THE PETROLOGY AND GEOLOGICAL SIGNIFICANCE OF SOME FAULT-GENERATED PSEUDOTACHYLYTES

by

Robert Huw Maddock

A thesis submitted for the degree of Doctor of Philosophy of the University of London

Department of Geology
Royal School of Mines
Imperial College
London SW7 2BP

June 1986

ABSTRACT

Different hypotheses for the origin of pseudotachylytes are examined with special emphasis on fault-generated pseudotachylytes. An origin for the latter by frictional fusion during co-seismic slip in dry upper crustal rocks proposed by Sibson (1975) is concurred with. The physical conditions and energetics of seismic faulting involving pseudotachylyte generation are considered. Frictional heating estimates for earthquakes, landslide and caldera-collapse 'faulting' are compared.

Field-studies of selected areas to the W of the Outer Hebrides Thrust are presented to illustrate the geological environment, geometry, style and chronology of pseudotachylyte faulting. Observed and inferred movement senses indicate broadly SE to NW-directed thrusting.

Pseudotachylytes from the Outer Hebrides, Gairloch and Tiree in Scotland, the Silvretta Nappe in the eastern Alps, Greenland, Guyana and the Vredefort Dome, S Africa have been examined in detail by optical and electron microscopy and by electron-microprobe analysis. A wide variety of textural and mineralogical types are distinguished. Textures resulting from primary crystallization from a melt are contrasted with those due to devitrification. The kinetics of these processes together with reactions involving partial melting and breakdown of included porphyroclasts indicate substantial disequilibrium behaviour. Various estimates of the physical conditions of pseudotachylyte generation are made from these data.

A critical examination of new whole-rock geochemical analyses, including trace elements, together with literature-reported analyses of pseudotachylytes is presented. For most pseudotachylytes these data indicate near-total, selective, preferential mechanical breakdown and fusion of hydrous ferromagnesian minerals together with some feldspar and quartz, followed by partial assimilation of remaining, largely quartz and feldspar porphyroclasts.

ACKNOWLEDGEMENTS

This project was made possible by a N.E.R.C. research studentship which is gratefully acknowledged. Drs Jack Nolan and Rick Sibson patiently supervised my studies in the field and at Imperial College. Other colleagues and friends, especially in the Structural and Mineralogy and Petrology sections at I.C., too numerous to name individually, greatly assisted in my understanding of pseudotachylytes as well as many other aspects of geology. Drs J. Grocott, M. van Nes and C. Passchier, who share my facination with pseudotachylytes, provided many hours of stimulating discussion. Prof H. Laubscher and Drs L. Masch, G. Park and H. Schmutz provided generous assistance in my field studies. The kindness of many people I met in the field, particularly in the Outer Hebrides, more than made up for some of wetter weather. More recently the encouragement of my present supervisor, Dr E.H. Rutter, and R. Holloway have brought this thesis closer to completion.

The technical and supervisory staff of cartography, photography, rock-cutting, rock-polishing, SEM, electron-microprobe and XRD gave freely of their services, advice and friendship. G. Briers, C. Leach and D. Johnston trained me in the use of transmission electron microscope facilities in the Department of Metallurgy at I.C. J. Glasser performed the C-H-N analyses in the Petroleum Geology section at I.C. C. Holloway and G. Davies assisted with typing. T. Ballard assisted greatly with photocopying and collation.

I am indebted to my parents and Sian whose material and other support made it possible to complete this thesis.

LIST OF CONTENTS

		Page
ABSTRACT		1
ACKNOWLEDGEMENTS		2
List of Contents		3
List of Figures		8
List of Plates		11
List of Tables		13
CHAPTER 1 INTRODUCTION		15
1.1 The Pseudotachylyte Problem		15
1.2 Scope of Thesis		15
1.3 Terminology and Origin of Pseudotachylytes		16
1.4 Types of Pseudotachylyte Occurrence		20
1.4.1	Fault-generated Pseudotachylytes	20
1.4.2	Landslide-generated Pseudotachylytes	21
1.4.3	Pseudotachylytes in Meteorites	21
1.4.4	Astrobleme Pseudotachylytes	22
1.4.5	Pseudotachylytes Associated with Igneous Activity	23
CHAPTER 2 THE MECHANICS AND ENERGETICS OF BRITTLE FAULTING WITH SPECIAL REFERENCE TO TEMPERATURE RISE		25
2.1 Basic Theorems		25
2.2 Earthquake Mechanisms		26
2.2.1	Earthquake Nucleation	30
2.2.2	Earthquake Termination	30
2.3 The Magnitude of Shear Stresses Acting on Faults		32
2.3.1	Direct Measurement of Shear Stress	34
2.3.2	Theoretical Estimates of Shear Stress	36
2.3.3	Seismological Estimates of Shear Stress	39
2.3.4	Geological Estimates of Shear Stress	41
2.3.5	Summary: Shear Stress and Pseudotachylyte Faulting	42
2.4 Energetics of Faulting		42
2.4.1	Gravitational Energy, E_g	43
2.4.2	Seismic Wave Energy, E_s	43

2.4.3 Shear Fracture Energy, E_c 45
2.4.4 Temperature Rise due to E_c 50
2.4.5 Frictional Energy, E_f 51
2.5 Frictional Shear Heating 51
2.5.1 Frictional Shear Heating Models 51
2.5.2 Effects of Fluids on Frictional Shear Heating 61
2.5.3 Experimental Observations on Frictional Shear Heating 62
2.5.4 Additional Effects of Frictional Shear Heating 66
2.6 Special Cases of Frictional Shear Heating 67
2.6.1 Caldera Collapse Faulting 67
2.6.2 Landslide Faulting 71
2.7 Aseismic Shear Heating 74

CHAPTER 3 CHARACTERIZATION OF FAULT-ROCKS AND THEIR FORMATION IN MAJOR FAULT ZONES OF CONTINENTAL CRUST 76

3.1 Introduction 76
3.2 Textures and microstructures of Fault-rocks: Deformation Mechanisms 78
3.2.1 Brittle Deformation and Cataclasis 78
3.2.2 Intracrystalline Plasticity: Dislocation Creep 79
3.2.3 Diffusive Mass Transfer 79
3.3 Textures and Microstructures of Fault-rocks: Classification 80
3.4 Distribution of Fault-rocks in Major Fault Zones 83
3.5 Fault-rock Mineralogy, Petrology and Geochemistry 84
3.6 A Conceptual Fault Zone Model 86
3.7 Terminology for the Field Description of Pseudotachylyte Veins 86

CHAPTER 4 FIELD STUDIES 91

4.1 Introduction 91
4.2 The Outer Hebrides Thrust 91
4.2.1 Background Geology of the Outer Hebrides 92
4.2.2 Background Thrust Geology 92
4.3 Greian Head, Barra 97
4.3.1 General Geology 97
4.3.2 Quasicomglomerate/Net-vein Complexes 99

4.3.3	Relationship of Quasiconglomerate to Lithology and structure	101
4.3.4	Injection Vein Arrays Associated with pseudotachylyte	101
4.3.5	Fault-Related Folding	104
4.3.6	Brittle Deformation Outside the Quasiconglomerate Zones	105
4.3.7	Imbrication and the Relation Between Different Types of Pseudotachylyte Faulting	110
4.3.8	Conclusions: Greian Head	118
4.4 Rubha Ardvule, South Uist		121
4.4.1	General Geology	121
4.4.2	Sub-Vertical Quasiconglomerate Complexes	121
4.4.3	Concordant and Sub-Horizontal Quasiconglomerate Complexes	126
4.4.4	Irregular Quasiconglomerate Zone	133
4.4.5	Microjointing	133
4.5 Field Studies: Conclusions		133
CHAPTER 5 PETROGRAPHY, MINERALOGY AND MICROSTRUCTURE OF PSEUDOTACHYLYTES		139
5.1 Introduction		139
5.2 Plagioclase Microlitic Pseudotachylytes		139
5.2.1	Description	139
5.2.2	Feldspar Chemistry	151
5.2.3	Interpretation of the Textures and Mineral Chemistry	159
5.2.4	Estimates of Temperature, Cooling Rate and Crystal Growth Rate	163
5.3 Amphibole Microlitic Pseudotachylyte		168
5.3.1	Sample SV15, Silvretta, Alps	169
5.3.2	Sample SA3, Vredefort Dome, South Africa	172
5.3.3	Interpretation and Discussion	172
5.4 Chlorite Spherulitic Pseudotachylytes		174
5.4.1	Sample GQ1A: Description	175
5.4.2	Sample GQ1A: Chemistry and STEM Analysis	177
5.4.3	Sample GQ1A: Interpretation	180
5.5 Pyroxene-Spherulitic Pseudotachylytes		181
5.5.1	Sample Series G80: Description	181

5.5.2 Sample Series G80: Vein and Mineral Chemistry 186
5.5.2 Sample Series G80: Interpretation 186
5.6 Phyllosilicate-spherulitic Pseudotachylytes 188
5.6.1 Sample SU802 188
5.6.2 Sample X 197
5.6.3 Sample G1B 200
5.6.4 Sample G1A 205
5.6.5 Sample GQ29 207
5.7 Flow-banded Pseudotachylytes 210
5.8 Porphyroclasts: Preamble 213
5.8.1 Quartz Porphyroclasts 213
5.8.2 Feldspar Porphyroclasts 216
5.8.3 Muscovite Porphyroclasts 220
5.8.4 Biotite Porphyroclasts 223
5.8.5 Amphibole Porphyroclasts 238
5.8.6 Accessory Phase Porphyroclasts 247
5.8.7 Lithic Porphyroclasts 251
5.9 Microjoints, Amygdales and Porphyroclast Replacement Pseudomorphs 264
5.9.1 Microjoints 264
5.9.2 Amygdaloidal Pseudotachylyte, Outer Hebrides 266
5.9.3 Amygdaloidal Pseudotachylyte, Ikertôq Shear Zone, Greenland 272
5.9.4 Porphyroclast Replacement Pseudomorph 276
5.9.5 Interpretation of Amygdales, Etc 277

CHAPTER 6 A CRITICAL INTERPRETATION OF PSEUDOTACHYLYTE WHOLE ROCK GEOCHEMISTRY 283

6.1 Preamble 283
6.2 Introduction 283
6.3 The Relative Volatile Content of Pseudotachylytes and Their Host-Rocks 286
6.4 The Oxidation State of Pseudotachylyte Rock and Melt 291
6.5 XRF Whole Rock Analyses: Comparative Geochemistry of Pseudotachylyte and Host-rocks 297
6.5.1 FV - Single Host-rock Relationships 298
6.5.2 IV - Single Host-rock Relationships 312
6.5.3 FV - IV - Multi Host-rock Relationships 313

6.6 EMP Analysis of Pseudotachylyte Matrix 323
6.6.1 Composition of Pseudotachylyte Matrix 324
6.7 A Model for Pseudotachylyte Melt Formation 333
6.7.1 Additional Considerations 336

CHAPTER 7 CONCLUSIONS 338

7.1 Conclusions 338
7.2 Suggestions for Future Research 339

LIST OF REFERENCES 340

APPENDICES 363
A1 Radiometric age dating of pseudotachylytes 363
A2 Analytical Techniques 366
A3 Mineral Analyses (EMP and STEM) 378
A4 Whole Rock Analyses (XRF) 413
A5 FeO Determinations 421
A6 Sample Localities 422

ENCLOSURES
Back Pocket
Map 1 Geological Map of the Outer Hebrides
Map 2 Geological Map of Greian Head, Barra
Map 2a Sketch Geological Section, Greian Head, Barra
Map 2b Sketch Geological Cross Sections, Greian Head, Barra
Map 3 Geological Map of Rubha Ardvule, South Uist
Map 4 Quasi-Conglomerate Zone, Rubha Ardvule, South Uist
Bound In
"Melt origin of pseudotachylytes demonstrated by textures" (reprint)
"Frictional melting in landslide-generated frictionites (hyalomylonites) and fault-generated pseudotachylytes - Discussion" (preprint)
"Partial melting of lithic porphyroclasts in fault-generated pseudotachylytes" (preprint)
"Vesicles, amygdales and similar structures in fault-generated pseudotachylytes" (MS accepted for publication)

List of Figures

2.1 Elastic rebound model for earthquakes 27
2.2 Stick slip behaviour 27
2.3 Seismic source parameters 29
2.4 Rupture arrest mechanisms 33
2.5 Stress cycle During Earthquake Faulting 35
2.6 Shear stress vs. depth projection 38
2.7 Single and multi strand fault models 40
2.8 Energy budget of faulting 44
2.9 Modes of fracture 46
2.10 Shear fracture energy 49
2.11 Plot of shear heating rate vs. time 53
2.12 Frictional heating models 54
2.13 Frictional heating model results 57
2.14 Effect of fault thickness on frictional heating 59
2.15 Plot of kinetic shear resistance vs. slip rate 60

3.1 Flow diagram for construction of a conceptual fault model 77
3.2 Fault-rock classification after Sibson (1977b) 81
3.3 Fault-rock classification after Obee (1985) 82
3.4 Conceptual fault zone model after Sibson (1983) 87
3.5 Terminology for description of pseudotachylyte veins 88

4.1 Tectonic setting of the Outer Hebrides Thrust 93
4.2 Stereoplot of minor fold axes, Greian Head 100
4.3 Pseudotachylyte-filled vein array, Greian Head 102
4.4 Stereoplot of 'single jerk' FVs, Greian Head 106
4.5 Conjugate FV system, Tangaval 109
4.6 Stereoplot of minor structures, Greian Head 113
4.7 Sketches of structures at Rubha Ardvule 124
4.8 Stereoplot of pseudotachylyte pavements, Rubha Ardvule 125
4.9 Pseudotachylyte-filled vein array, Rubha Ardvule 131
4.10 Microjoint orientation data, Rubha Ardvule 135

5.1 AFM diagram of STEM analyses of matrix biotites 150

5.2 An-Ab-Or diagram for porphyroclast and microlite feldspars 153
5.3 FeO^{*} vs. mol.% An in plagioclase microlites 154
5.4 Model for diffusion-controlled crystal growth 161
5.5 Model for crystallization of plagioclase microlitic pseudotachylyte 167
5.6 Si vs. $Mg/(Mg+Fe^{2+})$ of amphibole microlites 171
5.7 AFM plot of STEM analyses of matrix chlorites 195
5.8 Octahedral site occupancy of host and porphyroclast muscovites 222
5.9 Al^{vi} vs. Ti^{vi} of host and porphyroclast biotites 227
5.10 $(Na + Ca)^{xii}$ vs. K^{xii} of host and porphyroclast biotites 229-230
5.11 Fe vs. Mg of host and porphyroclast biotites 232
5.12 Chemical variation between host, porphyroclast and melted biotite in sample B1 236
5.13 Si vs. $Mg/(Mg + Fe^{2+})$ of host and porphyroclast amphiboles 244
5.14 Al^{vi} vs $(Na + K)^{A}$ plot of host and porphyroclast amphiboles 246
5.15 Ca-pyroxene quadrilateral plot for host and porphyroclast pyroxenes 248
5.16 Beginning of dehydration melting in granitic and dioritic mixtures 261
5.17 Mineral chemistry of amygdale phases, sample R15 270
5.18 Aspect ratios of amygdales, sample 2070 274
5.19 Mineral chemistry of amygdale carbonates, sample 2070 275
5.20 Fluid pathways involved in healing of microfractures and amygdales 282

6.1 H_2O in pseudotachylyte vs. H_2O in host-rock 287
6.2 CO_2 in pseudotachylyte vs. CO_2 in host-rock 290
6.3 LOI of pseudotachylyte vs. LOI of host-rock 294
6.4 FeO/Fe_2O_3 of pseudotachylyte vs. FeO/Fe_2O_3 of host-rock 296
6.5 - 6.12 Plots showing normalized chemical compositions of pseudotachylytes and their host-rocks 300-307

6.13 Geometry of FV's in sample G1A 309
6.14 Field relationships of analyzed samples 315
6.15 and 6.16 Plots showing normalized chemical compositions of pseudotachylytes and their host-rocks 317-318
6.17 Plot showing normalized chemical composition of cataclasite and peridotitic host-rock, Ivrea Zone 320
6.18 (a) Qz - Ab - Or plot of pseudotachylyte matrix compositions 327
(b) An - Ab - Or plot 327
(c) A - F - M plot 328
6.19 Qz - Ab - Or plot of pseudotachylyte whole-rock and matrix compositions 329
6.20 (a) Qz - Ab - Or plot of pseudotachylyte matrix and host-rock compositions 331
(b) An - Ab - Or plot 331
(c) A - F - M plot 332

A1.1 Rb-Sr isochron plot for OHT pseudotachylyte 364
A2.1 Relationship between BSE coefficient and atomic number 369

List of Plates

4.1 Quasiconglomerate and IV array, Greian Head 103
4.2 Discordant single jerk FVs, Greian Head 108
4.3 Minor structures in E-W section, Greian Head 111
4.4 N-S outcrop, Greian Head 115
4.5 N-S outcrop, Greian Head 116
4.6 N-S outcrop, Greian Head 117
4.7 Sub-vertical quasiconglomerate, Rubha Ardvule 122
4.8 Flat-lying quasiconglomerate, Rubha Ardvule 127
4.9 Irregular quasiconglomerate, Rubha Ardvule 129
4.10 IV array, Rubha Ardvule 130
4.11 Jointing of pseudotachylyte pavement, Rubha Ardvule 136

5.1 Plagioclase microlitic pseudotachylyte 143
5.2 Plagioclase microlitic pseudotachylyte detail 145
5.3 Zoned, skeletal plagioclase microlite 146
5.4 TEM detail of plagioclase microlitic pseudotachylyte 148
5.5 TEM detail of plagioclase microlitic pseudotachylyte 149
5.6 Amphibole microlitic pseudotachylyte 170
5.7 Chlorite spherulitic pseudotachylyte, sample GQ1A 176
5.8 TEM of chlorite spherulitic pseudotachylyte, sample GQ1A 179
5.9 Pyroxene-spherulitic pseudotachylyte, sample series G80 185
5.10 Phyllosilicate-spherulitic pseudotachylyte, sample SU802 189
5.11 TEM of phyllosilicate-spherulitic pseudotachylyte, sample SU802 193
5.12 TEM of phyllosilicate-spherulitic pseudotachylyte, sample SU802 196
5.13 TEM of phyllosilicate-spherulitic pseudotachylyte, sample X 198
5.14 TEM detail of phyllosilicate-spherulitic pseudotachylyte, sample X 199
5.15 Phyllosilicate-spherulitic pseudotachylyte, sample G1B 201
5.16 Phyllosilicate-spherulitic pseudotachylyte, sample

G1A 206
5.17 Flow-banded pseudotachylyte, sample B1 211
5.18 Quartz porphyroclast microstructures 215
5.19 Feldspar and biotite porphyroclast microstructures 218
5.20 Accessory phase porphyroclasts 250
5.21 Partially melted lithic porphyroclast, sample G804 253
5.22 Partially melted lithic porphyroclast, sample G1A 256
5.23 Healed microfractures 265
5.24 Amygdales, sample R15 267
5.25 Amygdales, sample 2070 and porphyroclast replacement pseudomorph, sample GQ34 273
5.26 Vesicular frictionite, sample 11256 278

List of Tables

2.1	Seismic source parameters	31
2.2	Fracture energy	47
2.3	Constants for frictional heating calculations	56
2.4	Experimental observations of Friedman et al (1974)	64
2.5	Comparison of source parameters for earthquake, caldera collapse and landslide faulting	68
2.6	Source characteristics of Fernandina caldera collapse	70
2.7	Source parameters for large landslides	72
4.1	Evolution of the Lewisian Gneiss Complex	94
4.2	Laxfordian fold phases in the Outer Hebrides	95
4.3	Deformation of the Outer Hebrides Thrust	98
4.4	Evolution of pseudotachylyte faulting, Greian Head, Barra	119
5.1	Classification of pseudotachylyte types	140
5.2	Crystal habit terminology	141
5.3	Feldspar characteristics in plagioclase microlitic pseudotachylytes	142
5.4	Microprobe analyses, plagioclase microlitic pseudotachylytes	156
5.5	Statistics of Fe site occupancy in plagioclase	158
5.6	XRF and microprobe analyses, sample GQ1A	178
5.7	Modal analyses, sample series G80	182
5.8	XRF and microprobe analyses, sample series G80	183
5.9	Microprobe and STEM analyses, sample series G80	184
5.10	XRF and microprobe analyses, sample SU802	192
5.11	Microprobe analyses, sample G1B	203
5.12	XRF and microprobe analyses, sample G1A	208
5.13	Microprobe analyses, sample GQ29	209
5.14	Microprobe analyses, sample B1	212
5.15	Characteristics of xenoliths in buchites	225
5.16	Amphibole stoichiometry limits	240
5.17	Microprobe analyses of lithic porphyroclast, sample G804	254

5.18 Modal analysis, sample G1A 257
5.19 Microprobe analyses of lithic porphyroclast, sample G1A 258
5.20 Modal data for sample G804 and melting experiment of Winkler (1967) 262
5.21 Amygdale and porphyroclast replacement mineralogy 268
5.22 Literature data for amygdaloidal pseudotachylytes 279

6.1 Volatile and LOI content of pseudotachylytes and host-rocks 292
6.2 Mixing model results for sample QD17 322
6.3 Normative compositions of pseudotachylyte matrix analyzed by EMP. 325
6.4 Normative compositions of Outer Hebrides biotite and amphibole 325

A2.1 Microprobe standards data 367
A2.2 STEM test analysis of quartz 370
A2.3 XRF whole rock analytical precision data 373
A2.4 XRF trace element detection limits and average relative errors 374
A2.5 ICP and AA trace element average relative errors 375
A2.6 Comparison of XRF, ICP and AA trace element analysis 376
A2.7 Standard FeO determination precision 377
A2.8 Sample FeO determination precision 377

CHAPTER 1 INTRODUCTION

1.1 The Pseudotachylyte Problem

Pseudotachylyte has been described, by igneous and metamorphic petrologists as well as structural geologists, from every continent in the world. The term pseudotachylyte has been applied to veinlets of dark, fine grained rock showing an intrusive habit found in major fault zones, around igneous intrusions, in meteorite impact scars (astroblemes), in meteorites themselves, and along the sole planes of landslides. However, a comprehensive review of the literature reveals that pseudotachylytes have most commonly been described from major fault zones cutting quartzofeldspathic crust - these may be termed fault-generated pseudotachylytes and form the subject matter of the greater part of this thesis.

In the same way that the origin and indeed the very defnition of mylonite has taxed geologists since the inception of that term (Lapworth, 1885) to the present day (Tullis et al., 1982), so pseudotachylytes present similar problems. The enigma of pseudotachylytes has centred largely on 3 questions: was the rock ever in a molten state? If so, by what mechanism did it become fused? What is the relationship between shear displacements and the generation of pseudotachylyte? Attempts to answer these questions have been vexed in part by the problems of studying such fine grained rocks and in part by problems over terminology. A consensus but by no means universally accepted view has now emerged that fault-generated pseudotachylytes are formed by frictional melting during seismic faulting, i.e. earthquakes (e.g. Sibson, 1975).

1.2 Scope of Thesis

Following a review of the terminology, origin and occurrence of various types of pseudotachylyte in this chapter, attention is given to the mechanics and energetics of seismic faulting in chapter 2. Power dissipation and frictional heating estimates for earthquake, landslide and caldera collapse 'faulting' are compared. In chapter 3 modern conceptual models for fault zones are briefly considered. Chapter 4 is devoted to field studies in the Outer Hebrides with emphasis laid on the small-scale geometry of fault-generated

pseudotachylytes. In chapter 5, the petrography (electron and optical), mineral chemistry and microstructure of pseudotachylytes are examined in detail; particular attention is given to kinetic aspects of melting and crystallization in pseudotachylytes. The 'whole-rock' chemistry of pseudotachylytes and their host-rocks is considered in chapter 6 and the usefulness of such data is critically assessed. Conclusions are summarized in chapter 7.

1.3 Terminology and Origin of Pseudotachylytes

Igneous and metamorphic rocks can be defined uniquely by reference to chemical and mineralogical criteria together with a type locality. The former criteria can only be used to define fault-rocks in exceptional cases, for example the micaceous phyllonites, because faults and shear zones may form in all rock types and at all metamorphic grades. Deformation mechanisms and degrees of metasomatism may vary greatly from one part of a fault zone to another, resulting in radically different fault rock chemistry, mineralogy and texture. The use of a type locality is implicit in many fault rock classification schemes simply because they were based on study of a single area. The pitfalls of this approach (which are especially pertinent to pseudotachylytes) were pointed out as long ago as 1935 by Waters and Cambell, but it is only recently that more broadly based schemes of classification have been published. Modern fault-rock classification uses a more mechanistic approach which is derived from an improved understanding of both microstructural and crustal scale deformation mechanisms. This will be discussed briefly in chapter 3.

The name pseudotachylyte was first appended to black, cherty/aphanitic rocks occurring in ramifying veinlets in the Old Granite of the Vredefort Dome structure, South Africa, by Shand (1916). Shand (1914) had originally believed that the veinlets were derived from an underlying body of basic magma, but in his later paper compared the Vredefort pseudotachylytes with mylonites and flinty crush-rocks from various localities. Shand (1916) categorically states that the pseudotachylytes were formed by melting of the granite attributable to mechanical processes, but he was unsure of the mechanism - favouring shock or gas-fluxing over frictional fusion because of the general absence of shear displacements associated with the veinlets. Indeed, he considered the term flinty-crush begged the question over their origin. Shand (1916) also suggested that the

pseudotachylyte might be related to earthquake processes.

The first recorded description of such rocks dates back almost a century earlier to Maculloch's (1819) "A description of the Western Isles of Scotland", in which Maculloch misidentified pseudotachylyte as veins of trap-rock. These fault-rocks associated with the Outer Hebrides Thrust were later recognized as flinty crush-rocks or pseudotachylyte (Jehu and Craig, 1923; Dougall, 1928; Kursten, 1957; Coward, 1969; Francis, 1969; Sibson, 1975).

Similar "trap-shotten" gneisses were described from Madras Province, India (King and Foote, 1864) and later described as "...mylonite (which is outwardly so tachylytic in appearance) ...probably the result of the heat produced during violent brecciation of the rock by which a temperature sufficient to frit the mylonite, but insufficient to melt the rock, was produced" (Holland, 1900, p.201). These rocks too have subsequently been recognized as pseudotachylytes (Pichamuthu, 1959).

The term "flinty crush-rock" seems to have emerged from Clough's (1888) description of "...hard fine-grained hornstone-like rock arranged in irregular streaks..." (ibid, p.23) in and around the Cheviot granite. Later workers found much of this flinty crush-rock was similar to mylonite (Carruthers et al., 1932). Because of the extremely fine-grained, flinty appearance of pseudotachylyte, ultracataclasite and ultramylonite they can be virtually indistinguishable in the field and the term flinty crush-rock has probably embraced all these rock types at one time or another.

A number of additional terms have been used more or less synonymously with pseudotachylyte or flinty crush-rock, particularly by European geologists: puree parfait (Termier and Broussac, 1911); gang mylonite or dyke mylonite (Hammer, 1914); pseudo-eruptive breccia (Bearth, 1933); and friksjonglass (Goldschmidt, 1941).

The problem of 'pigeon-holing' pseudotachylytes is exemplified in early fault-rock classifications. For example, Knopf (1931) relegated pseudotachylytes (together with trap-shotten gneiss and flinty crush-rock) to an appendix under the general heading of "rocks which have undergone mylonitization". The classification of Waters and Cambell (1935) is a more complete and useful scheme which attempts to include a mechanistic content. Following discussion of the original usage of the terms, and specifically whether or not shearing was observed, they classified pseudotachylyte and some flinty crush-rocks as cataclastic rocks whose temperature during deformation was high

enough to cause partial or complete fusion. It is implicit in their classification (Waters and Cambell, 1935, Table 1, p.480) that they consider this to have arisen from an increase in pressure and temperature related to depth.

In 1953 Scott and Drever described cryptomylonite and glassy hyalomylonite believed to have formed by frictional fusion along a thrust fault in the Langtang valley, Nepal. Subsequent work has shown that the 'fault' is in fact a landslide (section 1.4.2).

Reynolds (1954) applied her fluidization model to the origin of pseudotachylytes, specifically the Vredefort examples. Thus she believed that Shand's (1916) hypothesis of gas-fluxing was confirmed by her studies. The chief objection against this proposal is the lack of evidence for an abundant gas phase associated with the pseudotachylytes (cf. Francis, 1972).

Christie (1960) in his review of fault-rock terminology proposed that the term pseudotachylyte should be restricted to rocks not associated with mylonitization or shearing, preferring the term flinty crush-rock for these cases. Thus he conformed to the usage of Shand (1916) and following Reynolds' (1954) work, restricted the useage of pseudotachylyte to rocks formed by fluidization. Christie (1960) did not commit himself as to whether pseudotachylyte or flinty crush-rock were ever fused. Young (1967) describing ultra-fine grained intrusive fault-rocks from the Alpine Fault zone, New Zealand, which he acknowledged may have been molten used the term ultramylonite (Staub, 1915) - because of Christie's (1960) 'diktat'.

Describing pseudotachylytes from the Gairloch district of NW Scotland, Park (1961) presented convincing petrographic evidence for melting and suggested that pseudotachylytes form at considerable depth in crust of elevated temperature.

Because of doubts concerning the paragenesis of the 'type' (Vredefort) pseudotachylyte, Spry (1969) was wary of the name, but sensibly rejected the term hyalomylonite (Scott and Drever, 1953) because of its genetic conotations. In particular, he questioned the transition mylonite → pseudotachylyte favoured by some authors (e.g. Clough et al., 1909; Scott and Drever, 1953; Park, 1961; Bisschoff, 1962)

The first comprehensive review of the origin and occurrence of pseudotachylyte was presented by Philpotts (1964). He concluded that pseudotachylytes formed by frictional fusion could be distinguished from similar looking rocks of purely cataclastic origin, by the

presence of glass, vesicles and/or high temperature feldspar microlites. Philpotts believed pseudoatachylytes formed in the presence of an abundant gas phase, in rocks already elevated in temperature prior to frictional fusion during faulting. He also believed that pseudotachylyte and mylonite could not form contemporaneously.

Higgins' (1971) extensive and beautifully illustrated review of cataclastic rocks (a term he used to encompass all fault-rock types) unfortunately adds little to understanding the pseudotachylyte problem. He concurred with Philpotts' (1964) view that pseudotachylytes form by frictional fusion of already hot rocks, but differed in suggesting that every gradation exists between cataclasite or mylonite and pseudotachylyte. He therefore excluded pseudotachylyte from his classification preferring to use 'pseudotachylitic' as a prefix modifier. Higgins (1971) also made the sensible suggestion that flinty crush-rock should be restricted in its usage, only as a field term.

Francis (1972) provided the second review of the origin of pseudotachylytes. He pointed out that such rocks are probably much more abundant than initially realised - in part because of the confusion over terminology - and believed that they formed by high strain-rate faulting within intact crystalline rocks. In addition to frictional fusion, he postulated that glass found in some pseudotachylytes might be a product of shock-melting.

Sibson (1975) in discussion of fault-rocks from the Outer Hebrides Thrust Zone, NW Scotland, also believed that pseudotachylytes formed by frictional fusion. However, in contrast to Park (1961), Philpotts (1964) and Higgins (1971), mechanical considerations led Sibson to suggest that pseudotachylyte only forms in comparatively cold, dry crystalline rock and that it forms by frictional fusion during seismic shear displacements (i.e. earthquakes). Following this interpretation, Sibson (1977b) classified pseudotachylyes as random fabric, cohesive fault-rocks with a glassy or devitrified matrix.

Sibson's seismic frictional fusion hypothesis has now gained widespread but not universal acceptance (e.g. Allen, 1979; Watts and Williams, 1980; Jegouzo, 1980; Grocott, 1981; Passchier, 1982a, 1982b). Objections have been raised based principally on petrographic and petrologic interpretations by Wenk (1978), Wenk and Weiss (1982) and Masch et al (1985) who prefer an origin by brittle fracture, cataclasis and tensile fracture spallation. These interpretations have

been disputed however by Maddock (1986a). Macaudiere and Brown (1982) have postulated that crack tip energy dissipation may contribute significantly, in addition to frictional heat generation, to the temperature rise required for fusion.

The preferred definition of fault-generated pseudotachylyte in this study is simply a fault-rock which has cooled from a melt. Petrographic criteria supporting this definition are described in detail in chapter 5. To put the question of terminology in context, a quote from a report of a recent Penrose Conference on mylonites is presented (Tullis et al., 1982, p.230):-

> "...it is especially important for people to describe in some detail the textures (and inferred deformation mechanisms and conditions) that are observed in rocks {that they call mylonites}. As {structural} geologists, we are interested in the processes and conditions of deformation; we need to determine criteria for the recognition of faults and shear zones, rather than arguing about terminology".

The processes and conditions of deformation, particularly the nature of the melting process by which pseudotachylytes are formed are examined in detail in this thesis.

1.4 Types of Pseudotachylyte Occurrence

It is apparent from the previous section that the name pseudotachylyte has been applied to rocks of similar appearance and habit found in a variety of tectonic environments and perhaps generated by more than one mechanism.

1.4.1 Fault-generated Pseudotachylytes

Fault-generated pseudotachylytes have now been recognized in a large number of fault zones; they range in age from perhaps as young as 0.4 Ma along the Alpine Fault Zone, New Zealand (R.H. Sibson, pers. comm., 1982) to Precambrian (e.g. Philpotts, 1964). Fault-generated pseudotachylytes are almost invariably found in quartzofeldspathic crust, commonly in association with mylonites (and cataclasites) which the former usually postdate. Fault zones containing pseudotachylyte

generally have a large component of reverse slip, although in some cases only strike slip can be determined.

1.4.2 Landslide-generated Pseudotachylytes

Two important occurrences of 'pseudotachylyte' have recently been recognized as the product of frictional melting on the sole planes of landslides.

In the Öetztal valley of the Austrian Alps, the Köfels bimmstein (literally pumice-rock) and the associated Maurach (meaning fragmented massif) have long puzzled geologists. The bimmstein was recognized early on as having cooled from a melt and various origins were proposed: volcanic eruption (Pichler, 1863); melting due to forest fires (Heissel, 1938); and meteorite impact (Suess, 1937; Ampferer, 1937). Ampferer (1939) first proposed that the Maurach was a landslide block and Preuss (1971) suggested that the bimmstein formed by frictional melting. Subsequent geomorphological mapping and dynamic modelling have confirmed this hypothesis (Erismann et al., 1977).

The Himalayan Langtang valley pseudotachylyte (cryptomylonite and hyalomylonite of Scott and Drever, 1953) has also been demonstrated to be the product of frictional melting along a landslide surface (Masch and Preuss, 1977; Masch, 1979).

These two examples are important because they represent virtually the only truly glassy 'pseudotachylytes' demonstrably generated by frictional fusion so far described (Masch et al., 1985; but cf. Sibson et al., 1981). The name frictionite (Erismann, 1977) is preferable for such rocks.

Voight and Faust (1982) have postulated that landslide-generated frictionites may in fact be quite common in large, dry landslides with catastrophic rates of descent and cite 3 possible examples (section 2.6.2).

Further consideration of the energetics of landslides is given in chapter 2.

1.4.3 Pseudotachylytes in Meteorites

Many chondritic meteorites are traversed by minute black veinlets, some of which show evidence of shearing in addition to melting. Lacroix (1926) compared glassy veins in chondrites from Upper Volta and Argentina with pseudotachylytes from the Vredefort Dome and

the Outer Hebrides Thrust. He concluded that there were many similarities and that in both cases, fusion had resulted from "...l'exageration locale d'actions mecaniques..." (ibid., p.1584).

In 1940 Barnes published a comparative study of vein material (which he called pseudotachylyte) from 2 North American chondrites with Vredefort Dome samples and pseudotachylytes and mylonites and pseudotachylytes from Texas. Barnes considered meteorite pseudotachylytes and mylonites to have formed by crushing and shearing. Unfortunately Barnes' usage of the term pseudotachylyte - synonymously with mylonite - is particularly confusing, and he misunderstood Shand's (1916) original definition of pseudotachylyte.

Recent studies have shown that the majority of veinlets in meteorites contain high pressure mineral polymorphs (e.g. ringwoodite after olivine) indicating that the veins are shock-produced during extra terrestrial collisions (e.g. Price et al., 1979). Transmission electron microscopy (TEM) studies have also shown that many supposedly glassy veins are actually cryptocrystalline, with a grain size <2 um (Price et al., ibid.).

1.4.4 Astrobleme Pseudotachylytes

Glassy and pseudotachylyte-like rocks are found in association with many meteorite impact structures or astroblemes. In unequivocal astroblemes, such as the Ries Crater, Germany and Meteor Crater, Arizona, glassy rocks can be shown by the presence of high-P mineral polymorphs and certain deformation microstructures to have formed by shock melting (Kieffer et al., 1976).

A larger number of less well-characterized structures, also associated with pseudotachylyte-like rocks, are the subject of vigorous argument. Controversy centres over the interpretation of characteristic macro- and microstructures and the significance of high-P mineral polymorphs. Taking the Vredefort dome structure as a particularly pertinent example, two schools of thought have emerged: the first favours an exogenic origin (i.e. meteorite impact) propounded by Daly (1947) and Dietz (1961); the second favours an endogenic origin ('cryptoexplosion'), the case for which has chiefly been argued by Nicolaysen (1972, and later papers) and co-workers. (The presence of high-P SiO_2 polymorphs, coesite, stishovite and possibly diaplectic glass (Martini, 1979), would seem to be compelling evidence for the former origin.) The controversy is relevant to

fault-generated pseudotachylytes for 3 reasons. First, this is Shand's (1916) type locality for pseudotachylyte. Secondly, many textural and mineralogical similarities exist between fault-generated pseudotachylytes and fine grained meteorite impact/cryptoexplosion rocks suggesting similarities in deformation mechanisms and melting/cooling regimes. Thirdly, it is far from clear that all meteorite impact/cryptoexplosion rocks are generated by diaplectic (shock) melting per se; many may be related to shear displacement during or immediately after the cataclysmic event.

A sample of Vredefort Dome pseudotachylyte is described in chapter 5.

1.4.5 Pseudotachylytes Associated with Igneous Activity

Fault-rocks including flinty crush-rocks are frequently found in and around the margins of igneous intrusions, ranging from batholith dimensions to small fault or ring dyke intrusions. Fault-rocks developed in the intrusive lithology and directly related to the intrusion process have been termed protoclastic (Higgins, 1971). A classic example is the protoclastic marginal facies of the Colville Batholith, Washington U.S.A. (Waters and Krauskopf, 1941). Waters and Krauskopf (ibid, p. 1406) described a thick marginal zone of mylonitic gneiss with "...thin bands of lustrous material approaching pseudotachylyte..." which they considered to have formed during the final stages of the intrusion of a nearly solid batholith. (Note: Reynolds (1954) proposed an alternative hypothesis of intrusion by fluidization to account for these phenomena.) Perhaps descriptions of this type lead to the later idea that pseudotachylyte formed at depth in rocks of elevated temperature (cf. Park, 1961; Philpotts, 1964; Higgins, 1971).

Flinty crush-rocks have been described from most of the British Tertiary Volcanic Province igneous centres as well as a number of Caledonian intrusions. The most celebrated example is the flinty crush-rock associated with the Lower Old Red Sandstone age Glen Coe cauldron subsidence. Bailey and co-workers in a series of publications (Clough et al., 1909; Bailey and Maufe, 1916; Bailey, 1960) have described the flinty crush-rock in detail. They believed that the flinty crush-rock was formed by shearing of various country rocks, during faulting associated with igneous activity but not directly related to intrusion. Roberts (1966) on the other hand, believed that

the flinty crush-rock and the fault intrusion were emplaced together as a fluidized system.

Re-examination of these flinty crush-rocks using modern electron optical techniques might prove to be a fertile line of future research.

A model demonstrating that it is theoretically possible to generate pseudotachylyte by frictional fusion during caldera subsidence is presented in chapter 2.

CHAPTER 2 THE MECHANICS AND ENERGETICS OF BRITTLE FAULTING WITH SPECIAL REFERENCE TO TEMPERATURE RISE

2.1 Basic Theorems

This chapter is concerned with the mechanics and partitioning of energy during friction-controlled faulting in the upper crust ($Z < 15$ km) in an attempt to assess those factors which may be conducive to the formation of fault-generated pseudotachylytes. Certain basic theorems are fundamental to this discussion (they are described in most structural geology text books and reviewed in more detail by Sibson (1977b) and Moore (1980), so additional references will not be given). In a stress field with principal stresses $\sigma_1 > \sigma_2 > \sigma_3$:-

1) Brittle failure of intact homogeneous rocks may be described by the Mohr-Coulomb failure criterion, modified to include the effect of pore pressure:

$$\tau = C_o + \mu_i(\sigma_n - p) \qquad (2.1)$$

where τ = shear stress;
C_o = long term cohesive strength ($10 < C_o < 50$ MPa);
μ_i = coefficient of internal friction ($0.5 < \mu_i < 1.0$);
p = pore fluid pressure.
σ_n = normal stress

2) Frictional failure on existing fault planes is initiated when the applied shear stress is greater than the frictional resistance τ_f, given by:

$$\tau_f = C_o' + \mu_s(\sigma_n - p) \qquad (2.2)$$

where C_o' = cohesive strength of fault plane ($<C_o$);
μ_s = coefficient of internal friction ($0.5 < \mu i < 1.0$).

3) Acceleration continues so long as the applied shear stress exceeds the kinetic shear resistance, τ_k, where:

$$\tau_k = \mu_k(\sigma_n - p) \qquad (2.3)$$

where μ_k = coefficient of kinetic friction (usually $\mu_k < \mu_s$). Deceleration occurs once the applied shear stress is less than τ_k.

4) The pore fluid factor, λ_v, may be defined as the ratio of fluid to vertical overburden pressure, σ_v:

$$\lambda_v = p/\lambda_v = p/\rho gz \qquad (2.4)$$

where ρ = density;
g = acceleration due to gravity;
z = depth.

Or, alternatively λ_n may be defined as the ratio of fluid to normal pressure, σ_n:

$$\lambda_n = p/\sigma_n \qquad (2.5)$$

2.2 Earthquake Mechanisms

Earthquakes may be characterized according to hypocentral depth as deep, medium or shallow focus. In each case the earthquake results from a sudden or catastrophic mechanical instability causing radiation of seismic wave energy. The nature of the instabilities that nucleate medium and deep focus earthquakes is obscure but may be related to sudden phase changes (Benioff, 1964) or possibly shear melting (Griggs and Baker, 1969); medium and deep focus earthquakes will not be considered further. Here we are concerned only with shallow, crustal earthquakes.

From a study of the 1906 San Francisco earthquake, Reid (1911) formulated his elastic rebound hypothesis, where shallow earthquakes are explained by the sudden release of stored elastic strain energy (Fig. 2.1). This theory is still widely accepted to explain mainshock earthquakes though it does not account for foreshock and aftershock activity.

In the last 25 years, studies in rock mechanics, particularly frictional sliding experiments, have led to the widespread acceptance of the "stick-slip" mechanism for earthquakes (e.g. Brace and Byerlee, 1966). This idea is essentially an extension of Reid's elastic rebound theory, with the important qualification that the stress drop during slip is less than the shear stress required to initiate slip (Fig.

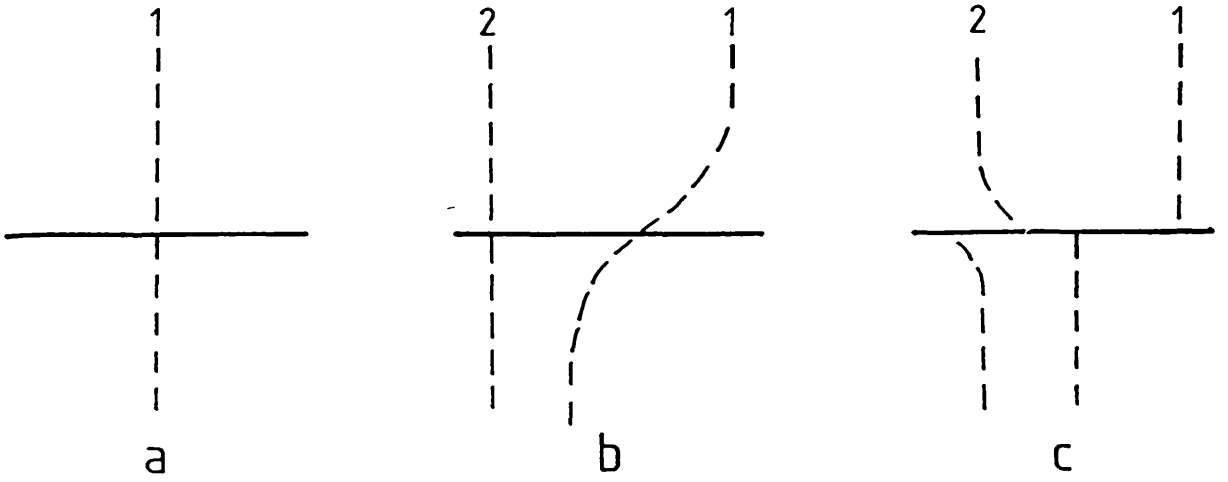


FIGURE 2.1 Schematic interpretation of Reid's elastic rebound hypothesis for earthquake faulting. (a) Survey line 1 (dashed) is made across the fault (F) at time t_0; (b) elastic strain energy accumulates during some time $t_1 - t_0$ causing distortion of the first survey line; (c) the stored elastic strain energy is released during an earthquake at time t_2 ($> t_1$) resulting in a finite displacement of the first survey line.

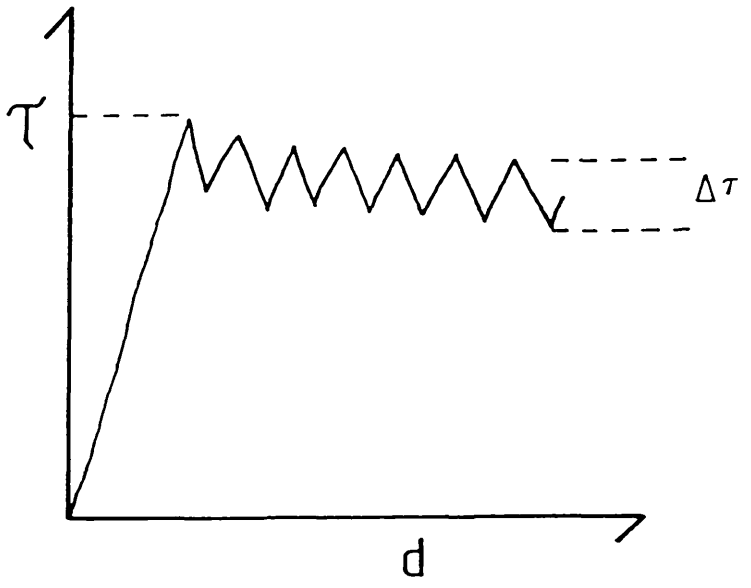


FIGURE 2.2 Plot showing relationship between shear stress (τ) and displacement (d) during stick-slip frictional sliding.

2.2). The stick-slip mechanism has been applied to earthquake faulting by numerous workers (see Paterson, 1978 for review). A number of parameters are found to influence the prevalence of stick-slip behaviour in the laboratory (reviewed by Paterson, 1978; Moore, 1980):-

(i) rock type;
(ii) pore fluid pressure;
(iii) confining pressure and normal stress;
(iv) temperature;
(v) displacement rate;
(vi) tribological characteristics of pre-cut (or pre-faulted) rock samples, including the presence or absence of gouge;
(vii) stiffness of the loading machine.

Summarizing the effects of the above factors, it is found that stick-slip is favoured by high modal quartz content, high normal stress and displacement rate and generally low temperatures. The influence of the other factors is more ambiguous (Paterson, 1978). In a natural fault zone, each of these factors may be expected to vary (non-independently) as functions of depth, time, slip and width across the fault zone, and from one fracture to another.

Earthquakes can be discussed and analyzed quantitatively by reference to various seismic source parameters. The following simple description of what is believed to happen during a single earthquake rupture should be read in conjunction with Fig. 2.3. A rupture nucleates at the focus (hypocentre) and propagates at close to the shear wave velocity (3 - 4 $km.s^{-1}$) over the rupture area, A = LW (defined in Fig. 2.3). For continental earthquakes the slip is < 10 m, and the slip rate is < 1 $m.s^{-1}$; the acceleration is generally less than 1g. At any one spot on the fault plane, slip is accomplished within the rise time of 0.5 - 10 s. The strains associated with earthquakes, measured as $\Delta\gamma = d/L$ are of the order of 10^{-4} - 10^{-5}. The size of an earthquake may be defined in terms of magnitude or seismic moment. Earthquake magnitude is determined from the amplitude of seismic waves at a given frequency within the seismic spectrum, and at a particular distance from the focus. Seismic moment, M_o, can be measured geologically (Aki, 1966):

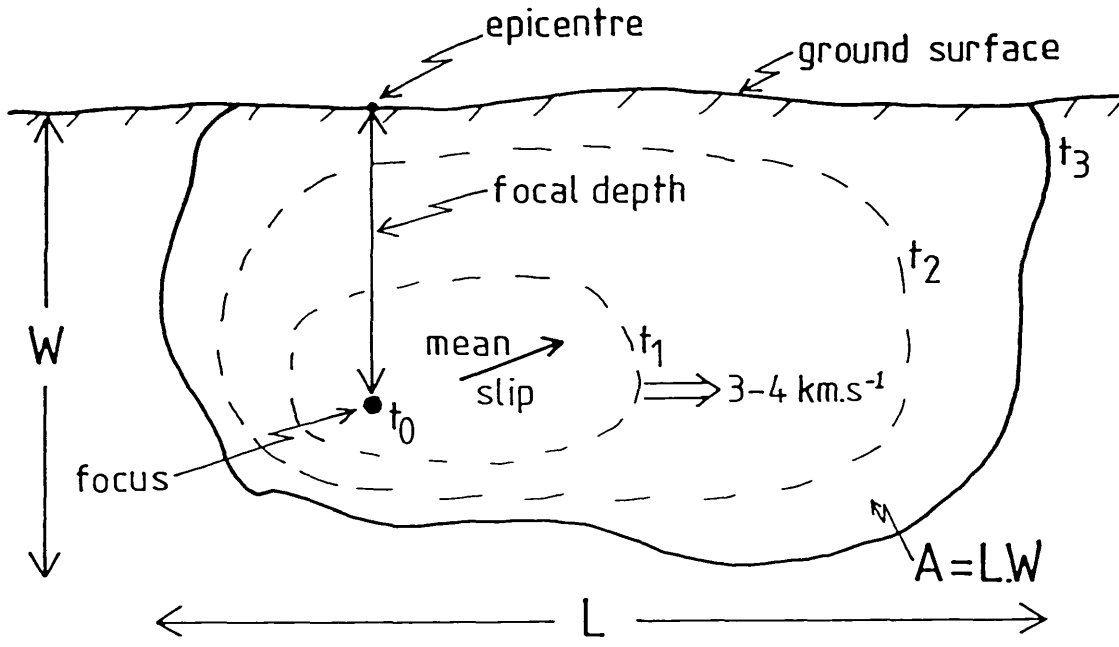


FIGURE 2.3 Schematic representation of a fault, with selected seismic source parameters indicated. Rupture nucleates at the focus at time t_0 and propagates at 3 - 4 km.s^{-1}. Note, rupture may or may not reach the ground surface and cause surface rupture (after Sibson, 1983, unpubl. data).

$$M_o = G.d.A = G.d.L.W \qquad \text{(dyne.cm)} \qquad (2.6)$$

where G = rigidity modulus

The measured values of some of these parameters for various historical earthquakes are shown in Table 2.1.

2.2.1 Earthquake Nucleation

Re-examining the Andersonian description (Anderson, 1951) of the principal stress field configuration for different types of faulting, Sibson (1974) found that the minimum level of shear stress required to overcome static friction and initiate slip on existing faults is in the ratio of 4:1.6:1 for thrust, wrench and normal faulting respectively, for a given depth and pore fluid pressure ratio (λ_v, eqn. 2.4). Defining the stored elastic strain energy per unit volume, E_d, as follows (Sibson, 1974):

$$E_d = \frac{\{(\sigma_1 - \sigma_3)^2(1 - k + k^2)\}}{6G} \qquad (2.7)$$

where G is the bulk modulus and $0 < k = (\sigma_2-\sigma_3)/(\sigma_1-\sigma_3) < 1$, E_d is in the ratio 16:2.56:1 for thrust, wrench and normal faults respectively, also at the same depth and pore fluid pressure ratio (λ_v). Clearly, the stress/strain energy conditions for the limiting types of faulting are very different. In chapter 1 it was noted that pseudotachylytes are most commonly associated with faults showing a major component of reverse slip; this suggests that pseudotachylyte may be formed during high stress faulting.

An alternative to the linear frictional failure approach is that of fracture mechanics to describe the nucleation of earthquakes. Using empirically derived expressions, Das and Scholz (1981) are able to explain many shallow earthquake phenomena. It is explicit in their model that fault planes are characterized by barriers (section 2.2.3) which necessitate high stress levels for continued rupture propagation.

2.2.2 Earthquake Termination

The cessation of fault rupture and slip propagation, in time and space, poses a trying seismological and geological question: how and

TABLE 2.1 COMPILATION OF EARTHQUAKE SOURCE DATA

Date	Location	Magnitude, M_S	Moment, M_o ($\times 10^{20}$ Nm)	Stress drop, $\Delta\tau$ (MPa)	Area, A ($\times 10^6 m^2$)	Displacement, d (m)	Rise time, t (S)	Fault Type
1/9/23	Kanto	8.2	8.5	-	91	2.1	7	T-S
27/3/27	Tango	7.75	0.46	-	460	3.0	6	S
2/3/33	Sanriku	8.3	43.0	-	18500	3.3	7	N
11/3/33	Long Beach	6.25	0.028	-	450	0.2	2	S
19/5/40	Imperial Valley	7.1	0.56	1.3	780	1.25	-	S
10/9/43	Tottori	7.4	0.36	-	430	2.50	3	S
28/6/48	Fukui	7.3	0.33	-	390	2.00	2	S
21/7/52	Kern County	7.7	2.0	-	1080	4.6	1	T-S
4/11/52	Kamchatka	8.25	350	-	42000	5.0	30	T
6/11/58	Etorufu, Kuriles	8.7	44	3.7	10500	8.4	-	T
13/10/63	Eruppa, Kuriles	8.1	67	1.2	30250	4.5	-	T
28/3/64	Alaska	8.4	820	1.8	130000	12.15	-	T
4/2/65	Rat Island	7.9	125	1.0	52000	4.8	-	T
27/6/66	Parkfield	6.4	0.03	0.4	370	6.0	0.7	T
13/2/67	Gibbs Fracture	6.5	-	-	600	1.6	7	S
9/4/68	Borrego Mountain	6.9	0.08	-	91	-	1.1	S
11/8/69	Shikotan, Kuriles	7.8	22	0.5	24150	1.8	-	T
9/9/69	Gifu	6.6	-	-	200	0.65	1	S
16/10/74	Gibbs Fracture	6.9	0.45	1.4	700	1.80	10	S
14/1/78	Izu-Oshima	6.8			170	1.85	2	S

Note: data from compilations of Kanamori and Anderson (1975), Kanamori (1977), Sibson (1978), Scholz (1982)
T = thrust dip slip, N = normal dip slip, S = strike slip.

why do faults terminate?

Dynamic models of earthquake mechanisms involve equations of motion which balance the energy flux into the crack tip with the energy absorbed by the newly-created surface area and other dissipative processes (e.g. Husseini et al., 1975; Richards, 1976; Das and Aki, 1977). Anticipating the form of these equations, it is clear that 2 types of 'arrest mechanism' are possible (Husseini et al, 1975). Either the shear fracture energy, E_c, increases along the trajectory of the running crack (Fig. 2.4a), or the available stress drop, $\Delta\tau$, decreases along the crack trajectory (Fig 2.4b). Both arrest mechanisms appear to be geologically realistic (e.g. Das and Scholz, 1981; Sykes, 1971), but the choice of a specific mechanism has important consequences for the estimation of the shear fracture energy (section 2.4.3) and the shear stress in fault zones (section 2.3).

The shear fracture energy arrest mechanism is the basis of barrier theory (Das and Aki, 1977). Fault plane (zone) barriers are expressed as obstacles of localized, high values of E_c. A geologically tenable example might be the passage of a rupture from a pre-existing fault, locked only by frictional traction, into virgin unfaulted rock. Structurally distinct, lithologically distinct or intrusive rock bodies may form such barriers in nature.

2.3 The Magnitude of Shear Stresses Acting on Faults

Some of the parameters which define an earthquake source are shown schematically in Fig. 2.3. In considering the generation of pseudotachylyte by fusion during seismic faulting, we are largely concerned with the equation for frictional heating energy, E_f, given by:

$$E_f = \tau_k . d . A \qquad (2.8)$$

where τ_k is the kinetic shear resistance, d is the displacement and A is the fault plane area. To estimate E_f we need to know the likely values of these earthquake source parameters; a collation of selected earthquake parameters has been given in Table 2.1. They are obtained in a variety of ways. Exceptionally, the scalar quantities of fault length, L, and displacement, d, may be measured directly if the rupture breaks surface; more commonly however, source parameters are derived from seismic data and empirical relationships (e.g. Kanamori

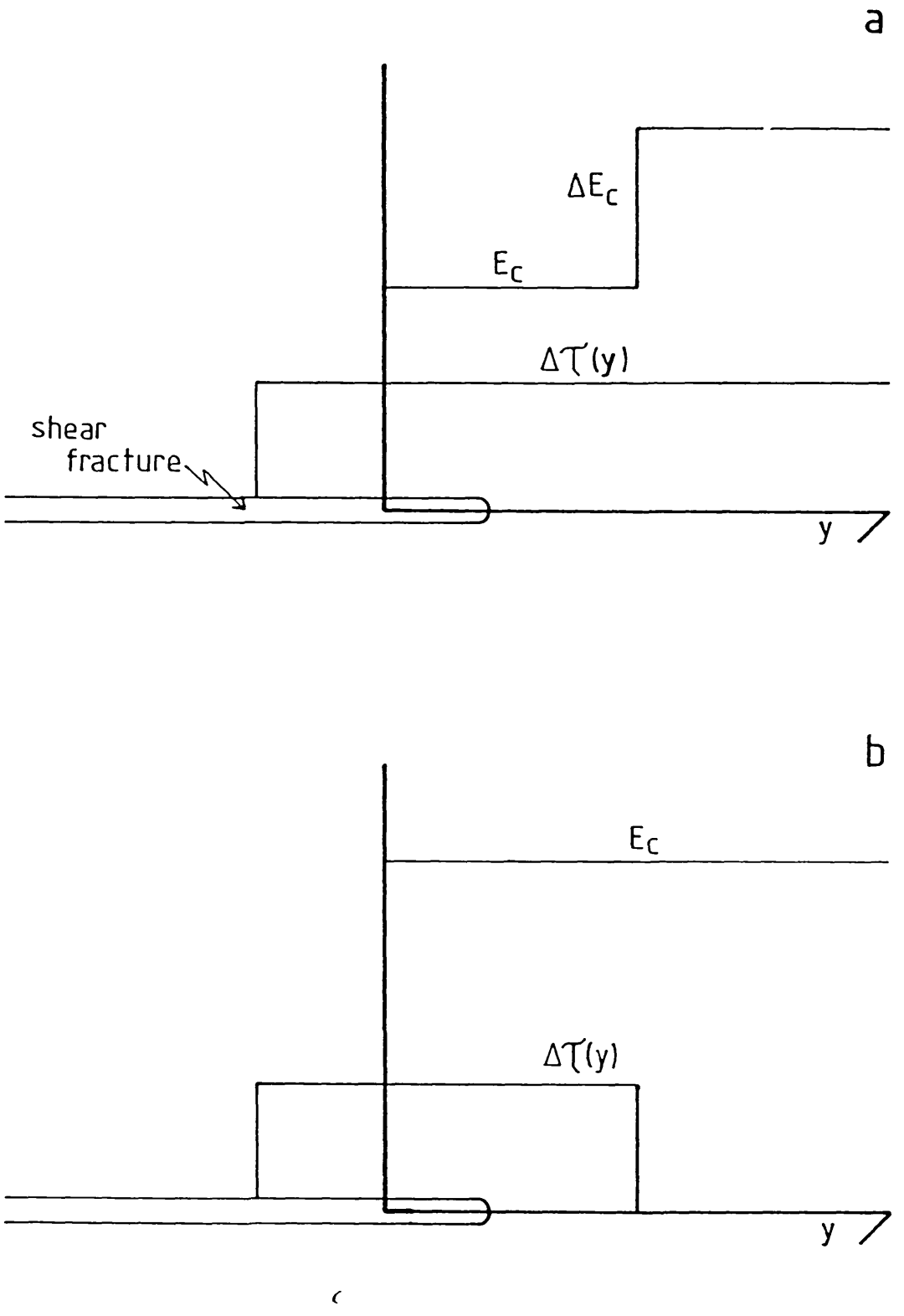


FIGURE 2.4 Propagating fracture termination mechanisms: (a) fracture energy (E_c) barrier; (b) stress drop barrier ($\Delta\tau$) (after Husseini et al., 1975).

and Anderson, 1975). An empirical relationship is used in section 2.6.1 to examine the possibility of frictional fusion during caldera collapse faulting.

The rise time, slip velocity and displacement during earthquake faulting are fairly well constrained by a large body of seismic and direct observations (Table 2.1).

One of the least well constrained parameters is the magnitude of the shear stress, τ, acting on faults. This is not a single quantity but varies during the earthquake process as a function of time and slip (Fig. 2.5). Obviously, from equation 2.8 we need to know the magnitude of the shear stress as accurately as possible in order to assess the energy available for frictional heating. Strictly speaking, we need to know the integrated value of the curve describing the kinetic shear resistance, τ_k, between t_1 and t_2 (the rise time of the earthquake) in Fig. 2.5:

$$\tau_k(t) = \int_{t = t_1}^{t = t_2} \tau_k \, dt \qquad (2.9)$$

What then is the magnitude of shear stresses acting on faults? A number of methods of estimating τ (described below) have led to estimates which vary by 1 or 2 orders of magnitude (see discussion by Hanks and Raleigh, 1982; Atkinson, 1982) even for the same data set. Proponents of high shear stresses acting on fault zones suggest $\tau >$ 100 MPa, and those of low stresses $1 < \tau < 10$ MPa.

2.3.1 Direct Measurment of τ

Greatest support for the high stress school of thought comes from compressive shear failure experiments on small rock samples. For a wide range of crystalline rocks the peak compressive shear strength is of the order of 100 - 200 MPa, increasing with increasing confining pressure (Paterson, 1978).

In situ shear stress measurements have been made to a depth of 4 km in hard rock of stable cratonic regions with the following significant observations (McGarr, 1980):-

(i) maximum shear stress increases linearly with depth;
(ii) maximum shear stress is greatest in compressional tectonic environments where σ_3 is near vertical, yielding a gradient of 8.7 $MPa.km^{-1}$;

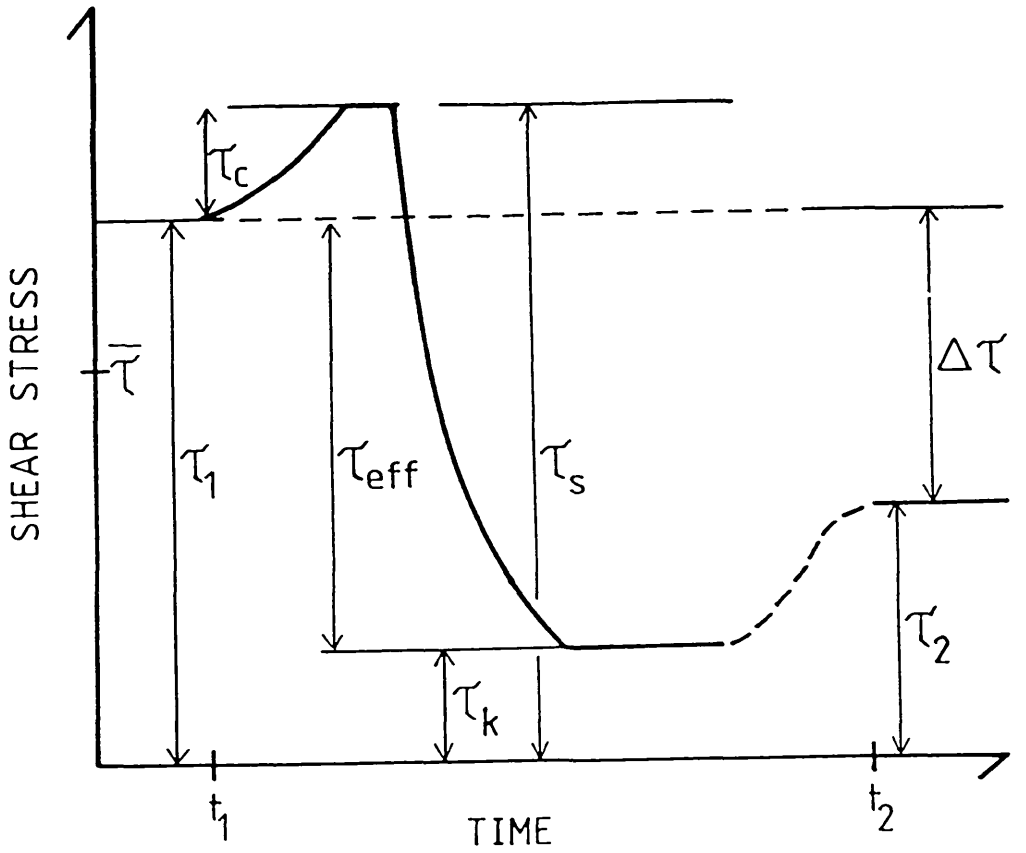


FIGURE 2.5 Stress cycle during earthquake faulting (modified from Yamashita, 1976; Kasahara, 1981).

$t_2 - t_1$: rise time of earthquake;

τ_1 : initial (static) shear stress;

τ_2 : final (static) shear stress;

τ_c : minimum incremental increase in shear stress required to overcome cohesion an static frictional shear resistance;

τ_s : static frictional shear stress;

$\Delta\tau = \tau_1 - \tau_2$: stress drop (static);

τ_k : kinetic shear stress or resistance;

$\tau_{eff} = \tau_1 - \tau_k$: effective stress (Brune, 1970) or accelerating stress;

$\frac{\Delta\tau}{\tau_1}$: fractional stress drop

$\bar{\tau} = \frac{\tau_1 + \tau_2}{2}$: mean shear stress;

$\Delta\tau/_k = \tau_1 - \tau_k$: dynamic stress drop.

(iii) maximum shear stress is least in extensional tectonic environments where σ_3 is horizontal, yielding a gradient of 6.69 $MPa.km^{-1}$.

The data of McGarr (1980) are extrapolated to a depth of 10 km in Fig. 2.6 for compressional (curve d) and extensional (curve e) tectonic environments. Note, these are minimum estimates of τ insofar as faulting did not occur immediately after measurement. It is not clear to what extent extrapolation of the curves, and thermal and cover-stripping effects vitiate inferred values of τ at depth. Nevertheless, the data would seem to support moderate to high stresses existing in the crust of the examined regions.

2.3.2 Theoretical Estimates of τ

From equation 2.8 the rate of frictional shear heating per unit area, $\dot{Q}$, on the fault plane may be expressed as:

$$\dot{Q} = \tau_k . v \qquad (2.10)$$

where τ_k and v are the time-averaged shear resistance and slip velocity respectively. Using this equation, with v constrained by plate tectonic data, Scholz et al (1979) have suggested that the rate of shear heating required to cause argon depletion against the Alpine Fault, New Zealand, implies a shear stress of 100 - 150 MPa (field 2, Fig. 2.6). Pseudotachylyte is fairly abundant along the Alpine Fault Zone (e.g. Wallace, 1978; Sibson et al., 1981).

In contrast, a comprehensive review of heat flow data for the San Andreas Fault (Lachenbruch and Sass, 1973; 1980) indicates a much lower shear stress magnitude at the same depth (field 1, Fig. 2.6). The nature of the overall San Andreas Fault zone heat flow anomaly (or lack of it!) has, however, been questioned (e.g. Scholz et al., 1979) and may yet allow shear stresses at least locally to 100 MPa (O'Neill and Hanks, 1980).

The theoretical estimates of τ required to initiate dry faulting, on pre-existing faults, determined by Sibson (1974) (section 2.2.1) are also shown in Fig. 2.6: curves a, b and c for thrust wrench and normal faulting respectively. The relationship between the magnitude of τ, depth and the mode of faulting is the same as for the in situ determinations. The values of τ derived by Sibson (1974) may

FIGURE 2.6 Plot of possible variation in shear stress (τ) with depth (z).

a, b, c : minimum values of shear stress required to initiate dry frictional sliding for thrust, wrench and normal faulting respectively, assuming μ_s = 0.75 (after Sibson, 1974);

d, e : variation in shear stress with depth for compressional and extensional tectonic regimes respectively, measured in-situ to a depth of 3.5 km and extrapolated to 10 km (after McGarr, 1980);

f, g : minimum and maximum seismological estimates of shear stress (see section 2.3.3 for references);

1 : estimate of shear stress acting on San Andreas Fault zone based on heat flow measurements (after Lachenbruch and Sass, 1973, 1980);

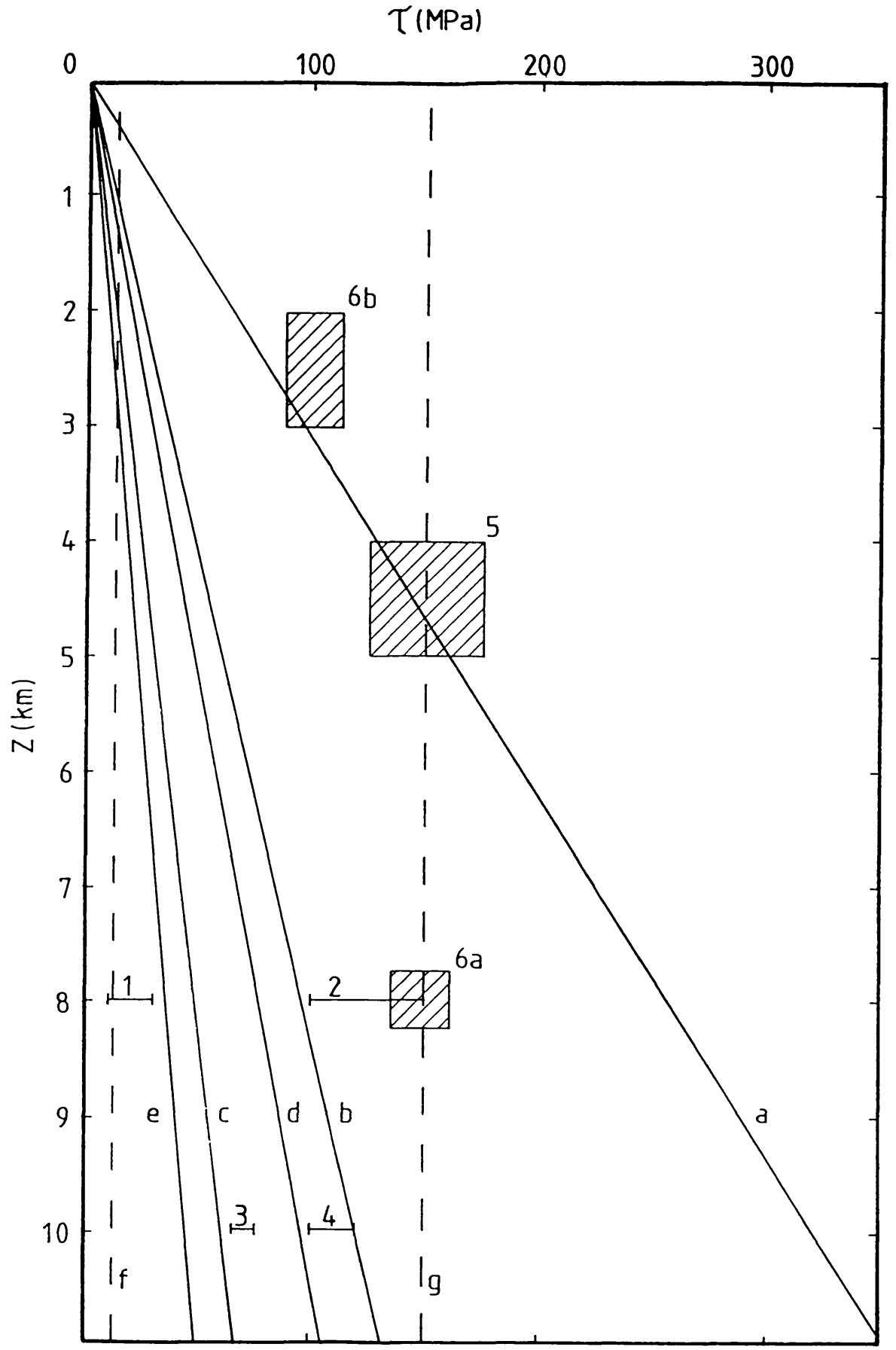
2 : estimate of shear stress acting on Alpine Fault zone, N Z, based on shear heating/Ar-depletion model (after Scholz et al., 1979);

3, 4 : estimate of shear stress in Nevada based on empirical frictional sliding law assuming hydrostatic pore fluid pressure (λ_0 = 0.36) or zero pore fluid pressure (λ_0 = 0) respectively (after Zoback and Zoback, 1980)

5 : estimate of palaeo- shear stress acting on Outer Hebrides Thrust zone based on displacement/width measurements of pseudotachylyte fault-veins (after Sibson, 1975);

6a : estimate of palaeo- shear stress acting on Ikertôq Shear zone, Greenland, based on displacement/width measurements of pseudotachylyte fault-veins and an assumed seismic stress drop of 100 MPa (after Grocott, 1977a);

6a : as for 6a based on vesicle/P_{fluid} relationships assuming σ_3 vertical.


τ (MPa)
0
100
200
300
Z (km)
1
2
3
4
5
6
7
8
9
10
6b
5
6a
1
2
3
4
a
b
c
d
e
f
g

be slightly underestimated since the cohesive strength of the faults has been ignored (C_o in Fig. 2.5).

Estimates of τ inferred from the long term strength of the lithosphere, based on models of crustally-supported loads and isostasy are of the order of 50 - 150 MPa (e.g. McNutt, 1980; Lambeck, 1980; Lambeck and Nakiboylu, 1980).

2.3.3 Seismological Estimates of τ

Minimum values of τ may be determined from the stress drop, $\Delta\tau$, (Fig. 2.5) during earthquake faulting. Note that the value of τ_2 (Fig. 2.5) may be larger or smaller than τ_k depending on the arrest mechanism of the propagating rupture (section 2.2.2).

The stress drop can be related to earthquake source parameters through the following equation (Kanamori and Anderson, 1975):

$$\Delta\tau = \tau_1 - \tau_2 = C.G.\frac{d}{L} \qquad (2.11)$$

where C = shape factor (constant), G = rigidity modulus, d = mean displacement and L = length dimension of rupture.

Observed earthquake stress drops are typically in the range $1 < \Delta\tau < 10$ MPa (Table 2.1) - plotted as curve f in Fig. 2.6. These data form a substantial argument for low stress faulting. Two lines of evidence may however refute this interpretation.

First, in equation 2.11, L is taken as the length of the entire rupture; the ratio d/L is typically 10^{-4} to 10^{-5} (Table 2.1). If instead of a 'single strand' fault model (Fig 2.7a), a 'multi strand' fault model is adopted (Fig 2.7b) the ratio d/L may be as much as an order of magnitude larger - yielding a similarly greater value of $\Delta\tau$ (Aki, 1979; Rudnicki and Kanamori, 1981). Near field seismic spectra (specifically strong motion displacements) sometimes do yield high stress drops for individual ruptures ($20 < \Delta\tau < 140$ MPa) compared to the stress drop integrated over the entire fault length ($1 < \Delta\tau < 10$ MPa) (e.g. Hanks, 1974; Hartzell et al., 1978; Hartzell and Helmburger, 1982).

Secondly, the relative magnitude of recorded stress drops and ambient stress levels depend upon the seismic efficiency:

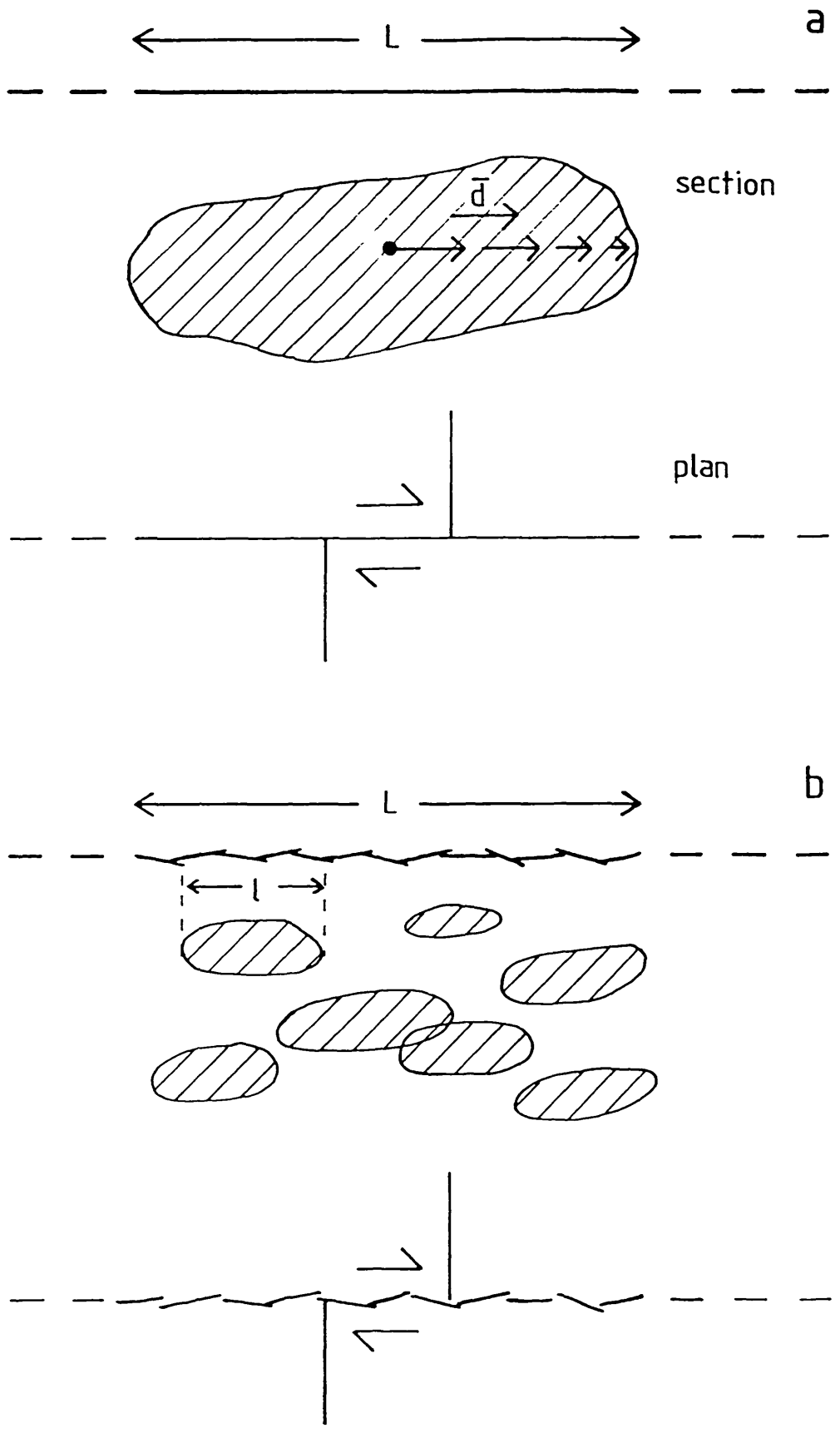


FIGURE 2.7 Fault zone geometries: (a) single strand model; (b) multi strand model.

$$\eta = \frac{E_s}{E} \qquad (2.12)$$

where E_s is the radiated seismic wave energy and E is the total energy released.

The stress drop can be related to the seismic efficiency and τ_1 by (Scholz et al., 1972; Sibson, 1977c):

$$\Delta\tau = 2\left[\tau_1 - \frac{\bar{\tau}_k}{1-\eta}\right] \qquad (2.13)$$

For reasonable values of τ_1/τ_k related to μ_s and μ_k and fractional stress drop, $\Delta\tau/\tau_1$, the seismic efficiency from equation 2.12 is about 16% (Sibson, 1977c). Only if τ_k decreases during slip due to a temperature enhanced increase in pore fluid pressure ratio (section 2.5.2) or frictional melting (section 2.5.1) is the fractional stress drop likely to approach unity and seismic efficiency approach 100% (Sibson, 1977c).

2.3.4 Geological Estimates of τ

Estimates of τ based on geological data support both high and low stress faulting (e.g. Sibson, 1977a; 1980a), the latter being enhanced by high pore fluid pressure ratios.

Palaeopiezometric studies of mylonites deformed aseismically in deep fault zones indicate shear stresses in the range 50 - 150 MPa (e.g. White, 1979; Kohlstedt and Weathers, 1980; Mercier, 1980). Note, such rocks have mostly been deformed below the base of the seismogenic layer which may be the limiting depth of maximum shear stress (Sibson, 1982).

From displacement-thickness measurements of pseudotachylyte fault-veins of the Outer Hebrides Thrust, Sibson (1975) derived the following empirical relationship:

$$\tau_k = 1.13 \times 10^8 d = 5.4 \times 10^6 w^{-1} \text{ (MPa)} \qquad (2.14)$$

where d is the displacement and w the thickness of the melt layer (c.g.s. units). Sibson (ibid.) observed that pseudotachylyte had just started to form on microfaults where d = 0.005 m and deduced from equation 2.14 an initial value of 160 MPa for τ_k. For dry thrust

faulting this implies a depth of 4 - 5 km (field 5, Fig. 2.6).

By Mohr circle construction, deriving τ_k from an empirical relationship similar to equation 2.14 and assuming $\Delta\tau$ = 100 MPa (following arguments outlined in section 2.2.3), Grocott (1977a) has estimated an initial shear stress of 140 MPa at 8 km depth (dry faulting) for early pseudotachylyte faulting in Greenland (field 6a, Fig. 2.6). (Note, this analysis requires a rather low coefficient of static friction, μ_s = 0.4). By similar construction , with σ_3 (vertical) determined from vesicle/P_{fluid} relations, Grocott (ibid) determined an initial value of τ_k = 100 MPa at 2 - 3 km depth for late glassy pseudotachylyte (field 6b, Fig. 2.6). (In this construction μ_s = 1.0).

2.3.5 Summary: τ and Pseudotachylyte Faulting

Three independent analyses indicate that pseudotachylyte faulting - in the Outer Hebrides, Greenland and New Zealand - occurred under conditions of high initial shear stress, close to that which may be inferred from the maximum seismologically derived stress drops (Fig. 2.6, fields 5, 6a and 2 and curve g, respectively). Where independent depth data is available, the initial value of τ_k is consistent with that which may be inferred theoretically for dry thrust faulting at the same depth (Fig. 2.6, field 6b and curve a).

These data suggest that pseudotachylyte generation should be favoured by dry thrust faulting, preferably on fault segments of smallish dimension, in intact rather than pre-faulted rock. If the initial shear stress is high and the seismic efficiency is low (i.e. $\Delta\tau/\tau_1 < 1$) the frictional heating energy given by equation 2.8 will be large. Once melting begins (or pore fluid pressure enhancement occurs in wet rocks), τ_k will decrease rapidly and the fractional stress drop may approach unity (Sibson, 1977c).

2.4 Energetics of Faulting

To gain a full understanding of the dynamics of faulting a complete description of the energy budget of faulting must be described. Ultimately, this should describe the accumulation of stored elastic strain energy, a criterion for the nucleation of an instability, energy dissipation during rupture propagation and during fault slip, and finally a description of the forces which terminate

rupture propagation and cause fault motion to cease. Such a description is not yet available, but the potential diversity of factors involved is illustrated in Fig. 2.8.

In a more tractable expression, the total energy dissipated during seismic faulting, E, is partitioned thus (Sibson, 1977c):

$$E = E_g + E_s + E_c + E_f \qquad (2.15)$$

where E_g = work done by or against gravity;
E_s = seismic wave energy;
E_c = work done at rupture front during propagation;
E_f = work done by frictional traction during slip.

2.4.1 Gravitational Energy, E_g

The magnitude of the term E_g in equation 2.15 is strongly dependent on the faulting mode: for dip-slip faulting, the gravitational energy change may be several orders of magnitude greater than energy released to other sinks. However, this is counterbalanced by a similar order of magnitude energy change in the elastic strain energy field (Dahlen, 1977; Savage and Walsh, 1978). E_g should be much smaller though probably non-zero, for strike-slip faulting.

2.4.2 Seismic Wave Energy, E_s

It is the radiation of seismic wave energy which uniquely characterizes earthquake faulting. The magnitude of E_s may be estimated from the Gutenberg-Richter relationship (Richter, 1958):

$$\log E_s = 1.5M_s + 11.8 \quad \text{(c.g.s. units)} \qquad (2.16)$$

where M_s is the surface wave magnitude.

Whilst this is a useful empirical formula, it has been suggested that errors in the determination of M_s may lead to orders of magnitude errors in E_s (Ben Menahem, 1977). Where the total energy, E, and E_s can be determined, the latter is usually orders of magnitude less than the former (cf. section 2.6.1), depending on the seismic efficiency. Sibson (1978) has determined values of radiated wave energy per unit area, E_s/A, between 10^5 and 10^8 $J.m^{-2}$.

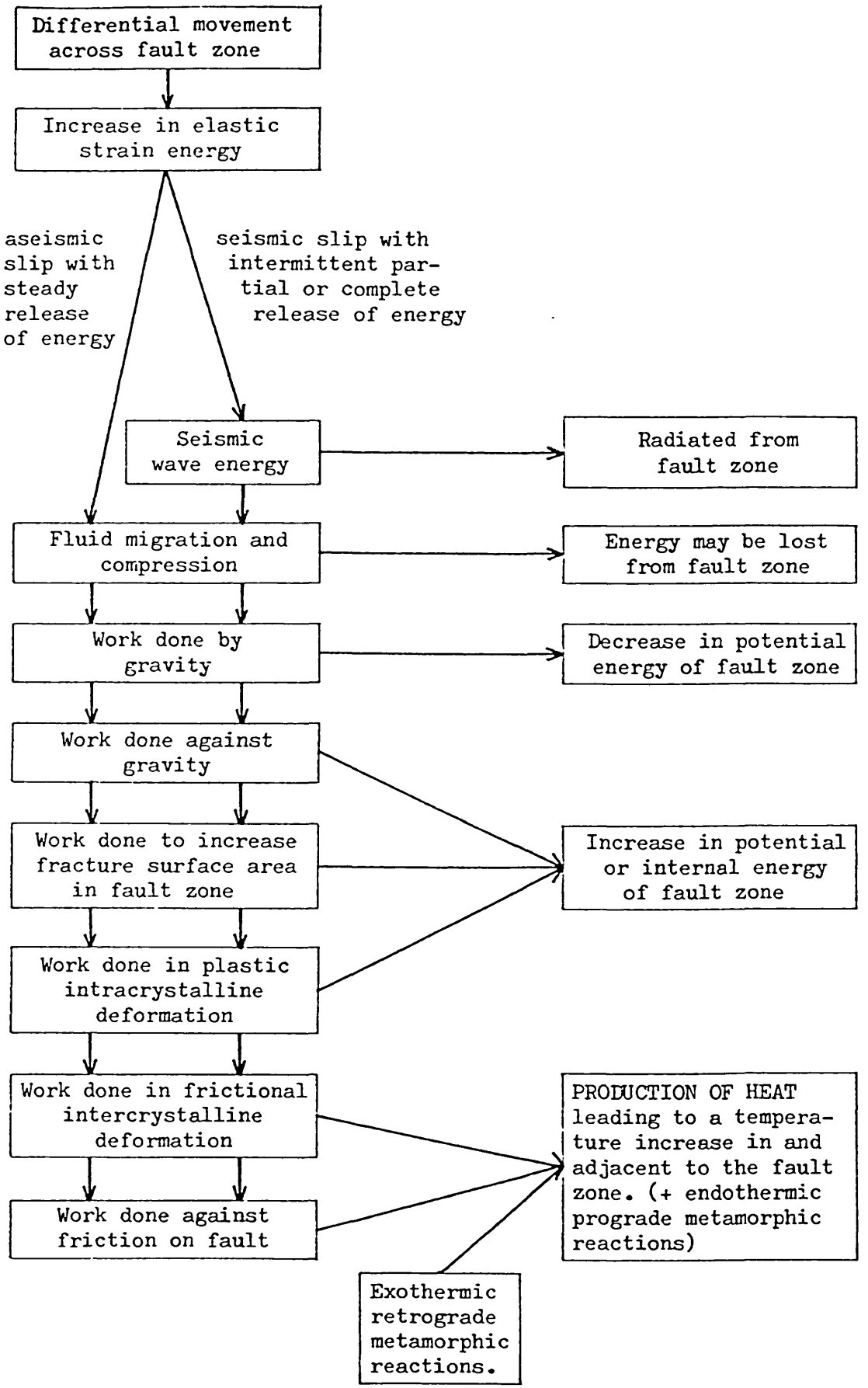


FIGURE 2.8 Flow diagram of possible energy budget during faulting (from Moore, 1980).

2.4.3 Shear Fracture Energy, E_c

A number of definitions and a corresponding number of estimates of the magnitude of E_c have been proffered. Physically, the fracture energy represents the energy flux for 'breakdown processes' or inelastic deformations at the crack tip during dynamic rupture propagation. It is the rate at which the sum of the potential energy of the loading system and the elastic strain energy of the specimen (fault zone) decrease with crack extension or rupture propagation.

The specific surface energy, γ, is the work done per unit area in creating new surface area; the shear fracture energy, E_c, includes γ and the energy dissipated by plastic deformation and heat at the moving crack tip. Several methods are available for determining γ and E_c:-

(i) γ may be measured directly during mode I tensile brittle fracture (Fig. 2.9a) of single mineral, intact rock or pre-fractured samples (Table 2.2);
(ii) E_c may be estimated from earthquake source models involving mode II and mode III rupture (Fig 2.9b and c; Table 2.2);
(iii) an apparent shear fracture energy, E_c', may be determined from laboratory study of pre- and post-failure behaviour of laboratory samples (Table 2.2).

Using $\gamma = 1\ J.m^{-2}$, Lachenbruch and Sass (1980) determined the resisting stress due to fracture, τ_γ, for a fault of half-width w, fractured into cubes of 1 μm side:

$$\tau_\gamma = \frac{3w}{d} \qquad (2.17)$$

According to this relationship, τ_γ will not exceed 3 MPa unless the ratio of half-width to displacement, d, exceeds unity. In fact this is likely to be a gross underestimate of τ, since the value of γ was derived from mode I rather than from shear fracture experiments.

In the dynamic model of Husseini et al (1975) an equation of motion balances the energy flux into an infinitely small crack tip volume with the specific fracture energy, γ, absorbed in creating new surface area for a mode III shear fracture. They find that for a fracture energy barrier rupture arrest mechanism (section 2.2.2):

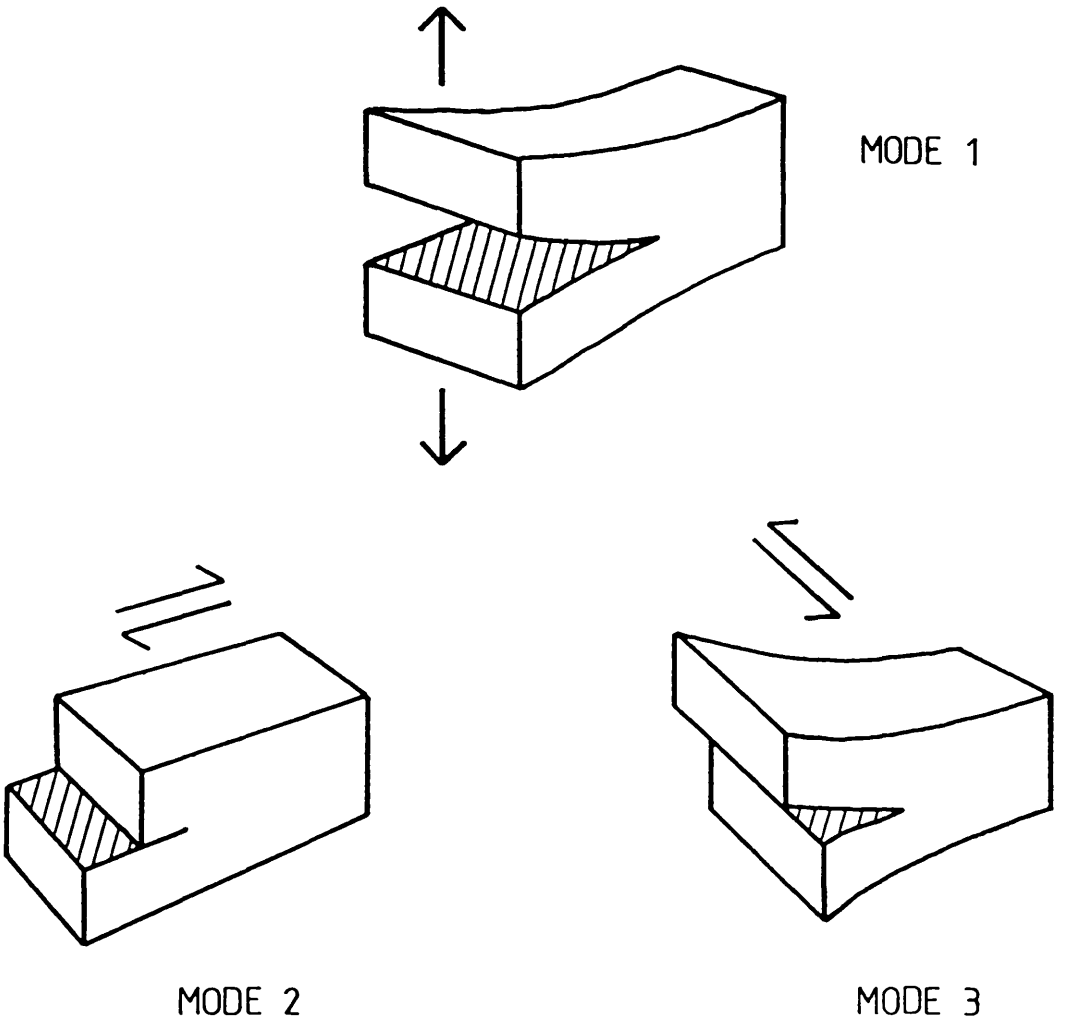


FIGURE 2.9 Classification of types of brittle fracture. Mode I, tensile fracture. Mode II plane shear fracture. Mode III, antiplane shear fracture.

TABLE 2.2 COMPILATION OF FRACTURE ENERGY MEASUREMENTS

Parameter/ magnitude ($J\ m^{-2}$)	Method of Determination	Reference
γ	Laboratory Measurement	
1 - 10	mode I fracture of quartz and orthoclase single crystals.	Brace & Walsh (1962)
$10-10^2$	mode I fracture of pre-fractured rock samples.	Atkinson (1979)
E_c'	Laboratory Measurement	
$0.3-7.3 \times 10^4$	analysis of postfailure behaviour in small samples of granite and quartzite for $0.1<\sigma_3<470$ MPa, $T \simeq 25^\circ C$.	compilation by Wong (1982)
0.06 - 0.8	analysis of postfailure behaviour in large sample of granite; E_c' increases linearly with $1.1<\sigma_n<4.6$ MPa.	Okubo and Dieterich (1981)
$1.7-5.1 \times 10^4$	SEM analysis of stress induced microstructures in small sample of Westerley Granite; $80<\sigma_3<250$ MPa $150<T<668^\circ C$.	Wong (1982)
E_c	Seismological Estimates	
10^2	minimum estimate from spatial distribution of slip during fault creep; field observations.	Rice & Simons (1978)
10^8	maximum estimate from stress drop and fault dimensions estimated from strong motion data, aftershock distribution and geological data.	Aki (1979)
$10 - 10^4$	estimate for fractured rock based on stress drop and fault dimension.	Husseini et al (1975)
$10^4 - 10^6$	estimate for intact rock based on stress drop and fault dimension.	

$$(E_c + \Delta E_c) > \frac{2R}{G} \qquad (2.18a)$$

and for a stress drop rupture arrest mechanism:

$$E_c = \frac{R}{2G} \qquad (2.18b)$$

where $(E_c + \Delta E_c)$ is defined in Fig. 2.4, R = fault radius and G = rigidity modulus.

Husseini et al (1975) concluded that earthquakes characterized by low $\Delta\tau$ and large R will occur along existing faults, whereas high $\Delta\tau$ and small R will be associated with fresh rupture. Similarly, higher values of E_c will be associated with rupture of intact rock (Table 2.2). Note, these deductions complement the discussion in section 2.3.3 concerning the relationship between $\Delta\tau$ and fault dimensions.

Both the work rate at the rupture front and the seismic efficiency are dependent on the rupture velocity. Physically realistic dynamic models suggest that the rupture velocity for mode III crack extension is slightly less than the shear wave velocity (Richards, 1976; Husseini and Randall, 1976). The results of Richards (1976) allow for a considerable temperature rise at the crack tip due to energy dissipation in excess of the surface energy, γ (see section 2.4.4).

Experimental determination of the apparent shear fracture energy for mode II shear fracture involves the adoption of a slip weakening model (Fig. 2.10). Initial slip is preceeded during fractions of a microsecond by a 'gradual' increase in shear stress to a peak, τ_p, resulting from cohesive forces initially resisting slip (Fig. 2.5); with the onset of slip the dynamic stress drop, $\Delta\tau = \tau_1 - \tau_k$, occurs over a finite critical displacement, dc, followed by sliding at the lower relatively constant kinetic shear stress, τ_k. The apparent fracture energy, E_c', is calculated from the shear stress versus slip curve (Fig. 2.10c).

In large scale biaxial experiments on pre-cut granite blocks, E_c' increases linearly from 0.06 $J.m^{-2}$ at 1.1 MPa normal stress to 0.8 $j.m^{-2}$ at 4.6 MPa normal stress (Okubo and Dieterich, 1981). These authors suggest that in natural fault zones containing gouge, the

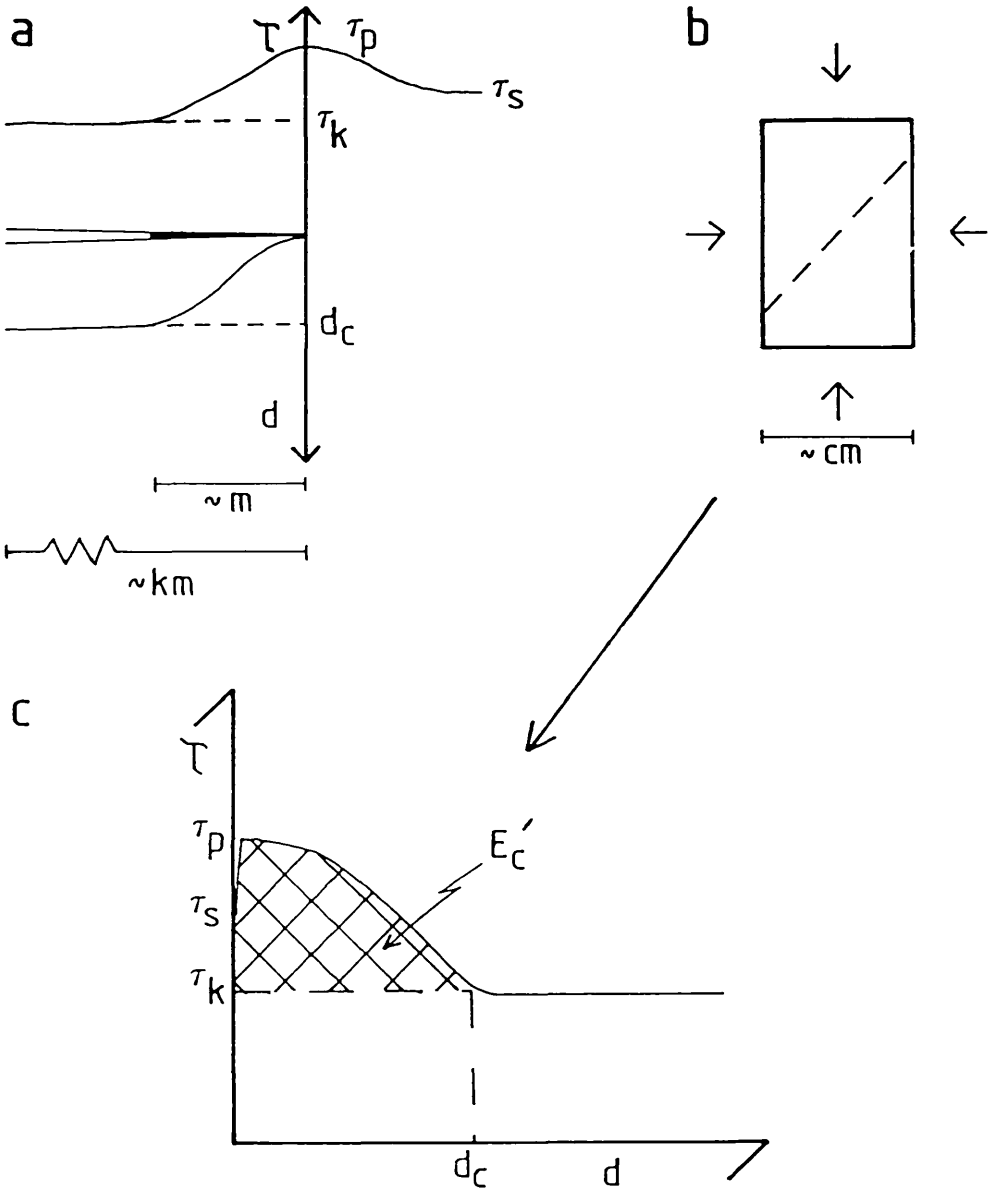


FIGURE 2.10 Shear fracture energy. (a) field scale; (b) laboratory scale; (c) plot of shear stress against displacement to show how the apparent shear fracture energy is calculated from laboratory measurements (from Wong 1982)

shear fracture energy may be 2 orders of magnitude greater. Complementary observations on post-failure behaviour in small specimens of Westerly Granite at varying temperatures ($25 < T < 700°C$) and values of σ_3 ($0.1 < \sigma_3 < 250$ MPa) have been made by Wong (1982). For the P-T conditions considered, $E_c' = 10^4$ J.m^{-2}; this is 2 orders of magnitude greater than the maximum values of γ, but several orders of magnitude smaller than seismologically inferred values of E_c. The variation of E_c' with P and T is ambiguous but Wong (1982) considers orders of magnitude variation in E_c possible over the natural range of P and T expected in fault zones. By SEM analysis of pre- and post-failure microcracks using assumed values of γ, Wong (ibid.) was able to show that the energy sinks of frictional heating and radiated wave energy are large compared to post-failure microcracking.

McGarr et al (1979) record values of $10^2 - 10^3$ J.m^{-2} for crushing of quartzite, but the partitioning of this 'crushing energy' into fracture, heat and wave energy is not defined. The process of comminution per se may be less than 1% efficient (Harris, 1966; Hukki, 1975), suggesting that almost all of the 'crushing energy' of McGarr et al (1979) is dissipated as heat. (Efficiency is defined empirically by Hukki (1975) as the total energy input relative to the specific surface energy during crushing of quartz.)

2.4.4 Temperature Rise due to E_c

It is evident from the above discussion that the shear fracture energy may considerably exceed the surface energy, and that much of this excess may be dissipated as heat. It is pertinent to ask therefore, whether melting temperatures can be achieved by crack tip energy dissipation? Wenk (1978) and Wenk and Weiss (1982) have argued that pseudotachylyte may be generated by crack tip energy dissipation and tensile fracture spallation rather than frictional fusion, whilst Macaudiere and Brown (1982), citing a personal communication with R.H. Sibson, suggest that crack tip heating may contribute significantly to the larger temperature rise produced by frictional shearing.

Experimental studies of high velocity ruptures in mode I extension in synthetic glasses demonstrate that temperature rises of several hundred degrees may be achieved in small volumes (Weichart and Schonert, 1975; Fuller et al., 1974). Weichert and Schonert (1975) have modelled numerically the temperature rise for a power dissipation of 20 J.m^{-2} in a crack tip of radius 30 Å undergoing mode I extension

at a velocity of 1000 $m.s^{-1}$. Assuming reasonable values of thermal conductivity and diffusivity, a maximum temperature rise in excess of 1000°C is predicted. If however, the crack tip radius is increased to 300 Å, the temperature rise is only 200 °C for the same power dissipation. For geologically realistic conditions of hybrid mode II/mode III shear fracture, a power dissipation some 5 orders of magnitude might be expected (Table 2.2) and a rupture velocity at least twice as large, but the breakdown zone radius may be 7-8 orders of magnitude larger (Wong, 1982).

If large temperature rises are to be achieved in this way, it appears that they will be transient and confined to a narrow zone during rupture of intact rock. This makes it highly unlikely that melt rock formed by crack tip processes contributes significantly to the volume of pseudotachylyte formed by frictional fusion.

2.4.5 Frictional Energy, E_f

It has been argued earlier that energy loss to comminution during frictional traction is rather small so that the greater part of the frictional energy should be dissipated as heat. This frictional heating energy is believed to be the source of heat by which fault-generated pseudotachylytes are formed. The fault source parameters τ_k and d, the product of which together with the fault area yields E_f (equation 2.8), have been discussed at some length. In the next sections the conversion of E_f to temperature rise and the likelihood of melting is considered.

2.5. Frictional Shear Heating

A large number of theoretical treatments of frictional shear heating, most of which describe the temperature rise up to the point of melting are available (e.g. Jeffreys, 1942; Anderson, 1951; Ambraseys, 1969; Price, 1970; McKenzie and Brune, 1972; Sibson, 1975; Richards, 1976; Cardwell et al., 1978; Moore, 1980). Most models involve the calculation of numerical or analytical solutions for the 1-dimensional unsteady transport of heat as a function of the rate of power dissipation, $\dot{Q}$, with respect to time, t, and dimension, x, given by Carslaw and Jaeger (1959):

$$\rho c_p \frac{\delta\theta}{\delta t} = k\frac{\delta^2\theta}{\delta x^2} + Q\,(x,t) \qquad (2.19)$$

where ρ, C_p and k are the density, specific heat capacity and thermal conductivity respectively. All the models involve simplifications and assumptions, particularly with respect to the rate of power dissipation per unit area, $\dot{Q}$, given by equation 2.10. Possible variations in the rate of power dissipation during slip are shown schematically in Fig. 2.11. Curve (a) shows the case used in most models. Curves (d) and (e) are probably more realistic geologically, with sudden changes in slope reflecting changes in kinetic shear resistance or slip rate as, for example, asperities are sheared or fluid (water or melt) is lost from the fault plane. Notice the integrated area beneath curve (a) equivalent to the cumulative power dissipation) is substantially greater than for the other, geologically more realistic curves; models using this type of relationship between rate of power dissipation and time will, therefore, tend to overestimate the temperature rise due to frictional heating. (Note, the ordinate axis in Fig. 2.11 could equally well be referred to kinetic shear stress or slip rate, remembering that the 2 quantities may be approximately inversely related.) Five other assumptions are made in the models: (i) convectional heat loss is ignored; (ii) heat loss due to the enthalpy of fusion is ignored; (iii) the faulting is assumed to occur under dry conditions (the important implications of this assumption are discussed in the next section); (iv) the conversion of frictional energy to heat and temperature rise is assumed to be 100% efficient; (v) the fault contact surface area is assumed to be 100%.

McKenzie and Brune (1972) have solved equation 2.19 numerically for 2 different types of slip regime shown schematically in Fig. 2.12. Using constant heat flux boundary conditions, the general solution to equation 2.19 yields the temperature rise, $\Delta\theta$, up to the point of melting (McKenzie and Brune, 1972):

$$\Delta\theta = \frac{\tau_k \, d}{\rho C_p (\pi K t)} \qquad (2.20)$$

Using mixed boundary conditions, involving constant temperature rather than constant heat flux, both the temperature rise and the thickness of the melt layer may be predicted. If a temperature rise, $\Delta\theta$ = 1000°C is taken to be sufficient to cause melting, then the

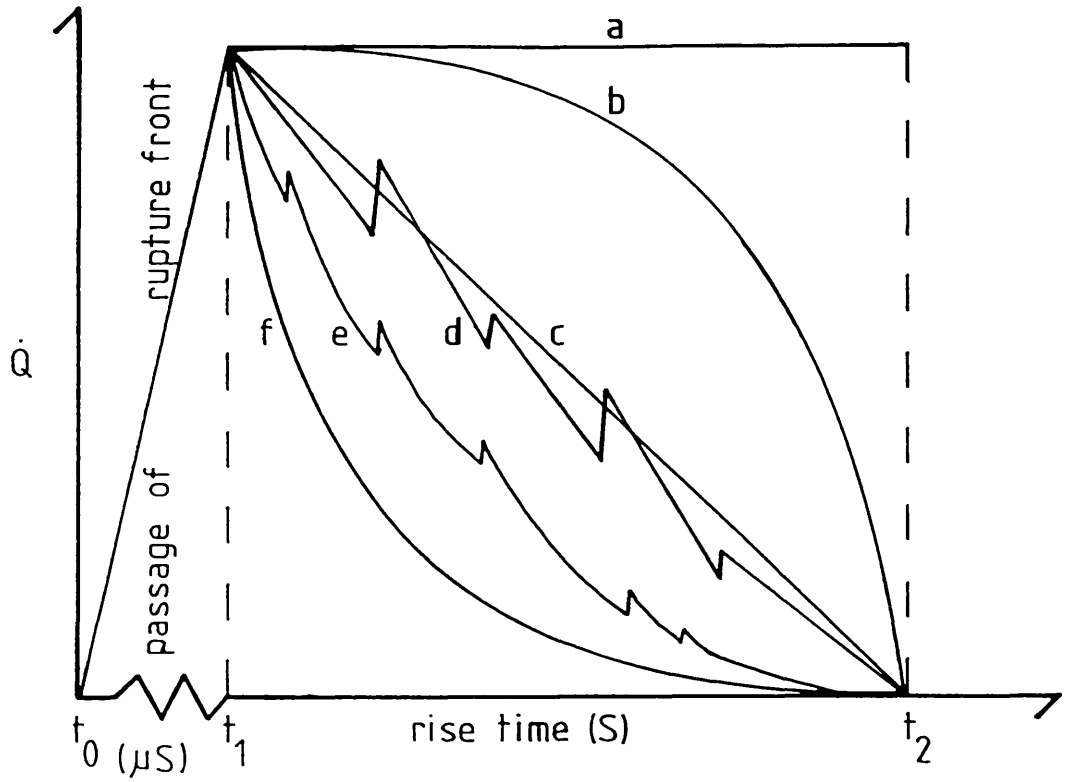


FIGURE 2.11 Schematic diagram to show possible variation in the rate of frictional shear heating ($\dot{Q}$) with time during earthquake faulting (see text of section 2.5 for discussion).

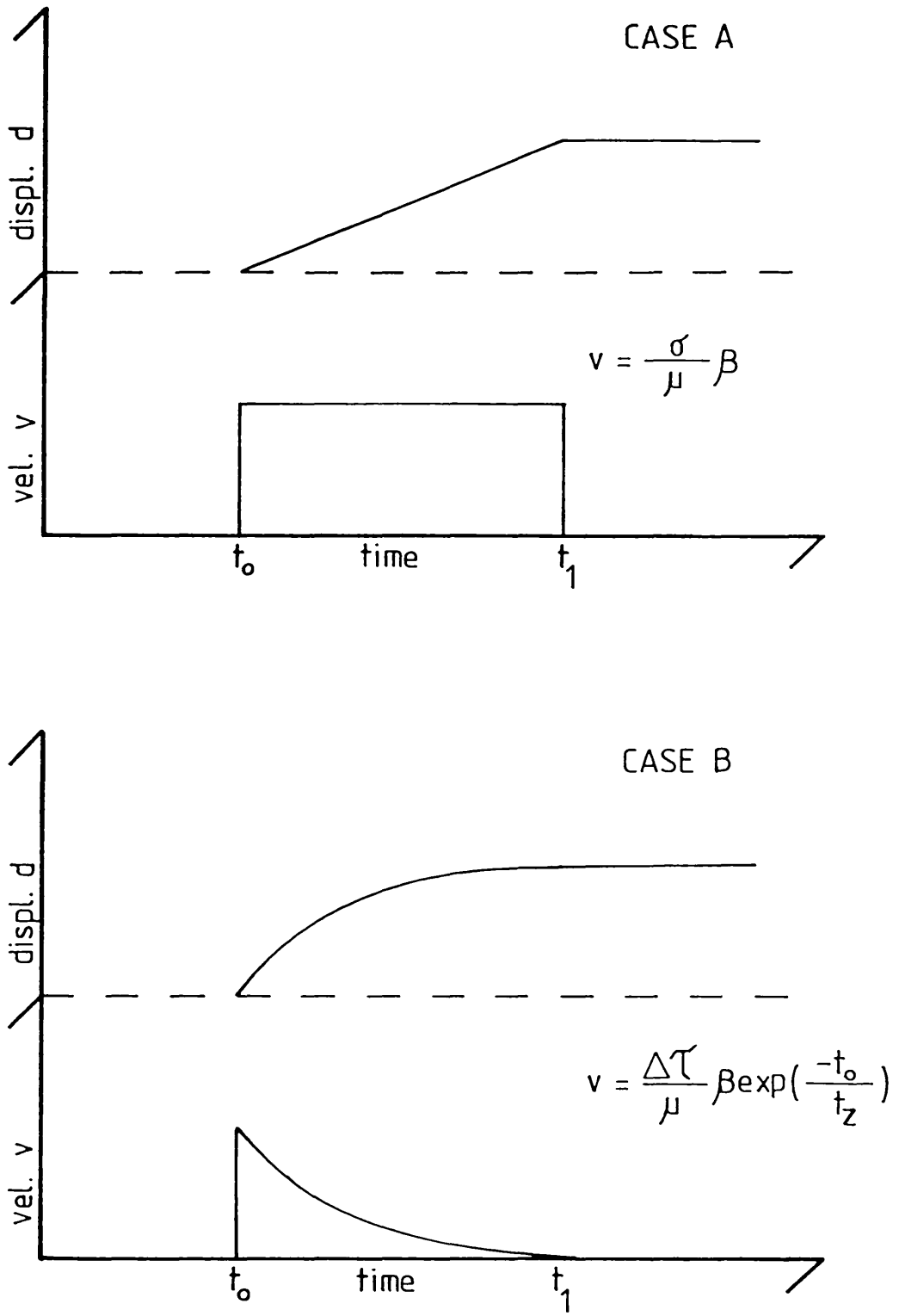


FIGURE 2.12 Velocity and displacement profiles used in the frictional shear heating models of McKenzie and Brune (1972).

critical minimum displacement, d_m, to achieve melting may be defined (McKenzie and Brune, 1972):

$$\text{for case A: } d_m = \frac{3.16 \times 10^2}{\tau_k^2 \tau_d} \qquad (2.21a)$$

$$\text{for case B: } d_m = \frac{1.07 \times 10^3}{\tau_k^2 \tau_d} \qquad (2.21b)$$

where τ_k and τ_d are the kinetic shear resistance and the difference between the initial shear stress and τ_k respectively expressed in MPa (material constants as given in Table 2.3). Plots of τ_k vs. d_m contoured for various values of τ_d required to achieve a temperature rise of 1000 °C are shown in Fig. 2.13. Using the mixed boundary conditions, case A describes the situation where a continuous layer of melt forms, τ_k is reduced and v may increase; case B describes the situation where melt occurs in pockets and there is less reduction in the kinetic shear resistance. In contrast to McKenzie and Brune (1972) who consider case A to be more realistic for real earthquake faulting, it is clear from field observations of pseudotachylyte fault veins that both cases may be applicable. For large fault displacements, case B predicts a thicker zone of melt (McKenzie and Brune, 1972, p. 74). Comparing Fig. 2.13 with likely values for the parameters, τ_k, d, and τ_d discussed earlier, it is evident that melting is predicted for dry faulting in most earthquakes of moderate to large displacement. Additional calculations by McKenzie and Brune (1972) indicate that if $\tau_k = \tau_d = 10$ MPa, slip must be confined to a zone <1 cm wide if melting is to occur. (The rupture speed of this model is infinite and therefore maximum temperature rises are predicted (Richards, 1976).)

The effect of fault thickness on temperature rise has been considered in more detail by Cardwell et al (1978) (see also Sibson, 1973) who use an identical approach to McKenzie and Brune's case A, and assume a constant rate of power dissipation uniformly distributed through a fault zone of thickness w. Their thin fault solution is identical to equation 2.20. A thick fault solution pertains when:

$$w > \frac{1}{(Kt)} \qquad (2.22)$$

For the value of K given in Table 2.3 and choosing a reasonable value

TABLE 2.3 MATERIAL CONSTANTS USED IN FRICTIONAL HEATING CALCULATIONS

Parameter	Symbol	Value	Dimensions
density	ρ	2.8×10^{3}	$kg\ m^{-3}$
thermal diffusivity	K	1.0×10^{-6}	$m^{2}.s^{-1}$
thermal conductivity	k	3	$W.m^{-1}.{}^{0}C^{-1}$
heat capacity	C_p	1.07×10^{3}	$J.kg^{-1}.{}^{0}C^{-1}$

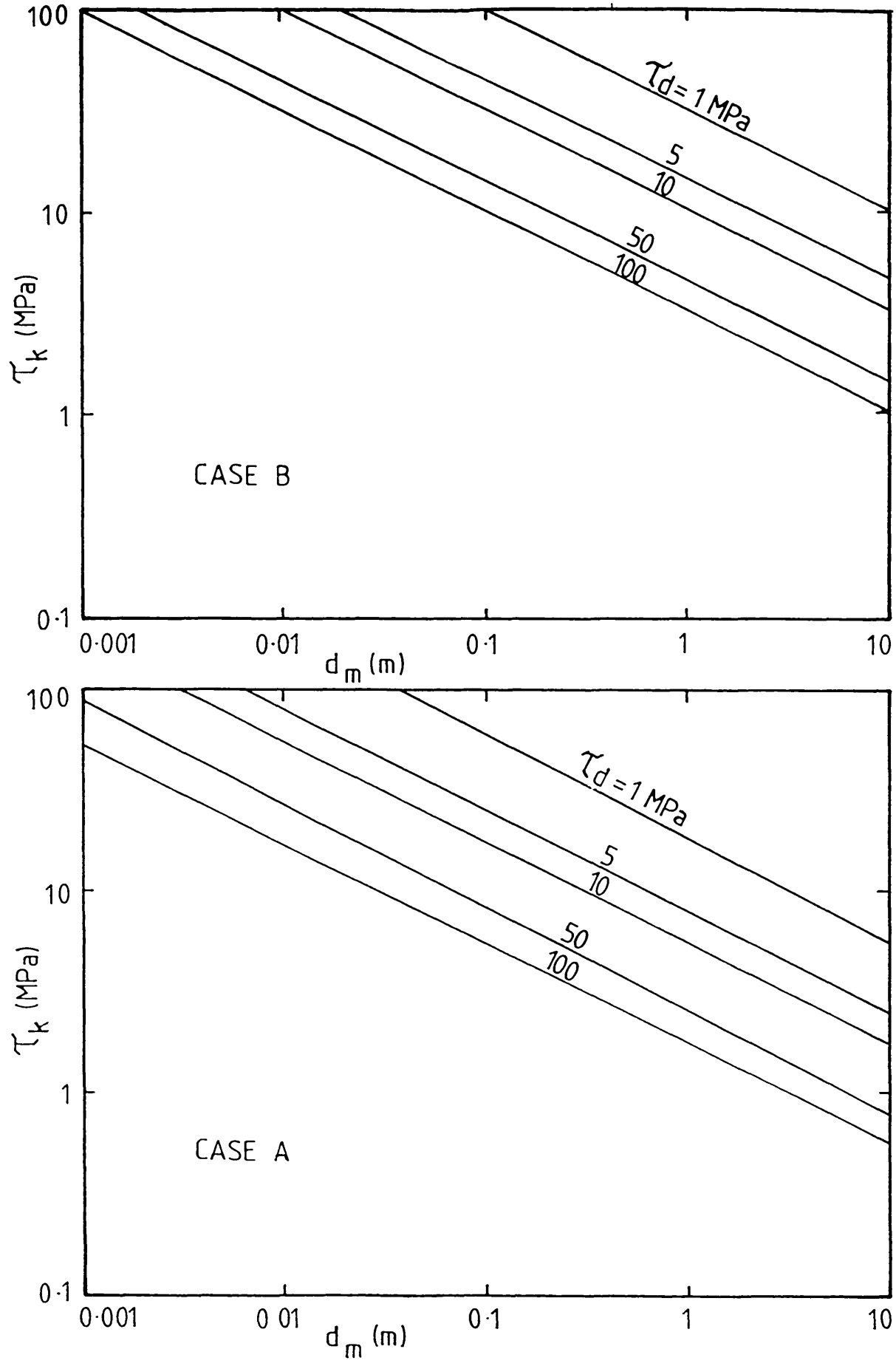


FIGURE 2.13 Plot of kinetic shear resistance (τ_k) against critical minimum displacement (d_m) required to obtain a temperature rise of 1000 C contoured for various values of difference between initial and kinetic shear stress (τ_d), according to the models of McKenzie and Brune (1972).

for the rise time, t, of 1-10s (Table 2.1) the inequality is satisfied for fault thicknesses, w > 1 cm. The temperature rise for thick faults is then given by (Cardwell et al., 1978; Sibson, 1973):

$$\Delta\theta = \frac{\tau_k \, d}{\rho C_p w} \qquad (2.23)$$

The effect of fault thickness on temperature rise for various values of the product $\tau_k d$ is shown in Fig. 2.14 (values of ρ and C_p are taken from Table 2.3). The model assumes that thermal conduction is unimportant, which for rise times of 1 - 10 s is probably reasonable (Lachenbruch, 1980; Voight and Faust, 1982), but note the comment in section 2.6.2. Clearly the effect of fault thickness is very considerable and suggests that pseudotachylyte should be preferentially generated on discrete fault planes - complementing the conclusions of section 2.2.3. Field study of pseudotachylyte fault veins (chapter 4) indicates that this is commonly the case. Furthermore, if a cataclasite layer is present it is far from clear that slip, and hence power dissipation, will be uniformly distributed throughout the layer; the stick-slip experiments of Engelder et al (1975) indicate that slip can be confined to the shear zone boundaries.

If the rate of power dissipation, $\dot{Q}$, is given by equation 2.10 when slip rate and kinetic shear resistance are assumed to be constant, Sibson (1975; 1980a) has shown that the temperature rise on a thin fault plane is given by:

$$\Delta\theta = 188 \, \dot{Q} t^{1/2} \qquad (2.24)$$

using the values of thermal diffusivity and conductivity given in Table 2.3. Using equations 2.10 and 2.24, plots of kinetic shear stress vs. slip rate may be contoured for power dissipation and associated temperature rise (Fig. 2.15). Temperature rises sufficient to cause melting (say > 1000°C) are achieved by power dissipations of ~ 5 MWm^{-2} or greater.

Most of the assumptions used in the above models tend to err toward overestimating temperature rise due to frictional shearing. However, 2 possible sources of underestimation exist. First, experimental studies indicate that thermal diffusivity and conductivity decrease in magnitude with increasing temperature, at

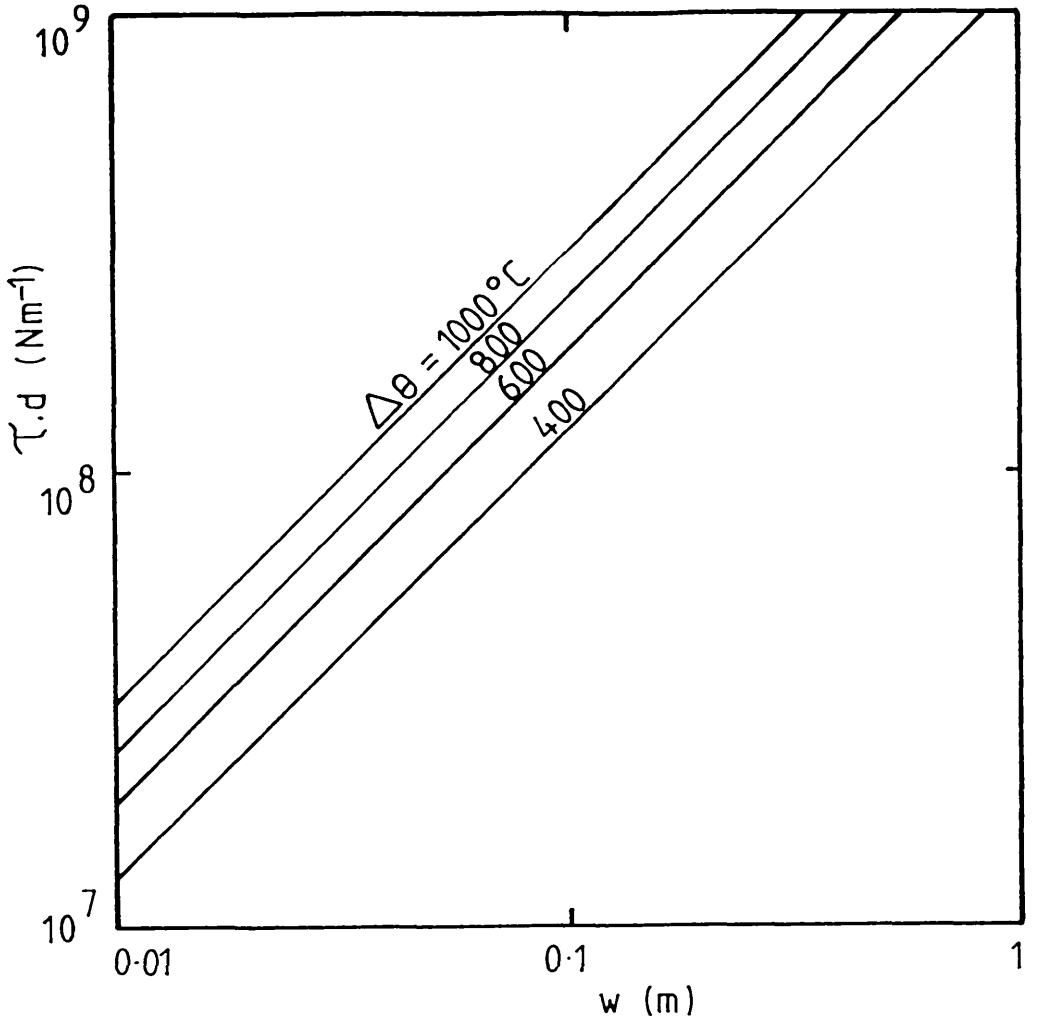


FIGURE 2.14 Plot showing the effect of fault thickness (w) on temperature rise ($\Delta\theta$) for likely values of the shear heating (after Cardwell et al., 1978).

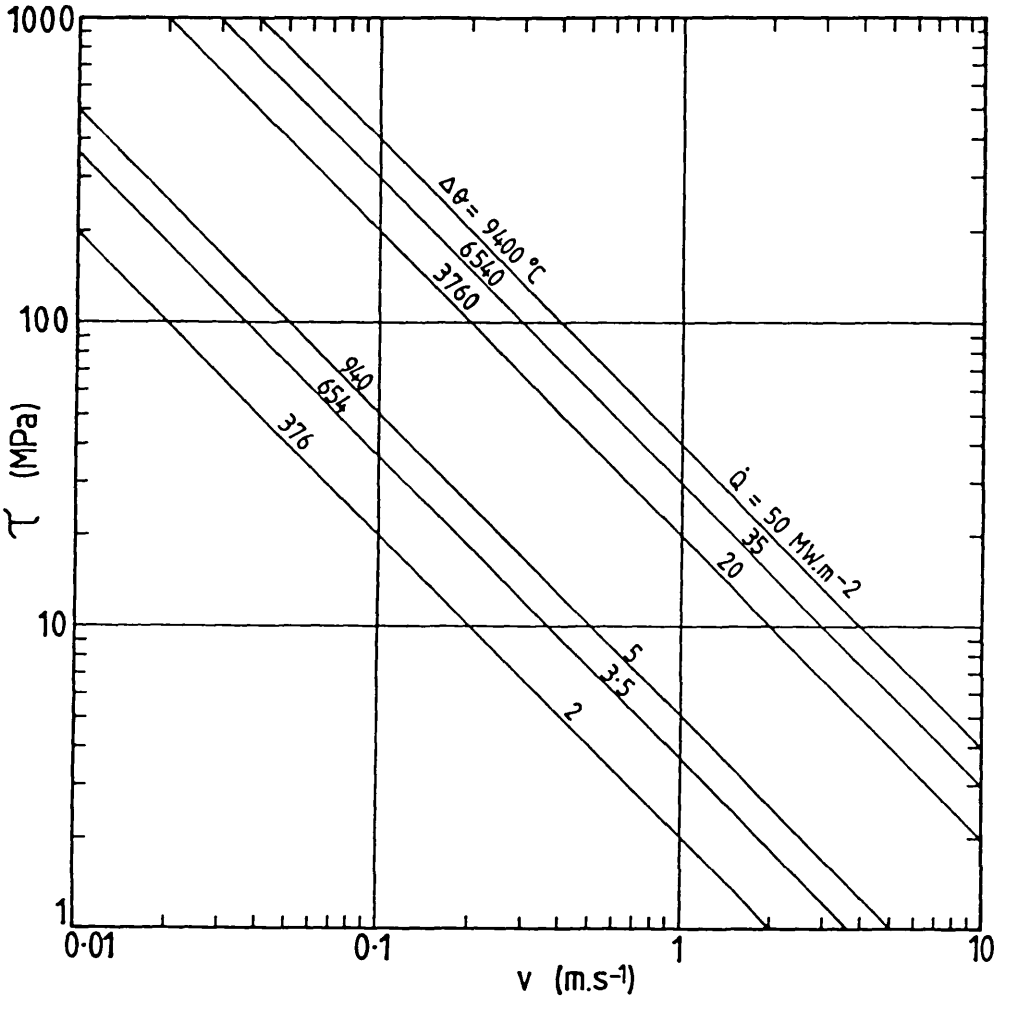


FIGURE 2.15 Plot of kinetic shear resistance (τ_k) against slip rate (v) contoured for various values of power dissipation ($\dot{Q}$) and associated temperature rise ($\Delta\theta$) (after Sibson, 1980a).

least in the range 25 - 400°C (Clarke, 1966). Second, the temperature rise required to achieve melting, rather arbitrarily chosen as 1000°C, may be an overestimate since no account has been made of the wall-rock temperature. For reasonable geothermal gradients (say 25°C.km^{-1}) maximum ambient temperatures toward the base of the seismogenic regime ($Z < 15$ km) could be as high as 375°C. Mitigating against this is the fact that a substantial quantity of heat energy may be required to overcome the enthalpy of melting, once the melting temperature is approached.

Petrological estimates of the melting temperatures are made in chapters 5 and 6.

2.5.2 Effects of Fluids on Frictional Shear Heating

It is clear from field observation that fluid flow frequently accompanies shear displacement in both the ductile (e.g. Beach, 1976) and brittle mode (e.g. Ramsay, 1980; Sibson, 1981). Hydrothermal vein textures are commonly directly referable to brittle faulting: for example, some slickensides, extensional veins which show a history of repeated incremental opening and healing by mineralizing fluids, and some fault breccias with a matrix of gangue minerals. Textures implying pulsatory movements may well be related to earthquake faulting (cf. Sibson et al., 1975; Sibson, 1985); this would be consistent with the dilatancy/fluid diffusion model for earthquake faulting (e.g. Nur, 1972; Scholz et al., 1973).

Combining the Terzaghi effective stress relationship with the equation for frictional power dissipation (equation 2.10), the rate of power dissipation as a function of time, $\dot{Q}(t)$, for wet faulting may be written (Voight and Faust, 1982):

$$\dot{Q}(t) = \{1 - \lambda_o - \Delta\lambda(t)\}\, \tau_k\, \sigma_n\, v \qquad (2.25)$$

where λ_o = initial pore fluid pressure ratio (p_o/σ_n);
$\Delta\lambda(t)$ = change in λ_o as a function of time;
τ_k = kinetic coefficient of friction;
σ_n = normal stress;
v = displacement rate.

Because of the thermodynamic properties of water ($\delta P/\delta\theta$ is strongly positive at constant volume) any rise in temperature due to

frictional heating will dramatically increase the pore fluid pressure; as $\lambda \rightarrow 1$ the frictional power dissipation in equation 2.25 becomes vanishingly small. For the special case of constant volume conditions, the temperature rise required to elevate the pore fluid pressure ratio from hydrostatic ($\lambda_v = 0.36$) to lithostatic values is less than 100°C, for shallow crustal depths less than 10 km (Sibson, 1973).

In general, the sign and magnitude of $\lambda(t)$ due to frictional heating will be a function of:-

(i) the initial values of τ_k, σ_n, λ_o;
(ii) the slip rate, v, and the rise time, t;
(iii) the thickness, w, and compressibility, β, of the slip zone;
(iv) the rate and sign of pore dilatation due to straining;
(v) the permeability of the slip zone and surrounding rock;
(vi) the rate of hydrofracturing.

Voight and Faust (1982) have shown that for slip distributed across zones of gouge, temperature rise is greater for large compressibilities. The effect of fault thickness on temperature rise during wet faulting is complex: it was shown above that temperature rise decreases with slip zone width for dry faulting (Fig. 2.14); however, in the wet case, thin slip zones show a more rapid pore fluid pressure enhancement than thick zones - thereby reducing the rate of frictional power dissipation.

2.5.3 Experimental Observations on Frictional Shear Heating

Thermo-mechanical rock deformation experiments providing information on frictional shear heating and the kinetics of melting may be classified into 5 categories:-

Type 1: small scale, low to moderate P-T frictional sliding experiments on unfaulted and pre-cut samples, with or without an artificial gouge layer;
Type 2: small scale, high P-T frictional sliding experiments where partial melting occurs;
Type 3: medium scale, high displacement rate frictional sliding at ambient T and low to moderate σ_n;
Type 4: large scale, moderate displacement rate frictional sliding at ambient T and low to moderate σ_n;

Type 5: medium scale, electrically-induced power dissipation without shear, but designed to simulate shear heating rates.

Large numbers of type 1 experiments have been performed (see Paterson, 1978), but few occurences of melting have been reported. The development of 'fused gouge' is restricted to dry frictional sliding of quartz-rich rocks, and is best developed on clean or polished pre-cut surfaces (29 - 45° with respect to σ_1 axis) (Friedman et al., 1974; Jackson and Dunn, 1974; Hundley and Moody, 1977; Teufel and Logan, 1978). Glassy gouge has also been found in un-pre-cut samples deformed under triaxial compression (Friedmann et al., 1974) and in similarly deformed artificial gouge layers (Jackson and Dunn, 1974).

The experimental observations of Friedman et al (1974) are shown in Table 2.4; interestingly, the coefficient of kinetic friction increases with ambient temperature and concomitant increase in the amount of indurated gouge. This they attributed to an increase in the real contact surface area of the sample fault zone, as predicted by Bowden and Tabor (1967). Glass was identified by SEM, and Friedman et al (1974) postulated local asperity hot spot temperatures as high as 1500 °C. They compared this glassy gouge with the Langtang frictionite described by Scott and Drever (1953) (see section 1.4.2). Also using Tennessee Sandstone, Teufel and Logan (1978) determined local asperity hot spot temperatures in excess of 1100 °C using thermodyes, for a sliding rate of 10^{-2} cm.s^{-1} and a confining pressure of 50 MPa. These authors estimated the real contact surface area as 5 - 14%, though this has recently been questioned by Lockner and Okubo (1983) who suggest that it may have been as little as 1%. (Byerlee (1977) has pointed out that the physico-chemical response of thermodyes to shear stress is not known.)

Other experiments on Tennessee Sandstone and Westerly Granite performed under both lower strain rates (although transient sliding rates are unknown) and wet conditions have failed to yield glassy gouge (Tullis and Yund, 1977; Rutter and White, 1979). These 2 factors are not strictly independent, since Brace and Martin (1968) have shown that dilatancy hardening is greater in low porosity rocks at higher strain rates. The results of Rutter and White (1979) indicate that at low strain rate ($\dot{e} = 10^{-6}$) and wet conditions when dramatic weakening occurs, most work may be done in the comminution of the gouge to a grain size <1 um in pre-faulted rather than pre-cut samples (cf. section 2.4.3). The authors note that if comminution and frictional

TABLE 2.4 EXPERIMENTAL OBSERVATIONS FOR TRIAXIAL COMPRESSION OF DRY, PRECUT TENNESSEE SANDSTONE (data from Friedman et al, 1974)

Type of gouge	Confining pressure (MPa)	Shortening rate (S^{-1})	Temperature ^{0}C
Welded clumps	14	10^{-4}	24
	100	10	24
Fibrous patches	50	10^{-4}	260 - 40
Welded patches	400 - 500	10^{-4}	24

Sliding mode	
Stick-slip	25
Episodic	150 - 250
Stable slip	410

Dynamic coefficient of friction μ_d	
0.58	25
0.72	410

melting are to some extent mutually exclusive, then estimates of the magnitude of shear stress acting on faults based on the presence or absence of glass need to be interpreted carefully (cf. Price, 1970).

In type 2 experiments (e.g. van der Molen and Paterson, 1979), partial melting is usually attributable to the high ambient temperatures, and as such little direct information about shear heating is provided. Useful information is, however, provided about the kinetics of melting and the migration and rheology of the melt phase; this is considered further in chapter 5.

Type 3 experiments were pioneered by Bowden (reviewed in Bowden and Tabor, 1967), although as long ago as 1929, Hawkes compared similar experiments with pseudotachylyte generation. The direct applicability of such experiments is questionable, since the asperity characteristics and real contact surface area of stressed, natural faults are poorly understood. By far the most pertinent experiment, designed to simulate the formation of landslip frictionite, was performed by Erismann et al (1977). Using circular sliders of gneiss, pumiceous glassy material was produced with a normal force of 20 000 N (approximate normal stress = 15 MPa) and an angular velocity of 300 s^{-1} ($\sim 10 m.s^{-1}$). These experimental conditions yielded an average kinetic coefficient of friction of 0.25 and an estimated temperature of dry fusion of 1200°C. (Similar temperatures have been estimated for the accidental dry fusion of impure quartzite during drilling by Bowen and Arousseau, 1932.) Erismann et al (1977) were also able to determine experimentally "the energy consumed per kg of rock destroyed" as 1.45×10^6 $J.kg^{-1}$, a figure which corresponds well with the energy required to heat and melt feldspar - 1.28×10^6 $J.kg^{-1}$.

Type 4 experiments are potentially the most informative with respect to frictional heating since the large sample dimensions minimize scaling effects. Unfortunately, few such experiments have been performed - principally because of the physical problems and costs involved.

Lockner and Okubo (1983) have biaxially deformed a 1.5 x 1.5 x 0.4 m, 45° pre-cut sample of granite at 0.69 - 6.41 MPa normal stress (corresponding to a maximum shear stress of 2.5 MPa) with a maximum displacement rate of 9 $\mu m.s^{-1}$ and a maximum finite displacement of 300 μm. Average temperatures of the entire fault surface were measured with thermistors 0.15 - 2.0 cm from the fault surface. In experiments with a dry, ground fault surface, frictional heating accounted for 94% of the energy released, implying (in the absence of energy loss to

comminution/fracture processes) a seismic efficiency of only 6% (cf. section 2.2.3). Temperature transients as large as 10 m°C were recorded up to 1.0 cm from the fault surface following stick slip events. The presence of water injected at pressures up to 2.76 MPa onto the fault plane held at constant normal stress of 3.45 MPa reduced frictional heating efficiency to 80%. Significant temperature rises were also found when a 0.15 cm thick layer of quartz sand 'gouge' was present, although the authors were unable to calculate the frictional heating efficiency because of experimental problems.

By scaling their experiments (equivalent to an earthquake of magnitude, $M_L = -1$) to observed earthquake source parameters, Lockner and Okubo (1983) concluded that frictional heating should be significant during both earthquake and creep displacement along faults. Their data also support evidence from small scale experiments that crustal stress levels may be 1 to 2 orders of magnitude greater than those inferred from seismic stress drops.

Experiments designed to simulate the power dissipation during seismic faulting by electrical means (Moore and Sibson, 1978; Moore, 1980) have produced melting in (quartz-rich) granite and gneiss but not quartz sandstone, and serpentinized peridotite. For a rate of power dissipation of 2.6 $MW.m^{-2}$ and cummulative dissipated power of 5×10^7 $J.m^{-2}$, surface temperatures of 1500°C were determined by thermocouple, whilst petrographic observations indicated a temperature of 1200°C. (The equivalent fault source parameters, τ_k and v for this rate of power dissipation may be estimated from Fig. 2.15.)

2.5.4 Additional Effects of Shear Heating

Frictional shear heating of rocks to even moderate temperatures can lead to thermal stress damage manifested by macro- and microstructural brittle deformations. These effects have recently been examined in detail by Moore (1980), who found 20 $kW.m^{-2}$ to be the lower limit for power dissipation on a fault surface inducing significant thermal damage. Values of τ_k and v producing power dissipations of this order may be read from Fig. 2.15. For an ideal solid, even if melting temperatures are achieved on the fault surface, initiation of large thermal fractures is restricted to within 10 mm of the fault surface (Moore, 1980).

Another potentially important deformation process is the thermally induced decrepitation of fluid inclusions (Sibson, 1975;

Moore and Sibson, 1978; Pecher, 1981). If a water-filled inclusion, initially at homogenized P-T conditions, is heated the pressure rise, ΔP, is given by (Sibson, 1975):

$$\Delta P = \frac{\Delta\theta}{0.47} \text{ MPa} \qquad (2.26)$$

for water initially at 140°C and a confining pressure of 130 MPa held at constant volume. The creation of an internal fluid pressure, P_i, gives rise to a tangential tensile stress, σ_t (Moore and Sibson, 1978):

$$\sigma_t = 0.5\ P_i \qquad (2.27)$$

Thus small temperature rises ($\Delta\theta$ = 50 - 100°C) should be sufficient to raise σ_t to values exceeding the tensile strength of most rock types (< 50 MPa).

2.6 Special Cases of Frictional Shear Heating

Two special modes of 'pseudotachylyte' generation were mentioned in chapter 1: those of caldera collapse and landsliding. Source parameters for these processes are compared with those deduced for earthquake faulting in Table 2.5. The table shows that similar power dissipations may be achieved by high normal stress/low slip rate faulting (earthquakes and caldera collapse) or low normal stress/high slip rate faulting (landslides). One example of each special case will be examined in detail.

2.6.1 Caldera Collapse Faulting

Accepting that the case for an igneous origin by fluidization for caldera collapse/ring fault pseudotachylytes remains unproven (section 1.4.5) it is reasonable to examine the possibility of frictional fusion in this context. Recent seismological, geophysical and geodetic studies have helped to elucidate some of the physical mechanisms of volcanic eruptions (e.g. Shaw, 1980). However, as far as the present author is aware, only a single such study of a caldera collapse event exists - the 1968 event on Fernandina in the Galapagos

TABLE 2.5 COMPARISON OF FAULT SOURCE PARAMETERS FOR EARTHQUAKE, CALDERA COLLAPSE AND LANDSLIDE FAULTING ASSOCIATED WITH POSSIBLE FRICTIONAL MELTING

Parameter (range of)	Earthquake	Caldera Collapse	Landslide
Displacement (m)	0.1 - 10	0.1 - 10?	< 2000
Rise time (s)	0.5 - 10	0.5 - 10?	40 - 200
Slip rate ($m.s^{-1}$)	0.1 - 1	0.1 - 1?	10 - 50
Normal stress (MPa)	10 - 100	1 - 50?	1 - 25
Kinetic shear stress (MPa)	1 - 200	1 - 50?	1 - 5
Power dissipation per unit area (MWm^{-2})	2 - 100	5 - 50?	5 - 250
Total energy dissipated per unit area ($J.m^{-2}$)	10^6 - 10^9	$\sim 10^7$	10^8 - 10^9

Note: data largely abstracted from Erismann et al (1977), Filson et al (1973), Sibson (1980a) and Scholz (1980).

Islands described by Filson et al (1973). Filson et al (1973) compared values of shear stress, energy and seismic moment derived from teleseismic observations with values calculated from a model based on known source parameters. A summary of their data is given in Table 2.6.

The caldera ring fault on Fernandina can be described as a sub-vertical normal fault with an elliptical trace and dimensions indicated in Table 2.6. From these source data the tangential stress due to gravity acting on the fault and the available potential energy can be calculated (Table 2.6).

Filson et al (1973) examined a large number of seismograms and determined 5 stages in the seismicity. By plotting cumulative seismic wave energy against time they found that the greater part of the seismic energy was released at a rather constant rate during a 9 day period. From a change in slope on a plot of frequency against magnitude, Filson et al postulated 2 types of seismicity: some 75 larger magnitude earthquakes were the result of faulting during caldera collapse and a larger number of smaller magnitude earthquakes were attributed to secondary faulting, landslipping and general stabilization of the volcano between collapse episodes. The 300 m cumulative slip (Table 2.6) could, therefore, have been accommodated by 75 earthquakes with average individual displacements of 4 m.

The fault source model chosen by Filson et al (1973) is a "Starr Fracture" (see Aki, 1966, for details) which allows calculation of pre-existing shear stress, τ, displacement, d, and thus the total energy dissipated during faulting (Table 2.6). Agreement between the values of parameters estimated from the model and from the fault source parameters and seismic data is fairly good (Table 2.6). In particular, the cumulative energy dissipated during faulting is substantially greater than the cumulative seismic wave energy, and is within an order of magnitude of the available potential energy.

Using the data calculated by Filson et al, the energy dissipated per unit area, per event, E_e, may be derived:

$$E_e = \frac{\Sigma E}{NA} = 5.3 \times 10^7 \ J.m^{-2} \qquad (2.28)$$

where N = 85 is the number of earthquakes with an average displacement of 3.5 m over the area A. For earthquake rise times of 1, 2, 5 and 10s, assuming a constant energy flux, rates of power dissipation , $\dot{Q}$,

TABLE 2.6 SEISMIC AND FAULT SOURCE DATA FOR FERNANDINA 1968 CALDERA COLLAPSE EVENT (after Filson et al, 1973)

Fault Source Parameters

Length, $l = 7.0 \times 10^3$m

Width, $2w = 1.0 \times 10^3$m

Area, $A = 7.0 \times 10^6 m^2$

Surface area of displaced block, $S = 8 \times 10^6 m^2$

Cumulative slip, $\Sigma d = 3.0 \times 10^2$m

Density, $\rho = 2.8 \times 10^3$ kg.m^{-3}

Rigidity, $G = 5.0 \times 10^9$N.m^{-2}

Acceleration due to gravity, $g = 9.81$ m.s^{-2}

Calculated from Source Parameters:-

Mass of displaced block, $m = 2w.s.\rho = 2.16 \times 10^{13}$kg.

Potential energy released, $Ep = m.g.\Sigma d \simeq 6.36 \times 10^{16}$J.

Tangential stress acting on fault plane due to gravity, $\tau_g = \frac{2.w.s.\rho.g}{L.2w} = 30$ MPa

Calculated from Seismic Data:-

Cumulative seismic energy, $\Sigma E_s = 7.25 \times 10^{13}$J
$\{\log E_s = 11.8 + 1.5 M_s\}$

Cumulative seismic moment, $\Sigma M_o = 9.8 \times 10^{18}$N.m.
$\{\log M_o = M_s + 19.2\}$

Calculated from Fault Source Model:-

Cumulative seismic moment, $\Sigma M_o = G.\Sigma d.A = 1.0 \times 10^{19}$N.m.

Tangential stress acting on fault plane, $\tau = \frac{2.G.E_p}{M_o} = 60$ MPa

Slip per event, $d = \frac{3\pi w \tau g}{8G} = \frac{60 \text{ MPa}}{\lambda}$ 3.53m

Cumulative energy dissipated during faulting, $\Sigma E = \frac{8d^2G.L.N.}{3\pi} = 3.15 \times 10^{16}$J

---

of 53, 26.5, 10.6 and 5.3 $MW.m^{-2}$ may be estimated. It is clear from the data of this study that the seismic efficiency was low and, therefore, the greater part of the energy may have been dissipated by frictional processes. It follows from equation 2.24 that for the same rise times of 1, 2, 5 or 10s maximum increases in temperature of 9964, 7045, 4456 and 3156°C respectively, may be inferred for a thin fault (ignoring heats of fusion).

Alternatively, making the gross assumption that τ_k = 30 MPa and d = 3.5 m from the data of Filson et al, $\Delta\theta$ may exceed 1000°C for fault thicknesses less than 3 cm (Fig. 2.14).

This analysis suggests that frictional melting during caldera collapse faulting is quite likely. However, in the particular case of Fernandina, important and perhaps unrealistic assumptions have been made. Those pertaining to the choice of a "Starr Fracture" model are discussed by Filson et al (1973). In estimating the temperature rise on the fault plane it has been assumed that dry faulting on a discrete fault plane has occurred. A possible fault plane solution for the Fernandina caldera collapse seems to preclude a single discrete fault plane between the blocks (Filson et al., 1973). Further, some of the available potential energy may well be lost to work done in compressing a vesicular magma body beneath the sunken caldera block.

2.6.2 Landslide Faulting

The occurence of landslide frictionite was briefly mentioned in chapter 1; it is restricted to large, catastrophic landslides involving the release of vast amounts of potential energy (Table 2.7). The effective 'rise time' of these events is thought to be of the order of 1 minute or less (Erismann, 1979; Voight and Faust, 1982), hence the rate of power dissipation is within a few orders of magnitude of that for large earthquakes (Table 2.5).

The 'problem' of large landslides is that their catastrophic rates of descent and large displacements imply very low coefficients of kinetic friction and hence kinetic shear resistance. Further, the main body of large landslide masses frequently remains coherent, unless it is shattered by impact with an obstruction in its path.

Melting (or dissociation in the case of carbonate rocks) during landsliding, like that during earthquake faulting, requires 3 conditions to be met:-

TABLE 2.7 COMPILATION OF LARGE LANDSLIDE SOURCE PARAMETERS

Name of Event	Langtang [1]	Köfels [2]	Vaiont [3]	Flims [3]	Goldau [3]	Huascaran [3]
Locality	Nepal Himalayas	Austrian Alps	Italian Alps	Swiss Alps	Swiss Alps	Peruvian Cordillera
Date	∿ 10,000 B.P.	∿ 8700 B.P.	1963	∿12,000 B.P.	1806	1970
Lithology	Felsic gneiss	Felsic gneiss	Carbonate	Carbonate	Carbonate	Ice, mud and rocks
Assumed mean density ($kg.m^{-3}$)	2.25×10^3	2.25×10^3	2.7×10^3	2.7×10^3	2.7×10^3	$\sim 1.25 \times 10^3$
Displaced volume (m^3)	3.0×10^9	2.1×10^9	2.5×10^8	1.2×10^{10}	3.5×10^7	4×10^7
Vertical travel (m)	∿ 350	350	200	1100	800	4000
Potential energy released	2.32×10^{16}	1.65×10^{16}	1.3×10^{15}	3.5×10^{17}	7.5×10^{14}	2×10^{15}
Landslide area (m^2)	3.0×10^7	1.2×10^7	-	-	-	-
Energy dissipated per unit area ($J.m^{-2}$)	7.73×10^8	1.38×10^9	-	-	-	-
Frictionite present	Yes	Yes	No	No	No	No

Sources of data: 1 Masch (1979); 2 Erismann et al (1977); 3 Erismann (1979)

(i) a large amount of the available energy (potential energy) must be converted to heat;
(ii) the heat must be dissipated over a small volume or area with respect to the total volume of the slipped mass;
(iii) there must be negligible heat loss during energy dissipation over this small volume or area.

Voight and Faust (1982) have examined the pore fluid pressure changes associted with frictional heating during landsliding, in a treatment akin to that of Sibson's (1973) for earthquake slip, and find that melting is only possible under essentially dry conditions.

For dry conditions, the equation obtained by Voight and Faust (1982) for the temperature rise due to frictional heating is identical to the 'thick fault' solution of Cardwell et al (1978) given in equation 2.23. From this solution, Voight and Faust (1982) predict that a 45 m thick slide could melt ($\Delta\theta$ = 1000°C) a 1 cm thick layer after 10 m displacement, assuming a kinetic coefficient of friction of 0.5.

Documented examples of catastrophic landslides, 2 of which involved melting, are given in Table 2.7. Voight and Faust (1982) postulate that melting may also have occurred in the Frank, Alberta, Madison Canyon, Montana and Hope, British Columbia slides - all of which are believed to have occurred under dry conditions.

Erismann (1979) and co-workers (Erismann et al., 1977) have examined how the above 3 requirements are met in both a general and a specific sense. They found that laminar and turbulent flow in the main body and the slip zone can be discounted. The absence of laminar flow within the slipped mass solves the coherency problem; and Erismann (1979) proposed a rule of lowest μ_k dominance which results in slip along a discrete plane.

The Köfels landslide has been modelled as a pendulum subjected to dry friction (Erismann et al., 1977). Using suitable differential equations of motion these authors found that a coefficient of kinetic friction of 0.15 - 0.20 satisfies best the known constraints imposed on the distance travelled and probable velocity. Scholz (1980) observed that this result is in good agreement with the result obtained by Sibson (1975), and indicates that the resistive shear stress <u>after</u> melting is non-zero. It will be attributable to the (non-Newtonian) viscous shear resistance of the melt plus clasts and possibly rock powder.

Using this value of τ_k = 0.15 and known or approximated source dimensions for the Langtang landslide (Table 2.7), Scholz (1980) has estimated that more than 2 m equivalent thickness of melt should have been produced according to the model of Cardwell et al (1978) (equation 2.23, Fig. 2.14). A 300 m long x 0.5 - 3 cm thick continuous layer of frictionite is present at Langtang but field observation apparently precludes loss of large amounts of melt by injection veining into the footwall and hanging-wall rocks (Masch, 1979). Because of this and because of the petrographic character of frictionites, which are locally a turbulent admixture of glass and rock powder (Erismann et al., 1977; Masch et al., 1985), Scholz suggested that the transformation of frictional heating energy into temperature rise might be only 10% efficient. The additional heat energy would be lost to the surroundings from the turbulent powder/melt mixture with almost infinite thermal conductivity.

Extending this argument to earthquake faulting (cf. 'acoustic fluidization' model of Melosh, 1979), Scholz (1980) concluded that if turbulent motion of gouge occurred then frictional heating models of the type employed by Cardwell et al (1978) would underestimate the shear stress acting on faults. A more realistic explanation for the apparently inefficient conversion of frictional heating energy to temperature rise might be a temperature-enhanced increase in pore-fluid pressure thereby reducing the value of τ_k and hence $\dot{Q}$ (section 2.5.2).

2.7 Aseismic Shear Heating

Combined field and microstructural observations indicate that pseudotachylyte is occasionally generated penecontemporaneously with mylonites in ductile shear zones undergoing aseismic shear (e.g. Sibson, 1980b; Passchier, 1982a). The question arises as to whether aseismic shear heating can lead to melting. A number of studies have modelled aseismic shear heating (e.g. Turcotte and Oxburgh, 1968; Yuen et al., 1978; Brun and Cobbold, 1980; Fleitout and Froidevaux, 1980) which yield the following qualitative conclusions, for velocities corresponding to steady state plate motions (i.e. 1 - 10 $cm.yr^{-1}$):-

(i) maximum temperature is obtained at the centre of the shear zone, its magnitude being a function of rock type rather than time;

(ii) thermal conduction causes widening of the region of elevated

temperature and hence the shear zone, proportional to the square root of time; shear stress decreases accordingly;
(iii) for homogeneous rock, sufficient softening occurs well below the solidus, allowing strain to be accomodated by intracrystalline plastic deformation (and/or grain boundary sliding), which precludes melting.

Fleitout and Froidevaux (1980) have specifically examined 3 cases which might lead to melting: narrow shear zones; shear relaxation in a visco-elastic medium; and shear across a stratified medium. For lithologies and flow laws pertaining to quartzo-feldspathic crustal rocks (where most pseudotachylytes are found) it is clear from their results that aseismic shear melting is extremely unlikely. These results support the hypothesis of Sibson (1980b) that pseudotachylyte formed penecontemporaneously with mylonite is the product of transient seismic slip (i.e. earthquakes) in an otherwise aseismic environment.

CHAPTER 3 CHARACTERIZATION OF FAULT-ROCKS AND THEIR FORMATION IN MAJOR FAULT ZONES OF CONTINENTAL CRUST

3.1 Introduction

Major fault zones, once established as loci of weakness in the continental crust by some form of strain or displacement softening, are extensive (in at least 2 dimensions) and frequently long-lived - of the order of 10^7 - 10^9 Ma (e.g. shear belts in W Greenland described by Bak et al., 1975). As a consequence of this, considerable spatial and temporal variations in style of faulting and deformation mechanism occur which reflect the changing mechanical behaviour of (fault) rocks. The mechanical behaviour of fault-rocks is a function of many variables including: the nature of the macroscopic stress field, effective confining pressure, temperature, fluid pressure and composition, strain or displacement rate, strain or displacement, permeability and porosity, and not least rock type. Obviously any approach to a comprehensive understanding of the nature and evolution of fault zone deformation must therefore draw on a large database. Such data are available from 3 sources:-

(i) study of active fault zones of which (for largely financial reasons) the largest database exists for the San Andreas Fault;
(ii) study of (usually) inactive, ancient exhumed fault zones;
(iii) rock deformation experiments, especially those designed to simulate fault zone deformation.

The information from these sources may be integrated to provide a conceptual model for a fault zone as indicated in Fig. 3.1. Since overlap exists in terms of input into the model, between active and ancient or inactive fault zones no discrimination is made between them in the diagram. The output - i.e. the conceptual model of a major fault zone - may be adapted to 2 purposes:-

(i) to provide a complete geological description of an ancient fault zone;
(ii) to provide a dynamic description of an active fault zone, ultimately perhaps, permitting accurate earthquake prediction.

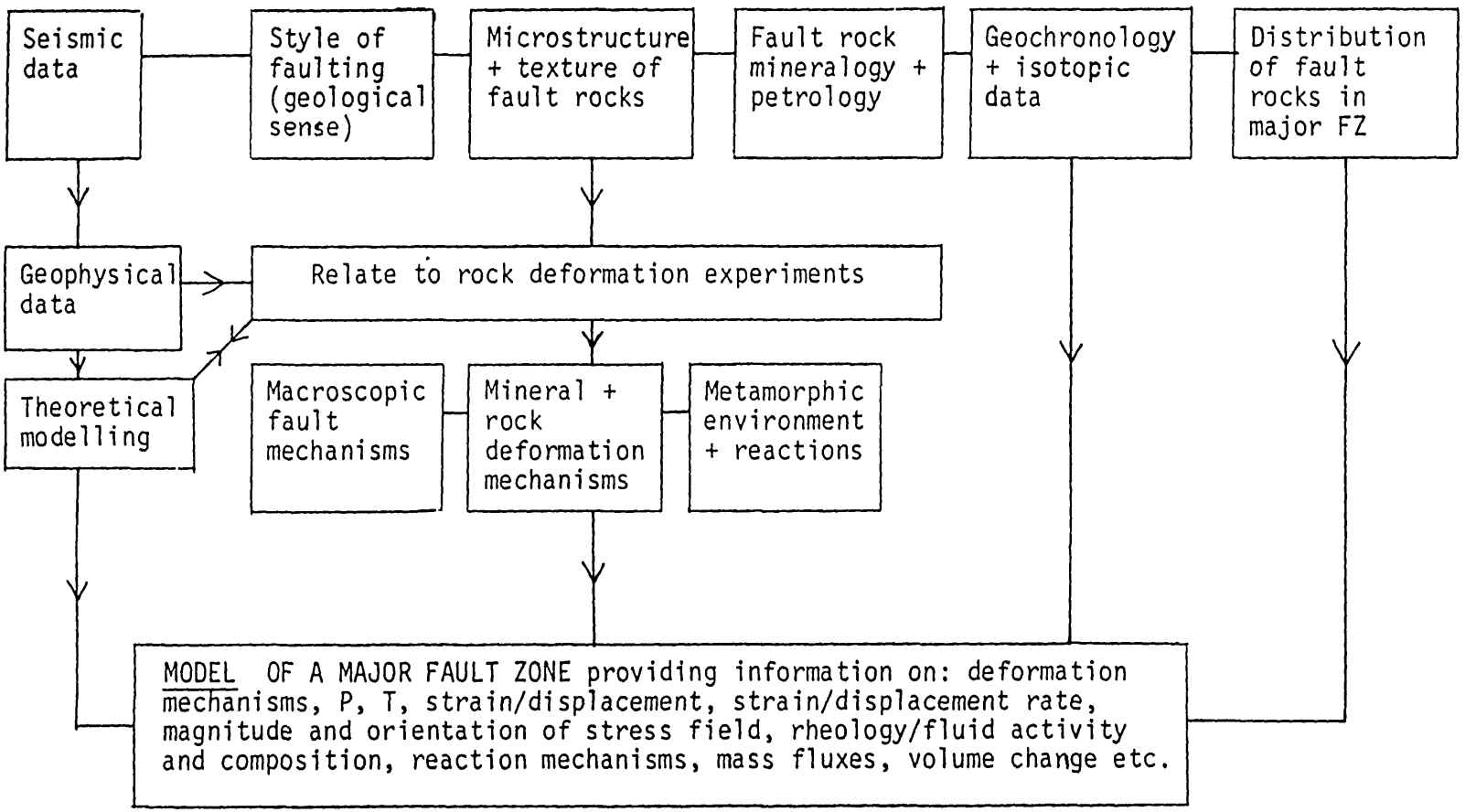


Fig. 3.1 Flow diagram illustrating information required to construct a conceptual model of a major fault zone (modified from Sibson, unpubl. data, 1979)

Some of the 'boxes' of Fig. 3.1 provide the section headings for this chapter. It is not intended to provide a comprehensive review but to provide a working framework of definitions with emphasis laid on specific aspects relevant to this study.

3.2 Textures and Microstructures of Fault-rocks: Deformation Mechanisms

The textures and microstructures of fault-rocks provide information about the deformation mechanisms active during their formation.

3.2.1 Brittle Deformation and Cataclasis

Brittle deformation is largely concerned with the process of cracking and crushing which result in particle size reduction. Cataclasis encompasses both the brittle deformation mechanisms and the movement which accompanies them. Cataclasis has been defined both on a grain scale (e.g. Handin, 1957) and on a larger scale, e.g. Stearns (1968, p.79) who states: "...once a rock layer loses cohesion along fractures and separates into discrete parts, no matter what their size, it can begin to flow by displacements of constituent parts relative to one another accompanied by mechanical granulation, breaking or crushing". Cataclastic flow is a macroscopically ductile process.

The important features of cataclasis may be summarized (Blenkinsop,1982):-

(i) distributed fracturing involving shear, extensional and/or hybrid fractures;
(ii) reduction in grain/aggregate size by fracture;
(iii) rotation and translation of grains/aggregates;
(iv) dominance of frictional sliding;
(v) crystal plasticity is subordinate or absent.

Because dilatancy accompanies cataclasis, the latter is a pressure-sensitive deformation mechanism.

3.2.2 Intracrystalline Plasticity: Dislocation Creep

With increasing confining pressure and temperature of a rock subjected to deviatoric stress, brittle behaviour gives way to plasticity when the stress required for frictional slip exceeds the long term creep strength of the rock. (The initiation of ductile shear zones has been attributed to softening by either diffusive mass transfer (Beach, 1980) or an initial phase of cataclastic deformation (White, 1982).) TEM studies of natural mylonites (e.g. Bell and Etheridge, 1973; White, 1973; White, 1976) and experimental analogues (e.g. Burrows et al., 1979) suggest that dislocation creep is the dominant deformation mechanism involved in the formation of quartzo-feldspathic mylonites in ductile shear zones. Dislocation creep overtakes brittle failure in quartz at temperatures around 300°C (Voll, 1976; Tullis and Yund, 1977) and in plagioclase feldspar at 450° C (Voll, 1976).

Dislocation creep involves a combination of dislocation glide and recovery. At low temperatures, gliding dislocations may be pinned by obstacles, such as voids, bubbles and dislocation tangles, causing an increase in dislocation density and stored strain energy which results in strain hardening. Thermally activated recovery, involving cross-slip and climb of dislocations, reduces the strain energy by dislocation disentanglement, annihilation and re-arrangement into low energy configurations such as sub-grain walls (White, 1976). Steady state dislocation creep involves a balance between the rate of strain hardening and the rate of recovery.

When recovery is unable to reduce the strain energy rapidly enough, this may be accomplished by recrystallization to new strain-free grains. With continued deformation the new grains may also be strained and undergo further recrystallization. This process of dynamic recrystallization, which usually involves grain size reduction (Bell and Etheridge, 1973), is distinct from static or annealing recrystallization which often involves grain growth (e.g. Hobbs, 1968).

Less commonly, at least in quartzofeldspathic fault-rocks, intracrystalline plastic deformation may be accomplished by twinning.

3.2.3 Diffusive Mass Transfer

Diffusive mass transfer may occur by diffusion creep or pressure

solution. Two types of diffusion creep are recognized (Poirier, 1985). Intracrystalline diffusion (Nabarro-Herring creep) is favoured by high temperatures and small grain sizes. Grain boundary diffusion (Coble creep) may occur at lower temperatures owing to its smaller activation energy. Under certain conditions, grain boundary sliding accomodated by diffusion (White, 1971) may be a significant deformation for achieving high strains.

Deformation by pressure solution involves (Durney, 1976): (i) pressure-enhanced dissolution at more stressed grain boundaries; (ii) solute transport through an intergranular film; (iii) precipitation of solute on less stressed grain boundaries (or pore walls). The importance of pressure solution during fault-rock evolution is poorly understood. However, in addition to hydrothermal mineralization (Stel, 1981) pressure solution offers a ready explanation for the induration of cataclasites. Further, Rutter and Mainprice (1978), Turcotte (1981) and Angevine et al (1982) have suggested that pressure solution creep may control steady state movement at deeper levels in some fault zones.

3.3 Textures and Microstructures of Fault-rocks: Classification

The history of controversy surrounding fault-rock terminology and classification was precied in chapter 1 (see White, 1982; Wise et al., 1984; Mawer, 1985 for recent discussion). It is not the writer's wish to further that controversy here but simply to present two alternative approaches.

The widely-used (e.g. Watts and Williams, 1980; Passchier, 1982a) non-genetic, textural scheme of Sibson (1977b) is shown in Fig. 3.2. The principal advantages of this field based scheme are that it relies on two easily identified discriminants - foliation and cohesion - and the simply quantified parameter of matrix to clast ratio. However, serious objections to this scheme are posed by the recognition of foliated gouges (e.g. Hall, 1982) and cataclasites (e.g. Chester et al., 1985) - where the latter are defined by deformation mechanism. Similarly, the terms 'random-fabric' and 'glassy' applied to pseudotachylytes in Sibson's classification appear from the present study to be quite inappropriate.

The alternative approach is to classify the fault-rocks entirely according to the dominant deformation mechanisms active during their formation. Obee (1985) provides the most recent and satisfactory

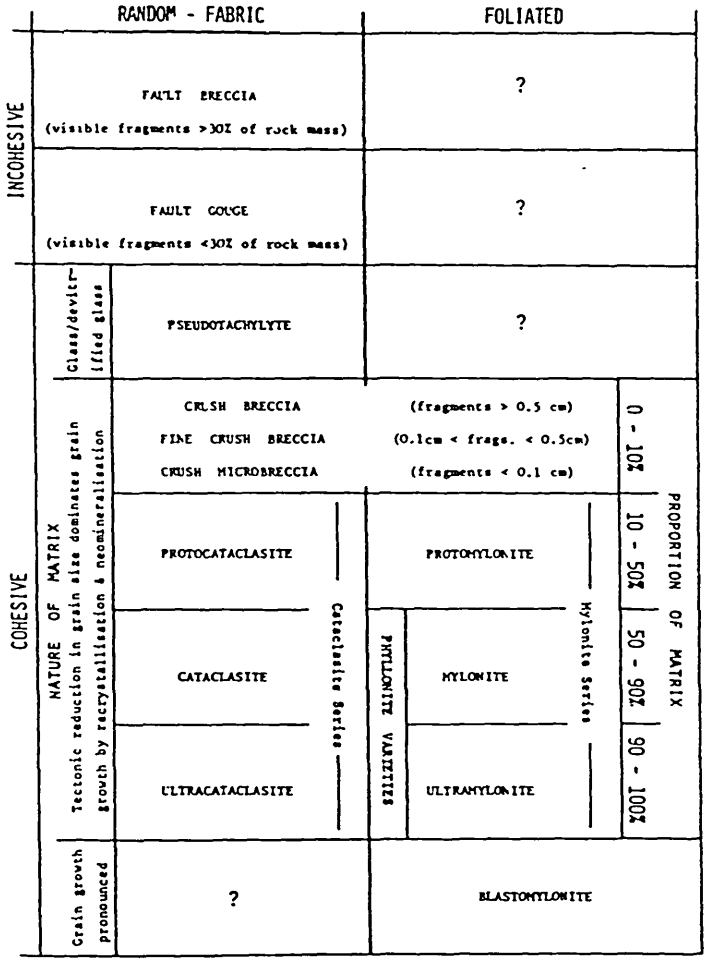


FIGURE 3.2 Textural classification of fault-rocks. From Sibson (1977b, Table 1, p.192).

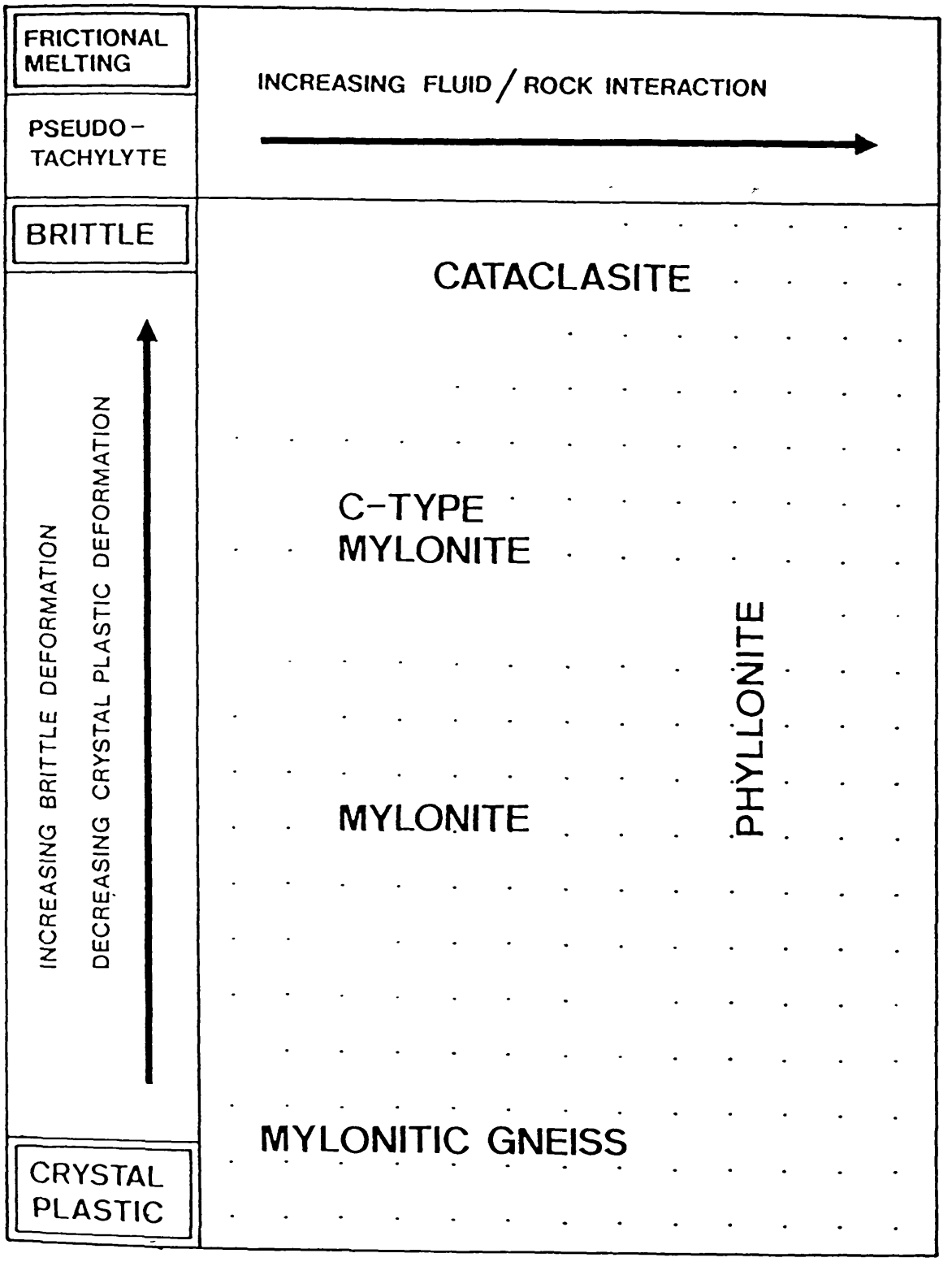


FIGURE 3.3 Mechanistic classification of fault-rocks; shaded area encompasses fault-rocks that are usually foliated; c-type mylonite as defined by White (1982). From Obee (1985, Fig. 1.2, p.19).

example of this approach (Fig. 3.3). The objection to this type of scheme is that it can be even more difficult to apply in the field.

Notwithstanding the objections, by combining these schemes, five distinctive fault-rock groups emerge:-

(i) incohesive fault-rocks which are 'sampled with a trowel rather than a hammer'; they may be foliated or unfoliated;
(ii) cataclasite series fault-rocks, largely formed by cataclasis; they may be unfoliated or, more rarely, foliated but generally lack a crystallographic preferred orientation;
(iii) mylonite series fault-rocks largely formed by crystal-plastic processes; they are generally L-S tectonites;
(iv) phyllonites which contain a significant proportion of phyllosilicate minerals and form by a combination of crystal-plastic and brittle deformation mechanisms together with substantial fluid-rock interaction; they are usually strongly retrogressed relative to their wall rocks.
(v) pseudotachylytes which possess glassy, devitrified or holocrystalline matrix - evidence of having cooled from a melt; believed to form by frictional melting.

3.4 Distribution of Fault-rocks in Major Fault Zones

Major fault zones, both active and inactive, frequently contain juxtaposed or interlayered cataclasites and mylonites. The data of section 3.2 suggests that it is unlikely that they formed contemporaneously at the same depth.

Two complementary models explaining the distribution of fault-rocks in ancient exhumed major fault zones were proposed in 1977. Across the Outer Hebrides Thrust (OHT), which shows a large component of reverse slip, Sibson (1977a and b) noted an increasing ratio of mylonites/cataclasites (and pseudotachylytes) passing up into the hanging wall. This he interpreted as reflecting a palaeodepth (i.e. P-T) gradient reorientated to a sub-horizontal attitude by reverse slip fault motion. In major shear belts of W Greenland, in which strike-slip dominates, Grocott (1977a and b) attributed the juxtaposition of mylonites with cataclasites and pseudotachylytes to uplift - i.e. the passage of the present erosion level through the brittle-plastic transition (s.l.) during dominant strike-slip displacement.

In both examples the authors conclude that cataclasites and pseudotachylytes formed in a seismogenic regime extending to ~15 km depth, overlying an aseismic, ductile shear zone in which mylonites formed. As uplift and/or reverse slip fault motion proceeded, so mylonites formed in an aseismic regime are subjected to brittle deformation.

The combined model has been applied by Sibson et al (1979) to the active, transform Alpine Fault Zone (AFZ) of South Island, New Zealand. This right-lateral oblique/reverse slip fault also shows an increasing ratio of mylonite to cataclasite passing up into the hanging wall. In the AFZ, pseudotachylyte cuts both cataclasite and mylonite, and gouge cuts all other fault-rock types. The pseudotachylyte is referred to seismic movements occurring in the relatively shallow brittle regime. All 'active' fault strands visible at the surface contain gouge (Sibson et al., 1979).

In spite of detailed direct sampling as well as numerous indirect and remote studies of the San Andreas Fault Zone (SAFZ) - including associated faults - the distribution of fault-rocks in this active, dominantly strike slip, major fault zone is poorly constrained. It is generally accepted that fault motion and deformation at depth (>15 km) along the SAFZ takes place by aseismic creep with formation of mylonites (see Prescott and Nur, 1981 for review). The nature and distribution of fault-rock types in the upper 15 km thick, seismogenic zone is however hotly debated (cf. Wu et al., 1975; Allen, 1979; J.R. Anderson, 1980; J.L. Anderson et al., 1980; Logan et al., 1981; J.L. Anderson et al., 1983). Pseudotachylyte has not been reported from the San Andreas fault to date.

3.5 Fault-rock Mineralogy, Petrology and Geochemistry

Studies of fault-rock mineralogy, petrology and geochemistry provide information on the metamorphic environment, fluid-rock interaction and reaction mechanisms during deformation of fault-rocks. In addition, the potentially important effects of chemical reaction (mineral transformation, grain nucleation and growth, etc.) on deformation mechanisms and kinetics - and hence mechanical behaviour of fault-rocks - can be studied. These effects include pressure solution, stress corrosion, reaction-enhanced ductility and reaction-enhanced embrittlement, which imply 'feedback' between reaction and deformation.

The paucity of data on mylonite mineral and bulk-rock chemistry noted by Carreras and White (1980, preface to J. Struct. Geol. 2, p.1) is matched by a similar dearth of data for cataclasite and gouge (F.T. Wu, pers. comm., 1984). A general summary is given here; the mineralogy, petrology and geochemistry of pseudotachylytes are examined in detail in chapters 5 and 6. It is emphasized that the syn-deformational chemical changes in fault-rocks encompass a complete P-T spectrum from weathering to high grade metamorphism.

1) Gouge. The mineralogy and petrology of clay-rich gouges is reviewed fully by Hall (1983) with the prime observation that clay crystallinity increases with depth of burial/formation of the gouge. In clay-poor gouge from the SAFZ of southern California, Anderson et al (1980) found no bulk chemical change for 11 elements between a tonalite protolith and the gouge. An increase in LOI of 2.2% from protolith to gouge was attributed to hydration. More significantly Anderson et al (ibid.) found that the mineral chemistries were not re-equilibrated to the assumed low P-T conditions during faulting.

2) Cataclasite. The few geochemical studies of cataclasite formed in crystalline rocks indicate the following:-

(i) mechanical mixing of protolith bulk chemistries dominates (Kasza, 1981; Anderson et al, 1983);
(ii) syn-faulting chemical equilibrium is rarely achieved, thus mineral chemistries are not significantly altered from those of the protolith (Anderson et al, 1983).
(iii) metamorphic alteration and neo-mineralization is restricted to grain boundaries, fractures and other defects together with any pore space; such alteration indicates sub-greenschist facies P-T conditions (Moore, 1980; Anderson et al, 1983).

3) Mylonite. The mineral chemistries of some mylonites indicate more or less complete re-equilibration to the metamorphic environment obtaining during deformation. In mylonites formed from crystalline protoliths the metamorphism is usually retrogressive (e.g. Beach, 1980 and references therein), although 'prograde' metamorphism during mylonitization of an amphibolite facies metagabbro has been described by Brodie (1981). In a study of mylonites cutting a metabasalt and an adamellite deformed under greenschist and amphibolite facies

conditions respectively, Kerrich et al (1977) observed:-

(i) in the lower temperature shear zone deformation was accommodated by pressure solution with bulk chemical and volume change;
(ii) in the higher temperature shear zone deformation was accommodated by mass-conservative dislocation creep with near isochemical and isovolumetric behaviour.

These observations may be expected to apply widely although subject to modification according to the fluid regime and rock type (cf. Kerrich et al, 1980).

Detailed studies of mineral-chemical changes occurring during mylonitization have been made by Brodie (1980; 1981), Beach (1973; 1976; 1980), Borges and White (1980) and Brown et al (1980).

3.6 A Conceptual Fault Zone Model

A qualitative model of a major fault zone in continental crust which utilizes the observations described above is illustrated in Fig. 3.4. Two aspects of this model require comment.

Firstly, the distribution with depth of fault-rock type, deformation mechanism, style of faulting, shear resistance, strain energy density and degree of chemical equilibrium will vary within a single fault zone and between different fault zones. It is the present writer's opinion that the most important factors controlling this distribution are rock type and the amount and accessibility (i.e. a function of permeability and porosity) of (usually hydrous) fluids.

Secondly, actual fault zones are demonstrably much more complex than the model because of their long life and large dimensions.

3.7 Terminology for the Field Description of Pseudotachylyte Veins

A scheme for the field description of pseudotachylyte veins adopted from Sibson (1975), modified and Francis and Sibson (1973), is shown in Fig. 3.5. The descriptive terminology of Fig. 3.5 is entirely geometric and largely self-explanatory; the distinction between concordant and discordant veins being made according to their relative orientation with respect to the gneissic foliation. Additional terms can be added where relevant: for example, thick (5 - 10 cm) planar lenses of sub-vertical orientation and with long traces (5+ m) may be

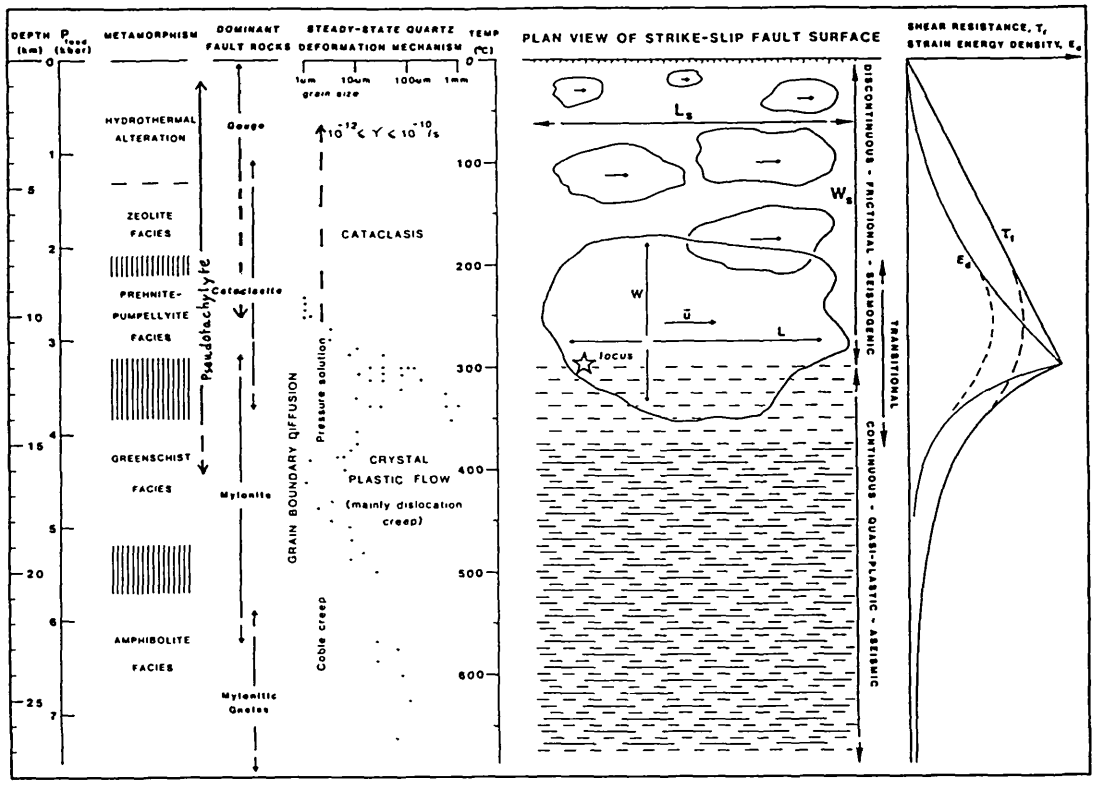


FIGURE 3.4 A conceptual model for a fault zone in continental crust which schematically relates fault-rock type to various physical and environmental parameters. Modified slightly from Sibson (1983) - see reference for details and sources of data. The probable depth range of pseudotachylyte has been added. Also, the field of gouge generation has been extended to greater depths, and the field of pressure solution to shallower depths based on this author's views and observations.

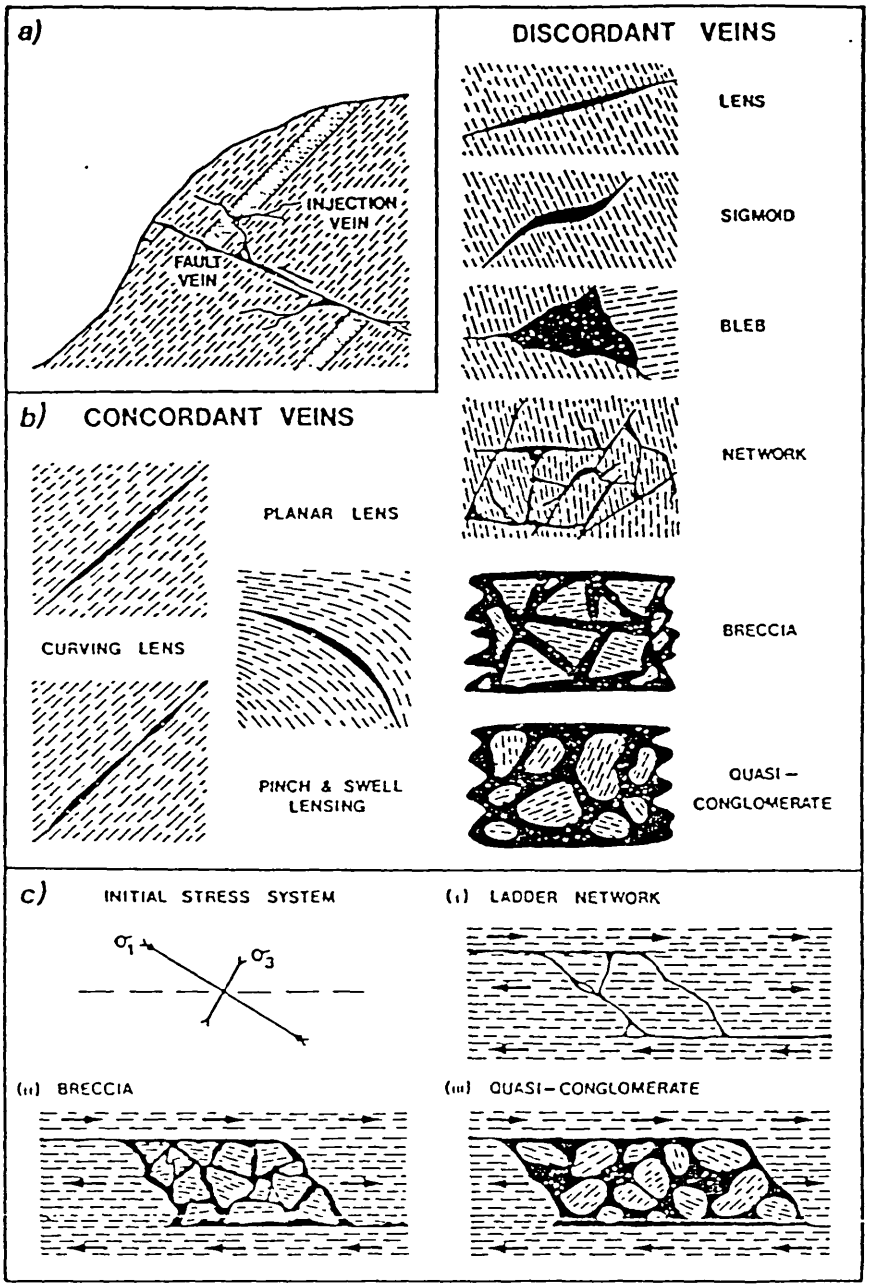


FIGURE 3.5 Classification of pseudotachylyte veins. From Sibson (1975, Fig. 2, p.772).

termed pseudotachylyte dykes.

Using geometric criteria Sibson (1975) recognized 2 genetic classes of veins (Fig. 3.5a):-

1) Fault Veins (FV) are pseudotachylyte generating surfaces (or volumes) characterized by the following features:-

(i) where the FV's are discordant or a suitable discordant marker intersects the FV a shear separation is visible;
(ii) they show planar habit, frequently with pinch and swell structure such that the thickness varies from vanishingly narrow (barren FV's) to a few cm;
(iii) their terminations are rarely exposed suggesting considerable areal extent;
(iv) dilational injection veins (IV) showing little or no shear separation intersect, often orthogonally, without crossing, the FV generating surface.

A further important distinction is made between 'single jerk' and 'multi-jerk' FV's relating to a single and several episodes of movement respectively (Sibson, 1975). Recognition of the latter in the field, perhaps augmented by thin-section observation, is dependant upon observation of features such as brecciated pseudotachylyte.

2) Injection Veins (IV) contain pseudotachylyte injected away from the FV generating surface. In addition to the features described above they are characterized by:-

(i) a more irregular form, usually thicker than FV's;
(ii) blind terminations are often visible (e.g. Fig. 3.5a) suggesting smaller planar dimensions than FV's.

The gneissic foliation is expected to be a plane of weakness (Borg and Handin, 1966) and for a fixed orientation of the principal stress axes, preferential shear failure along the foliation is likely for a fairly wide range of orientations of the foliation. Thus in many occurrences of pseudotachylyte in gneissic host rocks, concordant FV's are the rule. In the absence of suitable discordant markers (which might be earlier generations of IV's), elucidation of FV-IV relationships must rely on the geometric criteria outlined above.

Inferences concerning displacement vectors should be treated circumspectly and all the geological evidence invoked to assist in this.

Figure 3.5c illustrates Sibson's (1975) model for the generation of quasi-conglomerate in a continuous sequence passing through network veins and breccia to quasi-conglomerate with increasing displacement and pseudotachylyte/clast ratio. Note, for the principal stress orientation shown, the quasi-conglomerate structure will only be expected to form for right-stepping fault segments.

The classification detailed here is based on the study of pseudotachylyte veins in layered or foliated rocks. As such it is applicable to all the localities of this study and has been successfully applied (with slight modification) to other areas (e.g. Grocott, 1981). The applicability of FV-IV terminology to the rarer occurrences of pseudotachylytes in unfoliated rocks is uncertain however. The descriptions and illustrations of the Vredefort pseudotachylytes (e.g. Shand, 1916; Hall and Molengraaf, 1927) and the Canadian examples described by Philpotts (1964) do not appear to lend themselves fully to this terminology.

The origins of the different types of pseudotachylyte vein are considered further in the next chapter.

CHAPTER 4 FIELD STUDIES

4.1 Introduction

The following objectives were identified as being potentially rewarding and pursued in field studies:-

(i) the description and attempted explanation of the geometry of pseudotachylyte vein systems; this has been attempted by 4 previous workers (Sibson, 1975, 1977a; Grocott, 1977a, 1981; Passchier, 1982a, 1982b; Macaudiere and Brown, 1982);
(ii) the effects of pre-existing structure and lithology on pseudotachylyte faulting;
(iii) the relationship between minor, meso and macro scale structures in pseudotachylyte faulting and correlation with regional kinematic frameworks;
(iv) the attempted elucidation of earthquake source parameters related to pseudotachylyte faulting.

To these ends mapping was conducted on the following scales:-

1:1-1:100 by means of string grid photography and sketching, and section-measuring using a surveyor's tape;
1:2500 detailed mapping using O.S. plans;
1:10000 basic mapping using O.S. maps and photographs;
1:25000-1:50000 reconnaissance mapping using O.S. maps.

The main area of study, the Outer Hebrides Thrust Zone, is reasonably accessible and perhaps the classic locality for fault-generated pseudotachylytes. Pseudotachylyte faulting in Lewisian Gneisses has also been examined in Tiree, Inner Hebrides and Gairloch, NW Scotland. These latter examples together with other localities visited including the Silvretta Nappe and the Ivrea Zone will not be described although some of the ideas put forward in this chapter draw on observations in these places.

4.2 The Outer Hebrides Thrust

The Outer Hebrides comprises an arcuate archipelago of Precambrian Lewisian Gneisses trending NNE for some 200 km and

situated to the W of the Minch Basin off NW Scotland (Fig. 4.1). A major low-angle eastward-dipping fault, separates gneiss from gneiss and extends along the eastern seabord of the islands (map 1). Faultrocks associated with the fault include cataclasites, phyllonites and mylonites, and pseudotachylytes in approximate order of volumetric abundance.

4.2.1 Background Geology of the Outer Hebrides Lewisian Gneisses

The geology of the Outer Hebrides is shown chronologically in Table 4.1 and graphically in map 1. This geological history deduced by the combined efforts of a number of workers (e.g. Dearnley, 1962; Dearnley and Dunning, 1968; see Sibson, 1977a for later references) is closely similar to the classical interpretation of the scottish mainland Lewisian Gneisses (Table 4.1; Peach et al., 1907; Sutton and Watson, 1952).

To the W of the OHT the gross structure is largely determined by the attitude of Laxfordian F_3 folds (Table 4.2, map 1; Coward et al., 1970): large upright, open antiforms trending NW with cores of low to moderate finite strain are separated by tight synforms with high finite Laxfordian strain (map 1). To the E of the OHT considerable areas of Scourian meta-igneous rock are exposed (map 1; Coward, 1972).

Lithologically distinct terrains are divided by the thrust and by a NW-SE line through the Sound of Harris. In the southern islands, and also in northern Lewis, the rocks to the W of the thrust are largely monotonous amphibolite facies 'grey gneisses' (map 1) with the mineral assemblage: plagioclase (oligoclase/andesine) + quartz + hornblende ± biotite ± clinopyroxene ± K-spar ± accessories. Banding defined by modal variation in mineralogy and mainly concordant Scourie dykes was imparted during the Laxfordian F_2 event (Table 4.2). Structurally and lithologically distinct areas of Scourian metasediments (map 1) are characterized by aluminous phases: biotite, garnet, sillimanite and occassionally kyanite.

4.2.2 Background Thrust Geology

The history of study of the OHT is fully reviewed in Sibson's thesis and will not be duplicated here. Mention must however be made of the pioneering work of Jehu and Craig (1923, 1925, 1926, 1927, 1934) who presented the first systematic study of Outer Hebrides

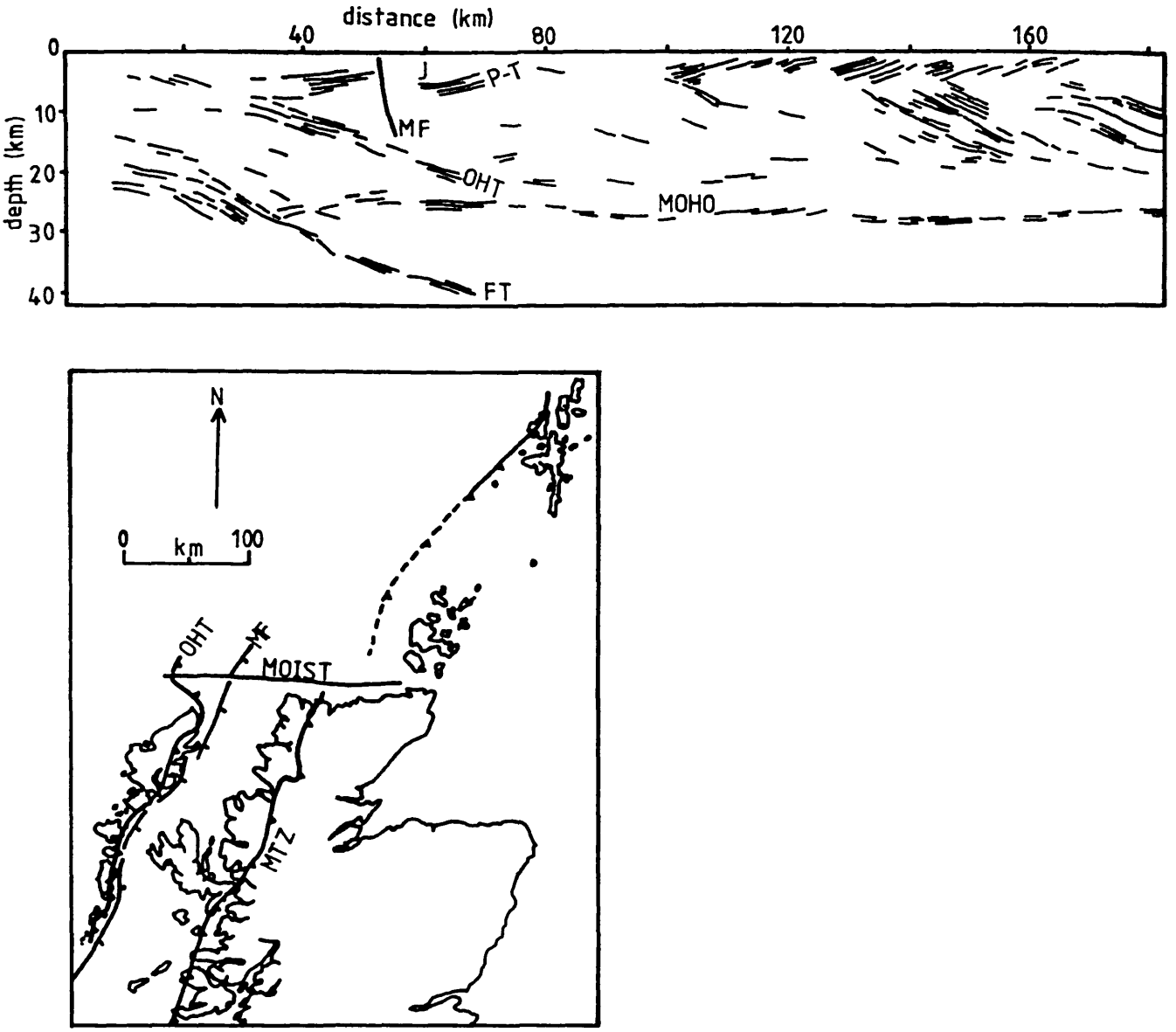


FIGURE 4.1 Tectonic setting of the Outer Hebrides Thrust (after Smythe et al., 1982).

(a) Interpretation of MOIST seismic reflection profile. FT = Flannan Thrust; J = Jurassic; MF = Minch Fault; OHT = Outer Hebrides Thrust; P-T = Permo-Triassic.

(b) Tectonic map. MTZ = Moine thrust zone.

TABLE 4.1 GENERAL HISTORY OF LEWISIAN COMPLEX

Time (Ga)			Major Events		Local Events	
					Mainland	Outer Hebrides
0			Tertiary dykes			
-			Minch normal faulting			
-			Permo-Comb dykes			Stornoway Beds deposited
-						
0.5			Moine Thrust	CALEDONIAN OROGENY	Moine Thrust	Outer Hebrides Thrust
-						
-						
-			Torridonian Sediments			
1.0						
-			Uplift and cooling of Lewisian complex		NW-trending crust zones	?
-						
1.5	L	Laxfordian	polyphase deformation, metamorphism and igneous activity			
-	E					
-	W					
2.0	I		scourie dyke intrusion			
-	S					
-	I		polyphase deformation, metamorphism, and igneous activity			
2.5	A	Scourian			Loch Maree + Gairloch sediments	
-	N					
-			formation of continental crust			deposition of sediments, S. Harris complex
3.0						

TABLE 4.2 LAXFORDIAN FOLD PHASES WEST OF THE THRUST BASE IN THE SOUTHERN ISLANDS (after Sibson, 1977a)

Phase	Characteristics	Metamorphism
F_4	locally developed; broad warps on W coast, isoclinal folds beneath thrust on S. Uist; absent in N. Uist and Harris; axial trends ENE to SE.	hydrous amphibolite facies metamorphism with variable but widespread migmatization; garnet mostly retrogressed; recrystallization outlasted deformation
F_3	∿ coaxial with F_2; large upright open antiforms, tight cuspate synforms with moderate plunge to NW; locally modified by F_4; minor structures highly variable.	
F_2	widespread, originally flat-lying tight to isoclinal folds plunging NW; main Laxfordian fabric forming event.	recrystallization at high-amphibolite facies, locally granulite facies condition; abundant garnet
F_1	folds rarely seen, deformation responsible for pre-F_2 fabrics in Scourie dykes.	

geology. In particular, Jehu (1923) realized at an early stage that "...the flinty crush phenomena are found in association with crush zones and shear lines..." (ibid, p.405) and that "...partial fusion of the mashed and ground down materials..." (ibid, p.406) had occurred.

In plan the OHT consists of 3 contiguous arcs, converse to the W, linking Barra and its adjacent islets, the Uists and South Harris, and North Harris with Lewis (map 1). At outcrop thrust zone topography is reflected by the ridge of hills traversing the E side of the southern islands and rising to 620 m. The thrust zone consists of a packet of imbricated slices of gneiss and faultrock or crush-melange (map 1) - some 1000 m thick in Barra and increasing in exposed thickness to the N. The average dip of the thrust plane is about 25°E. Seismic reflection profiling indicates that the thrust packet dips at this angle until it reaches, but does not cut, the moho at 25 km depth (Smythe et al., 1982; Fig. 4.1).

Suitable markers for determining the slip vector across the OHT are notable for their absence. Using 1 direct method (pertinent to the main thrust plane in Barra only) and 3 indirect methods Sibson (1977a) has estimated the finite reverse dip slip displacement of the thrust zone to be 10 ± 5 km with translation from ESE to WNW (i.e. normal to the overall strike). For an original dip of the thrust envelope of 25° this implies a vertical displacement of 4.2 ± 2.1 km. A moderate or large component of strike slip displacement has been postulated for parts of the thrust zone in Barra (Francis, 1969) and South Uist (Coward, 1969). It is also possible that rotation and transform type movement discordant to the NNE strike may have occurred. Assuming present day, time-averaged plate displacement rates of 1-10 $cm.yr^{-1}$, Sibson (1977a) has suggested that thrusting may have been achieved in the short time span of 10^5-10^6 years.

Sibson (1977a) concluded from his field studies that:-

(i) from W to E across the strike of the thrust zone there is a change from brittle pseudotachylyte faulting on discreet planes of dislocation to ductile shear zones with greenschist facies phyllonites (map 1); this palaeotemperature gradient is believed to have arisen through upward transport of the isotherms on the hanging wall region (to the E) during thrusting, perhaps with a minor contribution from shear heating;

(ii) from S to N along strike of the thrust zone there is a progressive decrease in the ratio of brittle to plastic deformation,

attributed to a deeper level of erosion prevailing in the N.

The deformation history recognized by Sibson (1977a) along much of the length of the fault is given in Table 4.3. This chapter will concentrate entirely on the 'forethrusts' W of the main thrust base because of their relatively simple geometry and faultrock associations of the former compared to the jumble of crush melange in the main thrust zone. Sibson believes the normal dip-slip (D_2 lag-sliding, Table 4.3) to have resulted in displacements of substantially smaller magnitude than the thrust sense movements. This is however an area of active research (S.H. White and J. Glasser, pers. comm., 1986).

The age of the thrusting is constrained geologically within the limits late Laxfordian to pre- Permian dyke intrusion (Sibson, 1977a). Radiometric age dating of Outer Hebrides fault-rocks is discussed in Appendix A1.

4.3 Greian Head, Barra

The main thrust on Barra has a curvilinear trace, convex to the NW (map 1); this form may be attributable to either a listric shape for the thrust (Francis, 1969) or alternatively the presence of an E-W transform segment in N Barra. To the W of the main thrust, significant pseudotachylyte faulting has occurred on the peninsulas of Greian Head and Tangaval (map 1). The main thrust has been described in some detail by Francis (1969), thus following Sibson's (1977a) observation that "...more information about the mechanics of brittle faulting and pseudotachylyte formation ..." can be got from areas to the W of the main thrust, attention is given here to the western areas.

4.3.1 General Geology

Greian Head peninsula is ~1.5 km long from E to W and ~1 km wide at its greatest breadth, attaining a maximum height of 97 m close to its eastern, landward margin.

The peninsula is composed of massive to well-foliated and banded grey gneisses, locally granitic in aspect, together with amphibolite bodies up to 50+ m thick that are broadly concordant to the foliation. The more massive amphibolite bodies present a rough impression of large boudins around which the foliation in the grey gneisses has been wrapped. At the western extremity of the peninsula (close to A in map

TABLE 4.3 OUTER HEBRIDES THRUST DEFORMATION HISTORY
(after Sibson, 1977a)

Event	Gross Structures	Fault-rock, fabric and metamorphism: at shallow level	at depth
D_3	late faulting at competency boundaries and along sub-vertical E-W lineaments.	crush breccia, gouge and hydrothermal quartz; supra-greenschist facies environment	(n.b. D_3 affects deep fault rocks exhumed subsequent to D_2).
D_2	low-angle ($\sim 25^0$) normal (oblique?) dip slip faulting	lag-sliding, extensional microfaulting; cataclasite formation; sub-greenschist facies environment.	lag-sliding in ductile SZ's forming down-dip verging folds; greenschist facies
D_1	low-angle ($\sim 25^0$) reverse (oblique) dip slip faulting	development of main imbricate crush zones; pseudotachylyte-cataclasite series rocks; sub-greenschist facies environment.	thrust sense mylonitic SZ's emphasizing and cutting early cataclastic foliation; greenschist facies recrystallization in high strain areas.
D_0	initiation of low-angle fault/SZ; development of fabric, especially by enhancement of gneissic foliation	brittle pseudotachylyte faulting in 'fore-thrusts' to W of main thrust base; microfault chopping and crushing	crushing, development of early cataclastic foliation; partial retrogression of amphibolite facies to greenschist facies.

↑ STRAIN SOFTENING

2) the gneisses are locally agmatitic with balls of verdant hornblendite 'swimming' in sub-isotropic pink granite-gneiss. This textural-mineralogical relationship is probably an expression of late-Laxfordian migmatization (Table 4.1).

Structurally, Greian Head occupies a shallow NNE-dipping limb region within the major Laxfordian F_3 fold pattern (map 1); poles to the foliation defining a strong maximum (map 2). Meso- and minor scale folding attributable to the major Laxfordian deformations (Table 4.2) are poorly developed. Minor F_3 folds showing S or M symmetry and plunging NW (vergence consistent with the regional F_3 fold geometry) occur sporadically; open F_4 folds plunge gently E. Orientation data for F_3 and F_4 folds are given in Fig. 4.2.

The entire peninsula is cut by a series of ~WNW and ~N-trending lineaments and fractures. Many of these correspond to Tertiary basaltic dykes, sometimes exposed but more usually largely removed by erosion. Such outcrops provide the most informative exposures of pseudotachylyte faulting.

4.3.2 Quasiconglomerate/Net Vein Complexes

The data presented in map 2 and accompanying sections (maps 2a and 2b) are necessarily somewhat stylized. Much of the peninsula is shot through with pseudotachylyte and the problems of representing individual FVs at this scale are self-evident. Map 2 essentially records the surface density distribution of pseudotachylyte faulting. This is considered the most satisfactory method of representing the geology, and believed preferable to attempts at delineating individual fault planes in areas W of the main thrust (cf. Sibson, 1977a, p. 23-24; Francis, 1969).

Zones of intense pseudotachylyte faulting containing intersecting FVs and IVs (net-vein complexes) and quasiconglomerate have been delineated according to the qualitative pseudotachylyte to undisturbed gneiss ratio observed in the field. Such zones may comprise 5% to a local maximum of 30% pseudotachylyte matrix. Within some zones blocks of gneiss which have suffered relatively little pseudotachylyte faulting may be mapped out and found to maintain a broad structural concordance with the regional foliation (map 2). These blocks might be described as 'fault-pips' (cf. Pettinga, 1982).

The thickness of the zones varies from less than 1 m of quasiconglomerate to about 5 m. The enveloping surfaces to the crush

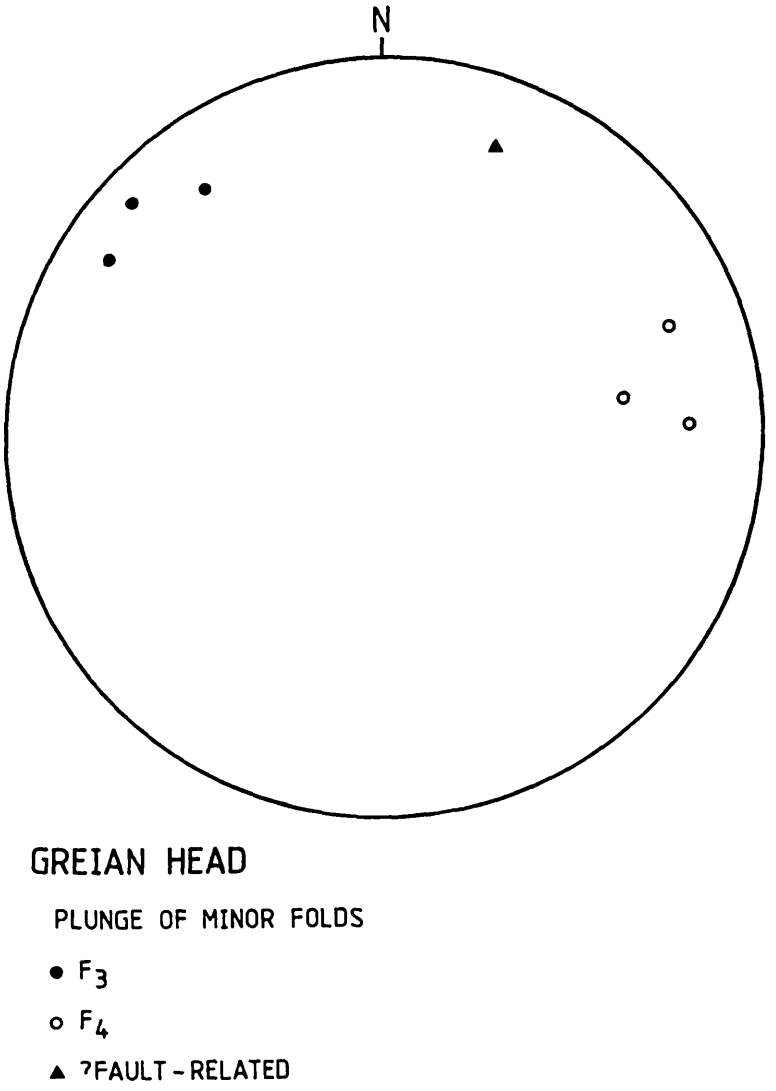


FIGURE 4.2 Plunge of minor folds at Greian Head, Barra.

zones appear to be approximately planar and are unfolded with a fairly consistent orientation dipping gently NNE to E, sub-parallel to the regional foliation. In a gross sense the regional structure (F_3 fold geometry) has guided this brittle deformation.

4.3.3 Relationship of Quasiconglomerate to Lithology and Structure

The development of the crush zones has been further guided by large scale litho-structural inhomogeneities. Crush zones are frequently pervasive in (originally) foliated and banded grey gneiss, whereas large amphibolite bodies are unfaulted except at their margins (Plate 4.1A). (The Laxfordian imposed fabrics in the amphibolite bodies vary from sub-isotropic to strong l-s tectonites.) The amphibolites have apparently acted as mechanically rigid and strong bodies during earthquake faulting. This has 2 important implications for the mechanics of the faulting. First, the amphibolite bodies may have acted as stress risers during stress accumulation and faulting leading to high strains at their margins (Sibson (1980b) has discussed this in a slightly different context). Secondly, the large amphibolite bodies should be prime candidates for earthquake fault plane barriers (section 2.2.2). Residual, post-slip stresses in the vicinity of the barriers might be expected to cause nucleation of further earthquakes or be dissipated by lower strain rate, anelastic or plastic deformation processes. No direct evidence of the latter has been observed.

The sub-isotropic agmatites are similarly largely devoid of pseudotachylyte faulting.

These direct observations made at outcrop scale have been extended to the construction of schematic geological cross sections through Greian Head (map 2a).

4.3.4 Injection Vein Arrays Associated With Quasiconglomerate

Figure 4.3 is a tracing of a photomosaic of pseudotachylyte-filled en-echelon injection veins; detail of part of the figure being shown in Plate 4.1B. The pseudotachylyte is believed to have been injected into relatively unfaulted grey gneiss from an overlying quasiconglomerate complex now eroded away. The complex may have been contiguous with that exposed some 50 m to the SE and illustrated in Plate 4.1A. A number of observations may be made:-

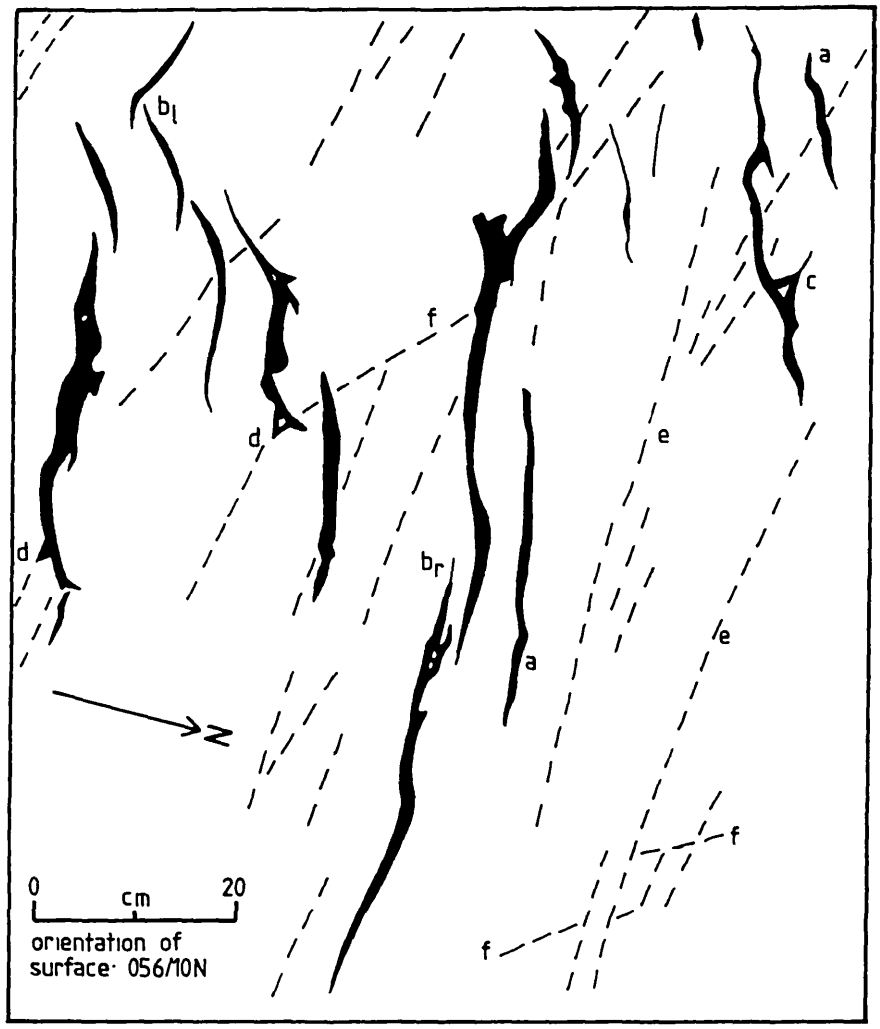
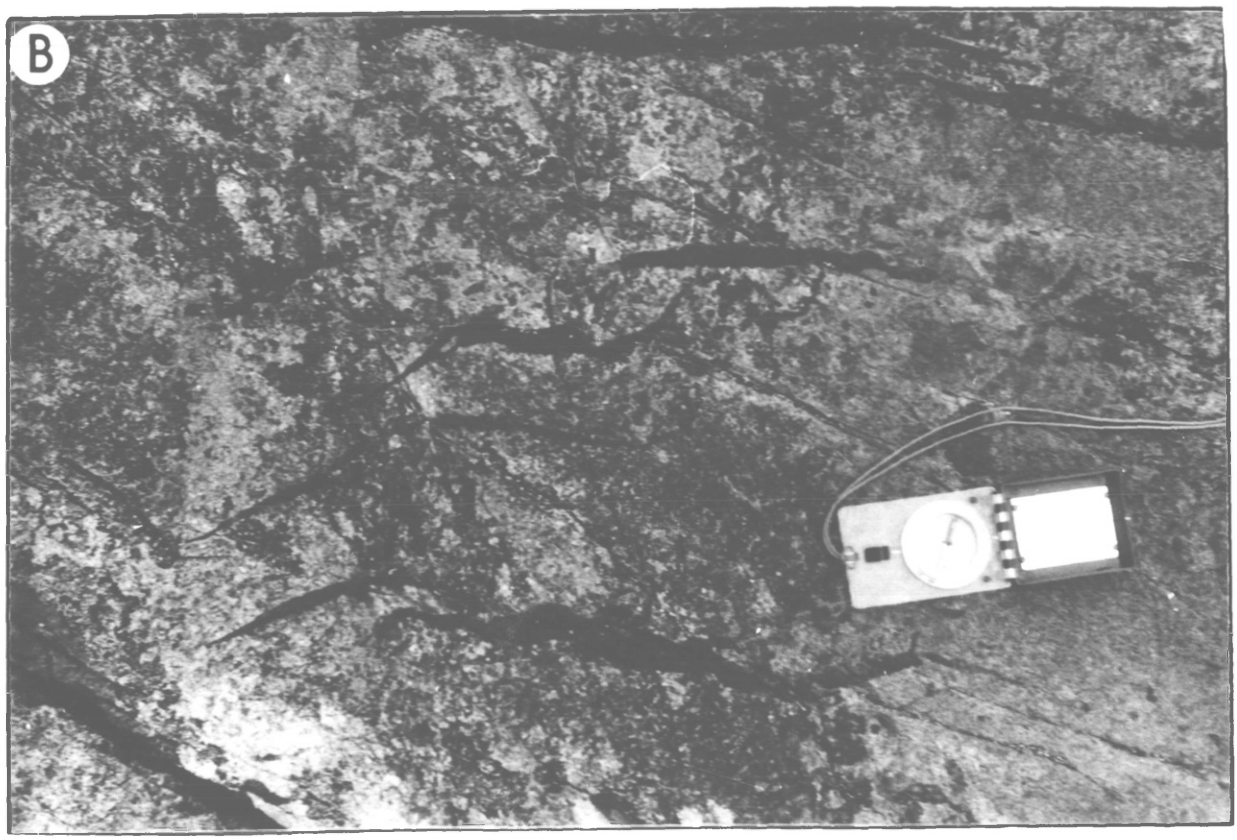


FIGURE 4.3 Pseudotachylyte-filled tension gash array, Cliad, 700 m E of Greian Head, Barra (NF667049). Traced from photomosaic. See text for details.

PLATE 4.1 (A) Unfaulted amphibolite body (foreground, with hammer) enveloped by quasiconglomerate generated in grey gneiss (contact indicated by arrow), Cliad, 750 m E of Greian Head, Barra (NF668049). (B) Detail of pseudotachylyte filled vein array shown in Fig. 4.3.


A


B

(i) the veins form conjugate arrays of sub-parallel, weakly sigmoidal veins; the acute angle between the conjugate arms is $\sim 40^{\circ}$.; the angle the veins themselves make with the conjugate arms is $<40^{\circ}$;
(ii) the conjugate arms have systematic left or right-stepping overlaps and propagation senses (b_l and b_r in Fig. 4.3);
(iii) dilational strain is heterogeneous, but measured normal to the vein elongation strains of up to 10^{-1} occur;
(iv) some of the veins have opposing mirror image walls which may be matched up (e.g. a in Fig. 4.3);
(v) vein shape was modified irreversibly by branching (d in Fig. 4.3) parallel to at least 2 joint sets (e and f in Fig 4.3), and by spallation of wall-rock re-entrants defined by the acute intersection of the veins and joints (c in Fig. 4.3);
(vi) closely-spaced jointing (<1 cm) in the veins (Fig. 4.3) developed after solidification of the melt, parallel to the more widely spaced ($\sim$10 cm) joint set (e) in the gneiss;
(vii) there is no evidence of pressure solution or cleavage development in the surrounding gneisses (cf. other examples of quartz/carbonate veins cited below).

Geometrically the pseudotachylyte vein arrays correspond to Beach's (1975) type 2 arrays. Beach (ibid.) suggests that such vein arrays initiate as primary en-echelon tensile fractures. However, other workers (e.g. Hancock, 1972; Gamond, 1983; Rickard and Rixon, 1983) have argued that such veins originate as extensional, hybrid extensional-shear or shear fractures in a secondary rotated stress field. In these cited examples quartz/carbonate vein arrays are believed to have developed under conditions of high pore fluid pressure and low effective confining pressure. The pseudotachylyte vein array certainly dilated under conditions of high fluid (pseudotachylyte melt) pressure, perhaps close to lithostatic pressure following near-total deviatoric stress relief during seismic faulting. It cannot be proved that they formed under these conditions; they may have nucleated during the first increments of pseudotachylyte faulting. It seems reasonable to assume from the array orientation that the primary maximum principal stress was orientated .ENE-WSW.

4.3.5 Fault-Related Folding

Within and adjacent to the crush zones highly irregular open folds of various amplitudes and wavelengths (cm-m) occur sporadically. Considerable care is neccessary to distinguish these features from F_4 folds and to ascertain that they do not simply refect chopping and reorientation of blocks of gneiss by the brittle faulting. The majority of the folds probably resulted from the latter process. A single plunge measurement for a fault-related fold (Fig. 4.2) combined with observations described in section 4.3.7 suggest that the axes of the folds trend NE. Similar, ill-defined thrust-related folds have been noted from S Uist (Coward, 1969) and N Uist (Sibson, 1977a). Sibson (ibid.) and Grocott (1980) have postulated that flexural slip folding may occur during stress accumulation prior to seismic failure and pseudotachylyte generation. This implies that pre-faulting stress accumulation is not wholly elastic.

4.3.6 Brittle Deformation Outside the Quasiconglomerate Zones

In the packets of gneiss structurally above and below the quasiconglomerate complexes a relatively simple brittle fault geometry exists, characterized by discrete FVs which allows some interpretation to be made of the kinematics and history of faulting.

1) Cataclastic Foliation. An early cataclastic fabric is developed predominantly in the better foliated grey gneisses. At outcrop the fabric consists of narrow (<1 mm), closely spaced, inosculating shear zones. Microscopically, individual shear zones contain small amounts of cataclastic debris. The fabric has largely developed through enhancement of the existing gneissic foliation.

The formation of the cataclastic fabric pre-dates the pseudotachylyte faulting and is comparable in both deformation mechanism and relative timing with the D_0 phase of deformation identified by Sibson (1977a) in the main OHT zone (Table 4.3).

Francis (1969) described mylonitic stringers folded around irregular thrust-related folds at Greian Head which may correspond to this cataclastic fabric.

2) Discrete Single-Jerk FVs. Orientation data for discrete single jerk FVs are presented in Fig. 4.4 Comparison of this stereoplot with that for the gneissic foliation (map 2) demonstrates the dominance of foliation parallel FVs. Sub-barren foliation parallel

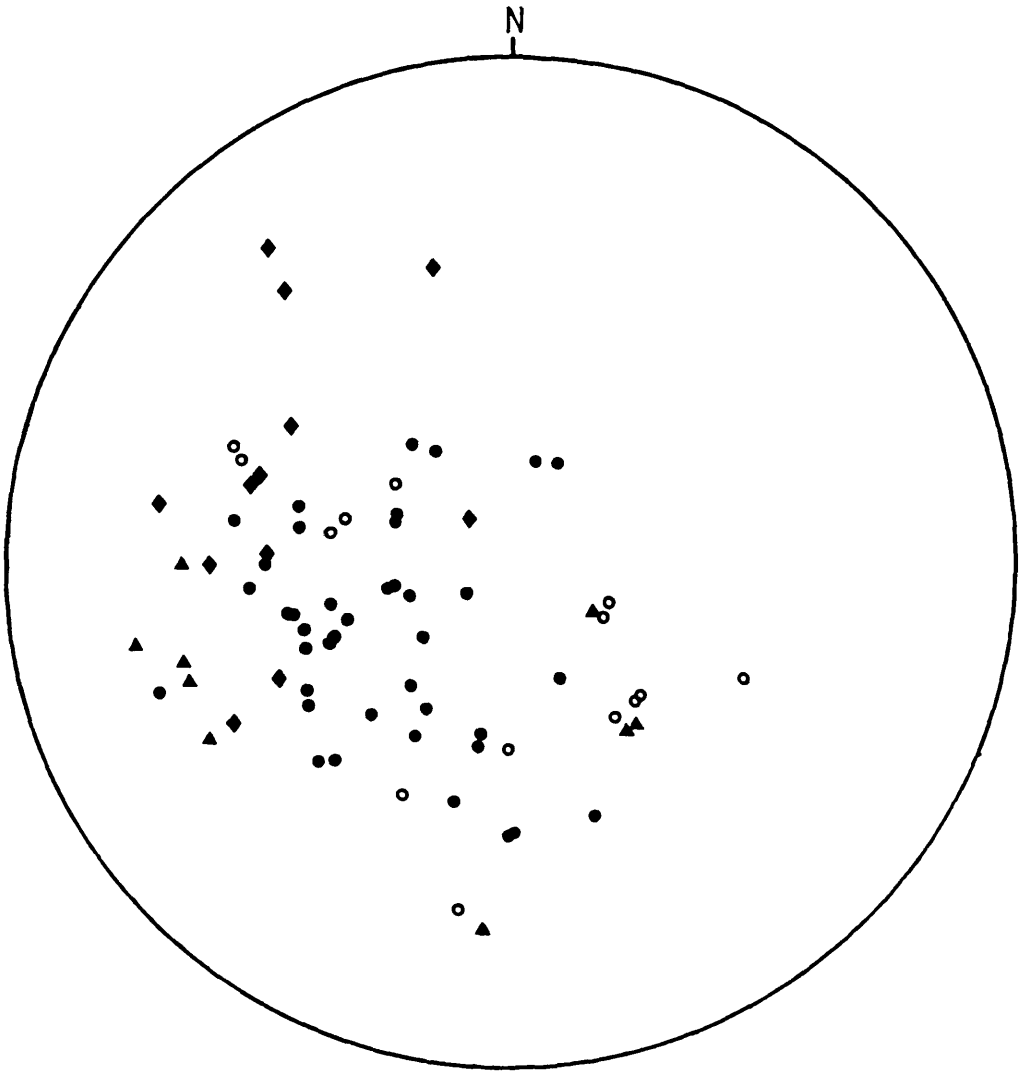


FIGURE 4.4 Stereoplot of poles to 'single-jerk' FVs at Greian Head, Barra.

FVs are distinguishable from the cataclastic foliation by the former's more sharply planar habit. Lithological contact FVs occur typically at the boundaries between amphibolitic and more feldspathic layers in the gneiss.

Discordant FVs invariably dip more steeply than the gneissic foliation, but in the absence of suitable linear markers, care is required in assigning movement sense and net slip to the FVs. Fortunately 3D outcrop assists in determining movement sense in many cases; in other cases the movement sense cannot be differentiated. The following three types of discordant, single-jerk FVs were recognized at Greian Head (see Ragan, 1985 for terminology):-

(i) Reverse dip separation FVs (e.g. Plate 4.2A and B) dip at moderate angles from SSE to NE (Fig 4.4). The movement sense on the FVs is inferred to be W to NNW-directed thrusting (Plate 4.2A). One or two W-dipping reverse dip separation FVs were also observed. These are possibly backthrusts (see also section 4.3.7).

(ii) Normal dip separation FVs (e.g. Plate 4.2C) show a weak bimodal distribution into E-ENE dipping and WNW dipping orientations (Fig. 4.4). The inferred movement sense on these FVs is normal (Plate 4.2C).

(iii) Undifferentiated FVs, showing various separations but with little possibility of determining movement sense, display a wide variety of orientations (Fig. 4.4). A typical example is shown in Plate 4.2D where a discordant FV (DFV) has displaced a thick amphibolite band and its associated concordant lithological contact FV (FV). The strike separation along DFV suggests sinistral strike slip. The separation could however be accounted for by pure normal dip slip, normal/sinistral oblique slip or reverse/sinistral oblique slip.

The relative age relations illustrated in Plate 4.2D are typical of all outcrops, with discordant FVs (regardless of orientation, separation or slip sense) invariably post dating concordant FVs.

The finite dimensions of FV are illustrated by an outcrop on Tangaval peninsula, south of Greian Head (map 2). The discordant (reverse separation) FVs terminate either by rotating into parallelism with the foliation (Fig. 4.5a) or by near-symmetrical branching or

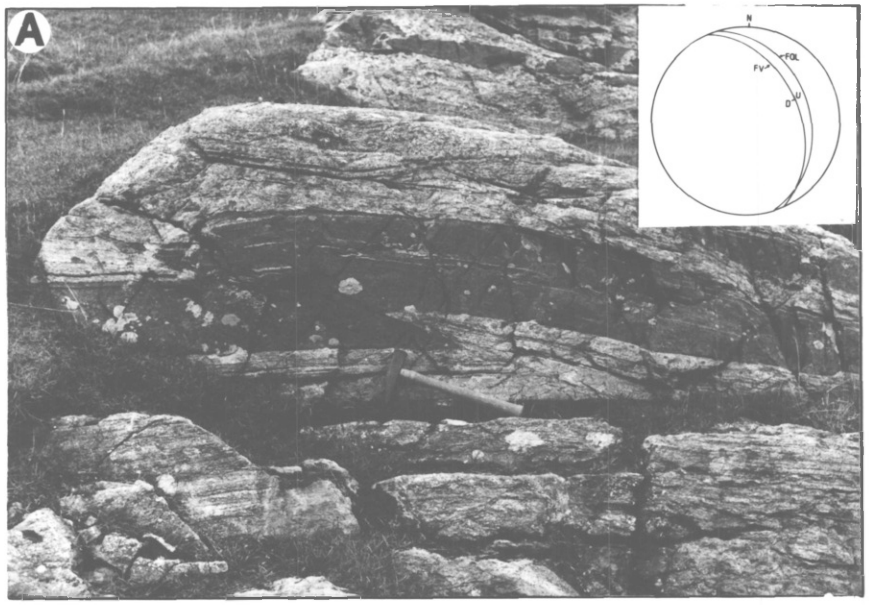
PLATE 4.2 Discordant 'single jerk' pseudotachylyte FVs, Greian Head, Barra.

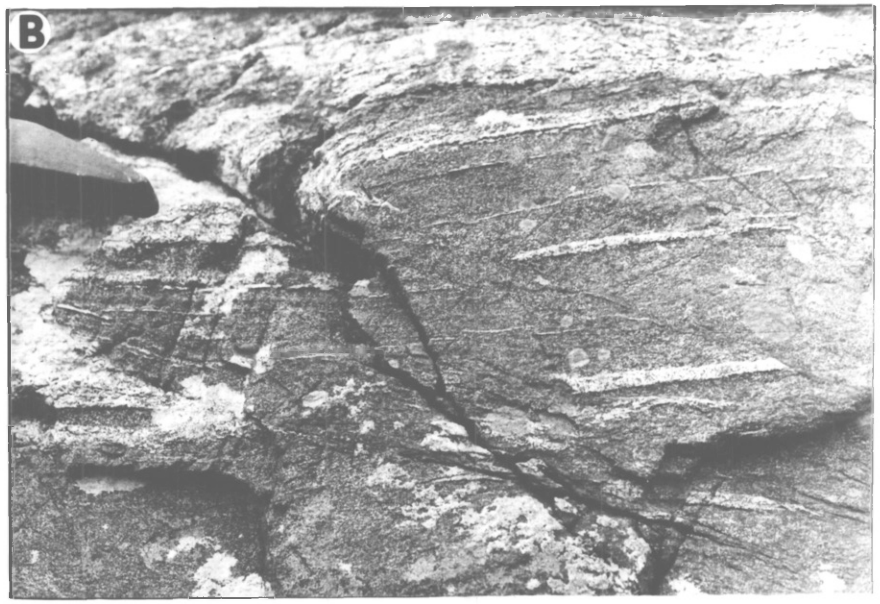
(A) E-dipping FV showing reverse dip separation of 10 cm on amphibolite layer (NF65980446).

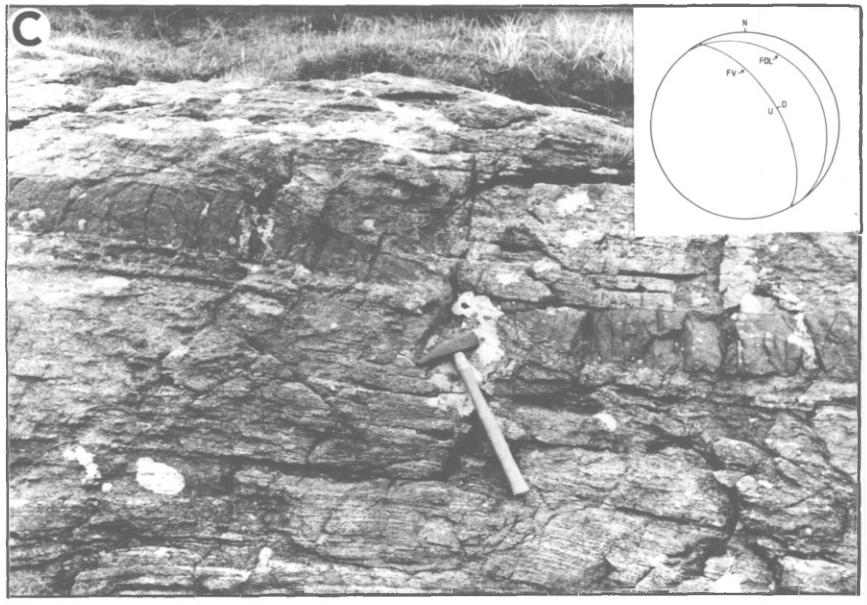
(B) Detail of (A) showing up-dip divergence of sub-barren FVs.

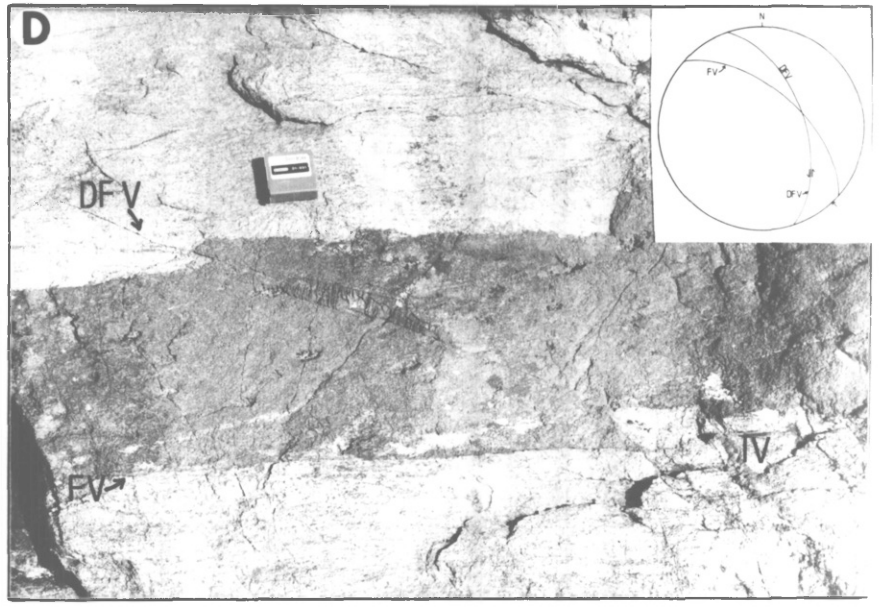
(C) E-dipping FV showing normal dip separation of 20 cm on amphibolite layer (NF65990446).

(D) FV trending 160/55E showing sinistral strike separation of gneissic banding and foliation which trends 130/58E. Note earlier concordant FV at lithological contact between base of amphibolite layer and grey gneiss (FV) with associated orthogonal IV (IV) and intensely jointed pseudotachylyte in FV swell in centre of amphibolite dyke (NF65580428).


A
N
FOL
FV
D
U


B


C
N
FOL
FV
U
D


D
N
FV
FOL
DFV
DFV
IV
FV

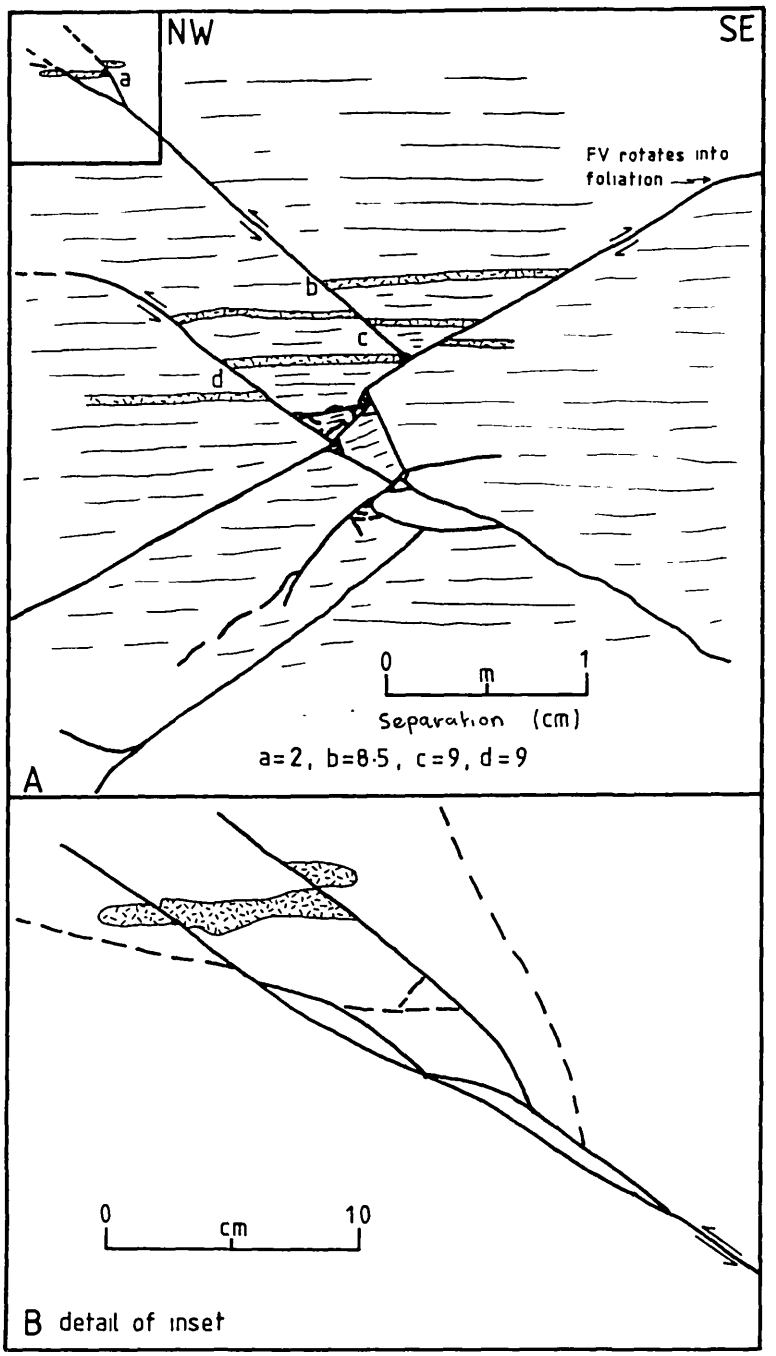


FIGURE 4.5 Detail of conjugate FV intersections and terminations revealed on vertical joint face at Tangaval, Barra (NF84209790). Quartzofeldspathic pegmatite shown in hachured ornament.

splaying (Fig. 4.5b) which conforms to theoretical analyses of fault and vein terminations (e.g. Chinnery, 1966; Beach, 1980). The dip separation gradient determined along a FV terminating by splaying is very large (Fig. 4.5). The absence of any pronounced lithological variation close to the termination of this FV may indicate that it was stopped by a driving stress barrier rather than a fracture energy barrier (see section 2.2.2).

4.3.7 Imbrication and the Relation Between Different Types of Pseudotachylyte Faulting

Maximum information information about the geometry of brittle faulting at Greian Head can be got from the WNW-ESE and N-S trending outcrops that are the former sites of Tertiary dykes.

1) WNW trending outcrops

Map 2b is a panoramic sketch of a 60 m long by 1-8 m high outcrop trending 110 from part of section A-A' (maps 2 and 2a) which lies 2-5 m below a major quasiconglomerate/net vein complex. Imbricate slabs of 5 recognizably different lithologies are separated by 6 pseudotachylyte faults.

Fault zone TP1, separating lithologic units I and II, has involved deformation of the entire exposed thickness of the basal lithologic unit. Within the faulted area 3 sub units (A, B and C) may be recognized (Plate 4.3A and B):-

(A) The base of the upper plate is largely unaffected by pseudotachylyte faulting or injection, but is gently folded (Plate 4.3A). The folds are moderate wavelength and low amplitude (<10 cm) and die out within 50-100 cm above. Their plunge is difficult to determine but appears to be broadly parallel with the dip of the fault zone immediately beneath (Plate 4.3B), i.e. plunging gently NE to ENE.

Elsewhere fault pips of the upper plate lithology have separated and become faulted into the lower plate (Plate 4.3C). The margins of the fault pips appear to be regions of locally high strain indicated by the intense shear fabric.

(B) Immediately beneath the upper plate is the main fault zone comprising 15-50 cm thickness of crushed rock, cataclasite and

PLATE 4.3 Detail of minor structures from E-W trending section shown in map 2b, Greian Head, Barra (NF653046)

(A) Fault contact between lithologies I and II (map 2b) showing 3 subzones A, B and C.

(B) Sketch showing fault contact between lithologies I and II showing zones A, B and C illustrated in (A).

(C) Fault contact between lithologies I and II showing fault pip of upper plate included in fault zone (indicated by arrow).

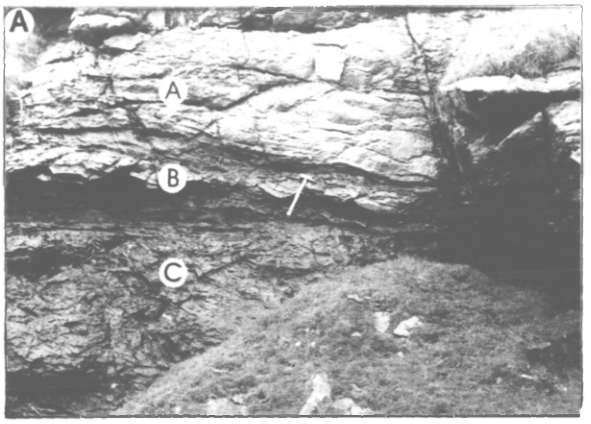
(D) NE striking, sub-vertical 7 cm thick IV which has been faulted by foliation-parallel faults. Arrows against IV indicate inferred movement direction. Note orientation of minor shears beneath hammer.

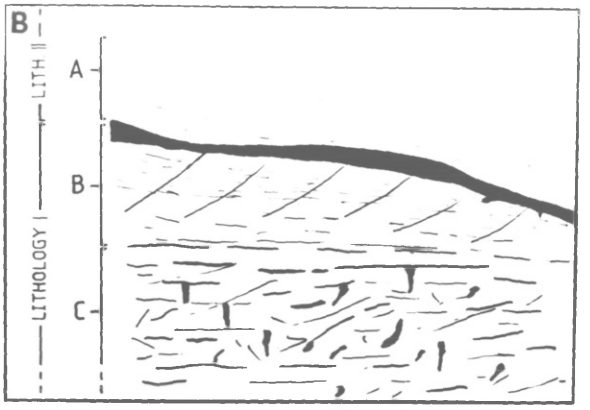
(E) Detail of D showing large clast (indicated by arrow) included in the IV.

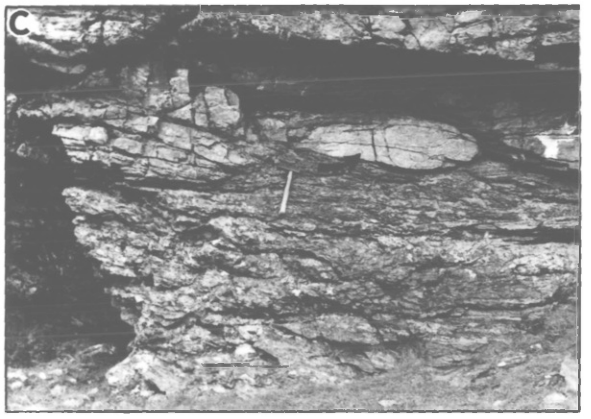
(F) NE striking, 3 cm thick IV affected by later foliation-parallel faulting.

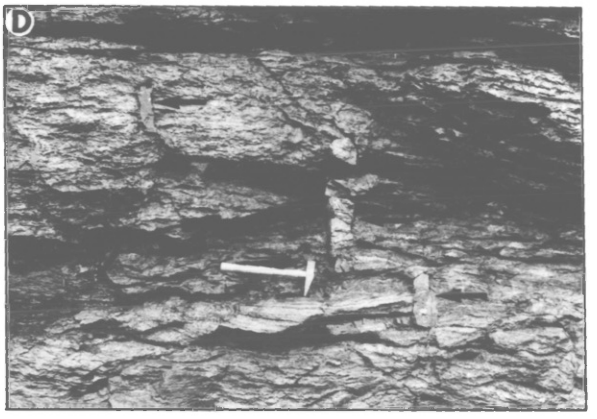
(G) Minor extensional shears.

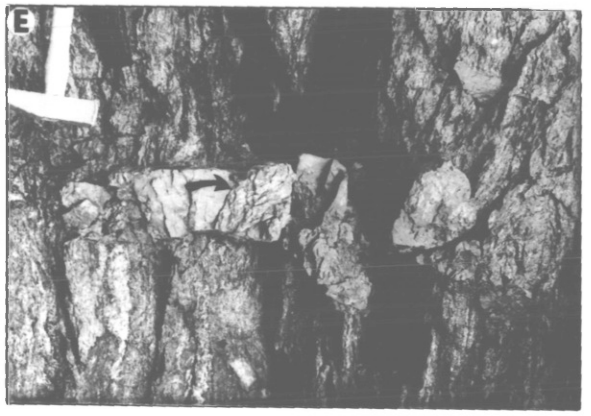
(H) Detail of G.

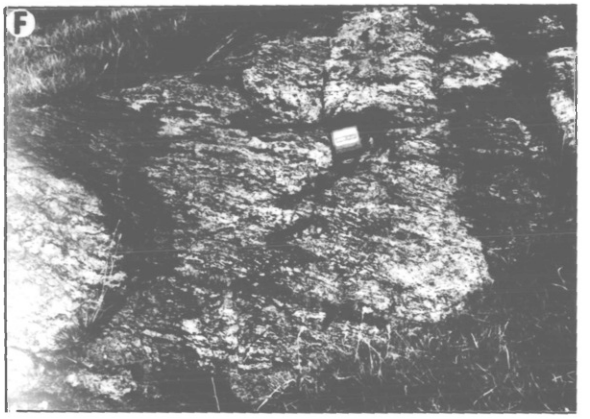

A
A
B
C

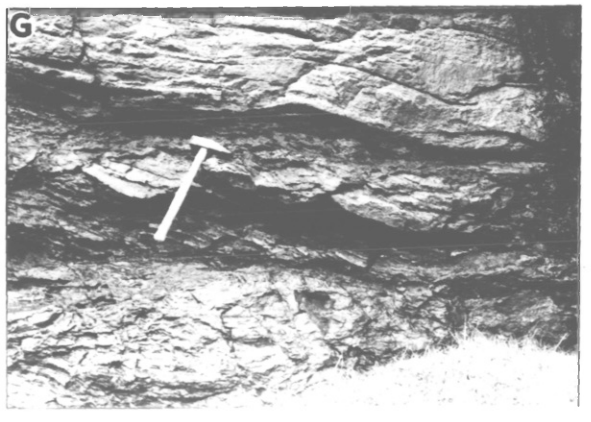

B
LITH II
LITHOLOGY I
A
B
C

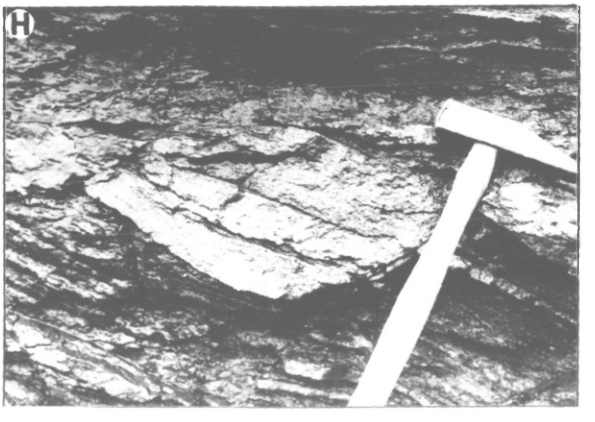

C


D


E


F


G


H

pseudotachylyte (confirmed by thin section observation). The maximum volumetric abundance of pseudotachylyte is close to the top of this zone, contained principally in vertical IVs. Deformation in this zone has been accomodated mainly by foliation parallel slip. Faulted IVs, which are sub-vertical and trend NNE, are testament to slip on several discontinuities involving separations of up to 50 cm (Plate 4.3D and F). The IVs contain large, rounded fragments of gneiss from the overlying plate (Plate 4.3E).

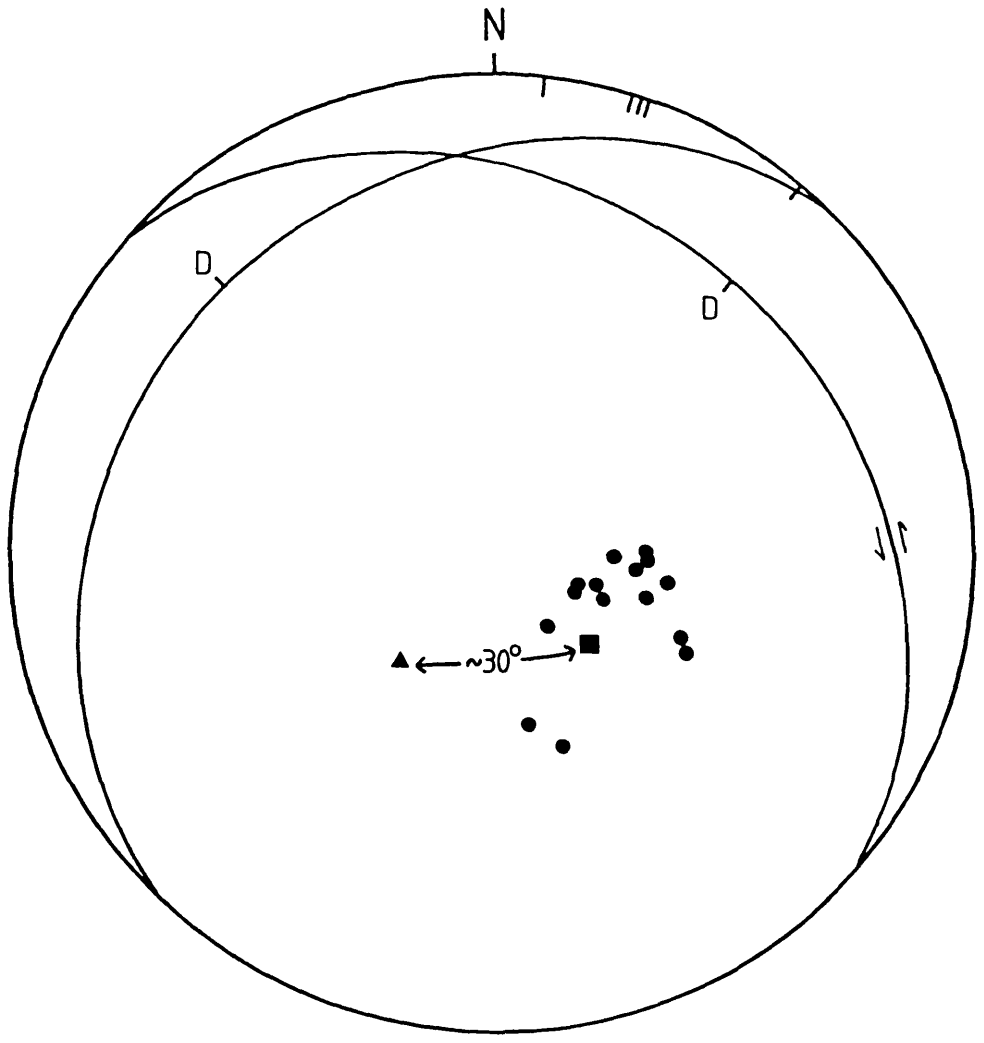
Minor normal sense separations (<1 cm) occur along discontinuous, sub-listric WNW to NW dipping minor shears (Plate 4.3G and H). These are in some cases coated with a thin smear of pseudotachylyte. Combined slip on these shears and the foliation parallel shears has resulted in a lozenge fabric due to partial transposition of the gneissic foliation.

(C) Below sub-zone B, the lower plate lithology is jumbled and shot through with pseudotachylyte (Plate 4.3B). Predominant slip appears to have been foliation parallel and along minor shears orientated similarly to those in sub-zone B.

Orientation data for various elements within this outcrop are presented in Fig. 4.6. The minor shears are believed to correspond to R_1 orientated Riedel shears. Reverse/sinistral oblique slip is inferred for the following reasons:-

(i) a general observation made in this study, and noted elsewhere (e.g. Grocott, 1981), is that FV-orthogonal IVs tend to dilate parallel to the movement direction;
(ii) the separation of IVs faulted by later foliation parallel FVs suggests WNW-directed thrusting;
(iii) the minor shear geometry is consistent with this movement sense, assuming that they are R_1 Riedel shears;
(iv) the orientation of the minor folds in zone A is consistent with ESE-WNW compression (see Grocott, 1981).

The faulted IV shown in Plate 4.3D suggests that perhaps 3 or 4 episodes of movement affected this outcrop. Other pseudotachylyte faults, structurally higher and exposed further E in the outcrop are broadly foliation parallel and dip to the ENE. No minor structures are exposed indicating slip sense or magnitude.



GREIAN HEAD

- ● POLES TO LOWER PLATE MINOR SHEARS, MS (n=15)
- ■ MEAN POLE TO LOWER PLATE MS
- ▲ POLE TO MAIN THRUST PLANE
- AZIMUTHS OF LOWER PLATE INJECTION VEINS (n=5)
- D DOWNTHROWN SIDE OF FAULT
- U UPTHROWN SIDE OF FAULT

FIGURE 4.6 Orientation data for structural elements and pseudotachylyte IVs from section shown in map 2b and Plate 4.3.

2) N-S Trending Outcrops

The exposures trending .N-S represented in Plates 4.4 and 4.5 lie structurally above the previously described outcrop and are separated from it by at least 1 major quasiconglomerate complex, although the general orientation of the gneissic foliation is similar (maps 2 and 2a). The pseudotachylyte faulting in these outcrops can be described chronologically.

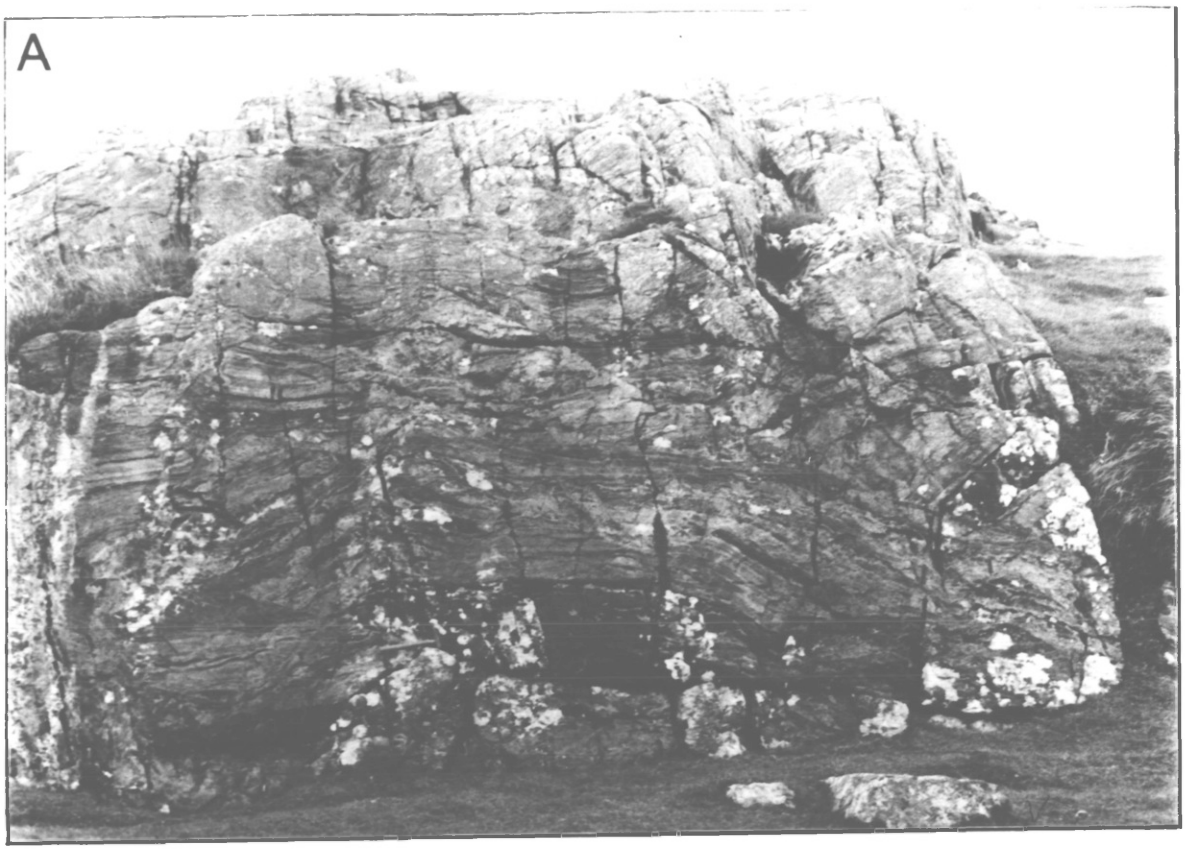
The earliest pseudotachylyte faulting occurred by repeated foliation-parallel slip, preferentially at lithological contacts, for example areas A and B in Plate 4.4. The magnitude of slip, indicated by faulted IVs, was probably of the order of centimetres. The direction of slip is difficult to determine due to imbrication by subsequent discordant faulting.

Following foliation parallel slip, faulting occurred on discordant FVs which dip ENE to SE at various angles (Plate 4.4). SE to NW directed thrusting is inferred from fault separations of the order of 10s of centimetres - e.g. displacement of the amphibolite layer in region A of Plate 4.4. The reorientation of this layer suggests that a rotational component of movement may also have occurred. The FVs vary from <1 cm of pseudotachylyte with small orthogonal IVs to zones of quasiconglomerate 5-10 cm thick. A subordinate set of .?N-dipping FVs which are older or possibly coeval and conjugate with the SE-dipping FVs are also developed. The displacement sense on these is unclear.

The youngest pseudotachylyte faulting comprises gently E-dipping quasiconglomerate complexes exposed at the base of the outcrop in Plate 4.4 and the top in Plate 4.5. Discordant discrete FVs are truncated at the contact with these zones and in the outcrop of Plate 4.5 a large, sub-vertical IV emanating from the upper quasiconglomerate layer cuts down through earlier SE-dipping and foliation parallel FVs.

Plate 4.6 shows another N-S trending outcrop with some interesting small-scale detail. Following foliation-parallel slip, .NW-directed thrust sense displacement along sub-barren microfaults occurred (e.g. A in Plate 4.6). This was followed by .SE directed thrust sense faulting along similar microfaults (e.g. C in Plate 4.6) which show considerable variation in dip. The resultant layer-parallel shortening structures are 'pop-ups' and triangle zones in the

PLATE 4.4 Photograph (A) and tracing (B) of N-S trending outcrop at Greian Head, Barra (NF65710468). Pseudotachylyte veins shown in heavy lines; quasiconglomerate cross-hatched ornament, amphibolite dotted, pegmatite hachured and grey gneiss unornamented. See text for discussion.


A

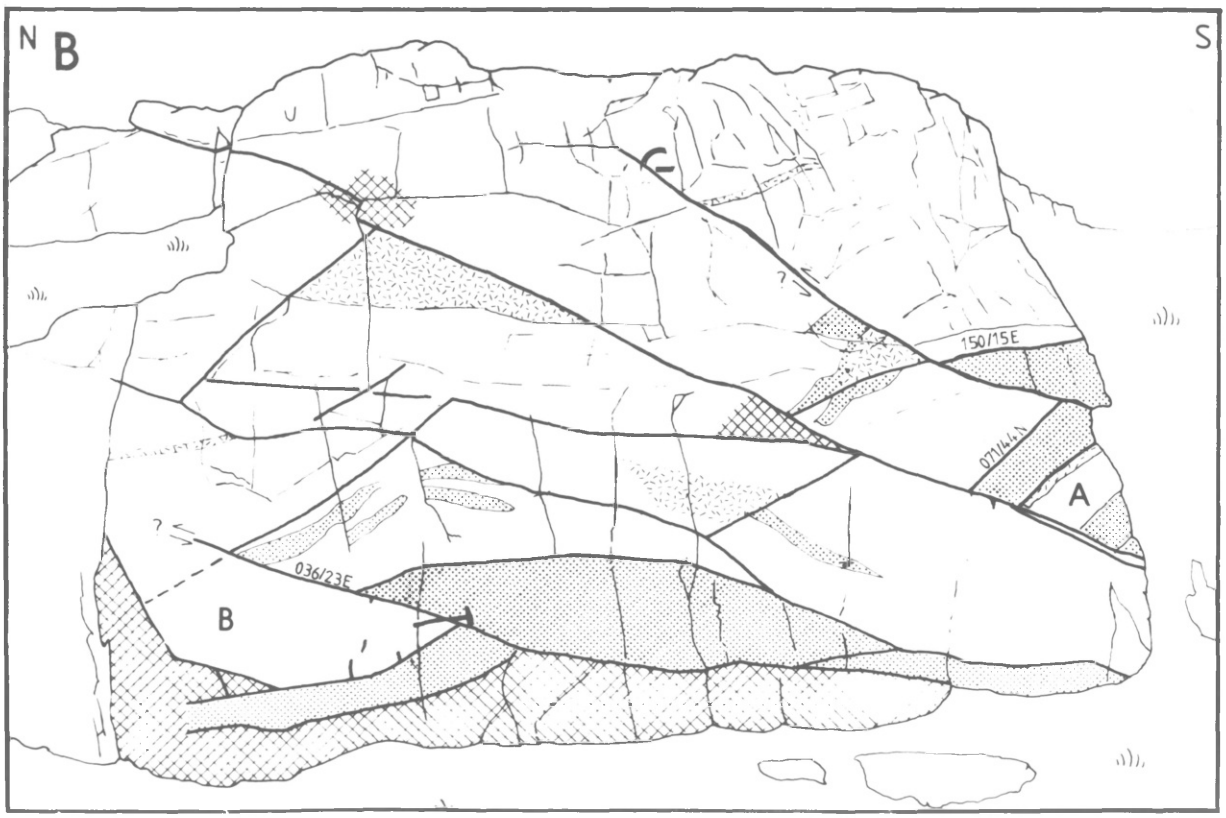
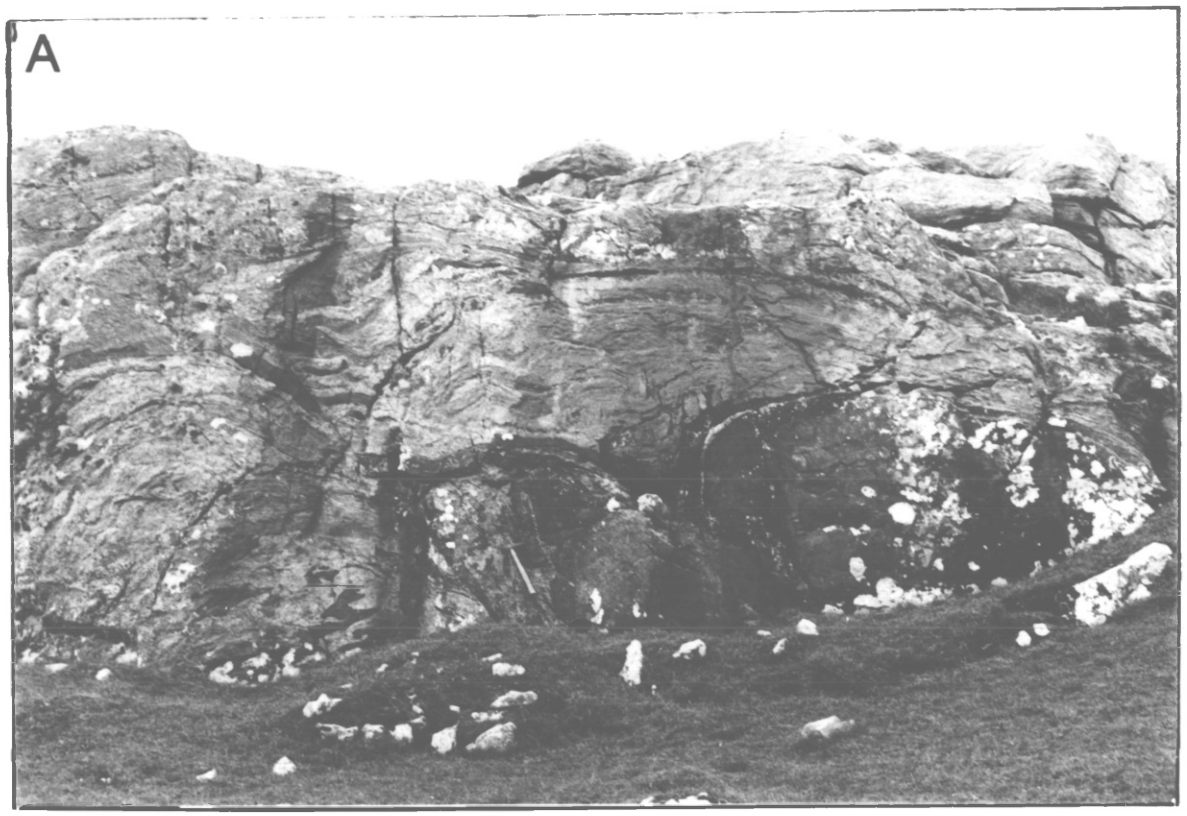

N
B
S
U
C
150/15E
071/44
A
036/23E
B

PLATE 4.5 Photograph (A) and tracing (B) of N-S trending outcrop at Greian Head, Barra (NF65710473). Ornament as for plate 4.4. See text for discussion.


A

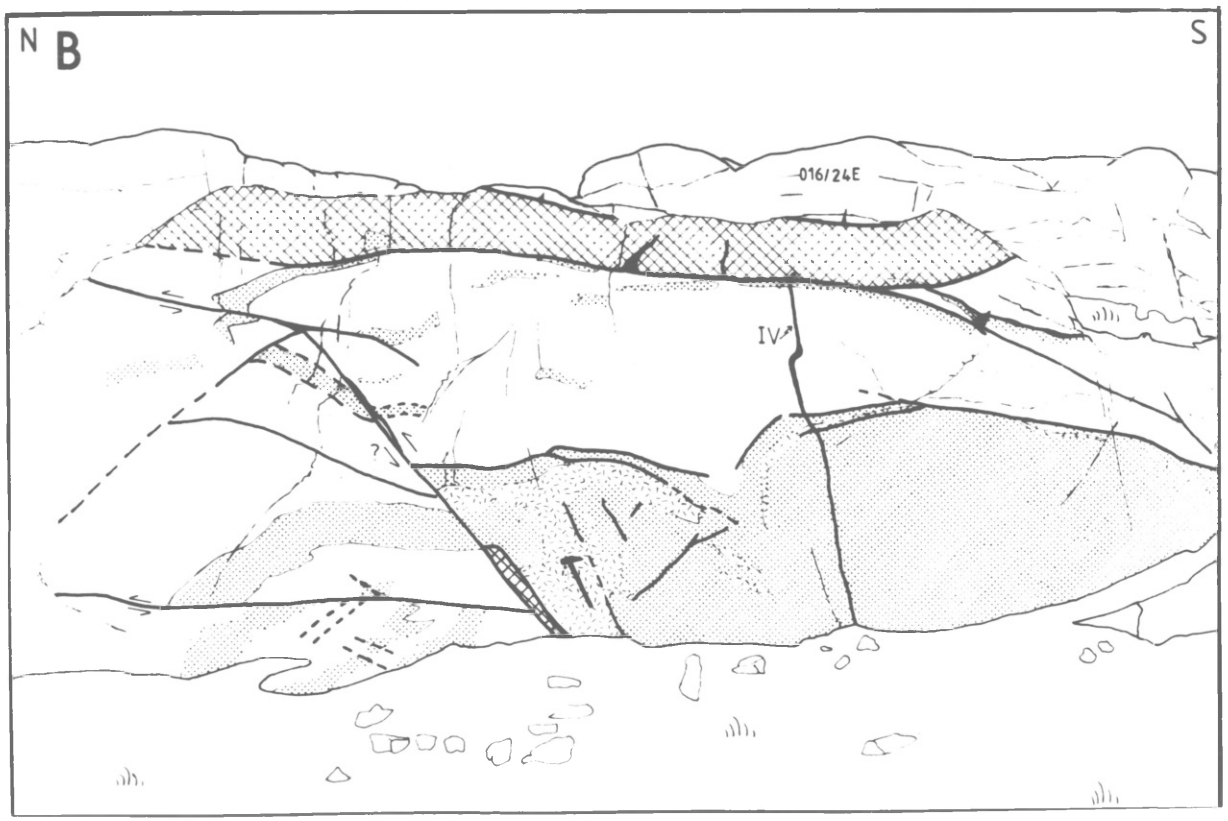
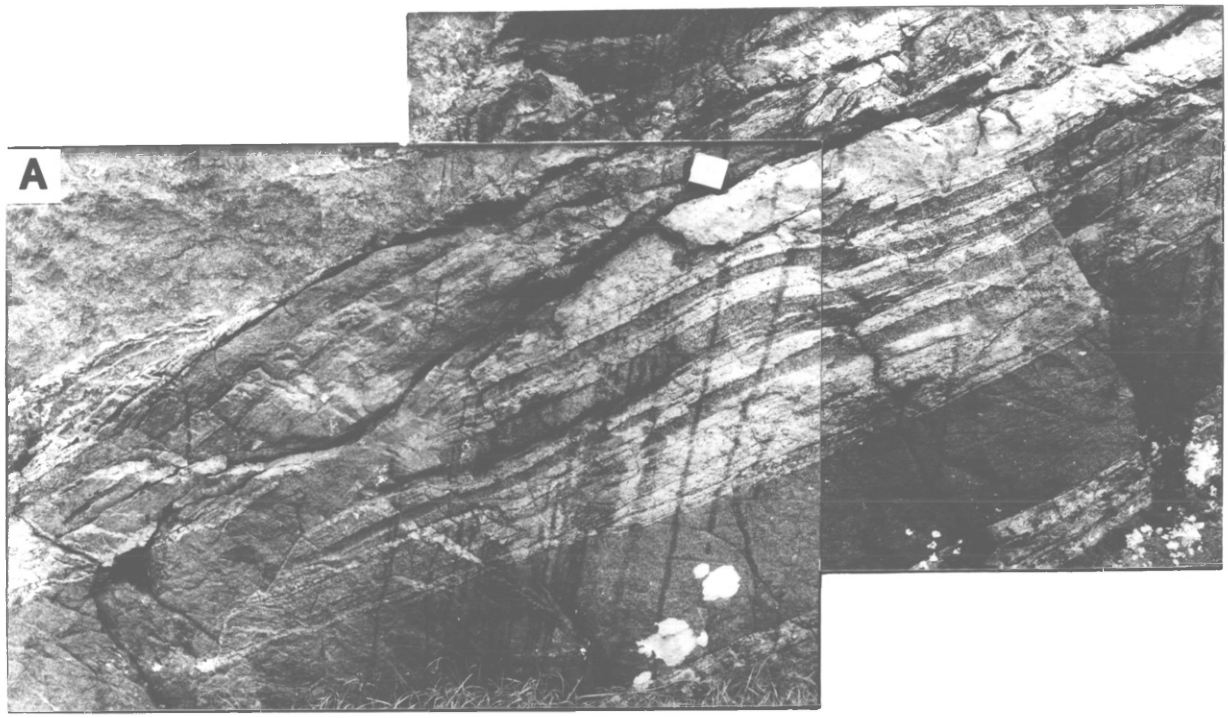
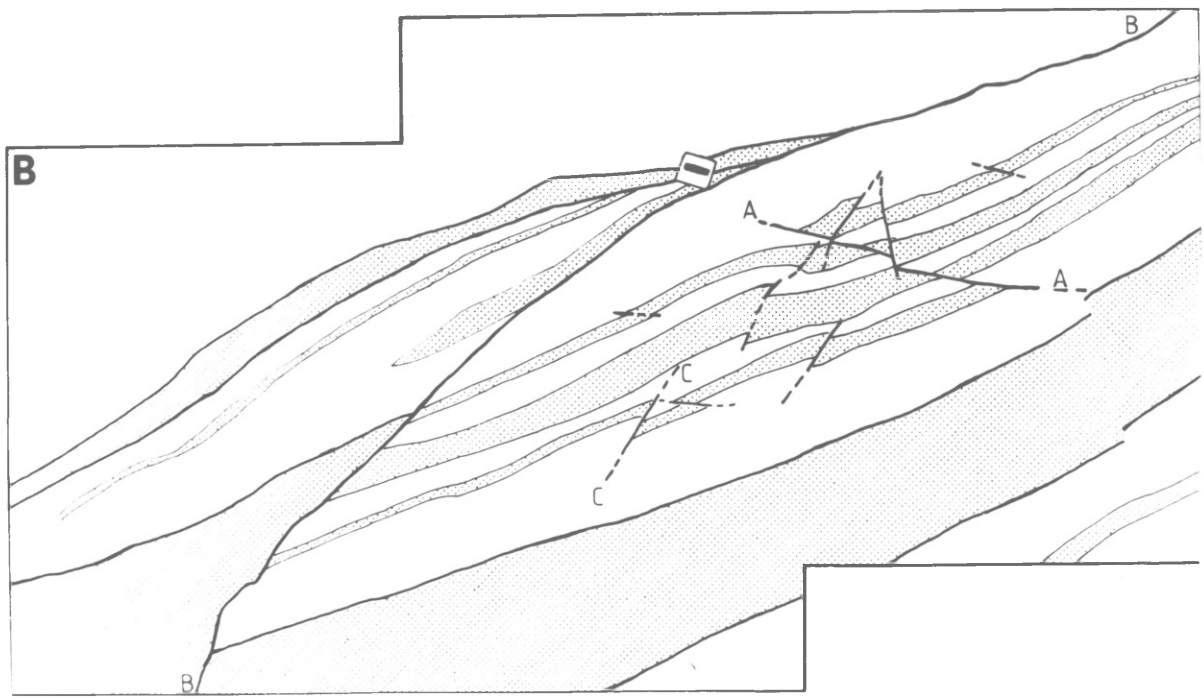

N
B
S
016/24E
IV
?

PLATE 4.6 N-S trending outcrop at Greian Head, Barra (NF65020489). Pseudotachylyte veins shown in heavy lines, amphibolite dotted and grey gneiss unornamented. See text for discussion.


A


B
A
A
C
C
B

terminology of Butler (1982). B and C are backthrusts which developed to accomodate layer-parallel shortening strain in excess of that which could be accomodated by the A-parallel microfaults. Possibly the major discordant FV, B formed after A and acted as a barrier to further slip on A-parallel FVs so inducing C-parallel slip. Extending this argument, B may have developed as a back thrust due to the presence of a larger unseen barrier - perhaps a large amphibolite body.

The microfault sets A and C are discontinuous and terminate either by rotating into parallelism with the foliation or sharply against one of the amphibolite layers. The latter may have acted as fracture energy barriers.

4.3.8 Conclusions: Greian Head

The observations made at Greian Head are summarized in Table 4.4. The initial foliation-parallel deformation and faulting can probably be ascribed to the effects of strength anisotropy in the gneisses. This is discussed by Sibson (1975; 1977a, p. 115-116) and it is concluded here that the foliation probably lay at a shallow to moderate inclination to a far-field ~E-W trending σ_1. The change to discordant faulting, particularly SSE-NNW directed thrusting may be due to 2 effects:-

(i) Successive foliation-parallel pseudotachylyte faulting may have resulted in substantial displacement-hardening of the gneiss by welding-up of planes of weakness with frozen pseudotachylyte melt. The occurrence of faulted orthogonal IVs combined with thin-section studies indicates that repeated episodes of slip are rare or absent along discrete FVs. There is some experimental evidence that a fracture toughness related parameter may increase in magnitude with decreasing grain size and increasing degree of interlocking of grains or fibres (Wood and Weidlich, 1982). The interpretation made here contrasts with but does not contradict a proposal made by Passchier (1982b). He suggested that ultramylonite bands developed from pseudotachylyte FVs due to their fine grain size and polyminerlaic character favouring diffusion-accomodated grain boundary sliding. It is possible that at P-T conditions favouring dominant plastic deformation, pseudotachylyte is weaker than the surrounding rock, whereas at P-T conditions favouring wholly brittle deformation pseudotachylyte is stronger than the surrounding rock.

TABLE 4.4 EVOLUTION OF BRITTLE DEFORMATION AT GREIAN HEAD, BARRA

Event	Nature of Brittle Deformation
D_3	Late faulting along WNW and NNE-trending, sub-vertical fractures probably involving small dip-slip and strike slip displacements; in part associated with Tertiary dyke intrusion
D_2	Multiple pseudotachylyte faulting within quasi-conglomerate/net-vein complexes which dip gently ∿NE, concordant or discordant with respect to the foliation; considerable imbrication, responsible for present gross structure of peninsula.
D_1	Discrete single jerk pseudotachylyte faulting on discordant FVs mainly involving oblique sinistral thrust displacements from E→E and SE→NW causing imbrication of the gneissic layering.
D_0	Development of cataclastic foliation in well-foliated grey gneiss followed by, and in part contemporaneous with discrete foliation-parallel pseudotachylyte faulting especially at lithological contacts.

(ii) The orientation of the principal stress axes may have changed because of a change in the regional stress tensor.

Distinct imbricate packets of gneiss sandwiched between quasiconglomerate complexes have been recognized in which E-W and SSE-NNW directed thrusting on discordant FVs occurred. It is possible that this variation is due to rotation of up to 70° about poles normal to the crush zones. However, it seems more likely that individual packets of gneiss were affected by westward and then NNW directed thrusting. Fault separations of centimetres to about 1 m have been recorded (i.e. within the range of earthquake displacements). The cumulative finite displacement on the discordant veins is estimated to be of the order of a few hundred metres.

The development of the quasiconglomerate complexes (D_2, Table 4.4) involves for the first time substantial strain/displacement localization. These zones post-date the single-jerk FVs. The larger volume of pseudotachylyte in the zones may reflect multiple slip events and perhaps larger increments of slip - generating a greater volume of pseudotachylyte.

4.4 Rubha Ardvule, S Uist

Rubha Ardvule occupies a somewhat similar geological and geographical position to that of Greian Head, lying some 9 km W of the main OHT base (map 1). Magnificent exposures of pseudotachylyte quasiconglomerate were recorded by Jehu and Craig (1923). Regrettably these are not noted on the recently published BGS 1:100 000 map.

4.4.1 General Geology

The W-facing peninsula of Rubha Ardvule is approximately 1 km long and 750 m broad at its maximum width. It is the only peninsula jutting out significantly from the 'machair' of S Uist and has clearly been hardened against erosion by the intense pseudotachylyte faulting. Outcrop is restricted to a narrow, largely inter-tidal, coastal strip.

Rubha Ardvule is composed of massive to well-foliated and banded grey gneiss, locally with more massive amphibolite bodies.

Like Greian Head, Rubha Ardvule lies on the S limb of a major Laxfordian F_3 fold whose axial trace trends NW. Statistically, the attitude of the foliation is regular and dips gently NE (stereoplot, map 3). Large areas (100s of m^2) however are flat-lying with a weak dome and basin structure with wavelength of a few metres and amplitudes of a few decimetres; elsewhere the foliation is vertical. This structure is believed to result from 2 processes: (i) F_3/F_4 fold interference (see Coward, 1969, p.48); (ii) repeated pseudotachylyte faulting along gently dipping fault zones of slightly different orientation.

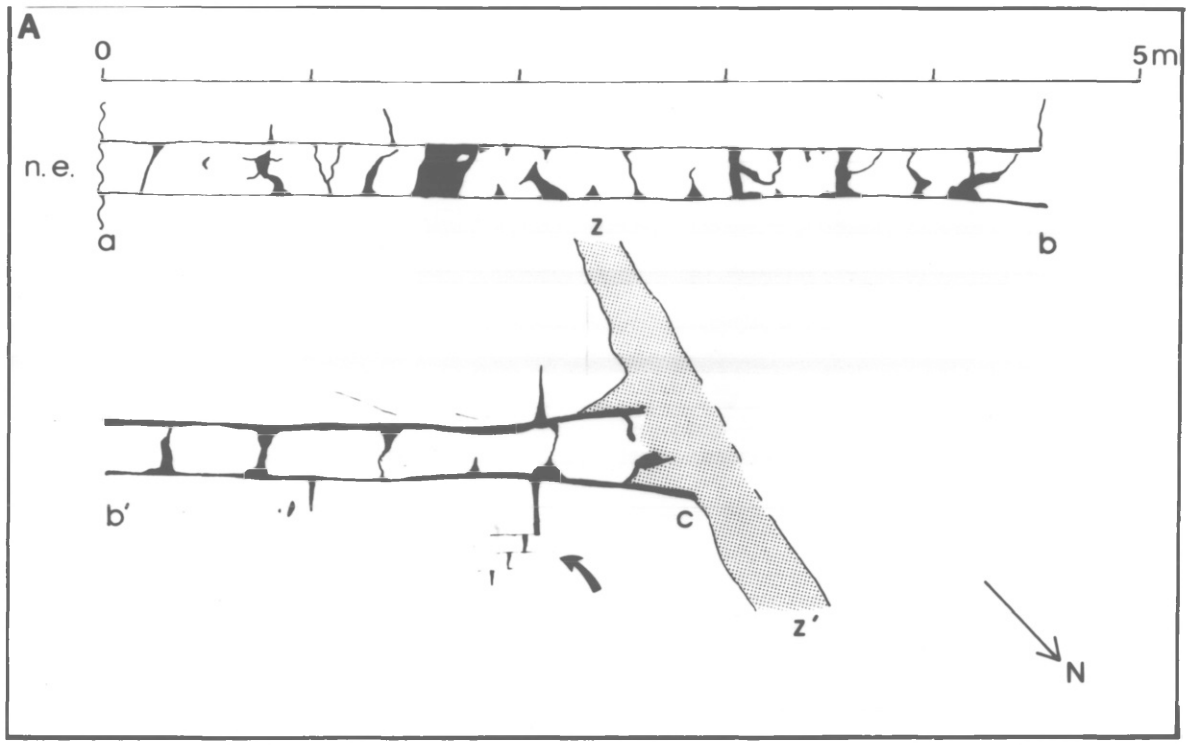
4.4.2 Sub-Vertical Quasiconglomerate Complexes

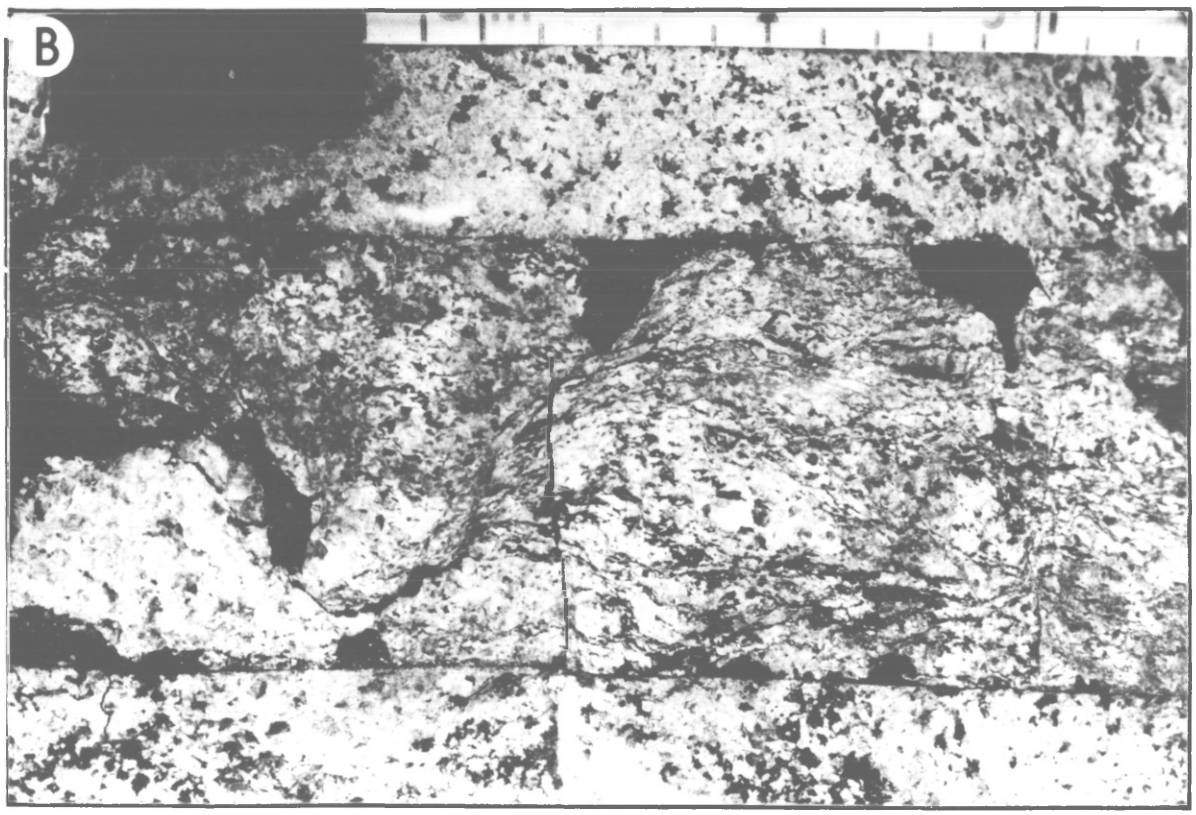
Discrete, single-jerk FVs, either concordant or discordant, are not abundant at Rubha Ardvule, perhaps due to the more weakly developed foliation in contrast to Greian Head. The earliest pseudotachylyte faulting appears to have taken place along predominantly NW-trending sub-vertical fault systems, often parallel to the strike of the more gently dipping foliation. Some variation in azimuth, with strike varying to NE and markedly discordant to the gneissic foliation exists (map 3). The zones cut massive and foliated grey gneiss and pegmatite, but were not observed cutting the larger amphibolite bodies. They vary in width from a few cm (Plate 4.7) to a

PLATE 4.7 Narrow, sub-vertical quasiconglomerate zone at Rubha Ardvule (NF715299).

(A) Sketch map of outcrop.

(B) Detail of part of quasiconglomerate.


A
0
5m
n.e.
a
b
z
b'
c
z'
N


B

few tens of cm wide and are traceable along strike for 10's of metres - usually restricted by the limit of exposure (Fig. 4.7a). Fault separations, fault drag, secondary faulting and faulted IVs indicate that movement is dominantly strike-slip with both dextral and sinistral slip senses. A maximum 2.4m sinistral strike separation was recorded in one case (Fig. 4.7c).

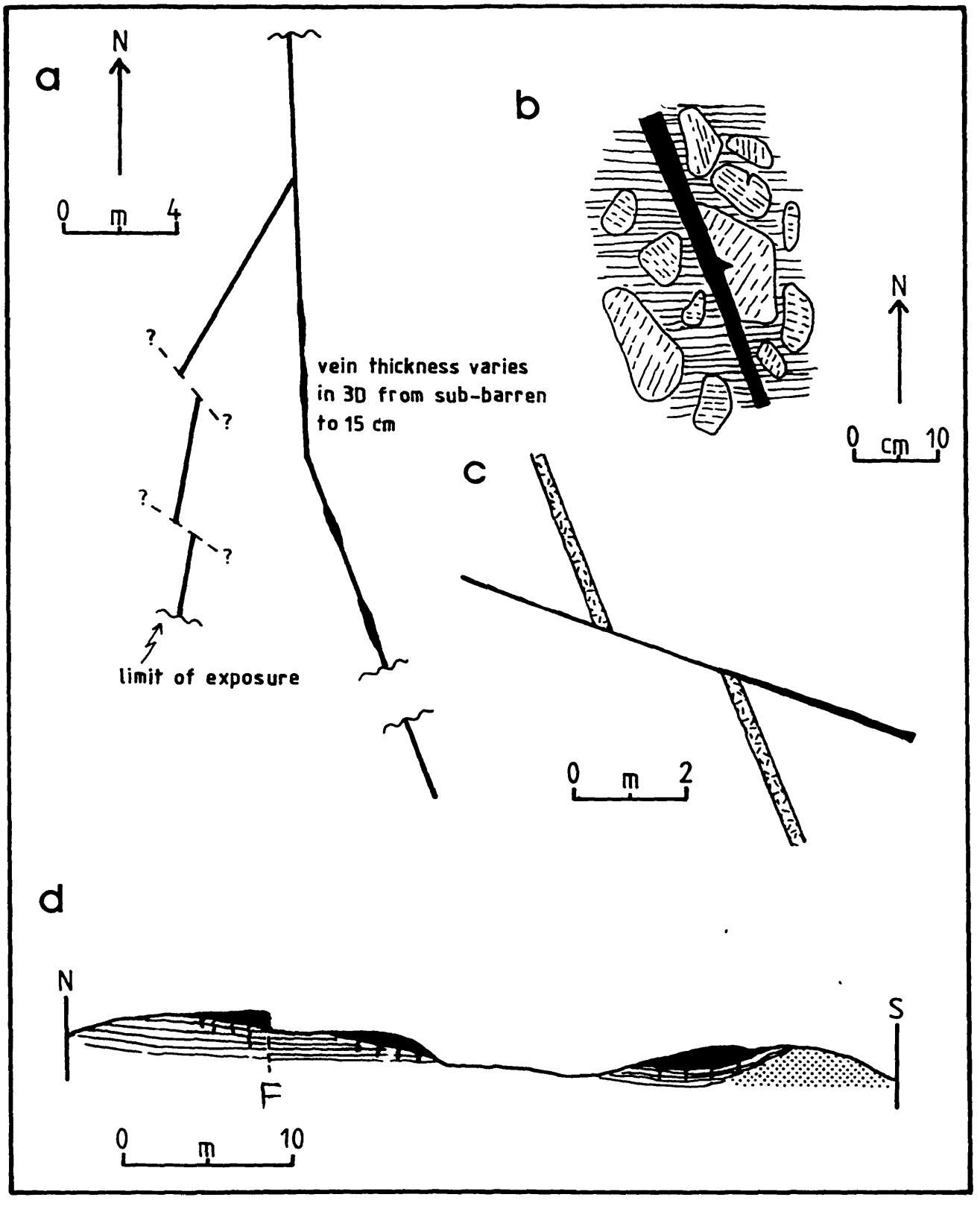
An example of one of the narrower sub-vertical zones is shown in Plate 4.7. The zone strikes 132°, traceable for 7 m until it intersects and is cut out by a later N-S striking, E-dipping quasiconglomerate complex. The FV envelopes vary along their length from knife-sharp, sub-barren transgranular fractures to cm-thick layers of pseudotachylyte. Fracturing, deformation and pseudotachylyte injection is intense within the layer between the FVs but restricted to occassional injection veining outside it. Within the layer both shear fractures, orientated at >50° to the margin and probable extension fractures orthogonal to the FVs have been dilated by pseudotachylyte intruded from the FVs. Dilatant strains, parallel to the FV system, of 10^{-2} - 10^{-1} are inferred. The genetic relationship in Plate 4.7 suggest high effective normal stresses were maintained locally on the FVs during movement with FV-generated pseudotachylyte being squeezed into and dilating the shear and extension fractures. In this way high kinetic shear stresses may persist during fault slip (cf. Sibson, 1975). The quasiconglomerate zone, whose movement sense is believed to be dextral strike slip, is considered to have resulted from a single slip event (earthquake).

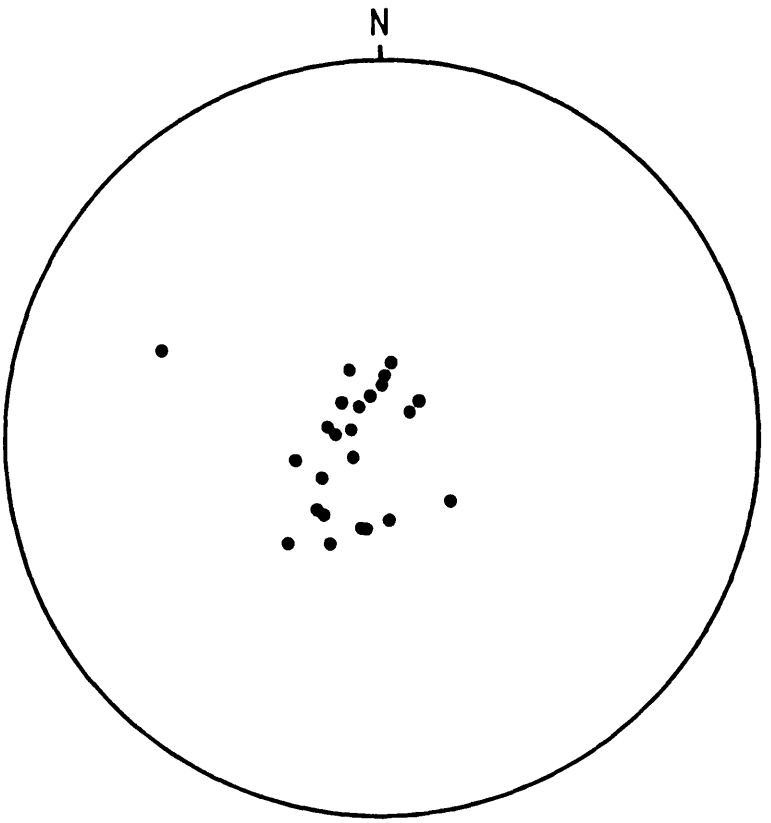
Coward (1969) has related these NW-trending, sub-vertical quasiconglomerate zones to similar zones exposed on Askernish (G.R. NF755237) some 8 km to the SE and at an altitude of 125 m. If these zones are contiguous, then fault plane areas of $>10^8$ m^2 may be estimated. These dimensions are comparable to those estimated by Grocott (1977a) for near 100% exposed (trace) FV systems in W Greenland.

4.4.3 Concordant and Sub-Horizontal Quasiconglomerate Complexes

Large areas (100's of m^2) of Rubha Ardvule are composed of gently-dipping to horizontal quasiconglomerate/net-vein complexes. For example, much of the intertidal outcrop S and W of Geodha Mor (map 3) is of this character. The enveloping surfaces to these zones are approximately foliation-parallel, usually dipping gently E to NE (Fig.

FIGURE 4.7 Sketches illustrating structures at Rubha Ardvule.
(a) Sketchmap showing trace of FV/IV system cutting flat-lying gneiss (NF71223016).
(b) Sketch showing 5 cm thick, NW-trending IV with chilled margin cutting jointed, horizontal pseudotachylyte pavement containing rounded and rotated clasts of foliated gneiss (NF71142967).
(c) Sketchmap showing 2-10 cm thick, WNW-trending FV displacing a quartzofeldspathic pegmatite with a strike separation of 2.4 m (NF71762995).
(d) Sketch cross-section showing relationship between flat-lying quasiconglomerate (black), foliated grey gneiss (lined) and amphibolite (dotted) (NF71172953).


a
N
0 m 4
?
?
?
?
vein thickness varies
in 3D from sub-barren
to 15 cm
limit of exposure
b
N
0 cm 10
c
0 m 2
d
N
S
F
0 m 10



RUBHA ARDVULE

POLES TO PSEUDOTACHYLYTE PAVEMENTS AND QUASI-CONGLOMERATE COMPLEXES (n=24)

FIGURE 4.8 Stereoplot of poles to 24 pseudotachylyte pavements and quasiconglomerate complexes at Rubha Ardvule. A further 51 pavements measured were horizontal and are not plotted.

4.8). Where (wave) erosion has stripped off the hanging wall, 'pavements' (cf. Jehu and Craig, 1925) of pseudotachylyte studded with rounded clasts of gneiss are exposed (Fig. 4.7b and Plate 4.11). The pavements attain a maximum thickness of 5-15 cm over areas of a few square metres; they are believed to represent swells in the enveloping surfaces (FVs) of the quasiconglomerate complexes. It is inferred from this that the enveloping surfaces are not perfectly planar but may possess irregular asperities with maximum amplitudes of a few 10s of cm and wavelengths of metres, with pseudotachylyte intrusion parallel to these surfaces (cf. Coward, 1969, p.274).

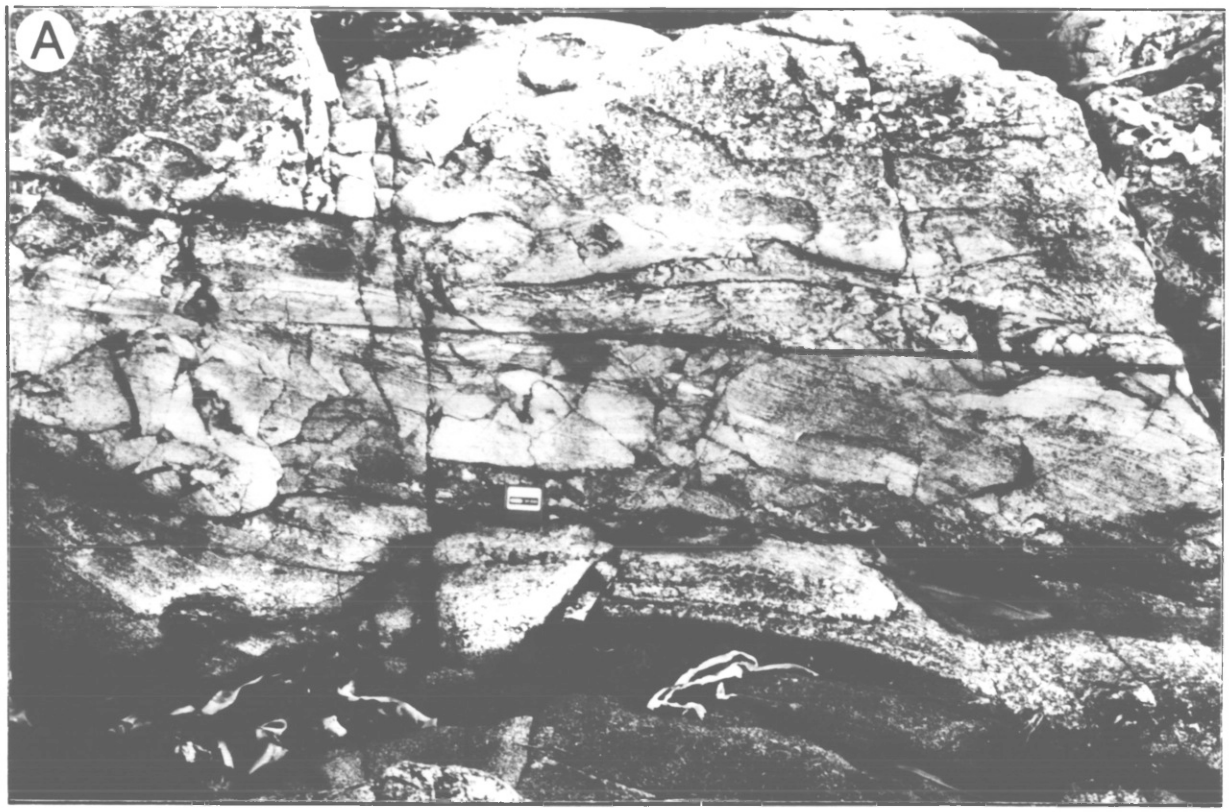
The relationship between these quasiconglomerate zones and structurally distinct bodies of amphibolite (e.g. Fig. 4.7d and Plate 4.8) is comparable to that seen at Greian Head; similar conclusions are drawn.

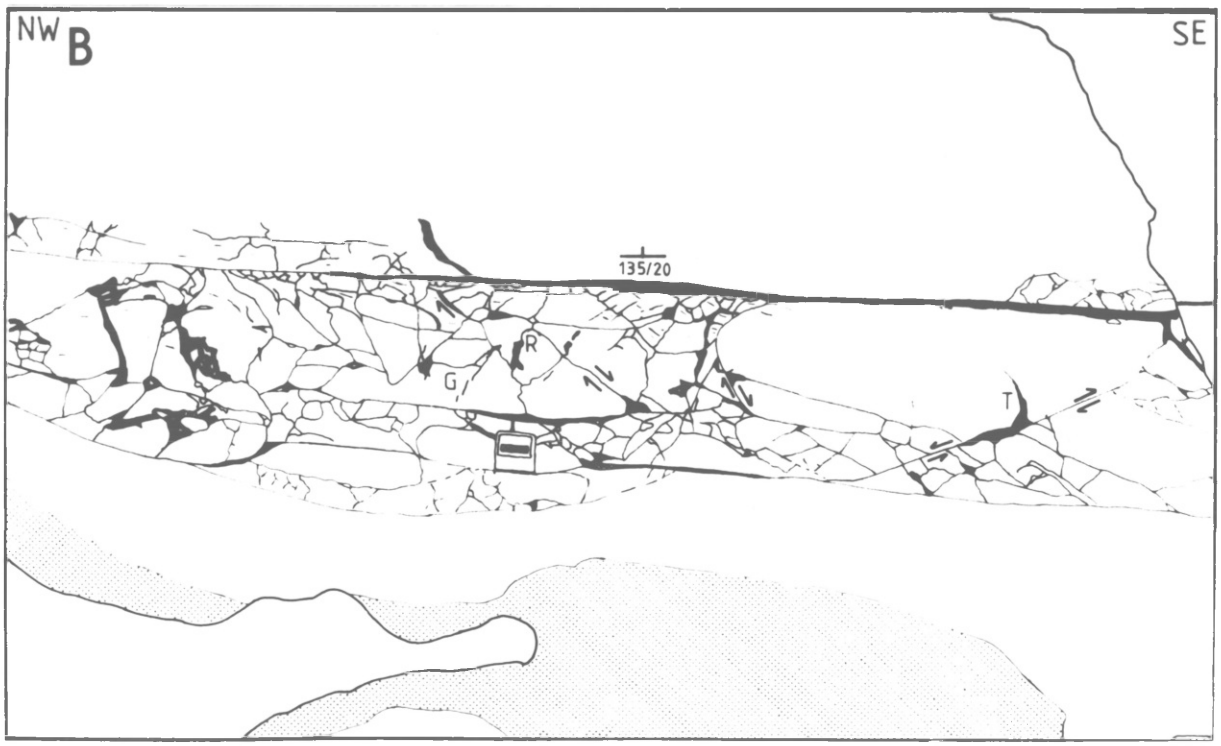
A narrow NE-dipping quasiconglomerate zone is illustrated in Plate 4.8. Significant differences exist between this zone and the sub-vertical zone shown in Plate 4.7. Many of the pseudotachylyte-bearing fractures within the zone are markedly curviplanar, having irregular, spidery traces which separate rounded blocks of gneiss (e.g. R in Plate 4.8). This demonstrates that 'rounding' of clasts in quasiconglomerate zones may result from initial fracturing and not only later spallation and attrition (cf. Sibson, 1975). Such fracture trajectories suggest complex dynamic stress trajectories during faulting. Shear separations on other minor fracture are small (<1 cm) although some pseudotachylyte may have been generated on these surfaces. Dilation of fractures by intrusion of pseudotachylyte melt (e.g. T in Plate 4.8) can lead to opposing senses of shear along the fracture. Rotation of the blocks increases with decreasing clast size and increasing matrix:clast ratio. This quasiconglomerate zone is believed to have suffered a rather small displacement although this cannot be proven. The curviplanar minor shear traces contrast with more planar traces described by Grocott (1981), and are a testament to not only rotated but also dynamic stress trajectories during pseudotachylyte faulting.

4.4.4 Irregular Quasiconglomerate Zone

Map 4 portrays the outcrop of an unusual and highly irregular quasiconglomerate zone. The exposed basal envelope to this zone is a strongly curviplanar surface (FV?), whose attitude varies from

PLATE 4.8 Photograph (A) and tracing (B) of quasiconglomerate layer with probable low displacement, Rubha Ardvule (NF71483002).


A


NW
B
SE
135/20
R
G
T

foliation-parallel to a 90° angular discordance to the consistently WNW-striking gneisses on either side of the outcrop (map4; Plate 4.9A).

Limited brittle (sub-barren) microfaulting occurs in the gneisses to either side of the quasiconglomerate zone (Plate 4.9B) and within clasts in the quasiconglomerate (Plate 4.9C). It clearly predates the pseudotachylyte faulting. This observation together with the jigsaw-like fit of many of the clasts and the lithological similarity between the clasts and the immediately surrounding gneisses suggests that translation of the clasts was limited. Where the pseudotachylyte:clast ratio is low the clasts tend to be angular and are separated by fractures which show little shear separation. Where the pseudotachylyte:clast ratio is higher, the clasts tend to be more rounded, rotated and polymict indicating greater translation.

The important feature about this outcrop is that it again demonstrates that considerable dilation has taken place during pseudotachylyte faulting. It also suggests that fracture involved a large component of extension. Careful field inspection of this outcrop and thin-section study of quasiconglomerale from similar outcrops, suggest that the quasiconglomerate formed during a single event; cross-cutting relationships were not observed. It is possible that this quasiconglomerate formed in a dilation fault-jog (Sibson, 1985). No explanation is offered to account for the remarkable form of the basal envelope.

A spectacular IV array extends some 1.1 m to 024 adjacent to the southern boundary of the quasiconglomerate zone (map 4). The veins were injected with pseudotachylyte from the now largely eroded away, overlying quasiconglomerate (see Plates 4.10A and B). The following observations are pertinent with respect to the origin of the veins:-

(i) the stepping direction is unsystematic, with 2 right-stepping and 1 left-stepping vein overlap (map 5; Plate 4.10A);
(ii) vein overlaps maintain near-constant dilation (Fig 4.9);
(iii) near mirror-image walls are modified slightly by spallation;
(iv) sinistral offset of wallrock markers and dilation of the veins increases approximately symmetrically from the vein ends to their mid-points;
(v) sinistral offset of the markers can be fully accounted for by oblique extension in a direction parallel to the strike of the transform microfault T in Fig. 4.9;

PLATE 4.9 Detail of irregular quasiconglomerate zone shown in map 4, Rubha Ardvule.

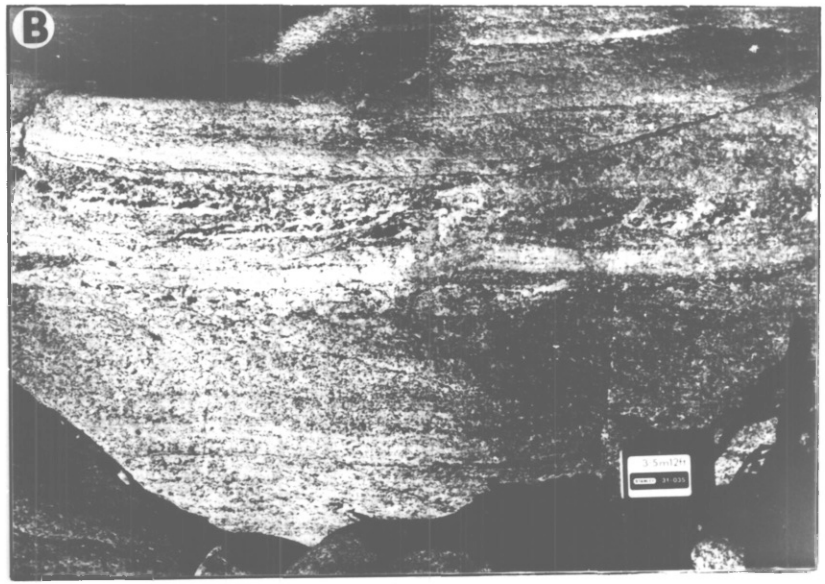
(A) NW contact between quasiconglomerate and grey gneiss. Note extensional microfault affecting amphibolite layer close to hammer handle. Gneissic foliation dips uniformly 20 to NE; apparent folding is a consequence of relief.

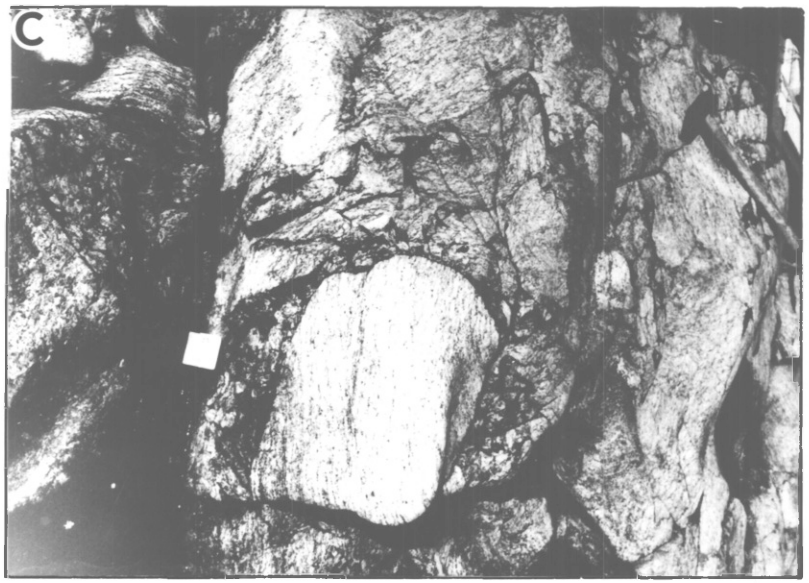
(B) Grey gneiss to SE of quasiconglomerate showing ramp-flat contractional microfaults.

(C) Quasiconglomerate with irregularly-shaped and sized clasts with local jigsaw fit.

(D) Quasiconglomerate. Clast above tape-measure is isolated by pseudotachylyte layer parallel to the plane of the photograph.


A


B


C

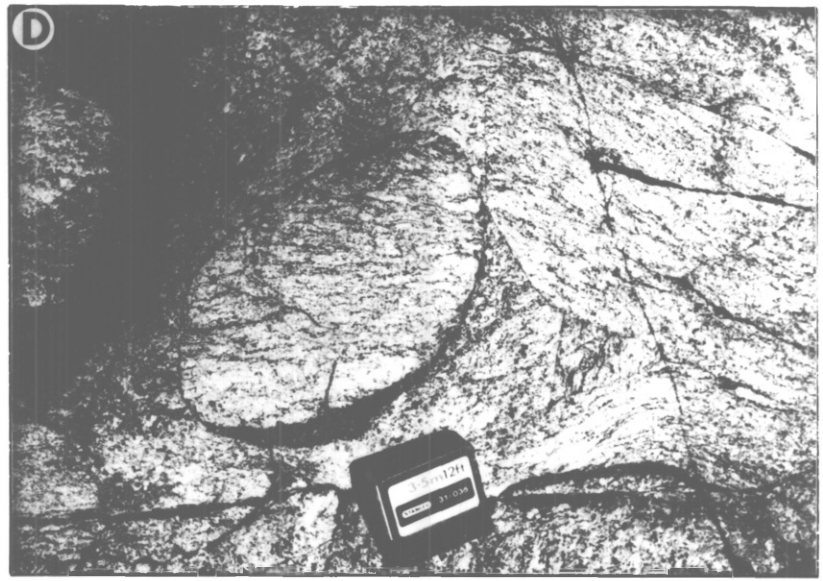

D

PLATE 4.10 Detail of IV array associated with quasiconglomerate zone shown in map 4, Rubha Ardvule.
(A) IV array comprising 4 veins (1-4) extending from southern margin of quasiconglomerate.
(B) Detail showing vein 1 and outlier of quasiconglomerate (O) which is structurally above the vein.


A
0
1
2
3
4

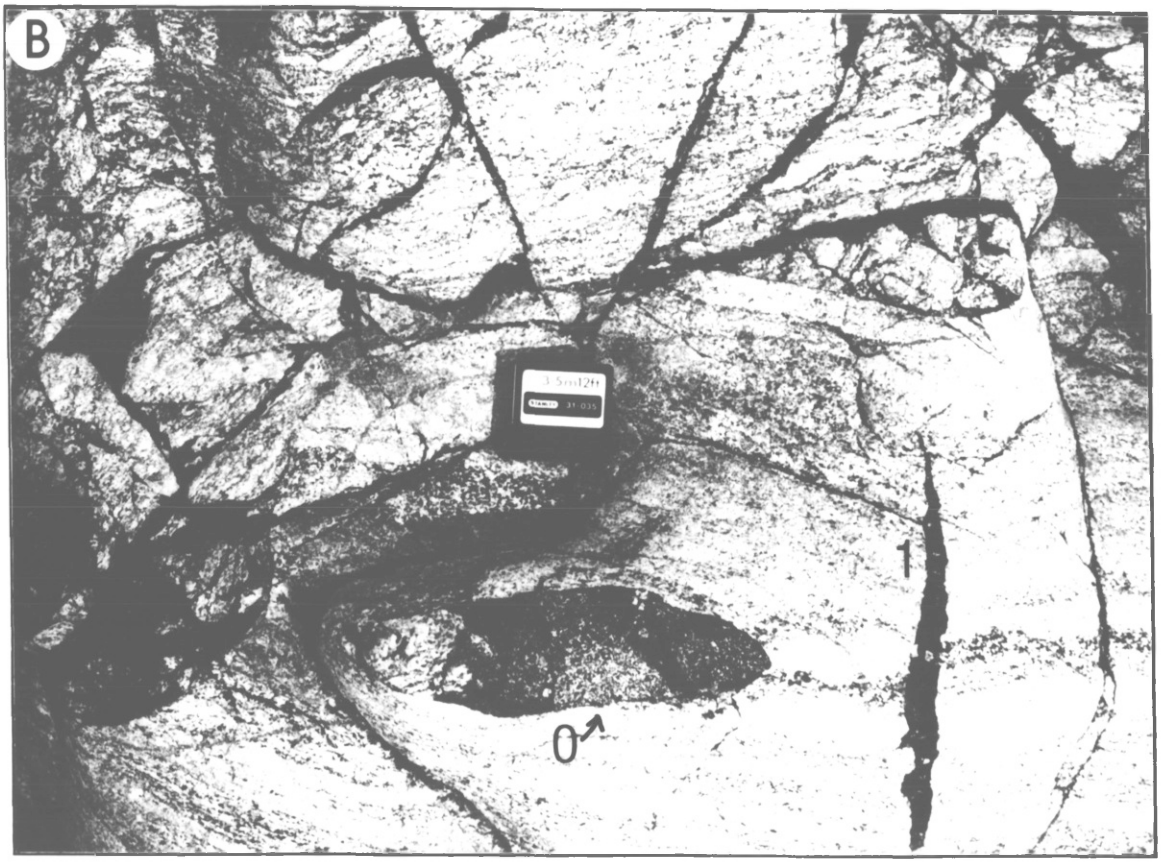
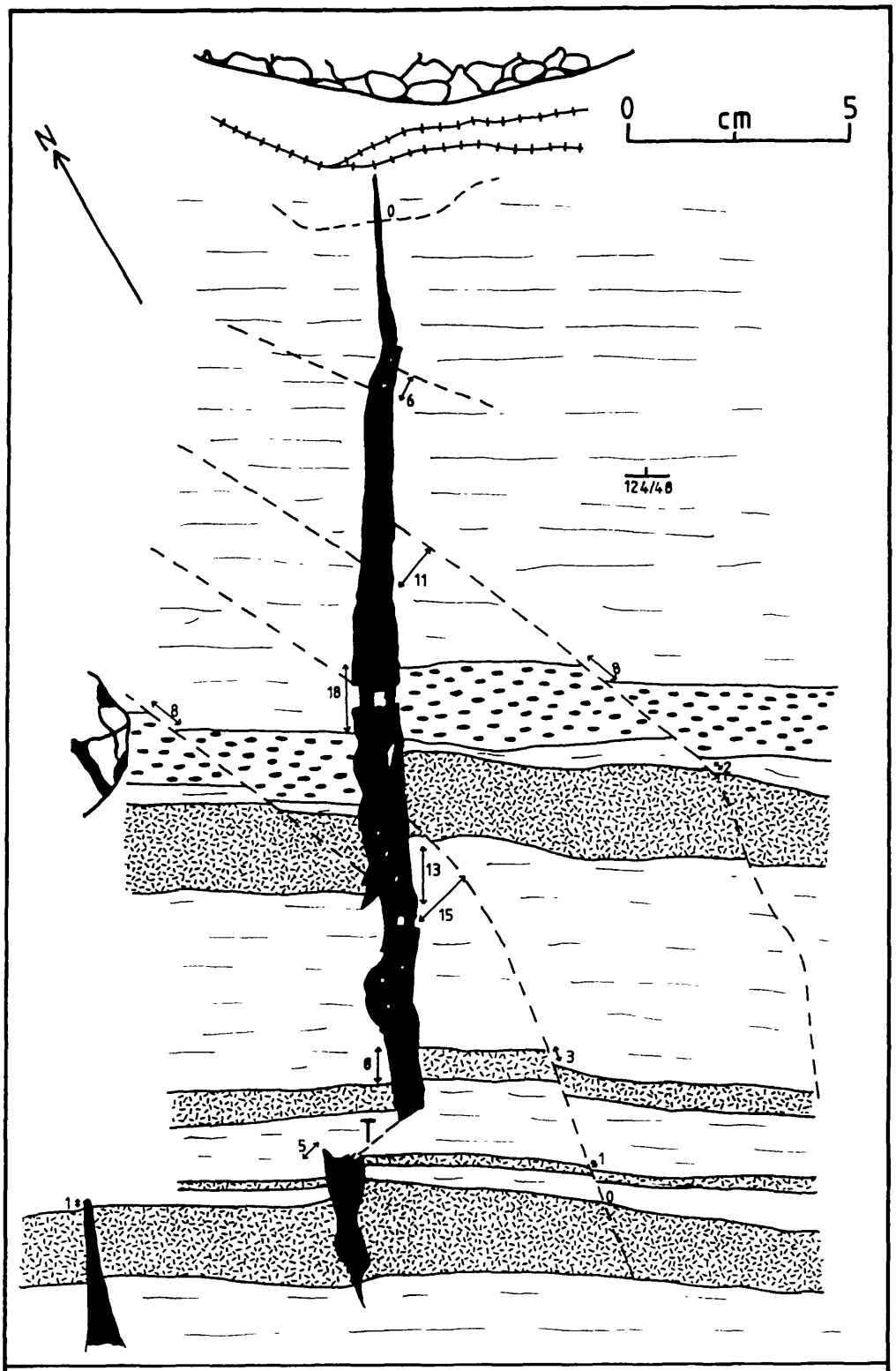

B
1
0

FIGURE 4.9 Detail of part of the IV array shown in map 5 and Plate 4.10. Note maximum extension direction is parallel to transform microfault T.


0
cm
5
N
124/48
0
6
11
18
8
8
2
13
15
6
3
T
5
1
1
0
KEY
acid gneiss
hornblende gneiss
pegmatite
pseudotachylyte
quasi-conglomerate
microfault
epidote vein
12 separation (mm)
T transfer microfault

(vi) the vein overlap trajectories between veins 2 and 3 (Plate 4.10B) are inconsistent with sinistral slip on a right-stepping shear fracture system (Segall and Pollard, 1980);
(vii) no conjugate array is developed;(viii) there is no visible evidence of related strain in the surrounding gneisses at the vein tips or elsewhere.

The geometrical relationship between the veins and the transform microfault (Fig. 4.9) are similar to those found in en-echelon shear fractures illustrated by Gamond et al (1983, p.35, Fig.s 3 and 4). It is suggested that these are hybrid extensional/shear fractures.

4.4.5 Microjointing

Pseudotachylyte is invariably intensely jointed. At the simplest, a single set of closely-spaced 'cross-joints' may cut IV's and FV's at a high angle to their walls (Fig. 4.10). These are probably extension joints resulting from differential volume changes in the cooling pseudotachylyte and host-rock (Hobbs et al., 1976, p.299).

The flat-lying pavements and quasiconglomerate zones are usually cut by a high-angle rectilinear joint set (Plate 4.11A, B and C). Joint frequency varies from decimetric or greater spacing in the gneiss to centimetric or millimetric spacing in the pseudotachylyte (Plate 4.11). Within quasiconglomerate, joint frequency and intensity decreases into the large clasts of gneiss (Plate 4.11C). The high joint frequency in pseudotachylytes may be attributed to the following factors:-

(i) the pseudotachylyte will possess more stored elastic strain energy than the gneiss due to volumetric contraction during rapid cooling of the melt. Price (1966, p.43) has suggested that joint frequency is dependant on the amount of stored elastic strain energy in the rock;
(ii) joint frequency tends to increase with decreasing layer thickness (Price, 1966).

The azimuths of high angle joint sets affecting selected pseudotachylyte pavements at Rubha Ardvule are plotted in Fig. 4.10. Two dominant trends separated by an angle close to 90 are typical.

FIGURE 4.10 Rose diagrams showing joint orientations in pseudotachylyte IV's and pavements and host gneisses at Rubha Ardvule. The joints in the gneisses are spaced about 40+ cm apart and the microjoints in the pseudotachylytes 0.5 - 5 cm apart, unless otherwise specified. (Frequency is proportional to length not area of rose 'petals'.)

a (i) Orientation of 24 sub-vertical IV's of exposed trace greater than 1 m; (ii) orientation of 59 sub-vertical microjoints in the IV's. (NF71142967)

b (i) Orientation of 70 sub-vertical joints in host gneisses; (ii) orientation of 58 sub-vertical microjoints in pseudotachylyte pavements. (NF71192957).

c (i) Orientation of 55 sub-vertical joints in host gneisses; (ii) orientation of 123 sub-vertical microjoints in pseudotachylyte pavements. (NF711301).

d (i) Orientation of 239 sub-vertical joints in host gneisses; (ii) orientation of 182 joints in gneiss and small areas of pseudotachylyte pavement (10 - 25 cm spacing); (iii) orientation of 229 microjoints in pseudotachylyte pavements. (NF708299).

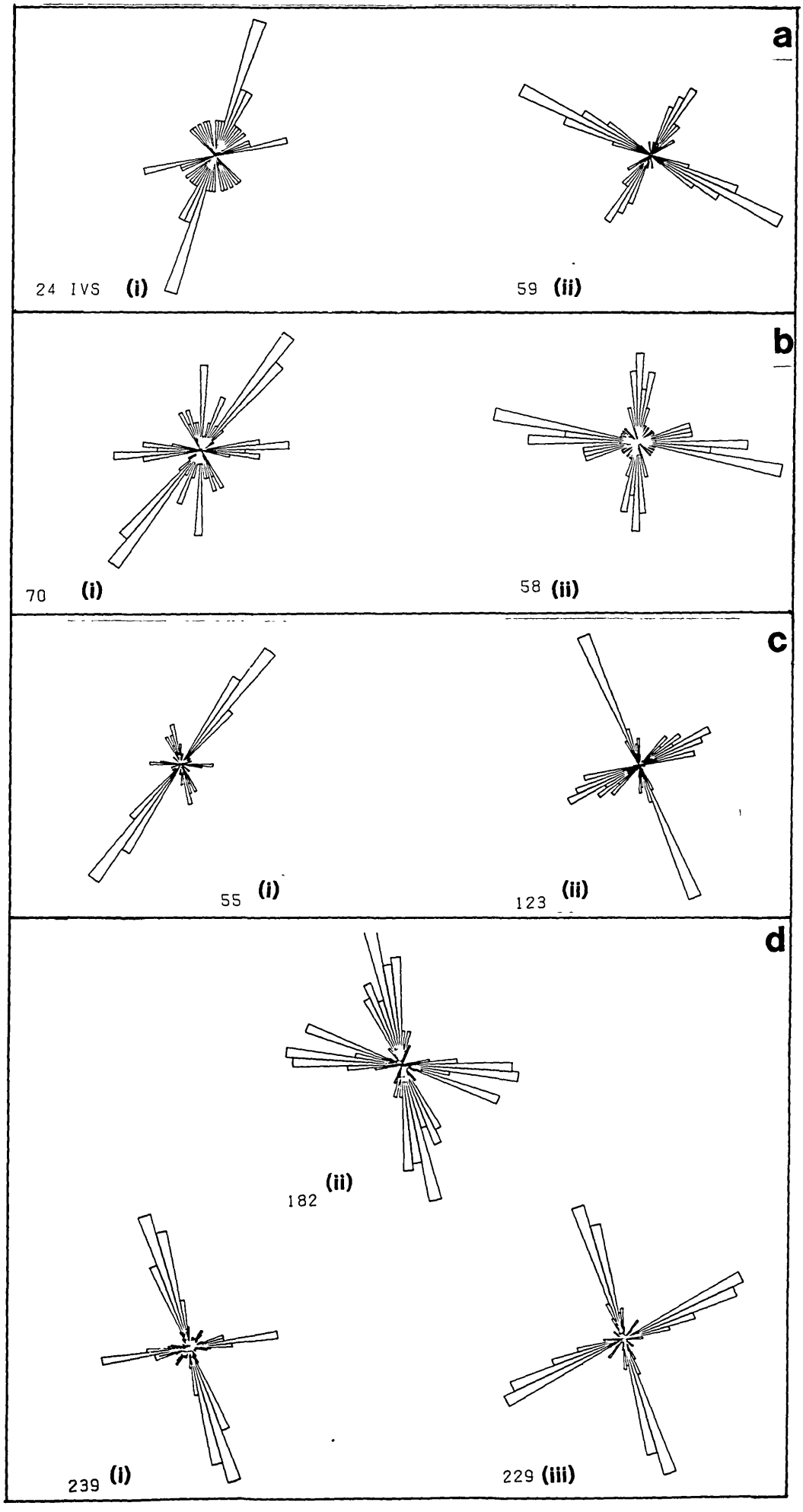

a
24 IVS (i)
59 (ii)
b
70 (i)
58 (ii)
c
55 (i)
123 (ii)
d
182 (ii)
239 (i)
229 (iii)

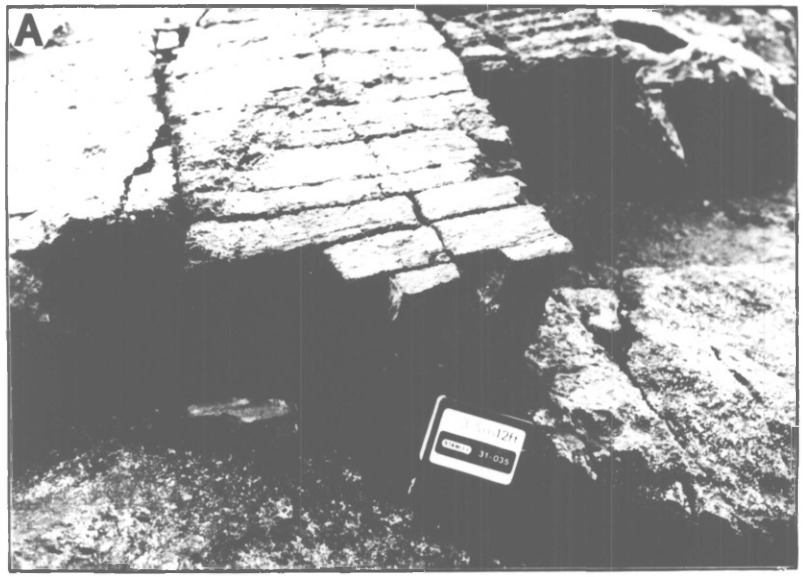
PLATE 4.11 Field photographs of jointing affecting pseudotachylyte pavements at Rubha Ardvule, S Uist.

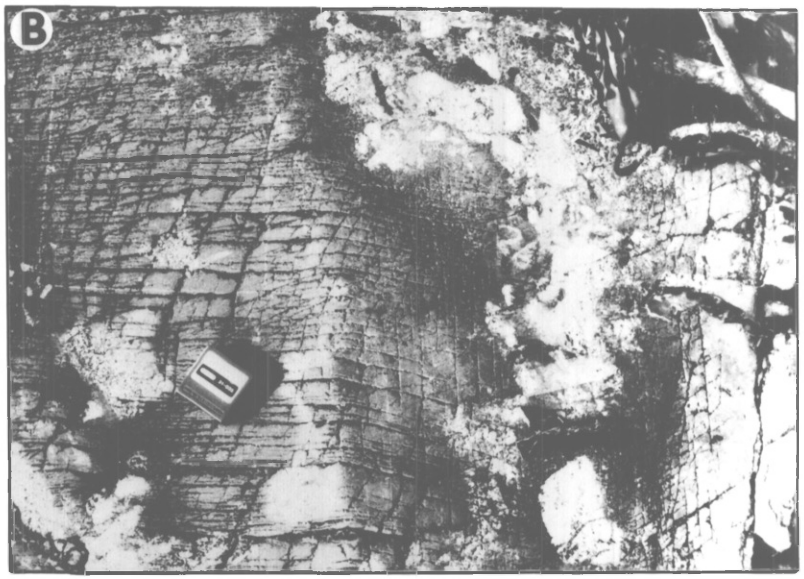
(A) Flat-lying 5 cm thick pseudotachylyte pavement cut by steep WNW and NNE-trending joint sets. Pseudotachylyte has a strong but irregular magnetic effect on compass readings. (The plagioclase-microlitic psedotachylyte sample R2 described in section 5.2 was collected here.) (NF71172957).

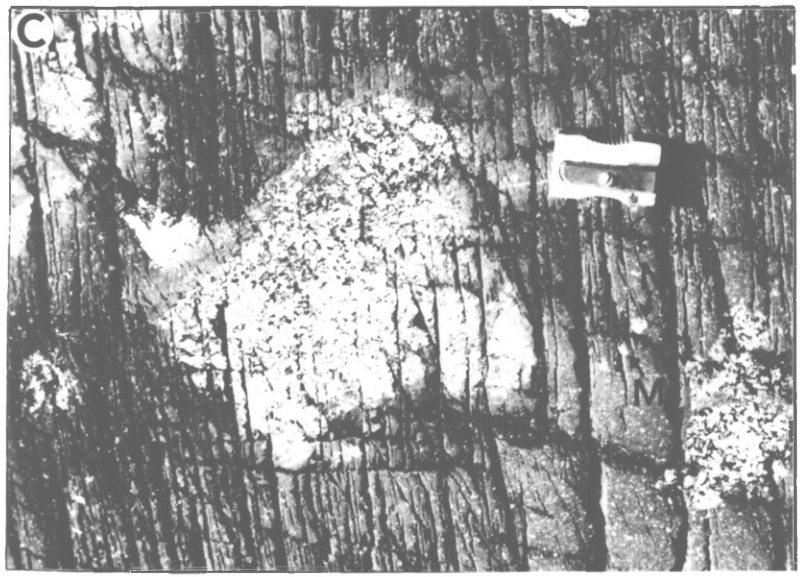
(B) Pseudotachylyte pavement with an 'antiformal' outcrop, resulting from wave-erosion, exposing gneissic clasts in the r.h.s. of the photograph. Prominent rectilinear joint set trends NNW and .E-W (NF71133009).

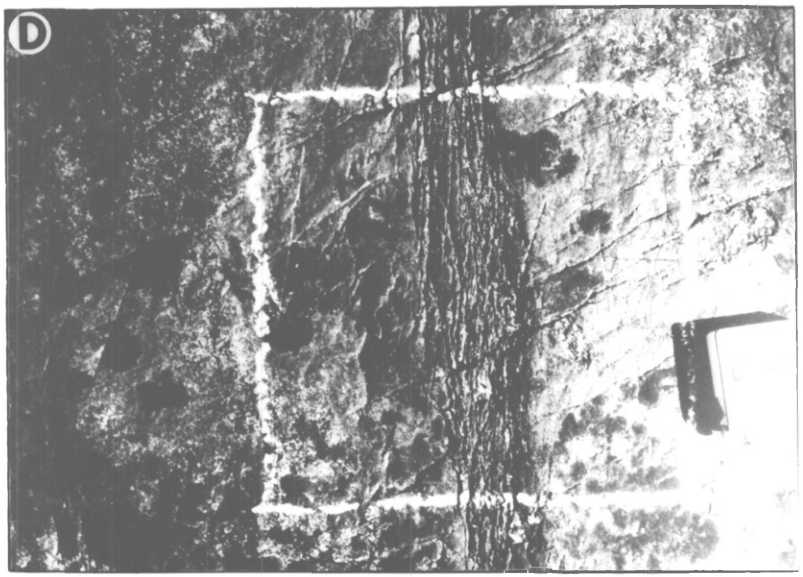
(C) Detail of (B) showing reduced joint development in gneissic clast. Note abundance of millimetric quartz and feldspar clasts in the pseudotachylyte.

(D) Brittle shear zone/intense jointing trending E-W in flat-lying pseudotachylyte pavement. Inferred shear sense is dextral. Subsidiary joint set trends NW. (NF70892994).


A


B


C


D

Generally these trend approximately WNW and ENE, though some variation is present.

4.5 Field Studies: Conclusions

Four objectives of fieldwork were given in section 4.1. General and specific conclusions may be summarized as follows.

1) Geometry of Pseudotachylyte Veins. Single jerk pseudotachylyte veins have a simple FV-IV geometry. Quasiconglomerate zones have variable geometry, from simple as in the sub-vertical zones at Rubha Ardvule to complex as in the flatter-lying zones at both Rubha Ardvule and Greian Head. At their simplest, they result from single jerk displacements. Curviplanar fractures within such zones are a testament to complex dynamic stress trajectories.

The more complex quasiconglomerate zones appear to result from larger displacements and/or more than one increment of slip. In many cases, substantial dilatancy must have occurred during slip.

2) Effects of pre-existing structure and lithology. Preferential failure along foliation planes and lithological contacts has been documented and ascribed to the relative weakness of these planes. The transition to discordant faulting at Greian Head may be due to displacement hardening associated with 'welding-up' of the gneisses by pseudotachylyte melt.

On both a small scale (metres) and on a larger scale (tens of metres), amphibolite bodies have been observed to be largely devoid of pseudotachylyte faulting. Such features are believed to be the physical expression of fault plane barriers discussed in section 2.2.2.

3) Kinematics. At Greian Head the majority of single jerk FV separations are consistent with E - W directed thrusting followed by SSE - NNW directed thrusting. Minor structures, including faulted IVs, IV arrays and single IV orientations, systematic minor shear orientations and possible fault-related folding are also consistent with this interpretation. At Rubha Ardvule the earliest pseudotachylyte faulting occurred along discrete, predominantly NW-trending FV/quasiconglomerate systems. Sinistral and dextral strike slip separations have been recorded. Movement sense along the more

flat lying quasiconglomerate zones at both localities is more difficult to infer.

The kinematic interpretation made here corresponds broadly to that made by Francis (1969) for Barra and Sibson (1977a) for elsewhere in the Outer Hebrides.

4) Palaeoseismic Source Parameters. Measured separations in the range a few cms to nearly 3 m correspond to the observed range for coseismic slip (Table 2.1). Limited outcrop unfortunately precludes proper estimates for fault dimensions. However, the sub-vertical quasiconglomerates at Rubha Ardvule certainly extend for 10s of metres; if they are contiguous with those exposed on Askernish then fault plane areas of tens of millions of square metres may be estimated. That pseudotachylyte faulting clearly involves considerable local dilatancy is evidenced by some quasiconglomerate zones. Following slip, the pseudotachylyte melt (fluid) pressure may have been close to lithostatic pressure.

CHAPTER 5 PETROGRAPHY, MINERALOGY AND MICROSTRUCTURE OF PSEUDOTACHYLYTES

5.1 Introduction

A general classification based on the petrography of the matrix of pseudotachylytes encountered in this study is given in Table 5.1. Examination of the literature suggests that this could be widely applied to the great majority of fault-generated pseudotachylytes. Examples of these types are described in detail in the following sections. In attempting to identify the controlling factors responsible for the textures and mineralogy of pseudotachylytes some descriptive repetition is inevitable.

The textures and mineralogy of the porphyroclasts contained within the pseudotachylytes are described separately as many features are common to the different types of pseudotachylyte. Finally, the mineralogy and significance of various 'filled cavities' (microfractures, amygdales and porphyroclast replacement pseudomorphs) are examined.

5.2 Plagioclase-Microlitic Pseudotachylytes

Plagioclase-microlitic pseudotachylytes are defined as having a matrix largely composed of acicular plagioclase microlites which may be arranged decussately, flow-aligned or grouped into open, wheatsheaf spherulites. They grade within a single vein and between veins into more closely-packed spherulitic types (Plate 5.1B and C). They are best developed in FV's and IV's with a minimum width > 2 cm, generated in more acid (feldspathic) gneisses. The samples described here were collected chiefly from Barra and Rubha Ardvule, South Uist (map 1) but are representative of similar veins collected along the length of the western OHT zone, from Tiree and Silvretta, Alps.

5.2.1 Description

The plagioclase microlitic pseudotachylytes are invariably strongly porphyroclastic, containing poorly sorted and rounded clasts of quartz, plagioclase and K-spar (if present in the host-rock), together constituting 15 - 35 modal % of the vein. Ferromagnesian and

TABLE 5.1 GENERAL CLASSIFICATION OF PSEUDOTACHLYTE TYPES DESCRIBED IN THIS STUDY

Name/Matrix Type	Typical Host-rock	Comments
Plagioclase-microlitic	leucocratic quartz of feldspathic gneiss	Dominated by skeletal plagioclase microlites; chilled margins; trachytic texture; occassionally amygdaliodal
Amphibole-microlitic	? leucocratic amphibolites	Skeletal amphibole and plagioclase microlites
Pyroxene-spherulitic	? garnet-biotite gneiss; (charnockites)	dendritic orthopyroxene and skeletal plagioclase microlites
Chloritic-spherulitic	amphibolite	heterogeneously nucleuted chlorite/plagioclase spherulites in chlorite-rich matrix
Phyllosilicate-spherulitic	biotite or white-mica rich gneisses	fine grained globulitic/ spherulitic K-mica matrix
Flow-banded types	various	flow banded streaks of chemically/ mineralogically distinct pseudotachylyte and ultracataclasite

Note: terminology explained further in Table 5.2

TABLE 5.2 DESCRIPTIVE TERMINOLOGY OF FINE-GRAINED CRYSTAL FORMS IN PSEUDOTACHYLYTES

Term	Definition
Acicular	needle-shaped
Dendrite	branching form of single crystal
Equant	crystal having similar dimensions in each direction
Globulite	irregular/spheroidal structure with definite nucleus but ill-defined fibro-radial or concentric halo
Microlite	small, usually acicular crystal
Skeletal	usually acicular crystal with (melt-filled) voids, with hollow or irregular form in thin section
Spherulite	radiating array of crystal fibres having same fibre axis; open spherulites contain visible inta-fibre material; closed spherulites have tightly woven fibres
Modifying Adjectives for spherulites:-	
axiolitic	spherulite fibres radiate from line rather than point
bow-tie	spherulite fibres whose 3D form is akin to 2 cones joined at apices.
fan	spherulite fibres whose 3D form is akin to a single cone with nucleation at its apex
plumose	spherulites which tend to be open, with side branching of fibres (i.e. fibres are dendritic)
wheat-sheaf	loosely constrained bundle of coarse (microlitic) fibres; coarser than bow-tie
swallow-tail	tabular, usually skeletal crystal with 2 pairs of tuning-fork-like projections
tabular	crystal flattened parallel to one crystal axis relative to the others.

Note: Modified after Lofgren (1974a).

TABLE 5.3 CHARACTERISTICS OF MATRIX FELDSPARS IN PLAGIOCLASE MICROLITIC PSEUDOTACHYLYTES

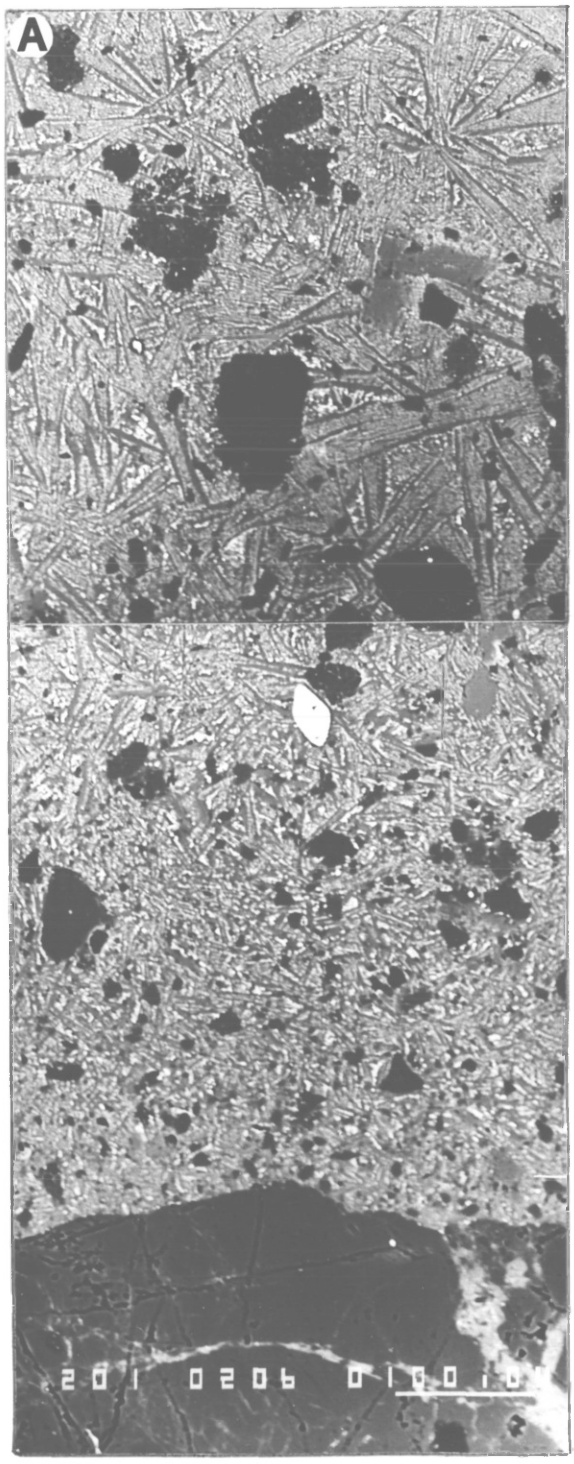
Crystal morphology:	Square tabular	Lath tabular	Acicular	Spherulitic
Maximum dimensions (μm)	40 x 40	36 x 50	200 x 20	200 x 2
Maximum growth parallel to	(010), (001)	(010)	(010)	(010)
Composition	An_{25-45}	An_{25-45}	An_{25-45}	An_{22-25}
Form	Chiefly filled	Skeletal filled	Skeletal filled	-
Twinning	Albite, Pericline	Albite, Pericline	Albite, Pericline	-
Zoning	Sector, normal	Sector, normal	-	-
Example	Plate 5.3	Plate 5.2F	Plate 5.2D	Plate 5.1

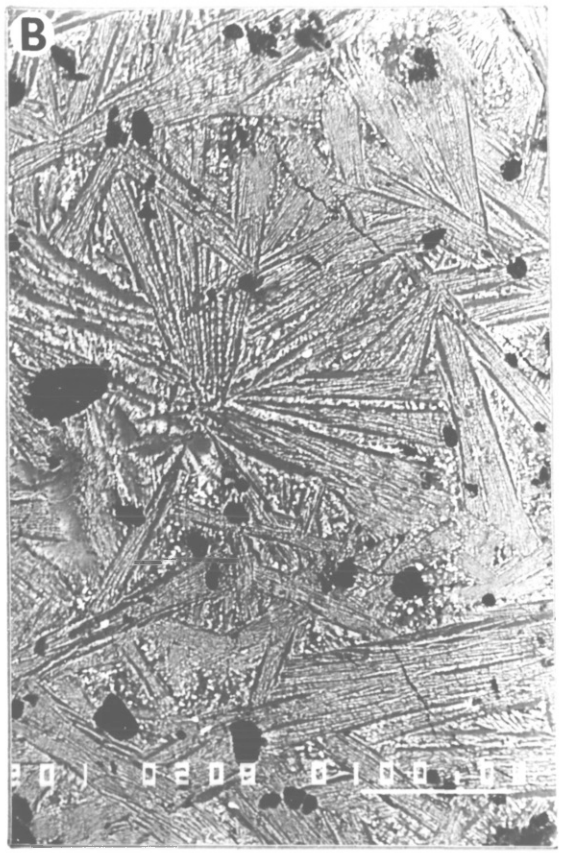
PLATE 5.1 BSE micrographs showing texture of plagioclase microlitic pseudotachylyte FV, sample SH1. Scale in microns

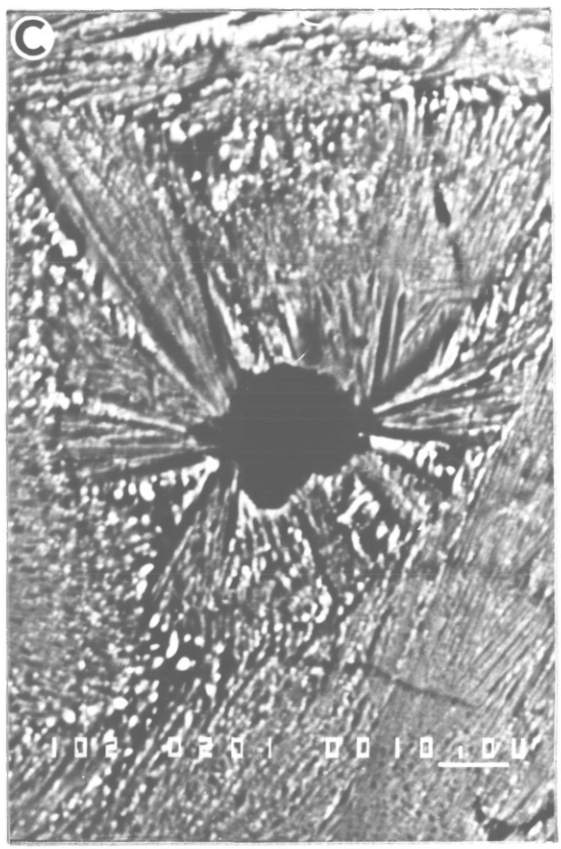
(A) Contact between plagioclase-rich host-rock (impure anorthosite) and pseudotachylyte with 450 μm wide chilled margin passing into axial zone of coarse microlites and bow-tie spherulites of plagioclase.

(B) Detail of axial portion of vein showing sheaf-like plagioclase microlites up to 200 x 50 μm. Note complex interlocking/decussate structure of microlites. Porphyroclasts are largely quartz which have not acted as nuclei for microlite growth.

(C) Detail of axial portion of vein showing individual plagioclase spherulite. The nucleus is an angular/ subrounded quartz clast mantled by a 5 μm wide rim of plagioclase (revealed by variation in the BSE contrast and Ca K_{α} X-ray mapping). Note the concentration of high mean atomic number phases (rich in Fe) between the plagioclase spokes of the spherulite structure.


A


B


C

accessory mineral clasts usually constitute <1 modal % of the pseudotachylyte whereas they may constitute up to 20% of the host-rock. Further detailed description of the porphyroclasts is deferred to section 5.8.

The pseudotachylyte matrix consists of microlitic feldspar set in an ultra-fine grained groundmass of quartz, plagioclase, biotite and magnetite. The salient features of the matrix feldspars are summarized in Table 5.3. The dimensional data of Table 5.3 refer to a 5 cm thick IV (sample R2), but in a general sense vary irregularly with vein width, though these figures are close to the maximum dimensions in any vein. Exceptionally, variation in microlite size normal to the vein margin provides convincing evidence for a chilled margin in the classic igneous sense (Plate 5.1A). Every gradation exists from filled tabular forms to feldspar microlites of highly skeletal and inequant shape, reflecting both actual and apparent variation in shape due to capricious sectioning. The dominant form of the larger plagioclases is a skeletal-prism morphology (Plate 5.2D and E) with elongation parallel to (010) becoming more pronouced in the finer grained forms.

The tabular, more or less filled, plagioclase microlites rarely possess an optically apparent heterophase nucleus and are structurally complex. Most sections exhibit albite twinning (Plates 5.2F and 5.3B) and less frequently pericline twinning; the twin planes are continuous either side of devitrified melt inclusions indicating quite complex 3D morphologies (Plate 5.3B). Normal and more rarely sector zoning are present in some of the tabular plagioclases (Plate 5.3B). The (010) sector zones, which have rational planar crystal faces, are slightly more calcic than the (001) zones which have irrational, skeletal faces (Plate 5.3B). Similar, but more calcic, sector zoned plagioclases found in submarine quenched ocean-floor basalts (Bryan, 1972a) are considered to be indicative of high cooling-rate crystal growth from a melt (Lofgren, 1980, p.515). The origin of sector zoning is poorly understood but may involve face-selective 'poisoning' by adsorbtion in the (001) zones (Dowty, 1980, p.440). (Note: recognition of sector zoning requires fortuitous sectioning, particularly with such a fine grain size, and it may be more prevalent in the pseudotachylytes than is immediately apparent.)

The more skeletal plagioclases are usually heterogeneously nucleated onto substrates of pre-existing tabular plagioclase (Plate 5.3A) or feldspar (but rarely quartz) porphyroclasts where

PLATE 5.2 Optical micrographs showing textures in plagioclase microlitic pseudotachylytes; all PPL except (F) partially crossed nicolsx. (A-G) sample R2. (H) sample SU804.

(A) Melt-corroded quartz porphyroclast set in matrix of skeletal plagioclase microlites and spherulitic phases.

(B) Incipiently melted plagioclase porphyroclast showing fingerprint texture along grain boundaries and mantle of new 'belt-buckle' plagioclase.

(C) Detail of (B) showing 'belt-buckle' plagioclase heterogeneously nucleated on plagioiclase porphyroclast.

(D) Swallowtail and belt-buckle plagioclase in wheatsheaf spherulite with its nucleus out of plane of section set in spherulitic matrix.

(E) Detail of (D) showing devitrified melt-filled cores. melt filled cores.

(F) Filled tabular plagioclase showing albite twinning and secondary growth prongs parallel to (010).

(G) Plumose fan-spherulite of plagioclase and biotite projecting from the blunt termination of an acicular plagioclase microlite which is fringed by small magnetite crystals.

(H) Dendritic opaques showing cruciform and christmas-tree morphologies.

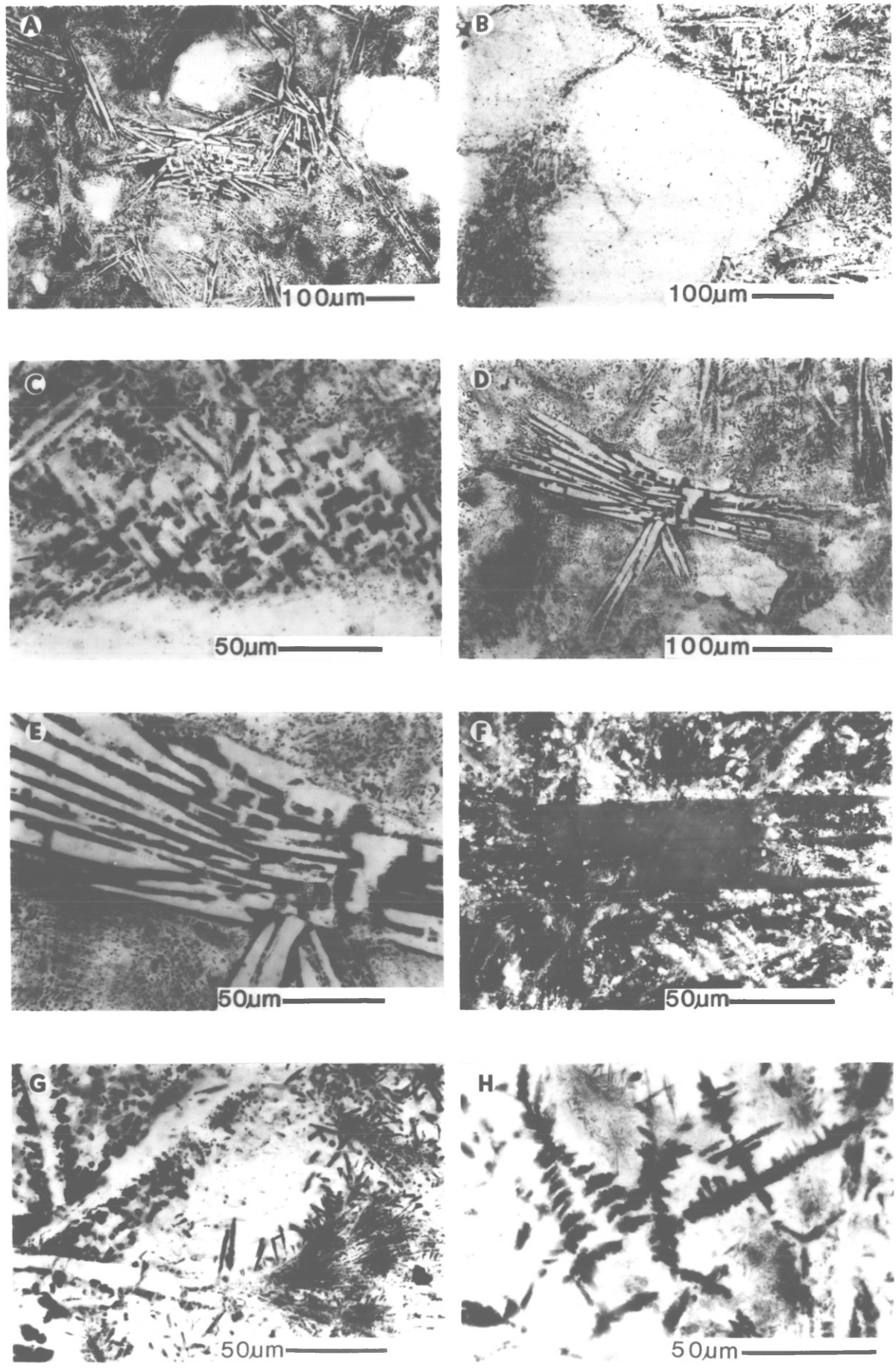
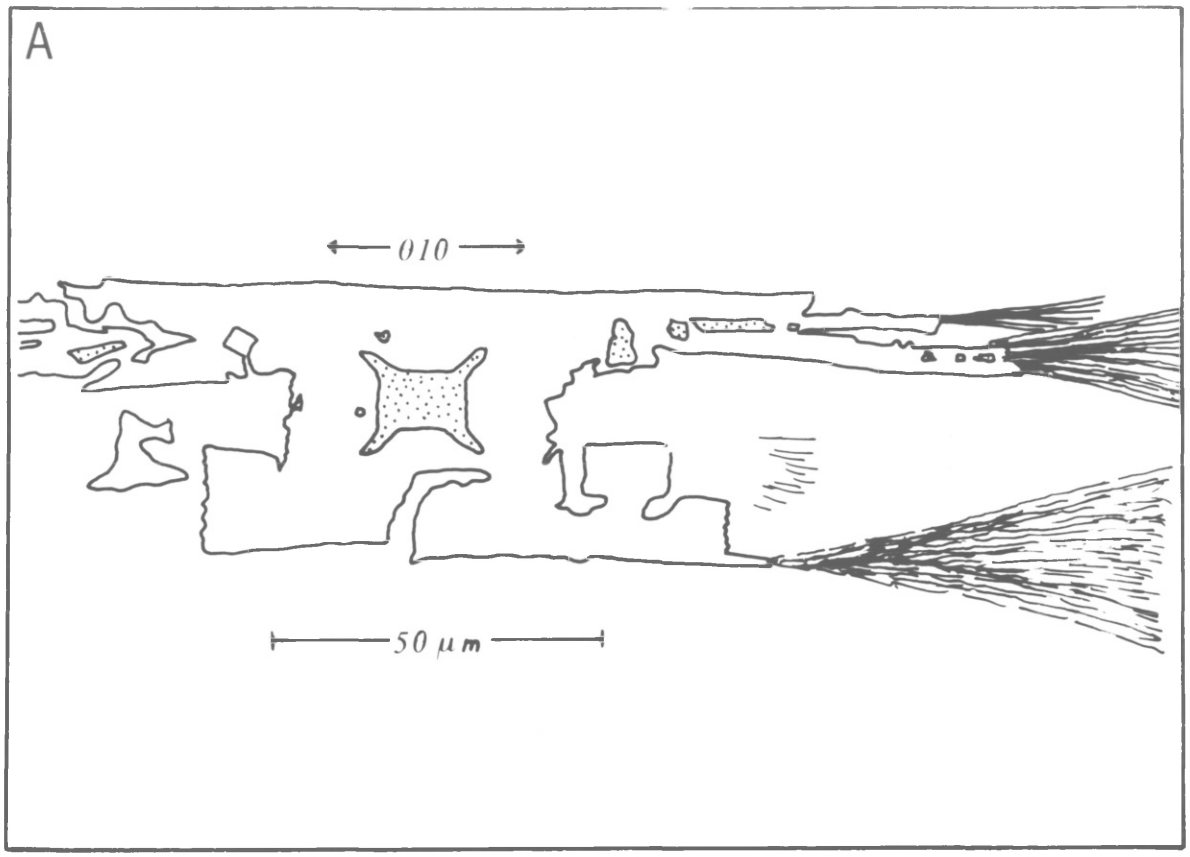
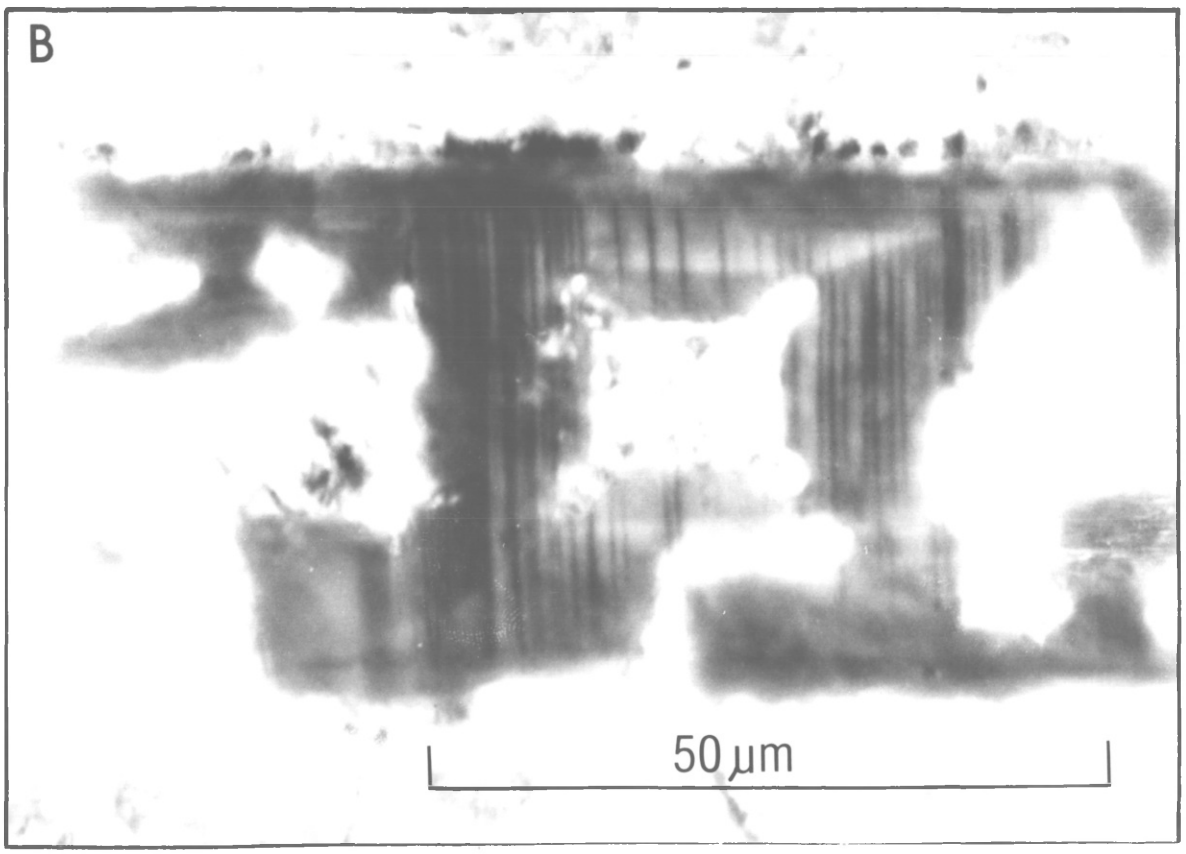

A
100μm
B
100μm
C
50μm
D
100μm
E
50μm
F
50μm
G
50μm
H
50μm

PLATE 5.3 Detail of plagioclase microlite, sample R2.
(A) Compound skeletal plagioclase showing 3 phases of growth: central tabular form of primary growth; secondary growth stage of skeletal acicular plagioclase elongated parallel to (010); and tertiary growth stage of fan-spherulite (mainly plagioclase). Drawn from photograph.
(B) Optical micrograph showing detail of central part of same crystal showing albite and pericline twinning, sector and normal zoning and crystallographically controlled form of melt inclusion.


A
010
50 µm


B
50 µm

'belt-buckle' shaped sections may be visible (Plate 5.2B).

Projecting from the blunt terminations of many of the acicular microlites are plumose fan spherulites composed largely of plagioclase intergrown with biotite (Plate 5.2D and G). Other optically resolvable phases in the groundmass include granular and dendritic opaques, chiefly magnetite (Plates 5.2H and G). Nucleation of the granular opaques on some of the microlite margins indicates late-stage precipitation of the former (although some of the granular opaque, derived from disequilibrium breakdown of biotite, may have been present in the melt prior to crystallization of the plagioclase) whilst late-stage dendritic opaques are common in igneous rocks (Tiller, 1964).

The ultra-fine grained groundmass interstitial to the feldspar microlites and fan spherulites has been examined by STEM. Foils from several different samples and different areas of the same thin section were prepared; representative transmission electron micrographs are presented in Plates 5.4 and 5.5. The greater part of the groundmass consists of euhedral quartz and plagioclase with a grain size <0.5 μm, and with quartz exceeding plagioclase modally (Plates 5.4A and 5.5A). Both the quartz and the feldspar are largely dislocation-free, which combined with an abundance of triple point grain boundaries (frequently close to 120°) indicates a 'well-annealed' or equilibrium texture. The third most abundant phase is biotite, present as small laths (0.2 x 1.0 μm) (Plates 5.4A and 5.5A) or occasionally as larger, more ragged plates to 1 um diameter (Plate 5.5B). Within the analytical limits of the STEM (Appendix A3), the laths and plates are compositionally indistinguishable (Fig. 5.1); both contain similar amounts of TiO_2 (Appendix A) suggesting that the plates as well as the laths are neocrystallized rather than porphyroclast relicts - which tend to be depleted in TiO_2 (section 5.8.4).

Small elongate rods (0.3 x 1.0 μm) of ilmenite and granules of magnetite (< 0.5 μm dia.) with rounded rather than faceted faces also occur in the groundmass (Plate 5.4B, C, and D). In Plate 5.4D a small rounded magnetite can be seen acting as a heterophase nucleus for the spherulitic growth of biotite. This foil was selected optically from a granular magnetite-rich area of the groundmass believed to be a palimpsest after the disequilibrium breakdown of a biotite porphyroclast. The neo-crystallized biotite may therefore have grown from a melt/glass domain enriched in biotite component. Pyrite of euhedral form and a grain size <0.5 μm (Plate 5.5E) occurs

PLATE 5.4 TEM micrographs showing microstructures and mineralogy of the groundmass of plagioclase microlitic pseudotachylytes. Sample SU803, foil 5.

(A) Large lath of biotite marked by pointer, surrounded by quartz, plagioclase and biotite.

(B) Groundmass of quartz (beam damaged), feldspar and ilmenite (dark).

(C) Ilmenite rod in quartz at edge of foil.

(D) Rounded magnetite grain with halo of spherulitic biotite.

(E) Euhedral pyrite grain surrounded by quartz (light grey) and biotite (mottled dark).

(F) Feldspar clast showing twinning and high dislocation density.

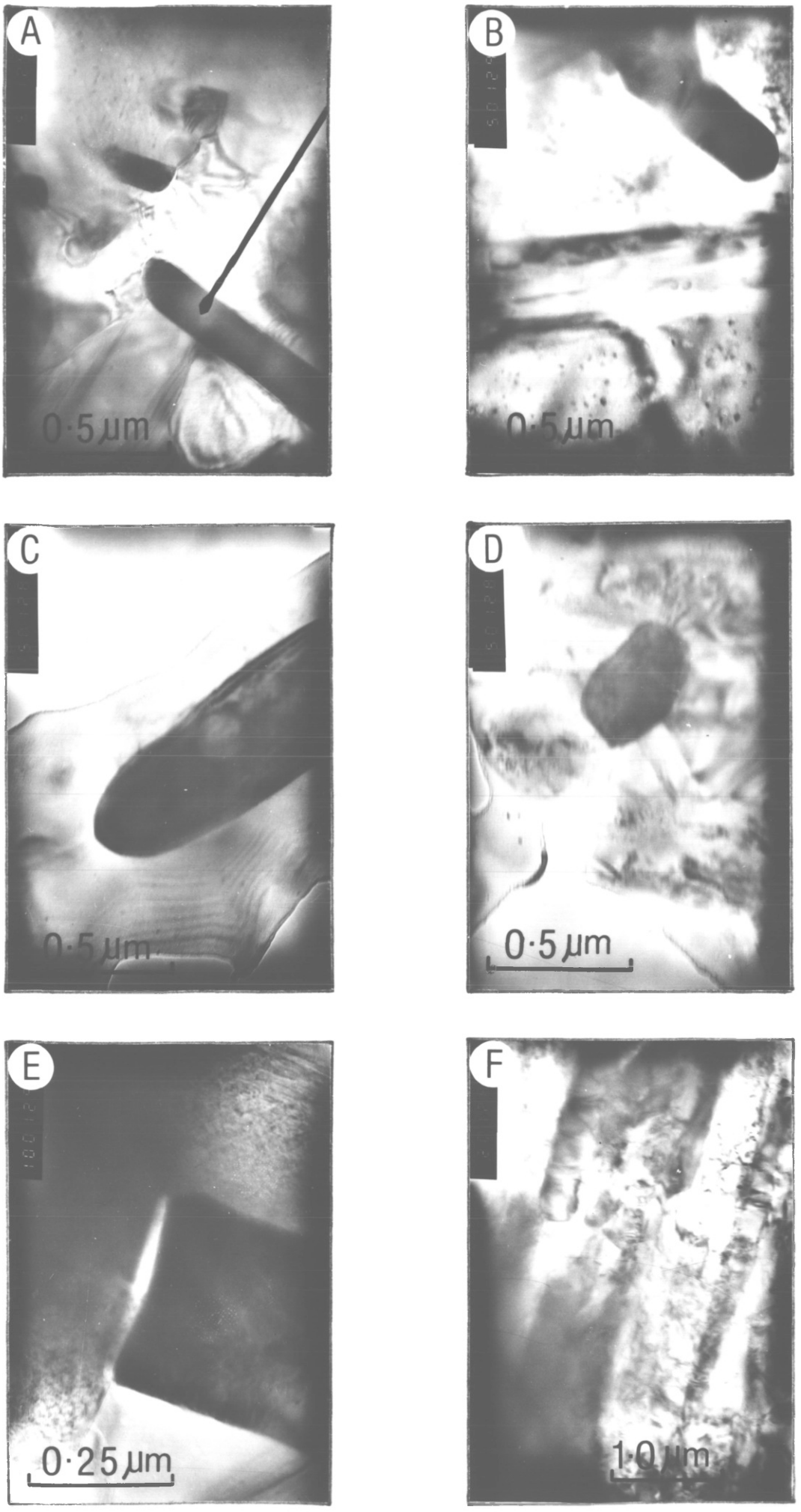
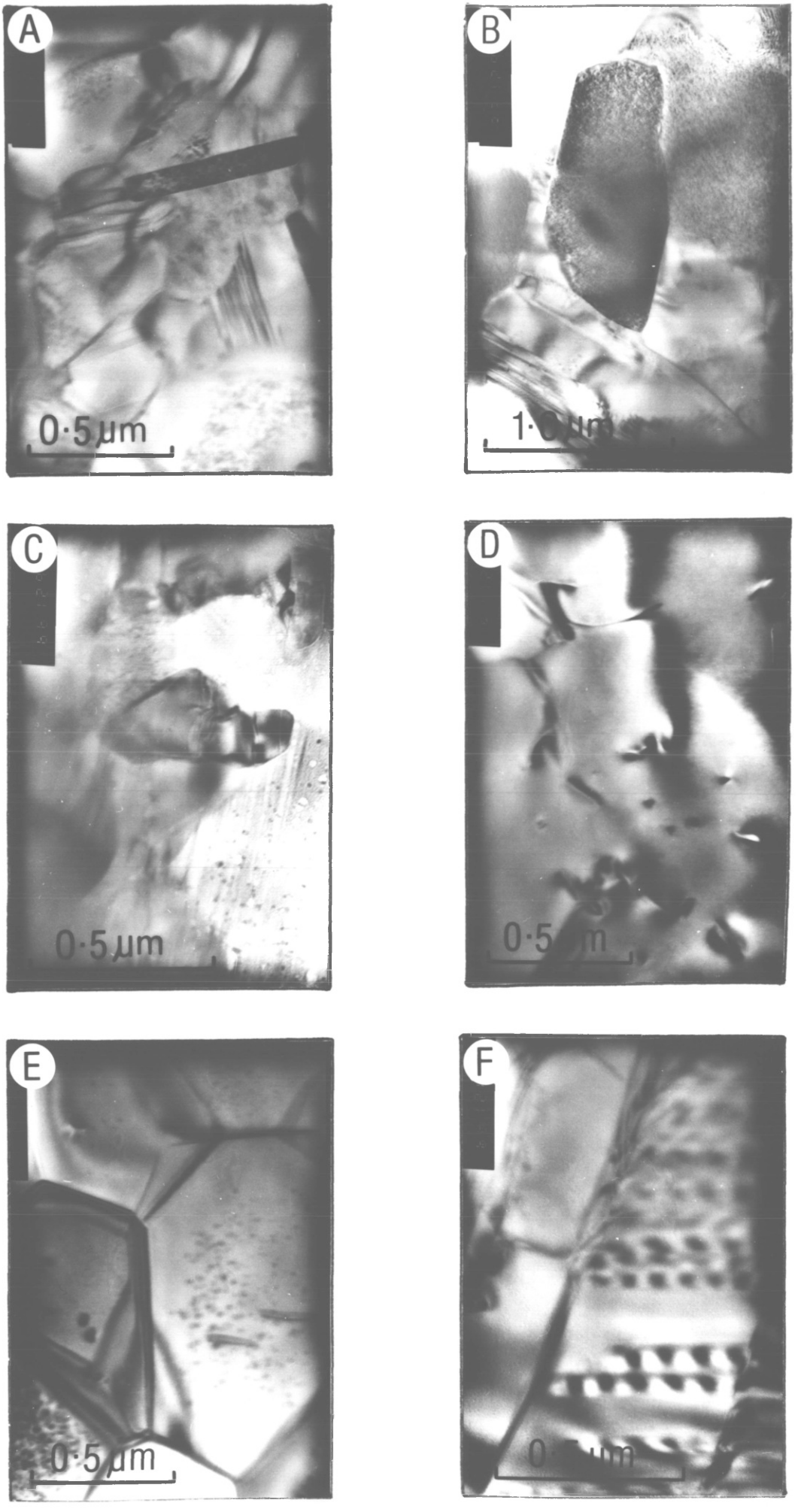

A
0·5 µm
B
0·5 µm
C
0·5 µm
D
0·5 µm
E
0·25 µm
F
1·0 µm

PLATE 5.5 TEM micrographs showing microstructure and mineralogy of the groundmass of plagioclase microlitic pseudotachylytes. (A), (B) sample SU803, foil 6; (C), (D), (E) and (F) sample R2, foils 3, 5 and 6.
(A) Groundmass of equant, dislocation-free quartz and plagioclase with laths of biotite showing slight beam damage.
(B) Large biotite grains surrounded by plagioclase showing picket fence subgrain boundaries.
(C) Small anhedral hornblende grain.
(D) Quartz clast showing low dislocation density.
(E) Equant quartz sub-grains showing annealed texture; believed to be recrystallized portion of a quartz clast.
(F) Detail of plagioclase clast showing picket-fence type dislocation wall.


A
0·5 µm
B
C
0·5 µm
D
E
0·5 µm
F

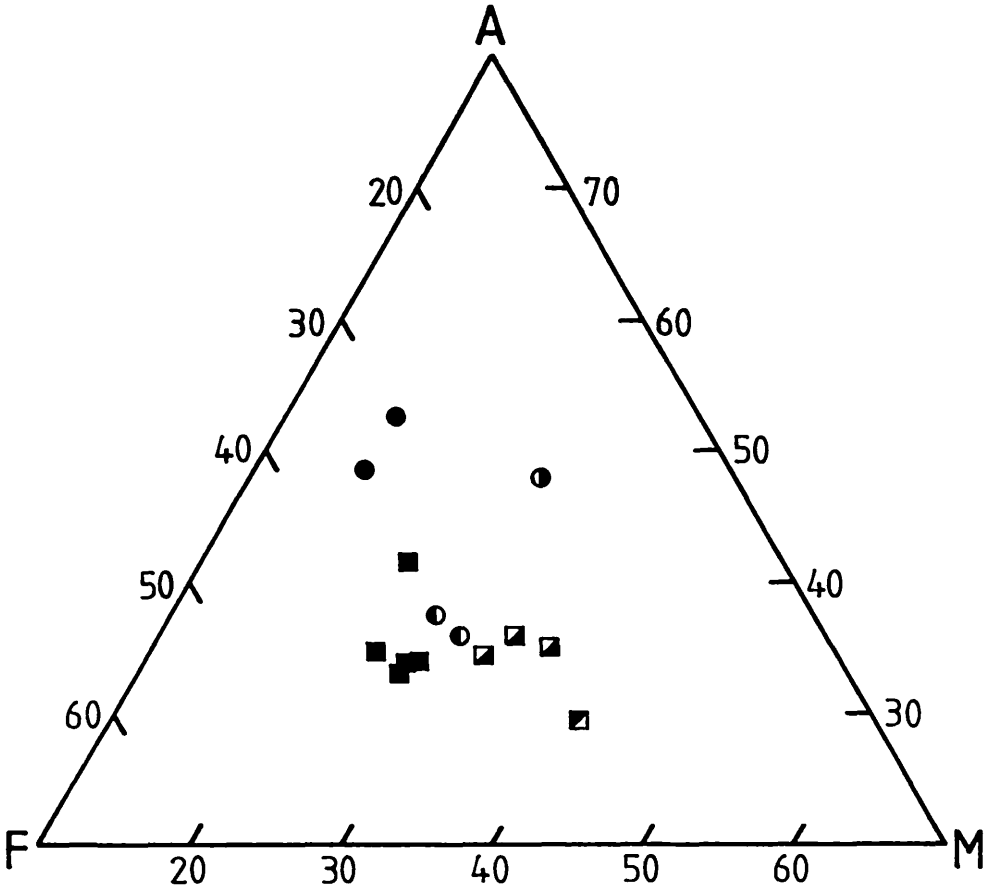


FIGURE 5.1 AFM diagram showing compositions of pseudotachylyte matrix biotites as determined by STEM microanalysis. A = Al_2O_3/SiO_2, F = FeO/SiO_2, M = MgO/SiO_2; A+F+M=100.

Plagioclase microlitic pseudotachylytes:

■ = biotite laths; sample R2, foils 3,5 and 6.

◪ = biotite laths; sample SU803, foil 6.

◪ = biotite laths; sample SU803, foil 5.

Phyllosilicate spherulitic pseudotachylytes:

● = spherulitic biotite; sample SU802, foil 5.

◑ = spherulitic biotite; sample X, foil 11.

◐ = spherulitic biotite; sample X, foil 6.

sporadically but was not observed acting as a nucleus for sherulitic crystallization.

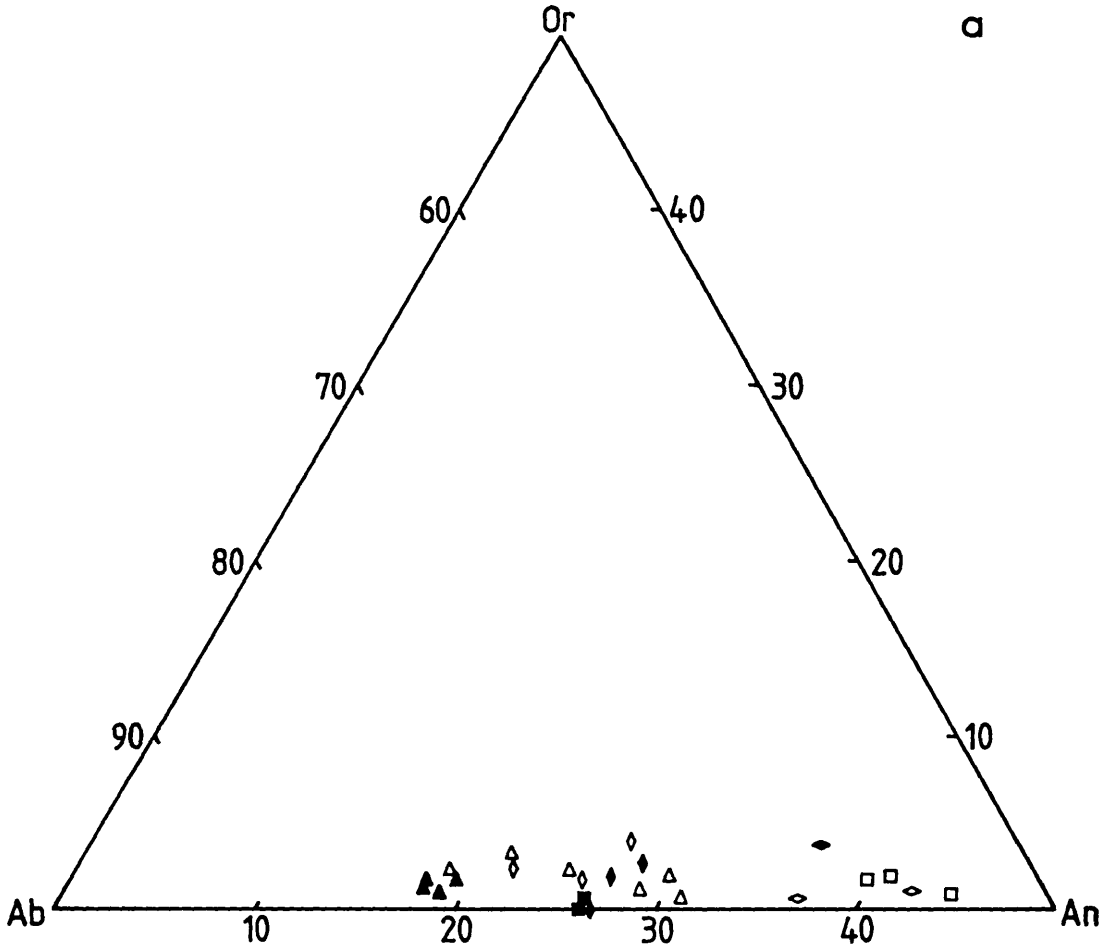
Epidote and rounded grains of amphibole (~0.5 μm dia.) also occur sporadically (Plate 5.5C). Analyses of the amphibole, 'hornblende' to 'actinolitic-hornblende' in composition, do not allow discrimination as to whether the grains are porphyroclastic or newly crystallized phases (Appendix A3).

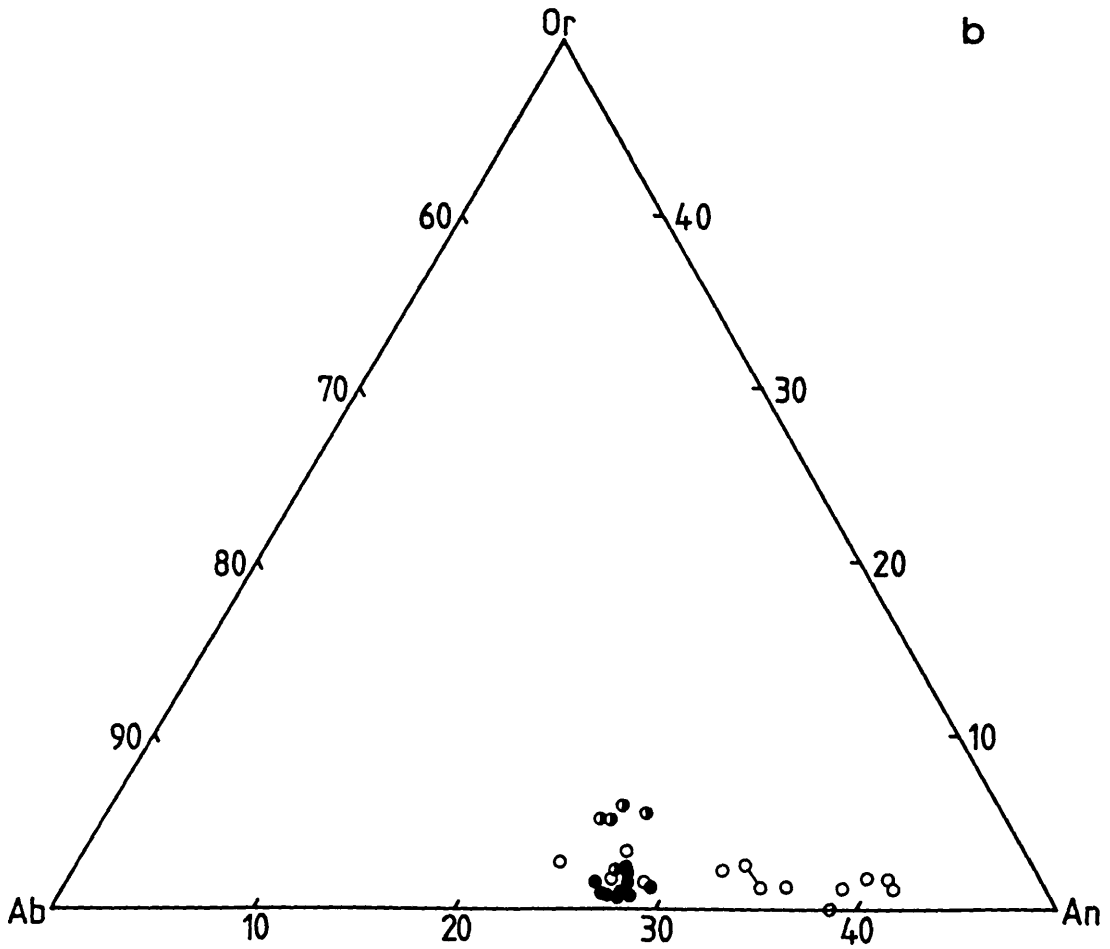
5.2.2 Feldspar Chemistry

The composition of feldspar microlites and associated host/porphyroclast plagioclases in plagioclase microlitic pseudotachylytes from the OHT, Tiree and Vredefort are plotted on an An-Ab-Or diagram in Fig. 5.2. The host/porphyroclast plagioclases occupy narrow, rather sodic compositional fields whereas the plagioclase microlites span larger compositional fields generally skewed to more calcic compositions (An_{22}-An_{45}) with respect to their associated host/porphyroclast plagioclases. Little correlation exists between An-content and microlite morphology, although 2 analyses of 'belt-buckle' sections of plagioclase are less calcic than the majority of microlites in sample R2 (Fig. 5.2b). The fine grain size did not permit quantitative characterization of the zoning within individual microlites, but the optical misorientation within such crystals is slight suggesting variation of a few mol.% An only. Individual prongs of swallowtail microlites vary in composition by up to 4 mol.% An (Fig. 5.2b). A few of the microlites analyzed plot in the alkali feldspar field (Fig. 5.2b). Such microlites are always found in embayments in lithic porphyroclasts after the disequilibrium breakdown of biotite. In general the tenor of K_2O in the microlites is low and is comparable to that of the host/porphyroclast plagioclases. The composition of the fan spherulites, determined optically, is An_{25}.

With the exception of Sibson (1975) who quotes microprobe determinations of An_{30}-An_{35} for OHT pseudotachylyte plagioclase microlites, all previous reported measurements were made optically. The majority fall in the range An_{20}-An_{30} (Shand, 1916; Pichamuthu, 1959; Philpotts, 1964; Grocott, 1977a). Philpotts and Miller (1963) and Philpotts (1964) apparently describing the same Canadian pseudotachylyte sample found normally zoned plagioclase microlites with a composition of An_{38}-An_{32} (note: the optics described suggest that this is a misprint for An38-An22) and An_{20}-An_{25} respectively.

FIGURE 5.2 Part of an An-Ab-Or diagram showing composition of host-rock (half-filled symbols), porphyroclast (filled symbols) and microlite (open symbols) plagioclases in plagioclase microlitic pseudotachylyte.
(A) △ = sample SA3, Vredefort Dome; □ = sample R4, Rubha Ardvule, S Uist; ◊ = sample SU802, Rubha Ardvule; <> = sample CT1, Tiree.
(B) ○ = sample R2, Rubha Ardvule, S Uist. Tie line joins 2 prongs of a swallowtail microlite.


a
Or
60
40
70
30
80
20
90
10
Ab
10
20
30
40
An


b
Or
60
40
70
30
80
20
90
10
Ab
10
20
30
40
An

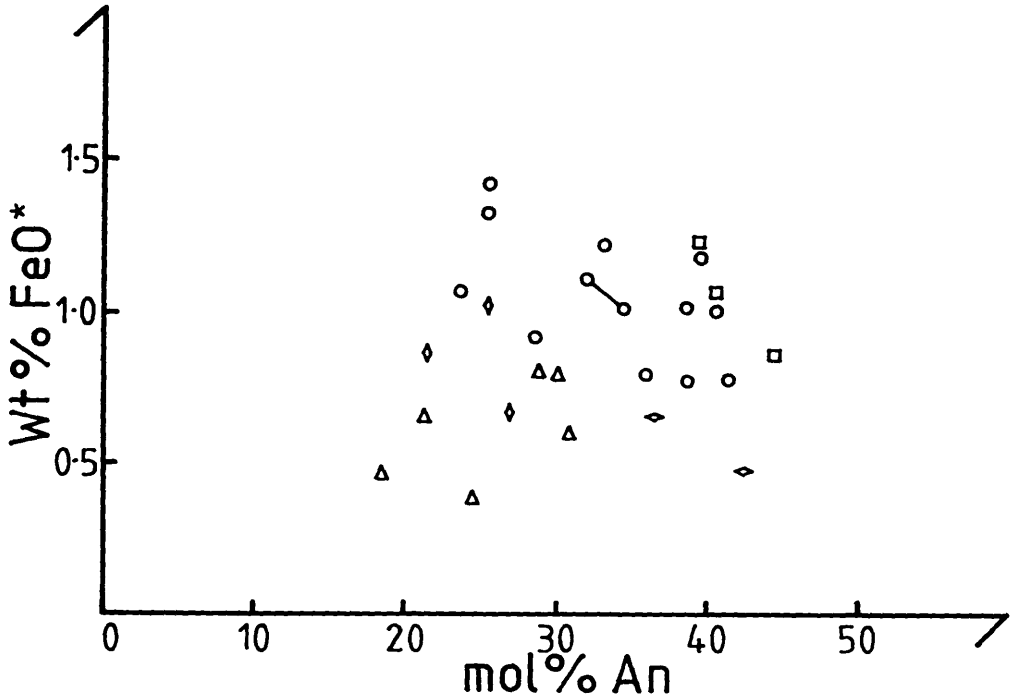


FIGURE 5.3 Plot showing variation of wt.% FeO* (total iron expressed as FeO) with mol.% An in plagioclase microlites. Symbols and tie-line as for Fig. 5.2.

Using XRD techniques, Philpotts (1964) determined an intermediate structural state for plagioclase microlites in the Canadian sample and also a Vredefort Dome sample. Dietrichson (1953) measured a composition of An_{60} and a high structural state for plagioclase microlites in a Norwegian pseudotachylyte. However, the large size of these microlites (500 x 100 μm; Dietrichson, ibid., Plate 3, Fig. 2, p.70) makes their origin somewhat suspect.

All of the microlites analyzed in this study contain unusually high Fe-contents (up to 1.5 wt.% FeO*) shown in Fig. 5.3. High concentrations of Fe in plagioclase have been attributed to the presence of exsolved phases and mechanical impurities (Smith, 1974, p.52 and 112) which may not necessarily be resolved from the host by the microprobe beam. Philpotts (1964), for example, tentatively identified hematite in pseudotachylyte plagioclase microlites. However, examination of the microlites in this study by high magnification (up to 2.3K) backscattered electron imagery in the SEM and concomitant EDS X-ray analysis indicates that the microlites are homogeneous. (This was independently confirmed by G. Lloyd using the SEM at the Centre for Materials Sciences, Birmingham University). A further source of anomalous Fe in plagioclase microprobe analysis can be that due to secondary fluorescence. Both the matrix surrounding the microlites and the devitrified melt inclusions contain Fe-bearing phases (Table 5.4) - principally biotite and magnetite. In order to guard against secondary fluorescence effects, analyses were made as far away from the melt inclusions and microlite margins as practicably possible. All analyses apparently containing Mg or Ti were rejected (about 60% of the determinations). Since secondary fluorescence of an element is proportional to the cube of its atomic number, it is believed that these rejection criteria minimized Fe secondary fluorescence. Unfortunately, this also means that any real Mg-content in the plagioclases (cf. Longhi et al., 1976) must be ignored. It is concluded therefore that most of the analyzed Fe is lattice-bound, but that secondary flourescence may be responsible for some scatter in the values.

Such high Fe-contents in naturally occurring plagioclases have only been found in lunar (e.g. Crawford, 1973), submarine quenched ocean-floor (e.g. Bryan, 1972b) and certain rapidly cooled terrestrial basalts (e.g. Kiel et al., 1972). The incorporation of Fe into the plagioclase lattice is attributable to kinetic disequilibrium crystallization whereby ions with small distribution coefficients,

TABLE 5.4 MICROPROBE ANALYSES OF PLAGIOCLASE PORPHYROCLAST CORE AND RIM, MICROLITE, AND DEVITRIFIED MELT INCLUSIONS AND FAN SPHERULITE

	1	2	3	4	5	6
SiO_2	60.40	50.13	58.69	58.30	55.37	57.13 (2.28)
TiO_2	-	2.49	-	-	-	1.74 (0.20)
Al_2O_3	23.79	16.24	25.35	24.34	21.96	18.00 (0.64)
FeO^*	0.91	9.83	-	1.30	4.75	6.98 (1.13)
MnO	-	0.23	-	-	-	0.19 (0.31)
MgO	-	4.08	-	0.74	2.89	2.69 (0.74)
CaO	5.89	7.65	8.27	7.51	1.74	5.53 (0.86)
Na_2O	7.91	4.20	6.41	5.92	0.76	5.43 (0.47)
K_2O	0.25	3.23	0.23	0.72	8.65	1.94 (0.43)
Total:	99.15	98.08	98.95	98.83	96.16	99.63

1. 'Belt-buckle' plagioclase microlite; sample R2.
2. Devitrified melt core of 1.
3. Core of plagioclase porphyroclast; sample G802/P.
4. Rim of 3.
5. Devitrified melt enclave in rim of 3.
6. Mean and Standard deviation (bracketed) of 10 raster analyses of fan spherulite, sample R2.

which would normally diffuse away from crystals grown under quasi-equilibrium conditions, are incorporated during rapid crystal growth (Albarede and Bottinga, 1972).

Observations on natural (e.g. Ujike, 1982) and synthetic plagioclases (e.g. Donaldson et al., 1975) together with theoretical considerations (Smith, 1974; Longhi et al., 1976) demonstrate that the Fe-content of plagioclase should increase with total Fe-content of the melt, increasing cooling rate and increasing Ab-component (note: the latter 2 factors are non-independent). In the pseudotachylyte plagioclase microlites there is a similar, but very weak positive correlation between the whole-rock Fe-content, and with the exception of the Vredefort examples, the Ab-component and the Fe-content of the microlites (Fig. 5.3).

Examination of the stoichiometry of the plagioclase microlites indicates that a better 'fit' is obtained by substitution of Fe^{3+} into the tetrahedral site than Fe^{2+} into the octahedral site (Table 5.5). The former substitution could be accomodated by a simple $Al^{3+} \rightleftharpoons Fe^{3+}$ exchange, which would suggest a moderately high oxygen fugacity (Longhi et al., 1976). A more exact consideration of the substitution mechanism on the basis of the stoichiometry however, seems unwarranted as Mossbauer spectra of lunar plagioclases indicate that Fe may occupy irregular site vacancies and lattice defects (Hafner et al., 1971), whilst (experimental) dynamically-crystallized plagioclases are frequently non-stoichiometric with Ca in excess of Si (e.g. Lofgren et al., 1974).

Although the scatter in Fig. 5.3 may in part be due to secondary fluorescence of Fe, it is interesting to note that Longhi et al (1976) suggest that scatter in a plot of An vs. Fe/(Fe + Mg) may be diagnostic of inhomogeneous impact melts - a useful analogue to 'poorly-stirred' fault-generated psedotachylyte melts. In summary, the high Fe-content of the plagioclase microlites complements the morphological evidence for fast crystallization at rapid cooling rates; the weak or poor correlation between Fe-content, Ab-component and morphology suggest that chemical and probably heat fluxes were strongly heterogeneous during freezing of the melt/clast system.

Raster microprobe analyses of the fan-spherulites (Table 5.4, column 6) are compatible with the optical identification of plagioclase intergrown with biotite. The optically determined composition of the plagioclase fan-spherulites, less calcic than the microlites is consistent with the former's later crystallization from

TABLE 5.5 STATISTICAL COMPARISON BETWEEN TETRAHEDRAL AND OCTAHEDRAL ASSIGNMENT OF Fe IN PSEUDOTACHYLYTE PLAGIOCLASE MICROLITES

Phase/ site occupancy	No. of Analyses	Tetrahedral site mean	s.d.	Octahedral site mean	s.d.
Host and porphyroclasts (Fe - free)	41	4.000	0.009	0.995	0.022
Microlites	24				
1. Fe^{3+} assigned to tetrahedral site		4.003	0.007	0.996	0.020
2. Fe^{2+} assigned to octahedral site		3.978	0.009	1.032	0.021

a cooler, less Ca-rich melt.

STEM analyses of the interstitial groundmass feldspars (Appendix A3) are of poor quality for reasons indicated in Appendix A2, but generally indicate an oligoclase composition ($\sim An_{20}$) - comparable to the fan-spherulites.

5.2.3 Interpretation of the Textures and Mineral Chemistry

Plagioclase-microlitic pseudotachylytes show extensive variation in textures across small domains; in some cases this can be related to distance from the vein margin and cooling rate considerations thereof (Plate 5.1); in other cases the variation is more complex (Plate 5.2A). The size, composition, distribution and melting behaviour of the porphyroclasts has governed the nucleation and growth of new phases from the melt and thus exerted an overriding control on the texture of these pseudotachylytes.

Mineralogically-specific heterogeneous nucleation has dominated. Heterogeneous nucleation tends to reduce the critical undercooling (ΔT) required for nucleation to occur because the surface energy (which contributes to the activation energy for nucleation) of solid-solid interfaces is less than that for solid-liquid interfaces (homogeneous nucleation) particularly if nucleation is epitaxial (Dowty, 1980). Nucleation is also enhanced by surface roughness (Kirkpatrick, 1981), a characteristic which might be expected of the brittly-deformed porphyroclasts (section 5.8) although mitigating against this is the corrosive action of the melt which would preferentially melt any asperities. Further, heterogeneous nucleation dramatically reduces the incubation time required for nucleation to occur once the requisite degree of undercooling is achieved. Experimental studies on basaltic melts demonstrate that the incubation time for homogeneous nucleation of plagioclase is sufficiently great that it may be suppressed from its normal appearance as a liquidus phase (Walker et al., 1976). The consequence of this is that in a rapidly chilled melt/clast system, such as these pseudotachylytes, nucleation can be expected to begin at lower values of ΔT and growth can be expected to continue over a greater temperature range than would be the case for an homogeneous clast-free melt of the same composition, cooling at the same rate.

Four different plagioclase morphologies have been recognized: tabular, chiefly filled crystals, skeletal acicular microlites,

fan-spherulites and the interstitial equant plagioclases intergrown with quartz in the groundmass. By analogy with isothermal and dynamic crystallization experiments on feldspar (Lofgren, 1974) and basaltic rock melts (Nabelek et al., 1978) respectively, the first 3 morphologies, listed from left to right in Table 5.3, may be referred to crystallization at increasingly greater values of ΔT. The compound form of the plagioclase crystal illustrated in Plate 5.3 is almost identical to the run products of isothermal drop experiments on feldspar melts (cf. Lofgren, 1974, Plate 3C, p. 259) where the charge is repeatedly rapidly quenched and held at successively lower temperatures (larger values of ΔT). In contrast to some lunar impactites, the cooling histories of pseudotachylyte melts seem unlikely to involve isothermal plateaus, unless perhaps sudden release of heat through the enthalpy of crystallization occurred, but apparently sudden changes in growth mechanism do appear to have occurred.

Three important rate-controlling processes govern crystal growth (Dowty, 1980; Kirkpatrick, 1981): (i) interface attatchment kinetics; (ii) material diffusion; (iii) heat transfer. The process which dominates is a function of the relative diffusion and heat transfer rates, the particular growth mechanism and the undercooling. In general, at low values of ΔT, when mass diffusion is facilitated by the high temperature and low viscosity of the melt, interface-controlled growth is the dominant mode, and diffusion or heat transfer become important at higher values of ΔT. Interface-controlled growth by a layer-spreading mechanism (Kirkpatrick, 1981) tends to give rise to tabular filled crystals; it may be inferred that the primary growth stage of the plagioclase crystals shown in Plates 5.2F and 5.3 grew by this mechanism.

As the degree of undercooling increases, mass diffusion usually becomes the rate-controlling process since thermal diffusivities are typically orders of magnitude greater than cation (mass) diffusivities (Henderson, 1982).

Two theoretically and experimentally derived aspects of diffusion controlled growth are shown in Fig. 5.4. The important feature of this figure is that small solid protrusions from the crystal-liquid interface, with dimensions of the order of δ, will be stabilized and growth enhanced relative to the planar interface because of the greater degree of undercooling and approach to equilibrium composition away from the interface. In order that growth

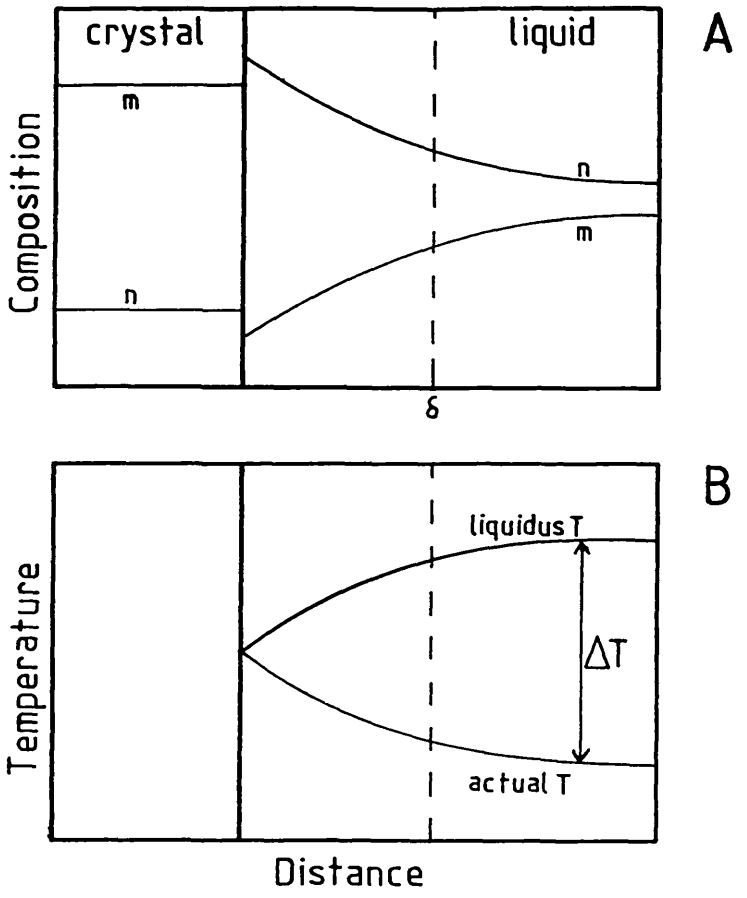


FIGURE 5.4 Schematic diagrams illustrating the factors affecting diffusion-controlled cellular crystal growth (modified from Kirkpatrick, 1981).

(A) Component n rejected by growing crystal increases in concentration close to crystal-liquid interface and must diffuse away; component m incorporated by crystal is depleted at the interface and must diffuse toward the crystal. Since the rejected components n are usually low temperature constituents the liquidus temperature is depressed and the value of ΔT is reduced (constitutional undercooling).

(B) Diagram showing effect on temperature of constitutional undercooling augmented by the release of latent heat from the growing crystal. Dimension δ is the length that random solid projections must achieve to be stabilized by near-equilibrium undercooling and composition away from the crystal-liquid interface.

may continue, the morphology of the protrusion takes on a cellular (skeletal, spherulitic or dendritic) aspect. Where convection and advection are unimportant, this approach to "equilibrium" undercooling and composition is more readily achieved at the corners of faceted crystals because of the larger melt volume to crystal surface area ratio at the corners than the centre of a face (Kirkpatrick, 1981). Thus the change in crystal morphology and probable transition in growth mechanism seen in the plagioclases of Plates 5.2F and 5.3 is predicted by crystal growth theory. Similar arguments may be applied to the transition from acicular to fan-spherulite morphology as the value of ΔT increases still further. Preferred growth parallel to (010) in the pseudotachylyte plagioclases also exemplifies the important effects of crystal (lattice) and growth anisotropy; these effects are common to both interface and diffusion controlled growth. Smith (1974) has argued that twinning may facilitate rapid growth in plagioclase.

By analogy with the experimental studies cited above, the plagioclase morphologies which can be resolved optically are all believed to have crystallized from the melt. (Further supporting evidence for this is given in section 5.2.4.) Turning attention to the interstitial, equant quartz + plagioclase groundmass it is clear that a further change in nucleation and growth mechanisms occurred, perhaps consequent upon changing melt composition in addition to decreasing temperature. The nucleation density as revealed by the fine grain size (on average < 0.5 um) is much higher, the crystal morphologies are equant and non-skeletal and quartz has crystallized for the first time. It is believed that this more annealed, equilibrium texture reflects devitrification under near-isothermal conditions. The texture is akin to snow-flake texture found in some devitrified volcanics and experimental charges (Lofgren, 1971a, 1980) where intergrown quartz and feldspar (more commonly alkali feldspar) poikilitically enclose plagioclase microlites. Snow-flake texture has been attributed to phase separation in glass prior to devitrification (Torske, 1975), and a similar process may have operated in the pseudotachylyte groundmass. In the absence of glass containing a readily identifiable devitrification front it is extremely difficult to discriminate between devitrification and primary crystallization (Lofgren, 1971b). Nevertheless, the groundmass texture described here is believed to have resulted from devitrification. Suitable experiments could be designed to test this hypothesis.

The present interpretation of the pseudotachylyte groundmass is radically different from that given by Wenk (1978) in a TEM study of pseudotachylytes including a sample from Greian Head, Barra (map 2). The electron micrographs presented by Wenk (ibid., Fig.s 3 and 4, p. 508-9) show a matrix of fine grained, high dislocation density (> 10^{12}) quartz and feldspar debris which is claimed to be partly recrystallized to polygonal strain-free grains, although only recrystallized quartz is illustrated. The highly-strained quartz/feldspar debris microstructure is unlike any seen in the pseudotachylytes of this study, but is closely similar to the microstructure of some cataclasites as revealed by TEM (cf. Moore, 1980). Recrystallization of quartz in the present samples is restricted to the margins of some of the quartz clasts, where the recrystallization product is quartz with a grain size > 1 μm (Plate 5.5E) - similar to the recrystallized quartz illustrated by Wenk (ibid., Fig. 3d, p. 509) - but distinct from the finer grained, unstrained equant quartz/feldspar matrix described above. Highly strained, high dislocation density quartz and feldspar in the present samples is restricted to the central portions of the quartz and feldspar porphyroclasts (Plate 5.5F).

Unfortunately Wenk (1978) provides no description of the optically resolvable microstructures in these pseudotachylytes (he evidently did not prepare ultra-thin sections) but it appears that his observations are descriptive of cataclasites rather than pseudotachylytes. Wenk's contention, which he applied to pseudotachylytes in general, that they result from crushing and cataclasis rather than fusion seems quite unwarranted (cf. Maddock, 1983). Cataclasite, of course, commonly occurs with pseudotachylyte (Sibson, 1977a, 1977b) and indeed is present at Greian Head.

5.2.4 Estimates of Temperature, Cooling Rate and Crystal Growth Rate

An estimate of at least 1000 °C for the melt temperature of plagioclase microlitic pseudotachylytes is proposed based on the following considerations:-

(i) the absence of partial melting in the vein wall-rocks implies a maximum wall-rock temperature < 650 °C assuming a granitic host with a reasonable water content (Winkler, 1967); from the data of Jaeger (1957) this implies a melt temperature of < 1100 °C;

(ii) fusion of biotite in lithic porphyroclasts requires that they were heated by the melt to at least 770°C (Nedelec and Paquet, 1981), whilst the presence of granular opaque, rather than fused opaque spherules as a result of the disequilibrium breakdown product of biotite and hornblende indicates a maximum temperature of < 1200 °C (Chao, 1967; see Grocott, 1977a for discussion);
(iii) corrosion of quartz and feldspar clasts, by analogy with published observations on buchites (Table 5.15) suggests a temperature of the order of 1000°C;
(iv) the 'whole rock' composition of plagioclase-microlitic pseudotachylytes (basaltic andesite/andesite/icelandite affinities, Appendix A4 and chapter 6) suggest a liquidus temperature at reasonable pressures (say 50 - 200 MPa) and volatile contents (up to 2 wt.% H_2O) of 1050°C.

The cooling rate of a pseudotachylyte vein may be considered in an approximate treatment using the analysis of Jaeger (1957) for the conductive cooling of an instantaneously injected, infinite planar sheet of melt of width w (see later discussion and reference for further assumptions). The position, X, of the plane at which crystallization is just complete is given by (Jaeger, 1957):-

$$X = 2\lambda(Kt)^{1/2} \qquad (5.1)$$

where K is the thermal diffusivity, t is the time after intrusion, and $0<\lambda<1$ is the parameter whose value is dependent on the initial temperature, the crystallization interval and the enthalpy of crystallization. Now, crystallization will be complete when X = W/2, thus the time, t', for complete crystallization may be found from equation 5.1:-

$$t' = w^2/16\ K \qquad (5.2)$$

A suitable value of K is given in Table 2.3. Values of λ for a wide range of conditions are tabulated by Jaeger (1957). Following the arguments outlined above an initial temperature of 900°C is chosen. The crystallization interval of andesitic melts is typically in the range 150 - 200°C (Eggler, 1972). In the pseudotachylyte it may be assumed from the evidence of heterogeneous nucleation that crystallization began almost immediately below the liquidus, whilst

the variety of plagioclase morphologies suggests crystallization at values ofΔT up to (and perhaps) exceeding 150°C. A conservative estimate of the crystallization interval of 100°C is chosen here which maximises the value of λ and should tend to underestimate the reduction in cooling rate due to the enthalpy of crystallization. To a first approximation the pseudotachylyte can be considered to have c ystallized plagioclase only. Jaeger (1957) tabulates λ for 2 values of the enthalpy of crystallization, ΔH, 334 and 418 $kJ.kg^{-1}$. Noting that the average composition of the plagioclase microlites is about An_{35} and that for albite, ΔH = 249 $kJ.kg^{-1}$ and for anorthite ΔH = 487 $kJ.kg^{-1}$ (Nicholls and Stout, 1982), a value of λ = 0.427 (assuming ΔH = 334 $kJ.kg^{-1}$) is chosen.

Substituting this value of λ into equation 5.2 yields the time taken for complete crystallization of a 5 cm thick vein as 1200s (20 minutes); similarly a 10 cm thick vein would be expected to crystallize in 4800s and a 1 cm thick vein in 48s. Since the maximum engtth parallel to (010) of the acicular microlites in a 5 cm thick vein (sample R2, Table 5.3) is 200 um, a linearized crystal growth rate of 1.66 x 10^{-5} $cm.s^{-1}$ may be deduced. The minimum linearized cooling rate at the centre of the vein is 300 $C.hr^{-1}$. Comparison with lagioclase growth rate data (also measured parallel to (010)) for various synthetic melts (compilation of Dowty, 1980) and natural melts (e.g. Kirkpatrick, 1981) indicate that the deduced growth rate is reasonable, falling in the middle of the published values.

The meaningfulness of the deduced linearized cooling rate of 300 $°C.hr^{-1}$ must be assessed in the context of the following factors:-

(i) the model assumes a melt sheet of infinite extent, convectional and volatile heat losses have been ignored and no account of heat loss to the porphyroclasts has been made;
(ii) not all the solidification involved crystallization of plagioclase; the ultra-fine grained groundmass almost certainly formed by devitrification which would not contribute to the enthalpy of crystallization;
(iii) the model assumes a wall rock temperature of 0°C;
(iv) the model assumes uniform liberation of latent heat throughout the crystallization interval;
(v) the deduced cooling rate has been linearized whereas theory predicts that the decay of temperature should be proportional to the square root of time.

Notwithstanding the conservative choice of parameters defining λ (which tend to maximise the cooling rate), (i) and (ii) above suggest that the cooling rate may be severely underestimated. However, this is considered doubtful for the following reasons. In dynamic crystallization experiments designed to promote heterogeneous nucleation of plagioclase on pre-existing crystals in Grande Ronde basalts (55% SiO_2, fO_2 maintained at the QFM buffer) the maximum cooling rate which will allow crystallization of any plagioclase during the linear cooling period is around 450°C.hr^{-1} (Schiffman and Lofgren, 1981). Near-equilibrium, filled tabular plagioclases do not form at such high cooling rates in the experiments. Although comparison between the crystallization of plagioclase in pseudotachylyte and in dynamic crystallization experiments must be circumspect, it is believed that such comparisons do justify the deduced linearized growth and cooling rates for the plagioclase-microlitic pseudotachylytes.

These results may be compared with the model adopted by Sibson (1975) who disregarded the enthalpy of crystallization. Using his model for the cooling 'half-life', $t_{1/2}$, of a vein:

$$t_{1/2} = 0.27\ w^2/K \quad \text{(c.g.s. units)} \qquad (5.3)$$

a 5 cm thick vein would cool from 900°C to 450°C in 950s. Regardless of the form of the cooling rate curve, any possibility of crystallization of plagioclase microlites would seem to be precluded by such rapid cooling. It is therefore concluded that Sibson's (ibid.) analysis substantially overestimates the cooling rate for thick veins of plagioclase microlitic pseudotachylyte.

A different approach may be used to estimate the growth rate of the fan spherulites. Adapting theories of spherulitic growth developed for organic polymers (Keith and Padden, 1963) to silicate melts, Lofgren (1971a, 1974) has shown that the diffusion rate, D, of impurities (component n in Fig. 5.4) away from the crystal-liquid interface and the growth rate, G, of the fibrous (cellular) projection are related to the thickness of the impurity layer (in Fig. 5.4) by the relationship:

$$\delta = D/G \qquad (5.4)$$

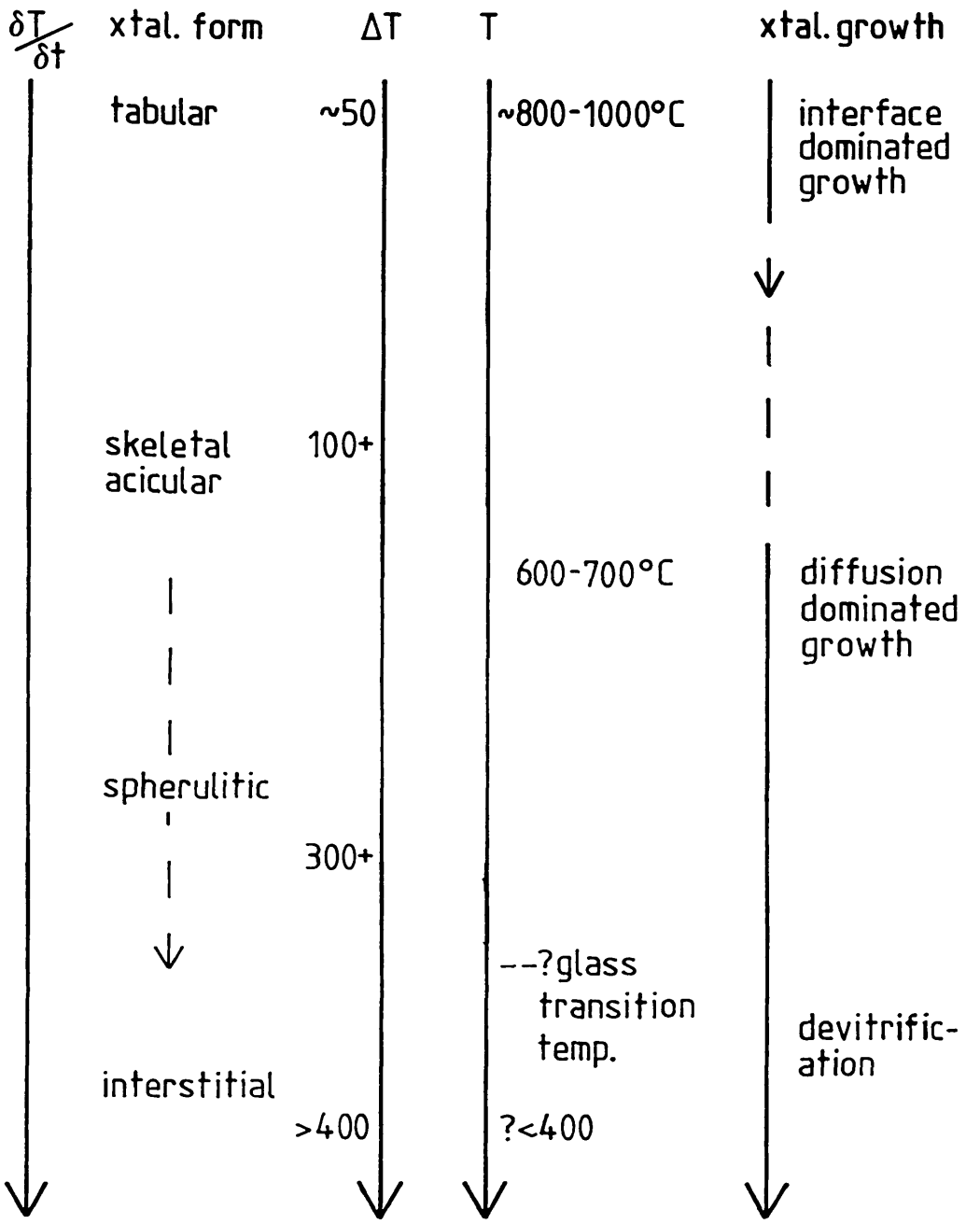


FIGURE 5.5 Generalized model for the crystallization of plagioclase in plagioclase microlitic pseudotachylytes. Temperature data is estimated from references cited in the text.

To a first approximation δ is equal to the diameter of individual fibres (Lofgren, 1971a). Using this approximation and noting that the spherulitic fibre diameter is of the order of 1 μm (Plate 5.1E), the growth rate may be estimated from equation 5.4 if D is known. During growth of plagioclase spherulites from the melt (or glass), the slowest, rate-controlling diffusing species is likely to be Si^{4+}. Diffusion data for Si^{4+} are restricted in number but self-diffusion rates for ^{31}Si of 10^{-7} $cm^2.s^{-1}$ in SiO_2-Cao-Al_2O_3 melt at 1430 C (Towers and Chipman, 1957) and 10^{-10} cm^2s^{-1} in SiO_2-SrO-K_2O glass at 750 °C (above the glass transition temperature) (Vareshnaya and Cooper, 1972) have been measured experimentally. A reasonable value for the diffusion rate of Si^{4+} in the pseudotachylyte melt at say 800 °C, might be 5×10^{-9} $cm^2.s^{-1}$. Substituting this value in equation 5.4 yields a growth rate of 5×10^{-5} $cm^2.s^{-1}$ for 1 um thick fibres. The 200 μm long fan-spherulites in a 5 cm thick vein (Table 5.3) could therefore have grown in 400s. If the assumptions made in this analysis are correct then the deduction, based on textural criteria, that the fan-spherulites grew during primary crystallization rather than devitrification is confirmed. If, however, the diffusion rate of Si^{4+} is any slower then the fan spherulites must have grown during devitrification: a diffusion rate of 10^{-10} $cm^2.s^{-1}$ would yield a (isothermal) growth time of 20000s. The higher growth rate indicated for the fan-spherulites which must have grown at larger values of ΔT than the microlites is predicted by both theory and experiment where the growth rate first increases with increasing undercooling up to ΔT = 200 C and then decreases (Kirkpatrick, 1981). The pseudotachylyte fan-spherulites fine slightly toward their distal ends suggesting growth under moderate/high cooling rate conditions with the diffusion rate decreasing as ΔT increases, and thus the fibre diameter decreasing according to equation 5.4. If growth had occurred under the more closely isothermal conditions of devitrification, fibre diameter would be expected to be constant.

An attempt to summarize the interpretations of this section is given in Fig. 5.5. A number of assumptions have been made, but any further refinements of this model would requi^re a complex experimental program.

5.3 Amphibole Microlitic Pseudotachylyte

In spite of the identification of hornblende microlites in Outer

Hebrides pseudotachylytes by Dougal (1928), few were found in the numerous thin sections examined in this study, with the exception of a few grains of amphibole seen in the TEM (e.g. section 5.2.1). Amphibole microlitic pseudotachylytes are however well known from the Silvretta nappe in the eastern Swiss Alps (e.g. Hammer, 1930; Masch, 1974) and the Vredefort Dome. Samples of each have been examined.

5.3.1 Sample SV15, Silvretta

Sample SV15 from Val Tasna, Silvretta is a 1-2 cm thick ?FV cutting quartz + plagioclase + hornblende gneiss. The axial portion of the vein consists of decussately arranged amphibole and plagioclase microlites (Plate 5.6B) with clots of epidote + amphibole + biotite + chlorite poikilitically enclosed by microcrystalline intergrown albite and alkali feldspar (Plate 5.6F). The relative proportions of amphibole and plagioclase microlites vary irregularly throughout the vein, although amphibole is generally absent from the vein margins and one phase usually exceeds the other in a given domain. Porphyroclasts of host-rock phases - feldspar and quartz show similar textures to those in plagioclase microlitic pseudotachylytes (section 5.2).

The amphibole microlites have maximum dimensions of 100 x 10 μm and are highly skeletal (Plate 5.6D and E). The skeleton walls are frequently <2 μm thick enclosing devitrified (?) melt inclusions with a crystallographically controlled form; these appear to contain phases similar to the surrounding matrix. By analogy with natural and experimentally crystallized clinopyroxenes (e.g. Bryan, 1972; Lofgren et al., 1974) it may be inferred that the skeletons are elongated parallel to the c-axis. In contrast to some of the plagioclase microlites, the amphiboles show no obvious heterogeneous nucleation either onto clasts or the plagioclase microlites. Fortuitously-sectioned cruciform microlites suggest that their 3D form may be likened to a star comprising 4 (or more?) skeletal spokes of square cross-section. Two analyses of the amphibole microlites plot as ferroan-pargasitic hornblende and magnesio-hornblende (Fig. 5.6).

The plagioclase microlites are similar to those seen in the plagioclase microlitic pseudotachylytes. They are swallowtails up to 75 μm long and 20 μm square about their nuclei with fan-spherulitic terminations extending several hundreds of microns (Plate 5.6C). The latter appear to be sub-micron intergrowths of plagioclase and amphibole; this observation combined with the overall textural

PLATE 5.6 Microstructure and mineralogy of amphibole microlitic pseudotachylyte. (A) optical micrograph (PPL), sample SA3; (B) - (F) BSE micrographs, sample SV15.

(A) Croundmass showing skeletal amphibole microlites (dark).

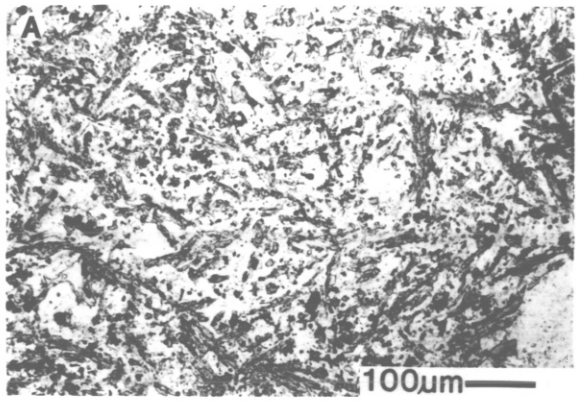
(B) General view of groundmass showing domains rich in skeletal amphibole microlites (white) and feathery plagioclase microlites/spherulites (grey).

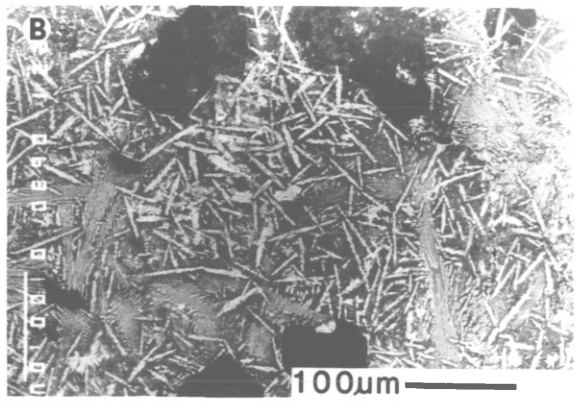
(C) Detail of feathery plagioclase microlites.

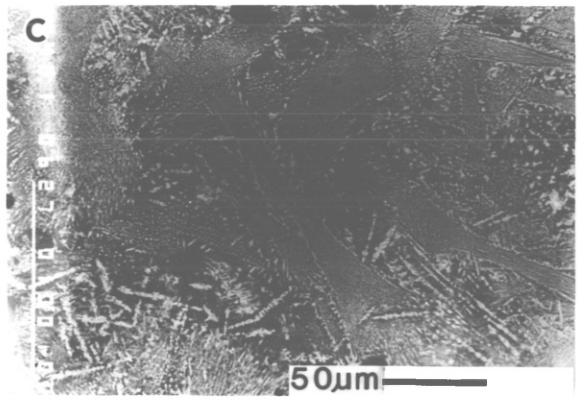
(D) Detail of skeletal amphibole microlites.

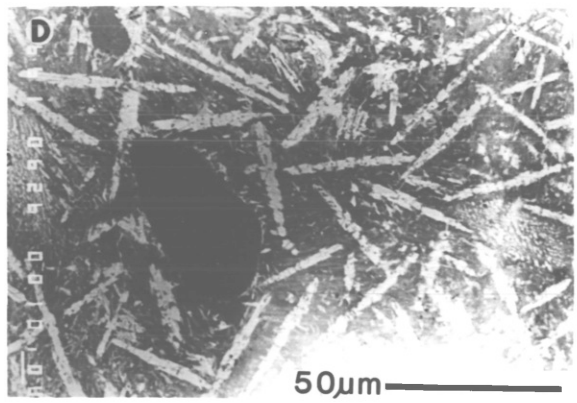
(E) Detail of skeletal amphibole microlites.

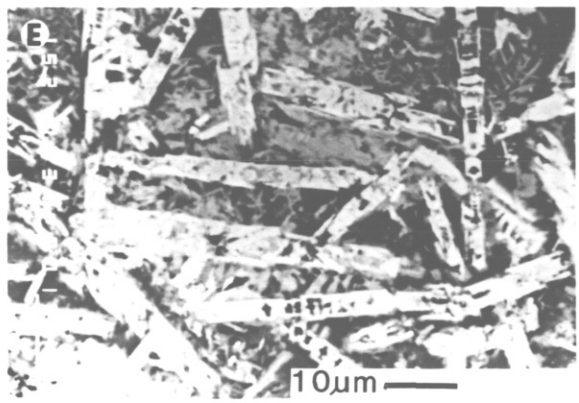
(F) Detail of groundmass which poikilitically encloses the amphibole and plagioclase microlites. e = epidote, ab = albite, k = K-spar.

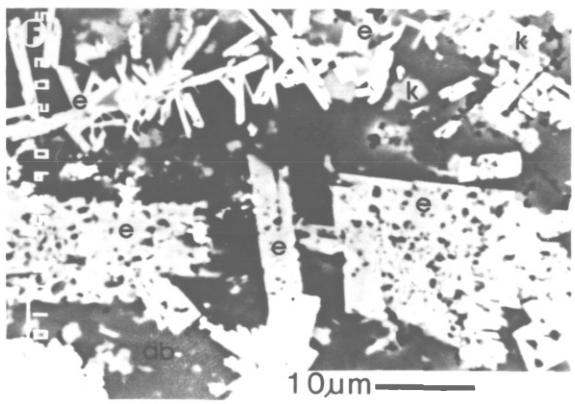

A
100µm


B
100µm


C
50µm


D
50µm


E
10µm


F
e
k
e
k
e
e
e
e
10µm

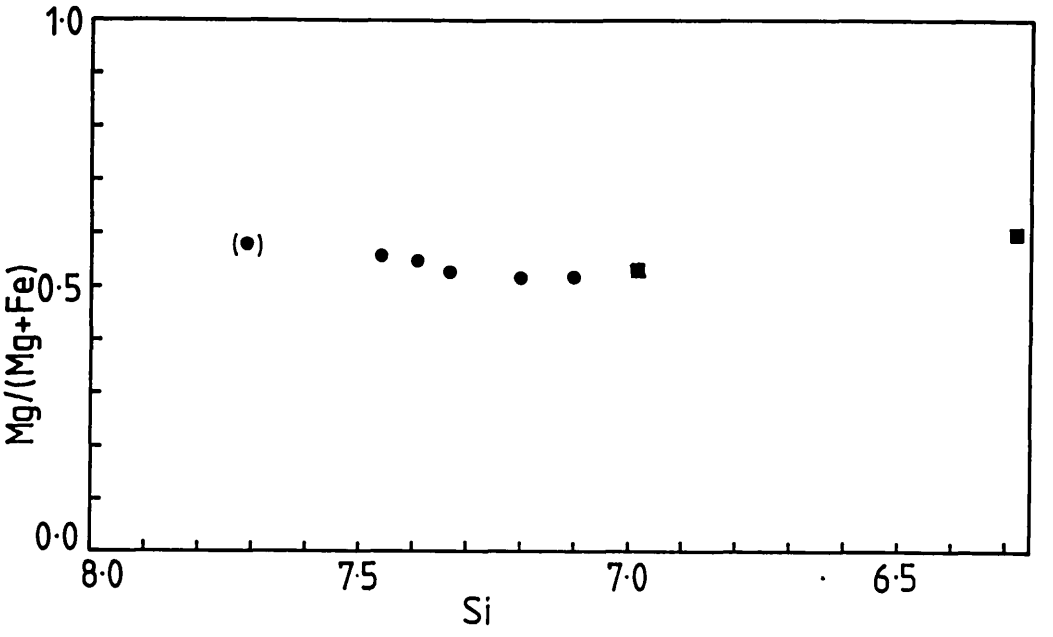


FIGURE 5.6 Plot of Si vs. Mg(Mg+Fe) formula units based on 23 (O) atoms showing composition of amphibole microlites in amphibole microlitic pseudotachylytes. ● = sample SA3, Vredefort Dome; ■ = sample SV15, Silvretta Alps. Bracketed sample has an octahedral site deficiency of 0.1 and residual charge imbalance of -0.2.

relationship between amphibole and plagioclase microlites (Plate 5.6B) indicate that the phases crystallized simultaneously over a considerable range of values of ΔT. The composition of the plagioclase microlites is approximately An_{35} (cf. albite microlites from Silvretta pseudotachylytes mentioned by Masch et al., 1985).

5.3.2 Sample SA3, Vredefort Dome

Sample SA3 is a large (5+ cm dia) IV fragment of pseudotachylyte from the "Old Granite' core of the Vredefort Dome (see Hall and Molengraaf, 1925, for map). It is considerably coarser grained than sample SV15, consisting of interfingering to sub-spherulitic microlitic plagioclase and amphibole, set in a matrix of the same phases plus quartz, small plates of partially chloritized biotite, abundant magnetite and small grains of carbonate and epidote (Plate 5.6A). Porphyroclasts of quartz, alkali feldspar and plagioclase (but not ferromagnesian phases) are abundant. The feldspars show incipient melting textures, whilst the quartz porphyroclasts are largely recrystallized to polygonized, unstrained (annealed) subgrains.

The amphibole microlites, modally subordinate to the plagioclase microlites, have maximum dimensions of 200 x 30 μm, typically arranged in sheaves or stellate groups. They are ragged rather than skeletal in habit and show weak green to colourless pleochroism, length slow character and a maximum extinction angle of 25°. Microprobe analyses confirm that they are hornblende with a composition varying from magnesio-hornblende to actinolitic hornblende (Fig. 5.6).

The plagioclase microlites have similar dimensions to the amphiboles and are also of ragged appearance. Analyses are given Fig. 5.2.

5.3.3 Interpretation and Discussion

Substantial differences in mineral texture and chemistry exist between the 2 amphibole microlitic pseudotachylytes: the Silvretta sample demonstrably crystallized from a melt; the texture of the Vredefort sample is more difficult to interpret. The latter appears to have undergone low grade metamorphism causing partial chloritization of the amphibole microlites (possibly preceeded by the making over of 'hornblende' to 'actinolite') and biotite grains, and sericitization

of both porphyroclast and microlite plagioclases. This observation is compatible with prevous suggestions that the Vredefort pseudotachylytes have suffered a static metamorphism subsequent to their genesis (Bischoff, 1962; Schreyer and Abraham, 1978). Whereas Bischoff (ibid.) inferred amphibolite facies metamorphism, the present observations are more consistent with greenschist facies metamorphism. With regard to the vexed question of whether the Vredefort pseudotachylyte ever existed as a melt (Shand, 1916; Wilshire, 1971), the combined observations of partially melted feldspar clasts and a microlitic groundmass (trachytic texture has been reported by Bischoff, 1962) is compelling evidence that it did.

It is outside the scope of this thesis - and would certainly be injudicious on the basis of 3 samples examined - to comment on the exact origin of the Vredefort pseudotachylytes (section 1.4.4). However, the similarities in texture, mineralogy and microstructure between fault-generated pseudotachylytes (this study), landslip frictionites (e.g. Scott and Drever, 1953), the Vredefort pseudotachylytes (this study; Bischoff, 1962), unequivocal meteorite impactites (e.g. Kieffer et al., 1976) and other contentious cryptoexplosion melt-rocks (e.g. the Onapping Formation at Sudbury, Ontario, Peredery, 1972) is testament to common factors in their genesis: i.e. catastrophic mechanical processes leading to melting followed by rapid disequilibrium crystallization/devitrification of a clast-laden melt.

Returning to sample SV15, the skeletal habit (by analogy with quench pyroxenes) and chemistry of the hornblende microlites indicates that they crystallized from a melt. Although the apparent rarity of amphibole microlites is undoubtedly a reflection of the sample population of pseudotachylytes which have been examined in this study, it is pertinent to question what factors would favour crystallization of amphibole rather than biotite + chlorite + epidote - believed to be the 'equivalent' hydrous phases in OHT pseudotachylytes generated in amphibole rich host-rocks.

As far as the author is aware, this is the first description of skeletal amphibole microlites (B.E. Leake, pers. comm., 1983). Equilibrium crystallization experiments yielding hornblende as a liquidus (or near liquidus) phase (see Helz, 1982, for review) are specifically designed to avoid quench crystallization, whereas dynamic crystallization experiments have largely been confined to anhydrous systems (but see Naney, 1983). Insofar as equilibrium experiments on

melts of tonalitic to andesitic composition (a reasonable analogue to pseudotachylyte and host-rock compositions) may be applicable, crystallization of amphibole is dependent upon many factors including (Helz, 1982):

(i) bulk rock composition, particularly Mg/(Mg + Fe) and X_{CaO};
(ii) the fugacity of H_2O (dependent on iii);
(iii) P_{total} and P_{H_2O}.

The crystallization of these amphiboles suggests a high a_{CaO} with respect to $a_{KAlSi_3O_8}$: this is demonstrated in the Silvretta pseudotachylyte by late crystallization of poikilitic K-spar. During crystallization of the plagioclase + amphibole assemblage, K would be strongly partitioned into the melt due to the small number of amphibole A sites available (for which K^+ ions would compete with Na^+ ions). Since Fe + Mg and H_2O would be partitioned into the amphibole rather than the melt, the final K-rich phase to crystallize is K-spar rather than biotite. Amphibole crystallization also requires moderate to high values of X_{H_2O}, a_{H2O} and P_{H2O} in the melt. Assuming the phase equilibria are relevant and that $P_{H2O} = P_{total}$ a minimum estimate of P = 100 MPa and T = 950 °C may be inferred for the crystallization of amphibole microlitic pseudotachylytes (Helz, 1982). A depth of 4 km inferred from the pressure estimate is of course reasonable for frictional melting during seismic faulting (chapter 2). The data of Naney (1983) indicate that the epidote must have formed by devitrification or metamorphic alteration rather than crystallization from the melt which requires excessive pressures (>800 MPa for granitoid melts).

5.4 Chlorite Spherulitic Pseudotachylytes

Chlorite spherulitic pseudotachylytes contain compound spherulites composed of intergrown plagioclase and Ca + Fe + Mg rich phases with a substantial proportion of inter-spherulite material believed to be devitrified/recrystallized glass. They are typical of FVs and IVs generated in amphibolitic gneisses (modal plagioclase + amphibole > 80%), most of the veins being rather narrow (< 2 cm). Pseudotachylytes of this type have been collected chiefly from Howmore Quarry, South Uist and Grimsay (map 1), in banded amphibolite (Scourie Dykes?) and felsic gneisses. Sample GQ1A, a representative 1 cm wide FV from Grimsay will be described in detail.

5.4.1 Sample GQ1A: Description

The host-rock consists of medium grained plagioclase (25%) of $An_{\sim 28}$ composition, green hornblende (61%), quartz (14%) with accessory sphene, magnetite, pyrite and epidote. The plagioclase is moderately sericitized and the hornblende is partially retrogressed to chlorite + epidote + opaque.

The pseudotachylyte vein contains a variable proportion, up to 25 modal %, of poorly sorted and rounded clasts of quartz, plagioclase and a few clasts of hornblende. Spherulitic structures mantling the plagioclase porphyroclasts and set in a dark greenish coloured matrix can just be made out in an optical thin section of normal thickness. BSE imagery reveals that the structure and mineralogy of the vein is complex, varying both across and along the length of the vein (Plate 5.7). The contact between the vein and its wall-rock is sharp against salic phases but more ragged abutting host hornblendes (Plate 5.7A and C). Adjacent to each contact is a narrow zone (~100 μm wide) consisting of angular clastic debris with a weak bimodal size distribution of small polyminerlic clasts < 20 μm and larger salic clasts < 100 um. Toward the centre of the vein, the next zone which varies in width from 0 - 500 μm, is made up of tightly-packed spherulites (Plate 5.7A and C). The individual spherulites vary in diameter from 20 - 80 μm and are round to polygonal in outline depending on the proximity of their neighbours and the orientation of the section through them. Where the spherulite nuclei are visible they are either angular plagioclase clasts or quartz-feldspar aggregates of 2 - 10 μm diameter. Monomineralic quartz clasts do not act as nuclei, but instead are either rejected to the spherulite margin, or included within the spherulite fibres apparently with little effect on the spherulites. The spherulites themselves are composed of narrow fibres (< 3 μm) of plagioclase intergrown with chlorite and epidote, which fine and branch away from the nuclei.

The axial portion of the vein is made up of more loosely packed spherulites to 100 μm diameter. The size, shape, density and packing of the spherulites is complexly related to the size , distribution, density and composition of the porphyroclasts which have acted as nuclei. This is illustrated by comparing 2 areas of the same vein shown in Plates 5.7A and 5.7C. In the area covered by Plate 5.7A the axial portion of the vein consists of rather uniform-sized spherulites

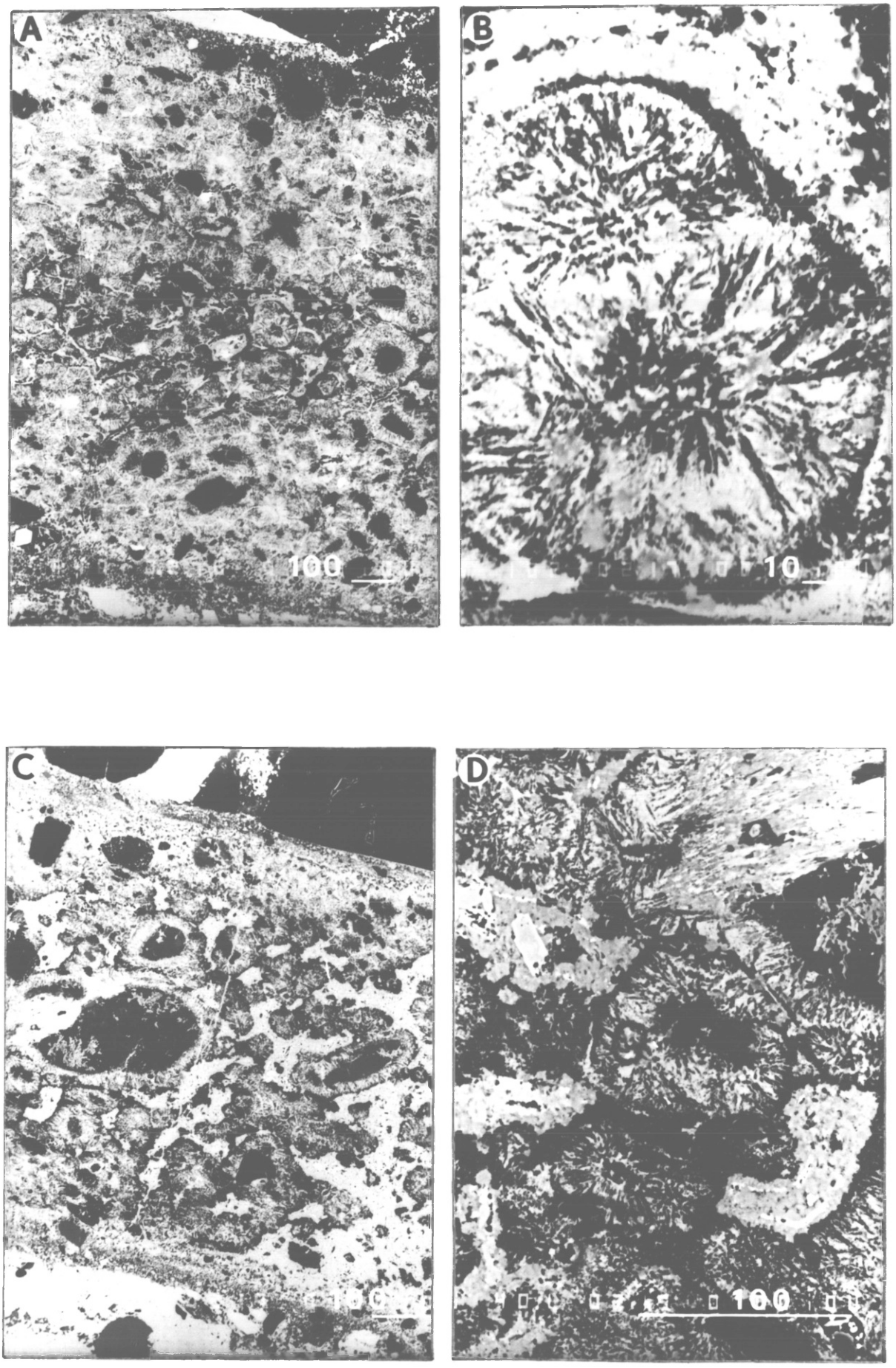
PLATE 5.7 BSE micrographs of chlorite spherulitic pseudotachylyte, sample GQ1A. (Scale in microns).

(A) Section across entire width of vein. Vein margins comprise a narrow zone of cataclastic debris against a sharp margin with the host-rock, passing into a 300 μm wide zone of polygonized plagioclase + chlorite spherulites; axial part of vein composed of loosely packed spherulites with plagioclase clast nuclei, separated by irregular patches of chlorite, epidote and quartz.

(B) Detail of A showing individual spherulite with rim of intergrown chlorite, epidote and quartz.

(C) Different part of same vein showing variation in spherulite density.

(D) Detail of (C) showing spherulites and interspherulite patches composed of intergrown chlorite, opaques and plates of zoned epidote. Note alteration of large plagioclase porphyroclast (top righthand corner).


A
100
B
10
C
D
100

with narrow interspherulite rims 10 - 20 μm wide; the majority of the spherulites are rounded rather than polygonal (Plate 5.7B). The plagioclase clast size and distribution in this area is also comparatively uniform, which has allowed nucleation and growth of similar-sized spherulites. In contrast, the area shown in Plate 5.7C is dominated by a few large plagioclase porphyroclasts which have dominated nucleation and growth of irregular spherulites, leaving large areas of inter-spherulite material (Plate 5.7D).

5.4.2 Sample GQ1A: Chemistry and STEM Analysis

Analyses of the pseudotachylyte are given in Table 5.6. The 'whole-rock' composition of the pseudotachylyte vein reflects the Ca + Fe + Mg-rich composition of the host gneiss and the moderate to high LOI reflects an H_2O content of 1.16 wt.% in the vein (Table 6.1).

In the BSE micrographs (Plates 5.7B and D), two types of interspherulite matrix can be resolved: dark areas (with a comparatively low BSE coefficient) composed mainly of quartz fringing many of the spherulites, and truly inter-spherulite areas which are bright and irregular in form. The latter consist of small plates of chlorite (<10 μm dia.) intergrown with trains of opaque minerals (pyrite and magnetite) and larger plates of zoned epidote to 20 μm long (Plate 5.7D). Chlorite-rich interspherulite areas could be resolved by the microprobe (Table 5.6, column 2; Fig. 5.7) indicating a rather Fe-rich chlorite; other analyzed areas clearly included more than one phase (Table 5.6, columns 3 and 4).

Foils from the axial portion of the vein were prepared for further examination of the mineralogy and microstructure by STEM. Much of the interspherulite area is composed of equigranular chlorite, plagioclase, quartz, sphene and epidote (Plate 5.8A). The quartz, plagioclase ($An_{<10}$) and chlorite occur as small euhedral plates up to 0.5 μm diameter, whilst sphene tends to have a more rounded shape and slightly smaller dimensions. Locally quartz-rich ares (Plate 5.8B) probably correspond to the felsic-rich interspherulite areas in the BSE micrographs (e.g. Plate 5.7D). Both the quartz and the plagioclase which shows good twinning, possess low dislocation densities. (Note: the microstructure is again unlike that described by Wenk, 1978 - although the cataclastic vein margins in this sample may have a microstructure similar to that illustrated by Wenk, ibid.) Large areas of the foils are composed of equant to elongate platelets of chlorite

TABLE 5.6 ANALYSES OF PSEUDOTACHYLYTE MATRIX, SAMPLE GQ1AP

	1	2	3	4
SiO_2	48.54	25.68	48.79	44.80
TiO_2	1.27	-	1.19	1.89
Al_2O_3	16.56	19.82	13.97	13.06
$Fe_2O_3^*$	14.88	n.d.	n.d.	n.d.
FeO^*	n.d.	26.90	13.26	15.60
MnO	0.23	0.48	-	0.24
MgO	6.24	13.76	6.63	7.46
CaO	8.66	0.33	10.81	12.37
Na_2O	2.63	-	2.89	1.48
K_2O	0.37	-	0.62	0.69
P_2O_5	0.11	n.d.	n.d.	n.d.
H_2O^-	0.08	n.d.	n.d.	n.d.
LOI	1.74	n.d.	n.d.	n.d.
Total	99.31	86.97	98.16	97.59

1. Mean of 2 XRF whole rock analyses of vein matrix plus clasts

2. Mean of 2 microprobe defocussed spot analyses of light coloured interspherulite phase (chlorite).

3, 4. Microprobe defocussed spot analyses of dark coloured interspherulite phases.

Note: (a) $Fe_2O_3^*$ is all iron determined as Fe_2O_3

(b) FeO^* is all iron determined as FeO.

(c) - is below detection limit.

(d) n.d. is not determined.

(e) H_2O^- is weight loss after drying at 110°C.

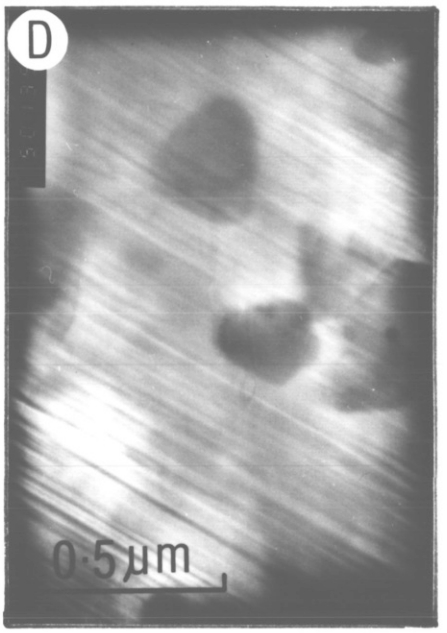
(f) LOI is weight loss after ignition at 950°C.

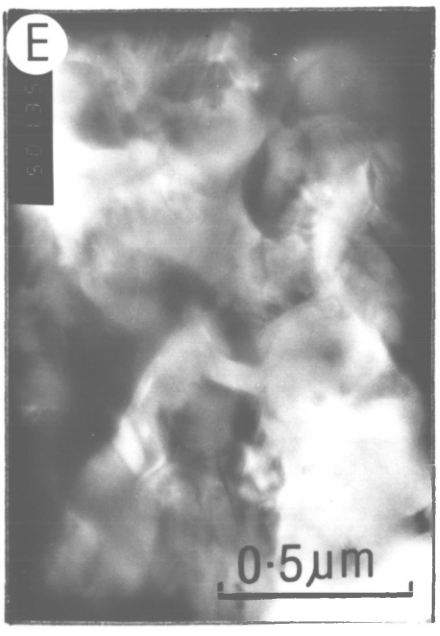
PLATE 5.8 TEM micrographs showing microstructure and mineralogy of chlorite spherulitic pseudotachylytes, sample GQ1A, foil 2.
(A) Equigranular groundmass composed of chlorite, plagioclase, sphene, quartz, epidote and oxides with a typical grain size of 0.5 μm.
(B) Quartz containing small grains of chlorite and sphene.
(C) Interspherulite area composed of large plates of chlorite with 120 triple point grain boundaries.
(D) Detail of large chlorite plate containing small rounded grains of sphene.
(E) Feldspar, possibly part of a spherulite .
(F) Triple point grain boundary between chlorite, quartz and plagioclase.


A
1·0 µm


B
1·0 µm


C
0·5 µm


D
0·5 µm


E
0·5 µm


F
0·5 µm

to 1 um diameter (Plate 5.8C and F) corresponding to the chlorite-rich interspherulite areas visible in the BSE micrographs (Plate 5.7D). Within the analytical limits of the STEM there is good agreement between the STEM and the microprobe analyses of the chlorites (Fig. 5.7). Small grains of sphene, poikiloblastically enclosed in the chlorite, are common (Plate 5.8D). Some difficulty was experienced in sucessfully thinning and locating electron-transparent areas of the spherulites, but the cellular intergrowth of plagioclase shown in Plate 5.8E is believed to be part of a spherulite.

5.4.3 Sample GQ1A: Interpretation

As with the plagioclase microlitic pseudotachylytes, the clast size, distribution, density and composition have to a large extent governed the textural development of this chlorite spherulitic pseudotachylyte. In addition, however, there is a systematic textural/mineralogical variation across the vein. It is clear that in this FV at least, melting followed cataclasis - frictional fusion - but that insufficiently high temperatures were obtained at the vein margins to permit melting. The variation in spherulite size and density is related at least in part to the variation of suitable spherulite nucleation sites - i.e. plagioclase clasts. There is some evidence for the axial entrainment of larger clasts (Plate 5.7C). It may also be related to the more rapid rate of cooling close to the vein margins.

Following the arguments outlined in section 5.2.4, the narrowness of this vein combined with the fine spherulite fibre diameter suggest that the spherulitic crystallization resulted from devitrification of a glass. Recrystallization of a fine grained, poorly sorted rock powder is discounted because of the presence of cataclastic margins and the improbability of a fine grained silicate rock powder recrystallizing to spherulitic morphologies (G. Lofgren, pers. comm., 1982). The interspherulite phases presumably (re-?) crystallized from glass enriched in Fe, Mg, Ca and Ti rejected by the growing plagioclase-rich spherulites.

The 'whole rock' composition of the pseudotachylyte vein (Table 5.5, column 1) is broadly similar to a ferro-basalt, and it is instructive to compare the texture of the pseudotachylyte with the textures found in devitrified basalts. The normal course of devitrification in, for example, 'recent' ocean floor basalts involves

palagonitization followed by the formation of clay and zeolite minerals (e.g. Mevel, 1978). The assemblage chlorite + albite + quartz + sphene + epidote seen in the pseudotachylyte is more akin to that seen in ancient metamorphosed pillow basalts (e.g. Dimroth and Lichtblau, 1979). This mineral assemblage suggests that higher temperature and drier conditions, close to greenschist facies, existed during devitrification of the pseudotachylyte than those applicable to the devitrification of recent ocean floor basalts.

Assuming a geothermal gradient of 25 -30°C.km^{-1} and a minimum (sub-) greenschist facies temperature of 300°C (Winkler, 1967), which would seem to be indicated by the mineral assemblage, a depth of 10 - 15 km may be estimated for the devitrification of the pseudotachylyte. From the data of chapters 2 and 3 this must be close to the maximum depth of pseudotachylyte generation before plastic deformation mechanisms become dominant. An alternative possibility, allowing a slightly shallower depth of devitrification is that ambient temperatures were raised by shear heating during continued faulting.

5.5 Pyroxene-spherulitic Pseudotachylyte

The pseudotachylyte described here was generated in aluminous biotite-garnet paragneisses and is distinguished by the presence of orthopyroxene dendrites.

5.5.1 Sample Series G80: Description

Seven samples of pseudotachylyte were collected along the length of a 40+ m long, concordant FV which varies in thickness from 0.1 to 5 cm. The host paragneisses are weakly foliated, medium grained and have a modal mineralogy given in Table 5.7. Five vein samples contain an average of 27 modal % clasts: about 15% less quartz than the host-rock, a quarter as much plagioclase and almost no garnet or biotite (Table 5.7).

The pseudotachylyte matrix has a globulitic structure which, like the chlorite-spherulitic varieties (section 5.4), varies both across and along the vein. Optically, the pseudotachylyte has a rather uniform fine-grained character being khaki-brown in PPL and a felted appearance of medium birefringent phases under X-nicols. Globulites are absent from an approximately 500 μm wide chilled/cataclastic margin (Plate 5.9A). The globulites are defined by their coarser grain

TABLE 5.7 MODAL COMPOSITION (VOLUME %) OF G80 SAMPLE SERIES

	1	2	3	4	5	6
Quartz	23	19	22	21	20	15
Plagioclase	39	5	8	8	10	5
Biotite	28	-				
Garnet	9	-				
Opaque	1	-				
Pseudolachylyte Matrix	-	76	70	71	70	80

1. G801H - host rock
2. G801P - pseudotachylyte
3. G802P - "
4. G803P - pseudotachylyte
5. G904P - "
6. G805P - "

Note: 1000 points counted for each sample

TABLE 5.8 ANALYSES OF PSEUDOTACHYLYTE MATRIX, SAMPLE SERIES G80

	1	2	3
SiO_2	60.31 (0.71)	55.64 (0.51)	57.31
TiO_2	0.63 (0.02)	0.63 (0.06)	0.76
Al_2O_3	17.22 (0.24)	19.08 (0.37)	16.00
Fe_2O_3*	7.26 (0.23)	n.d.	n.d.
FeO*	n.d.	7.47 (0.53)	7.00
MnO	0.12 (0.01)	0.20 (0.04)	-
MgO	4.18 (0.11)	4.57 (0.36)	5.43
CaO	3.60 (0.18)	4.76 (0.12)	2.65
Na_2O	3.41 (0.21)	4.24 (0.17)	2.64
K_2O	2.52 (0.17)	1.69 (0.14)	4.15
P_2O_5	0.12 (0.02)	n.d.	n.d.
H_2O^-	0.06 (0.05)	n.d.	n.d.
LOI	0.64 (0.22)	n.d.	n.d.
Total	100.07	98.27	96.34

1 Mean and standard deviation (bracketed) of 6 XRF analyses of vein matrix plus clasts (G801P-G806P)

2 Mean and standard deviation (bracketed) of 4 microprobe raster analyses of vein matrix

3 Mean of 3 microprobe raster analyses of matrix

TABLE 5.9 MICROPROBE AND STEM ANALYSES OF PYROXENE-SPHERULITIC PSEUDOTACHYLYTE MATRIX PHASES, SAMPLE SERIES G80

	1		2		3		4		5	
SiO_2	44.95 (0.50)		43.44		34.43		38.74		63.05	
TiO_2	0.79 (0.10)		0 75		2.10		2.46		0.24	
Al_2O_3	12.21 (0.89)		11.65		17.00		17 73		22.62	
FeO*	24.29 (0.90)		29.31		17 23		17.36		0.79	
MnO	0.79 (0.14)		1.25		-		0.41		-	
MgO	15.14 (0.83)		12.26		11.30		13.81		0.48	
CaO	0.94 (0.32)		1.04		1.03		-		6 70	
Na_2O	0.50 (0.26)		-		0.67		0.25		5.13	
K_2O	0.48 (0.42)		-		8.57		9.31		0.58	
Total	100.09		99.70		92.33		100.07		99.59	
Si	1.707		1.697		5.390		5.532		2.800	
Al	0.293	2.000	0.303	2.000	2.610	8.000	2.468	8.000	1.184	3.984
Al	0.253		0.234		0.536		0.516		0.000	
Ti	0.023		0.022		0.242		0.264		0.008	
Fe	0.771		0.958		2.266		2.073		0.032	
Mn	0.025		0.041		0.000		0.000		0.000	
Mg	0.857		0.714		2.640	5.684	2.939	5.792	0.032	
Ca	0.038		0.044		0.176		0.000		0.320	0.072
Na	0.037		0.000		0.198		0.069		0.440	
K	0.023	2.027	0.000	2.016	1.716	2.090	1.696	1.765	0.032	0.792
O	6.000				22.000		22.000		8.000	
En	50.6									
Fs	47.1									
Wo	2.3									

1 Mean and standard deviation (bracketed) of microprobe anlayses of orthopyroxene dendrites

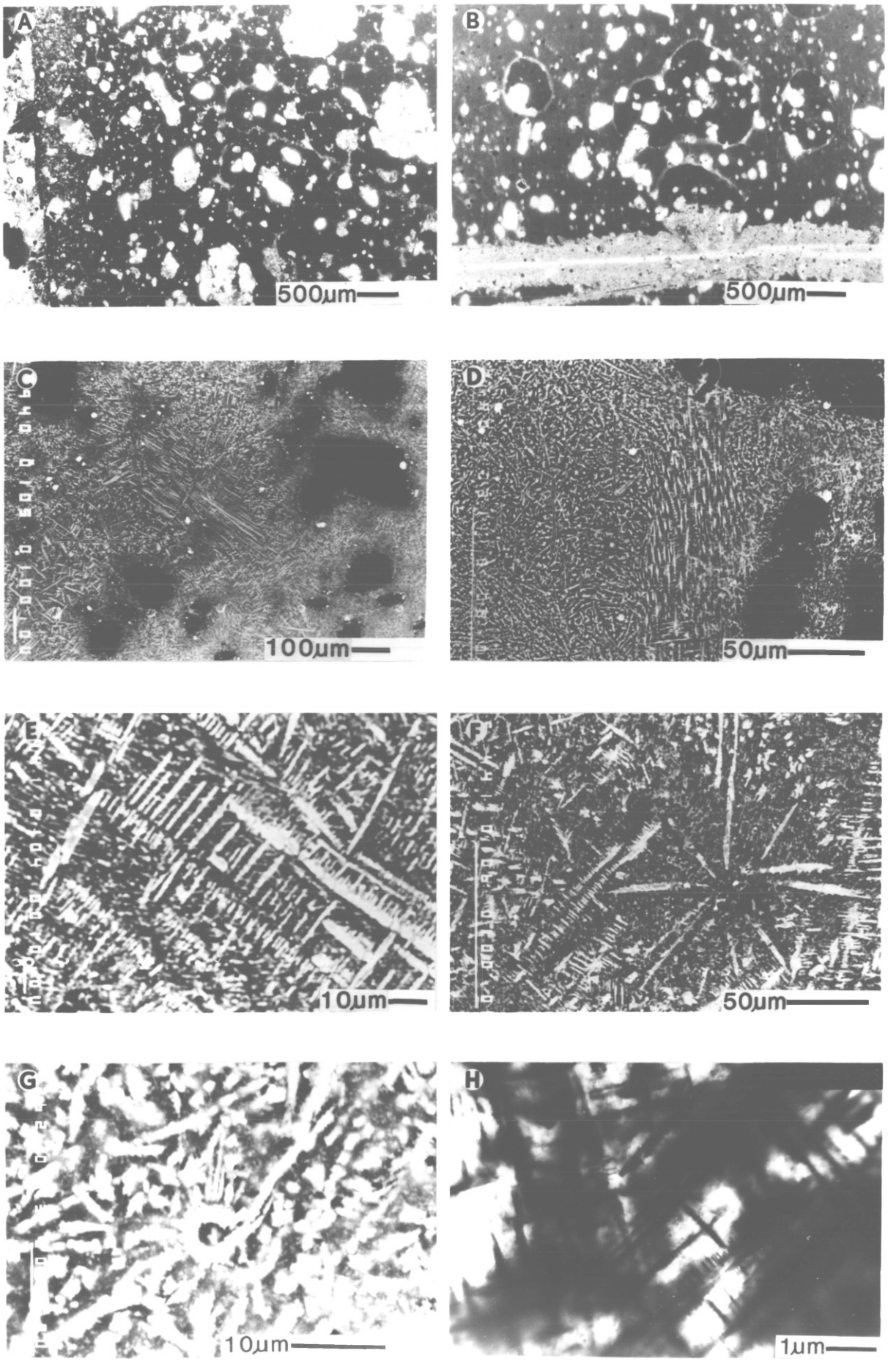
2 STEM analysis of orthopyroxene dendrite

3 Microprobe analysis of xenoblastic biotite

4 STEM analysis of xenoblastic biotite

5 Microprobe analysis of plagioclase feldspar poikilitically enclosing orthopyroxene dendrites

PLATE 5.9 Pyroxene-spherulitic pseudotachylyte, sample series G80.
(A) Optical micrograph (X-nicols) showing chilled/cataclastic margin and closely-packed globulites.
(B) Optical micrograph (PPL) showing loosely-packed, coalescent globulites. Note late cross-cutting quartz/chlorite-healed microfracture with halo of bleaching which affects the globulites.
(C) BSE micrograph showing general view of the groundmass. A globulite composed of pyroxene dendrites occupies the central area.
(D) BSE micrograph showing randomly and systematically orientated pyroxene dendrites. The systematically orientated dendrites correspond to a globulite as seen optically.
(E) BSE micrograph of pyroxene dendrites showing cock's comb texture.
(F) BSE micrograph of spherulitic and cock's comb pyroxene dendrites.
(G) BSE micrograph of small spherulitic structure.
(H) TEM micrograph of cock's comb pyroxene dendrites.


A
500μm
B
500μm
C
100μm
D
50μm
E
10μm
F
50μm
G
10μm
H
1μm

size and a narrow (<20 μm) lighter coloured halo (similar haloes mantle the quartz clasts) (Plate 5.9A and B). They are irregular to circular in section with a maximum diameter of about 1 mm and vary in density from close-packed, occasionally coalescent but non-polygonal)Plate 5.9A), to 2 - 3 mm separation (Plate 5.9B). They generally have plagioclase clast nuclei (often non-central) fringed by plagioclase microlites; the microlites have morphologies and chemistries comparable to those in plagioclase-microlitic pseudotachylytes. The greater part of the globulites are made up of high-relief, straight-extinguishing dendrites arranged in a loosely spherulitic (Plate 5.9C) or more regular latticework fashion (PLATE 5.9D). In the SEM and TEM the dendrites are seen to be up to 75 μm long X 5 μm wide and with secondary fibrillar growths or cock's comb texture (Plate 5.9E and H). The groundmass interstitial to the microlites and dendrites appears optically to be largely composed of phyllosilicate. In the SEM and TEM this is seen to be made up of small equant grains of biotite, quartz, plagioclase and chlorite. The inter-globulite portions of the vein are made up of the same phases as the globulites but witha smaller grain size (Plate 5.9F and G). Throughout the vein (globulites and outside and in fractures in quartz clasts) small blebs (<50 μm) of sulphide occur, including pyrite, chalcopyrite and sphalerite.

The pseudotachylyte is cut by chlorite/quartz-healed microfractures which possess a bleached halo. The bleaching is demonstrably later than the globulite formation (Plate 5.9B).

5.5.2 Sample Series G80: Vein and Mineral Chemistry

Whole-rock chemical analyses of the host-rock and pseudotachylyte vein are given in Table 5.8. The whole-rock chemistry is considered further in section 6.5.1.

Microprobe and STEM analyses of various matrix phases are given in Table 5.9. The orthopyroxene of composition $Fs_{47.1}$-$En_{50.6}$-$Wo_{2.3}$ (probe analysis) is unusual in being highly aluminous (~12 wt.% Al_2O_3). Analyses of the other phases are of rather poor quality due to their extremely fine grain size.

5.5.3 Sample Series G80: Interpretation

The globulitic texture of this pseudotachylyte, dominated by

microlitic plagioclase and dendritic orthopyroxene almost certainly resulted from primary crystallization from the melt. As in the previously described pseudotachylytes the porphyroclasts have strongly influenced the nucleation and growth of new phases from the melt. The morphology of the plagioclase and orthopyroxene together with the high Al_2O_3-content of the latter suggest a rapid cooling rate and/or crystallization at large values of .T. In an experimental study, Wood (1974) found that the Al_2O_3-content in complex (Ca-Fe-Mg) orthopyroxenes crystallized with garnet took 54 hours to decrease to an equilibrium value at 1 GPa and 900°C. Whilst the pseudotachylyte pyroxenes undoubtedly crystallized at lower pressures, a strongly disequilibrium phase chemistry may be inferred.

Hypersthene microlites have been tentatively identified optically in pseudotachylytes cutting charnockites from Mysore Province, India (Pichamuthu, 1959). The texture of these pseudotachylytes are somewhat similar to those described here. Aluminous calcic clinopyroxene (21 wt.% Al_2O_3) has been described from a pseudotachylyte vein cutting gabbro in the Musgrave Ranges, Australia (Wenk and Weiss, 1982). The clinopyroxene corresponds chemically to the whole-rock composition of the gabbro.

The conditions favouring crystallization of orthopyroxene (or clinopyroxene - cf. Wenk and Weiss, 1982) in pseudotachylytes are not clear. The chemical compositions of the paragneiss host-rock of this study and the charnockite host-rock mentioned above are radically different. It is obvious from the data of Table 5.7 that the pseudotachylyte melt form largely from a mixture of biotite, plagioclase, garnet and a small amount of quartz. Examination of the partial melting textures of lithic porphyroclasts in this sample suggest that the melt was undersaturated with respect to water (section 5.8.7)

5.6 Phyllosilicate-Spherulitic Pseudotachylytes

A variety of different types of pseudotachylyte, all with an ultra-fine grained groundmass rich in K-phyllosilicates are grouped under this heading. In contrast to most other types of pseudotachylyte, similar textures are found in phyllosilicate spherulitic pseudotachylyte FV 's and IV 's independently of their width; the common factor between the veins in addition to their K-phyllosilicate matrix, is the presence of K-rich phases (biotite + K-spar + muscovite) in the host (protolith) rocks. Because extensive small scale variation exists from one sample to another, representatives of a number of textural/mineralogical types will be described separately and an attempt to explain some of their differences will be made.

5.6.1 Sample SU802

1) Description

Sample SU802 was collected from an IV complex cutting 'granitic' gneisses (quartz + plagioclase + K-spar + biotite + accessories) at Rubha Ardvule, S Uist. A definitive cross-cutting vein relationship was visible in the field. This is clearly seen in thin section where the later biotite-spherulitic pseudotachylyte appears to have chilled against an earlier generation of plagioclase microlitic pseudotachylyte (Plate 5.10A). The latter is an irregular IV 'squirt' with a texture comparable to those described in section 5.2 and containing about 25 modal % angular and poorly sorted clasts of quartz and feldspar. Analyses of the plagioclase microlites are included in Fig.s 5.2 and 5.3.

The cross-cutting IV is much finer grained, consisting of a light brown/yellow globulitic groundmass with 5-20 μm diameter clots of optically darker phases between the globulites (Plate 5.10D; note: the optically darker areas appear brighter in the BSE micrographs). The irregularly coalesced globulites are chiefly nucleated on minute (<5 μm diameter) rounded opaques (Plate 5.10D). Under crossed-nicols, the globulitic groundmass shows yellow to upper first order birefrigence. A weak flow banding, parallel to the vein margins, is defined by variations in colour and the distribution and density of the dark clots and darker brown, more homogeneous mantles to some of

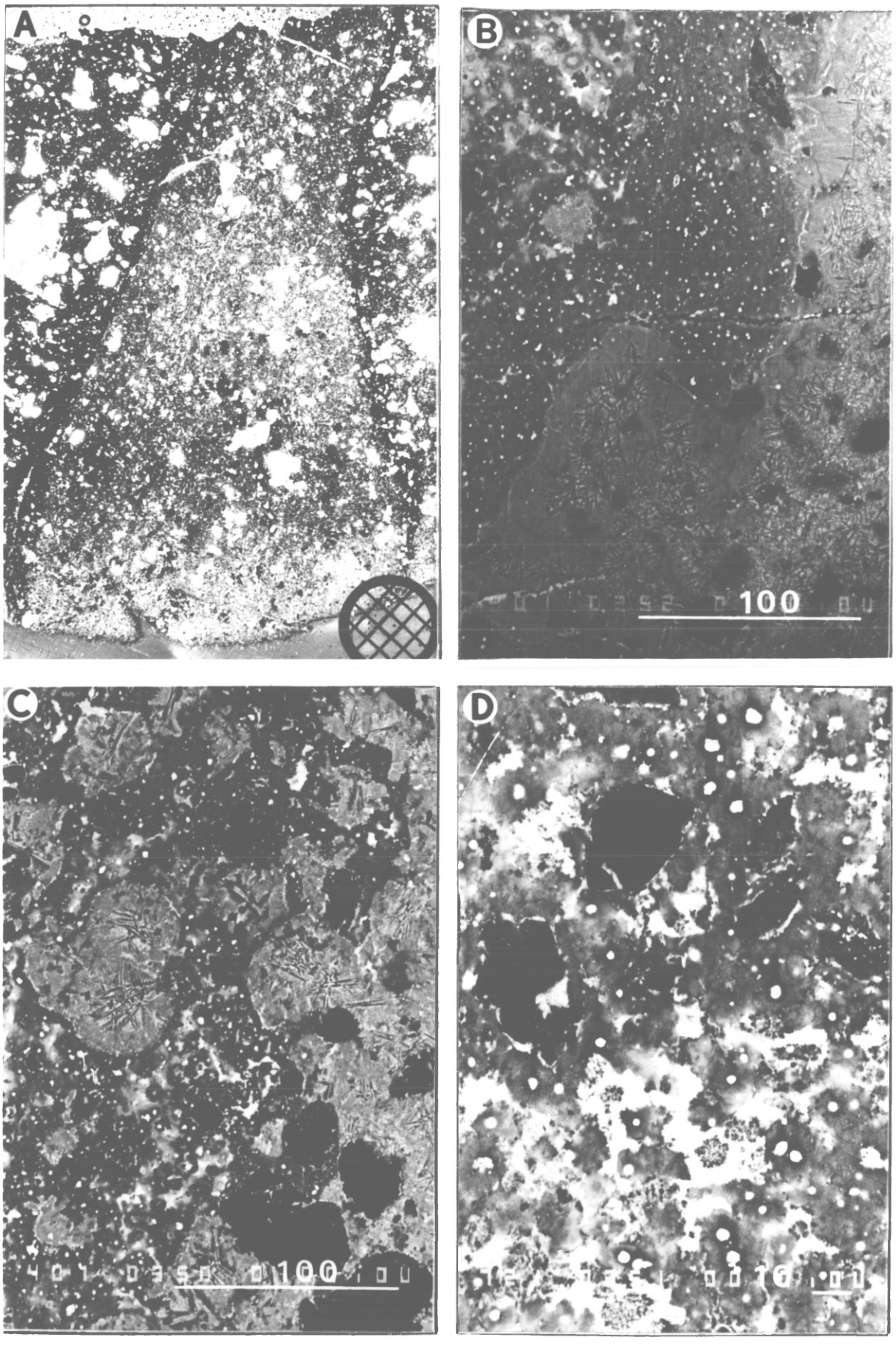
PLATE 5.10 Phyllosilicate-spherulitic pseudotachylyte IV cross-cutting plagioclase microlitic vein, sample SU802.

(A) Photomicrograph showing tapering phyllosilicate-spherulitic pseudotachylyte IV cutting earlier generation of plagioclase microlitic pseudotachylyte; note dark reaction zone between the 2 generations of pseudotachylyte and dark patches within the later vein. Partially crossed nicols; grid is 3 mm across.

(B) BSE micrograph showing contact between microlitic and spherulitic pseudotachylytes. First generation pseudotachylyte is composed of plagioclase microlites with abundant quartz porphyroclasts. Partial rheomorphism has occurred and the contact itself is composed of ultra fine grained fibro-radial phases. Bright phases in second generation pseudotachylyte are oxides.

(C) BSE micrograph showing more advanced stage of rheomorphism where globulites of microlitic pseudotachylyte from first generation are enclosed in spherulitic pseudotachylyte of second generation.

(D) BSE micrograph showing detail of axial region of cross-cutting pseudotachylyte showing ultra fine grained biotite spherulites chiefly nucleated on opaque phases and other high mean atomic number phases in inter-spherulite areas.


A
B
100
C
100
D

the quartz clasts.

The contact with the earlier microlitic pseudotachylyte is marked by a dark chocolate-brown coloured zone which varies in width from 100 to 500 μm (Plate 5.10A), and locally shows a flow structure defined by colour. More detail is revealed in the BSE images where the textural change across the contact can be seen to affect both generations of pseudotachylyte. In the earlier microlitic vein, the plagioclase microlite size decreases toward the contact from 200 x 20 μm acicular skeletons to 20 x 4 μm swallowtails with a concomitant increase in volume of ultra fine grained fibro-radial phases nucleated on the swallowtails (Plate 5.10B). In the later biotite-spherulitic vein, the size of the globulites decreases and their density and packing increases against the contact (Plate 5.10B). The contact itself remains sharp, although its trace varies from planar to interfingering or necking (Plate 5.10B). Elsewhere along the contact, spherulites to 40 μm diameter apparently derived from the microlitic pseudotachylyte are detatched and isolated within the globulitic groundmass of the cross-cutting vein (Plate 5.10C). These spherulites are microstructurally and mineralogically similar to the fine-grained margin of the microlitic pseudotachylyte; they consist of a single, or a bundle of interfingering plagioclase swallowtails up to 20 μm long on which fibro-radial phases have nucleated (Plate 5.10C).

Within the main part of the cross-cutting vein irregular patches to 400 μm across of a darker chocolate-brown phase occur, similar in appearance to the fibro-radial phases of the contact zone (Plate 5.10A). The structure of these patches, seen optically at the thin edge of the section, is raggedly fibro-radial; under crossed nicols they show anomalous grey-brown birefringence. In the SEM they appear as ragged aggregates with a moderate to high mean BSE coefficient.

The clast content of the cross-cutting vein is slightly lower than the microlitic pseudotachylyte but, more significantly, consists of about 90% quartz and 10% feldspar clasts in contrast to the sub-equal proportions of the same clasts in the microlitic vein. The clasts vary in size from 10 μm to 2 mm diameter; all are more or less brittley-deformed showing varying degrees of brittle fracture, cataclasis, undulose extinction and melt-corrosion. The larger clasts are sub-rounded whereas the smaller clasts tend to be more angular. Nucleation of opaques along fractures within the quartz clasts is restricted and a greater proportion of opaques are present in the groundmass (cf. section 5.8.1).

2) Chemistry and STEM Analysis

XRF whole-rock analyses of the two veins and microprobe raster analses of the yellow/brown globulite matrix, the irregular dark-brown patches and the dark-brown fibro-radial part of the contact zone are presented in Table 5.10. The whole-rock analyses of the two veins are remarkably similar - probably due in part to the weighting effect of clasts included in the analyzed material (section 6.2). The globulitic vein however is richer in K_2O, poorer in Na_2O and has a larger LOI than the microlitic vein - consistent with the presence of abundant K-phyllosilicate in the former (Table 5.10, columns 1 and 2 respectively). The microprobe analyses show up substantial differences in the Ca and alkali contents of the various groundmass phases. The brown/yellow globulitic groundmass is greatly enriched in K_2O and depleted in FeO, MgO, CaO and Na_2O relative to the dark brown patches and the contact zone (Table 5.10, columns 3, 4 and 5 respectively). The marginal brown zone contains higher FeO, MgO and CaO but lower Na_2O than the brown patches. Microprobe raster scans were made of areas up to 20 x 20 μm and although obvious heterogeneities such as opaque globulite nuclei were avoided, it is clear from the detail of Plate 5.10 that the analyses include more than one phase; in spite of this the reproducibility of the analyses is satisfactory (Table 5.10).

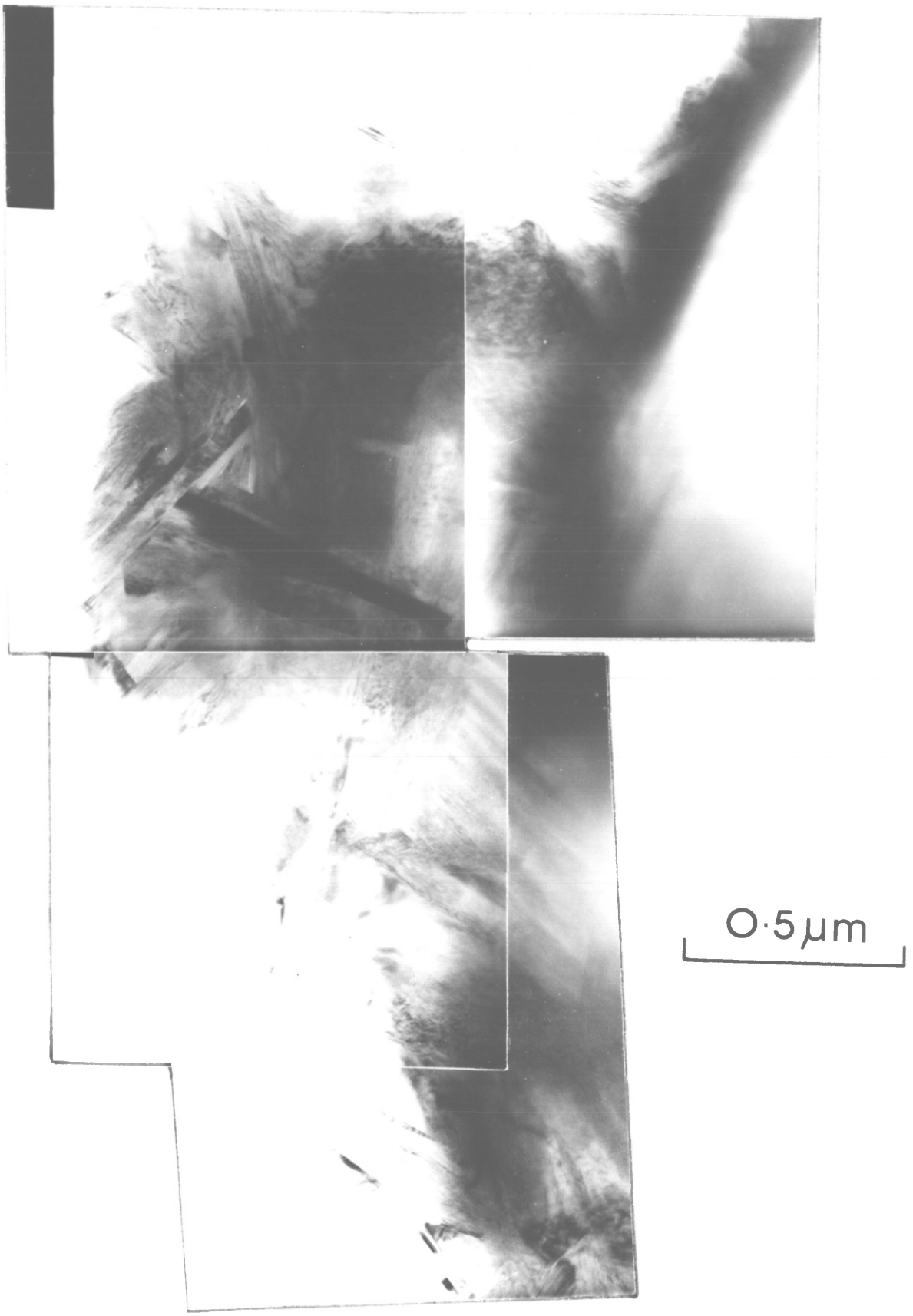
TEM foils of the globulite groundmass and the dark brown patches were prepared to facilitate more detailed examination of the mineralogy and microstructure. (Attempts to prepare thin foils of the contact zone were unsuccessful.) Plate 5.11 illustrates the typical microstructure of the globulitic groundmass. The globulites consist of irregular phyllosilicate spherulites nucleated on rounded magnetite or plagioclase grains. Individual phyllosilicate fibres elongated parallel to (001) are <0.1 μm across, although the narrowness may in part be accentuated by splicing along the (001) cleavage during ion-thinning and due to electron beam damage. Because the fibres interfinger (reflecting coalescence of the globulites visible in the SEM) and because only small areas of the foils are transparent to 100 kv electrons, the lenghth of the fibres is difficult to determine. However, it is reasonable that the fibre lenghth should equal the globulite radii visible in the SEM - i.e. ~20 μm. Fibrillar overgrowths and branching of the fibres were not found. Analysis of the fibres proved difficult, even in the STEM, because of their

TABLE 5.10 ANALYSES OF BIOTITE SPHERULITIC PSEUDOTACHYLYTE, SAMPLE SU802P

	1	2	3		4		5	
SiO_2	64.26	64.23	60.28	(1.36)	60.68	(1.15)	58.82	(1.32)
TiO_2	0.76	0.65	0.65	(0.15)	0.27	(0.08)	0.76	(0.12)
Al_2O_3	15.26	15.05	18.01	(1.01)	18.24	(0.66)	17.09	(0.63)
Fe_2O_3*	6.05	5.82	-		-		-	
FeO*	-	-	4.42	(1.30)	5.32	(1.04)	5.43	(0.15)
MnO	0.10	0.10	trace		trace		trace	
MgO	1.14	1.02	0.91	(0.26)	1.01	(0.36)	1.87	(0.14)
CaO	4.58	4.26	2.77	(0.33)	3.06	(0.53)	5.71	(0.23)
Na_2O	4.02	3.39	3.67	(0.82)	8.43	(0.48)	6.85	(0.52)
K_2O	1.89	2.56	7.45	(1.30)	0.79	(0.31)	0.56	(0.11)
P_2O_5	0.33	0.27	-		-		n.d.	
H_2O^-	0.12	0.19	-		-		n.d.	
LOI	0.94	1.25	-		-		n.d.	
Total	99.45	98.79	98.15		97.80		97.09	

1. XRF whole rock analysis of plagioclase microlitic pseudotachylyte generation 1.
2. XRF whole rock analysis of biotite spherulitic pseudotachylyte generation 2.
3. Mean and Standard deviation (bracketed) of 5 microprobe raster analyses of biotite spherulitic pseudotachylyte groundmass.
4. Mean and Standard deviation (bracketed) of 5 microprobe raster analyses of dark brown phase in 3.
5. Mean and Standard deviation (bracketed) of 5 microprobe raster analyses of marginal dark brown phase in 3.

PLATE 5.11 TEM micrograph showing microstructure of phyllosilicate-spherulitic pseudotachylyte shown in plate 5.10A. The spherulite is composed of biotite and subordinate chlorite laths, with minor interfibre quartz and plagioclase and is nucleated on feldspar..


0·5 µm

narrowness and susceptibility to beam damage. The majority of the fibres are biotites with high SiO_2 and Al_2O_3 and low MgO contents (Fig. 5.1; Appendix A3) indicating considerable substitution of the dioctahedral mica component. Smaller numbers of chlorite fibres, which are discrete rather than interlayers within the biotites, are also comparitively MgO-poor (Fig. 5.7; Appendix A3, STEM biotite analyses 10-11). Within the triangular interstices between diverging phyllosilicate fibres are small (<0.25 μm diameter), sub-equant, dislocation-free grains of quartz and plagioclase (Plate 5.11). The microprobe raster analses of the globulitic groundmass evidently correspond to this polymineralic assemblage. Around the margins of some of the feldspar porphyroclasts, similar quartz and feldspar occurs displaying an equilibrium texture (Plate 5.12A and B).

The microstructure of the dark brown patches is shown in Plates 5.12C and D. They consist of jumbled wispy laths of biotite and chlorite (<1 μm long), small rounded grains (~0.1 μm diameter)of amphibole and minute euhedral magnetites (<0.05 μm dimeter) largely enclosed in dislocation-free quartz and plagioclase. The biotite and chlorite are similar in composition to the globulitic groundmass and the amphibole is an actinolitic-hornblende (Appendix A3). No trace of a systematic spherulitic structure could be seen in the TEM.

3) Interpretation and Discussion

In addition to the chemistry, mineralogy and microstructure of the globulitic pseudotachylyte, the nature of the contact with the microlitic pseudotachylyte is of particular interest in this sample. The form of the contact has resulted from reaction between the intruding hot pseudotachylyte melt and the cooler microlitic pseudotachylyte host. The necking of the contact and the fact that textural changes affect both veins strongly suggests that rheomorphism involving mobilization of the microlitic pseudotachylyte has occurred. The most advanced effect of this is demonstrated by the relationships shown in Plate 5.10C. It is not clear whether the isolated spherulites, apparently derived from the microlitic pseudotachylyte, represent imperfect mechanical mingling or liquid-liquid silicate immiscibility (cf. Carstens, 1982). They appear to have been partially melted when incorporated into the later melt and their near spherical, locally coalesced form (Plate 5.10C) certainly suggests large differences in viscosity between the two melts.

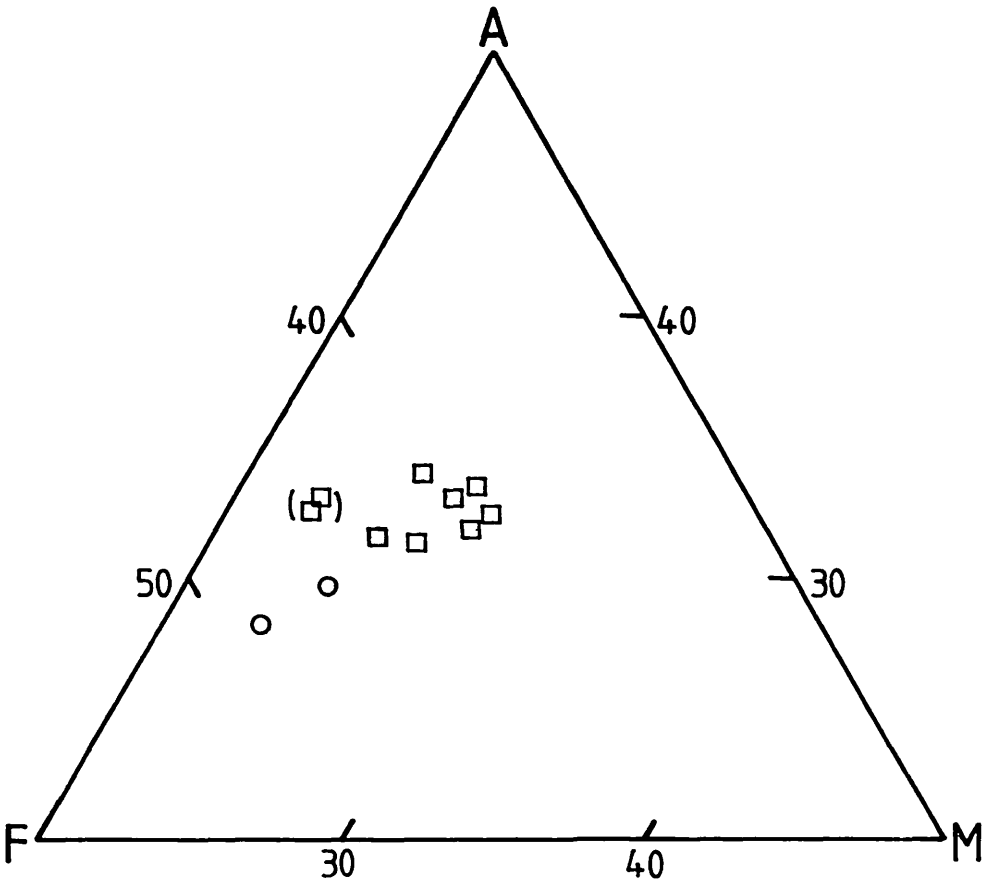


FIGURE 5.7 AFM diagram showing composition of pseudotachylyte matrix chlorites determined by STEM microanalysis. Components as for Fig. 5.1.

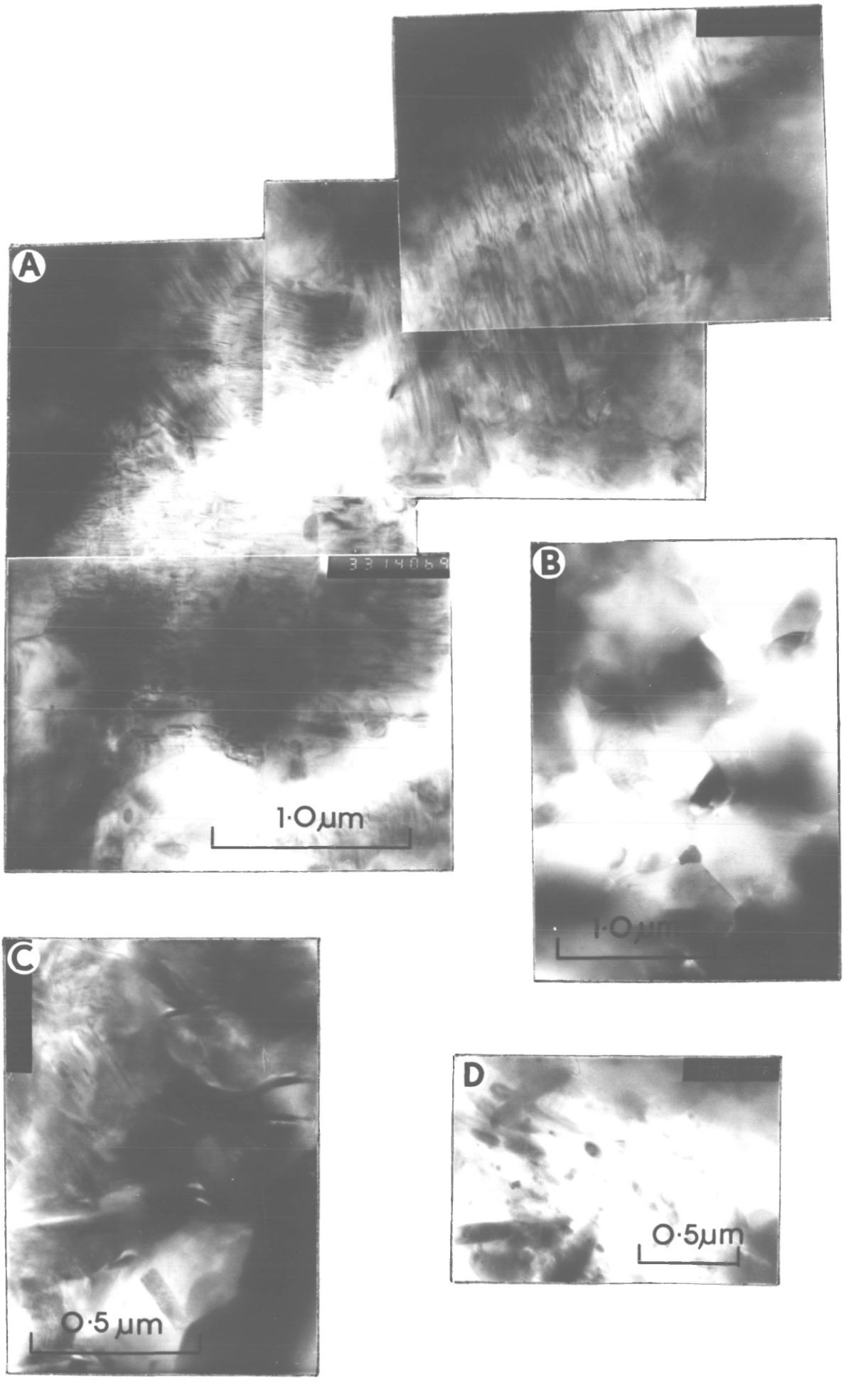
Chlorite spherulitic pseudotachylyte:

□ = interspherulite chlorite plates, sample GQ1A, foil 2, Grimsay. Bracketed symbols are microprobe analyses.

Phyllosilicate spherulitic pseudotachylyte:

○ = spherulitic chlorite intergrown with biotite; sample SU802, foil 3, Rubha Ardvule.

PLATE 5.12 TEM micrographs showing microstructure of phyllosilicate-spherulitic pseudotachylyte shown in Plate 10A.
(A) Plagioclase clast with mantle of (?) new plagioclase, equant quartz and small biotite laths.
(B) Equant euhedral to rounded quartz grains adjacent to feldspar clast shown in (A).
(C) Wispy laths of biotite with feldspar and quartz adjacent to quartz porphyroclast. Foil prepared from optically dark area of vein shown in Plate 5.10A.
(D) Fine-grained groundmass composed of quartz, feldspar, biotite and equant rounded grains of hornblende.


A
1·0μm
B
1·0μm
C
0·5 μm
D
0·5μm

Noting the narrow width of the cross-cutting vein and the thermal considerations detailed in section 5.2.3 the question arises as to how rheomorphism/partial melting of the microlitic pseudotachylyte could possibly have occurred. It is possible that the later pseudotachylyte was superheated, although there is a general lack of wall-rock alteration adjacent to pseudotachylyte veins. An alternative possibility however, and one which is compliant with the field relations, is that the later vein was intruded into still-hot microlitic pseudotachylyte. Given that perhaps 80% of the heterogeneously nucleated microlitic plagioclase may have crystallized over a temperature range of $T < 200°C$ (Fig. 5.5), the amount of heat required to remelt a small amount of the microlitic pseudotachylyte might be quite small. A possible objection to this, that brittle fracture/ intrusion of the hot microlitic pseudotachylyte seems inherently unlikely may be overruled on the basis of a number of recent studies (e.g. see summary by Shaw, 1980) indicating that hot igneous rock containing <30% melt is weak but can deform by brittle failure.

5.6.2 Sample X

Sample X was collected as a beach pebble at Rubha Ardvule, S Uist. In spite of the poor field control (!) a brief description is included to illustrate further the microstructure of a pseudotachylyte which appears 'glassy' optically.

The cobble consists of medium-grained microperthite + plagioclase + quartz + muscovite + epidote gneiss containing a 6 cm thick pseudotachylyte vein.

TEM Microstructure

Foils from part of the vein comprising a 5 mm thick zone of yellow-brown optically structureless material were prepared. The microstructures revealed by the TEM are shown in Plates 5.13 and 5.14. The pseudotachylyte consists of a fine grained assemblage dominated by K-phyllosilicate (Plate 5.13A, D and E, and Plate 5.14) with domains richer in feldspar and quartz (Plate 5.13C). The grain size of all the phases is <1 μm - i.e. below the limit of optical resolution. The spherulitic structure is well-illustrated in Plate 5.14. Plagioclase, believed to be newly-crystallized/devitrified, with a cellular

PLATE 5.13 TEM micrographs showing mineralogy and microstructure of phyllosilicate-spherulitic pseudotachylyte, sample X.

(A) New microlitic plagioclase with small laths of biotite (dark).

(B) Feldspar, quartz and biotite rich groundmass.

(C) Groundmass of rounded quartz and feldspar with spherulitic biotite laths.

(D) Spherulitic and randomly orientated biotite laths adjacent to (?) new plagioclase.

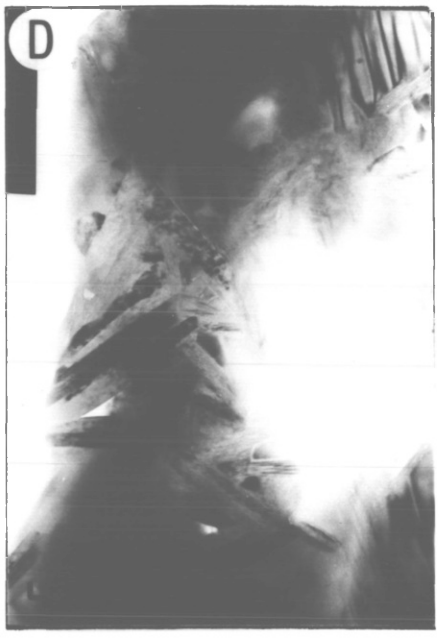
(E) Biotite lath surrounded by quartz. Note beam damage in area of analysis.

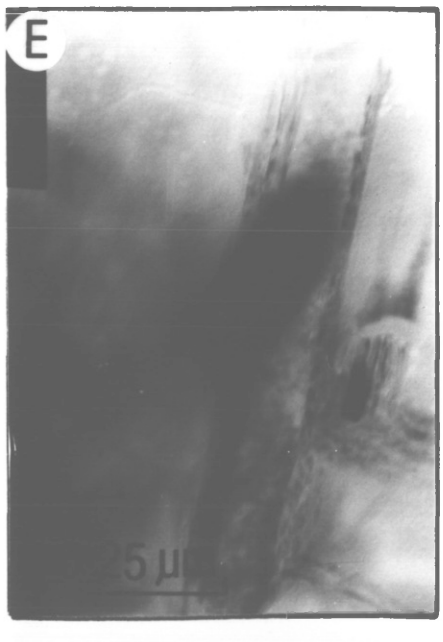
(F) Equant dislocation-poor quartz sub-grains on rim of quartz porphyroclast.


A
1·0 µm


B
1·0 µm


C


D

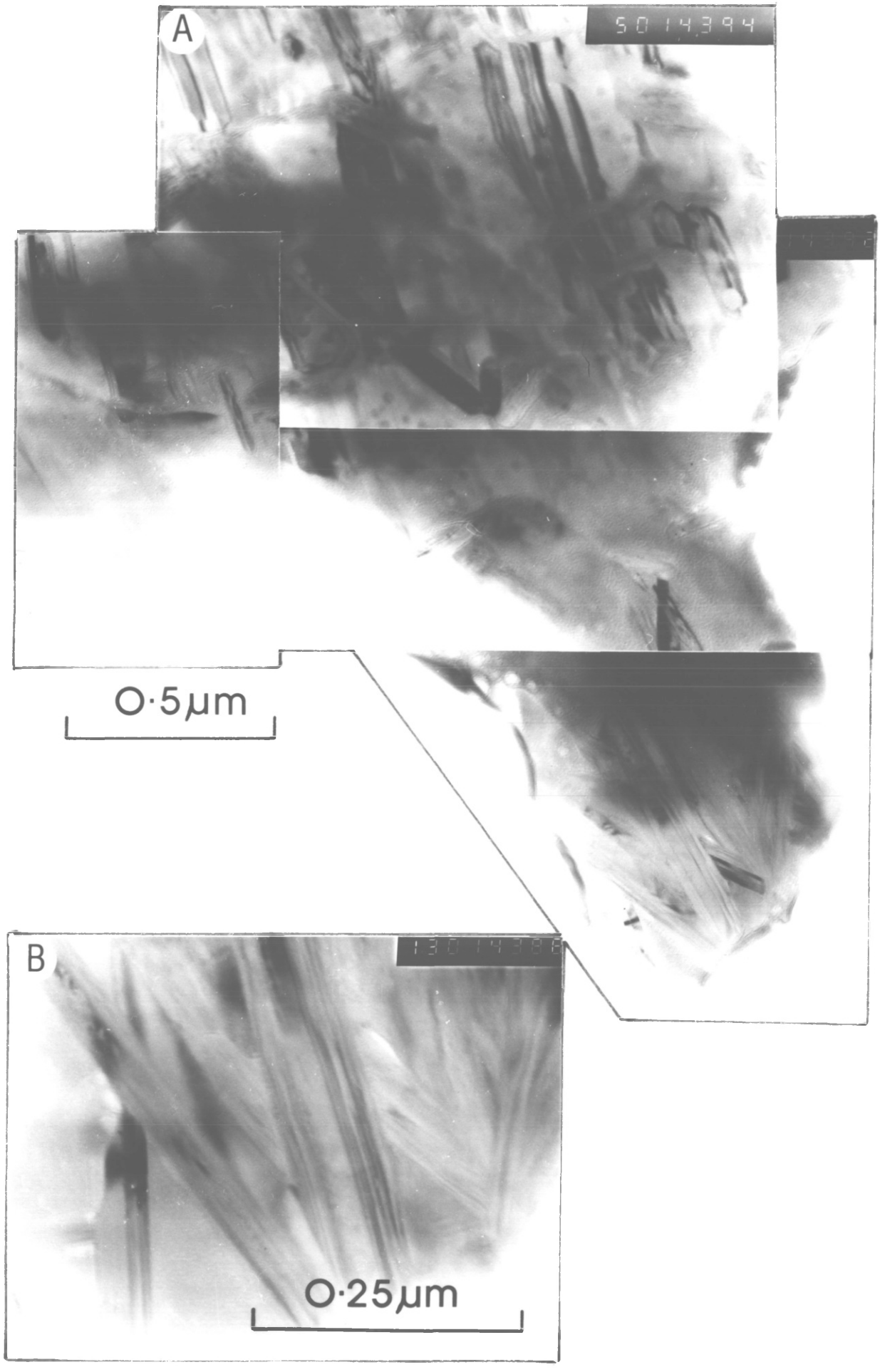

E


F
0·5 µm

PLATE 5.14 Detail of biotite spherulite shown in Plate 5.13A. Sample X, foil 6.

(A) Spherulitic biotite laths diverging away from the hole towards a plagioclase grain.

(B) Detail of spherulitic biotite showing extremely fine grain size.


A
0·5μm
B
0·25μm

structure comprising equant (euhedral?) cells of about 0.5 um across is surrounded by radially arranged (spherulitic) K-phyllosilicate. The latter consists of laths or fibres <0.1 μm wide and a few microns long (Plate 5.14B).

Analyses of some of the phyllosilicates are included in Fig. 5.1.

5.6.3 Sample G1B

1) Description

Sample G1B is a concordant 2 - 3 mm thick FV cutting fine-grained paragneiss from Gairloch, NW Scotland. The gneiss contains quartz + plagioclase + K-spar + biotite + muscovite + epidote + sphene, with chlorite + opaque locally replacing biotite and has a strong foliation defined by irregularly spaced centimetric layers of felsic and mafic phases. Shears parallel to the foliation occur at the contact with and within ferromagnesian mineral rich bands - demonstrating on a small scale the control of anisotropy/layers of weakness on pseudotachylyte faulting (cf. section 4.3.5). The foliation-parallel shears vary from knife-sharp discontinuities of less than 100 μm thickness of optically isotropic ultracataclasite or pseudotachylyte to the 2 - 3 mm wide pseudotachylyte FV shown in Plate 5.15A. Where the shears enclose mica-rich gneiss, the gneiss is strongly sheared by irregular transgranular and intergranular shears and a prominent set of discrete, systematic shears making an angle of <25° with the main FV (Plate 5.15A). IV 's of pseudotachylyte occur in both sub-orthogonal orientation and parallel to the minor shears (V and X respectively in Plate 5.15A).

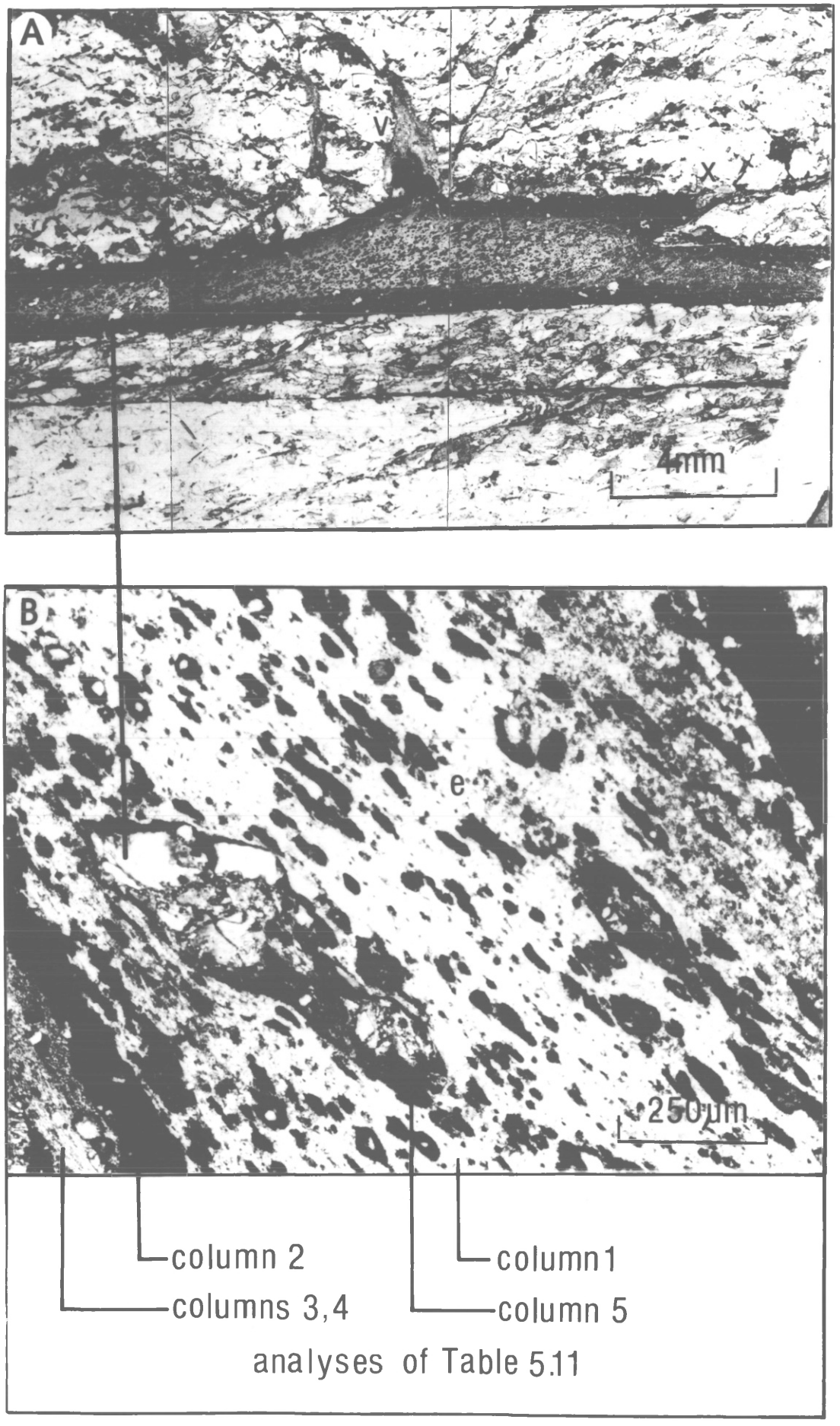
The main pseudotachylyte vein is divisible into two marginal zones and an axial zone. The marginal zones, <300 μm wide, show a delicate flow banding defined by dark-brown to black colouration which is parallel to the vein margins. They contain small clasts of host rock phases, predominantly quartz and feldspar (Plate 5.15A and B). The margins consist of mainly ultracataclasite rather than pseudotachylyte.

The axial part of the vein is made up of a more homogeneous golden brown coloured matrix, whose birefringence is partly masked by the strong absorbtion. It contains predominantly felsic clasts which are haloed by dark brown or black mantles (Plate 5.15B). A strong

PLATE 5.15 Concordant biotite-rich pseudotachylyte FV; sample G1B, Gairloch, NW Scotland.

(A) Photomicrograph showing general relationship between 2 foliation parallel FV's, associated low angle minor shears (X), a high angle IV (V) and the gneissic banding defined by modal variation. Note the foliation in the thicker FV orientated from lower left to top right and folded into the minor shear at X. PPL.

(B) Photomicrograph showing detail of A. The main FV is divisible into light and dark marginal zones with a delicate flow banding, and a thicker axial zone. The foliation in the axial zone is defined by the lattice-preferred orientation of the phyllosilicate matrix and the dimensional-preferred orientation of porphyroclasts and their haloes. Small granular high relief phases are epidotes (e). Partially crossed nicols.


A
V
X
X
4mm
B
e
250µm
column 2
columns 3,4
column1
column 5
analyses of Table 5.11

planar fabric, orientated sub-parallel to the systematic minor shears, is defined by the lattice-preferred orientation of the phyllosilicate matrix and the dimensional-preferred orientation of the porphyroclasts and their haloes (Plate 5.15B). The porphyroclasts do not however show evidence of intracrystalline plastic deformation associated with the formation of this fabric. The optical slow ray of the matrix phyllosilicate is orientated approximately parallel to the fabric, such that the whole vein extinguishes almost uniformly upon rotation of the microscope stage. On closer examination however, the fabric can be seen to be folded; for example, the nose of an open fold projects into the minor shear/IV X in Plate 5.15A. The optical extinction fans around this fold.

The porphyroclast content of this pseudotachylyte is rather low (about 10%), perhaps resulting from generation of the pseudotachylyte in a mica-rich layer in the gneiss. Small grains of a high relief colourless phase (e in Plate 5.15B) are probably newly-crystallized (metamorphic/alteration) epidote rather than porphyroclast-derived. Opaque granules and globules are not present, and apart from the dark porphyroclast haloes no trace of globulitic or spherulitic structure is visible optically.

2) Chemistry

Microprobe defocussed spot analyses of the main pseudotachylyte vein are presented in Table 5.11. The golden brown phyllosilicate matrix of the axial portion of the vein is chemically homogeneous and largely composed of K-mica (Table 5.11, column 1). The high SiO_2 content and moderate (Fe + Mg) suggests a moderate content of the dioctahedral mica component, although without TEM study it is not possible to determine the precise mineralogy. The 2% CaO content of this material may be referable to the small grains of epidote. The vein margins are more inhomogeneous (Table 5.11, columns 2, 3 and 4), the variation in colour reflecting variations in the proportions of salic and mafic phases - especially Fe-content. Analysis 4 (Table 5.11) corresponds to a biotite grain (chemically similar to the melt-corroded biotite clasts described in section 5.8.4), suggesting that the vein margins may be ultracataclasite rather than pseudotachylyte. The dark haloes to the porphyroclasts are strongly heterogeneous, but all are Fe-rich (Table 5.11, column 5). No systematic relationship was found between porphyroclast and halo

TABLE 5.11 MICROPROBE ANALYSES OF PSEUDOTACHYLYTE MATRIX, SAMPLE G1B

	1		2		3	4	5	
SiO_2	46.78	(0.71)	50.46	(1.85)	65.03	46.57	53.68	(2.29)
TiO_2	1.38	(0.16)	1.11	(0.18)	0.18	0.32	1.54	(0.74)
Al_2O_3	22.95	(0.57)	17.52	(0.83)	12.76	22.93	18.24	(0.85)
FeO*	7.09	(0.44)	10.85	(2.07)	7.43	8.73	17.40	(1.46)
MnO	-		0.12	(0.09)	-	-	-	
MgO	4.43	(0.44)	5.02	(0.68)	4.56	5.32	1.88	(1.04)
CaO	2.14	(0.13)	3.10	(0.56)	0.68	0.91	2.64	(0.84)
Na_2O	trace		4.59	(0.54)	-	-	4.94	(1.99)
K_2O	9.60	(0.27)	4.48	(0.75)	6.07	9.79	3.73	(2.04)
Total	94.37		97.25		96.71	94.57	104.05	

1. Mean and Standard deviation (bracketed) of 10 defocussed spot microprobe analyses of yellow/brown matrix.
2. Mean and Standard deviation (bracketed) of 9 defocussed spot microprobe analyses of dark vein margin.
3, 4. Defocussed spot microprobe analyses of light margin.
5. Mean and Standard deviation (bracketed) of 3 defocussed spot microprobe analyses of dark brown porphyroclast haloes in axial part of vein.

compositions. The analyses suggest that the haloes are largely composed of plagioclase, possibly spherulitic, intergrown with magnetite and K-mica.

3) Interpretation

The petrographic and mineral-chemical observations suggest that the pseudotachylyte was preferentially generated in a mica-rich band in the host gneiss forming a melt rich in $KAlSi_3O_8$ component and containing clasts of quartz and feldspar. Crystallization, or more likely, devitrification of the melt/glass formed an ultrafine grained matrix of K-phyllosilicates. The composition of the phyllosilicate matrix indicates that at least some of the salic clast components entered the melt. In contrast to sample SU802 (section 5.6.1), the Fe-component of the melt (which must have been derived largely from the breakdown of ferromagnesian phases) did not remain/form as opaque magnetite globules but diffused to the margins of the salic clasts - apparently favourable nucleation sites for magnetite in this pseudotachylyte. This diffusion and nucleation process must have occurred prior to, or simultaneously with the deformation of the pseudotachylyte which resulted in the imposition of the fabric.

The geometric character of the fabric is believed to result from viscous flow/deformation of the pseudotachylyte melt rather than subsequent plastic deformation of the pseudotachylyte after its solidification. This is supported by the following observations:-

(i) the fabric is sub-parallel to and folded into the systematic minor shears (e.g. X in Plate 5.15A). Slip on these minor shears appears to have occurred during movement of the main FV, or at least whilst the pseudotachylyte was still molten;
(ii) the fabric is also folded into the sub-orthogonal IV; (V in Plate 5.15A);
(iii) the oblique fabric does not affect the margins of the vein. This probably results from differing mechanical properties of the marginal and axial portions of the vein. Such mechanical differences would be most pronounced if the axial portion of the vein was still molten.

The fold orientation and shear sense of the minor shear fracture at X (Plate 5.15A) strongly suggest that the overall sense of shear on the FV is dextral. The orientation of the phyllosilicate fabric would

then be comparable to the P-foliation in fault gouges and cataclasites (see Rutter et al., 1986 for discussion).

The evidence cited above for the geometric character of the fabric does not exclude an origin by mimetic crystallization after a 'flow fabric' developed in a glass. The vanishingly small solidification time for a vein of this thickness would seem to favour mimetic crystallization, yet the delicate fold microstructures and the long range diffusion evinced by the porphyroclast haloes seem to indicate deformation of incipiently crystallized pseudotachylyte.

It is clearly important to distinguish fabrics of this type from fabrics resulting from intracrystalline plastic deformation of solidified pseudotachylyte (cf. Allen, 1979; Passchier,1982a).

5.6.4 Sample G1A

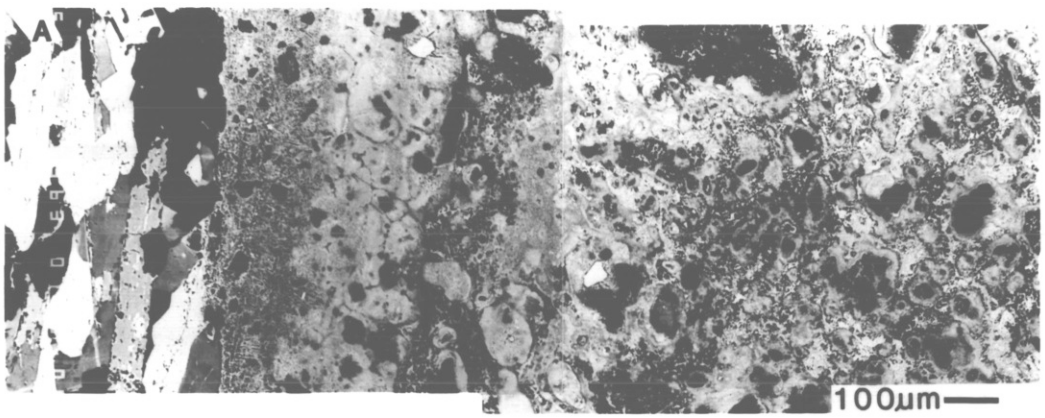
1) Description

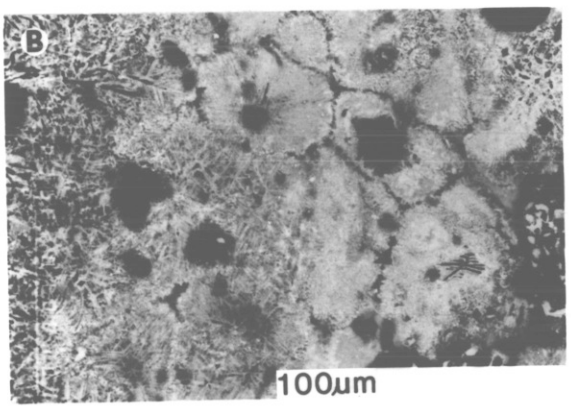
Sample G1A is a K-spar + plagioclase + hornblende + sphene + epidote + chlorite paragneiss (see Table 5.18) with a foliation-parallel FV from Gairloch whose modal mineralogy is given in Table 5.18.

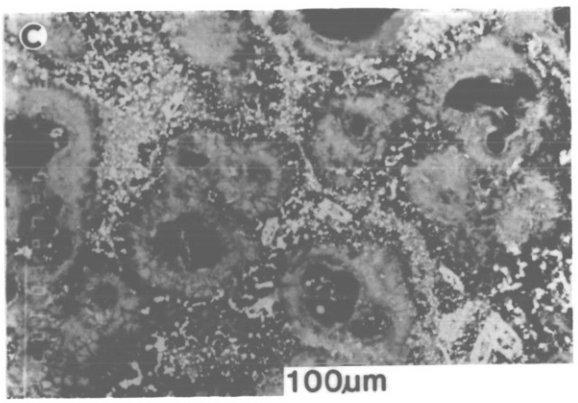
The FV is about 1 cm wide with 100μm wide, dark chilled/cataclastic margins visible to the naked eye. Under the microscope the axial portion of the vein has a typical 'honeycomb' arrangement of spherulites. In the SEM the pseudotachylyte is seen to consist of three axially bi-symmetric zones (Plate 5.16):-

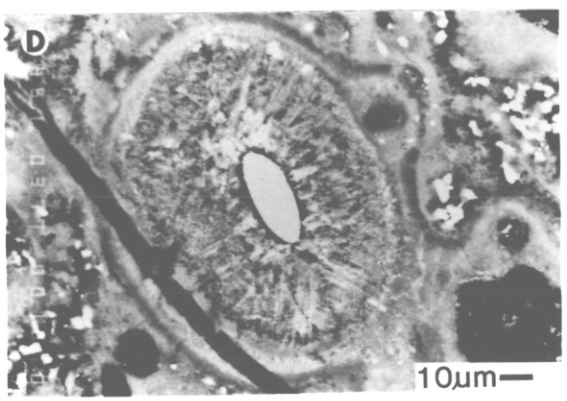
(i) a chilled/cataclastic margin about 100 μm wide (Plates 5.16A and B);
(ii) a marginal zone about 100 μm wide consisting of close-packed to polygonal spherulites, 50 - 100 μm across (Plate 5.16B); these typically have plagioclase clast or microlite nuclei;
(iii) an axial zone forming the greater width of the vein which consists of loosely-packed spherulites (Plate 5.16D) up to 200 μm across. These consist of spherulitic fringes to a variety of different porphyroclasts including plagioclase, quartz and magnettite (e.g. Plate 5.16D). The spherulites are largely composed of biotite, K-spar and magnetite fibres. Irregular inter-spherulite zones consist of decussately arranged epidote platelets (Plate 5.16C) and dendritic magnetites (Plate 5.16E) set in a reddish-brown groundmass of grain

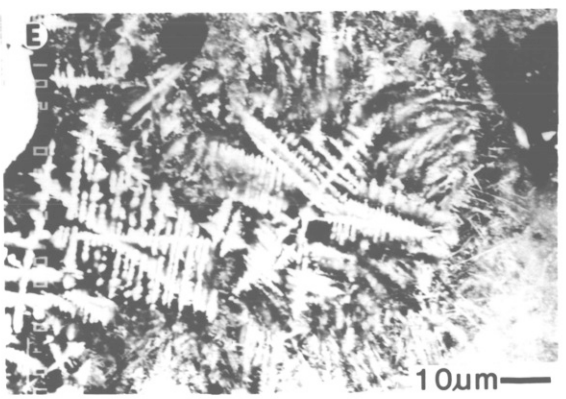
PLATE 5.16 BSE micrographs showing texture of phyllosilicate-spherulitic pseudotachylyte, sample G1A.
(A) General view showing zonation comprising (from left to right) host-rock, a chilled/cataclastic margin, close-packed polygonized spherulites and an axial region of more loosely-packed spherulites.
(B) Detail of (A) showing polygonized spherulites close to vein margin. Note small microlitic plagioclase nucleus in one spherulite.
(C) Detail of (B) showing loose-packed spherulites in vein centre.
(D) Axial spherulite with a magnetite nucleus surrounded by a fibro-radial halo of biotite and magnetite. Note later cross-cutting chlorite-healed veinlet which post-dates the finest crystallization/devitrification microstructures.
(E) Dendritic magnetites which crystallized in proximity to a magnetite porphyroclast.


A
100μm


B
100μm


C
100μm


D
10μm


E
10μm

size beyond the resolution of the SEM.

2) Chemistry

The whole-rock chemistry of this vein (Table 5.12, column 1) is considered in detail in section 6.5.1. Microprobe analyses of the reddish-brown inter-spherulite groundmass, determined avoiding the epidote and magnetite grains, suggest that it is largely made up of K-phyllosilicates, chlorite and epidote (Table 5.12, column 2). The anlaysis is notable for its very low Na_2O-content. Analyses of various porphyroclast phases and their spherulitic haloes demonstrate a porphyroclast crystal-chemical control on the spherulite mineralogy (Table 5.12, columns 3 - 8). Lithic porphyroclasts in this pseudotachylyte are considered in section 5.8.7.

3) Interpretation

The texture, but not the mineralogy, of this pseudotachylyte bears a remarkable similarity to the chlorite-spherulitic pseudotachylyte (sample GQ1A) described in section 5.4 and illustrated in Plate 5.7. Similar conclusions are drawn, as for sample GQ1A, concerning the nucleation, crystallization and devitrification of this pseudotachylyte. In particular, the inter-spherulite material probably devitrified from glass under low-grade metamorphic conditions.

5.6.5 Sample GQ29

Sample GQ29 is a 1 cm thick pseudotachylyte IV cutting quartz + plagioclase + biotite + hornblende + accessories leucocratic gneiss from Grimsay, N Uist. The vein is divisible into 3 zones bilaterally symetrical about the vein axis.

The marginal zones) are about 500 μm wide and consist of small (<10 um diameter) brown, loosely-packed to close-packed polygonal globulites set in a matrix of yellow/brown phyllosilicate

The greater part of the axial portion of the vein is made up of a dense globulitic/spherulitic mantle on filamental to swallowtail plagioclase microlites (about 10 x 2 μm) and on plagioclase clasts.

The centre of the vein, approximately 2 mm wide consists of loosely-packed brown spherulites to about 50 μm diameter which have

TABLE 5.12 ANALYSES OF BIOTITE PHYLLOSILICATE PSEUDOTACHYLYTE, SAMPLE G1A

	1	2	3	4	5	6	7	8
SiO_2	54.05	38.11 (2.11)	62.19	53.16 (1.51)	67.55	52.36	57.92	51.03
TiO_2	1.50	2.49 (0.42)	0.34	2.01 (0.23)	-	1.80	1.61	1.95
Al_2O_3	13.25	13.49 (1.65)	21.36	15.95 (0.75)	20.56	15.63	16.84	15.20
Fe_2O_3*	14.39	n.d.	n.d.	n.d.	n.d.	n.d.	n.d.	n.d.
FeO*	n.d.	17.97 (1.83)	0.70	12.50(2.47)	-	15.32	10.84	16.27
MnO	0.12	0.24 (0.10)	0.20	-	-	-	-	-
MgO	2.83	10.30 (0.61)	0.46	0.34 (0.30)	-	-	-	-
CaO	3.48	4.63 (1.18)	0.97	1.87 (0.10)	1.22	1.99	1.97	1.83
Na_2O	3.28	0.31 (0.21)	4.98	1.10 (0.48)	10.24	4.07	7.94	0.71
K_2O	4.58	3.13 (0.34)	7.82	11.75 (0.56)	0.52	6.92	2.42	11.85
P_2O_5	0.21	n.d.	n.d.	n.d.	n.d.	n.d.	n.d.	
H_2O^-	0.27	n.d.	n.d.	n.d.	n.d.	n.d.	n.d.	
LOI	1.36	n.d.	n.d.	n.d.	n.d.	n.d.	n.d.	
Total	99.32	90.67	99.02	98.68	100.09	98.09	99.54	98.84

1. XRF whole rock analysis of pseudotachylyte vein + clasts
2. Mean and standard deviation (bracketed) of 7 defocussed spot microprobe analyses of interspherulite matrix.
3. Microprobe analysis of partially-melted K-spar porphyroclast.
4. Mean and Standard deviation (bracketed) of 5 defocussed spot microprobe analyses of spherulitic haloes surrounding K-spar porphyroclasts.
5. Microprobe analysis of albite porphyroclast.
6. Mean of 2 defocussed spot microprobe analyses of spherulitic haloes surrounding albite porphyroclasts.
7. Microprobe analysis of spherulitic halo surrounding a quartz porphyroclast.
8. Microprobe analysis of spherulitic halo surrounding a magnetite porphyroclast.

TABLE 5.13 MICROPROBE ANALYSES OF PSEUDOTACHYLYTE MATRIX, SAMPLE GQ29

		1	2	3	4	5
SiO_2	48.77	(0.89)	59.61	60.50	53.92	48.54
TiO_2	0.32	(0.07)	0.62	0.68	0.39	0.51
Al_2O_3	26.95	(0.91)	19.93	19.69	24.27	28.31
FeO*	4.86	(0.38)	4.01	3.82	4.08	4.38
MnO	-		-	-	-	-
MgO	2.71	(0.28)	1.81	1.95	2.18	2.28
CaO	0.22	(0.15)	5.39	4.52	0.93	0.41
Na_2O	0.24	(0.17)	7.52	7.11	2.10	0.49
K_2O	10.43	(0.25)	0.59	1.03	7.82	10.41
S	-		0.27	-	-	-
Total	94.50		99.75	99.30	95.76	95.33

1. Mean and Standard deviation (bracketed) of 9 defocussed spot analyses of interglobulite matrix.
2. Globulite nucleus
3. Globulite core
4. Globulite rim
5. Interglobulite matrix

overgrown plagioclase microlite or clast nuclei set in a yellow/brown phyllosilicate matrix. The matrix shows first order yellow to uppermost first order birefringence and may be in optical continuity over several hundred microns. The matrix contains minute crystals of epidote and small granular opaques to 5 μm diameter with poorly defined globular haloes.

Analyses of the axial zone matrix and globulites are given in Table 5.13. The matrix is largely composed of K-phyllosilicate with a large component of dioctahedral mica component. Avoiding the opaque and epidote grains it was possible to obtain good reproducible analses (Table 5.13, column 1). The globulite/spherulite analysed has a plagioclase nucleus (Table 5.13, column 2) with a spherulitic overgrowth of feldspar and increasing proportions of K-mica with distance from the nucleus (Table 5.13, columns 2 - 5).

5.7 Flow-Banded Pseudotachylyte

Pseudotachylytes may show a variety of different types of fabric or foliation (hence the rejection of Sibson's (1977b) term 'random-fabric" - section 3.3). Banding resulting from chilled and cataclastic margins and an unusual phyllosilicate fabric have been (sample G1B, section 5.6.3) have been illustrated in this study. Other fabrics may result from plastic deformation of pseudotachylytes (e.g. Sibson, 1980b; Passchier, 1982a). Less regular flow fabrics can result from flowage and intimate mixing of melts and ultracataclasite. Rather few examples of this were encountered in this study, though they may be more common elsewhere (H. Obee, pers. comm., 1985).

5.7.1 Sample B1

An example of a flow-banded pseudotachylyte is shown in Plate 5.17; complementary analyses are given in Table 5.14. At least three different melt and ultracataclasite domains are recognizable optically (Plate 5.17). The most distinctive, a dark-coloured melt zone (dotted ornament in Plate 5.17B) contains a large component of biotite (Table 5.14, column 1; see also section 5.8.4 and Fig. 5.12). The other zones more heterogeneous both optically and chemically, believed to reflect a transition texture from ultracataclasite to pseudotachylyte melt.

The preservation of such delicate mixing may indicate that insufficient heat was available for complete melting.

PLATE 5.17 Flow-banded pseudotachylyte, sample B1.
(A) Optical micrograph (PPL) showing intimately mixed, colour-banded pseudotachylyte and ultracataclasite. The darkest phase, which partly mantles a lithic porphyroclast, is pseudotachylyte enriched in a biotite component. Grid is 3 mm in diameter.
(B) Line drawing of (A) showing location of microprobe analyses given in Table 5.14 and Fig 5.12 (B_1, B_2, B_3 and C). m = muscovite, p = plagioclase, q = quartz.

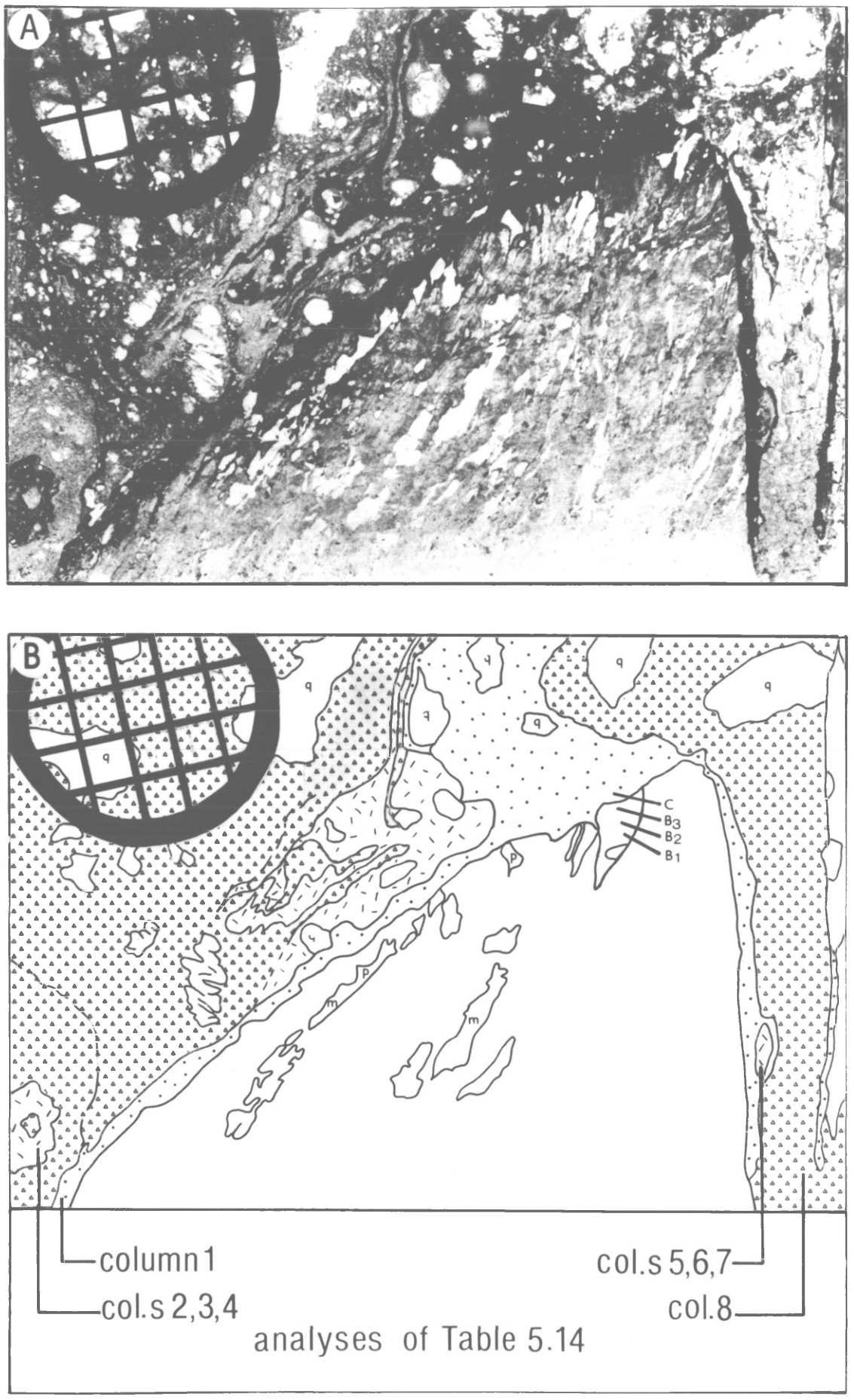

A
B
q
C
B3
B2
B1
p
m
column 1
col.s 2,3,4
col.s 5,6,7
col.8
analyses of Table 5.14

TABLE 5.14 MICROPROBE ANALYSES OF PSEUDOTACHYLYTE MATRIX, SAMPLE B1

	1	2	3	4	5	6	7	8
SiO_2	43.15 (1.64)	62.44	66.89	61.51	58.54	57.79	55.94	64.68 (0.44)
TiO_2	2.43 (0.47)	1.35	0.95	1.49	1.72	2.60	1.77	1.63 (0.12)
Al_2O_3	19.27 (0.47)	16.73	13.73	17.49	19.61	19.96	19.05	18.16 (0.50)
FeO	16.44 (1.74)	9.50	4.26	11.16	6-78	4.01	10.80	4.51 (0.41)
MnO	0.17 (0.15)	-	-	0.25	-	-	-	-
MgO	6.62 (1.06)	2.81	1.24	3.69	2.76	0.87	3.51	1.26 (0.13)
CaO	0.42 (0.25)	1.61	0.72	0.55	0.43	1.28	1.89	0.42 (0.11)
Na_2O	0.24 (0.26)	1.37	0.40	0.48	0.19	1.24	0.91	0.30 (0.07)
K_2O	7.32 (0.79)	2.05	10.25	1.71	4.82	6.46	4.18	3.73 (0.10)
S	trace	0.28	0.20	0.31	trace	trace	trace	0.25 (0.07)
Total	94.06	98.14	98.64	98.64	94.85	94.21	98.05	94.69

1 Mean and standard deviation of 5 defocussed spot analyses of dark melt zone C in Plate 5.17

2, 3, 4 Defocussed spot analyses of light brown, inhomogeneous flow-banded melt in Plate 5.17

5, 6, 7 Defocussed spot analyses of light brown, inhomogeneous flow-banded melt in Plate 5.17

8 Mean and standard deviation of 3 defocussed spot analyses of ultracataclasite - triangle ornament in Plate 5.17

5.8 Porphyroclasts: Preamble

The gneissic host rocks to the pseudotachylytes collected from various localities during this study contain more than a dozen different phases. These same minerals occur as porphyroclasts, but in radically different proportions to that of the host-rock: ferromagnesian clasts are scarce whereas anhydrous salic clasts, especially quartz are abundant. This mineral-specific sorting is believed to be a consequence of two processes both of which favour the selective breakdown of hydrous ferromagnesian minerals: (i) mechanical deformation during pseudotachylyte faulting; (ii) the thermomechanical response of porphyroclasts to hot, corrosive silicate melt. Further complexities arise from localized solid-state or fluid/solid metamorphic reactions after consolidation of the pseudotachylyte melt. All 3 processes will be addressed in this section.

The porphyroclasts have been examined by optical microscopy, microprobe and a limited amount of SEM/BSE imagery. A TEM study of the clasts has not been made because in the limited machine time available it was considered more profitable to concentrate on the more complex and cryptic pseudotachylyte matrix. Future TEM study of the porphyroclasts should be made however with a view to characterizing small scale mineralogical/chemical changes in the ferromagnesian clasts and detailing more precisely the deformation and reaction mechanisms.

The descriptions which follow apply to porphyroclasts in most pseudotachylyte types, FV 's and IV 's. Where relevant however the differences are noted.

5.8.1 Quartz Porphyroclasts

Quartz porphyroclasts derived from a typical quartz-rich host (about 30 modal% quartz) are invariably the most abundant porphyroclast phase (Table 5.7). Clast size varies from <10 μm to that of the host rock grain size; where quartz and feldspar clasts coexist qualitative microprobe 'point-counting' indicates that the smallest clasts are always quartz (cf. Ermanovics et al., 1971). The significance of this observation is uncertain, but it may result from quartz clasts having a higher melting point than feldspar.

All the quartz clasts show moderate to strong undulose extinction (Plate 5.18A), sometimes appearing more strongly developed than that seen in the host rock quartzes. It is inferred from this that the quartz clasts have undergone marked strain-hardening due to an increase in dislocation density and probably dislocation pile-up (White, 1976). This is consistent with high strain rate deformation at low temperature during pseudotachylyte faulting.

Further evidence of the highly brittle nature of the deformation is manifested by the presence of intragranular fractures within the quartz clasts (Plate 5.18B and C). Many of the fractures show no evidence of displacement, are randomly orientated with respect to the quartz crystallography and appear as cascades with plumose branches (Plate 5.18C). The 2-D form of these fractures probably reflects the (3-D) conchoidal fracture seen in quartz. Fractures of this type are interpreted as having formed by cataclastic rupturing during fault movement - perhaps involving Hertzian impingements.

Two additional aspects of these fractures are of interest. First, new sub-equant unstrained subgrains of quartz have grown along some of the fractures (Plate 5.18A). These probably grew statically by 'nucleation recrystallization' (Watts and Williams, 1979) recovering small strains present in the fracture walls. The ultimate stage in this process is a trail of inclusions and a small lattice mismatch but without optically visible (i.e. < 1 μm) subgrains. Secondly, many of the fractures found in quartz clasts contain minute (< 10 μm) specks of opaque phases (Plate 5.18D), usually pyrite but sometimes magnetite. Nucleation of opaques along the fractures is largely restricted to quartz clasts and is very rare (usually entirely absent) in the host rock quartz grains. The opaques have clearly been derived from the pseudotachylyte melt (breakdown of ferromagnesian phases?); the fracture surfaces apparently providing energetically favourable nucleation sites. The reason for this is not understood. Similar features have been described by Passchier (1982a) and may be usefully diagnostic of a pseudotachylyte protolith in, for example, plastically-deformed pseudotachylytes where all other traces of a former melt phase may be lost.

Shear fractures with displacements of a few microns are found both in clasts and quartz grains within brittle shear zones in the host rocks

PLATE 5.18 Microstructures of quartz porphyroclasts in pseudotachylytes.

(A) Clast showing fracturing and strongly undulose extinction. Note recrystallization along some fractures. Sample E1.

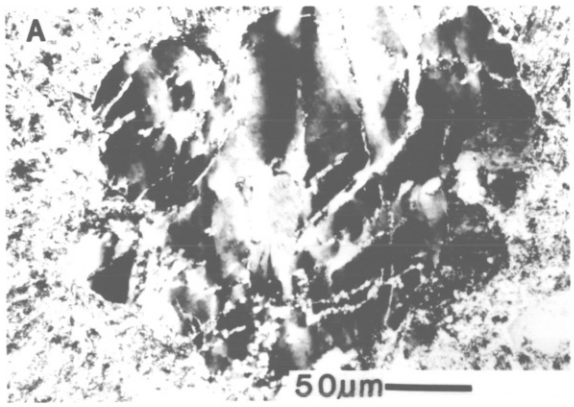
(B) Clast showing extensive plumose fracturing. Sample E5.

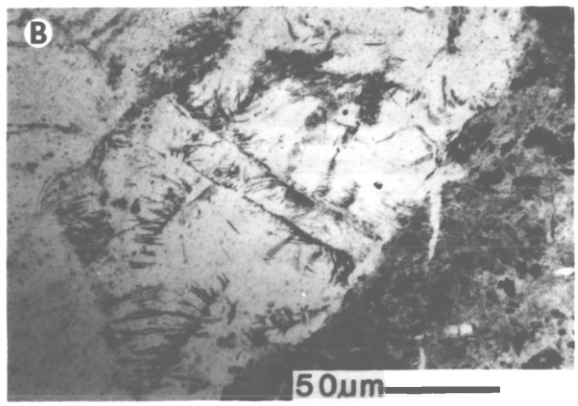
(C) Detail of (B). Note healed fractures represented by an inclusion trail (arrowed).

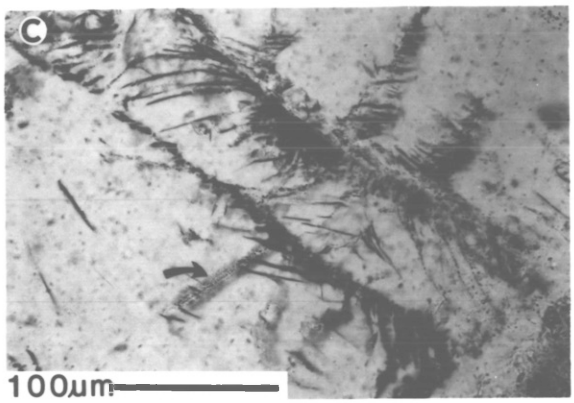
(D) Clast containing fractures decorated by pyrite blebs (white). Sample G804.

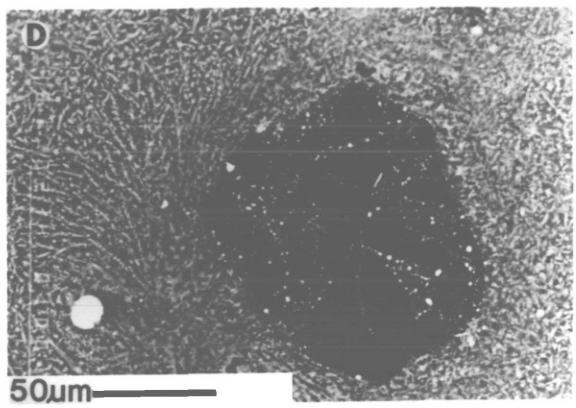
(E) Clast showing cataclasis and melt corrosion. Sample G802.

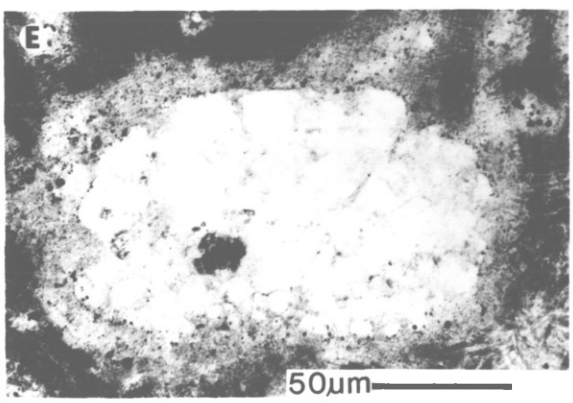
(F) Clast showing melt corrosion and cuspate margins. Sample A.

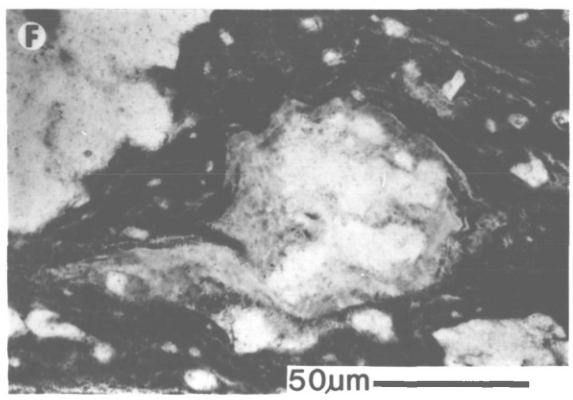

A
50μm


B
50μm


C
100μm


D
50μm


E
50μm


F
50μm

In some examples, the quartz clasts comprise a mass of strained subgrains 10 to 50 μm in diameter, sometimes with a relict larger grain (Plate 5.18E). This structure is believed to result from cataclasis and shattering of the grains rather than static or dynamic crystallization. Rather similar cataclastic flow of 'ductile stringers' is seen in natural and experimentally-deformed fault gouges (Logan et al., 1982).

Quartz deformation lamellae, occassionally noted in the literature (e.g. Bischoff, 1962), were not observed in the pseudotachylytes of this study.

2) Dissolution/Melting Related Microstructures

Many of the quartz clasts display evidence of corrosion by the surrounding pseudotachylyte melt involving the formation of melt filled embayments within the clasts. Fingerprint textures, ballen structure (Carstens, 1974) and tridymite are not seen however. Tongues of melt forming the embayments frequently exploit grain and sub-grain boundaries (Plate 5.18E) together with the fractures described above.

Some of the quartz clasts exhibit fluidal textures characterized by trails of recrystallized quartz, cusps (Plate 5.18F) or irregular swirls. Masch (1974; 1979) has attributed similar vortex structures in quartz clasts in the Silvretta pseudotachylytes to plastic deformation during pseudotachylyte faulting and excludes a strictly melt-related origin. In the present study, these textures are interpreted as resulting from a combination of cataclastic flow and partial melting and flow at high temperature; this is supported by observations of similar structures in feldspar clasts (next section).

5.8.2 Feldspar Porphyroclasts

In most of the pseudotachylytes examined, plagioclase porphyroclasts are second in abundance to quartz, or where the host rock contains little quartz they are the dominant clast phase. In the majority of the samples examined the degree of saussuritization of the plagioclase is comparable to that seen in the host-rock plagioclases - except where later microfractures intersect the clasts.

1) Deformation Related Microstructures

Plagioclase porphyroclasts tend to show weak to moderate undulose extinction - generally comparable to that of the host plagioclases immediately adjacent to the fault plane (pseudotachylyte). There is no optical evidence that the intra-crystalline plastic deformation microstructures differ between clast and host plagioclases.

Brittle microcracking manifests itself by shear fractures with apparent displacements of a few microns (Plate 5.19A). Plumose fracture cascades like those found in the quartz clasts are not present, this is probably attributable to the stronger cleavage in feldspar influencing the fracture trajectories. Albite twin lamellae are often bent as well as displaced by shear fractures (Plate 5.19A); the twins are indistiguishable optically from those in the host plagioclases thus their origin as mechanical or growth twins is uncertain. Little or no recrystallization along the fractures is observed. (Deformation lamellae reported in plagioclase clasts in Silvretta pseudotachylytes (Masch, 1974) have subsequently been recognized as mechanical twins (L. Masch, pers. comm., 1984).)

Evidence for mechanical twinning in K-spar was found in a quasi-conglomerate sample from Rubha Ardvule, S Uist. The K-spar grain, a microperthite, is part of a 2 cm diameter lithic clast set in a matrix of fine grained plagioclase-microlitic pseudotachylyte. The twin lamellae are discontinuous, locally lensoid and show en-echelon propagation parallel to (010) (Plate 5.19B). The microperthitic exsolution is continuous across the twins which are faulted by micro shear fractures.

2) Dissolution/Melting Microstructures

Microstructures directly attributable to solid/silicate melt reaction are most clearly seen in plagioclase (and plagioclase-bearing lithic) clasts.

Fingerprint or sieve texture (Plate 5.2B) is well-developed along grain and sub-grain boundaries together with the cleavage and the fractures described above. This 'defect'-related distribution of melting suggests that melting occurred by a heterogeneous nucleation process at energetically favourable sites (Tsuchiyama and Takahashi,

PLATE 5.19 Optical micrographs showing microstructures of feldspar and biotite porphyroclasts.

(A) Plagioclase clast (with plagioclase-microlitic halo) showing microfaulting of albite twin lamellae (X-nicols). Sample GW11 of R.H. Sibson.

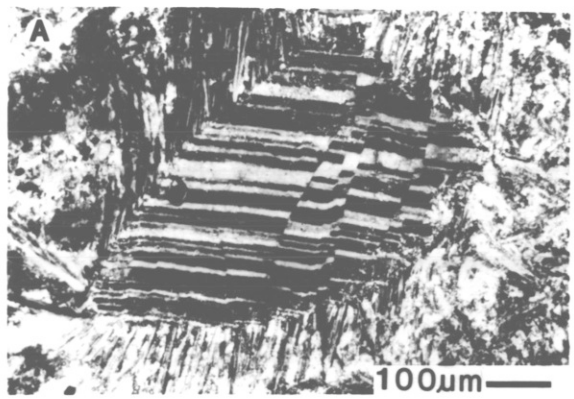
(B) Microperthite in lithic porphyroclast (quasiconglomerate) showing deformation twinning (X-nicols). Sample R7.

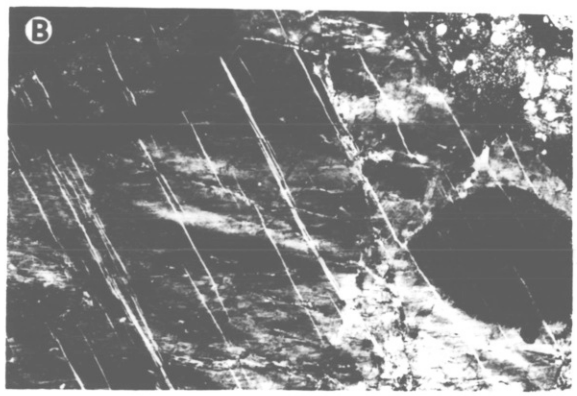
(C) Ab-rich plagioclase clast displaying 'swirl' structure believed to result from fusion (PPL). Sample GQ12.

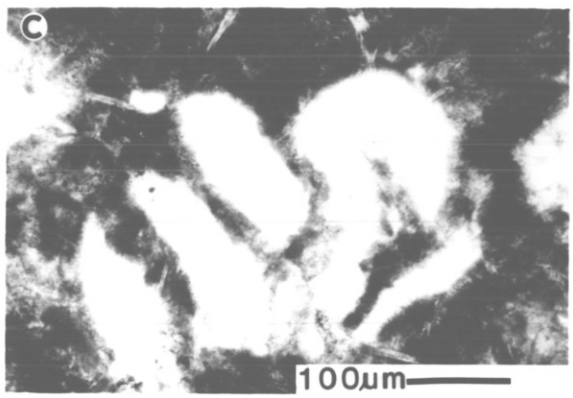
(D) As for (C) X-nicols.

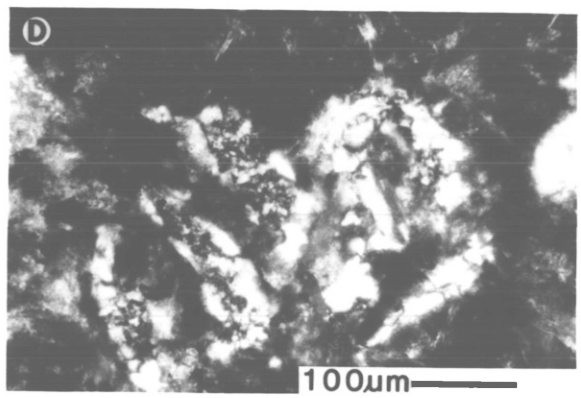
(E) Biotite porphyroclast showing exsolution of granular magnetite (PPL). Note light halo in adjacent pseudotachylyte matrix which is depleted in opaque phases. Sample R4.

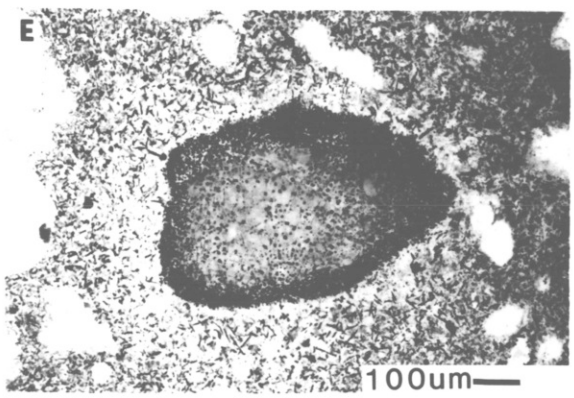
(F) Granular magnetite in pseudotachylyte matrix believed to be a palimpsest after a biotite porphyroclast (PPL). Sample R4.

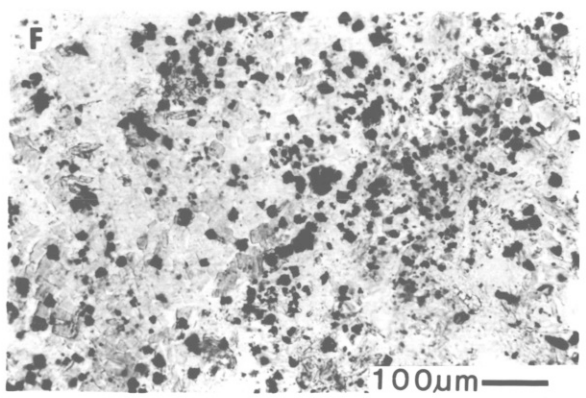

A
100μm


B


C
100μm


D
100μm


E
100um


F
100μm

1983). The positive volume change associated with melting of plagioclase would tend to increase the number and density of defects. The fingerprint texture clearly demonstrates that the temperature of the feldspar clasts was elevated by thermal conduction and possibly diffusion of hot volatiles (cf. section 5.8.7) from the surrounding pseudotachylyte melt such that dissolution and partial melting occurred. Lofgren and Norris (1981) have shown experimentally that plagioclase dissolving in basaltic melt may aquire sieve textures at temperatures well below the plagioclase solidus though observations on natural buchites suggest that temperatures of the order of 1000 C are required (Table 5.15).

Many of the plagioclase clasts are mantled by a skeletal or seive textured rim of more calcic plagioclase of similar composition to the microlites in plagioclase microlitic pseudotachylytes. In most cases the rims are too narrow (<5 μm) to probe satisfactorily but are clearly visible by BSE or Ca Kα X-ray imagery (e.g. Plate 5.21C and D). Two interpretations of this feature are possible: (i) it may reflect the abstraction of a low temperature Ab-rich component into the melt by fractional melting; (ii) or, it may result from heterogeneous but crystal-specific nucleation of new plagioclase from the melt. In both cases a skeletal texture could result by crystallographic control (cf. Tsuchiyama and Takahashi, 1983; and Hibbard, 1981). Philpotts (1964) suggested that similar zoned plagioclase porphyroclasts in Canadian pseudotachylytes resulted from fractional melting. Experimental melting of homogeneous single crystals of labradorite yield An-enriched rims on residual crystals for short run times (Tsuchiyama and Takahashi, 1983). In this study the first interpretation is favoured for very narrow rims such as that illustrated in Plate 5.21C and D. However, the occurrence of a rim of plagioclase on a K-spar clast demonstrates that heterogeneous nucleation also causes this texture. This rapakivi-like structure is a quench texture which can form when there is a dearth of available plagioclase nuclei (Hibbard, 1981).

Plagioclase clasts showing 'fluidal' textures (similar to the quartz described above) were found in pseudotachylytes from the OHT, NW Scotland, Silvretta and Vredefort (Plate 5.19C and D). Such clasts are invariably recrystallized to an aggregate of small (5 - 10 μm) unstrained grains. Microprobe analyses (Appendix A3, feldspar analyses 73-81) demonstrate that these grains are significantly less calcic (An_{10-23}) than other (non-fluidal) clasts as well as host-rock

plagioclases (An_{28-35}) in the same sample. Clearly fractional melting has not occurred in these examples. It is inferred that this structure results from advanced partial fusion - enhanced by the low melting point composition - and viscous flow, followed by static recrystallization/annealing during freezing of the pseudotachylyte melt. This behaviour is to be expected from the experimental studies referred to above, where "crystals more refractory than the equilibrium plagioclase require temperatures well above the liquidus of the basalt before they will melt and crystals less refractory will melt very quickly at near liquidus temperatures" (Lofgren and Norris, 1981, p.498). Similar recrystallized plagioclase clasts in Pyrennean pseudotachylytes are illustrated by Passchier (1982a) who found irregular compositional variation.

5.8.3 Muscovite Porphyroclasts

Up to 10 modal% of muscovite is present in the quartz + microcline + biotite + muscovite + sillimanite + plagioclase paragneisses (sample B1) from Market Stance Quarry, Benbecula, Outer Hebrides (section 5.7). The pseudotachylytes in these rocks (usually generated at the contact between paragneiss and muscovite-free basic schists) contain rare porphyroclasts of muscovite. The muscovite clasts are wispy, up to 100 μm long and show an increase in R.I. and decrease in birefringence relative to the host grains. Apart from the absence of a halo of opaque phases they are difficult to distinguish from biotite porphyroclasts in the same pseudotachylyte; this observation however demonstrates that the clasts examined are 'primary' paragneiss-derived muscovite clasts and not pseudomorphs after biotite clasts (cf. Schleicher and Lippolt, 1981).

Microprobe analyses of 5 host and 2 clast muscovites (Appendix A3) indicate that they are all phengitic and that no systematic variation in total Fe, Mg or Fe/Mg exists between host and clasts. Both host and clasts show slight overfilling of the octahedral sites (1.47% and 0.98% respectively) but slightly different 12-fold stoichiometry (0.88% underfilled and 2.88% overfilled respectively). The clast muscovites however show a substantial decrease in Ti-content with respect to the host phases (clast average 0.56 wt.% TiO_2 against 1.44 wt.% in the host), and small gains in SiO_2, Al_2O_3 and oxide totals. A generalized reaction between host and clast muscovites may be written as follows:-

$$(K_{1.90}Na_{0.07}Ca_{0.01})(Mg_{0.14}Fe_{0.32}Ti_{0.15}Al^{vi}_{3.44})(Al^{iv}_{1.85}Si_{6.15})O_{20}(OH)_4 + K_{0.05} + Na_{0.01} + Ca_{0.01} + Si_{0.05} + Al_{0.03} + Mg_{0.02}$$

$$(K_{1.95}Na_{0.08}Ca_{0.02})(Mg_{0.16}Fe_{0.30}Ti_{0.06}Al^{vi}_{3.52})(Al_{1.80}Si_{6.20})O_{20}(OH)_4 + Fe_{0.01} + Ti_{0.09} \qquad (5.5)$$

Given the small number of analyses, lack of Fe_2O_3/FeO data and possible partial devolatilization of the clast muscovites (suggested by the higher analysis totals), significant changes between host and clast are considered to be the marked increased in Alvi/Aliv ratio, the loss of Ti and gain in Si.

The generally accepted substitution model for Ti in (metamorphic) muscovites has been given as (Holdaway, 1980):-

$$Al^{vi} = Ti_{0.5}(Fe + Mg)_{0.5} \qquad (5.6)$$

Notwithstanding the apparent fit of the data to this model (Fig. 5.8) it is clear from the analyses and equation 5.5 that (Fe + Mg) was not important in the substitution. A more satisfactory model for the substitution of Ti is given by:-

$$Ti^{vi} + Al^{iv} = Si^{iv} + Al^{vi} \qquad (5.7)$$

although the slight increase in total Al is not taken into account. Comparable clast/host muscovite analyses determined by Allen (1979) in Arunta Block (Australia) pseudotachylytes show similar chemical changes, especially the marked loss in Ti and gain in Alvi (Fig. 5.8). Acknowledging that substitution of Al for Ti has occurred, regardless of the actual substitution, two possible mechanisms may be responsible for it:

(i) diffusional ion exchange between the muscovite clasts and the pseudotachylyte melt;
(ii) diffusional ion exchange between the clasts and solidified pseudotachylyte during retrogressive solid-state metamorphic reaction (a decrease in Ti-content of muscovite usually correlates with decreasing grade (Holdaway, 1980))

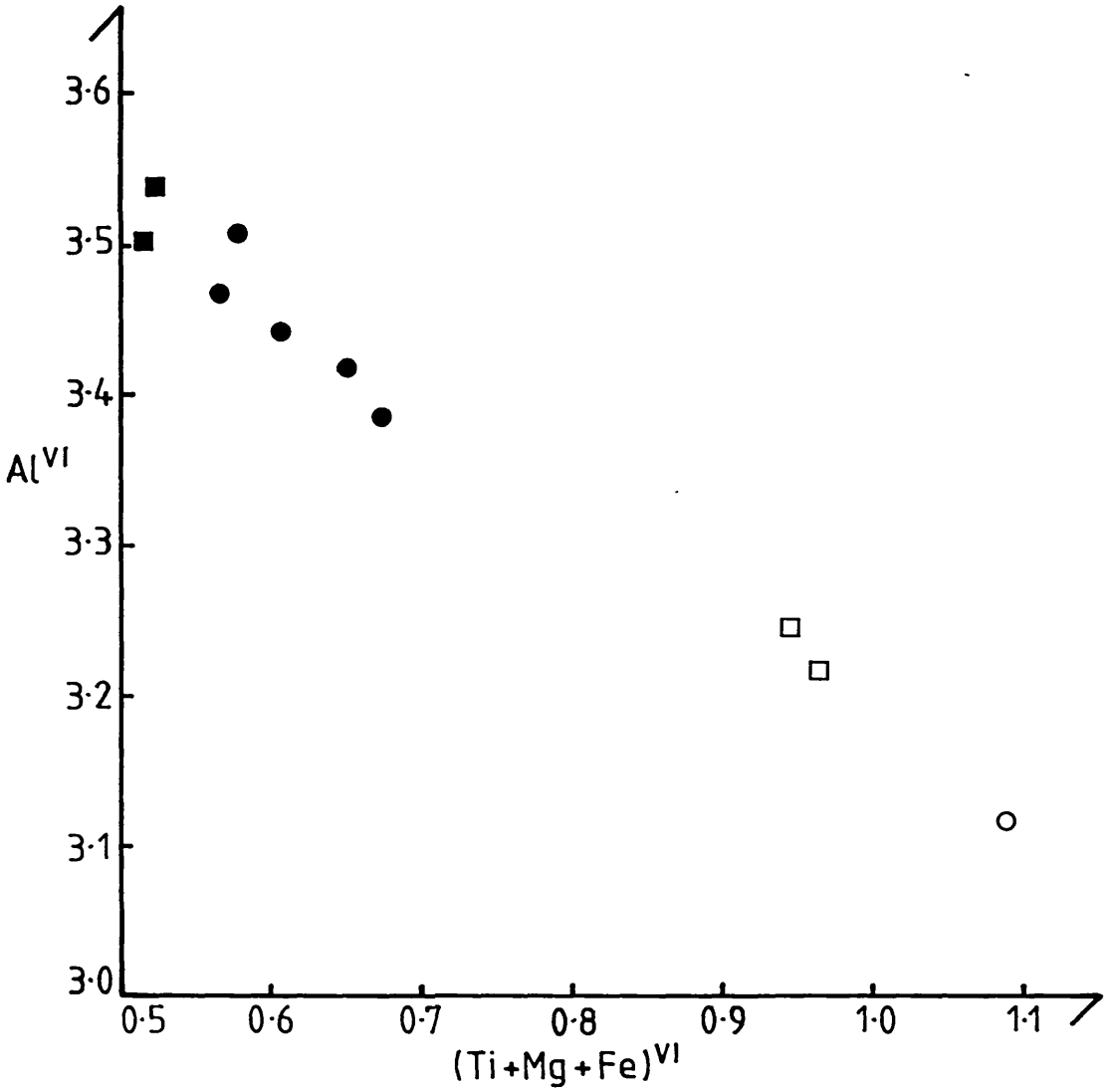


FIGURE 5.8 Plot showing variation in octahedral site between host (circles) and porphyroclast (squares) muscovites. Filled symbols, sample B1, this study; open symbols, data of Allen (1979).

By analogy with the direct petrographic and chemical mineralogical evidence for reaction between clasts and melt in the case of feldspar, biotite, and other minerals the first mechanism is considered to have been dominant. Also, little evidence for extensive retrogression/alteration is seen in the majority of clasts. The pseudotachylyte melt, formed largely of mica and feldspar components, would provide a ready source of Al^{3+} ions and sufficient heat for the activation energy barrier for diffusion to be overcome. The formation of Ti-bearing oxides and/or sphene (present in association with biotite clasts in many pseudotachylytes, although not observed in association with the muscovite in this sample) would provide a suitable sink for the Ti.

5.8.4 Biotite Porphyroclasts

Biotite is a major constituent of many of the host gneisses, where it is found as the sole ferromagnesian phase or together with amphibole ± garnet ± clinopyroxene.

1) Optical Characteristics

Biotite porphyroclasts attain maximum dimensions of 1 mm; this is substantially less than the host grains and associated felsic porphyroclasts. The clasts tend to show an increase in absorbtion and a loss of birefringence. The most significant optical feature of the clast biotites is the exsolution of opaques - largely magnetite - as well as ill-defined clots (found by probe analysis to be sphene; Appendix A3). The opaques are granular and subhedral in contrast to the skeletal or dendritic opaques in the pseudotachylyte matrix (compare Plates 5.19E and 5.16E). The former occur in 3 modes:

(i) as a narrow halo (5 - 50 μm wide) fringing the larger clasts and occupying fractures within the clasts; commonly a similar width fringe of opaque-depleted pseudotachylyte matrix surrounds this (Plate 5.19E);
(ii) in equant distribution throughout the smaller clasts;
(iii) as a palimpsest comprising granules of opaque with effectively no optically visible biotite remaining (Plate 5.19F) (strictly, it is impossible to distinguish between a biotite or an amphibole precursor, although this may often be inferred from the host rock mineralogy).

The textural/mineralogical progression from (i) to (iii) is correlated qualitatively with decreasing clast size and/or increasing vein mass, and it is inferred that these changes reflect an increasing degree of breakdown/melting of the biotite. (The opaque-depleted haloes in the pseudotachylyte matrix may be an indication of the length of the diffusion path of Fe species during crystallization of a given pseudotachylyte.)

These optical observations are comparable to those on biotites in buchites (Table 5.15) with respect to the exsolution of opaque phases but dissimilar in that no glass or incongruent melting solid silicate residua (pyroxene, hornblende or olivine) are found in the pseudotachylytes. The optical and mineralogical character of the clast biotites are however very similar to partially resorbed biotites in many andesites (s.l.) (e.g. Washington, 1896; Day and Allen, 1925). In experimental studies performed by Day and Allen (ibid) on Lassen Peak andesite, biotite breakdown of this type occurred at 925 C in a neutral atmosphere at 1 atmospheric pressure.

Clast biotites are typically more strongly deformed than their host equivalents; well-developed kink bands with axial traces at a high angle to (001) and shears sub-parallel to (001), which may be dilated by melt (cf. Allen, 1979) are common. The shears or fractures are usually bleached relative to the surrounding biotite. Deformation of the biotite clasts is believed to be dominantly related to fault slip, although it may result in part from volume changes occurring during melting, cooling and crystallization/devitrification of the pseudotachylyte (cf. Schlichert and Lippolt, 1981).

2) Mineral Chemistry

Some 200 host-rock and clast grains of biotite were analyzed for this study. Of these, 113 determinations from 13 host-rock/pseudotachylyte pairs are presented in Appendix A3; these show a range in composition from 45-70 mol.% phlogopite. Only 3 analyses are available from the literature for comparison (Allen, 1979). Variation diagrams of selected formula components (based on 22 (O)) in clast and host biotites are given in Fig.s 5.9, 5.10 and 5.11. (Note, the plots a, b, c, etc. are arranged in order of increasing phlogopite component and correspond in each figure.)

The plots show a large degree of scatter both within and between

TABLE 5.15 CHARACTERISTICS OF XENOLITHS IN BUCHITES

Reference	Magma Inclusion Type	P-T conditions	New Phases	Feldspar Clasts	Quartz Clasts	Mafic Clasts	Accessory Clasts	Comments
Ackermann and Walker (1960)	arkose in dolerite	T<1100°C	gt,cord,px + plag + trid microlites	Kspar inverts to san + cord microlites, plag less corroded than Kspar, cord + plag microlites	corroded, fringed by trid ±opx±gl		Sph recrystallized to ilm, alm rimmed by cord±px±spinel, opx rimmed by op zir rounded + embayed Ap has reaction rim	Resistance to melting Kspar<plag<qtz
Wyllie (1961)	arkose in picrite	T> 1000°C P_{H_2O} ~ 4 } MPa	gt,cord,trid, opx, cpx microlites	Kspar + plag show fingerprint texture + mechanical disaggregation	corroded,fringed by trid,gl or recrystallized qtz	sericite replaced by gl + opq.	hematite reduced to mt, carbonate with rosettes	melt fluxed by H_2O-released from sericite
Larsen and Switzer (1939)	granodiorite in andesite	870>T>570°C	<50% gl,plag (An_{15}) and cpx microlites, qtz	Kspar and plag strongly corroded	less strongly corroded than feldspar	bte replaced by cpx + mt, hnbl completely lost		selective fusion of Kspar + bte fluxed by H_2O from bte
Al-Rawi and Carmichael (1967)	granite in basaltic andesite	T~1000°C?	<60% gl,opx, plag microlites, mt,qtz	Kspar/plag/qtz grain boundary melting,fingerprint texture	corroded, maintains sharp contact with glass	bte replaced by red bte+opq±opx± sodic plag microlites,hnbl by mt	sph rimmed by opaques	selective fusion of hydrous mafics with fluxing by H_2O from bte
Sigurdsson (1968)	granite in basalt	T~1170°C	gl in granite xenoliths, spherulitic trid,plag (An_{65-55}) mull, px microlites in pyrometamorphic xenoliths	Kspar turbid and corroded, plag recrystallized and corroded	corroded, rimmed by trid in pyrometamorphic xenoliths	bte +hnbl replaced by gl + px microlites and mt		selective fusion of mafics Kspar, plag then qtz, pyrometamorphics immiscible in basalt magma
LeMaitre (1974)	granite in basalt	T>1000°C p>0.1 MPa	gl, mt, olivine			replaced by "titanomagnetite" + ol		b down of bte rel H_2O pro moting fusion of salic phases
Harris and Bell (1974)	syenite in trachyandesite	T~1000°C?	gl, Kspar + px + opq microlites, opaque Fe-silicate	fusion greatest along qtz/feldspar and cpx/feldspar boundaries, least along qtz/cpx and bte/feldspar boundaries		bte replaced by gl + opq,px-feldspar contacts fused	Zir and ap are refractory	no evidence for preferential fusion of bte
Maury and Bizouard (1974)	(a)quartzofeldspathic gneiss	T>1100°C?	rhyolitic gl,trid + mull + cpx microlites	plag/Kspar melted to fingerprint text Kspar inverted to sanidine	corroded, rimmed by trid			vapour phase transfer between host magma + xenolith glasses
	(b)biotite gneiss in basanite		brown gl,opx + cpx + cord + ol + plag microlites	Kspar replaced by gl + corundum crystallites Plag rimmed by An_{70} microlites		bte replaced by gl + opq		

Note alm = almandine, ap = apatite, bte = biotite, cord = cordierite, cpx = clinopyroxene gl = glass, hnbl = hornblende, ilm = ilmenite, Kspar = alkali feldspar, mt = magnetite, mull = mullite, opq = opaque, opx = orthopyroxene, plag = plagioclase, trid = tridymite, san = sanidine, sph = sphene, Zir = zircon, gt = garnet

FIGURE 5.9 Plot of Al^{vi} vs. Ti^{vi} formula units based on 22 (O) atoms for host (filled symbols) and porphyroclast (open symbols) biotites. The diagrams are arranged in order of increasing phlogopite content from 45% (a) to 70% (f). Tie lines join multiple analyses of the same grain, with arrows pointing from core to rim.

(a) ● = sample GQ49; ■ = sample A; ▲ = Allen (1979).

(b) ● = sample GQ39;

(c) ● = sample GQ34, dashed line encloses field of partially chloritized biotites; ■ = sample GQ38; ▲ = sample GQ19.

(d) ● = sample GH4; ■ = sample GH5.

(e) ○ = sample R4; ◊ = fractures within biotite of tie line 3.

(f) ● = sample G1B; ■ = sample G2D; ▲ = sample CT1; ♦ = sample CT2.

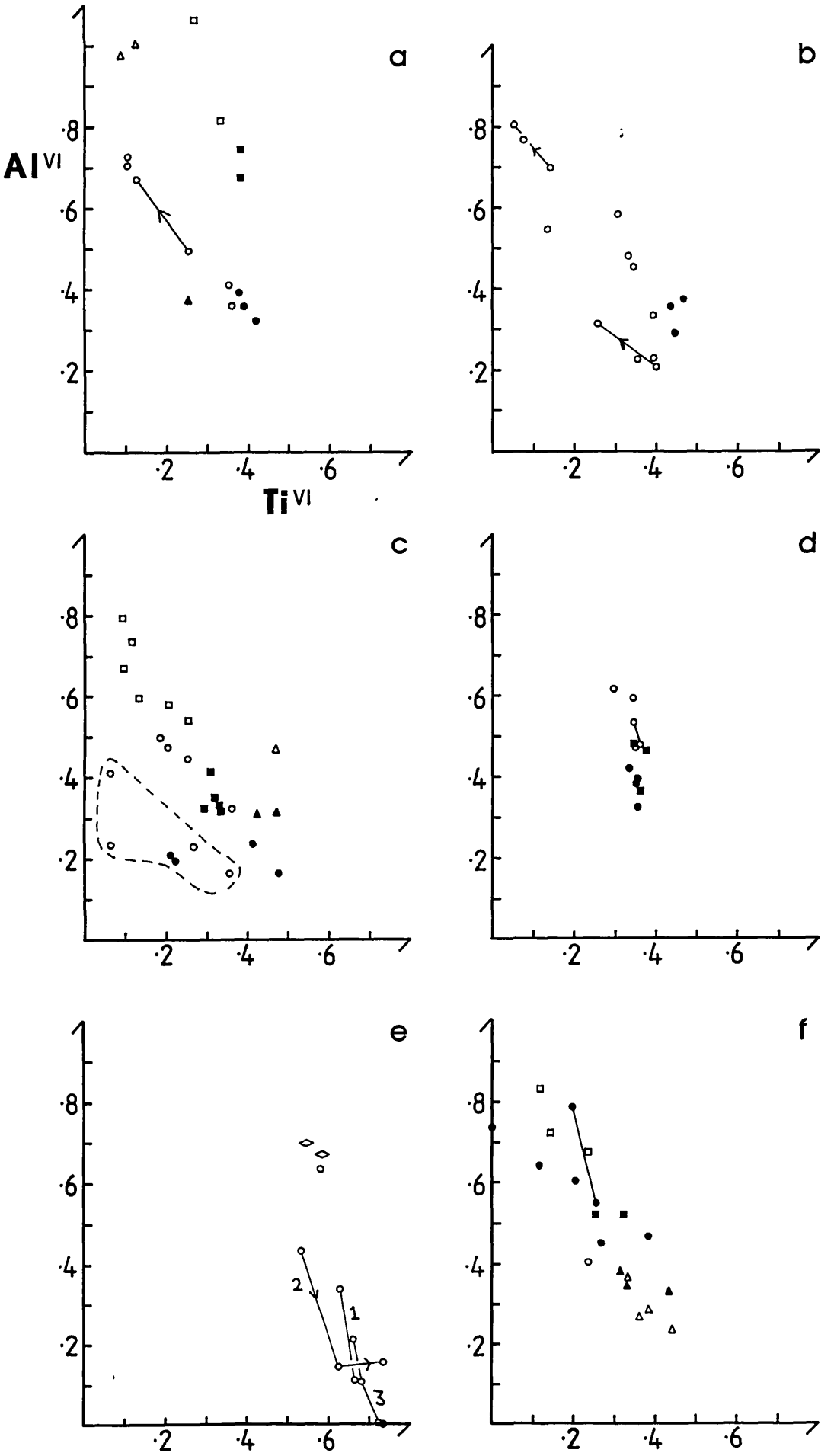
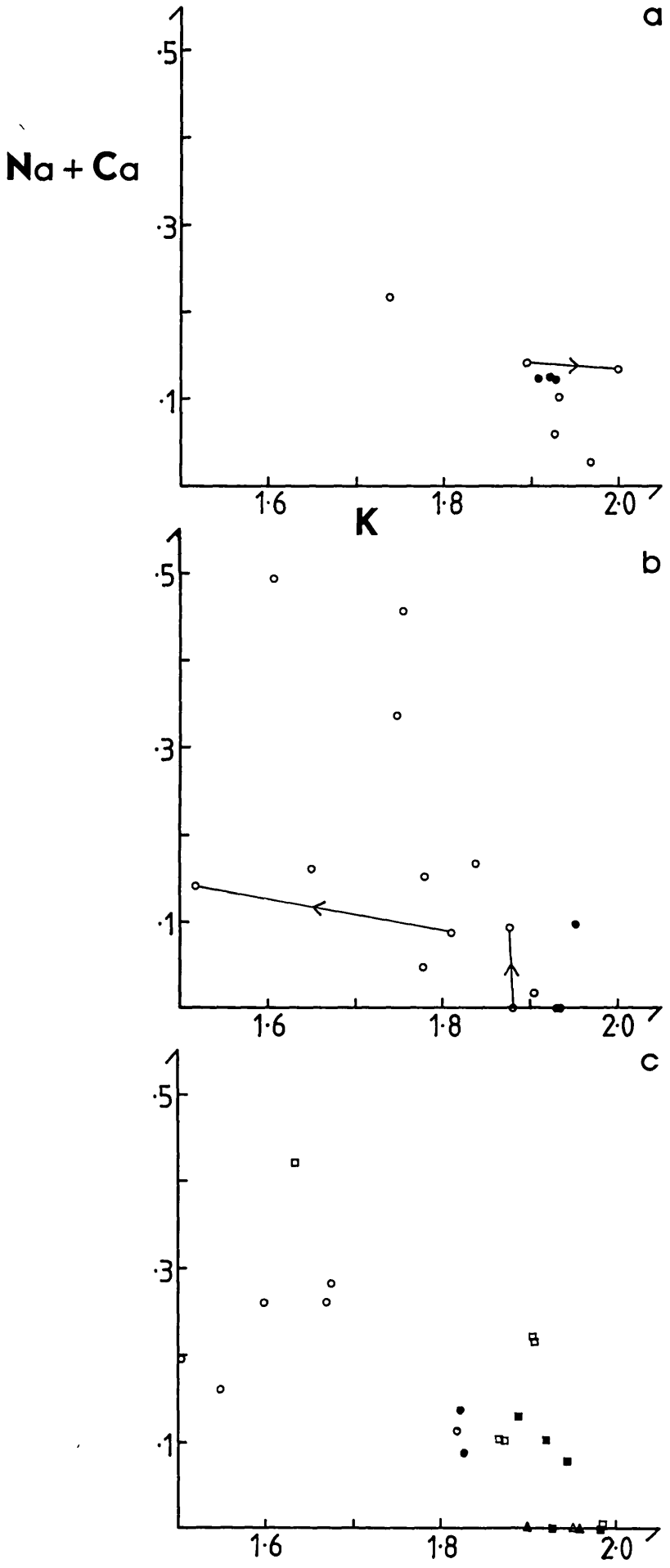

a
b
c
d
e
f
Al^{VI}
Ti^{VI}
·2
·4
·6
·8
1
2
3

FIGURE 5.10 Plot of $(Na + Ca)^{xii}$ vs. K^{xii} formula units based on 22 (O) for host (filled symbols) and porphyroclast (open symbols) biotites. Figure and sample identity as for Fig. 5.9.


a
b
c
Na + Ca
K
·5
·3
·1
1·6
1·8
2·0

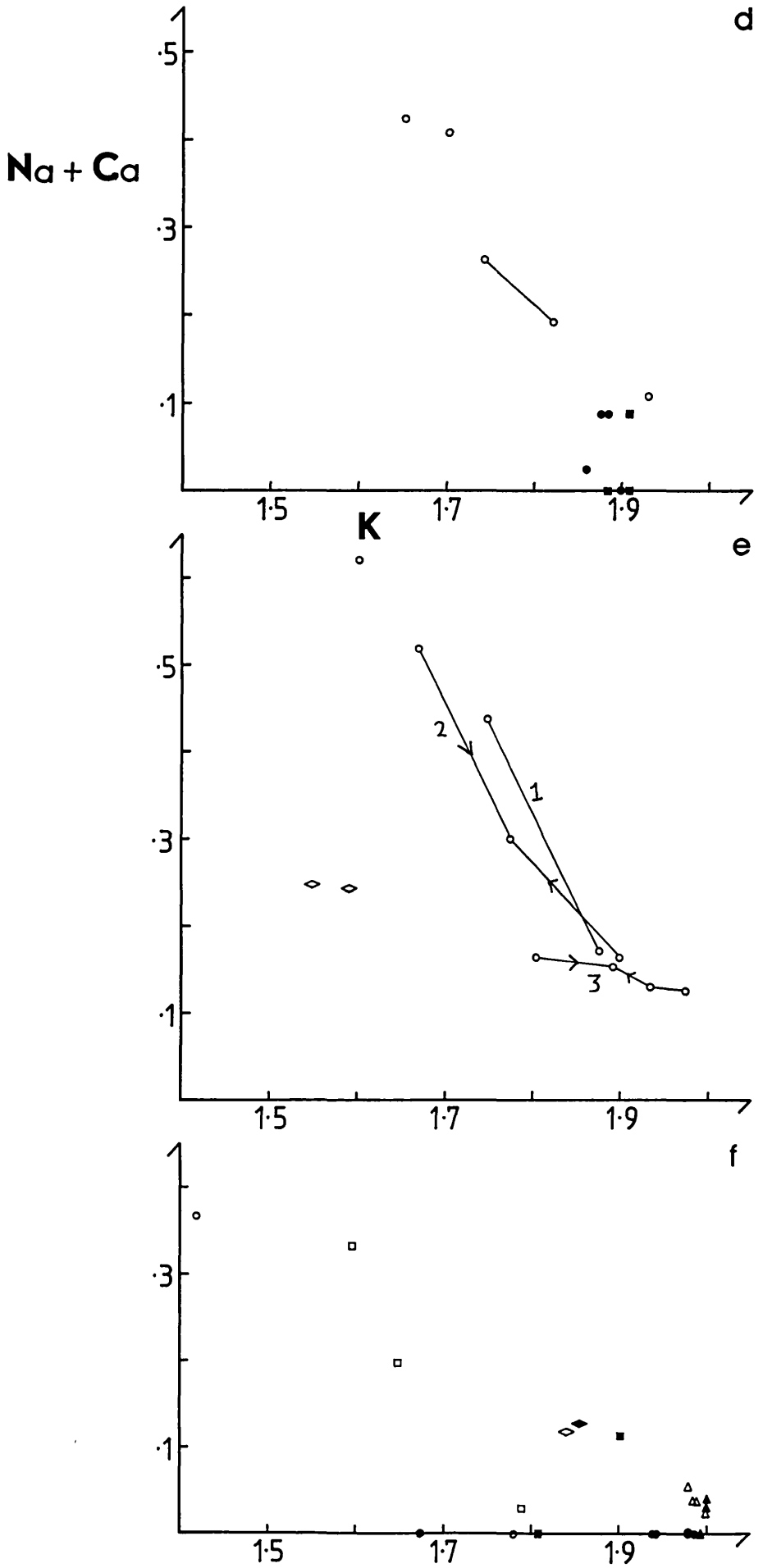
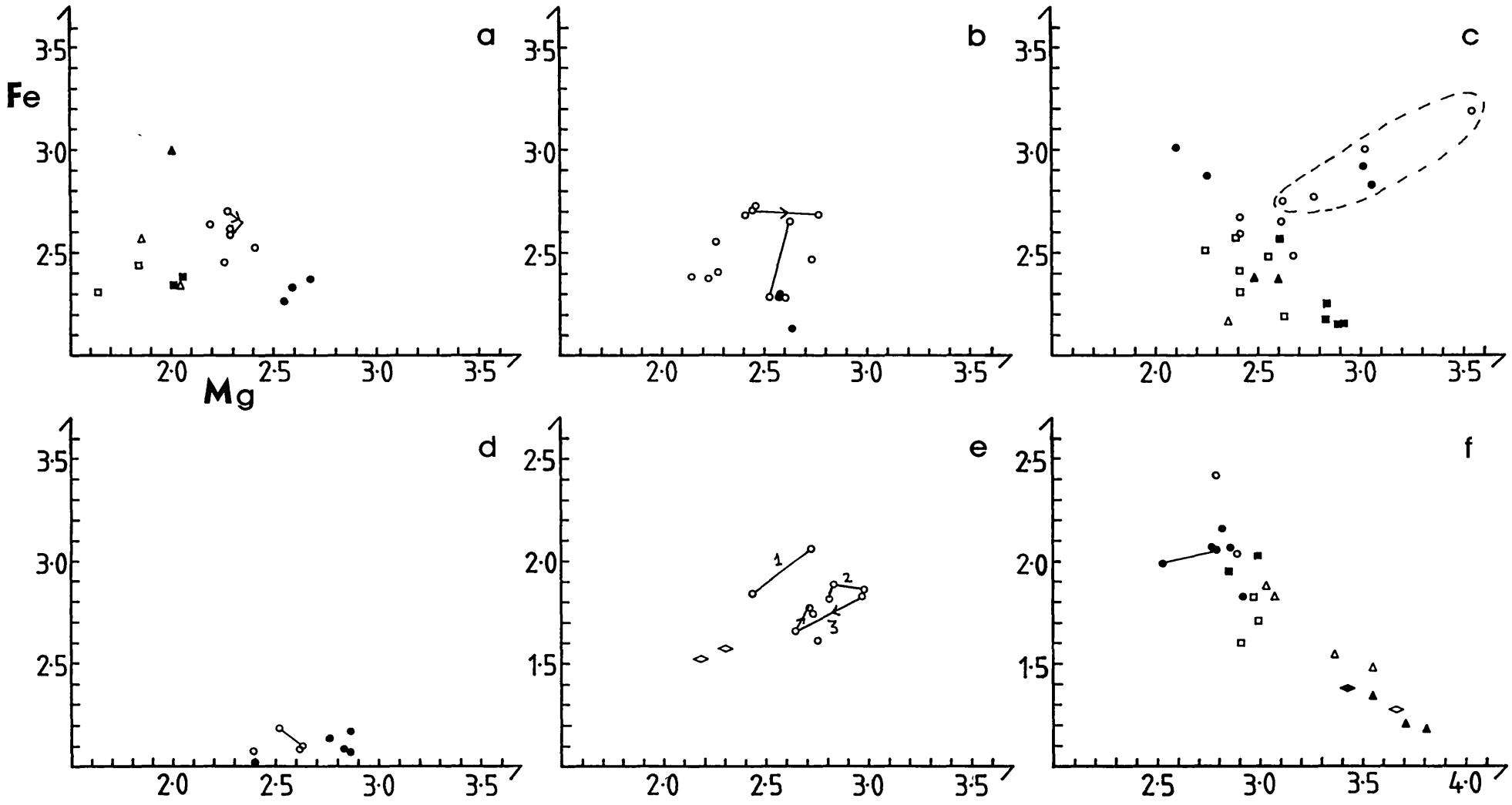

d
Na + Ca
·5
·3
·1
1·5
1·7
1·9
K
e
2
1
3
f

FIGURE 5.11 Plot of Fe vs. Mg formula units based on 22 (O) for host (filled symbols) and porphyroclast (open symbols) biotites. Figure and sample identity as for Fig. 5.9.


a
b
c
d
e
f
Fe
Mg
3·5
3·0
2·5
2·0
1·5
4·0
1
2
3

samples, thought to be a consequence of several interacting factors:-

(i) variation in the host/protolith biotites with respect to Fe/Mg zoning and to a lesser extent Ti;
(ii) variable degrees of disequilibrium reaction between clasts of differing compositions and pseudotachylyte melts of differing compositions; (note, variations in the ferrous/ferric ratio and volatile content between the host and clast biotites are impossible to determine by microprobe);
(iii) retrogressive metamorphic reactions, possibly post-crystallization of the pseudotachylyte melt, including chloritization of the biotites and the making over of ilmenite? to sphene;

The most significant and widespread chemical difference between host and clast biotites is the reduction in Ti-content of the latter, which corresponds with the petrographic observations described above. This chemical change is considered to be a direct consequence of reaction between the biotite clasts and pseudotachylyte melt rather than retrogression.

Samples GQ39, GQ49, GQ38, GQ34, and G1B show a good correlation between Ti^{vi} and Al^{vi}, decreasing and increasing from host to clast respectively (Fig. 5.9), and an increase in $\leq Al$ whilst $\leq$(octahedral ions) remains approximately constant at ~90% trioctahedral maximum or increases slightly. With the exception of GQ49, the same samples show a decrease in K and an increase in (Na + Ca) from host to clast, with overall 12-fold stoichiometry remaining approximately constant. The sum of the divalent octahedral ions (Fe + Mg + Mn) in these samples shows only slight variation from host to clast. This suggests that a possible coupled substitution of the type:-

$$Ti^{vi} + K^{xii} = Al^{vi} + Ca^{xii} \qquad (5.8)$$

may be involved. In addition to the change in 12-fold site chemistry, the influx of Ca^{2+} ions into the biotite clasts is recorded by the presence of clots of sphene (after ilmenite?) (see Appendix A3, biotite analyses 98, 109 and 111).

An additional substitution/oxidation reaction which may be significant is:-

$$Ti^{vi} + (Fe^{2+})^{vi} = Al^{vi} + (Fe^{3+})^{iv} \quad (5.9)$$

Unfortunately the importance of this reaction cannot be assessed from the microprobe analyses. Allen (1979) has suggested that the oxidation of Fe in biotite during pseudotachylyte generation may be important in releasing lattice bound water promoting melt formation. However it should be noted that this reaction consumes oxygen and might therefore diminish the amount of water available to flux the melt. In natural rocks and in experimentally melted samples the change in optical properties of biotite phenocrysts in disequilibrium with andesitic melt (at atmospheric pressure) has been correlated with an increasing ferric/ferrous ratio (Day and Allen, 1925)

Samples A, GH4 G2D and Allen (1979) show an increase, from host to clast, in Al^{vi} (near constant ΣAl), a small decrease in Ti^{vi} (Fig. 5.9) and a small decrease in Σoctahedral, but a moderate to large increase in Si. This is effectively a trioctahedral to (more phengitic) dioctahedral substitution of the form (ignoring Ti and 12-fold site variation):-

$$Al^{iv} + 2(Fe + Mg + Mn) = Al^{vi}\,\square^{vi} + Si^{iv} \quad (5.10)$$

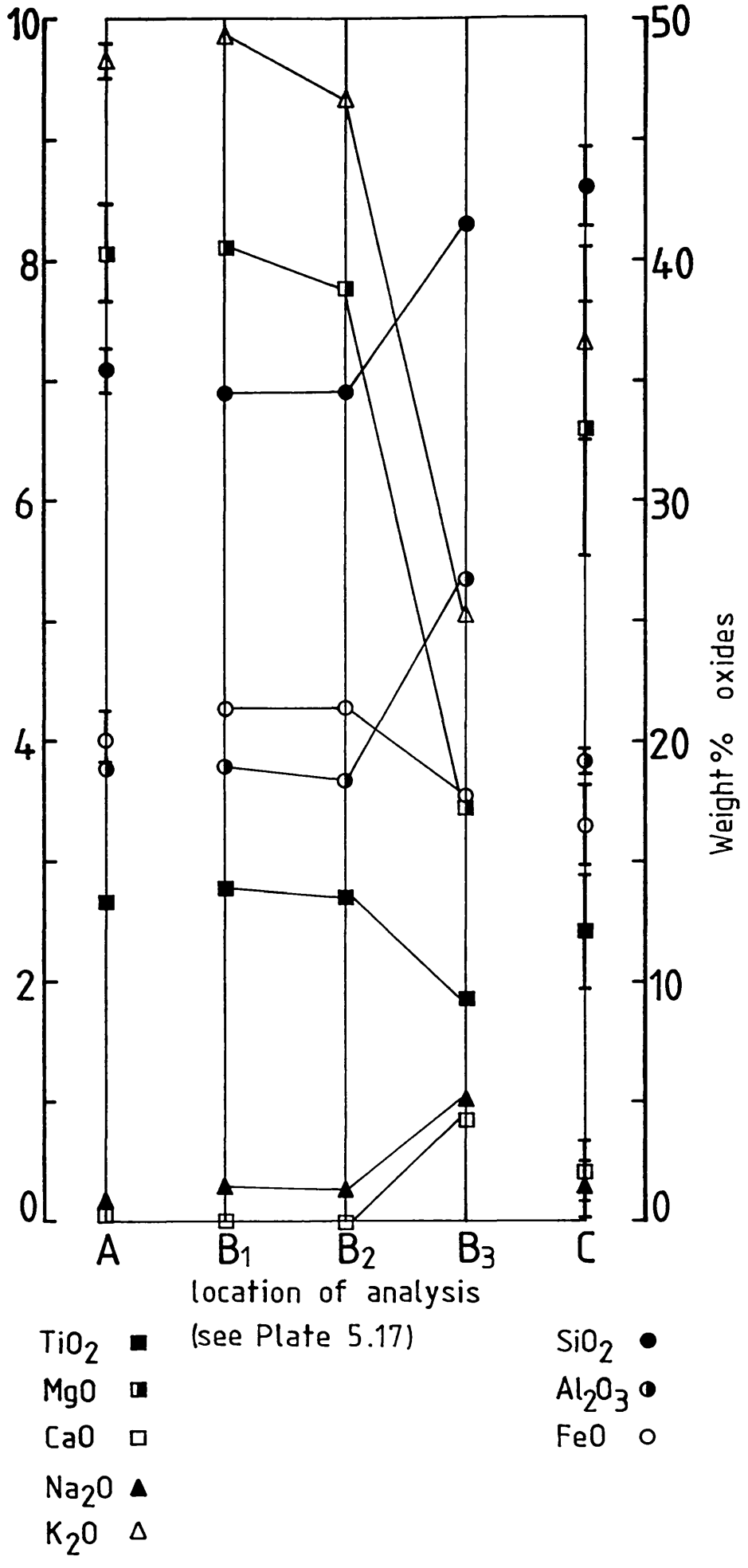
where $\square$ denotes a vacancy.

Since this change involving a gain in Si has been observed in samples from widely differing localities (OHT, NW Scotland and S America in this study and Australia by Allen (1979)) it appears likely that it is a consequence of clast-melt interaction rather than subsequent retrogressive metamorphism.

Considering the samples in a more general sense, the loss of K and gain in (Ca + Na) is common to nearly all of the samples analysed (Fig. 5.10). The behaviour of Fe and Mg is much more complex (Fig.5.11) - perhaps for the reasons stated above.

As an alternative approach in assessing the chemical reactions between a biotite clast and pseudotachylyte melt a microprobe traverse across a biotite clast into the surrounding pseudotachylyte was made. The clast and the location of the analyzed spots are shown in Plate 5.17 and the chemistry in Fig. 5.12. The core region of the biotite (within a lithic porphyroclast) is chemically similar to other host biotites in the rock (analyses B1 and A respectively, Fig. 5.12). Approximately 100 μm from the melt interface (analysis B2) the biotite

FIGURE 5.12 Plot showing chemical variation between host and porphyroclast biotites and associated melt phase in pseudotachylte sample B1.
A= mean of 6 analyses of host biotites (error bars represent + 1σ); B_1, B_2, B_3 = traverse across biotite porphyroclast into melt rimmed margin (see Plate 5.17 for location); C = mean of 5 defocussed beam microprobe analyses of dark melt phase (Table 5.14, column 1).


10
8
6
4
2
0
50
40
30
20
10
0
Weight % oxides
A
B1
B2
B3
C
location of analysis
(see Plate 5.17)
TiO2
MgO
CaO
Na2O
K2O
SiO2
Al2O3
FeO

shows slight depletion in K and Mg. At a few microns from the melt interface (analysis B3) substantial variation has occurred: the biotite shows severe depletion in K, Mg, Fe and Ti, a large gain in Si and Al and small gains in Ca and Na. Concomitant with these changes is a 10% decrease in octahedral site occupancy, a 30% decrease in 12-fold site occupancy and a gain in wt.% oxide total from about 95% to 98%. The latter observation may indicate dehydration.

A further chemical transformation is related to the deformation of some biotite clasts. An example of this is shown by sample R4 collected from a 6 cm thick IV of plagioclase microlitic pseudotachylyte. Biotite porphyroclasts in this rock are dark red/brown to light brown pleochroic with marked exsolution of opaques and are deformed by kink-band type fractures. Analyses of a number of clasts and their fractures are given in Appendix A3 (biotite analyses 60-71). Relative to the surrounding biotite, the fractures show large gains in SiO_2 (up to 7 wt.%) and Al^{vi} (Fig. 5.11e) and a loss of (Fe + Mg + Ti) (Figs. 5.11e and 5.12e) resulting in a 10% reduction in octahedral site occupancy in spite of the $Al^{iv} = Al^{vi}$ exchange (ΣAl constant). The fractures also show a loss of K but slight gain in Na + Ca (Fig. 5.12e) resulting in an overall 10% reduction in 12-fold site occupancy relative to the host. Oxide totals are little changed. A generalized reaction describing the chemical changes from host (n = 4) to fracture (n = 2) may be written:-

$$(K_{1.90}Na_{0.13}Ca_{0.01})(Mg_{2.90}Fe_{1.82}Ti_{0.70}Al^{vi}_{0.08})(Al^{iv}_{2.52}Si_{5.48})O_{20}(OH)_4 + Na_{0.07} + Ca_{0.04} + Si_{0.76} =$$
$$(K_{1.57}Na_{0.20}Ca_{0.05})(Mg_{2.24}Fe_{1.54}Ti_{0.56}Al^{vi}_{0.69})(Al^{iv}_{1.76}Si_{6.24})O_{20}(OH)_4 + K_{0.33} + Mg_{0.66} + Fe_{0.28} + Ti_{0.14} + Al_{0.15} \quad (5.11)$$

By analogy with similar examples it is assumed that the deformation occurred during fault slip (host rock biotites were not available for direct comparison in this sample). There is no a priori reason to assume that the reaction is a stress corrosion effect (cf. Kerrich et al., 1981), rather the mechanical disruption of the biotite lattice by brittle fracturing facilitated diffusion and ion exchange along the fracture path. The reaction (equation 5.11) is retrogressive involving a trioctahedral to dioctahedral substitution and may have occurred at any time during and/or after freezing of the

pseudotachylyte melt, though the absence of substantial hydration (e.g. chloritization) suggests it may have been thermally activated by the pseudotachylyte melt.

In summary, the observations and analyses allow the following conclusions to be made:

(i) biotite preferentially enters the melt phase, probably mixing with the complementary components of feldspar and/or quartz;
(ii) disequilibrium partial melting of biotite immersed in pseudotachylyte melts of various compositions results in substantial depletion of K, Mg, Ti and in many cases Fe, and gains in Si, Al, Ca and Na. At least two different substitutions are involved. One involves mainly an increase in total Al, with Alvi replacing Tivi, charge balance being maintained by changes in the octahedral site vacancies, substitution of Ca^{2+} for K^{+} or possibly the oxidation of Fe^{2+} to Fe^{3+}. The second substitution involves a gain in SiO_2 and depletion in in total octahedral site occupancy. Both of these types of reactions are believed to result from clast/melt interaction;
(iii) reactions assisted by brittle fracture are similar to the second type of substitution. Insofar as the brittle fracture has occurred during pseudotachylyte faulting, this reaction is related to pseudotachylyte genesis, but it is not clear whether it occurred whilst the pseudotachylyte was molten or solid;
(iv) increasing phlogopite component does not appear to stabilize the biotites in the pseudotachylyte melt;
(v) it is intuitively likely that volatiles, OH^{-}, Cl^{-} and F^{-} were important during the disequilibrium breakdown of the biotites, perhaps complexing cations involved in exchange reactions. The extent of devolatilization of the micas is difficult to assess from the probe analyses in the absence of FeO/Fe_2O_3 analyses;
(vi) reactions which post date crystallization of the pseudotachylyte may include the formation of sphene after a Ti-bearing exsolved phase.

5.8.5 Amphibole Porphyroclasts

Amphibole, like biotite, is a major constituent of many of the host gneisses yet it too rarely occurs as a porphyroclast, indicating selective mechanical and/or thermal breakdown during pseudotachylyte

faulting.

1) Optical Characteristics

Amphibole porphyroclasts vary in size from close to that of the host (up to 1 mm) to relicts <<100 μm in diameter. The host amphiboles are typically straw yellow and light to dark green pleochroic, xenoblastic hornblendes. Metamorphic retrogression/alteration to epidote + chlorite + sphene + quartz + opaque + carbonate of both host and clast amphiboles is not uncommon, but these have largely been excluded from the analyses.

The clast amphiboles tend to show a stronger and browner colouration but weaker birefringence than the host grains; the petrographic description 'oxy-hornblende' is not warranted however. Marginal exsolution of opaques and sphene is comparable to that seen in the biotite clasts. The optical characteristics are similar to amphibole xenocrysts in buchites (Table 5.15), with the exception that pyroxene incongruent melting/dehydration products were not observed.

Deformation of the clasts involves cataclasis - also seen in host amphibole grains at FV margins - and shearing, frequently guided by the cleavage. Undulose extinction is often intense in the clasts and also in host-rock grains of amphibole which are close to the vein margins. Recrystallization of the amphibole clasts was not observed.

2) Mineral Chemistry

Microprobe analyses of host and clast amphiboles were recast on the basis of 23 (O) following the method of Papike et al. (1974) to assess ferric iron and the stoichiometric quality of the analyses. (Note: minimum Fe203 was assumed in all cases for consistency.) All analyses of host amphiboles, selected from a total of 200+ determinations, meet the fairly stringent stoichiometric requirements of this method (Table 5.16). From a total of 80+ analyses of clast amphiboles, 49 have been used of which 24 meet the 'Papike criteria' whilst the remaining 25 fall within the relaxed stoichiometric limits given in Table 5.16 (see Appendix A3 for individual analyses). The use of the relaxed stoichimetric limits is considered justifiable for the following reasons:-

(i) the majority of the analyses rejected by the 'Papike criteria'

TABLE 5.16 AMPHIBOLE STOICHIOMETRY LIMITS

Stoichiometric limits	ΣOctahedral sites	ΣEx. oct + Ca.	M4 Site	A Site	Charge imbalance
1. Papike et al. (52 host amphiboles)	> 4.98	≪ 2.02	2±0.02	≪ 1.02	< 10.021
2. Relaxed limits (24 out of 49 clast amphiboles)	> 4.80	≪ 2.02	2±0.10	≪ 1.02	< 10.41

involve only small octahedral site deficiencies (<0.15) and residual charge imbalances (<-0.15); where M4 is in excess (4 analyses) the Ca could be assigned to the octahedral site thus removing that site deficiency (see Robinson et al., 1982 for discussion);
(ii) some clast analyses showing the largest divergences from the host analyses were accepted by the 'Papike criteria';
(iii) although an attempt has been made to determine ferric iron, the proportions of volatile components OH^-, F^- and Cl^- are unknown;
(iv) the purpose of the analyses is to assess mineralogical and chemical variations between the host and clast amphiboles; the chemical changes can be assessed at least semi-quantitatively even if the mineralogical changes can only be treated qualitatively.

Notwithstanding these qualifications it is clear from the consistent octahedral site deficiency and negative charge imbalance (2.2% and -0.17 average respectively for 20 analyses) that an imperfectly characterized mineralogical transformation is occurring. The oxide totals (wt.%) of the clast analyses show some scatter, skewed toward low totals. It is inferred from this that the mineralogical transformation may involve the breakdown of amphibole to phyllosilicate. Further STEM analysis would be required to resolve this problem.

Host and clast amphibole analyses are plotted on a 'Leake diagram' {$(Mg/Mg + Fe^{2+})$ vs. Si} in Fig. 5.13 and Al^{vi} vs (Na + K)A in Fig. 5.14; note, the same data set is shown in plots a, b, c, etc. in each figure. Common to all the samples, except GQ38, is an increase in SiO_2 and a decrease in (Na + K)A from host to clast; the behaviour of other elements and site occupancies is more complex and will be described for groups of samples.

(A) Samples GQ36 and CT1 show similar variation from host to clast involving gains in SiO_2, MgO and CaO (approximately constant in CT1) and losses in FeO, Na_2O, TiO_2, Al_2O_3 (Aliv and Alvi) and (Na + K)A (Figs. 5.13a and 5.14a). The host amphibole in GQ36 is ferro-edenitic to ferroan-pargasitic hornblende and the clast magnesio- to actinolitic-hornblende; in CT1 the host is tschermakite and the clasts tschermakitic-hornblende. In addition to the exchange Fe = Mg, the following coupled substitutions may have been active in GQ36:-

host clast

(i) $Al^{vi} + Al^{iv} = Mg^{vi} + Si^{iv}$ {tschermakite} (5.12)

(ii) $(Na + K)A + Al^{iv} = \square + Si^{iv}$ {edenite} (5.13)

(iii) $(Na + K)A + NaM4 = \square A + CaM4$ {richterite} (5.14)

(iv) $Ti^{vi} + 2Al^{iv} = Mg^{vi} + 2Si$ {titanoamphibole} (5.15)

In CT1 little variation in Ca and Ti exists between host and clast amphibole and only the tschermakite and edenite substitutions may have been active.

In general terms the change in chemistry is compatible with the retrogressive metamorphism of host amphibole of amphibolite facies paragenesis to clast amphibole of greenschist facies paragenesis. It is difficult to assess to what extent this is a consequence of clast/melt reaction and of retrogressive metamorphism, sensu stricto, perhaps during microfracture formation.

(B) Samples GQ5, GQ14, GQ19 (Fig.s 5.13c and 5.14c) and GQ6 (Fig.s 5.13d and 5.14e) show variation from host to clast involving: gains in SiO_2, Al_2O_3, Al^{vi} and losses in FeO, MgO, CaO, (Na + K)A and Al^{iv} whilst Na_2O, K_2O, TiO_2 and MnO show irregular or little variation. The host amphiboles are ferro-edenitic to ferro-pargasitic hornblendes and the clasts of ferro-hornblende to magnesio hornblende composition. In contrast to GQ36 and CT1, little variation in $Mg/(Mg + Fe^{2+})$ exists between host and clasts. Possible substitutions involved include Fe = Mg, the edenite substitution (ii) and:-

(v) $Ca = 2Na$, $Ca = Na + K$, $Na = K$ (5.16)

(vi) $2(Fe + MG)^{vi} + Al^{iv} = Si^{iv} + Al^{vi}$ (5.17)

Analyses of weakly altered fractures in host amphiboles in sample GQ5 (Figs. 5.13c and 5.14c) indicate that similar chemical variation exists in this environment as between pristine host and clast amphiboles. Again this suggests that the chemical variation determined between host and clast amphibole, although probably activated by the heat content of the melt, are essentially retrograde metamorphic reactions. This is further demonstrated by a probe traverse across a host amphibole abutting a pseudotachylyte vein, sample QD1 (Figs. 5.13 and 5.14; Appendix A3, amphibole analyses 100-109). The traverse across the fresh and apparently unaltered amphibole grain shows increasing SiO2 and decreasing (Na + K)A toward

FIGURE 5.13 Plot of Si vs. $Mg/(Mg + Fe^{2+})$ formula units based on 23 (O) showing compositional variation between host (filled symbols) and porphyroclast (open symbols) amphiboles.

(a) ● = sample GQ36; ■ = sample CT1;

(b) ● = sample GQ38;

(c) ● = sample GQ14; ■ = sample GQ5; ▲ = GQ19;

(d) ● = sample GQ6;

(e) ● = sample QD1, arrows point from grain centre to margin at vein edge

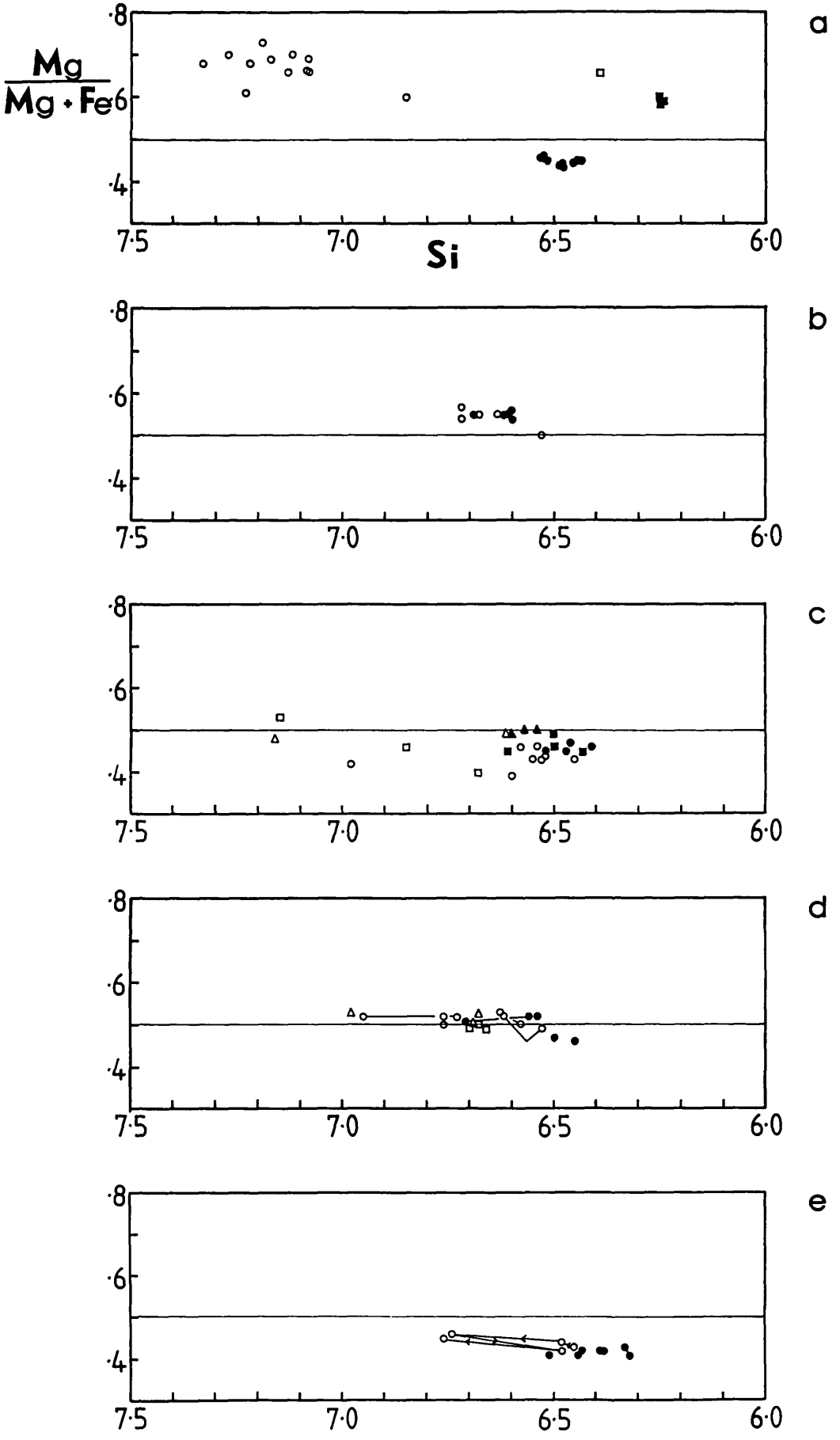
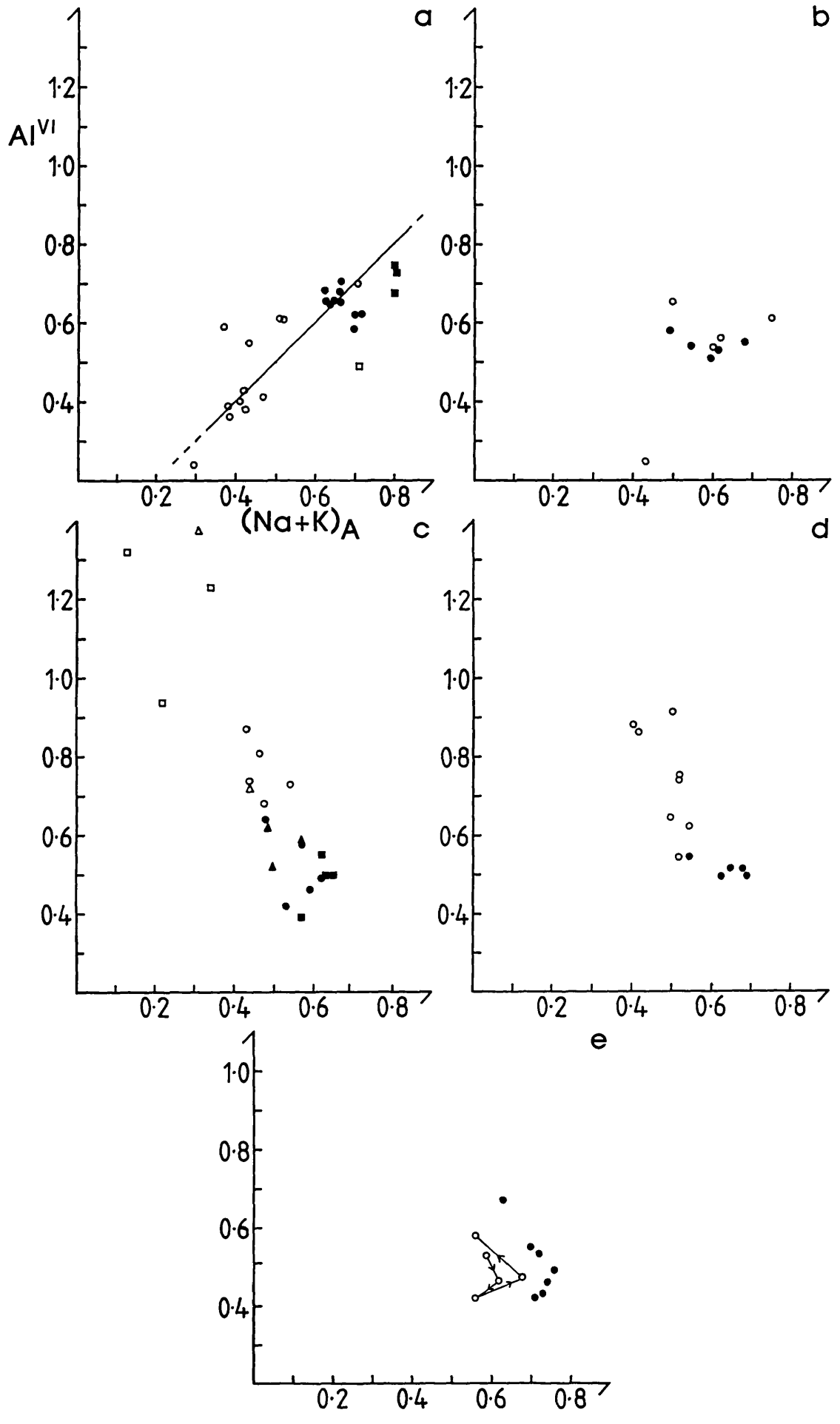

Mg / Mg + Fe
·8
·6
·4
7·5
7·0
6·5
6·0
Si
a
b
c
d
e

FIGURE 5.14 Plot of Al^{vi} vs. $(Na + K)^{A}$ formula units based on 23 (O) showing compositional variation between host (filled symbols) and porphyroclast (open symbols) amphiboles. Sample identity as for Fig. 5.13.


a
b
c
d
e
Al^{VI}
$(Na+K)_A$
1·2
1·0
0·8
0·6
0·4
0·2
0·4
0·6
0·8

the vein, similar to that seen between host and clast in the above samples, although the variation is unsystematic along the traverse. The causes of the unsystematic variation are unclear.

(C) Sample GQ38 (Figs. 5.13b and 5.14b) shows alteration (including partial retrogression to biotite) of both host and clast amphiboles. The alteration has obscured any differences between host and clast amphiboles.

5.8.6 Accessory Phase Porphyroclasts

1) Clinopyroxene of diopsidic composition is an essential constituent of some of the more basic gneissic host rocks, particularly those of Scourie dyke affinities in the Outer Hebrides and Tiree. The clinopyroxene often shows some retrogression to amphibole (presumed to be a Laxfordian effect) and exsolution of magnetite along cleavage planes.

Porphyroclasts of clinopyroxene are not abundant even in pseudotachylytes with host rocks with up to 20 modal% clinopyroxene. Typically they occur as small cleavage fragments, to 250 μm diameter compared with a typical host rock grain size of 500 - 1000 μm. The clasts show similar cleavage-located magnetite exsolution and usually posssess a dark halo up to 100 um wide in the pseudotachylyte matrix.

Microprobe analyses of clinopyroxenes from 2 different samples show little chemical variation between host and clast grains, apart from a slight decrease in Fs-component - i.e. a loss of Fe (Fig. 5.15).

2) Sphene constitues up to 5 modal% of some gneisses from Gairloch and Tiree and is an accessory in nearly all the host rocks. Porphyroclasts are usually cleavage fragments of the commonly euhedral host grains, and are darker coloured and possess a dark halo. Analyses of host and clast sphenes (Appendix A3) show negligible variation. A qualitative analysis of a dark halo region shows that it is enriched in Fe with respect to the sphene and the surrounding pseudotachylyte matrix. It is not certain whether this is a corrosion or a nucleation feature. Ilmenite was not found in the halo within the spatial resolution of the microprobe (cf. buchites in Table 5.15) Rutile and minute grains of calcite have been identified in the groundmass of a few pseudotachylytes by X-ray mapping using the SEM and may have formed

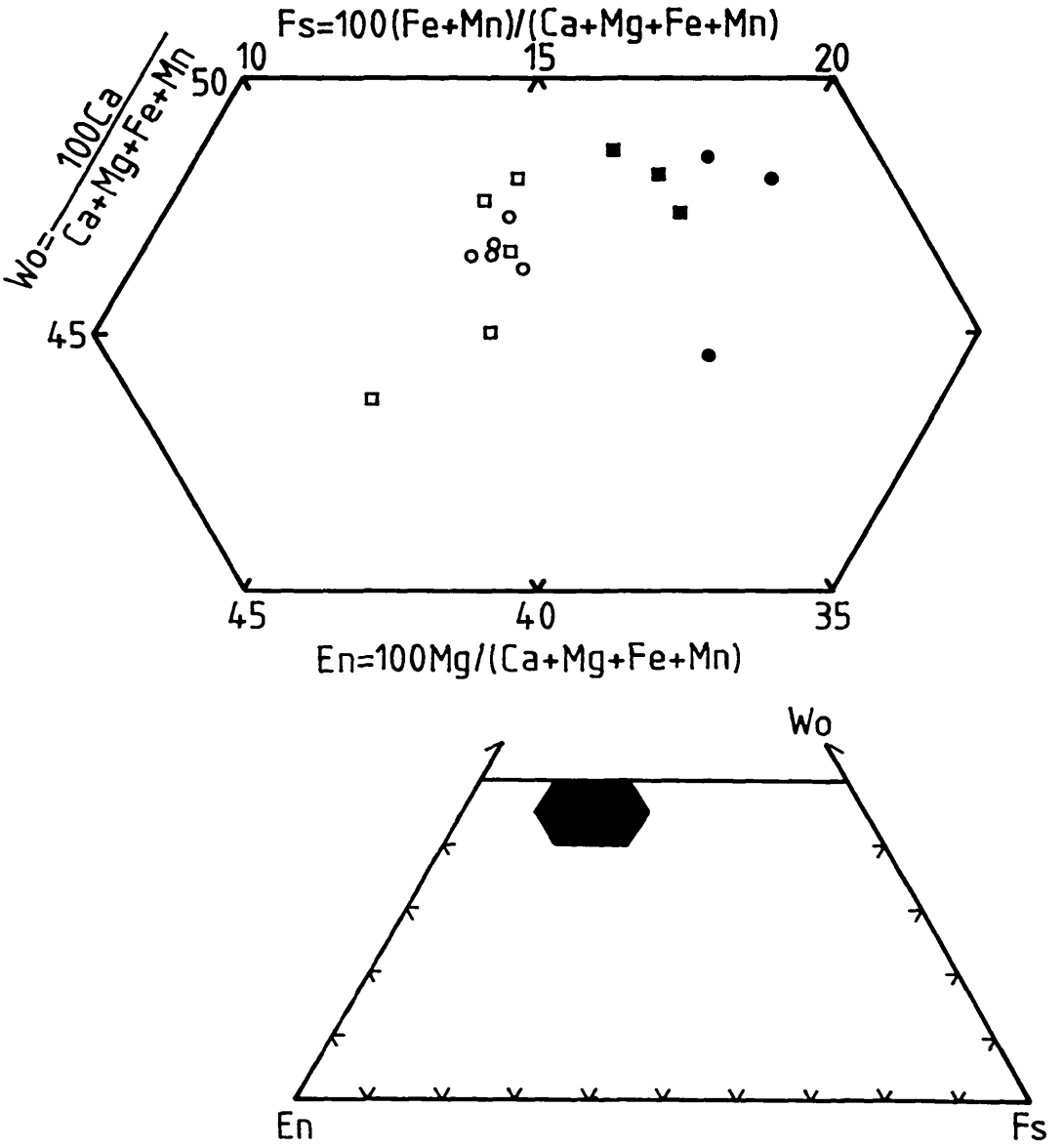


FIGURE 5.15 Part of Ca-pyroxene quadrilateral diagram showing composition of host-rock (circles) and porphyroclast (squares) clinopyroxenes. Filled symbols, sample CT3; open symbols, sample GQ6.

according to the reaction:-

$$CaTiO_5 + CO_2 = TiO_2 + CaCO_3 + SiO_2 \qquad (5.18)$$

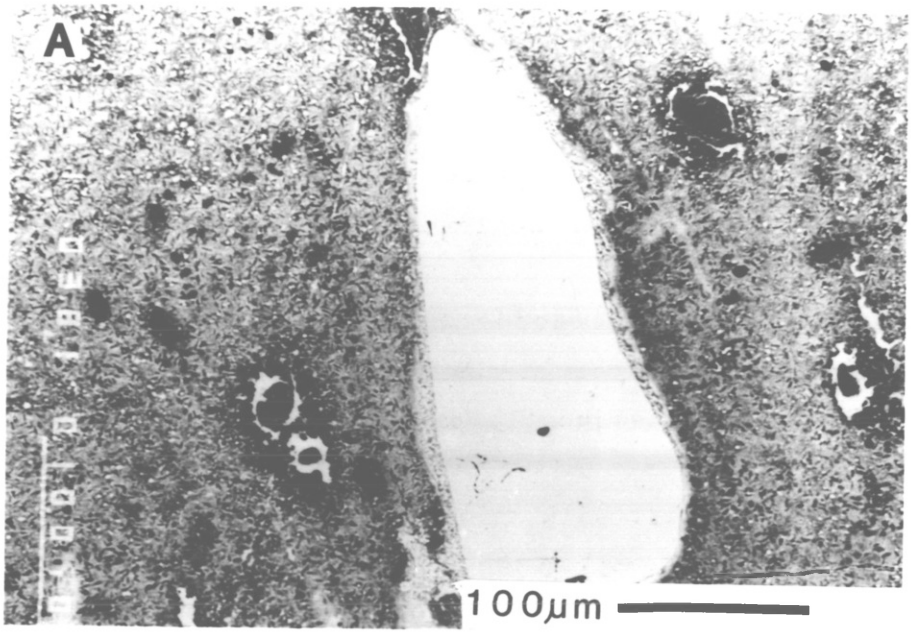
Sphene contained in partially-melted lithic porphyroclasts shows rather different behaviour and is described in section 5.8.7.

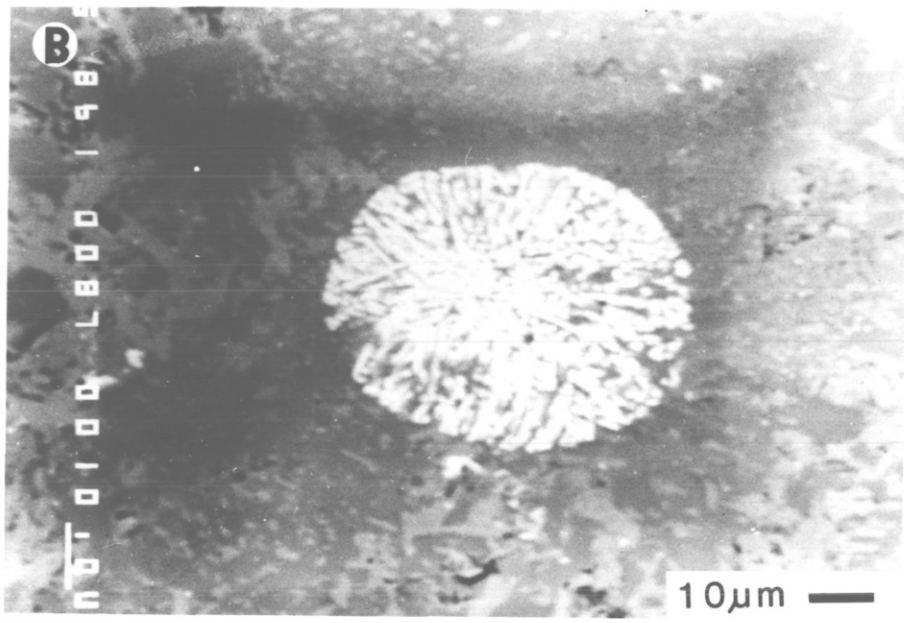
3) Garnet is a major constituent of certain paragneisses and amphibolites from the Outer Hebrides and the Silvretta area. Porphyroclasts of garnet are abundant in pseudotachylytes generated in such host rocks but no optical distinction exists between the host and porphyroclast phases. Garnet does not appear to act as a favourable nucleation site for either crystallization or devitrification.

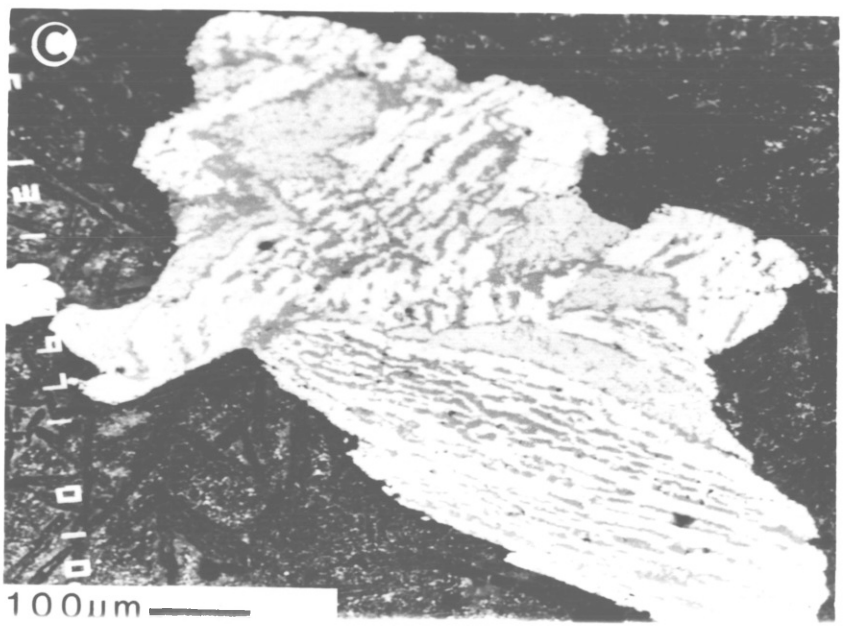
4) Sillimanite occurs as porphyroclasts in pseudotachylytes generated in the Benbecula sillimanite-bearing paragneisses (section 5.7). Apart from brittle fracturing believed to be associated with the pseudotachylyte faulting, no differences were observed between the porpohyroclasts and host sillimanites. Neither mullite nor fibrolite could be found by optical examination. Passchier (1982a) made similar observations in Pyrennean pseudotachylytes.

5) Apatite is a ubiquitous host rock accessory phase, although as a porphyroclast it is easily overlooked under the microscope - by virtue of its small size (<50 μm) and indifferent optics - but is soon apparent in the SEM. Plate 5.20A shows an apatite clast in a biotite-spherulitic pseudotachylyte matrix, which has a narrow mantle of apatite crystallites (identified by P $K\alpha$ X-ray mapping). The clast/mantle contact is sharp and is interpreted as a nucleation phenomenon rather than a corrosion feature. Microprobe raster analyses of various pseudotachylyte groundmasses consistently indicate the presence of small amounts of P which may be held in newly crystallized apatites, although this has not been confirmed by STEM analysis. Passchier (1982a) describes apatite clasts with 'frayed edges' - an apposite optical description of the texture shown in Plate 5.20A.
Apatite is conventionally considered to be a refractory phase, though the data from buchites is ambiguous (Table 5.15). Experimental studies indicate that apatite dissolution in felsic magmas is rate-limited by diffusion of phosphorous into the melt and is strongly dependant upon the water content of the melt (Harrison and Watson, 1984).

PLATE 5.20 BSE micrographs of accessory phase porphyroclasts.
(A) Apatite clast with nucleation or corrosion halo enriched in apatite. Sample GQ16.
(B) Zircon clast with dendritic structure included in lithic porphyroclast. This grain was originally included within a biotite crystal, which subsequently partially melted and reacted with plagioclase (see Plate 5.21). Sample G804.
(C) Magnetite clast with exsolved blebs of ilmenite (light grey) partially altered to sphene (dark grey). Sample R15.


A
100μm


B
10μm


C
100μm

6) Zircon, an abundant accessory phase in many of the more 'granitic' host gneisses, occurs with similar frequency as a porphyroclast. Optically the only difference between host and clast zircons (both <50 um diameter) is that the latter tend to show a brown discolouration (cf Passchier, 1982a) and may possess a narrow dark halo.

Other reported occurrences of zircon in pseudotachylytes (e.g. Allen, 1979; Passchier, 1982a) and in buchites (e.g. Schidlowski, 1963) generally confirm the expected refractory behaviour of this mineral, although the buchite data (Table 5.15) further suggest that its stability may be strongly dependent on melt composition and volatile content rather than temperature per se.

Like sphene, zircons contained in a partially melted lithic porphyroclast show unusual textures (section 5.8.7, Plate 5.20B). Experimental studies indicate that the dissolution of zircon in hydrous granitoid melts undersaturated with respect to Zr is rate-limited by the diffusivity of Zr (Harrison and Watson, 1983). For example, a 50 μm diameter zircon reacting in a nominally dry felsic melt at 750°C would take 200 Ma to dissolve compared to about 100 years in a wet melt.

7) Magnetite containing little or no Ti, Mn etc in solid solution, behaves very similarly to apatite as a porphyroclast. Clasts of magnetite maintain their (host rock) rounded form and corrosion/embayment textures are generally absent in clasts varying in size from 10 to 500 μm. Melting is suggested however from the proximity of newly crystallized dendritic crystallites of magnetite (Plate 5.16E). The migration of Fe in the pseudotachylyte melt and subsequent nucleation on fractures in quarz clasts has already been mentioned. Magnetite clasts frequently act as heterogeneous nuclei for spherulitic phyllosilicate growths (Plates 5.16B and 5.4B).

An unusual textural relationship was found in a magnetite clast in sample R15 - an amygdaloidal pseudotachylyte (section 5.9.2). A large opaque clast of magnetite (<3 wt.% TiO2) with exsolved blebs and lamellae of ilmenite (approx. 55 wt.% TiO2 and 5 wt.% MnO) shows retrogressive alteration of the ilmenite to sphene (Plate 5.20C). The timing of this alteration is uncertain though as host rock magnetites were not available for examination.

5.8.7 Lithic Porphyroclasts

Textures indicative of partial melting in quartzofeldspathic porphyroclasts in plagioclase microlitic pseudotachylytes have already been mentioned in section 5.8.2. Here, two examples of porphyroclasts with more complex mineralogies and found in pyroxene- and phyllosilicate-spherulitic pseudotachylytes are described.

1) Sample G804. The pseudotachylyte matrix to this sample has been described in some detail in section 5.5.; the whole rock chemistry of the vein and its host-rock is considered in section 6.5.1. The host-rock mineralogy is given in Table 5.7 and illustrated in Plate 5.21A. The FV contains abundant quartz and feldspar porphyroclasts, a few lithic clasts but no biotite clasts (Table 5.7).

The lithic clasts range in size up to 4 mm. A typical example is shown in Plate 5.21B, where the porphyroclast can be seen to be made up of 3 phases or assemblages: (i) plagioclase; (ii) quartz; (iii) zones composed of an assemblage of plagioclase microlites with minor sulphides and accessory phases, poikilitically enclosed by biotite and minor chlorite. A rather similar 'external' zone mantles the entire porphyroclast (Plate 5.21D).

The internal microlitic zones constitute approximately 40 modal % of the porphyroclasts - i.e. slightly more than the modal proportion of biotite in the host-rock/protolith (Table 5.7; compare Plates 5.21A and B). The texture of the internal zones is shown in detail in Plates 5.21C and D. The plagioclase microlites (8 x 100 μm max) are heterogeneously nucleated on the original plagioclase grains of the lithic clast. The margins of the plagioclase grains show slight enrichment in CaO (Plate 5.21C) extending over distances of <5 μm. This is believed to be due to either fractional melting or possibly, 'plating on' of new, more An-rich plagioclase (see section 5.8.2). Semi-quantitative analyses of the plagioclase microlites (their fine grain size precluded fully quantitative analysis) indicates that they are also more An-rich than the relict plagioclase grains (Table 5.17). Interstitial to the microlites is a non-pleochroic, freckly-brown substrate with a texture varying from ill-defined spherulitic to platey with optically recognizable plates of birefringent biotite (<10 μm dia.). In the SEM this poikilitic matrix is found to be dominantly biotite with minor chlorite, sulphides and accessory phases. The biotite contains less TiO_2 but greater SiO_2 and Al^{vi} than the host biotite (Table 5.17). Amongst the accessory phases, zircon is of

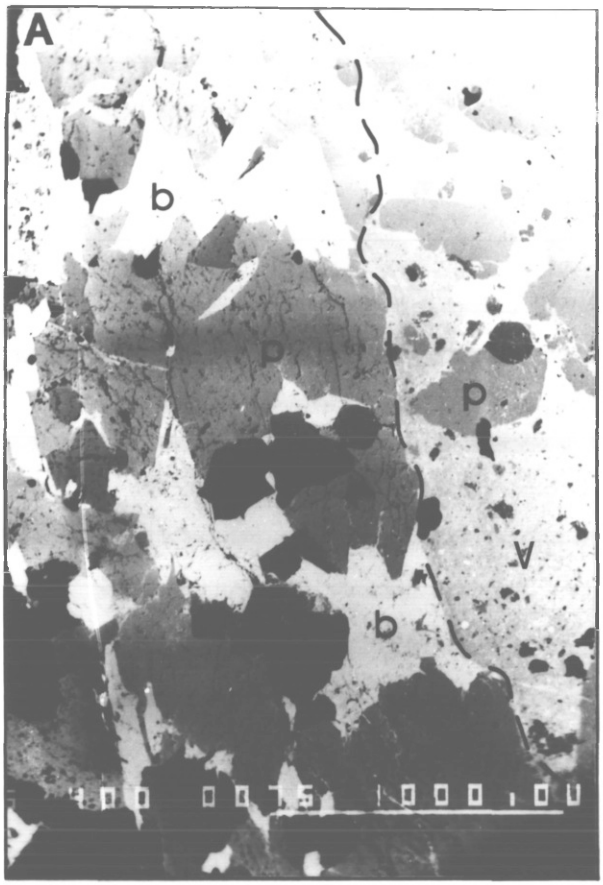
PLATE 5.21 BSE micrographs of a partially melted lithic porphyroclast in sample G804.

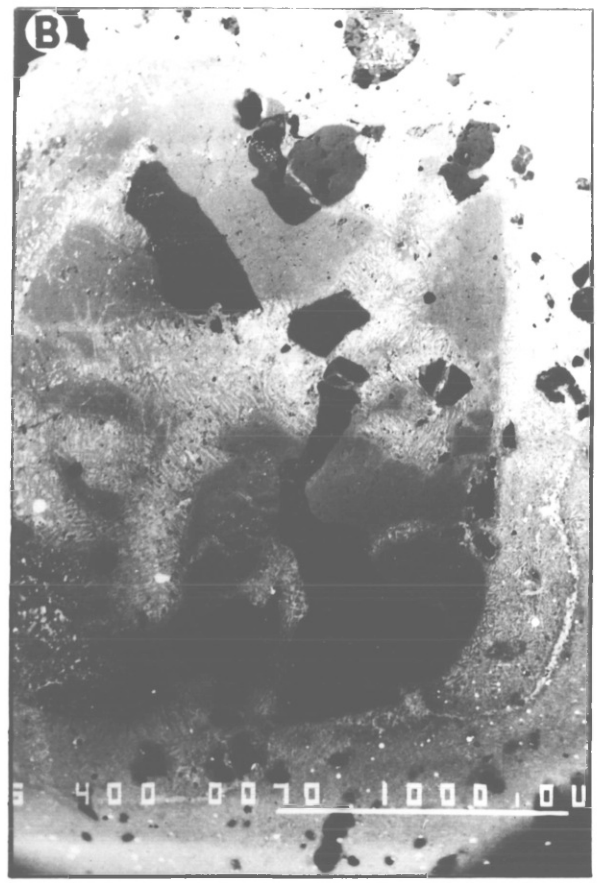
(A) Host-rock paragneiss containing quartz (q), plagioclase (p) and biotite (b). Pseudotachylyte vein is labelled v.

(B) Partially melted porphyroclast. Note distribution of microlitic melt zones (m) and absence of large biotite grains.

(C) Detail of (C) showing relict quartz grains with microfractures decorated by sulphide blebs. Note contact between porphyroclast melt zones (m) and pseudotachylyte vein (v) marked by dashed line.

(D) Detail of (B) showing plagioclase microlites heterogeneously nucleated on relict grains of plagioclase which have An-enriched margins (arrowed).


A
b
p
p
A
b


B


C
q
p


D
p
p

TABLE 5.17 ELECTRON MICROPROBE ANALYSES OF PORPHYROCLAST MINERAL PHASES, SAMPLE G804P

	1	2	3	4	5
SiO_2	59.61	56.57	37.06	38.44	26.77
TiO_2	0.00	0.00	2.88	1.89	0.00
Al_2O_3	25.62	25.79	16.59	16.95	
FeO	0.00	0.38	15.15	14.14	20.38
MnO	0.00	0.00	0.00	0.00	0.00
MgO	0.00	0.00	14.10	13.95	19.09
CaO	7.44	8.71	0.00	0.07	0.00
Na_2O	6.71	5.63	0.00	0.28	0.40
K_2O	0.20	0.39	9.87	9.73	0.00
TOTAL	99.58	97.47	95.65	95.75	86.01

1 Mean of 4 analyses of relict plagioclase grains

2 Plagioclase microlite

3 Mean of 6 analyses of host-rock biotites

4 Mean of 6 analyses of new poikiloblastic biotite

5 Chlorite in porphyroclast

particular interest. Whereas in the pseudotachylyte groundmass proper, grains of zircon are simply darker coloured relative to those in the host-rock (cf. section 5.8.6), the zircons in the porphyroclast have sufferred reaction and complete recrystallization to a spherulitic habit (Plate 5.20B).

The microlitic habit and general texture of these zones indicates that they were once melt. The external melt zones contain essentially the same phases as the internal zones together with orthopyroxene, but the crystallites tend to exhibit a more platey habit (Plate 5.21D).

Both the (relict) quartz and plagioclase grains show extensive brittle microfracturing and moderate to strongly undulose extinction, which are not present in the host-rock. Additionally, the quartz microfractures are decorated by minute blebs (<5 μm dia.) of sulphide.

2) Sample G1A. The host-rock to this sample is a fine grained (para-?) gneiss whose modal mineralogy is given in Table 5.18 and shown in Plate 5.22A. The pseudotachylyte FV (~1 cm thick) has a well developed phyllosilicate spherulitic texture (Plate 5.16B) believed to have resulted from devitrification of a glass. The whole rock chemistry of the vein and its host-rock is considered in section 6.5.1.As in the previous sample, quartz and feldspar clasts are abundant but ferromagnesian mineral clasts are very scarce.

The scarce lithic clasts are typically ovoid, up to 3 mm in length, with their long axes aligned parallel to the vein margins and the host-rock foliation. A typical example is shown in Plate 5.22A. With the exception of hornblende and chlorite, all of the phases present in the host rock occur with broadly similar habits, grain sizes and modal abundances in the lithic porphyroclast (Table 5.18; compare Plates 5.16A and 5.22B). The inferred former sites of hornblende and chlorite are now occupied by fine grained, texturally and mineralogically complex zones - an analagous relationship to that of biotite in the previous sample. The fine grained zones are composed of epidote + chlorite + muscovite + sphene + magnetite + K-spar + plagioclase, varying in grain size from 1 - 30 μm (Plates 5.22B, C and D). Their habit varies from platey/decussate, especially phyllosilicates and epidote, to dendritic/microlitic form favoured by sphene, magnetite and feldspar. Analyses of some of the phases are given in Table 5.19. As in the previous sample unexpected textures are shown by the accessory phases. In Plate 5.22D a relict grain of sphene

PLATE 5.22 BSE micrographs of a partially melted lithic porphyroclast in sample G1A.

(A) Partially melted lithic porphyroclast with annotated melt zones (m).

(B) Detail of (B) showing microlitic feldspar heterogeneously nucleated on relict feldspar grain at margin of porphyroclast.

(C) Detail of (B) showing fine grained melt zone within enclave in feldspar, composed of dendritic sphene (s) and magnetite (mt), epidote (e) and muscovite (mu).

(D) Detail of (B) showing relict sphene (s) rimmed by sphene microlites and surrounded by a fine grained matrix of epidote, muscovite, magnetite and chlorite.

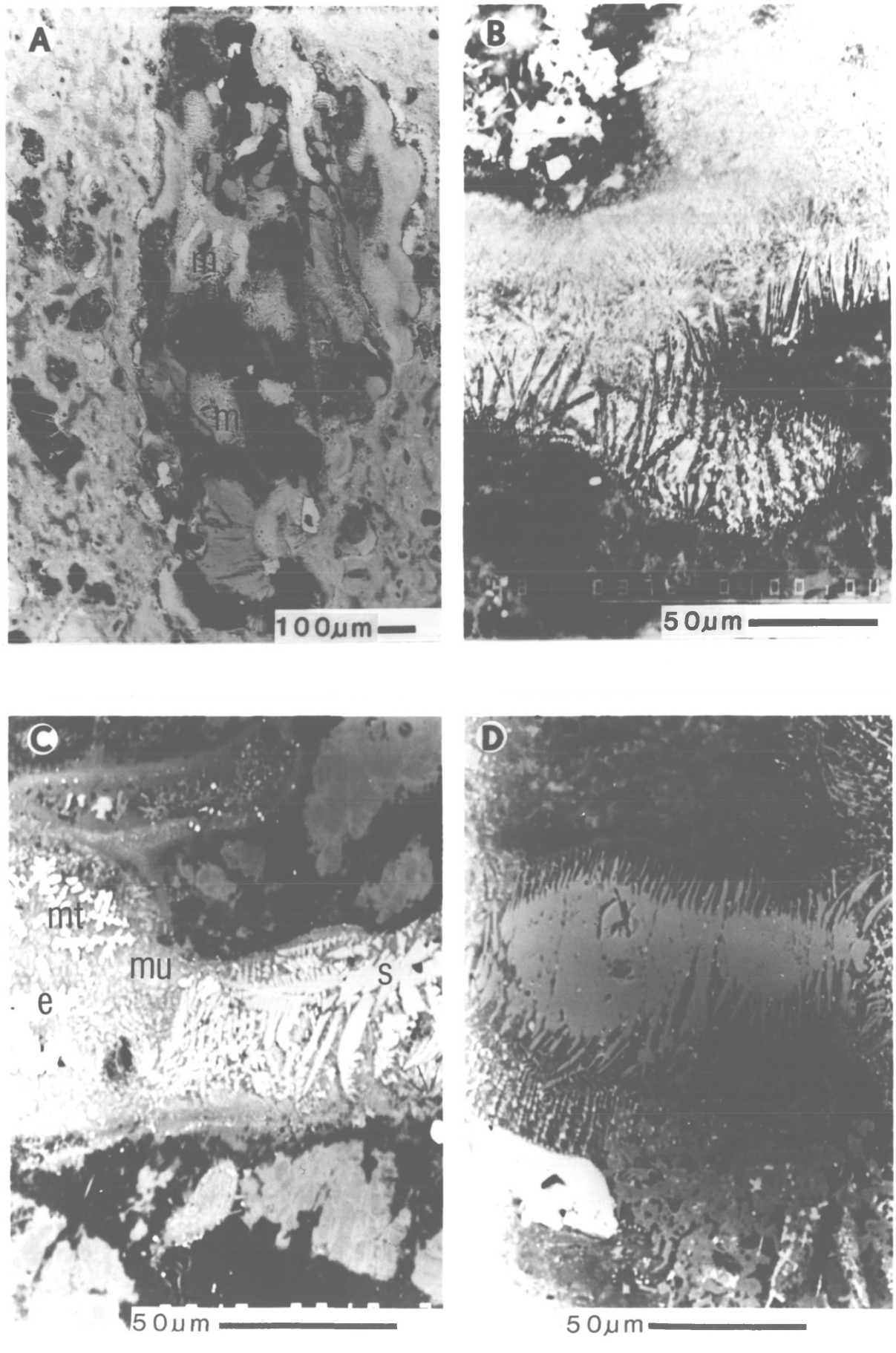

A
m
m
100µm
B
50µm
C
mt
mu
e
s
50µm
D
50µm

TABLE 5.18 MODAL COMPOSITION (VOLUME %) OF HOST-ROCK, SAMPLE G1AH

Quartz	15.1	
Plagioclase	19.6	
Microperthite	12.4	
Hornblende	36.2	(part chloritized)
Epidote	11.3	
Sphene	3.0	
Magnetite	2.4	

TABLE 5.19 ELECTRON MICROPROBE ANALYSES OF PORPHYROCLAST MINERAL PHASES, SAMPLE G1AP

	1	2	3	4	5
SiO_2	29.58	28.88	46.78	28.69	61.68
TiO_2	38.36	38.86	0.17	0.00	0.00
Al_2O_3	1.15	1.25	32.63	19.16	18.30
FeO	0.68	1.38	4.55	22.19	1.97
MnO	0.00	0.00	0.00	0.65	0.00
MgO	0.00	0.00	0.90	14.57	0.26
CaO	28.82	27.18	0.00	0.24	0.40
Na_2O	0.34	0.00	0.40	0.00	0.98
K_2O	0.00	0.00	10.24	0.00	14.11
TOTAL	98.93	97.55	95.67	85.50	97.70

1 Relict Sphene (Plate 5.22B)

2 Sphene microlite (Plate 5.22B)

3 Muscovite (Plate 5.22C)

4 Chlorite (Plate 5.22C)

5 K-spar microlite (Plate 5.22B) - also contains BaO

is fringed (epitaxially?) by heterogeneously nucleated microlites of newly grown sphene; both have the same composition (Table 5.19).

These zones are also considered to be former melt zones, now largely devitrified glass though the feldspar, sphene and magnetite microlites and dendrites may have grown directly from the melt.

The relict quartz and plagioclase grains show brittle deformation features comparable to the last sample; although the microfractures are undecorated. The plagioclase in both host-rock and clasts is heavily sericitized; in the latter however, it has a marked brown discolouration - perhaps due to exsolution of hematite, though this could not be resolved in the SEM.

Interpretation

The textures of the lithic porphyroclasts in these 2 pseudotachylytes indicates that melting occurred as a consequence of heat derived from the surrounding pseudotachylyte melt and transported over distances <1000 μm.

In both examples melting was initiated at and advanced to the greatest degree, in and around sites formerly occupied by hydrous ferromagnesian minerals (principally biotite and hornblende). Also in both cases, feldspar has been 'wetted' by the melt to a greater degree than quartz (e.g. Plate 5.21 C and D). Selective fusion of hydrous ferromagnesian phases and preferential 'melt-wetting' of feldspar relative to quartz has been observed in certain granitic and arkosic xenoliths in basalt (see Table 5.15). In these examples the temperature of the melt was of the order of 1000 °C. As with the monomineralic porphyroclasts described above, the lithic porphyroclasts in pseudotachylyte differ from xenoliths in buchites, in that silicate solid residua resulting from incongruent melting of biotite and hornblende, are not seen in the porphyroclasts.

A number of partial melting and rock deformation experiments on granitoid/gneissic rocks, with mineralogies appropriate to the pseudotachylyte host-rocks/lithic clasts, are pertinent to the porphyroclast observations. In experiments where $P_{H2O} = P_{total} > 200$ MPa, 'equilibrium' partial melting begins at quartz + K-spar + plagioclase or quartz + plagioclase (K-spar absent) grain boundaries; breakdown or melting of hydrated ferromagnesian phases does not occur until higher temperatures are reached (e.g. Mehnert et al., 1973; Busch et al., 1974; Arzi, 1978; van der Molen and Paterson, 1979). In

the 3-phase system, quartz + K-spar + plagioclase, at $P_{H2O} = P_{total} =$ 200 MPa, minimum melts may form at temperatures > 670°C, depending on the Ab/An ratio of the plagioclase (Winkler, 1967). In contrast to the above experiments, when $P_{H2O} < P_{total}$ partial melting is delayed until higher temperatures are reached and is initiated in and around hydrated ferromagnesian phases (e.g. Auer et al., 1981; Paquet et al., 1981). These observations also concur with phase equilibria studies. Naney (1983) for example, has shown that the thermal stability of biotite and hornblende increase as water is added to a granitoid system at $P_{H2O} < P_{total} = 200$ MPa.

In general such studies indicate that for confining pressures in the range 200 - 400 MPa (appropriate to equivalent depths of pseudotachylyte generation), dry melting of granitoid rocks requires temperatures 100 - 300°C greater than melting under water-saturated conditions (e.g. Brown and Fyfe, 1970).

Comparison of the textures seen in the lithic porphyroclasts and those of the above experimental studies strongly suggests that melting in the clasts occurred with $P_{H2O} < P_{total}$. It is specifically noted that many quartz + plagioclase + microperthite triple point grain boundaries in sample G1A are unwetted by melt. If these observations are correct, then it may be further inferred that the pseudotachylyte melt itself was also undersaturated with respect to H_2O. Otherwise, the easy ingress of vapour allowed by mechanically and thermally induced fractures should have allowed 'wet' initial melting. A further consequence of dry melting is that heat transport from the surrounding pseudotachylyte melt must have been conductive rather than convective. Given the low thermal conductivity of silicates, a considerable overshoot must have existed between the temperature of the pseudotachylyte melt and the maximum temperature achieved by the porphyroclasts.

A generalized P-T diagram indicating the beginning of melting of granite and granodiorite mixed with various hydrated phases is shown in Fig. 5.16. Assuming $P_{total} < 200$ MPa, temperatures in excess of 740 and 860°C should have been attained in the centres of samples G804 and G1A respectively. The influence of much lower confining pressures (considered unlikely) and hydrated phase solid-solution are difficult to assess.

A further constraint on the minimum temperature of melting of sample G804 may be made by comparison with experimental data reported by Winkler (1967). In this experiment a biotite gneiss of similar

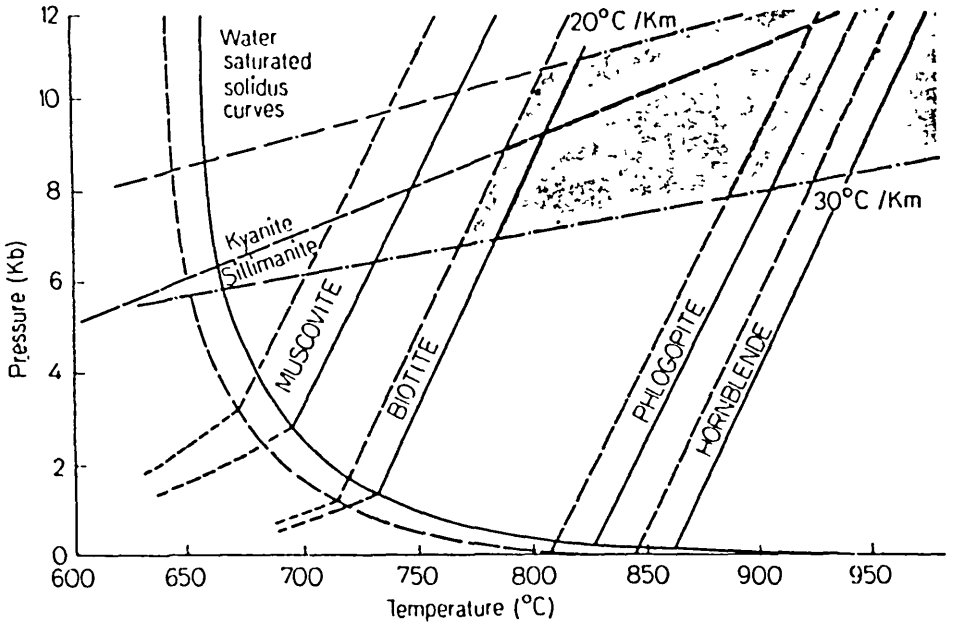


FIGURE 5.16 The beginning of melting of dry granitic (dashed lines) and dioritic (solid lines) mixtures resulting from the decomposition of muscovite (m), biotite (b), phlogopite (p) and hornblende (h). Water-saturated solidus curves for granitic and dioritic mixtures also shown. After Brown and Fyfe (1970).

TABLE 5.20 MODAL ANALYSIS AND DATA FOR SAMPLE G804H AND EXPERIMENTALLY MELTED ROCK OF WINKLER (1967)

	1	2	3
Quartz	23.5	25.8	21.0
Plagioclase	38.8	42.68	45.0
Biotite	28.0	30.8	30.0
Garnet	8.9	-	-
Opaque	0.8	-	-
Plagioclase composition	An_{38}	An_{38}	An_{21}
Beginning of melting (P_{H_2O} = 200 MPa)			690 ± 10 °C
Amount of melt at 720 °C			50%

1. Sample G804H host rock (n = 1000)
2. Recalculated modal analysis of G804
3. Experimentally melted rock of Winkler (1967)

mineralogy and chemistry to the host-rock of sample G804 (Table 5.20) was melted at $P_{H2O} = P_{total} = 200$ Mpa. Melting began at 690 °C and 50% melt was formed at 720 °C. Noting the higher An-content of the pseudotachylyte host-rock plagioclases (Table 5.17), more refractory behaviour would be expected in the latter compared to the experimental sample. During dry melting of a biotite gneiss at a confining pressure of 210 MPa, Nedelec and Paquet (1981) found that melting began at 770 °C.

In both the porphyroclast examples, formation of a melt phase has been assisted by water released during dehydration/breakdown of hydrous ferromagnesian minerals. Additionally, it may be anticipated that a $KAlSi_3O_8$ component released by biotite in the first sample and microperthite in the second, should tend to lower the liquidus temperature of any melt forming (Winkler, 1967, p.214).

The textures of the accessory phases, zircon and sphene, suggest partial dissolution in the surrounding melt followed by heterogeneous nucleation and growth of new spherulitic/microlitic forms. Corrosion of these rather refractory phases, not seen in the main pseudotachylyte vein, may have been assisted by unusual local melt compositions within the porphyroclasts, perhaps enriched in H_2O relative to the surrounding pseudotachylyte melt. Since a high proportion of the rare earth elements and U reside in accessory phases such as zircon and sphene, the melting behaviour of these phases is of crucial importance in trace element, REE and isotopic petrogenetic studies.

5.9 Microjoints, Amygdales and Porphyroclast Replacement Structures

'Filled cavities' - healed microjoints, amygdales and porphyroclast replacement pseudomorphs - in pseudotachylytes tend to contain systematic mineral assemblages. The presence of these structures and their mineral infillings can provide information about the conditions of formation and subsequent history of pseudotachylytes.

5.9.1 Microjoints

The microfractures, whose field characteristics have been described in section 4.5, vary in thin section from knife-sharp shears with no visible filling to healed fractures up to 150 μm in width. The microfractures invariably post-date the most delicate crystallization/devitrification microstructures in the pseudotachylyte matrix (e.g. Plate 5.16D and 5.23D), and cannot therefore be interpreted as perlitic fractures causing hydration/devitrification. Microfracture frequency varies from regular 200 - 1000 μm spacing to irregular centimetric spacing - visible in the field. The former, typical of narrow injection veinlets of pseudotachylyte, usually show no shear displacement and terminate against the vein walls which they meet at a high angle (Plate 5.23A). These are interpreted as tensile fractures formed in response to cooling stresses. Shear fractures with displacements of the order of 10's of microns also occur, either singly or in conjugate sets. Propagation of such microfractures occurs by en-echelon nucleation of new fractures which show consistent stepping directions and ultimately coalesce. The microfractures often terminate in narrow cataclastic shear zones, which they meet at a high angle, a few grain diameters into the host-rock.

The phases healing the fractures are ubiquitous in pseudotachylytes from all the localities of this study and several published studies (e.g. Philpotts, 1964; Bisschoff, 1962). The most common minerals are quartz, chlorite, epidote and K-spar (adularia?); pyrite, carbonate, Fe-hydroxide and rutile are less abundant; albite was found in a single example only. A marked mineralogical/chemical correlation exists between fracture filling, pseudotachylyte type and host-rock type. Thus in six phyllosilicate spherulitic pseudotachyltes containing K-spar healed microfractures, K-spar is also present in the host-rocks. Many of the observations made by Ramsay (1980) on crack

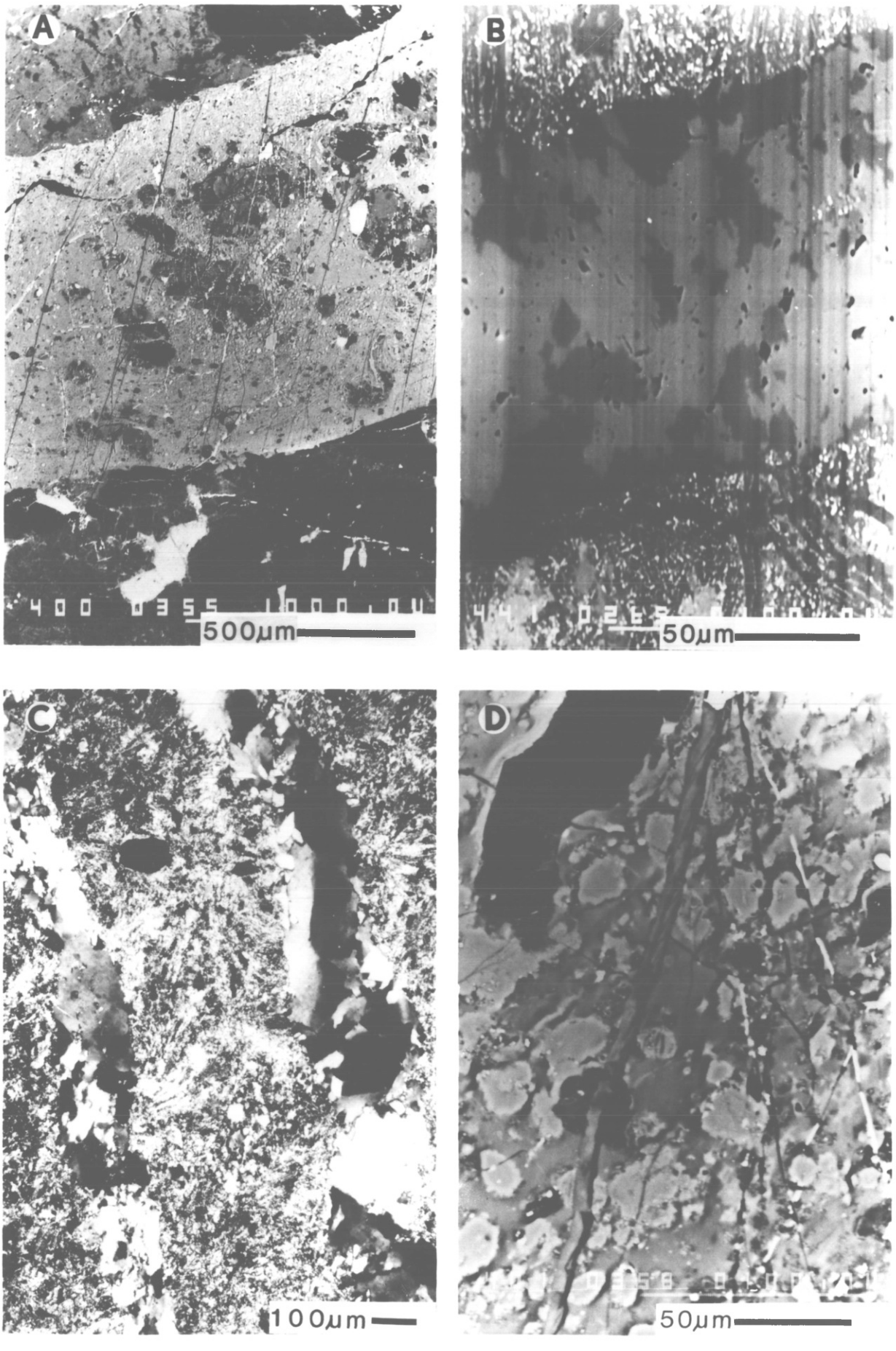
PLATE 5.23 Micrographs of healed microfractures cutting pseudotachylyte veins.

(A) BSE micrograph of injection veinlet of pseudotachylyte cut by irregular opaque-healed fractures and regularly-spaced microfractures healed by chlorite. Note that the latter do not continue into the host-rock. Sample CT2.

(D) Detail of (A) showing braided chlorite healed microfracture which is later than the fine spherulitic/devitrification stuctures in the pseudotachylyte matrix. (Irregular open fractures are an artefact of section making.)

(C) Optical micrograph of a microfracture healed by quartz which shows undulose extinction. Sample E5.

(B) BSE micrograph of microfracture healed by a xenoblastic intergrowth of albite (a) and adularia (k) which crosses a plagioclase porphyroclast in plagioclase-microlitic pseudotachylyte. Sample R15.


A
500µm
B
50µm
C
100µm
D
50µm

seal veins in polymineralic rocks can be applied to healed microfractures in pseudotachylytes.

The fabric of the fracture fillings varies from drusy (especially quartz, epidote and K-spar) to fibrous (especially chlorite - Plate 5.23D) or xenoblastic. In quartz porphyroclasts the microfractures show every gradation from platey quartz crystals filling an obvious dilational feature (Plate 5.23C) to a hairline trail of inclusions flanked only by a narrow line of slight optical misorientation in the quartz. A median, dusty inclusion trail, in some examples containing ripped-off fragments of wall-rock, is often present - demonstrating axially-directed growth. Fibrous fillings are often synthetically orientated to the direction of shear, perhaps due to mineral growth during slow crack propagation. Xenoblastic quartz infillings may show undulose extinction (Plate 5.23C) indicatin that further small strains were accomodated by intracrystalline plasticity following healing of the fractures (cf. White and Johnson, 1983).

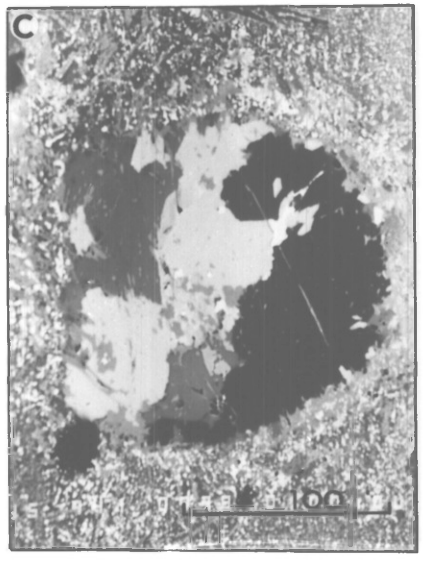
5.9.2 Amygdaloidal Pseudotachylyte, Outer Hebrides Thrust

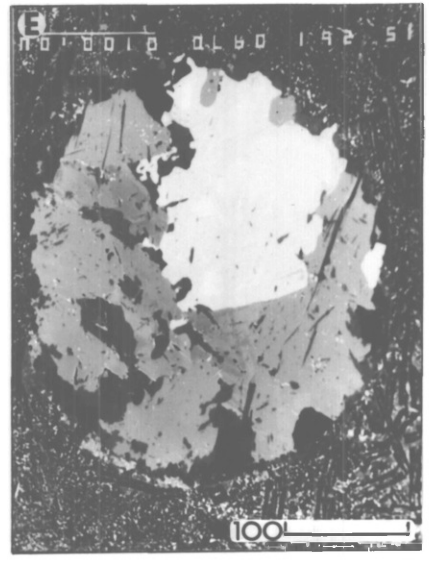
Amygdales have not previously been recognized in OHT pseudotachylytes, their absence having been used by Sibson (1975) to estimate a minimum depth of 2 km for pseudotachylyte-generation in the OHT zone. In this study they were found in a single suite of plagioclase-microlitic pseudotachylytes collected from a sub-vertical quasi-conglomerate complex at Rubha Ardvule, S Uist (Plate 4.7). The pseudotachylyte veins of maximum thickness 3 cm were generated in quartzo-feldspathic gneisses. The amygdales vary from almost perfectly circular (beleived spherical in 3-D) to elliptical in section with increasing size over the range 20 - 200 μm maximum dimension. The larger elliptical examples are flattened parallel to the vein walls and have maximum aspect ratios of about 2 (thin-section cut normal to the vertical dip of the vein). There is no evidence of microlite nucleation on the vesicle walls, but locally the microlite long axes are aligned parallel to the elongation of the vesicles. The amygdales constitute a maximum of 5 modal% and are randomly distributed apart from being absent within 1 mm of the vein margin.

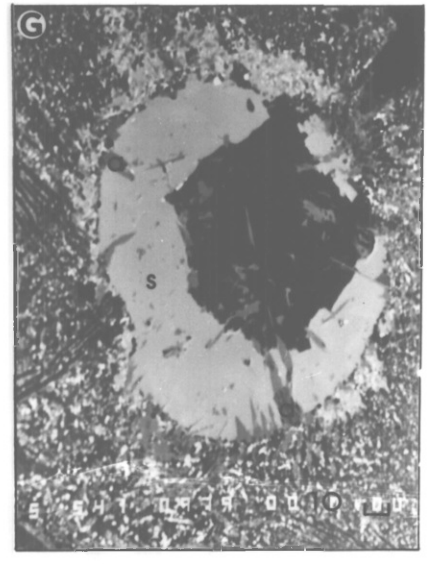
The mineral assemblage filling the amygdales is shown in Table 5.21. Each amygdale contains 3 - 7 subhedral grains of one or more of the 'essential' phases which occupy most of the volume and exhibit quasi-drusy habit; the accessory phases occupy the grain boundaries,

PLATE 5.24 BSE micrographs and line drawings of amygdales in plagioclase-microlitic pseudotachylyte, sample R15.
a = actinolite, b = biotite, e = epidote, f = Fe-hydroxide (grain boundaries shown by dashed lines), k = K-spar, p = pyrite (diagonal hachuring in F), pl = plagioclase, q = quartz, s = sphene.
Scale in microns.


A
100


C


E
100


G
S


B
s
e
s
k
a
a
e
s
s
a
q


D
s
k
s
s
p
a
e
s
q
s
k
a


F
q
e
s
s
a
e
f
a
s
a
e
s
k
s
s
q
k

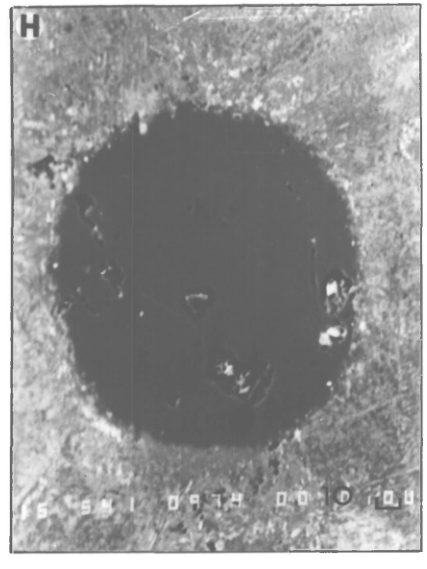

H

TABLE 5.21 AMYGDALE AND PORPHYROCLAST REPLACEMENT PSEUDOMORPH MINERAL ASSEMBLAGES

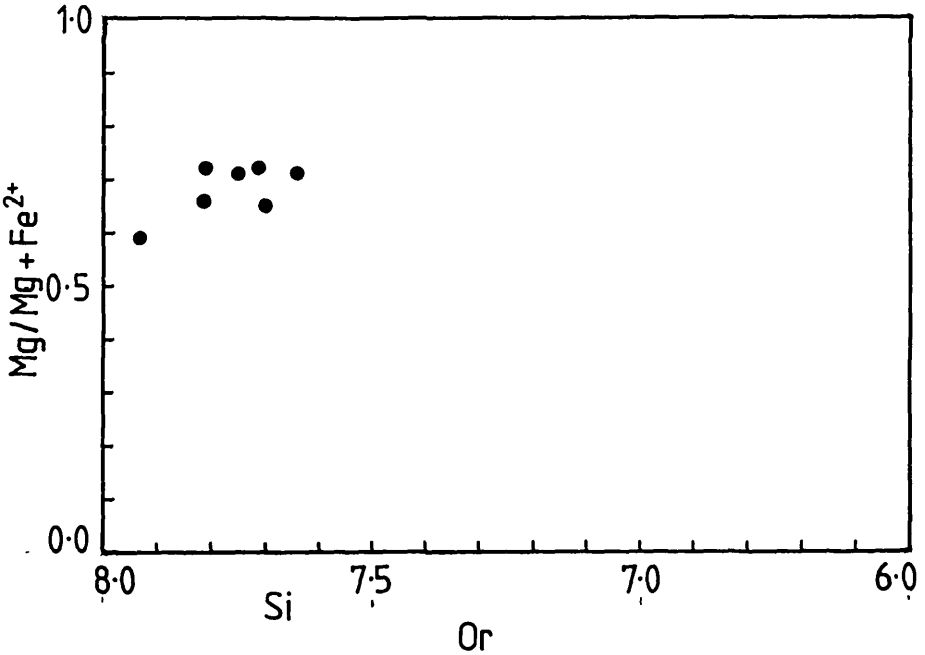
Sample	Phases	Composition (Probe analysis)	Zonation/Occurrence
R10 - R15 amygdales in plagioclase microlitic pseudotachylyte, OHT	K-spar	$Or_{95.37}Ab_{4.19}An_{0.44}$	'essential' phases
	quartz		
	sphene	$Ca_{4.05}(Ti_{3.64}Fe^{3+}_{0.14}Al_{0.29})Si_{4.00}O_{20}$	
	epidote 1		
	epidote 2		
	actinolite	$(Ca_{1.94}Na_{0.11}K_{0.01})(Mg_{3.28}Fe^{+}_{1.58}Fe^{3+}_{0.06}Mn_{0.07}Ti_{0.04}A^{VI}_{0.04})(Si_{7.78}Al^{IV}_{0.22})O_{22}(OH)_2$	'accessory' phases
	biotite	$(K_{1.57}Ca_{0.03})(Fe_{2.24}Mg_{3.11}Mn_{0.04}Ti_{0.28}Al^{VI}_{0.29})(Si_{5.63}Al_{2.37})O_{20}(OH)_4$	
	apatite		
	magnetite		
	pyrite		
	chalcopyrite		
	chlorite	$(K_{0.68}Ca_{0.06})(Mg_{4.78}Fe_{3.20}Mn_{0.06}Ti_{0.21}Al^{VI}_{2.50})(Si_{6.68}Al_{1.14})O_{20}(OH)_{16}$	'alteration' phases microjoints
	Fe-hydroxide		
	albite	$Or_{0.63}Ab_{98.64}An_{0.76}$ (with K-spar)	
2070 amygdales in biotite-spherulitic pseudotachylyte, Greenland	ferroan dolomite 1	$sid_{4.76}Magn_{43.60}Rhod_{1.06}Calc_{50.58}$	axial zone
	ferroan dolomite 2		
	ferroan dolomite	$Sid_{8.91}Magn_{40.82}Rhod_{0.62}Calc_{49.65}$	marginal zone
	ankerite	$Sid_{16.44}Magn_{34.19}Rhod_{0.45}Calc_{48.92}$	
	barite		marginal zone and grain boundaries
	magnetite		
	celadonite	$(K_{1.91}Ca_{0.06})(Mg_{1.58}Fe^{3+}_{2.38})(Si_{7.90}Al_{0.02})O_{20}(OH)_4$	
	quartz		
	calcite	$Sid_{1.31}Magn_{1.87}Rhod_{0.51}Calc_{96.31}$	
GQ34 replacement pseudomorph in chlorite-rich pseudotachylyte, OHT	calcite	$Sid_{0.36}Magn_{0.47}Rhod_{0.25}Calc_{98.95}$	axial zone
	quartz		
	chlorite		marginal zone
	actinolite (relict)		

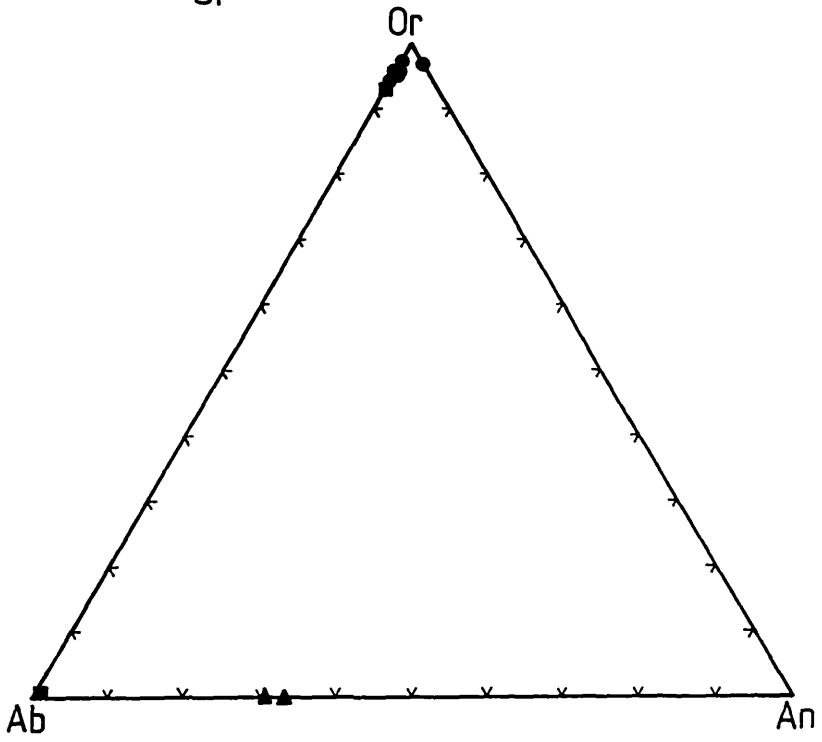
FIGURE 5.17 Diagrams showing the compositions of selected phases occupying amygdales in plagioclase microlitic pseudotachylyte sample R15.

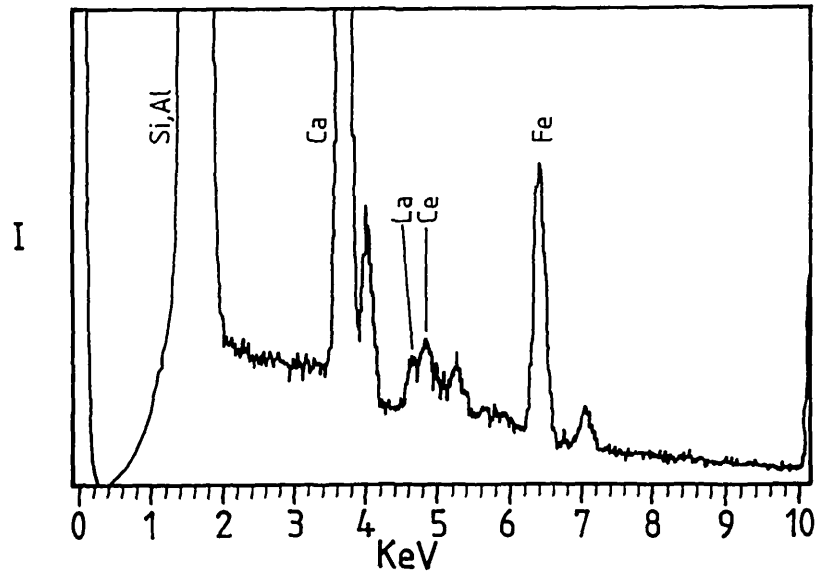
(a) Plot of Si vs. $Mg(Mg + Fe_{2+})$ formula units based on 23(0) showing composition of acicular amphiboles.

(b) An-Ab-Or diagram. ● = K-spar in amygdales; ▲ = relict feldspar porphyroclast (?) in amygdale; ■ = feldspars in microfractures.

(c) Intensity (I) vs. energy (keV) plot showing qualitatively the presence of La and Ce in epidote 2 (only the lowest energy peaks are annotated).


a
1·0
0·5
0·0
Mg/Mg+Fe2+
8·0
7·5
7·0
6·0
Si


b
Or
Ab
An


c
I
Si,Al
Ca
La
Ce
Fe
0
1
2
3
4
5
6
7
8
9
10
KeV

inclusions within the essential phases and other interstices (Plate 5.24). Extreme modal variation between the amygdales is considered prima-facie evidence that they are indeed amygdales and not immiscible silicate liquid droplets (cf. Roedder, 1979, p. 44). In amygdales where quartz and/or K-spar dominate, sometimes to the total exclusion of all other phases (e.g. Plate 5.24H), substantial optical misorientation exists between the grains but there is no optical evidence of strain. Both the sphene and epidote type 1 show strong absorbtion and appear dusty in thin-section due to inclusions of the accessory phases as revealed in the SEM. Little chemical variation in essential or accessory phases exists within or between amygdales.

The accessory phases occur in varying proportions and restricted combinations: neither of the pairs actinolite and biotite or magnetite and sulphide were observed coexisting in the same amygdale. Epidote type 2 is found as laths (~10 x 40 μm max.) within epidote type 1 (Plate 5.24A and B) and contains up to 10 wt.% Ce_2O_3 and La_2O_3 substituting for CaO - estimated from semi-quantitative analyses (Fig. 5.17c) - and could be described as an allanite. Actinolite, perhaps the most abundant accessory phase, occurs in needles 15 x 100 μm maximum dimensions which are included within, and cross without deflection grain boundaries between, the essential phases (Plate 5.24C and D). This textural relationship implies growth of actinolite and subsequent inclusion within the essential phases. The actinolite approaches end-member composition (Fig. 5.17a containing very low Al2O3 and alkalis (Appendix A3). Biotite is also found in lath-like or platey form. The average composition of the biotite is shown in Table 5.21, but some of the grains are partially chloritized - indicated by the loss of SiO2, TiO2 and K2O and gain in FeO and MgO and reduced oxide wt.% totals (Appendix A3).

Pyrite, the most abundant opaque phase, may achieve dimensions comparable to the essential phases (Plate 5.24E and F). Magnetite occurs as small rounded grains to 40 μm diameter. Both pyrite and magnetite are altered marginally and along grain boundaries to an brown/red Fe-hydroxide (goethite?) of bladed habit (Plate 5.24F). Chalcopyrite and apatite were found in a single instance only.

In one amygdale a large, rather angular grain of plagioclase of composition similar to the porphyroclasts (Fig. 5.17b) was identified (Plate 5.24G). Although the grain appears to contain inclusions of actinolite, it seems most likely that it is a plagioclase clast which became trapped during vesiculation.

The amygdale walls vary from sharp boundaries to narrow zones (< 10 μm wide) of replacement/alteration of the pseudotachylyte matrix by the phases within the amygdale proper.

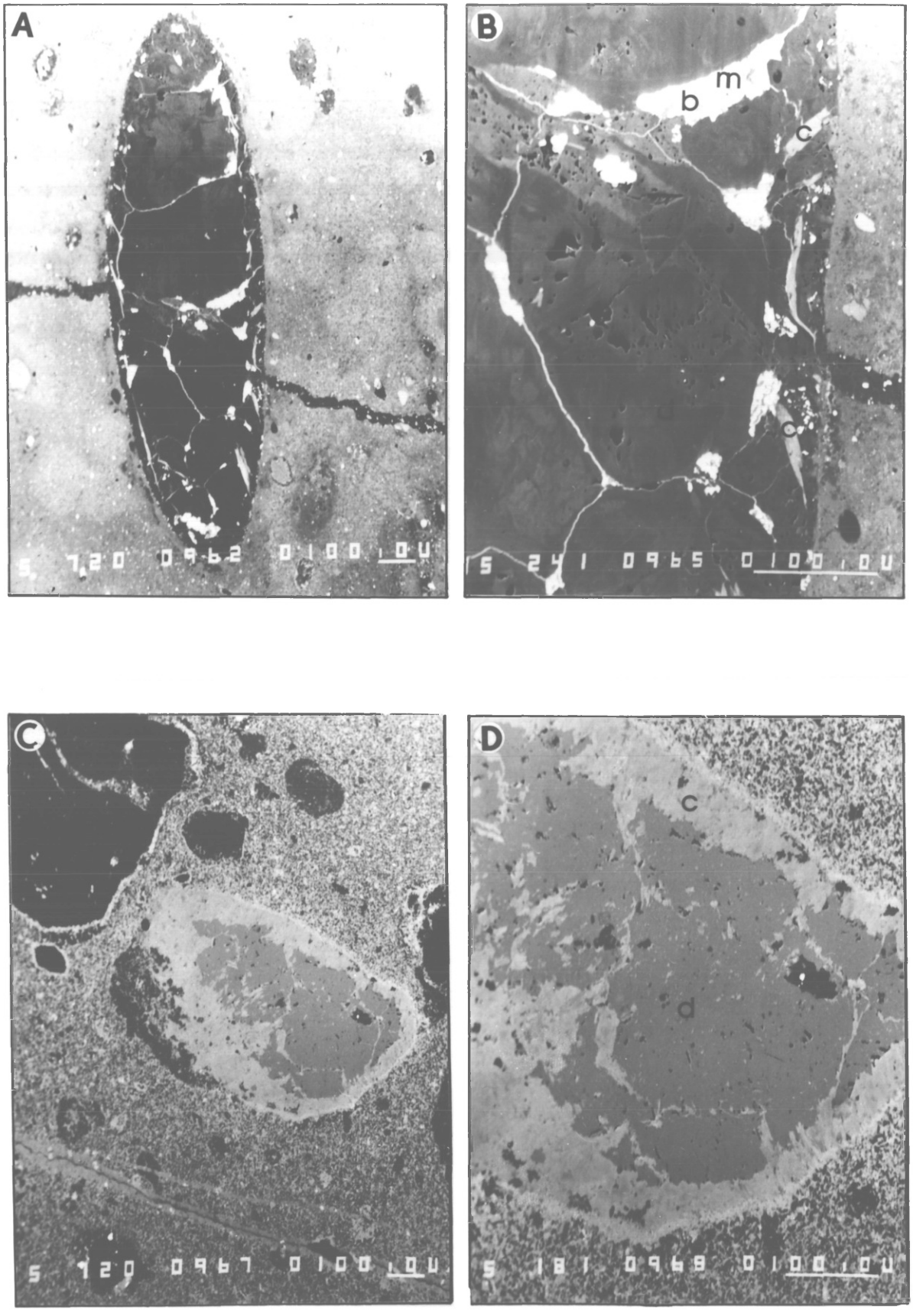
At least 2 generations of microfractures cut the pseudotachylyte. The earliest, <10 μm wide, are healed largely by K-spar apparently contemporaneous with infilling of the amygdales. It is stressed however that only a minority of the amygdales are visibly connected to microfractures. A later set of microfractures, up to 100 μm wide, demonstrably postdate amygdale infilling. These microfractures are healed by a xenoblastic intergrowth of K-spar and albite in the approximate ratio 60:40 respectively, but with albite occupying most of the microfracture margin (Plate 5.23B). The K-spar in the microfractures is comparable in composition to that in the amygdales whilst the Na-feldspar is near-pure albite (Fig. 5.17b). A weak buff red colour may be imparted to the microfractures by Fe-bearing impurities.

5.9.3 Amygdaloidal Pseudotachylyte, Ikertôq Shear Zone, Greenland

For comparison an amygdaloidal pseudotachylyte collected by J. Grocott from the northern boundary of the Ikertôq shear zone, W Greenland (Grocott, 1977a) has also been examined. The pseudotachylyte is a biotite spherulitic type vein occupyiny the contact between plagioclase + quartz + biotite gneiss and lamproite, both slightly altered by fractures containing carbonate. The 1.5 cm thick vein contains 2-3 modal% elliptical amygdales of maximum dimension 250 μm, flattened parallel to the vein walls (Plate 5.25A). Aspect ratios up to 10 (Fig. 5.18), possibly result from simple shear or flattening of still hot and viscous pseudotachylyte. The larger amygdales contain a zoned arrangement of minerals given in Table 5.21 and Fig. 5.19 and illustrated in Plates 5.25A and B (analyses are given in Appendix A3). The overall structure suggests vesicle infilling with nucleation dominating over growth initially (marginal zone) followed by growth dominating over nucleation (axial zone). Similar geometries and indeed mineralogies are frequently seen in vug and pore space cementation and are explicable in terms of changing substrate structure and chemistry during crystallization. Growth of non-carbonate phases in these amygdales may have been relegated to grain boundary environments for similar reasons.

The dolomite is presumably secondary, perhaps after calcite

PLATE 5.25 BSE micrographs of amygdale (sample 2070) and porphyroclast replacement pseudomorph (sample GQ34). Scale bar = 100 um.
(A) Flattened vesicle with intersecting microfracture infilled by large grains of carbonate with barite, celadonite and magnetite along grain boundaries.
(B) Detail of (A) showing irregularly zoned plates of ferroan dolomite (d) and grain boundary location of barite (b), celadonite (c) and magnetite (m). Note increase in grain size away from margin and continuity of microfracture and amygdale infilling.
(C) Porphyroclast replacement pseudomorph structure in chlorite-rich pseudotachylyte; note proximity of chlorite-healed microfracture (m).
(D) Detail of (C) showing zoned arrangement with rim of chlorite (c) enclosing calcite (d) with small grains of quartz.


A
B
m
b
c
c
C
D
c
d

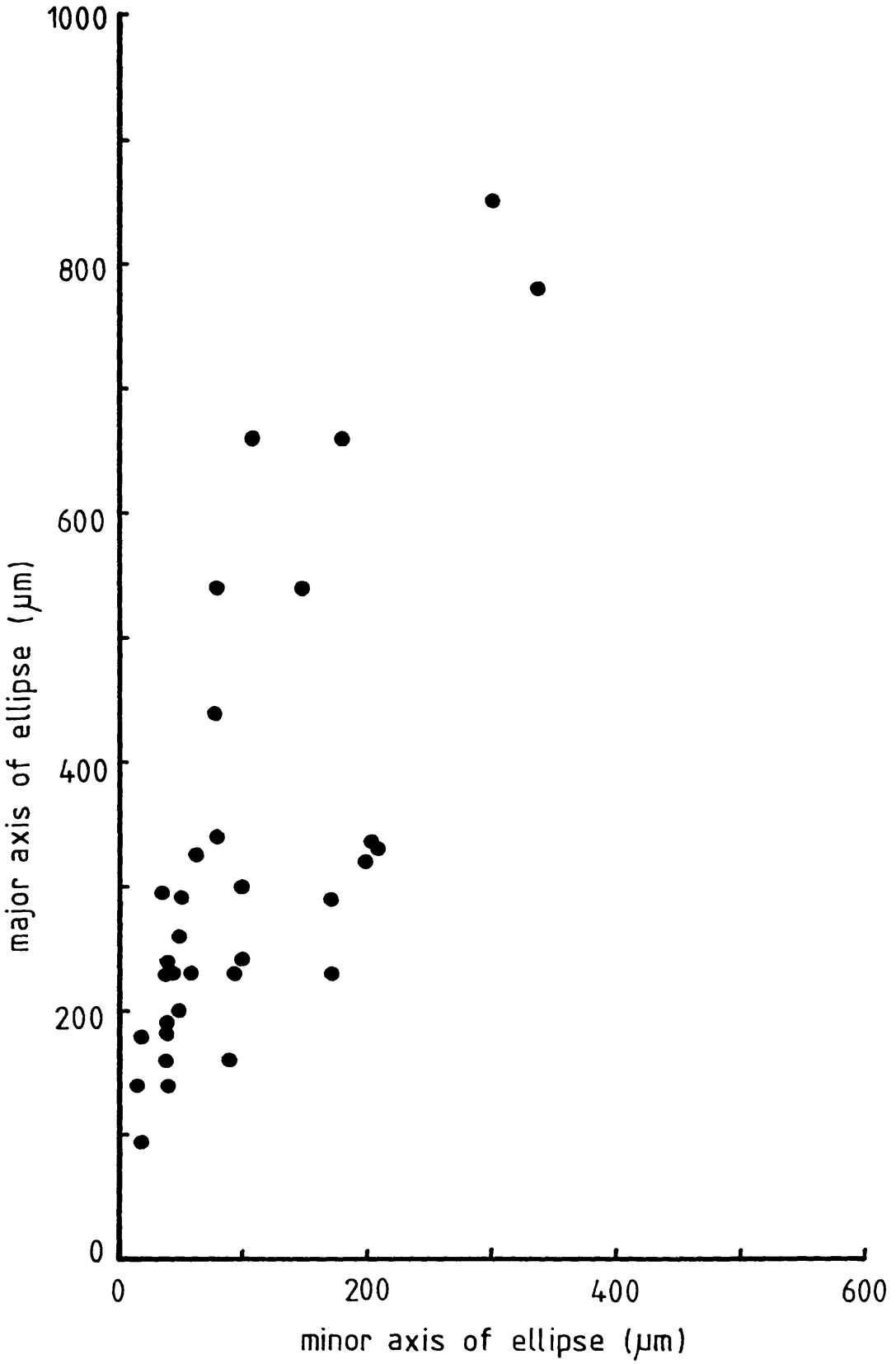


FIGURE 5.18 Plot of major vs. minor axes for ellipsoidal amygdales in sample 2070 (J. Grocott); mean axial ratio = 4.41, σ = 2.27, n = 33.

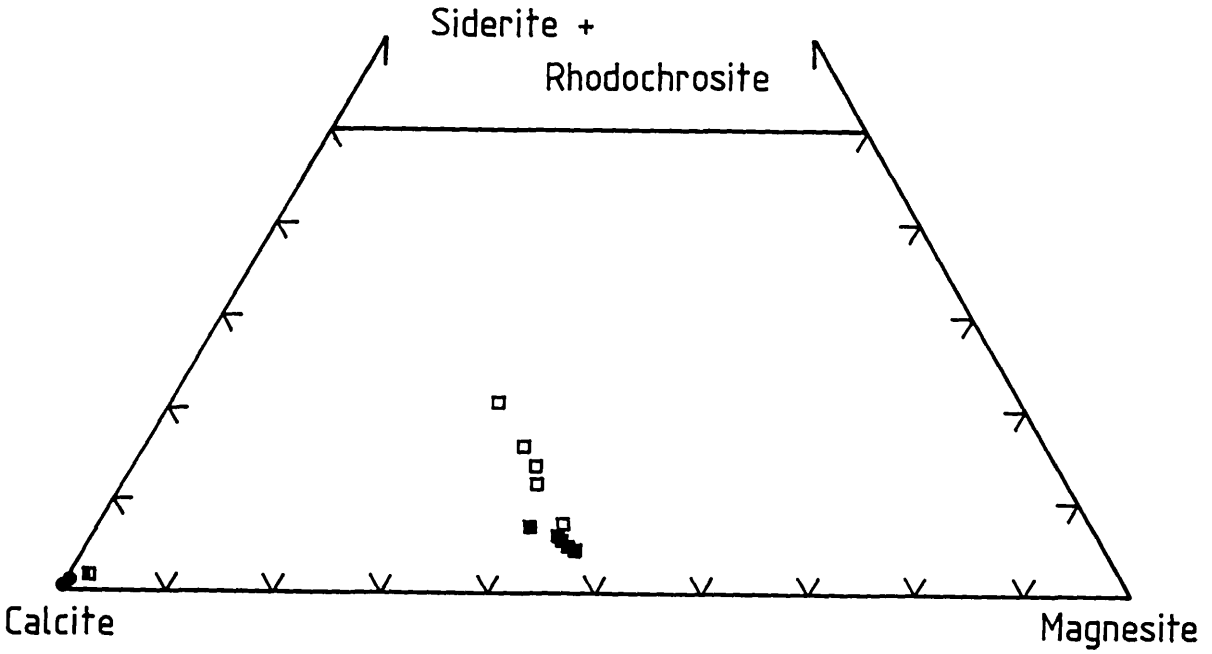


FIGURE 5.19 Pseudoternary plot showing compositions of carbonates, in amygdales and porphyroclast replacement pseudomorphs.

● = porphyroclast replacement pseudomorph, sample GQ34;

■ = axial zone of amygdale, sample 2070;

◻ = marginal zone of amygdale, sample 2070;

◧ = inclusion in barite, sample 2070.

although no porosity increase is apparent. It is not clear whether the zoning in the dolomite is primary (i.e. it formed during growth of the dolomite) or a later exsolution feature.

Celadonite, distinguished from glauconite by the former's negligible Alvi content (Buckley et al., 1978), occurs as wispy, verdant green laths to 75 x 15 um maximum dimensions (Plate 5.25B). Analyses of this phase (obtained on 2 separate occasions both with stable machine conditions: Appendix A3) contain less than 8 formula units Si per 22 (O) and little or no Al suggesting that some of the (inferred) Fe^{3+} may be tetrahedrally coordinated.

Carbonate and barite bearing microfractures intersect some, but not all, of the amygdales with textures clearly demonstrating coeval, contemporaneous filling of both structures (Plate 5.25A and B)

5.9.4 Porphyroclast Replacement Pseudomorphs, OHT

Porphyroclast replacement pseudomorphs are distinguished from amygdales by their more irregular form and generally larger dimensions. In the amygdaloidal pseudotachylyte from the OHT described above, incipient marginal alteration of the plagioclase porphyroclasts to epidote + clinozoisite + sericite + calcite has occurred, especially adjacent to the microfractures. Similar marginal alteration of porphyroclasts has been noted in the literature (e.g. Philpotts, 1964; and Table 5.22).

In a more general sense, replacement pseudomorphs are best developed in pseudotachylytes with a high content of chlorite in their groundmass (e.g. the chlorite-spherulitic types) and with a high density of microfractures. The petrography and mineralogy of one example is shown in Table 5.21 and Plate 5.25C and D. The Plate shows a porphyroclast largely replaced by a rim of fibrous chlorite enclosing plates of weakly ferroan calcite, about 200 μm across and with finely saw-toothed grain boundaries. Detailed examination in the SEM reveals that the chlorite is replacing actinolitic hornblende and the calcite includes small grains of quartz (Plate 5.25D). The concentric pattern of replacement could result from either nucleation effects or partial dissolution followed by void-infilling, or both. Chlorite-healed microfractures occur in close proximity to the replacement pseudomorph (Plate 5.25C).

5.9.5 Interpretation of Amygdales Etc

In the Langtang and Köfels frictionites (section 1.4.2) an unequivocal vesicular texture is observed (Scott and Drever, 1953; Erismann et al., 1977; Plate 5.26, this study). The vesicles are a testament to the exsolution of a vapour phase from the melt under conditions of low confining (lithostatic) pressure, estimated at 20 MPa by Masch et al (1985) for the Langtang slide. In both examples the vesicles are deformed and folded indicating that flowage of the melt continued after vesiculation.

Amygdaloidal pseudotachylytes have been described from at least four other localities in addition to the Ikertôq shear belt and the OHT (Table 5.22). The presence of vesicles in pseudotachylytes offers the possibility of estimating the depth of melt formation which may assist in determining other palaeoseismic source parameters during pseudotachylyte faulting (cf. Sibson, 1975; Grocott, 1981). Maddock et al (1986, in press - see enclosure) have examined in detail the physical conditions permitting vesiculation of pseudotachylyte melt. Using published data relating volatile (H_2O and CO_2) solubilities and vesicle abundances in basaltic and andesitic melts they were able to estimate likely depths for vesiculation of pseudotachylyte melt. Their model assumes that vesiculation occurs in response to a pressure drop associated with extensional injection veining of pseudotachylyte. For the amygdaloidal, Greenland pseudotachylyte described above, Maddock et al estimated a depth of generation (vesiculation) of 1.6 km. The precision of this estimate, a factor of 2-3, is limited largely by the quality of the solubility data. A similar depth may be calculated for the amygdaloidal hebridean pseudotachylyte described above, using their model together with the volatile data given in Table 6.1.

Allen (1979) has suggested that vesicles and feldspar microlites are mutually exclusive in pseudotachylytes and that both are related to depth of generation. The former suggestion is demonstrably not the case in the present hebridean example and in the Canadian pseudotachylytes described by Philpotts (1964) (see Table 5.22). The presence or absence of microlites should not therefore be used to infer the depth of generation of pseudotachylytes.

The mineralogy of the microfractures, the replacement pseudomorphs and the Greenland amygdales together with those described in the literature is markedly uniform. The common assemblage of quartz + epidote + chlorite + carbonate suggests mineral precipitation at low

PLATE 5.26 BSE micrograph of highly vesicular landslide frictionite from Langtang, Himalayas. Sample 11256.

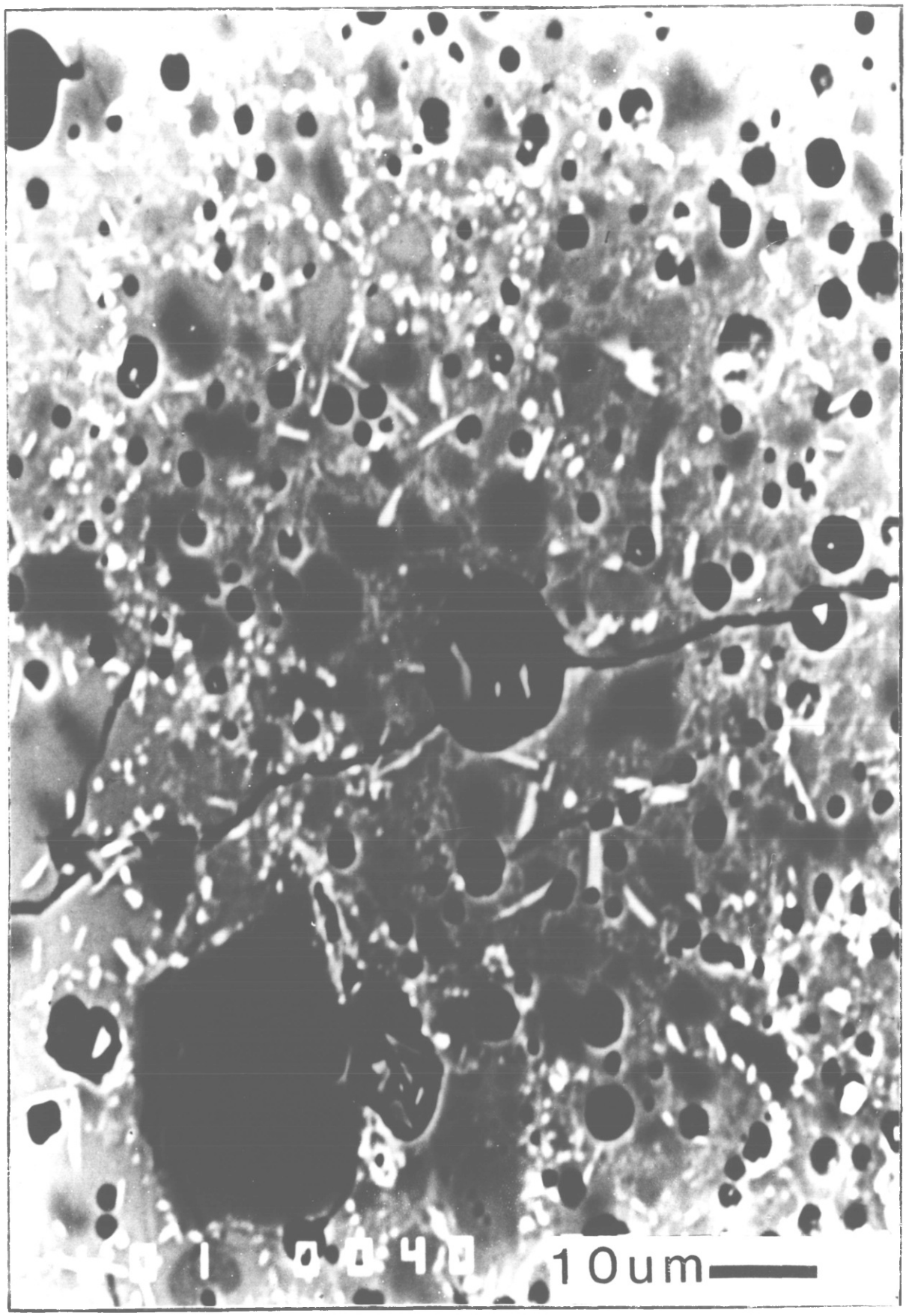

10um

TABLE 5.22 LITERATURE - REPORTED OCCURRENCES OF AMYGDALES AND SIMILAR CAVITIES IN PSEUDOTACHYLYTES

Reference	Locality	Description
Beckholmen (1982)	Sweden	irregular cavities to 3 mm, filled with drusy quartz and calcite; ore minerals in spherulitic pseudotachylyte zoned around cavities; interpreted as amygdales.
Bisschoff (1962)	Vredefort (S.Africa)	irregular or elliptical cavities parallel to flow banding filled with drusy calcite ± quartz ± chlorite ± chalcopyrite; interpreted as amygdales.
Grocott (1977)	Greenland	spherical or ellipsoidal, 100μm-5mm filled with drusy carbonate± quartz ± opaque; quartz or carbonate first crystallized, magnetite last; up to 25 modal % of glassy and microlitic pseudotachylytes; interpreted as amygdales.
Nockolds (1944)	Antarctica	irregular or elliptical cavities filled with calcite ± chlorite ± epidote ± quartz; microfractures containing similar phases may connect cavities; interpreted as amygdales.
Philpotts (1964)	Canada	spherical to slightly irregular 50μm, filled with quartz ± calcite ± magnetite ± pyrite; pyrite in microfractures; magnetite first; up to 20 modal % of microlitic pseudotachylyte; vesicle filling attributed to vapour precipitate enriched in H_2O, CO_2, Fe and S; derived from pseudotachylyte melt; rims of feldspar porphyroclasts locally replaced by carbonate.

P and T - below that of greenschist facies metamorphism (Winkler, 1967). The frequent presence of carbonate also suggests that the cavity filling took place under conditions of moderate partial pressure of CO_2 - favouring breakdown of Ca-silicates to calcite plus an aluminous phase (i.e. chlorite). Microprobe analyses demonstrate chemical heterogeneity (i.e. disequilibrium) between, for example, chlorite in a replacement pseudomorph and associated microfractures in the same thin section (Appendix A3). For this reason it is difficult to write precise reactions describing the alteration/replacement/cavity-filling process. However, for the replacement pseudomorph described above an appropriate end-member reaction involving the phases present is:-

$$\text{Actinolite} + \text{clinozoisite} + CO_2 + H_2O = \text{calcite} + \text{chlorite} + \text{quartz} \quad (5.19)$$

with reaction tending to the r.h.s. favoured by moderate to high P_{H2O} and P_{CO2}.

Summarizing, the mineralogy indicates that a low temperature (<200 °C) assemblage was precipitated from a hydrous fluid, locally or temporally enriched in CO_2 and containing solutes Si, Al, Ca, K, Fe, Mg and S. The timing of vesicle infilling and origin of the infilling fluids is difficult to ascertain. Philpotts (1964) suggested that pseudotachylyte amygdale minerals might be precipitated directly from vapour phases exsolved from the pseudotachylyte melt. This possibility seems unlikely in the present examples because of the mineralogy of the amygdales. Further, it is clear that in at least some cases vesicle infilling was related to healing of the microfractures (e.g. Plate 5.25A and B), and the sub-drusy habit is good evidence that the amygdales contain a primary assemblage precipitated in vesicle void space. In addition to the microfractures, the vesicles themselves may have locally provided a gross porosity allowing ingress of fluids.

In contrast to the mineralogy discussed above, the mineralogy of the Hebridean pseudotachylyte amygdales constitute a much higher temperature assemblage, similar to that found in greenschist facies metavolcanics (e.g. Morrison, 1979; Studemeister, 1983). The assemblage (albite+) actinolite + epidote + quartz + sphene is indicative of greenschist facies conditions with T > 350 °C and P > 2 kb (Winkler, 1967). Further, the absence of carbonate suggests a low partial pressure of CO2. The chemistry and mineralogy of these

amygdales suggests that the phases were precipitated from a hydrous fluid enriched in Si, K, Ca, Ti, Al and Fe, with lesser amounts of Mg, S, P, Na, Ce and La. The LREE content of the epidote confirms that short range LREE mobility at least is possible in a hydrous fluid at low metamorphic grade (cf. Hellman et al., 1977; Nystrom, 1984), and that the LREE's are preferentially partitioned into epidote rather than sphene. The minimal compositional variation between analyses of the same phase suggests that a reasonable degree of equilibrium was obtained. The extreme modal variation is perhaps due to different times of filling and kinetic nucleation effects.

As with the amygdales and filled cavities described above, this mineral assemblage appears to be restricted to structures with suitable mechanical pathways allowing fluid ingress. Thus the plagioclase microlites (An_{25}-An_{40}) and porphyroclasts (An_{25}) show no sign of albitization or adularization. Possible mechanical processes and fluid pathways associated with cavity-filling are summarized in Fig. 5.20.

A problem arises with the Hebridean pseudotachylytes as to how vesicles, stated above to be likely to have formed at depths <2 km, may contain a greenschist facies mineral assemblage implying T > 350 °C. A palaeogeothermal gradient of 175 °C.km^{-1} is unlikely even in a potentially shear-heated thrust fault environment! An explanation for this may lie in the geological setting of these particular pseudotachylytes.

It was noted earlier (section 4.4.2) that the sub-vertical quasiconglomerate vein systems at Ruhba Ardvule, in which the amygdales occur, represent the earliest stages of pseudotachylyte generation, followed by E to W directed low angle thrusting. Sibson (1977a) has estimated a finite vertical component of thrust-sense movement across the main Outer Hebrides Thrust of 4.2 ± 2.1 km. Ignoring the subaerial erosion that must accompany thrusting, it is possible that the early amygdaloidal pseudotachylytes were buried by a substantial thrust pile, with higher P-T conditions achieved through a combination of burial and shear-heating.

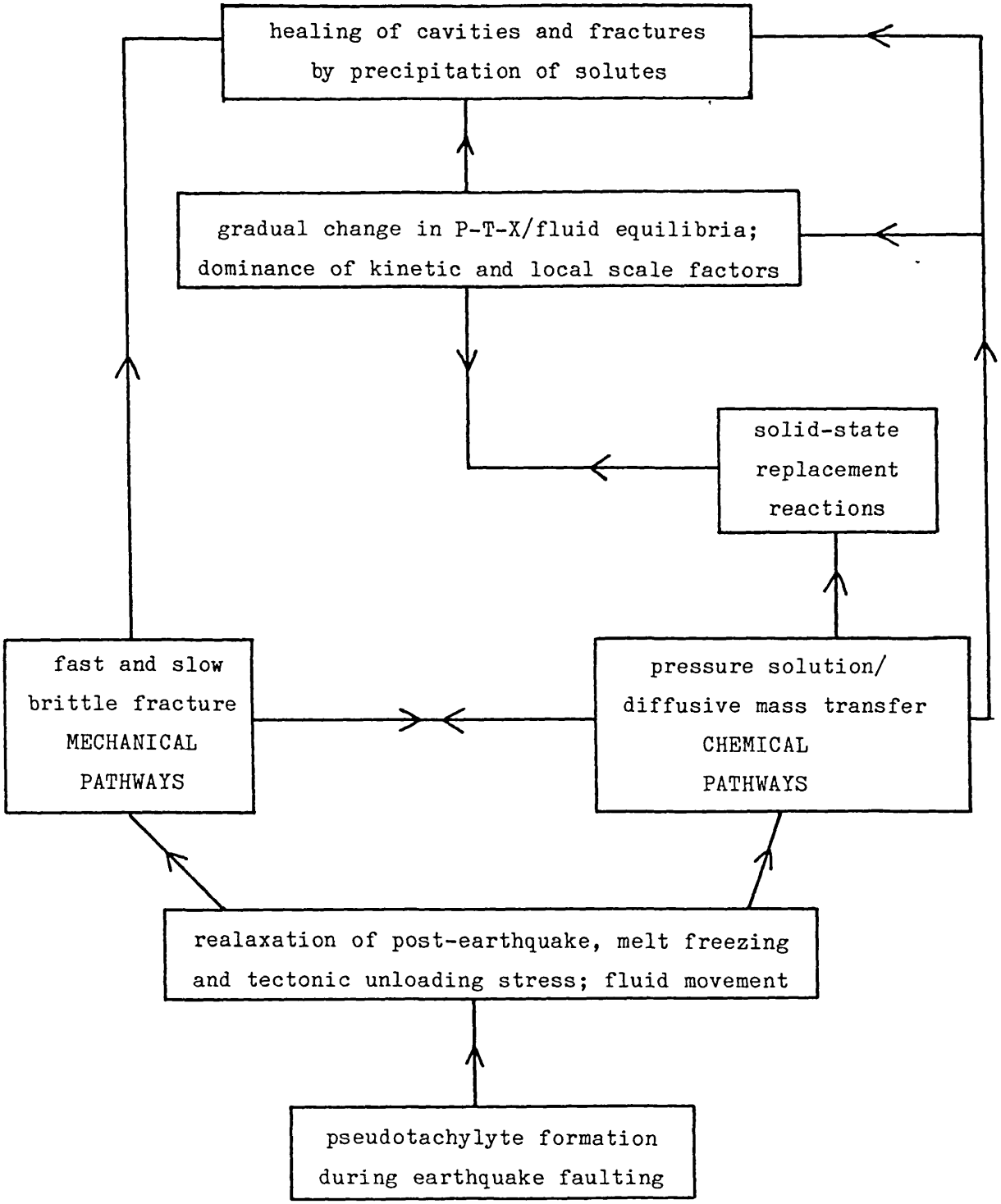


FIGURE 5.20 Flow diagram illustrating some of the factors affecting the healing of cavities and solid state reactions involving low-temperature phases.

CHAPTER 6 A CRITICAL INTERPRETATION OF PSEUDOTACHYLYTE GEOCHEMISTRY

6.1 Preamble

The purpose of this chapter is 2-fold. First, to present new analytical results from this study. Secondly, to interpret these results within constraints provided by a critical assessment of the methodologies adopted - including field, laboratory and theoretical approaches - in this, and in published studies. It is hoped to demonstrate that whole-rock chemical analyses of pseudotachylytes cannot be interpreted satisfactorily in isolation, e.g. in terms of igneous or metamorphic geochemistry/petrology, but that the analytical data must be combined with field and petrographic observations in an attempt to unravel the geochemical story of these mechanically-generated rocks.

6.2 Introduction

Whole rock geochemical analysis of pseudotachylytes and their host-rocks has been carried out both in this and in previous studies (e.g. Shand, 1916; Salop, 1945; Dietrichson, 1953; Philpotts, 1964; Ermanovics et al., 1972; Sibson, 1975) by conventional bulk analysis (including classical, AA, XRF, and ICP methods) and by raster or defocussed electron beam microprobe analysis. Such analyses have been directed towards answering 3 questions pertinent to pseudotachylyte genesis:-

(i) what is the overall geochemical relationship between pseudotachylytes and their host-rocks? (i.e. are pseudotachylytes derived from immediately local rocks and is their any evidence for metasomatic alteration?);
(ii) what is the igneous mechanism of melting? (i.e. does partial or total or some other type of melting occur?);
(iii) what information does the geochemistry of pseudotachylytes provide about the mechanical processes involved during their formation? (this question has largely been ignored in published studies).

Published chemical analyses of pseudotachylytes and their host rocks have led to radically divergent hypotheses in answer to these questions. For example, Bhattacharjee (1963, p.51) interpreted his analyses as indicating selective fusion of "...competent acid gneiss layers rather than incompetent hornblende schist...", whereas Philpotts and Miller (1963, p.339) inferred from their analyses that "...hornblende and biotite ... have decomposed and been assimilated by the liquid much more readily than ... quartz and feldspar..." Hypotheses put forward in answer to the second question vary from total fusion (Masch, 1974; Sibson, 1975) to generation of a near-minimum melt composition at 655 - 685°C and PH_2O = 500 - 700 MPa (Sinha-Roy, 1981). Although a unified theory of pseudotachylyte formation/melting is perhaps not to be anticipated, the contradictions in these published hypotheses seem excessive. These examples have been chosen specifically to highlight the problems and limitations of interpreting whole rock analyses of pseudotachylytes. Four of these problems will be considered here, whilst others are examined in later sections.

1) The Clast Problem. Questions (i) and (iii) above may be addressed by comparative geochemical analysis of host-rocks and the assemblage of pseudotachylyte matrix plus clasts. To determine the igneous mechanism of melting analysis of the pseudotachylyte matrix without clasts is necessary. The latter requirement was appreciated during the earliest geochemical studies on pseudotachylytes (e.g. Shand, 1916). Removal of the clast component has been attempted directly by handpicking (e.g. Shand, ibid.) and heavy-liquid separation (e.g. Philpotts, 1964), and indirectly by subtraction of a point counted clast fraction from the chemical analysis (Sibson, 1975). Because of the small clast size and common occurrence of the same mineral phase (e.g. plagioclase) both as clasts and in the pseudotachylyte matrix, none of these methods can be considered wholly satisfactory. EMP raster/defocussed beam analysis of clast-free pseudotachylyte matrix, first attempted by Ermanovics et al (1972), seems to be the best technique adopted so far. However, because of the physics of electron beam/sample interaction (and other factors) this method should be restricted to ultra fine grained (<5 um) pseudotachylytes (cf. Wallace, 1976; Schwarzman et al., 1983).

In the present study it was recognized that different analytical techniques could be applied to the different problems posed in the

questions above.

2) IV vs. FV Analyses. Sibson's (1975) classification of FV-IV relationships (Fig. 3.5) allows a simple distinction to be made between the immediate host or wall rocks and the protolith from which the pseudotachylyte was generated. (Note: using this terminology the protolith and host-rock would be identical for a FV but need not be for an IV.) Failure to identify such relationships will clearly lead to problems when interpreting geochemical data; an example of this is given in section 6.5.2.

3) Equilibrium vs. Kinetically Controlled Processes. In spite of abundant petrographic evidence for disequilibrium melting and crystallization in fault-generated pseudotachylytes (e.g. chapter 5, this study), a number of workers have made a priori assumptions of equilibrium to interpret their data (cf. Dietrichson, 1953; Wallace, 1976; Sinha-Roy, 1981). In a general sense, whilst providing a framework for kinetic interpretations, strict application of petrologic equilibria, in most cases, tends to overestimate likely confining pressures ($PH_2O = P_{total}$) and underestimate likely temperatures involved during pseudotachylyte melting (cf. Sinha-Roy,1981).

4) Comparative Geochemistry: Composition-Volume Relationships. A common approach to the study of transformational reactions, such as serpentinization or mylonitisation, is to compare the geochemistry of the protolith with that of the transformation product. A complete chemical description of a transformational reaction requires accurate and precise analyses of protolith and product, and in addition, a quantitative description of any volume and density changes resulting from the transformation (Gresens, 1966). This mass balance approach has been applied to fault-rocks by only a few workers (e.g. Kerrich et al., 1980; Brodie, 1981; F. Wigley, 1984 unpubl. data). Even using mass balance calculations, a priori assumptions concerning volume, density and element (component) mobility must be made (Gresens, 1966).

The transformation of gneissic rock to pseudotachylyte is believed to be approximately isochemical, isovolumetric and at constant density for the following reasons:-

(i) small volume increases during melting are probably balanced by

volume changes of similar magnitude but opposite sign during crystallization;
(ii) density measurements of Hebridean gneisses and pseudotachylytes given by Sibson (1977a) suggest that only small and unsystematic variations exist between the 2 rock types;
(iii) Rb/Sr isotopic data for one FV/host-rock pair support the idea of a closed system bulk transformation reaction (Appendix A1);
(iv) there appears to be no evidence for large scale metasomatism or hydration of pseudotachylyte; although it is clear from the next section that a small degree of hydration occurs.

6.3 The Relative Volatile Content of Pseudotachylytes and Their Host-Rocks

The H_2O contents of 8 host-rock/vein pairs determined by C-H-N analysis using a Perkin Elmer elemental analyser are plotted in Fig. 6.1. A number of observations may be made from this diagram:-

(i) the pseudotachylytes are generally more hydrated than their host rocks (note: for sample series G1A, additional chemical data suggests that the actual protolith may be less hydrated than the analysed sample);
(ii) the maximum absolute increase in H_2O^+ content from host to vein is around 1%, and the greatest relative increase in H_2O^+ content (by a factor of 3) is shown by the sample whose protolith has the lowest H_2O^+ content;
(iii) there is a positive correlation between the content of H_2O^+ in the host-rock and that in the pseudotachylyte;
(iv) the H_2O^+ contents of the host-rock samples are broadly commensurate with the modal contents of hydrous minerals;
(v) the high H_2O^+ content of sample GQ1AP (2.5 wt.%) correlates well in a qualitative sense with the high chlorite content of this pseudotachylyte (section 5.4); apart from this example, no significant correlation can be made, from this admittedly small data set, between pseudotachylyte petrography and H_2O^+ content.

These observations indicate that the assemblage pseudotachylyte matrix plus clasts is, in general, only slightly more hydrated than the host-rock from which it is derived. This finding, combined with the evident low porosity and permeability of pseudotachylytes,

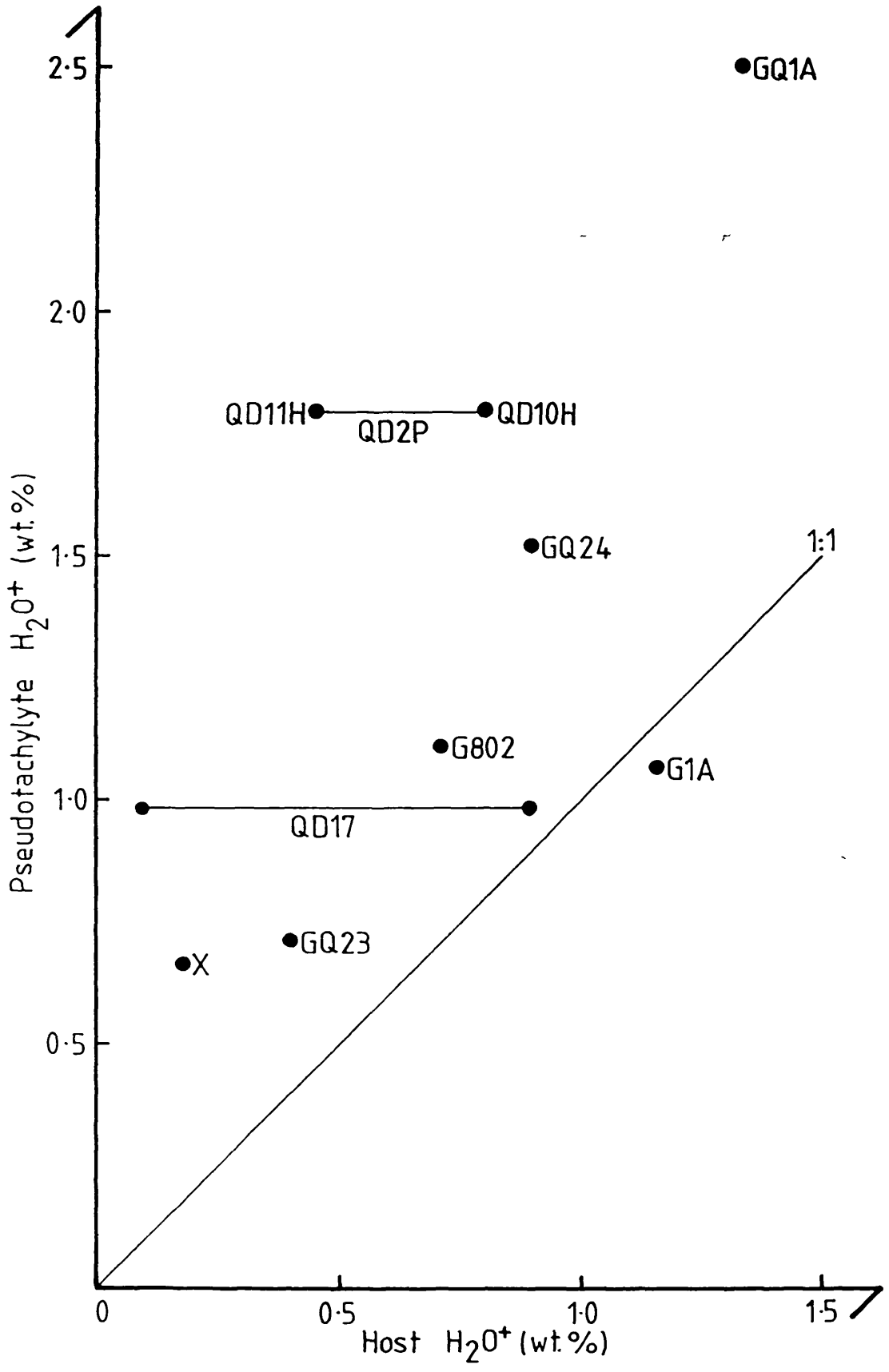


FIGURE 6.1 Plot of H_2O^+ content in pseudotachylyte vs H_2O^+ content in host-rock. Tie lines join host-rock values where pseudotachylyte generated at contact between 2 host-rocks. Sample series as annotated.

suggests that unlike many other brittle-deformed fault-rocks pseudotachylytes do not act as conduits for fluid flow.

The CO_2 contents, simultaneously determined in the same host-rock/vein pairs, are plotted in Fig. 6.2a. Both host-rock and pseudotachylyte contain very little CO_2, but the figure indicates that the latter tends to contain slightly more than the former. The CO_2 is probably largely contained in small amounts of carbonate sometimes visible as an alteration/cavity-filling phase (section 5.9.).

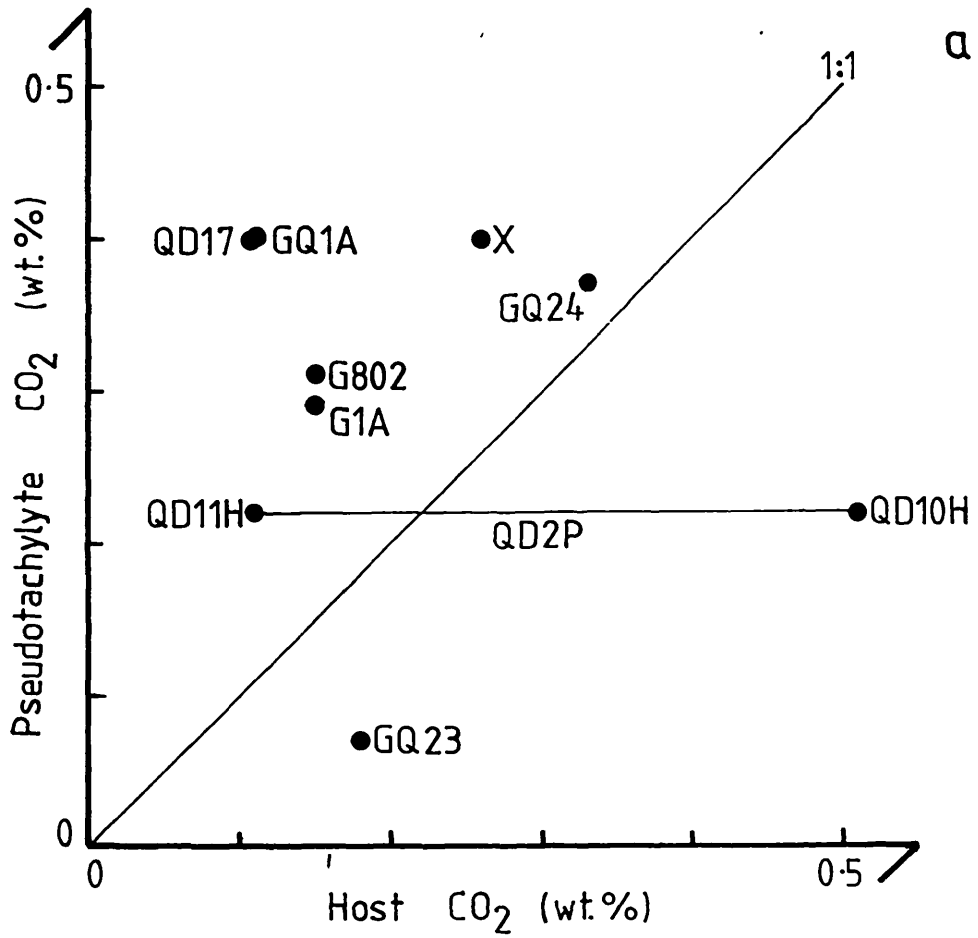
Two sets of analyses of CO_2 in host-rock/vein pairs have been published previously and are plotted in Fig. 6.2b. Philpotts (1964) found more CO_2 in crystalline than glassy pseudotachylyte derived from the same host-rock. In the crystalline vein he ascribed the CO_2 to carbonate replacing feldspar porphyroclasts, but considered the smaller amounts of CO_2 in the glassy vein to be actually dissolved in the glass.

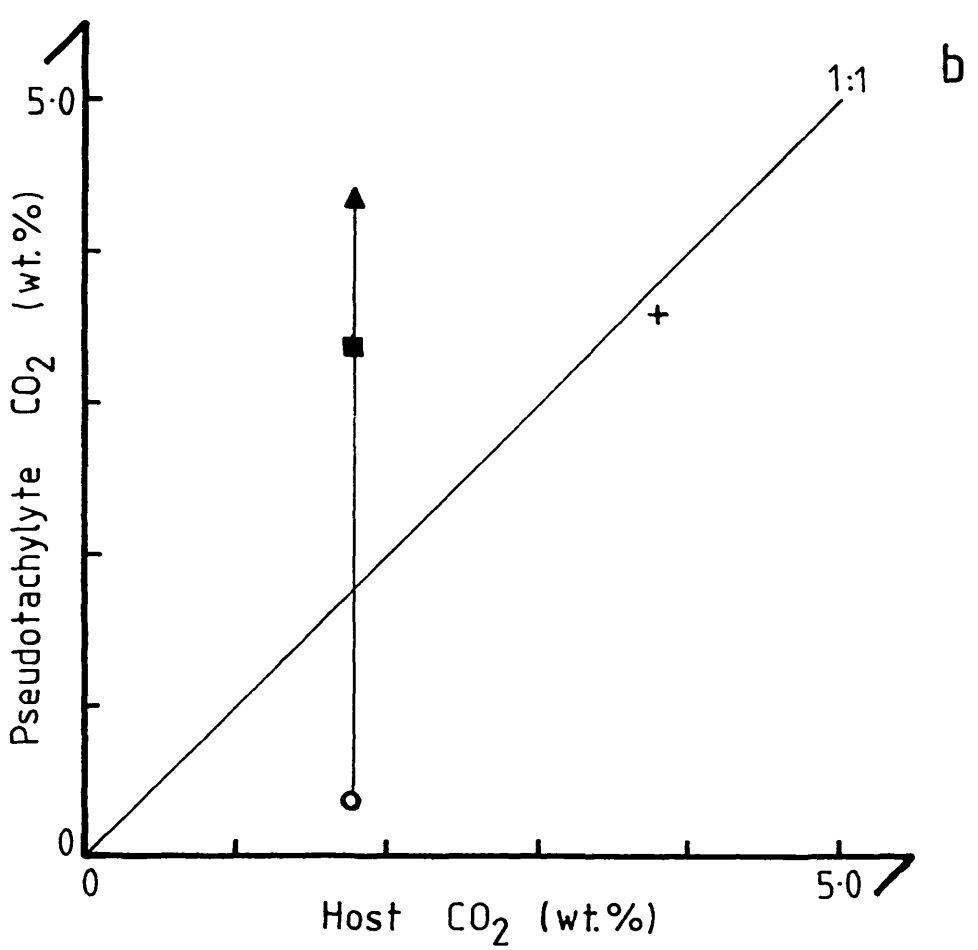
In addition to the small number of samples in which H_2O^+ and CO_2 has been determined, the loss on ignition (LOI) was measured for the same and additional samples. LOI was determined as the percentage weight change of dry rock powder after ignition at 950 °C for half an hour. The LOI is not a direct measurement of the volatile content but is a compound quantity involving:-

(i) weight loss due to loss of H_2O^+, CO_2 (possibly S, and F and Cl which are present only in trivial amounts), principally from phyllosilicates and to a lesser extent amphibole (differential gravimetric analysis of amphibole from Outer Hebrides gneisses demonstrates that amphibole dehydration and breakdown is incomplete at 950 C (F. Wigley, pers. comm., 1984));
(ii) weight gain due to partial oxidation of FeO to Fe_2O_3, greatest in rocks with high total iron and/or pyrite (this is apparent in samples QD18H, QD18P and QD24P which are pyritiferous and contain 16 wt.% Fe_2O_3*, and which gained weight during ignition (Appendix A4)).

Recalculation of the volatile content from the LOI values would require additional determinations of FeO, total iron and S before and after ignition. Comparison of the H_2O^+, CO_2 and LOI values for the 8 host-rock/vein pairs indicates that the increase in volatile content from host to pseudotachylyte is also reflected in increasing LOI

FIGURE 6.2 Plot of CO_2 content in pseudotachylyte vs CO_2 content in host-rock.
(a) this study, sample series as annotated;
(b) data from literature: ▲ = crystalline pseudotachylyte, ■ = partially glassy pseudotachylte, O = glassy pseudotachylyte in monzonite (Philpotts, 1964); + = pseudotachylyte in schist (Bryn, 1959).


a
1:1
0·5
QD17
GQ1A
X
GQ24
G802
G1A
QD11H
QD2P
QD10H
GQ23
0
0·5
Pseudotachylyte CO_2 (wt.%)
Host CO_2 (wt.%)


b
1:1
5·0
0
5·0
Pseudotachylyte CO_2 (wt.%)
Host CO_2 (wt.%)

values, irrespective of the total iron content of the samples (Table 6.1). On average for the 18 samples analyzed, the LOI values underestimate the measured volatile content by a factor of slightly less than 2 with a maximum absolute difference of just over 1 wt.%. The difference between the measured LOI value and the measured volatile content increases broadly with increasing $Fe_2O_3^*$, but a less than perfect correlation may indicate a mineralogical control on oxidation during ignition and devolatilization during C-H-N analysis. For 7 of the host-rock/vein pairs (selected on field criteria) the average increase from host to pseudotachylyte is 0.84 and 0.63 wt.% for volatile content and LOI respectively.

In summary, it appears from the data of Table 6.1 that although the LOI significantly underestimates the true volatile content of these rocks (especially when $Fe_2O_3^* > 5$ wt.%) the trend of increasing volatile content from host to pseudotachylyte is mirrored by the LOI values in direction (sample G1A excepted) and not grossly dissimilar in magnitude.

On this basis, additional measured (this study) and previously published LOI values for host-rock/vein pairs are plotted in Fig. 6.3. The general trend of these data is also consistent with the proposal that pseudotachylytes are slightly more hydrated (or at least have a higher volatile content) than their host-rocks. Again, no consistent variation in LOI with pseudotachylyte petrography can be discerned from this data. Six plagioclase microlitic pseudotachylytes, for which host-rock analyses are not available (due to ambiguous field relationships) show a large variation in LOI (0.15 - 0.94 wt.%) independant of their $Fe_2O_3^*$ content (4.47 - 9.26 wt.%).

Finally, it should be stressed that the (measured and inferred) increase in degree of hydration from host-rock to vein refers to the assemblage pseudotachylyte matrix plus clasts and not the matrix (i.e. crystallized or devitrified melt) in isolation.

The oxide totals of EMP analyses provide a rough estimate of the volatile content of pseudotachylyte matrix (mainly devitrified glass in the phyllosilicate-spherulitic types). Totals range from about 94% to 99%, the lower figure being broadly consistent with the expected stoichiometric water content of micas.

6.4 Oxidation State of Pseudotachylyte Rock and Melt

Thirty-eight samples of gneiss and pseudotachylyte were analyzed

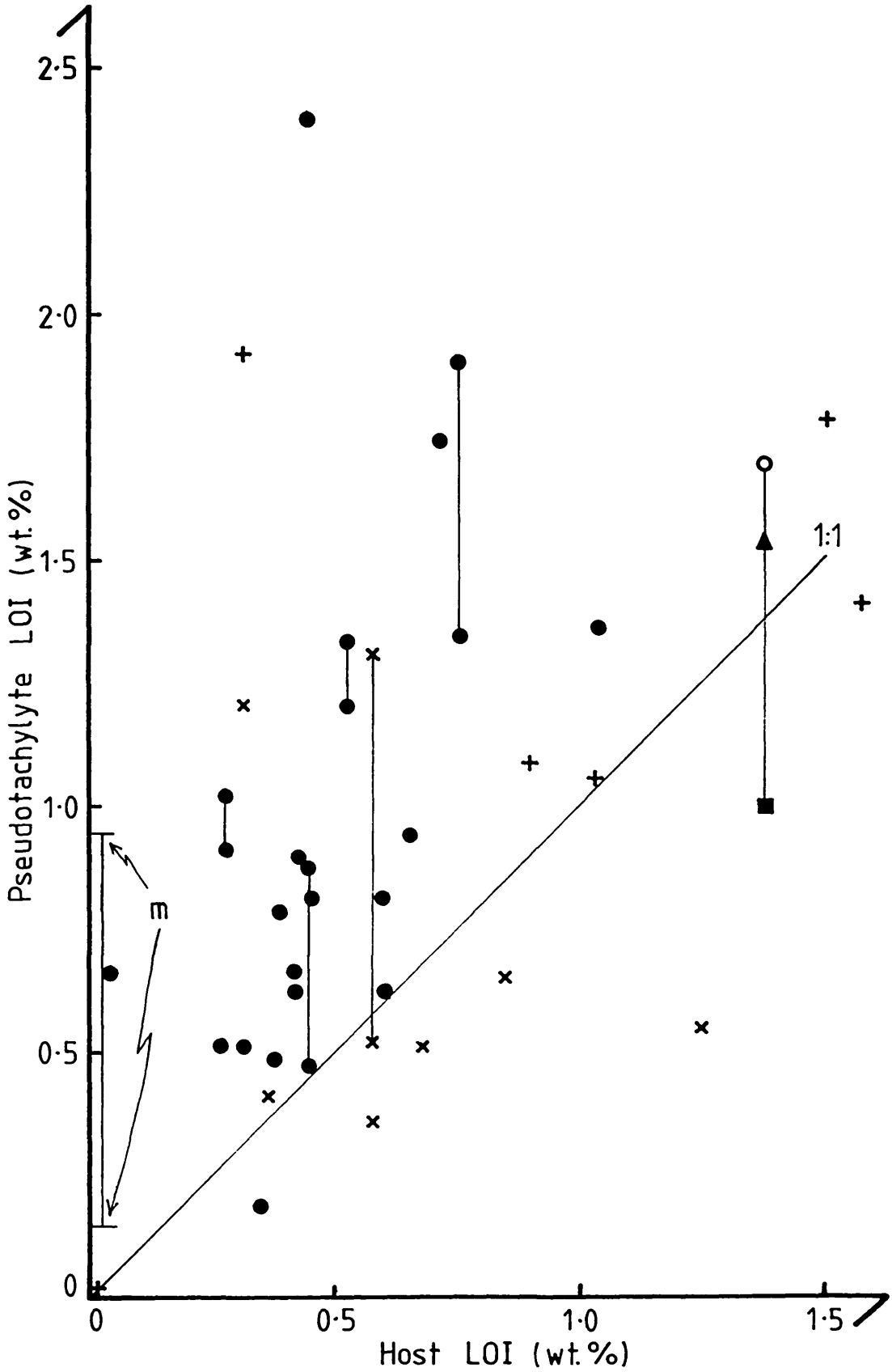
TABLE 6.1 COMPARISON OF H_2O^+, CO_2, LOI and Fe_2O_3* IN PSEUDOTACHYLYTES AND THEIR HOST ROCKS

Sample No.	H_2O^+ wt.%	CO_2 wt.%	$H_2O^+ + CO_2$ wt.%	LOI wt.%	Fe_2O_3* wt.%
X/H	0.18	0.26	0.44	0.42	3.85
X/P	0.65	0.40	1.05	0.62	4.26
QQ23H	0.40	0.18	0.58	0.27	6.07
GQ23P	0.71	0.07	0.78	0.14	13.94
G802H	0.71	0.15	0.86	0.66	7.19
G802P	1.1	0.31	1.41	0.94	6.94
GQ24H	0.89	0.33	1.22	0.43	14.94
GQ24P	1.52	0.37	1.89	0.89	14.62
GQ1AH	1.34	0.11	1.45	0.72	14.63
GQ1AP	2.50	0.40	2.90	1.74	14.88
G1AH	1.16	0.15	1.31	1.04	14.16
G1AP	1.07	0.29	1.36	1.36	14.39
QD17MH	0.89	0.11	1.00	0.27	16.75
QD17FH	0.09	0.11	0.20	0.32	2.09
QD17P	0.98	0.40	1.38	0.45	12.69
QD11	0.45	0.11	0.56	0.82	2.91
QD10	0.80	0.51	1.31	0.72	13.81
QD2P	1.79	0.22	2.01	1.91	13.31

Note: Fe_2O_3 is total iron as determined by XRF

FIGURE 6.3 Plot of weight loss on ignition (LOI) of pseudotachylyte vs LOI of host-rock.

● = this study, tie lines join analyses of different pseudotachylyte veins generated in the same host-rock; m = range of LOI values for 6 plagioclase microlitic pseudotachylytes (host-rocks unknown), this study; + = data from Bryn (1959), Masch (1974), Salop (1945), Sinha-Roy (1981) and Wenk and Weiss (1982); ■, ▲ and O = data from Philpotts (1964) annotated as for Fig. 6.2; x = data for Vredefort pseudotachylytes from Shand (1916), Willemse (1937) and Wilshire (1971); note, certain literature values of LOI may in fact be measured H_2O^+.


2·5
2·0
1·5
1·0
0·5
0
Pseudotachylyte LOI (wt.%)
m
1:1
0
0·5
1·0
1·5
Host LOI (wt.%)

titometrically for FeO (Appendix A5). Of the 38 analyses, almost one third yielded wet chemical FeO values expressed as Fe_2O_3 greater than or equal to the $Fe_2O_3^*$ values determined by XRF. This is attributable to the presence of sulphide (principally pyrite) in the samples; and brought about by the reducing action of S during the titration. In the absence of sulfur analyses all of the data are considered suspect. For example, a suite of samples taken from the same FV in homogeneous paragneiss host with a FeO/Fe_2O_3 ratio of 41, the associated pseudotachylyte produced FeO/Fe_2O_3 ratios from 9.48 to 31.8 (Fig. 6.4). The variation probably reflects real differences in the FeO/Fe_2O_3 ratio, variation in the amount of sulphide in the analysed samples, and imperfect acid-digestion of the samples (XRD analysis of insoluble residues present in some samples yielded ambiguous results).

Published values of FeO/Fe_2O_3 ratios in host-rock/vein pairs are also shown in Fig. 6.4. Using part of this data set and additional FeO/Fe_2O_3 values of Vredefort samples given in Shand (1916) and Willemse (1938), Philpotts (1964) concluded that pseudotachylytes are more oxidized than their host-rocks.

Qualitatively, the petrography of many pseudotachylytes suggests that they are more oxidized than their host-rocks. This is particularly so for magnetite-rich pseudotachylytes generated in biotite-bearing gneisses.

In contrast to the above data, partial analyses of glassy frictionite from Langtang, published by Scott and Drever (1953) yield very high values of FeO/Fe_2O_3 (30.4 and 76.5, with $Fe_2O_3^*$ = 3.44 and 3.45 wt.% respectively); unfortunately, analyses of the host-rocks are not given so direct comparison is not possible. Melting of biotite is considered important in the genesis of these frictionites (derived from granitic precursors) but exsolution of magnetite from the biotite is rare (Scott and Drever, ibid., p.129). It appears that the iron may have entered the frictionite melt and remained in the glass, largely in the ferrous state. By analogy with dry-fused borehole arkoses (Bowen and Arousseau, 1932) and taking in to account the chemical and petrographic data, Scott and Drever (ibid.) suggested that the frictionite melt was fluxed by Fe^{2+} and OH^- derived from the selective breakdown of biotite. These ideas have been extended to the generation of pseudotachylyte melt by a number of authors (e.g. Allen,1979).

However, it has already been noted (section 5.8) that petrographic evidence exists for the oxidation of biotite yielding magnetite, a reaction which consumes oxygen and will therefore release

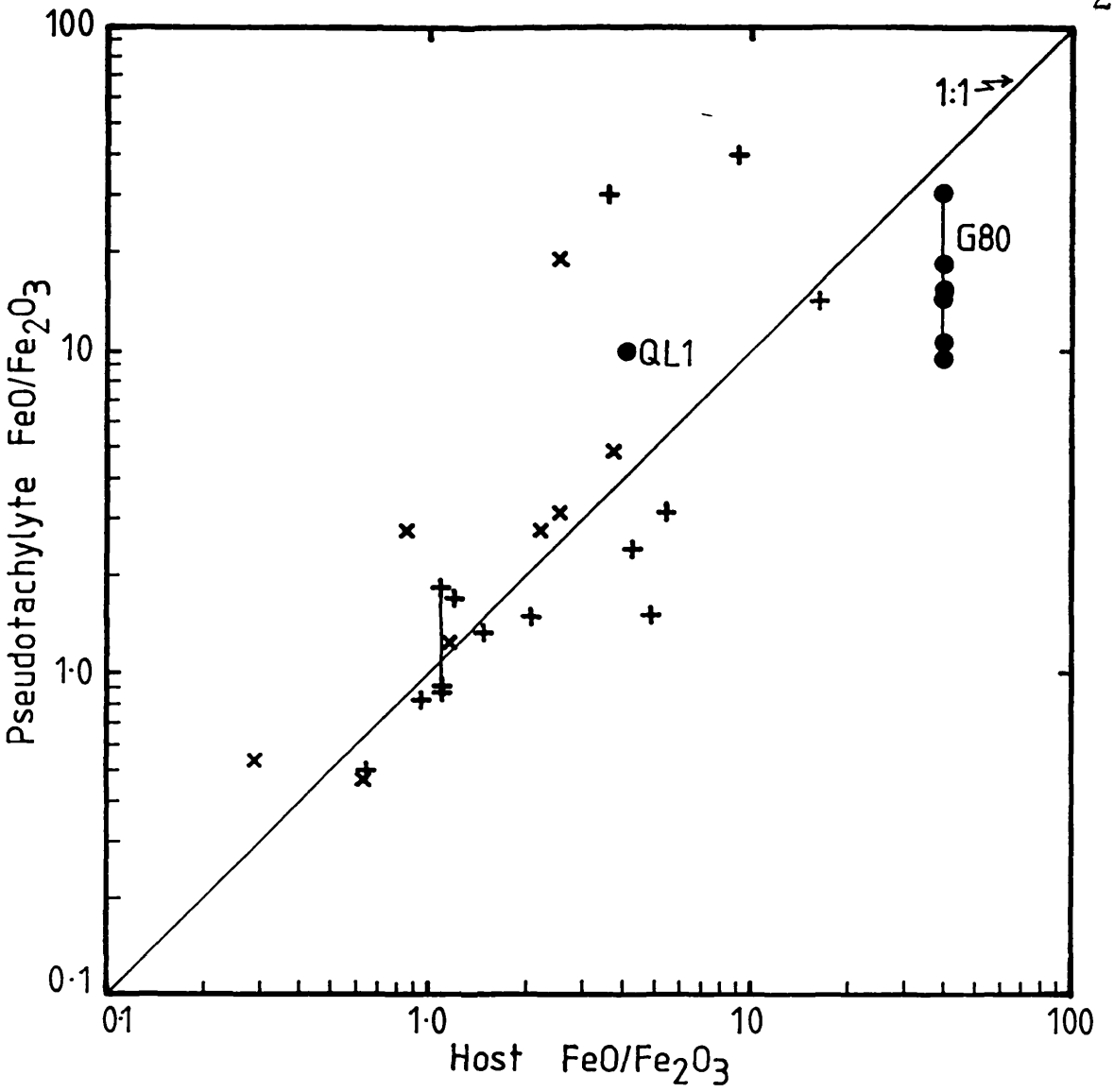


FIGURE 6.4 Plot of FeO/Fe_2O_3 in pseudotachylyte vs FeO/Fe_2O_3 in host-rock. Tie lines join samples with common host rock. ● = this study; + and x as for Fig. 6.3.

protons rather than OH^- groups. The Fe^{3+} formed by this reaction may enter the melt as a network former (cf. likely network modifying behaviour of Fe^{2+}) or remain as magnetite. In either case the iron is unlikely to flux the pseudotachylyte melt.

More recently Masch et al (1985, Table 2, p.152) have determined FeO/Fe_2O_3 values of 6.78 and 5.11 in brown and white Langtang frictionite respectively.

The factors responsible for any differences in oxidation state between glassy frictionite and holocrystalline/devitrified pseudotachylyte, if they exist, are not obvious but are worthy of further investigation. (FeO/Fe_2O_3 data for the Köfels frictionites are not yet available.)

6.5 XRF Whole-rock Analysis: Comparative Geochemistry of Pseudotachylyte and Host-rocks

More than 110 rock samples were analyzed by XRF to determine the major, minor and trace element compositions in an attempt to answer the questions posed in section 6.2. Specifically, the analyses were made to ascertain the similarities and differences in composition betweeen the host-rocks and pseudotachylyte veins, and to allow interpretation of the differences. The composition of the pseudotachylyte may be considered in terms of the contribution from differing host-rocks and their varying mineralogy. This 'mechanical mixing' (no implication of igneous processes is inferred at this stage) approach has been applied with some success to cataclasites from the San Andreas Fault zone (Anderson et al., 1983) and to Vredefort Dome pseudotachylytes (Schwarzman et al., 1983), but otherwise has not been applied to pseudotachylytes in general. As indicated in section 6.2, previous work has largely concentrated on attempts to deduce melting mechanisms/processes from whole-rock analyses of pseudotachylytes and has tended to ignore mechanical mixing aspects, apart from general observations on the often-observed similarity in composition between pseudotachylytes and their host-rocks.

The concentrations of 10 major and minor oxides and 10 trace elements in 25 pseudotachylytes and 25 host-rocks are presented in comparative form in Fig.s 6.5 to 6.12, 6.15 and 6.16 (additional analyses, not plotted in the figures, are given in Appendix A4). To minimize the dilution effect due to varying volatile content (i.e.

between host and vein samples) the analyses were recast to 100% following subtraction of H_2O^- and LOI. The data of Table 6.1 suggest that the remaining errors due to the dilution effect should be small. Assumptions concerning constant density and volume between pseudotachylyte and protolith have already been discussed (section 6.2).

Two further cautionary notes are appropriate. First, it should be realized that whereas large masses (>1 kg) of host rock were available for analysis (allowing preparation of a homogeneous sample split), the amount of pseudotachylyte vein material was typically less than 50 g. Large clasts (>0.5 cm) only were removed from the pseudotachylyte at the sawing or jaw-crushing stage of preparation. Second, whilst the method of presentation of geochemical data in Fig.s 6.5 to 6.12, 6.15 and 6.16 is well-suited for comparative purposes, attention is drawn to the analytical precision data given in Appendix A2 and the error bars given in some of the plots.

The pseudotachylytes and their host-rocks, from all the areas of this study, occupy a broad compositional field from granite to (ferro-) basalt.

Prior to this study, the only trace element study of pseudotachylytes and their host-rocks was performed by Wilshire (1971) on Vredefort Dome material. He was unable to recognize any systematic variation or make any sensible interpretation of the data.

6.5.1 FV - Single Host-rock Relationships

The oxide and element concentrations for 18 host-rock/vein pairs are compared in Fig.s 6.5 to 6.12. Overall, the diagrams demonstrate a rather close correspondance between the composition of the pseudotachylytes and their host-rocks, a feature which has been noted before (e.g. Shand, 1916; Philpotts, 1964; Ermanovics et al., 1972). The diagrams also illustrate expected major/trace element correlations which are referable to the mineralogy of the rock samples. Thus, for example, high K_2O and Rb contents are present in samples rich in biotite (e.g. G80 sample series, Fig. 6.5), and high TiO_2 and V in samples rich in sphene or iron-titanium oxides (e.g. GQ1A sample series, Fig. 6.10). However, by combining field and petrographic observations with the comparative chemical analyses it is possible to make more subtle and detailed interpretations of the chemical relationship between host-rock and pseudotachylyte.

FIGURE 6.5 Plot showing normalized chemical composition of pseudotachylytes and their host rocks. Major and minor elements expressed as wt.% oxides, total iron as Fe_2O_3, and trace elements (V - Y) as ppm.

———— = pseudotachylyte;

———— = 'mafic' host-rock (< 55 wt.% SiO_2);

-------- = 'felsic' host-rock (> 55 wt.% SiO_2);

..... = no data or below detection limit for element concerned;

G801P, etc. = sample number;

note factor at top of diagram by which each oxide or element value is multiplied, and error bars (showing analytical precision) where relevant.

FIGURES 6.6, 6.7, 6.8, 6.9, 6.10, 6.11 and 6.12 For explanation see caption to Fig. 6.5 and text.

Fig. 6.5

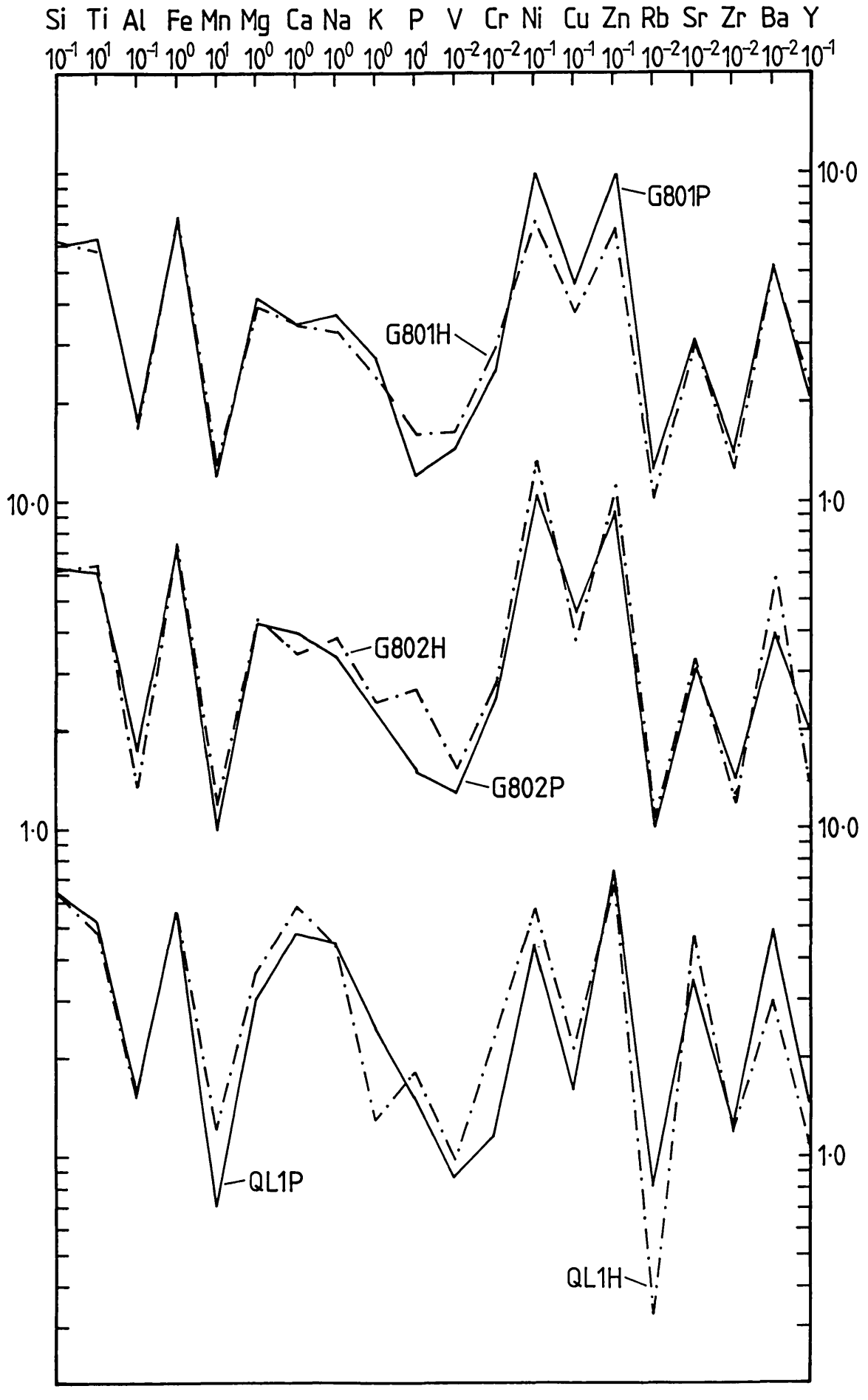

Si Ti Al Fe Mn Mg Ca Na K P V Cr Ni Cu Zn Rb Sr Zr Ba Y
10·0
1·0
G801P
G801H
G802H
G802P
QL1P
QL1H

Fig. 6.6

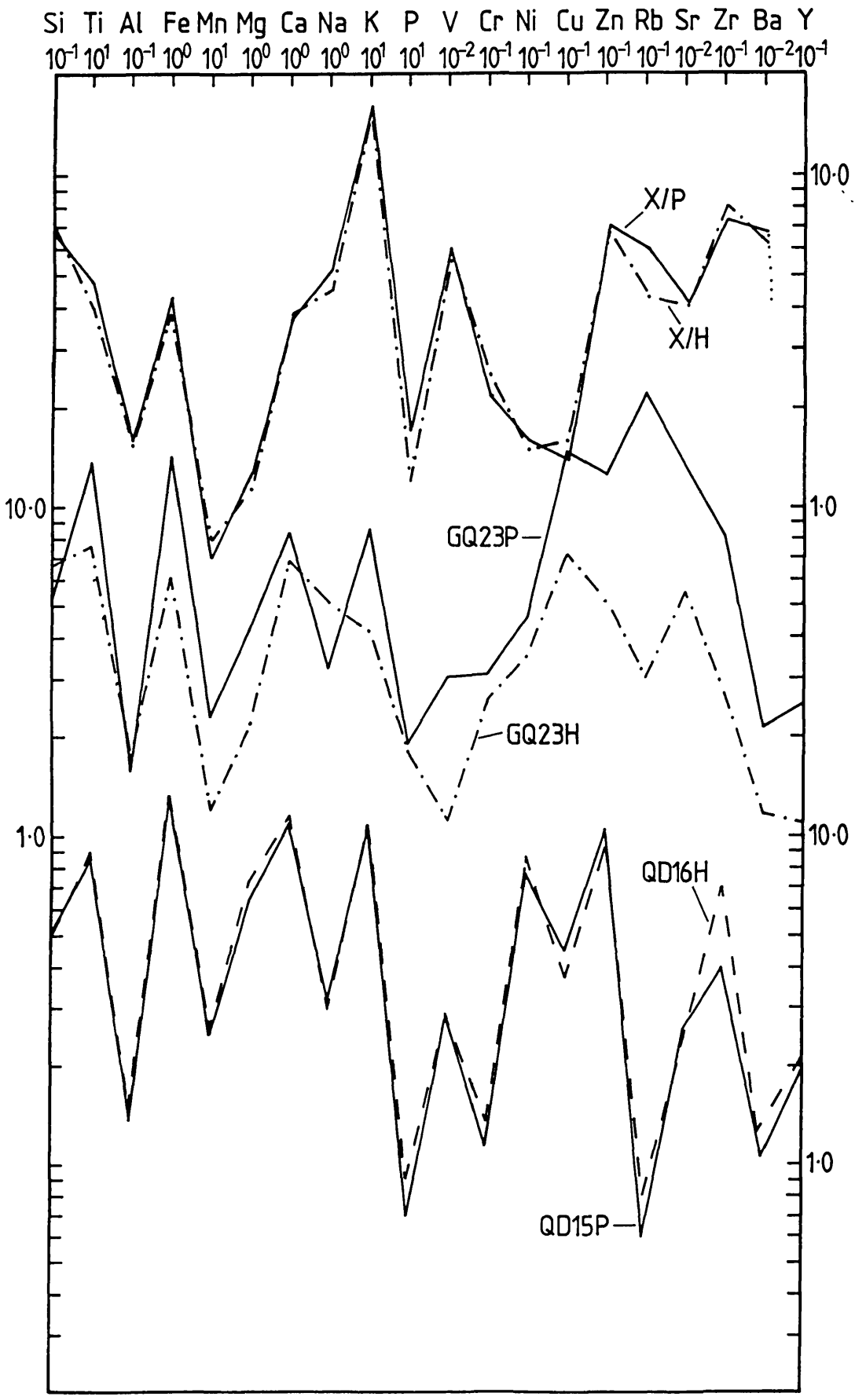

Si Ti Al Fe Mn Mg Ca Na K P V Cr Ni Cu Zn Rb Sr Zr Ba Y
10·0
1·0
X/P
X/H
GQ23P
GQ23H
QD16H
QD15P

Fig. 6.7

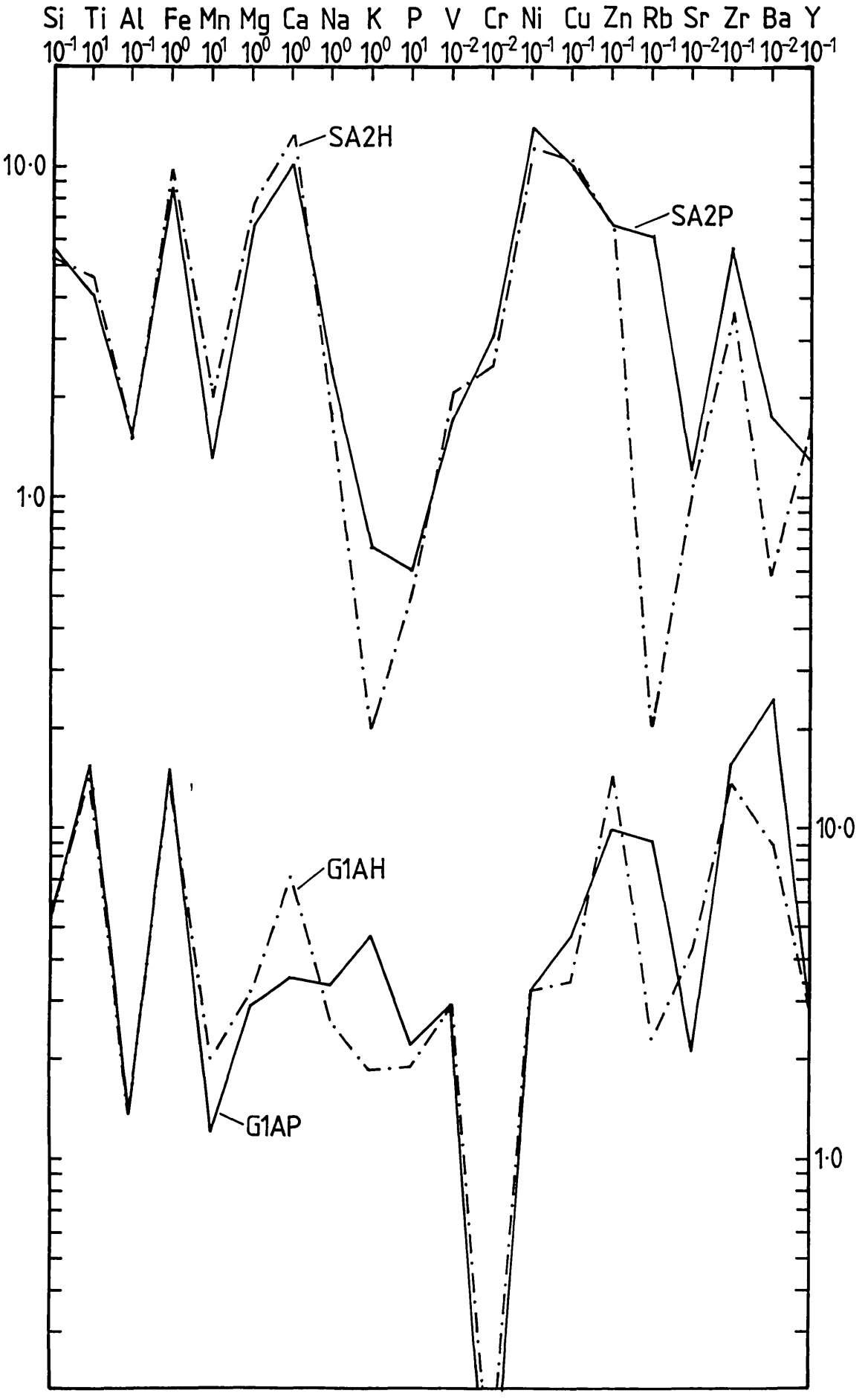

Si Ti Al Fe Mn Mg Ca Na K P V Cr Ni Cu Zn Rb Sr Zr Ba Y
10⁻¹ 10¹ 10⁻¹ 10⁰ 10¹ 10⁰ 10⁰ 10⁰ 10⁰ 10¹ 10⁻² 10⁻² 10⁻¹ 10⁻¹ 10⁻¹ 10⁻¹ 10⁻² 10⁻¹ 10⁻² 10⁻¹
10·0
1·0
SA2H
SA2P
G1AH
G1AP
10·0
1·0

Fig. 6.8

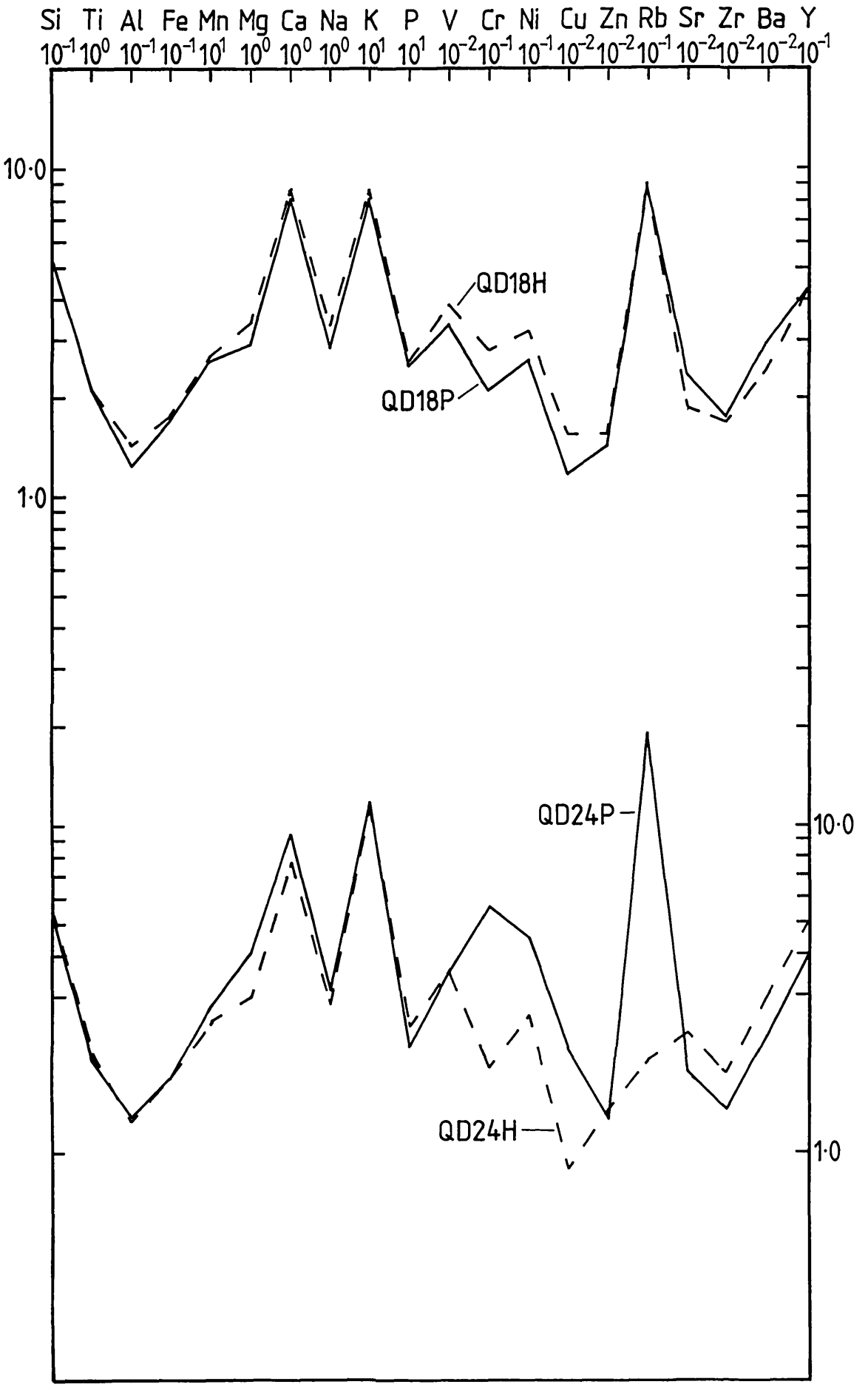

Si Ti Al Fe Mn Mg Ca Na K P V Cr Ni Cu Zn Rb Sr Zr Ba Y
10·0
1·0
QD18H
QD18P
QD24P
QD24H
10·0
1·0

Fig. 6.9

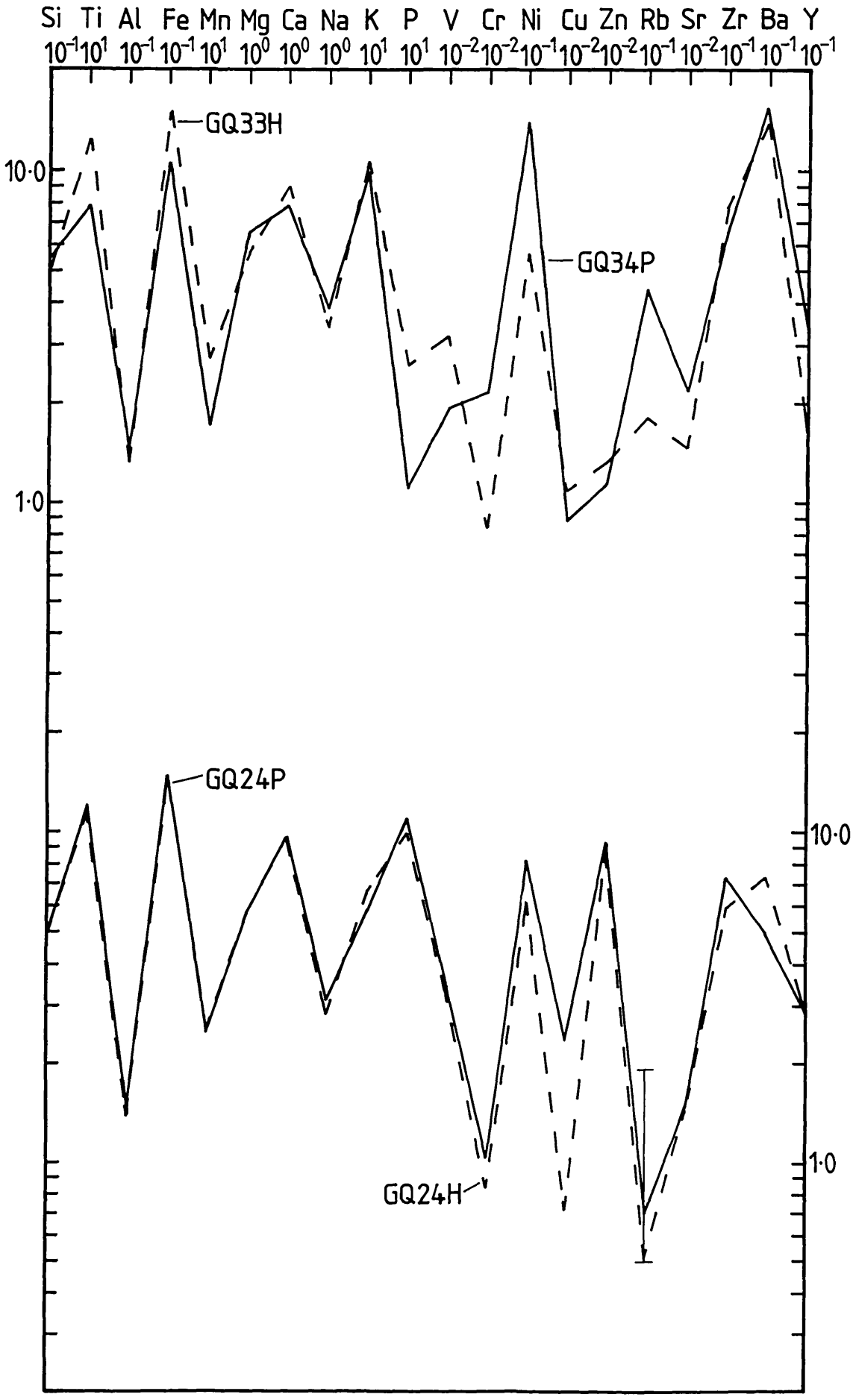

Si Ti Al Fe Mn Mg Ca Na K P V Cr Ni Cu Zn Rb Sr Zr Ba Y
10^{-1} 10^{1} 10^{-1} 10^{-1} 10^{1} 10^{0} 10^{0} 10^{0} 10^{1} 10^{1} 10^{-2} 10^{-2} 10^{-1} 10^{-2} 10^{-2} 10^{-1} 10^{-2} 10^{-1} 10^{-1} 10^{-1}
GQ33H
GQ34P
10·0
1·0
GQ24P
GQ24H
10·0
1·0

Fig: 6.10

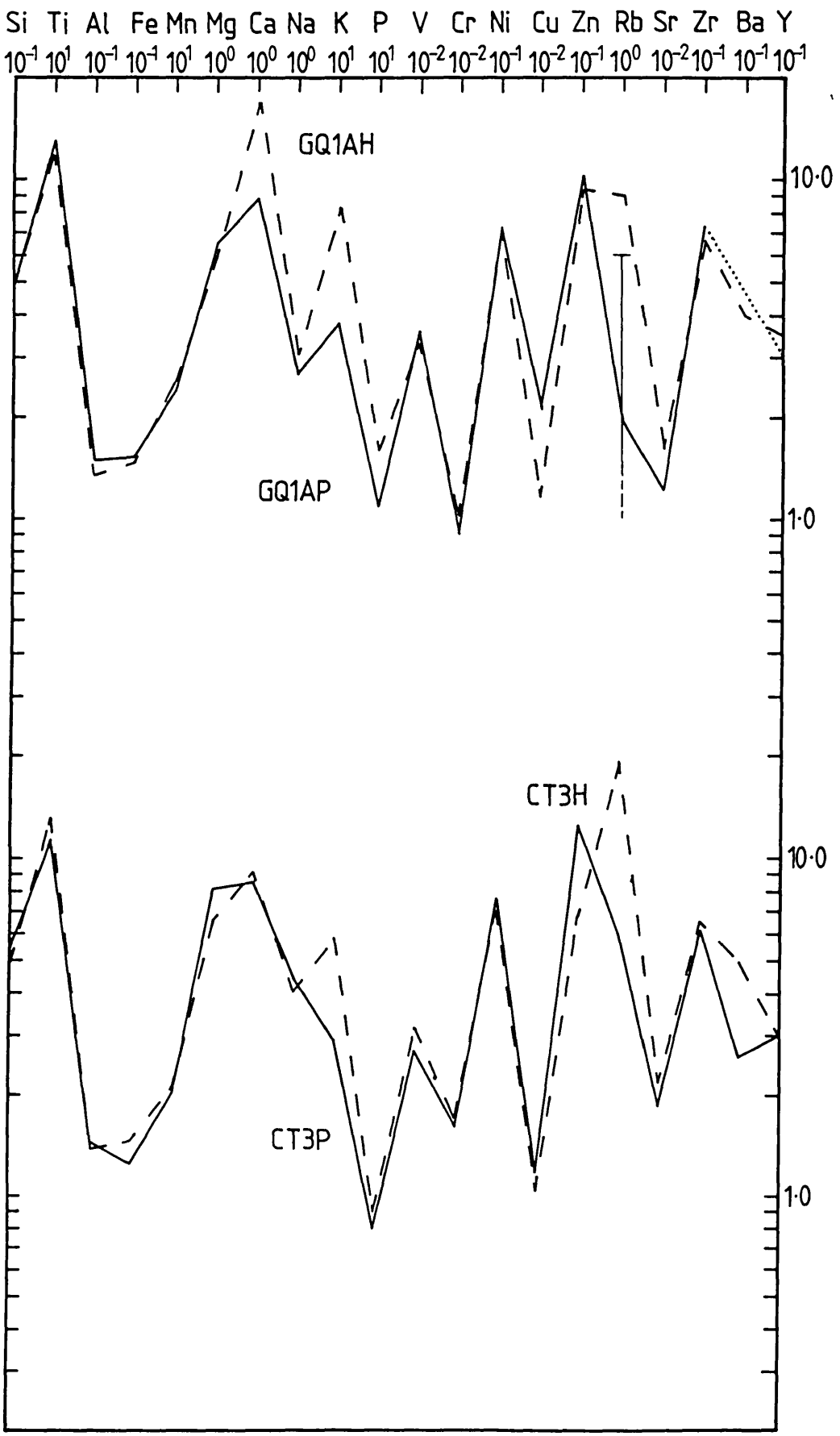

Si Ti Al Fe Mn Mg Ca Na K P V Cr Ni Cu Zn Rb Sr Zr Ba Y
10^{-1} 10^{1} 10^{-1} 10^{-1} 10^{1} 10^{0} 10^{0} 10^{0} 10^{1} 10^{1} 10^{-2} 10^{-2} 10^{-1} 10^{-2} 10^{-1} 10^{0} 10^{-2} 10^{-1} 10^{-1} 10^{-1}
GQ1AH
GQ1AP
10·0
1·0
CT3H
CT3P
10·0
1·0

Fig. 6.11

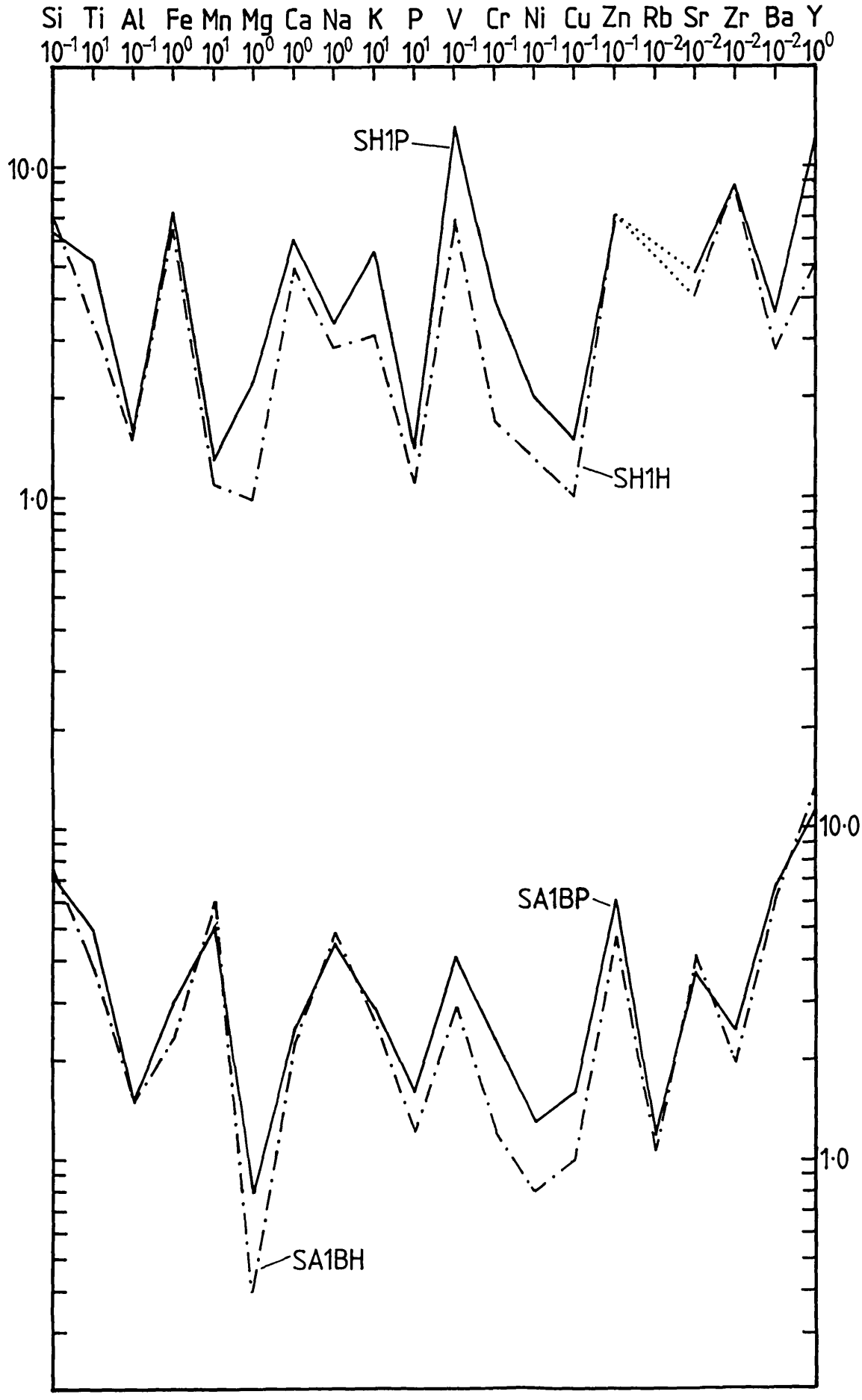
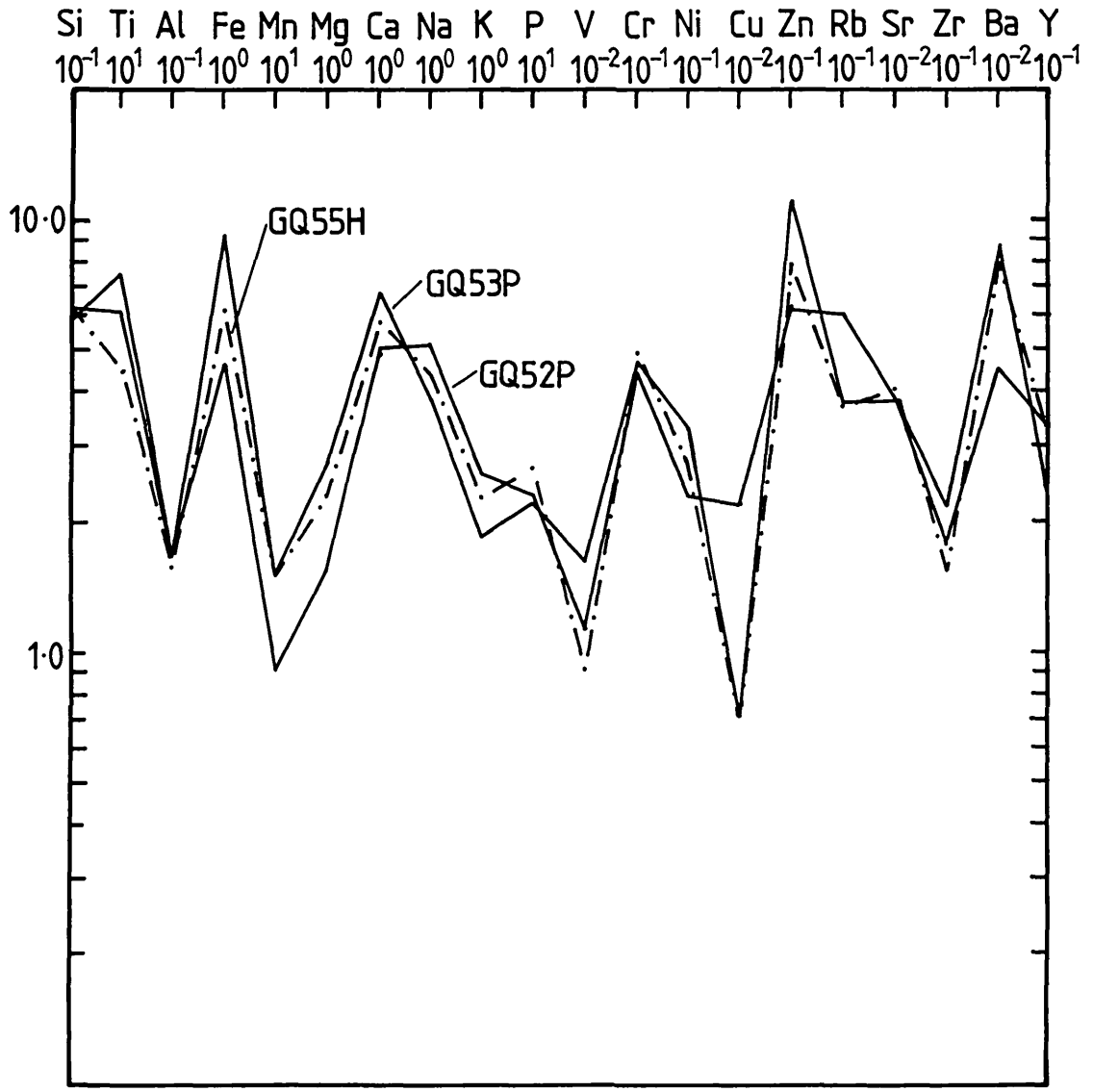

Si Ti Al Fe Mn Mg Ca Na K P V Cr Ni Cu Zn Rb Sr Zr Ba Y
10·0
1·0
SH1P
SH1H
10·0
1·0
SA1BP
SA1BH

Fig. 6.12


Si Ti Al Fe Mn Mg Ca Na K P V Cr Ni Cu Zn Rb Sr Zr Ba Y
10·0
1·0
GQ55H
GQ53P
GQ52P

The closest compositional similarity exists between FV pseudotachylytes - which have been uniquely identified as such in the field - and homogeneous host-rocks, especially those which are fine-grained and in which the foliation is weak or absent. Sample suites meeting these criteria include the G80 series of paragneisses and FV's whose chemical compositions are shown in Fig. 6.5. Two FV/host-rock pairs sampled from the same FV at an interval of 7.6m are plotted in the figure. All 4 rocks contain closely similar absolute abundances of the plotted oxides and elements. Small, but significant (with respect to analytical precision), discrepancies exist for P_2O_5, Ni and Zn. In sample series G801 the vein contains relatively larger amounts of Ni and Zn than the host, whereas the reverse is true of sample series G802. The host-rock, G802H, contains nearly twice as much P_2O_5 as the vein, G802P. Such discrepancies most likely arise from modal differences in accessory mineral content between the analyzed host rock and the volume of the host-rock which was transformed to pseudotachylyte (i.e. the protolith now represented by the analyzed pseudotachylyte). This effect will of course, be aggravated by the fact that only small volumes of pseudotachylyte were available for analysis. In the G80 sample series apatite and Cu-Zn-Ni sulphides are present as minor accessories in the host and as porphyroclasts (sulphides possibly neo-crystallized) in the pseudotachylyte (see section 5.5). Clearly, modal variation of a few grains of apatite could account for the differences in P_2O_5 content without having any significant effect (in the plagioclase-rich rock) on the CaO content.

If this interpretation is correct, then similar discrepancies may be expected for other minor and trace elements. This does appear to be the case. For example, the host-rock sample QD15H and FV sample QD15P of near identical composition in all other elements, contain 71 and 40 ppm Zr respectively (Fig. 6.6). This difference could be accounted for by a variation in zircon content.

Other FV/host-rock pairs showing very close compositional correspondance include sample series QD18 (Fig. 6.8) and QL1 (Fig. 6.5).

Where host-rock fabrics, particularly layering, become more strongly developed the geochemical relationship between host-rock and concordant FV's can become more complex, though interpretation may still be possible. The structural relationship of such an example is sketched in Fig. 6.13 and the comparative geochemistry is shown in

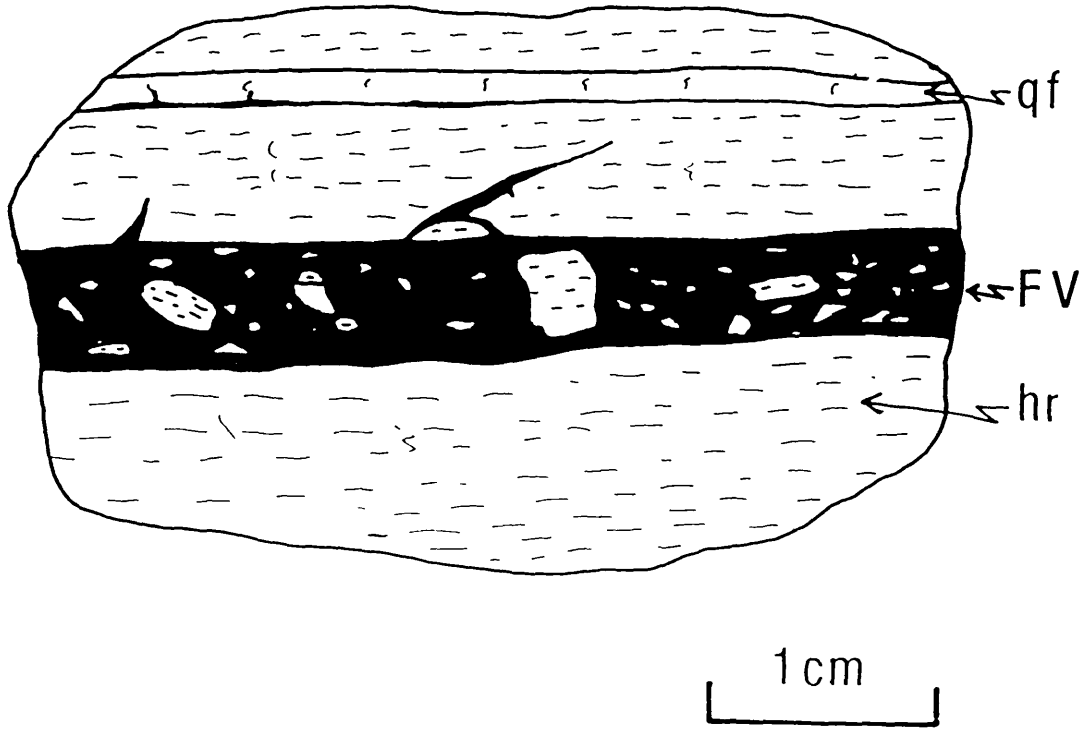


FIGURE 6.13 Sketch drawn from thin section illustrating geometric relations of pseudotachylyte FV's in sample G14. FV = pseudotachylyte fault vein, hr = host-rock, qf = quartz-feldspar veinlet.

Fig. 6.7. The host-rock, G1AH, is a strongly banded paragneiss whose modal mineralogy is given in Table 5.18.

The layering is defined by the dimensional and lattice-preferred orientation of the amphibole, weak irregular variations in modal mineralogy and occasional narrow (<5 mm wide) quartz-microperthite veinlets (Fig. 6.13). The FV is concordant to the foliation and 6 - 8 mm in width. Figure 6.7 demonstrates that considerable divergence in the major and minor oxide and trace element concentrations exists between the host rock and the pseudotachylyte. Most significantly, the K_2O, Rb and Ba contents of the pseudotachylyte are markedly greater than the host-rock, whilst the CaO and Sr contents are markedly less. EMP analysis of the host-rock and porphyroclast phases demonstrate that microperthite is the major K_2O bearing phase and also, that it contains up to 0.5 wt.% BaO (i.e. a celsian component). These observations, together with the petrographic relationships shown in Fig. 6.13, strongly suggest that the pseudotachylyte FV was generated within a layer of host rock containing a relatively greater proportion of microperthite than the bulk host-rock. The microperthite layer, or its boundary, probably constituted a mechanical anisotropy favourable to faulting and pseudotachylyte generation (cf. sub-barren FV in Fig. 6.13); the layer was presumably 'consumed' during the faulting and pseudotachylyte-generation process. Enrichment of such a layer in microperthite requires concomitant depletion in some other phase(s); the data of Fig. 6.7 indicate that this is a CaO-rich phase. Given that the TiO_2 contents of both host and vein are similar (Fig. 6.7), sphene is rejected, leaving hornblende, epidote and plagioclase. Fe_2O_3 and Al_2O_3 are likely to be rather insensitive discriminants (because of their abundance in more than one phase), but if it can be assumed that the majority of the Sr is partitioned into the plagioclase, then this mineral may have been depleted from the pseudotachylyte forming layer. This would also require that the Rb is partitioned into the alkali-feldspar rather than the plagioclase. (In the pseudotachylyte matrix a ready 'sink' exists for Rb - phyllosilicate - not present in the host-rock.)

In the above discussion strong evidence has been presented to explain the differences in K_2O and BaO contents between the vein and host-rock, and a plausible explanation to account for the other chemical differences. The whole-rock composition of the pseudotachylyte vein is believed to be influenced by selective mixing effects consequent upon faulting/pseudotachylyte generation along a

mechanically anisotropic layer, rather than any direct effects of melting. However, mineralogical variation along such layers undergoing sliding/frictional melting under otherwise identical conditions of frictional traction may control both the composition and the amount of melt formed. In the present example, a quartz/microperthite veinlet might be expected to have a rather low melting point, particularly if water is available - say from the dehydration of amphibole or chlorite (Winkler, 1967)

The following conclusions may be made from this section on the geochemical relationship between FV's and single host-rocks:-

(i) the overall similarity in composition between pseudotachylyte FV's and their host-rocks demands that the former are locally derived from the latter, in an essentially isochemical fashion (excepting the qualifications listed below);
(ii) small differences in the concentrations of certain minor and trace elements between host-rock and pseudotachylyte can be accounted for by modal variation of accessory phases; examples concerning P_2O_5 and Zr in apatite and zircon respectively have been given;
(iii) the mechanical behaviour of layered gneissic rocks may exert a control, through selective mechanical mixing, on the whole rock composition of the pseudotachylyte (matrix plus clasts) and so indirectly affect the composition and/or amount of pseudotachylyte melt.
(iv) subtle differences in composition, especially of trace elements contained in modally important phases, may reflect significant processes involved in pseudotachylyte generation - such as selective mechanical mixing; an example involving Ba in alkali-feldspar has been given;
(v) the concentrations of major element oxides, such as SiO_2, Al_2O_3 and Fe_2O_3 and CaO may be quite insensitive to mechanical mixing effects because of the high concentrations of these components in more than one modally important phase (e.g. CaO and Al_2O_3 in plagioclase and epidote);
(vi) these observations have been made on pseudotachylyte veins with simple field relationships involving concordant FV's; geochemical relationships between discordant FV's and inhomogeneous host-rocks are expected to be much more difficult to interpret.

The effects of selective mechanical mixing can also be seen in other fault-rock types. In Fig. 6.17 the normalized compositions of a peridotitic host-rock and an included cataclasite vein ('FV') from the Ivrea Zone are plotted. In this example the cataclasite was formed within a layer enriched in An-rich plagioclase resulting in a cataclasite composition enriched in Al_2O_3 and CaO relative to the host rock composition.

6.5.2 IV - Single Host-rock Relationships

With the exception of sample GQ23 (Fig. 6.6) every attempt was made in the field to relate the IV pseudotachylytes to a pseudotachylyte generating surface or FV, and hence the ultimate protolith. Host-rock is used here and in the figures to describe the field-identified protolith; it is not neccessarily the immediate wallrock to the veins.

When comparing the composition of IV/host-rock pairs, greater chemical differences (than for FV/host-rock pairs) emerge, which are believed to be dependant upon a number of contributory factors. Compositional variation may be as little as that seen in sample series X (Fig. 6.6) or GQ24 (Fig. 6.9) - where the differences are minimal and similar to FV/host-rock pairs, or as great as that seen in sample series GQ23 (Fig. 6.6). In Fig. 6.6 analyses are plotted of an IV (GQ23P) and its immediate host or wallrock (GQ23H) collected as a handspecimen of float. The data are plotted simply to highlight the dangers of making gross comparisons between the composition of pseudotachylyte and its host-rock without regard for the field relationships. Cursory inspection of this figure suggests that the pseudotachylyte was generated in a more mafic rock than its immediate leucocratic wallrock.

In general, the IV and host-rock pairs possess similar chemical compositions with variations most easily seen in the trace element patterns. No systematic differences are common to all the examples. The composition of the IV's may indicate generation from a protolith with a greater felsic component (e.g. SA2 sample series, Fig. 6.7) or mafic component (e.g. SH1 sample series, Fig. 6.11) than that of the analyzed host-rock. A particularly large compositional variation exists between pseudotachylyte from a quasi-conglomerate and its host-rock (samples GQ33P and GQ33H respectively, Fig. 6.9).

In addition to the factors outlined at the end of the previous

section, compositional variation between IV pseudotachylytes and their host (protolith) rocks may result from:-

(i) poor field identification of the host (protolith) rock;
(ii) inclusion in the analysed pseudotachylyte of lithic and/or mono-mineralic porphyroclasts ripped-off the immediate wallrocks during injection of the pseudotachylyte vein.

6.5.3 FV - IV - Multi Host-rock Relationships

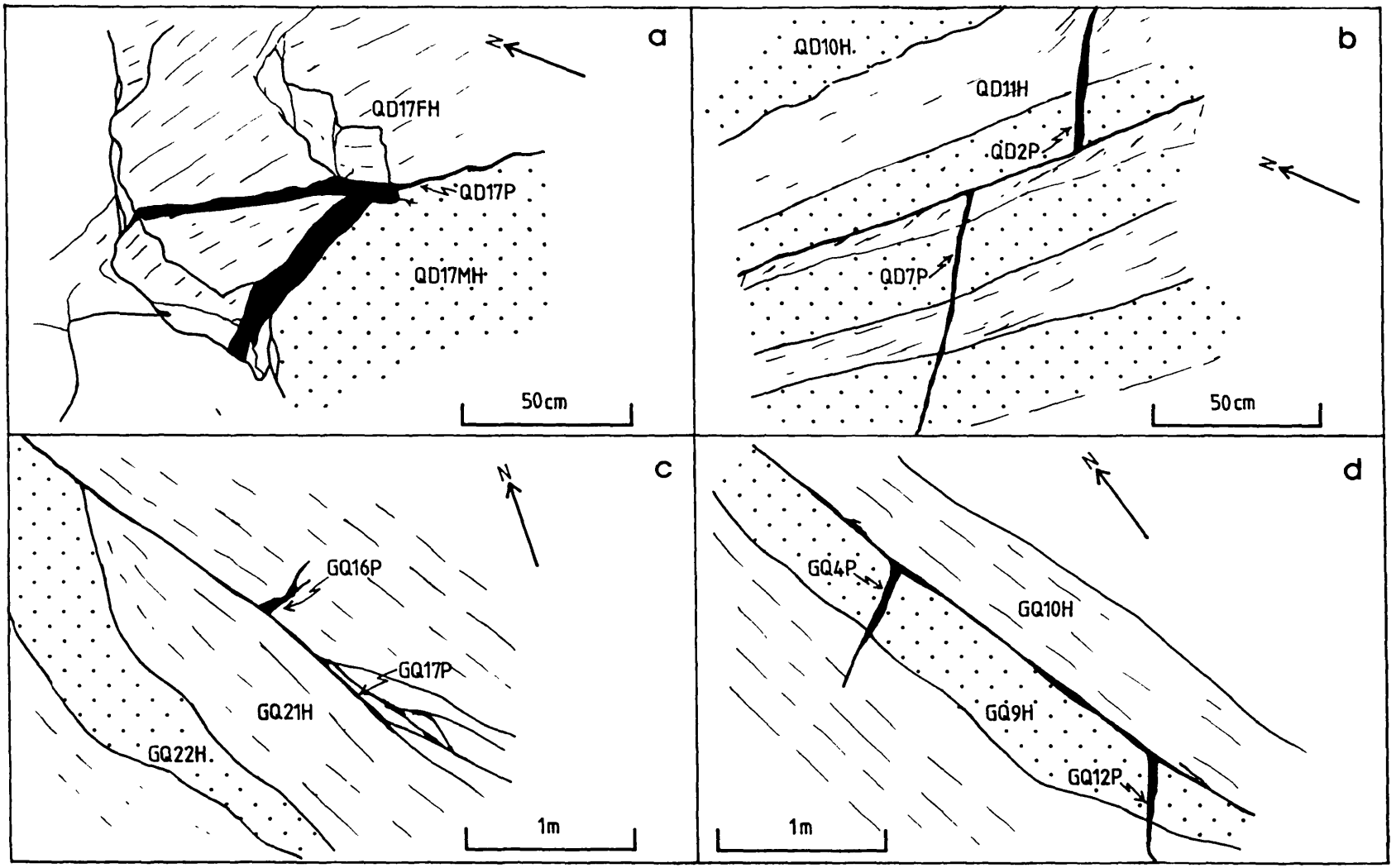
Mechanical controls (selective mechanical mixing) on the whole-rock composition of concordant pseudotachylyte FV's were emphasized in section 6.5.1. Where pseudotachylyte is generated at a lithological boundary it should be possible to assess the relative contributions, to the composition of the pseudotachylyte of unlike hangingwall and footwall host-rocks. Four examples are considered here, the field relationships of each vein system - believed critical to the interpretation of the data - are shown in Fig. 6.14 .

Sample series QD17 possess the best-constrained field relationships (Fig. 6.14a). The chemical composition of the pseudotachylyte (QD17P) and its juxtaposed quartzofeldspathic and amphibolitic host-rocks (QD17FH and QD17MH, respectively) are shown in Fig. 6.15. For all the elements analyzed, the composition of the pseudotachylyte is 'enveloped' by the compositions of the 2 host-rocks. However, for all the major and minor oxides and the majority of the trace elements, the composition of the pseudotachylyte is much closer to that of the amphibolite than the quartzofeldspathic host-rock. Using the normalized oxide concentrations, the reaction x% QD17MH + y% QD17FH = 100% QD17P was modelled according to the least squares generalized mixing model of LeMaitre (1979). (To the author's knowledge this is the first time a mixing model has been applied to pseudotachylytes or any fault-rocks.) A best fit solution (Table 6.2) yielded the result:-

71.76% QD17MH + 28.24% QD17FH = QD17P

The 'fit' of this calculation, indicated by the residual sum of the squares of the differences between the input and calculated oxide values, is very close (Table 6.2, column 3). Using these calculated proportions, the trace element concentrations have been modelled -

FIGURE 6.14 Field sketches showing geometric relationships between pseudotachylyte veins and host-rocks whose compositions are plotted in Fig.s 6.15 and 6.16. Quartzofeldspathic gneiss, lined ornament; amphibolitic gneiss, dotted ornament; pseudotachylyte, black. See Appendix A6 for sample localities.


a
N
QD17FH
QD17P
QD17MH
50cm
b
QD10H.
QD11H
QD2P
N
QD7P
50cm
c
N
GQ16P
GQ17P
GQ21H
GQ22H.
1m
d
N
GQ4P
GQ10H
GQ9H
GQ12P
1m

FICURES 6.15 and 6.16 (overleaf) Plots showing normalized chemical composition of pseudotachylytes and their host-rocks. For each sample set the pseudotachylyte was generated at the contact between unlike host-rocks; see Fig. 6.14 for details of field relationships between samples.

Fig. 6.15

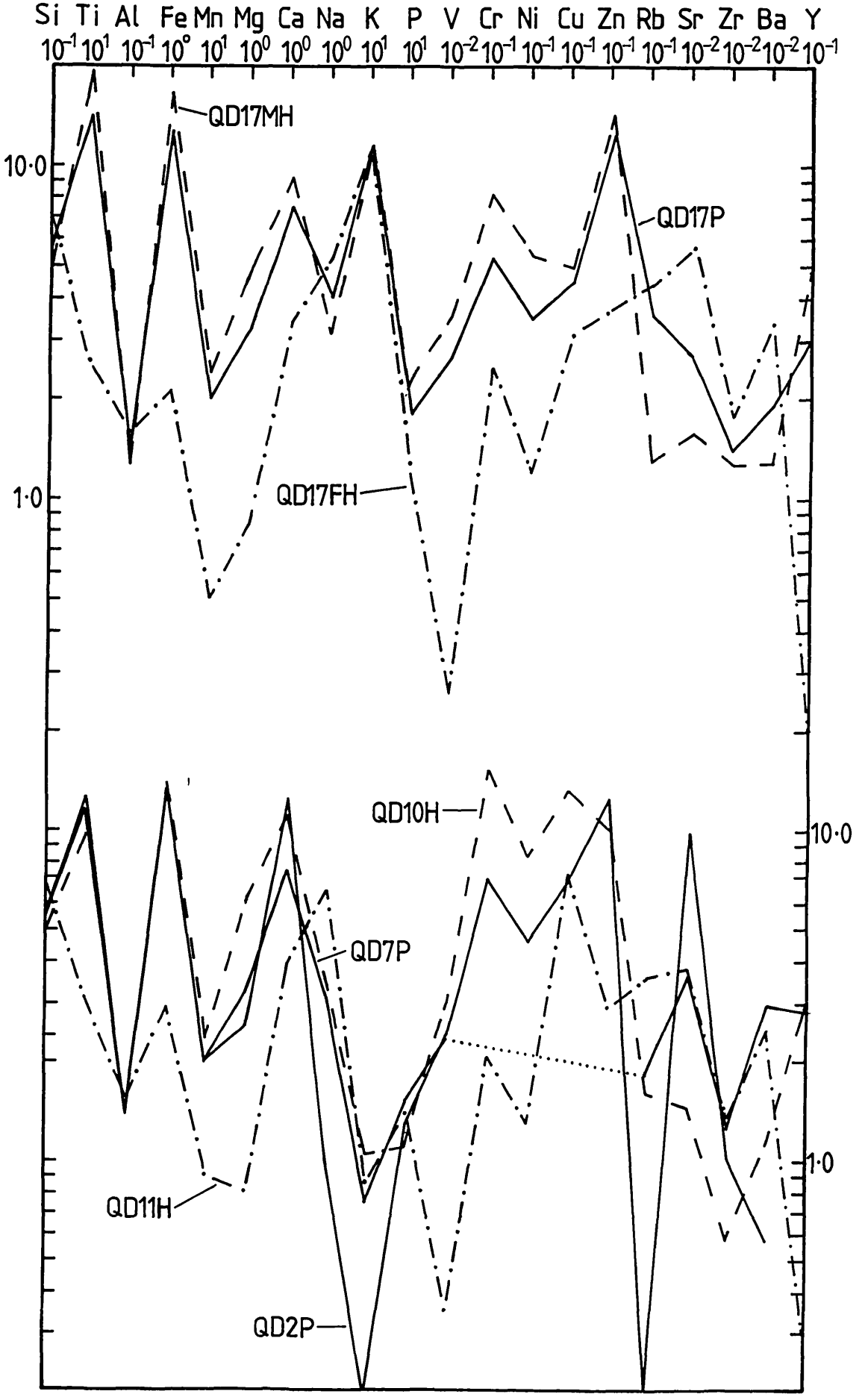

Si Ti Al Fe Mn Mg Ca Na K P V Cr Ni Cu Zn Rb Sr Zr Ba Y
10·0
1·0
QD17MH
QD17P
QD17FH
QD10H
QD7P
QD11H
QD2P
10·0
1·0

Fig. 6.16

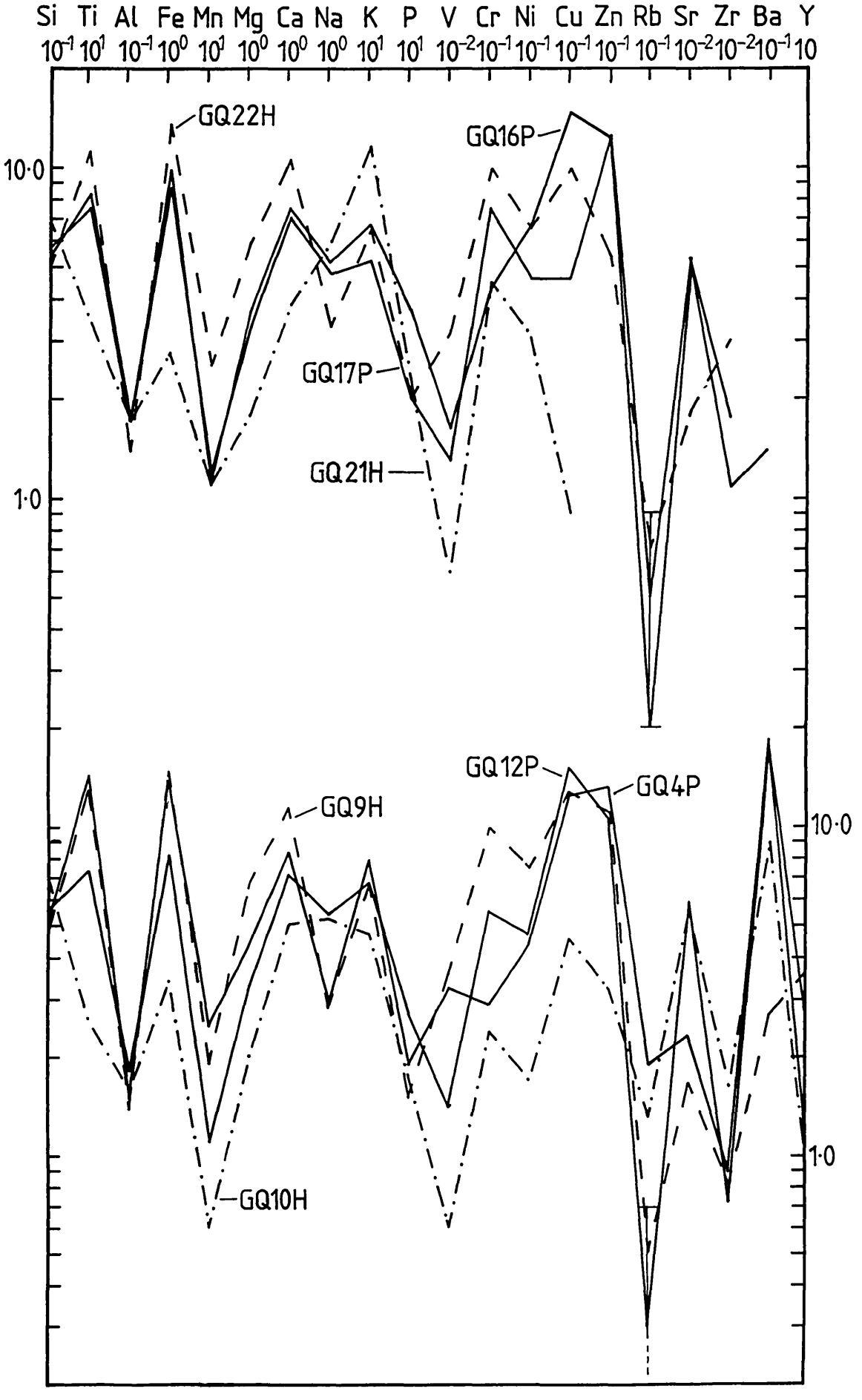
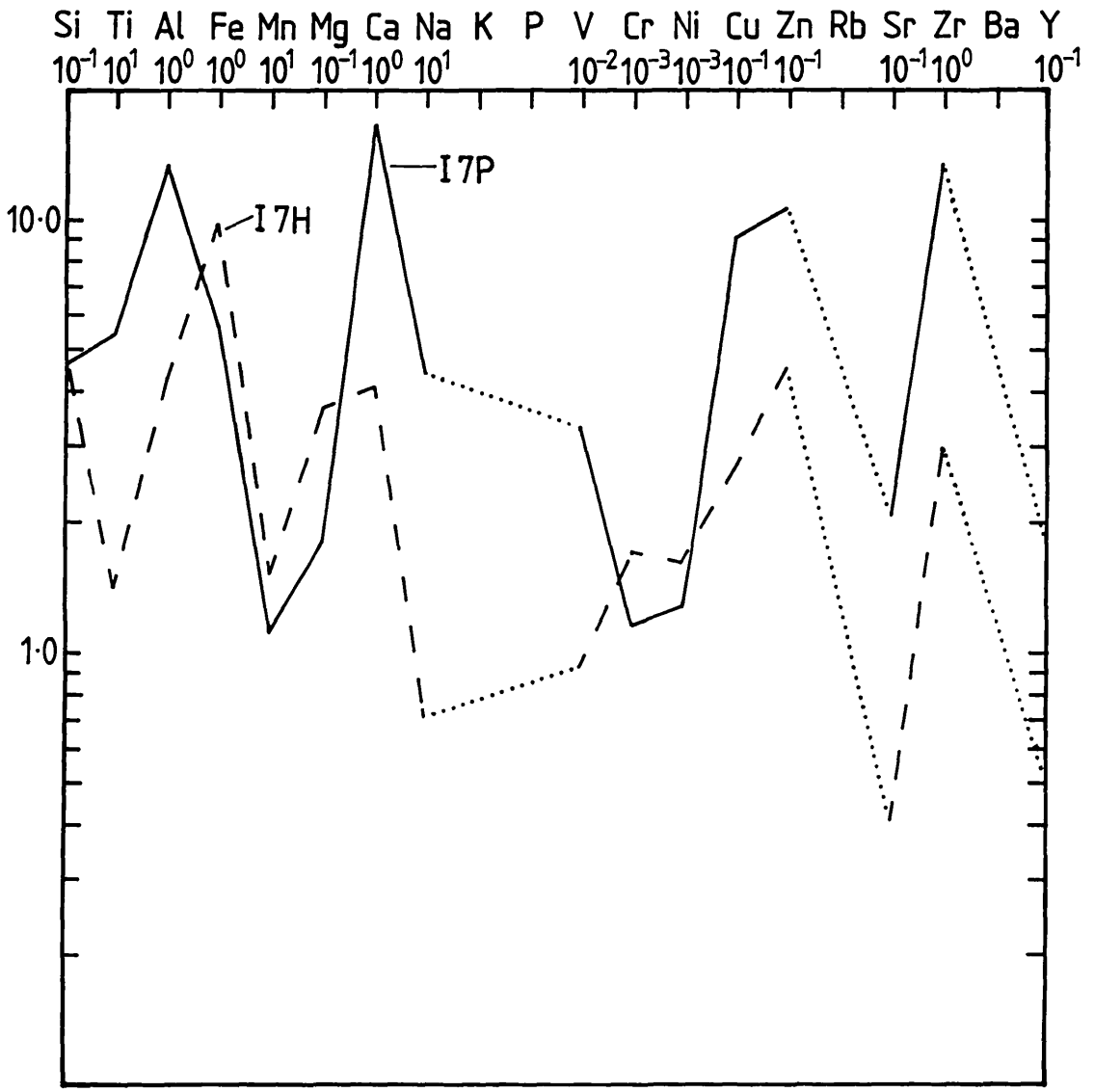

Si Ti Al Fe Mn Mg Ca Na K P V Cr Ni Cu Zn Rb Sr Zr Ba Y
10⁻¹ 10¹ 10⁻¹ 10⁰ 10¹ 10⁰ 10⁰ 10⁰ 10¹ 10¹ 10⁻² 10⁻¹ 10⁻¹ 10⁻¹ 10⁻¹ 10⁻¹ 10⁻² 10⁻² 10⁻¹ 10
GQ22H
GQ16P
10·0
GQ17P
GQ21H
1·0
GQ12P
GQ4P
GQ9H
10·0
1·0
GQ10H

FIGURE 6.17 Plot showing normalized chemical composition of cataclasite (I7P) and peridotitic host rock (I7H) from Ivrea zone, Italy.

Fig. 6.17



also resulting in a very good fit (Table 6.2).

The data for sample series QD17 indicates that a substantially greater proportion of the amphibolitic host than the quartzofeldspathic host contributed to the formation of the pseudotachylyte. It appears then that rock-type may exert a mechanical control on the whole-rock composition of pseudotachylyte. In many respects this behaviour may be viewed as a large scale analogue of the effect of mineralogical layering described in section 6.4.1.

The field relations of 3 other suites of host-rocks and pseudotachylytes are illustrated in Fig. 6.14b, c and d, and the chemical compositions of some of these rocks are plotted in Fig.s 6.15 and 6.16. The fit of the pseudotachylyte compositions to the compositional envelopes defined by the host-rocks is less good than for sample series QD17. Least squares mixing calculations, determined as for sample series QD17, yielded the following results:-

'mafic' host + 'felsic'host = pseudotachylyte	sum squares differences
68.41% QD10H + 31.59% QD11H = QD7P	13.8777
81.05% QD10H + 18.95% QD11H = QD12P	30.3345
62.80% QD10H + 37.20% QD11H = QD11P	10.2030
53.89% GQ22H + 46.11% GQ21H = GQ17P	5.0582
60.73% GQ22H + 39.27% GQ21H = GQ16FP	15.9507
68.85% GQ22H + 31.15% GQ21H = GQ16IP	14.6794
80.44% GQ9H + 19.56% GQ10H = GQ4P	10.5149
50.77% GQ9H + 49.23% GQ10H = GQ12P	20.2210
47.08% GQ9H + 52.92% GQ10H = GQ13P	18.3641

In these 3 suites also, the concentrations of the majority of major, minor and trace elements in the pseudotachylyte correspond more closely to the more mafic host-rocks. For the major and minor oxides, substantial relative differences between the pseudotachylyte and the more mafic host-rock are limited to those elements present in only very small absolute amounts - e.g. MnO in GQ22H, GQ16P and GQ17P (Fig. 6.16). For the trace elements the most significant differences are for Sr and Ba. The poorer fit of the mixing models for these 3 suites, in comparison to sample series QD17, is probably due to a combination of factors including:-

TABLE 6.2 GENERALIZED MIXING MODEL RESULTS FOR SAMPLE SERIES QD17

	1	2	3
SiO_2	55.57	55.40	0.17
TiO_2	1.47	1.42	0.05
Al_2O_3	13.57	13.96	0.39
Fe_2O_3*	12.69	12.79	0.10
MnO	0.19	0.20	0.01
MgO	3.80	3.25	0.55
CaO	7.65	7.50	0.15
Na_2O	3.71	4.11	0.40
K_2O	1.15	1.18	0.03
P_2O_5	0.20	0.18	0.02
Σx^2			0.69
V	261	265	4
Cr	67	53	14
Ni	42	35	7
Cu	45	45	0
Zn	113	124	11
Rb	21	36	15
Sr	275	270	5
Y	35	29	6
Zr	141	141	0
Nb	15	12	3
Ba	189	194	5
Σx^2			702

1 Best fit least squares solution to mixing model (oxides only) QD17MH + QD17FH = QD17P; trace element data derived from mixing model

2 XRF whole rock analysis of QD17P (normalized to 100% following deduction of LOI and H_2O)

3 Differences ($|1-2|$); Σx^2 = residual sum of squares of differences

(i) the field constraints on vein/host-rock are poorer;
(ii) samples QD1P, QD2P, QD7P, GQ4P, GQ12P, GQ13P and GQ16IP are IV's and therefore liable to differ in composition from their host rocks for reasons outlined in section 6.5.2; in this context it is noted that the smallest residual is yielded by a reaction involoving a FV (GQ17P).

Several of the conclusions reached in sections 6.5.1 and 6.5.2 also apply to FV - IV multi host-rock relationships. Additionally, it has been shown that:-

(i) where pseudotachylyte is generated between 2 lithologies richer and poorer in hydrated minerals (hornblende and/or biotite), the former appears to contribute in larger amount to the pseudotachylyte (matrix plus clasts); this is believed to be a function of mineralogy per se rather than grain size, pre-existing fractures etc.; this is however in contrast to the behaviour of sample G1AP, where K-feldspar contributed preferentially to the melt (section 6.5.1);
(ii) because of the large differences in chemical composition (i.e. a function of modal mineralogy) between the mafic and felsic host rocks in the 4 examples described, major element oxides as well as trace elements are sensitive to the preferential mechanical mixing described in (i);
(iii) the preferential mechanical mixing should have an effect on the composition and/or amount of pseudotachylyte melt produced, all other things being equal.

The first conclusion above complements the results of a geochemical study by Anderson et al (1983) on fault rocks along the San Gabriel fault, California. These workers found that cataclasite generated along faults separating 2 differing lithologies preferentially incorporated the more inhomogeneous rock-type richer in hydrated ferromagnesian minerals.

6.6 EMP Analysis of Pseudotachylyte Matrix

In this study raster/defocussed beam EMP analysis of pseudotachylyte matrix was restricted, for reasons indicated above, to matrix material with a grain size < 5 um. Consequently, a somewhat biassed sample - the phyllosilicate-spherulitic types of

pseudotachylyte (devitrified from glass) - is considered in this section. All available published EMP analyses of pseudotachylyte and frictionite (excluding the Vredefort Dome samples analysed by Schwarzman et al (1983)) have also been collated; these include samples originally described as glassy and as microlitic.

6.6.1 Composition of Pseudotachylyte Matrix

EMP analyses of some of the pseudotachylytes have been presented in chapter 5 where the mineralogy was considered. These and additional analyses, including the published data, have been recast to their normative components. (Fe_2O_3/FeO ratios of 0.35 and 0.25 were chosen for the pseudotachylyte and their host-rocks, respectively - see Appendix A5).

Summarized normative data are given in Table 6.3. In Fig. 6.18a the analyses are plotted on a ternary Qz-Ab-Or diagram, together with various experimentally-determined minimum melt compositions (see figure caption for details). The majority of pseudotachylytes anlalysed are depleted in normative quartz relative to the experimentally-determined minimum melt compositions. Taking into account the rather low Ab/An ratios of many of the pseudotachylytes (Fig. 6.18b), it is clear that they did not form by classical, equilibrium or near-equilibrium partial melting under either excess water or dry conditions. Noting this, Sinha-Roy's (1981) hypothesis of partial melting yielding a near minimum melt composition is rejected. His interpretation was based on XRF whole-rock (matrix plus clasts) analyses.

Also plotted in Fig. 6.18 are the average compositions of some landslide frictionite glasses. These plot closer to the minimum melt compositions, probably reflecting their granite precursors (see host-rock analyses given in Masch et al (1985)). Other EMP analyses of of Kofels frictionite (not plotted) include glasses whose compositions correspond closely to alkali feldspar and to chlorite (Kurat and Richter, 1972). These glasses together with the lechatelierite described by Milton (1964) argue for extremely high temperatures and also extremely rapid quenching (Masch et al., 1985). Similar glasses have not been found in fault-generated pseudotachylytes - perhaps due to slower cooling rates influenced by higher ambient temperatures.

Figure 6.19 demonstrates that the whole-rock (matrix plus clasts) compositions of 5 pseudotachylytes are enriched in normative

TABLE 6.3 SUMMARIZED NORMATIVE COMPOSITION OF PSEUDOTACHYLYTE MATRIX ANALYSES BY EMP

	Qz-normative	Ol-normative	Co-normative	Ne-normati
This study (n=35)	14	20	8	8
Masch (1974) (n=1)	-	1	-	-
Ermanovics et al. (1972) (n=10)	9	1	7	-
Wallace (1976) (n=7)	4	3	5	1

TABLE 6.4 NORMATIVE COMPOSITIONS (WT.%) OF TYPICAL OUTER HEBRIDES BIOTITE AND AMPHIBOLE

	1	2
SiO_2	37.06	42.66
TiO_2	2.88	1.57
Al_2O_3	16.59	10.99
Fe_2O_3	2.00	2.48
FeO	13.35	16.51
MnO	0.00	0.28
MgO	14.10	8.99
CaO	0.00	11.34
Na_2O	0.00	1.63
K_2O	9.87	0.74
TOTAL	95.85	97.19
Qz	0.00	0.00
Or	0.00	4.37
An	0.00	20.49
Ab	0.00	7.77
Le	35.74	0.00
Ne	0.00	3.26
Ks	7.25	0.00
Di	0.00	29.75
Wo	0.00	0.00
Hy	0.00	0.00
Ol	38.59	24.97
Co	5.91	0.00
Mt	2.90	3.59
Ilm	5.47	2.98

1 Mean of 6 biotite analyses, sample G802
2 Mean of 4 amphibole analyses, sample GQ14

FIGURE 6.18a Qz - Ab - Or (recalculated normative wt.%) plot showing ternary composition of pseudotachylyte matrix analyzed by EMP.

● = this study (n = 30);

■ = Alpine Fault Zone, N.Z. (n = 7), Wallace (1976);

◆ = Canada (n = 4), Ermanovics et al (1972);

▼ = Silvretta (n = 1), Masch (1974);

▲ = Langtang frictionite (n = 2), Wallace (1976);

▲ = Langtang frictionite (n =1), mean of 24 analyses of brown glass, Masch et al (1985, Table 1, p.150);

▲ = Langtang frictionite (n=1), mean of 24 analyses of white glass, Masch et al (1985, Table 1, p.150);

⬮ = Kofels frictionite (n =1), mean of 3 analyses of brown glass, Storzer et al (1971, Table 1, p.239);

⬮ = Kofels frictionite (n = 1), mean of 6 analyses of light glass, Kurat and Richter (1972, Table 4, p.34);

⬮ = Kofels frictionite, (n = 1), mean of 9 analyses of dark glass, Kurat and Richter (1972, Table 4, p.35);

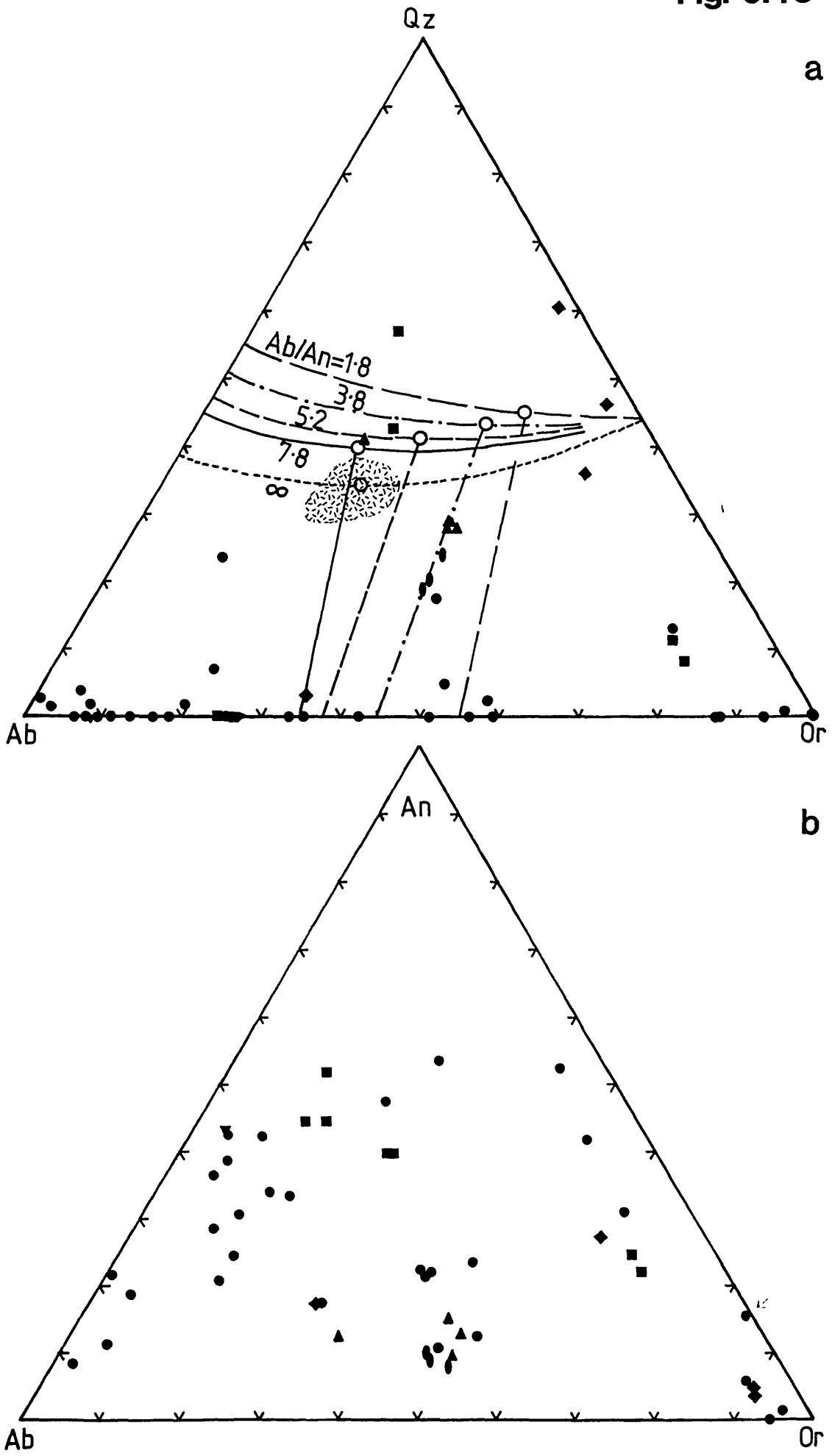
○ = ternary minimum melt compositions projected from the system Qz - Ab - An - Or - H_2O, for various AB/An ratios at P_{H2O} = 200 MPa; cotectic lines also shown (after Winkler, 1967);

stippled field = ternary minimum melt compositions for 'dry' melting of biotite/muscovite/amphibole + granite/granodiorite (after Brown and Fyfe, 1970; see text).

(b) An - Ab - Or plot, symbols as for (a).

(c) (overleaf) A - F - M plot where A = $Na_2O + K_2O$/A+F+M, F = FeO^*/A+F+M and M = MgO/A+F+M; symbols as for (a).

Fig. 6.18



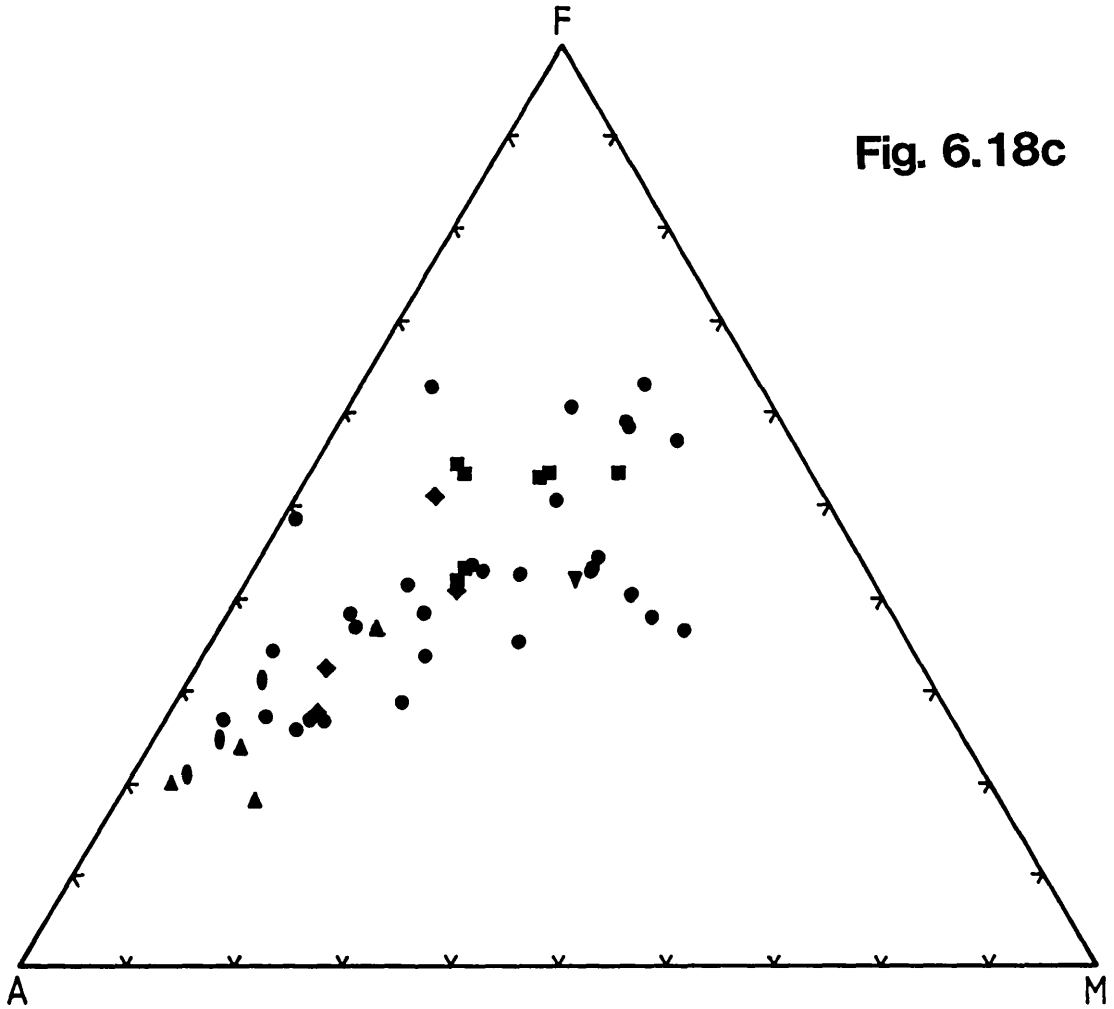


Fig. 6.18c

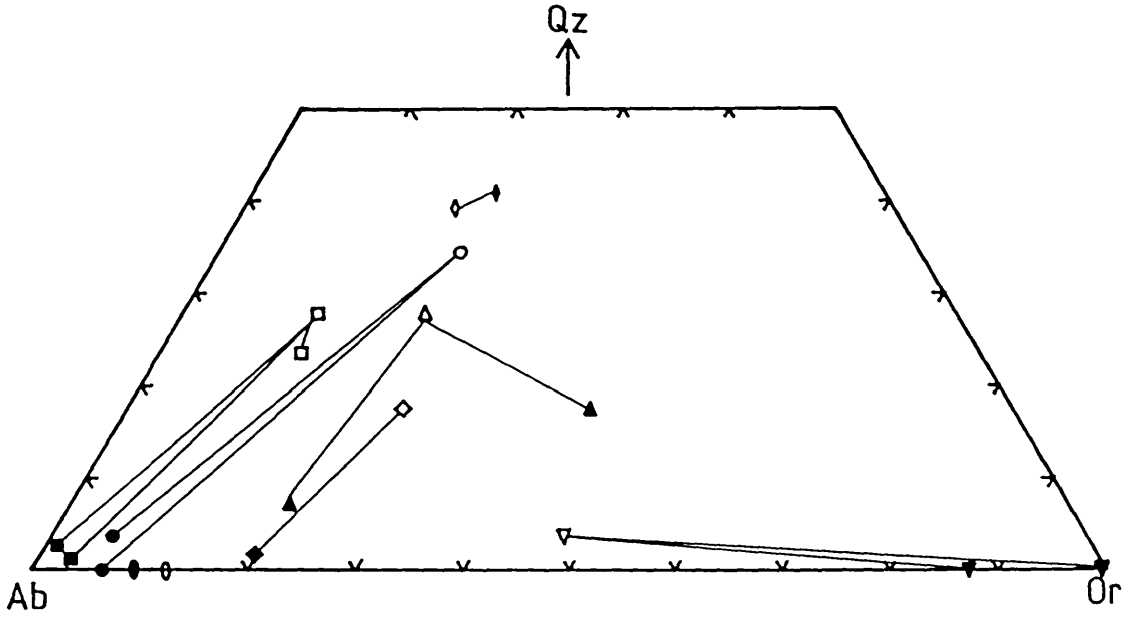


FIGURE 6.19 Qz - Ab - Or (recalculated normative wt.%) plot showing relationship between pseudotachylyte whole rock (matrix + clasts) composition determined by XRF (open symbols) and pseudotachylyte matrix composition determined by EMP (closed symbols). Tie lines join whole rock to one or more mineralogically/texturally distinct matrix component.

● = sample SU802B;

■ = sample X;

◆ = sample R2;

▼ = sample G1A;

▲ = sample G802;

⬮ = sample GQ33.

FIGURE 6.20a Qz - Ab - Or (recalculated normative wt.%) plot showing relationship between host-rock composition determined by XRF (open symbols) and pseudotachylyte matrix composition determined by EMP (closed symbols). Tie lines join host-rock to one or more texturally/mineralogically distinct matrix component.

■ = sample X

▲ = sample G802

▼ = sample G1A

⬮ = sample GQ33

◆ = Silvretta, Masch (1973);

● = Canada, Ermanovics et al (1972).

(b) An - Ab - Or plot, symbols as for (a).

(c) (overleaf) A - F - M plot, components as for Fig. 6.18, symbols as for Fig. 6.20a.

Fig. 6.20

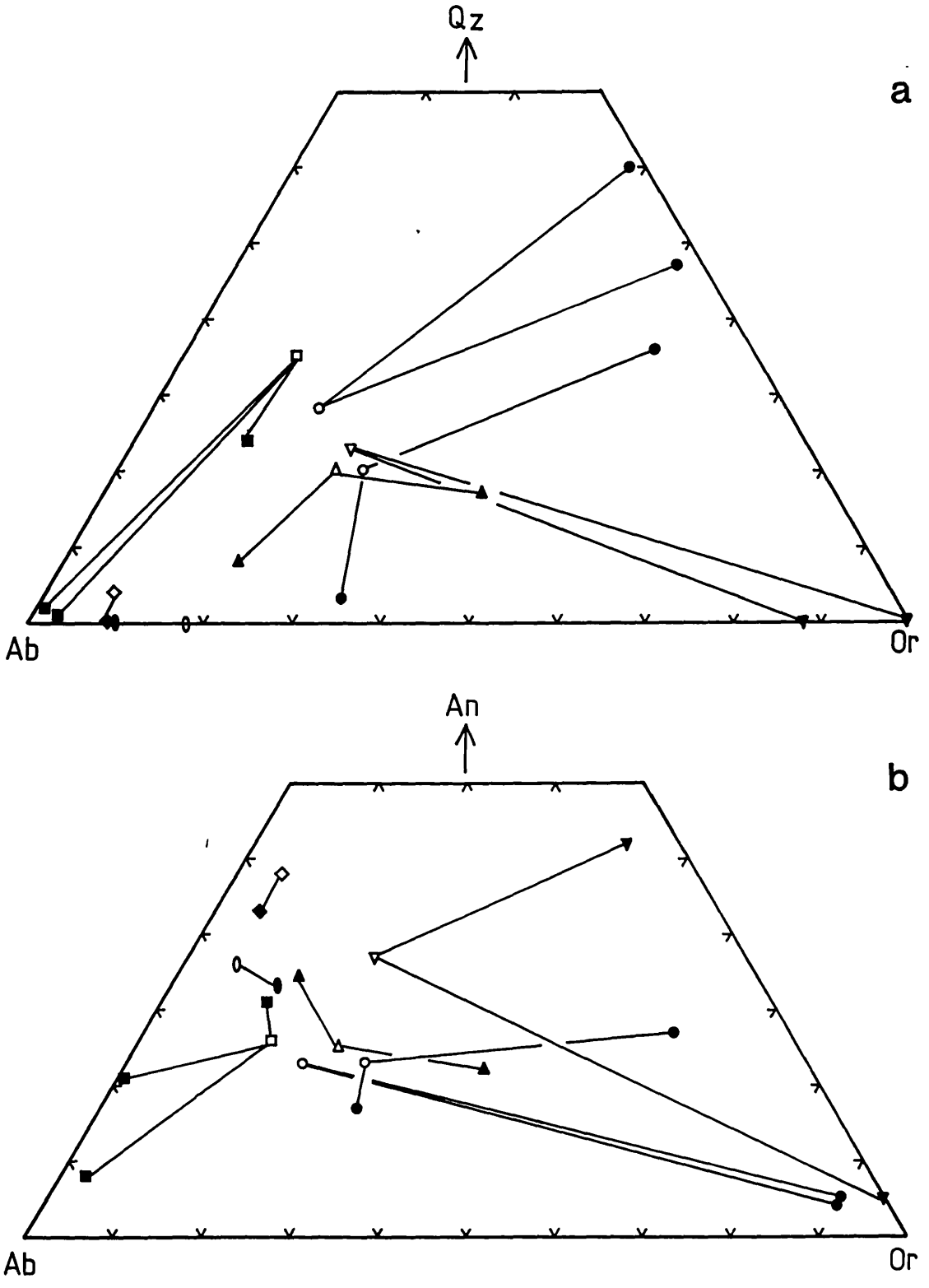
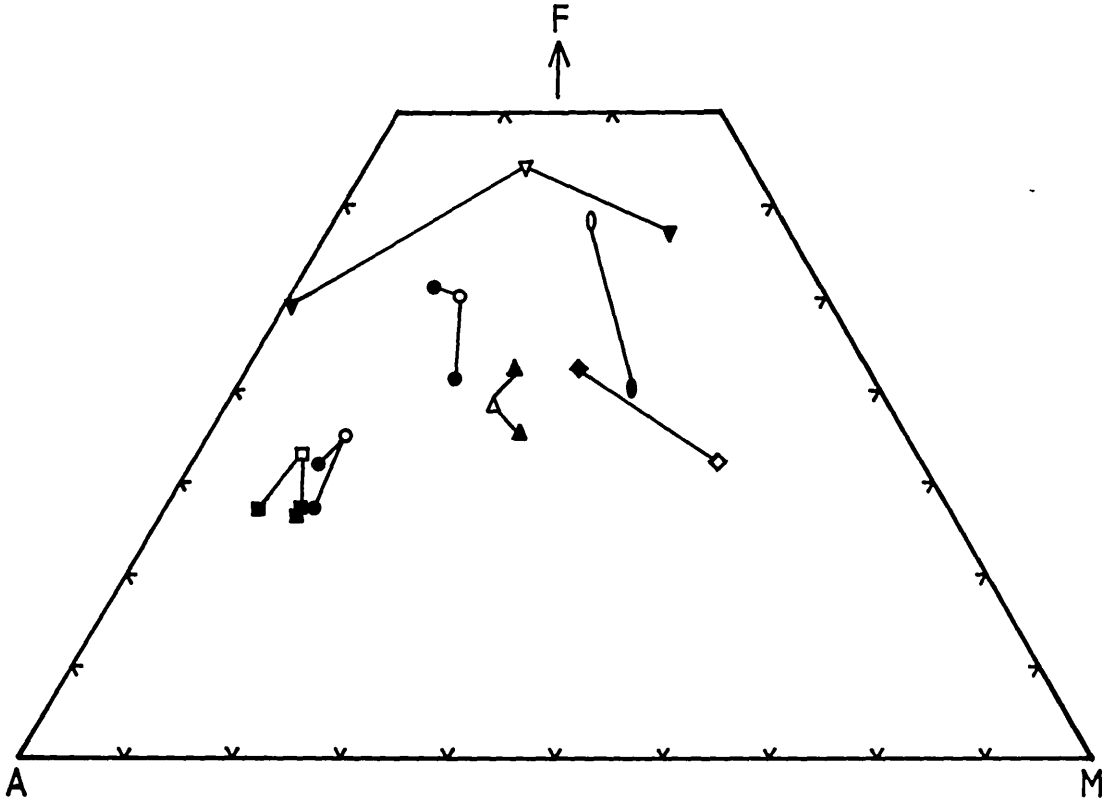


Fig. 6.20c



quartz relative to the composition of the matrix; the former would therefore plot closer to the experimentally-determined minimum melt compositions. (This is of course the 'clast problem' referred to in section 6.2.)

The normative plots (Fig.s 6.18a and b) combined with the AFM plot of Fig. 6.18c illustrate the wide range in composition of pseudotachylyte matrix. This variation undoubtedly results in large part from the variation in host-rock chemistry and mineralogy (Appendix A4). This is also evident from a comparison of the published analyses of Ermanovics et al (1972) and Wallace (1976) with the analyses from this study (Table 6.3, Fig.s 6.18 and 6.19). In the former case, the pseudotachylytes were generated in granitic rocks, richer in SiO_2 than the gneissic host rocks of this study. The large number of olivine-normative analyses in this study (Table 6.3) reflects the important contribution of olivine-normative hornblende and biotite (Table 6.4) to the compositions of hebridean and Gairloch pseudotachylytes. This is supported by the petrographic observation that hydrated ferromagnesian phases are preferrentially consumed during melt formation.

In Fig. 6.20 the composition of pseudotachylyte matrix is compared to its host-rock composition. With the exception of the data of Ermanovics et al (1972) the pseudotachylyte shows enrichment in either normative Ab or Or at the expense of Qz. In terms of the matrix mineralogy, the Ab-rich compositions correspond to plagioclase-rich portions of the matrix (e.g. in proximity to nucleation haloes surrounding porphyroclasts) and the Or-rich compositions to phyllosilicate-rich portions of the matrix. In contrast to the Qz-Ab-Or and An-Ab-Or plots, little variation is seen between host-rock and pseudotachylyte matrix composition on an A-F-M plot (Fig. 6.20c). Taken together, these data indicate that pseudotachylyte melt does not form by total melting as suggested by Masch (1974) and Sibson (1975). The ferromagnesian components, in these examples derived chiefly from hornblende and biotite, are preferentially incorporated into the melt. This is believed to occur at an earlier rather than a later stage during pseudotachylyte melt formation, as will be explained below.

6.7 A Model for Pseudotachylyte Formation

Published hypotheses that suggest pseudotachylyte melt forms by

partial melting of a low melting point granitic fraction, or by total melting, have been rejected on the evidence of both chemical and petrographic data.

In addition to selective mechanical mixing (section 6.5.1), 4 dominant processes are believed to influence the composition of pseudotachylyte melt:-

(i) cataclasis during fault slip (it is assumed a priori that cataclasis preceeds or accompanies melting - cf. Rutter and White, 1979);
(ii) initial melting;
(iii) assimilation of porphyroclastic material by the initially formed melt;
(iv) freezing/crystallization of the pseudotachylyte melt.

It is emphasized that these are not a set of rigidly defined stages in the formation of pseudotachylyte, but an approximate sequence of processes which may overlap in time and space along a fault during and after slip.

Petrographic and chemical data have been presented (sample G1A, section 6.5.1, excepted) which strongly suggest that during pseudotachylyte melt formation the major host-rock phases are consumed in the following order:-

biotite and hornblende > feldspars > quartz

This is clearly shown, for example, by the modal analysis of sample series G80 given in Table 5.7. Two features of this sequence are significant. First, it corresponds to the dry 1-atmosphere melting and/or breakdown points of these minerals (Clarke, 1966). Secondly, it is suggested that this sequence may also reflect an increasing resistance to comminution during cataclastic deformation. This idea is supported by the observation that biotite and amphibole tend to be preferentially 'smeared out' along sub-barren microfaults. Biotite shows similar behaviour in high temperature/high strain rate triaxial deformation experiments on granite (Stesky, 1977); although in the experiments it probably deforms plastically. A high degree of resistance to comminution of quartz relative to other minerals has also been proposed by Philpotts (1964), Allen (1979) and Schwarzman et

al. (1983) in discussion of the chemical composition of pseudotachylytes. Unfortunately there appears to be little published quantitative data concerning the relative rates of comminution of minerals during crushing or shearing of silicate rocks.

Initial melting may be expected to affect first the finest grain size fraction having a high surface area/volume ratio and a high density of defect and damage structures. (There is abundant evidence that these parameters exert a kinetic control on initial melting in both hydrostatic and non hydrostatic partial melting experiments - e.g. van der Molen and Paterson (1979).) On the basis of the chemical and petrographic data given above, it is argued that the finest grain size fraction will contain abundant biotite or amphibole, depending on the host-rock mineralogy. It has been shown in chapter 2 that frictional heating, sufficient to cause melting, requires very low pore fluid pressures. In low porosity/low permeability crystalline rocks, this demands that the total water content is small. In this situation it appears likely that initial melting is largely controlled by dehydration breakdown of hydrous ferromagnesian minerals. This will affect melting in the following ways:-

(i) release of water by dehydration will lower the melting points of further mineral phases entering the melt;
(ii) released water will also lower the viscosity of the melt perhaps assisting heat transfer (i.e. the rate of heating of unmelted domains) by convection and advection;
(iii) incorporation into the melt of network-modifying cations, such as Fe, Mg, Ca, Na and K will also tend to reduce the viscosity of the melt;
(iv) released water may act as a catalyst in the melting process;
(v) the reaction products of dehydration breakdown will be extremely fine grained enhancing their susceptibility to melting (A.J. Brearly, pers. comm., 1985);
(vi) in the case of dehydration breakdown of biotite, an orthoclase component ($KAlSi_3O_8$) should be released and enter the melt tending to reduce the 'liquidus' temperature, depending on the melt composition (Winkler, 1967).

The importance of biotite (when present in the host-rock) during initial melting of pseudotachylytes (and frictionites) has been stressed by Scott and Drever (1953) and Allen (1979); these authors

mentioned some of the effects outlined above. In contrast, Philpotts (1964) suggested that corundum-normative pseudotachylytes might result from assimilation of biotite or chlorite porphyroclasts into an already formed melt. In the present study, 7 of the 8 Co-normative microprobe analyses (Table 6.3) were from pseudotachylytes whose host-rocks contained 15 modal% or more biotite. The above considerations point to biotite involvment in the initial melting, rather than later assimilation.

The infrequent occurrence of mixtures of pseudotachylyte and rock flour/cataclastic debris (cf. sample B1, section 5.7; Francis, 1972; Wenk, 1978) suggests that initial melting is pervasive except perhaps at the cooler margins of some FV's. Following initial melting, larger and/or more refractory porphyroclasts (mainly quartz and feldspar according to the above model) will begin to be corroded and assimilated by the melt. Ample evidence that this occurs has been documented in section 5.8, but the degree of assimilation of clasts and the extent to which it affects the ultimate composition of pseudotachylyte melt/matrix is difficult to assess. This will be largely dependant upon: (i) the initial composition and temperature of the melt; (ii) the porphyroclast mineralogy; (iii) the time-integrated amount of heat available. Irrespective of all other factors, the net effect of porphyroclast assimilation can only be to direct the melt composition toward that which would result from total fusion. It is clear from Fig. 6.20 however, that this is rarely if ever achieved, probably because of fast cooling rates, high melt viscosities and rapid nucleation.

6.7.1 Additional Considerations

Any universal application of the above model must be questioned. Allen (1979), for example, has postulated that hydrous ferromagnesian minerals may be a pre-requisite for pseudotachylyte melt formation. He suggests that this may account for the scarcity of pseudotachylytes in granulite facies rocks. The majority of pseudotachylytes are certainly found in amphibolite-facies or lower grade rocks, although examples are known in granulites (H.K. Obee, pers. comm., 1985). In the present authors opinion, a more fundamental constraint on this relationship is the fact that fewer fault zones cut granulites as compared to amphibolites or lower grade rocks.

The model accounts reasonably well for the matrix composition of

the pyroxene-, chlorite- and phyllosilicate-spherulitic types of pseudotachylyte. However, the volumetrically important (at least to the W of the OHT) plagioclase microlitic pseudotachylytes clearly contain a large fraction of plagioclase component in the melt - as demonstrated by the high modal content of plagioclase microlites (~40%) in the veins. (Similarly, it has been shown in section 6.5.1 that a large proportion of alkali feldspar entered the pseudotachylyte matrix/melt in one vein.) In spite of this, the presence of magnetite and biotite in the devitrified matrix surrounding the microlites demonstrates that a ferromagnesian component also enters the melt. The role of hydrated ferromagnesian minerals in the melting process in these pseudotachylytes may still be important regardless of the reduced volume of these phases.

CHAPTER 7 CONCLUSIONS

7.1 Conclusions

Important observations and results are noted at the end of the relevant sections in this thesis. The most significant conclusions, concentrating on new data are re-iterated here:-

1) Fault-generated pseudotachylytes are widespread in major fault-zones cutting (especially) quartzofeldspathic crust.
2) Mechanical considerations indicate that they are generated by frictional fusion during co-seismic slip (Sibson, 1975). This requires that the host-rocks are dry, of low permeability and rather cold. The occurrence of fault-generated pseudotachylyte is a compelling argument for high shear stresses (of the order of 100 MPa) in some fault zones.
3) The geometry of pseudotachylyte veins in the Outer Hebrides, W of the main thrust base, is consistent with thrust-sense displacements directed to the W and NW. At Rubha Ardvule, earlier transcurrent faults trending NW and NE, are also associated with pseudotachylyte generation.
4) Existing structures and lithologies exert a strong influence on pseudotachylyte faulting. Possible structural/geometric expressions of (theoretical) fault plane barriers have been recognized.
5) Pseudotachylyte faulting may under certain circumstances 'weld' together its host-rocks resulting in a form of displacement hardening.
6) Considerable dilatancy is associated with quasiconglomerate formation. The exact origin of quasiconglomerates is not yet understood.
7) Fault-generated pseudotachylytes, from many localities, have igneous textures and microstructures which can be interpreted in terms of primary crystallization (from a melt) and/or devitrification (from a glass). The textures are dominated by heterogeneous nucleation onto porphyroclasts, and crystal growth dominated by kinetic factors. This is visible on all scales from low magnification optical microscopy to 100K magnification transmission electron microscopy.
8) Minimum temperatures of about 800°C for pseudotachylyte melt formation are suggested from various data. Maximum temperatures may be considerably higher, perhaps 1100°C or more.
9) The compositions of pseudotachylyte matrix material (approximating melt composition), as determined by electron microprobe analysis,

indicate preferential decomposition and fusion of hydrous ferromagnesian phases (principally hornblende and biotite), together with a relatively smaller component of feldspar and quartz. Pseudotachylyte melts do not form by classical partial melting or by total fusion.

10) The whole-rock compositions (major and trace elements) of pseudotachylyte veins (matrix plus clasts), as determined by XRF analysis, are closely similar to the compositions of the rocks from which they were generated. Where pseudotachylyte has been generated between two unlike rock types, the host-rock richer in hydrous ferromagnesian minerals contributes a relatively larger proportion to the composition of the pseudotachylyte. This is interpreted in terms of a selective mechanical mixing effect, and is complementary to 7.

7.2 Suggestions for Future Research

As a result of this study four areas of potential future research on pseudotachylytes are identified:-

(i) there is scope for further analytical transmission electron microscopy (cf. Wenk and Weiss, 1983; Masch et al., 1985) applied particularly to the investigation of porphyroclast/melt phase reactions, and to better-characterizing the crystallography of the matrix mineralogy (e.g. twinning in plagioclase microlites);
(ii) dynamic crystallization experiments involving melts 'seeded' with mineral grains, thereby enhancing heterogeneous nucleation, could provide better constraints on melt temperatures, cooling rates and crystal nucleation and growth rates in natural pseudotachylytes;
(iii) rock deformation experiments involving frictional melting could provide further information on the mechanical significance of melting during earthquake faulting, together with data on the textures and whole rock chemistry of pseudotachylytes; novel experimental procedures are probably required (cf. Weiss and Wenk, 1983) and indeed, preliminary studies have been made using industrial friction welding apparatus (J.G. Spray, pers. comm., 1984); in particular, it would be interesting to try to test the hypothesis of 'welding-up' of rocks by pseudotachylyte melt;
(iv) many aspects of the brecciation and dilatancy associated with pseudotachylyte faulting are poorly understood; these problems might be addressed both in field and theoretical studies.

ADDENDA

Beach, A., 1973. The mineralogy of high temperature shear zones at Scourie, N.W. Scotland. J. Petrol. 14, 231-248.

Bryn, K.O., 1959. Et funn pseudotachylitt i S. Trondelag, og en teori for dannelsen. Norges-Geol. Unders. 211, 8-17.

Parker, R.J., 1979. A computer-based system of XRF analysis and its application to a study of volcanic rocks from Vulsini, central Italy. Unpubl. Ph.D thesis, Univ. Lond.

Ragan, D.M., 1985. Structural Geology. 3rd ed. John Wiley, New York, 208pp.

References

Abbey, S., 1980. Studies in "standard samples" for use in the general analysis of silicate rocks and minerals. Part 6: 1979 edition of usable values. Geol. Soc. Can. Pap. 80-14.

Abbott, J.T., 1972. Rb-Sr study of isotopic redistribution in a Precambrian mylonite-bearing shear zone, Northerh Front Range, Colorado. Geol. Soc. Amer. Bull. 83, 487-494.

Ackerman, P.B. and Walker, F., 1960. Vitrification of arkose by Karoo dolerite near Heilbron, Orange Free State. J. Geol. Soc. 116, 239-254.

Albarede, F. and Bottinga, Y., 1972. Kinetic disequilibrium in trace element partitioning between phenocrysts and host lava. Geochem. Cosmochim. Acta. 36, 141-156.

Al-Rawi, Y. and Carmichael, I.S.E., 1967. A note on the natural fusion of granite. Amer. Miner. 52, 1806-1814.

Aki, K., 1966. Generation and propagation of G waves from the Niigata earthquake of June 16, 1964, part 2, Estimation of earthquake moment, released energy, and stress-strain drop from the G wave spectrum. Bull. Earthquake Res. Inst. Tokyo Univ. 44, 73-88.

Aki, K., 1979. Characterization of barriers on an earthquake fault. J. Geophys. Res. 84, 6140-6148.

Allen, A.R., 1979. Mechanism of frictional fusion in fault zones and pseudotachylytes as indicators of uplift. J. Struct Geol.

Allen, C., 1981. The modern San Andreas fault. In, W.G. Ernst (ed.) The geotectonic development of California. Prentice Hall, New Jersey.

Ambraseys, N.N., 1969. Maximum intensity of ground movements caused by faulting. 4th World Conf. on Earthquake Engineering, Chilean Assoc. on Seismol. and Earthquake Engineering, Santiago, Chile.

Amferer, O., 1939. Die geologische hypothesen uber die formung des talraumes zwischen Umhausen und Langfeld im Otztale. Akad. Wiss. Wien. Sitzungsber. Math.-naturwiss. Kl., Abt. I, 148, 123-140.

Anderson, F. J., 1951. Dynamics of faulting. (2nd ed.) Oliver and Boyd, Edinburgh, 206pp.

Anderson, J.L., Osborne, R.H. and Palmer, D.F., 1980. Petrogenesis of cataclastic rocks within th the San Andreas fault zone of southern California, USA. Tectonophys. 67, 221-249.

- , Osborne, R.H. and Palmer, D.F., 1983. Cataclastic rocks of the San Gabriel fault - an expression of deformation at deeper levels in the San Andreas fault zone. Tectonophys. 98, 209-251.

Anderson, J.R., 1980. A study of mylonitic rocks from major fault zones. Summary of technical repts., 10, U.S. Geol. Surv. Open File Rep. 80-842.

Angevine, C.L., Turcotte, D.L. and Furnish, M.D., 1982. Pressure solution lithificaltion as a mechanism for the stick-slip behaviour of faults. Tectonics 1, 151-160.

Arzi, A.A., 1978. Fusion kinetics, water pressure, water diffusion and electrical conductivity in melting rock, interrelated. J. Petrol. 19, 153-169.

Atkinson, B.K., 1982. Shear stress in fault zones. Nature 296, 708.

- 1979. A fracture mechanics study of sub-critical tensile cracking of quartz in wet environments. Pageophys. 117, 1011-1024.

Auer, F., Berckhemer, H. and Oehlschlegel, G., 1981. Steady state creep of fine grain granite at partial melting. J. Geophys. 49, 89-92.

Bailey, E.B., 1960. The geology of Ben Nevis and Glen Coe. (Sheet 53) 2nd ed. Mem. Geol. Surv. U.K.

- and Maufe, H.B., 1916. The Geology of Ben Nevis and Glen Coe. Mem. Geol. Surv. Scotland.

Bak, J., Sorensen, K., Grocott, J., Korstgard, J.A., Nash, D. and Watterson, J., 1975. Tectonic implications of Precambrian shear belts in western Greenland. Nature, 566-569.

Barnes, V.E., 1939. Pseudotachylyte in meteorites. Univ. Texas Publ. No 3945, 645-656.

Beach, A., 1976. The interrelations of fluid transport, deformation, geochemistry and heat flow in early proterozoic shear zones in the Lewisian complex. Phil. Trans. Roy. Soc. A280, 569-604.

- 1980a. Retrogressive metamorphic processes in shear zones with special reference to the Lewisian complex. J. Struct. Geol. 2, 257-263.

- 1980b. Numerical models of hydraulic fracturing and the interpretation of syntectonic veins. J. Struct. Geol. 2, 425-438.

Bearth, P., 1933. Uber gangmylonite der Silvretta. Schweiz Min. Petr. Mitt. Bel. 13, H2, 347-355.

Beckholmen, M., 1982. Mylonites and pseudotachylytes associated with thrusting of the Koli Nappes, Tannsforsfaltet, central Swedish Caledonides. Geol. Foren. Forh. 104, 23-32.

Bell, T.H. and Etheridge, M.A., 1973. Microstructures of mylonites and

their descriptive terminology. Lithos 6, 337-348.

Benioff, H., 1964. Earthquake source mechanisms. Science 143, 1399-1406.

Ben-menahem, A., 1977. Renormalization of the magnitude scale. Phys. Earth Plan. Inter. 15, 315-340.

B.G.S., 1981.1:100 000 scale geological map of the Outer Hebrides.

Bhattacharjee, C.C., 1963. The late structural and petrological history of the Lewisian rocks of the Meall Deise area, N of Gairloch, Ross-shire. Trans. Geol. Soc. Glasgow 25, 31-60.

- 1964. The Lewisian geology of the Little Sand dioritic mass, Gairloch. Geol. Mag. 101, 48-62.

Bischoff, A.A., 1962. The pseudotachylyte of the Vredefort Dome. Trans. Geol. Surv. S. Afr. 65, 207-226.

Blenkinsop, T. 1983. Cataclasis and the thrust tectonics of south west Sleat, Isle of Skye. Unpubl. M.Sc thesis, Univ. Lond.

Borg, I.Y. and Handin, J., 1966. Experimental deformation of crystalline rocks. Tectonophys. 3, 249-368.

Borges, F. and White, S.H., 1980. Microstructural and chemical studies of sheared anorthosites, Roneval, South Harris. J. Struct. Geol. 2, 273-280.

Bowden, F.P. and Tabor, D., 1967. Friction and lubrication of solids. Methuen, London, 166pp.

Bowen, N.L. and Arousseau, M., 1932. Fusion of sedimentary rock in drill holes. Geol. Soc. Amer. Bull. 34, 431-448.

Brace, W.F., 1980. Permeability of crystalline and argillaceous rocks. Int. J. Rock Mech. Min. Sci. Geomech. Abstr. 17, 241-251.

Brace, W.F. and Byerlee, J.D., 1966. Stick-slip as a mechanism for earthquakes. Science 153, 990-992.

Brace, W.F. and Martin, R.J., 1968. A test of the law of effective stress for crystalline rocks of low porosity. Int. J. Rock Mech. Min. Sci. 5, 415-426.

Brace, W.F. and Walsh, J.B., 1962. Some direct measurements of the surface energy of quartz and orthoclase. Am. Miner. 47, 1111-1122.

Brodie, K.H., 1980. Variations in mineral chemistry across a shear zone in phlogopite peridotite. J. Struct. Geol. 2, 265-272.

- 1981. Variation in amphibole and plagioclase composition with deformation. Tectonophys. 78, 385-402.

Brown, G.C. and Fyfe, W.S., 1970. The production of granitic melts during ultrametamorphism. Contrib. Mineral. Petrol. 28, 310-318.

Brown, W.L., Macaudiere, J., Ohnenstetter, D. and Ohnenstetter, M., 1980. Ductile shear zones in a meta-anorthosite from Harris, Scotland: textural and compositional changes in plagioclase. J. Struct. Geol. 2, 281-287.

Brun, J.P. and Cobbold, P.R., 1980. Strain heating and thermal softening in continental shear zones: a review. J. Struct. Geol. 2, 149-158.

Brune, J.N., 1970. Tectonic stress and the spectra of seismic shear waves from earthquakes. J. Geophys. Res. 75, 4997-5009.

Bryan, W.B., 1972a. Morphology of quench crystals in submarine basalts. J. Geophys. Res. 77, 5812-5819.

- 1972b. Mineralogical studies of submarine basalts. Carnegie Inst. Washington Yearbook 71, 396-403.

Buckley, H.A., Bevan, J.C., Brown, K.M., Johnson, L.R. and Farmer, V.C., 1978. Glauconite and celadonite: two separate mineral species. Mineral. Mag. 42, 373-382.

Burrows, S.E., Humphreys, F.J. and White, S.H., 1979. Dynamic recrystallization and textural development in magnesium deformed in compression at elevated temperatures. 5th Int. Conf. on Strength of metals and alloys. Aachen, p.607-615.

Busch, W., Schneider, G. and Mehnert, K.R., 1974. Initial melting at grain boundaries. Part II: Melting in rocks of granodioritic, quartzdioritic and tonalitic composition. N. Jb. Miner. Mh. 8, 345-370.

Butler, R.W.H., The terminolgy of structures in thrust belts. J. Struct. Geol. 4, 239-245.

Byerlee, 1977. Friction of rocks. Proc. Conf. II; experimental studies of rock friction with application to earthquake prediction. p.55-79. U.S. Geol. Surv., Menlo Park, California.

Cardwell, R.K., Chinn, D.S., Moore, G.F. and Turcotte, D.L., 1978. Frictional heating on a fault zone with finite thickness. Geophys. J. R. Astr. Soc. 57, 525-530.

Carruthers, R. G., Burnett, G. A. and Anderson, W., 1932. The geology of the Cheviot Hills. Mem. Geol. Surv. Eng. Wales

Carslaw, H.S. and Jaeger, J.L., 1959. Conduction of heat in solids, (2nd ed.). Clarendon Press, Oxford.

Carstens, H., 1975. Thermal history of impact melt rocks in the Fennoscandanavian Shield. Contrib. Mineral. Petrol. 50, 145-155.

- 1982. Spherulitic crystallization in lamphrophyric magmas and the origin of ocelli. Nature, 297, 493-494.

Chao, E.C.T, 1967. Ries and the progressive stages of impact metamorphism. Fortschr. Mineral. 44, 139-140.

Chester, F.M., Friedman, M. and Logan, J.M., 1985. Foliated cataclasites. Tectonophys. 111, 139-146.

Chinnery, M.A., 1966. Secondary faulting 1. Theoretical aspects. Can. J. Earth Sci. 3, 163-174.

Christie, J.M., 1960. Mylonitic rocks of the Moine thrust zone in the Assynt region, North-West Scotland. Edin. Geol. Soc. Trans. 18, 79-93.

- and Ord, 1980. Flow stress from microstructures of mylonites: example and current assessment. J. Geophys. Res. 85, 6253-6262.

Clarke, S.P., 1966. Handbook of physical constants. Mem. Geol. Soc. Amer. 97.

Clough, C.T., 1888. The geology of the Cheviot Hills (English side). Mem. Geol. Surv. Eng. Wales (New Series 5).

- , Maufe, H.B. and Bailey, E.B., 1909. Cauldron subsidence of Glencoe. J. Geol. Soc. 65, 611-668.

Coward, M.P., 1969. The structural and metamorphic geology of South Uist, Outer Hebrides. Unpubl. Ph.D thesis, Univ. Lond.

- 1972. The eastern gneisses of South Uist. Scott. J. Geol. 8. 1-12.

- , Francis, P.W., Graham, R.H., Myers, J.S. and Watson, J., 1969. Remnants of an early metasedimentary assemblage in the Lewisian Complex of the Outer Hebrides. Proc. Geol. Assoc. 80, 387-408.

Crawford, M.L., 1975. Crystallization of plagioclase in Mare basalts. Proc. Lunar Sci. Conf. 4th, 705-717.

Dahlen, F.A., 1977. The balance of energy in earthquake faulting. Geophys. J. 48, 239-261.

Daly, R.A., 1947. THe Vredefort Ring structure of South Africa. J. Geol. 55, 125-145.

Das, S. and Aki, K., 1977. Fault plane with barriers: A versatile earthquake model. J. Geophys. Res. 82, 5658-5670.

- and Scholz, C. T., 1981. Theory of time dependent rupture in the earth. J. Geophys. Res. 86, 6039-6051.

Day, A.L. and Allen, E.T., 1925. The volcanic activity and hot springs of Lassen Peak. Pubn. 360, Carnegie Inst., Washington.

Dearnley, R., 1962. An outline of the Lewisian complex of the Outer Hebrides in relation to that of the Scottish mainland. J. Geol.

Soc. Lond. 188, 143-176.

- and Dunning, F.W., 1968. Metamorphosed and deformed pegmatites and basic dykes in the Lewisian complex of the Outer Hebrides and their geological significance. J. Geol. Soc. 123, 335-378.

Deer, W.A., Howie, R.A. and Zussman, J., 1966. An introduction to the rock-forming minerals. Longman, London, 528pp.

Dietrichson, B., 1953. Pseudotachylit fra de kaledonske Skyresoner i Jotunheimens forgarder, Gudbrandsdalen, og deres dannelsesbetingelser. Norges. Geol. Unders. 184, 23-70.

Dietz, R. S., 1961. Vredefort Ring structure: meteorite impact scar? J. Geol. 69, 499 - 516.

Dimroth, E. and Lichtblau, A.P., 1971. Metamorphic evolution of Archean hyaloclastites, Noranda area, Quebec. Part I: Comparison of Archean and cenozoic sea-floor metamorphism. Can. J. Earth Sci. 16, 1315-1340.

Donaldson, C.H., Usselman, T.M., Williams, R.J. and Lofgren, G.E., 1975. Experimental modelling of the cooling history of Apollo 12 olivine basalts. Proc. Lunar Sci. Conf. 6th, 843-869.

Dougal, J.W., 1928. Observations on the geology of Lewis. Trans. Geol. Soc. Edin. 12, 12-18.

Dowty, E., 1980. Crystal growth and nucleation theory and the numerical simulation of igneous crystallization, in Hargraves, R.B. (ed.), Physics of magmatic processes. Princeton.

Durney, D.W., 1976. Pressure-solution and crystallization deformation. Phil. Trans. Roy. Soc. Lond. A283, 229-240.

Eggler, D.H., 1972. Water-saturated and undersaturated melting relations in a Paracutin andesite and an estimate of water content in the natural magma. Contrib. Mineral. Petrol. 34, 261-271.

Engelder, T., Logan, T. and Handin, J., 1975. The sliding characteristics of sandstone on quartz fault gouge. Pure Appl. Geophys. 113, 69-86.

Erismann, T.H., 1977. Der bimmstein von Kofels, impaktit oder friktionit? Material und Technik. 5, 190-196.

- 1979. Mechanisms of large landslides. Rock Mechanics 12, 15-46.

- , Heuberger, H. and Preuss, E., 1977. Der bimmstein von Kofels (Tirol), ein bergstrutz-"friktionit". Tsch. Min. Petr. Mitt. 24, 67-119.

Ermanovics, I.F., Helmstaedt, H. and Plant, A.G., 1972. An occurrence of Archean pseudotachylyte from southeastern Manitoba. Can. J. Earth Sci. 9, 257-265.

Evernden, J.F. and James, G.T., 1964. Potassium-argon dates and the Tertiary floras of North America. Amer. J. Sci. 262, 945- .

Filson, J., Simkin, T. and Lew, L., 1973. Seismicity of a caldera collapse: Galapagos Islands 1968. J. Geophys. Res. 78, 8591-8622.

Fleitout, L. and Froidevaux, C., 1980. Thermal and mechanical evolution of shear zones. J. Struct. Geol. 2, 159-164.

Francis, P., 1969. Some aspects of the Lewisian geology of the isle of Barra and adjacent small islands. Unpubl. Ph.D thesis, Univ. Lond.

- 1972. The pseudotachylyte problem. Comm. Earth Sci. Geophys. 3, 35-53.

- and Sibson, R.H., 1973. The Outer Hebrides Thrust. In: The early Precambrian of Scotland and related rocks of Greenland, R.G. Park and J. Tarney (eds.), Univ. Keele.

Freidman, M., Logan, J.M. and Rigert, J.A., 1974. Glass-indurated quartz gouge in sliding friction experiments on sandstone. Geol. Soc. Amer. Bull. 85, 937-942.

Fuller, K.N.G., Fox, P.G. and Field, J.E., 1975. The temperature rise at the tip of fast-moving cracks in glassy polymers. Trans. Roy. Soc. A341, 537-557.

Gamond, J.F., 1983. Displacement features associated with fault zones: a comparison between observed examples and experimental models. J. Struct. Geol. 5, 33-45.

Goldschmidt, V. M., 1943.Om friksjonglas (pseudotachylitt); fjelkjeden. Geol. For. Stockh. Forh. 65, 83-84.

Gresens, R.I., 1967. Composition-volume relationships of metasomatism. Chem. Geol. 2, 47-65.

Griggs, D.T, and Baker, D.W., 1969. The origin of deep focus earthquakes. In, H. Mark and S. Fernbach (eds.), Properties of matter under unusual conditions. p.23-42. Interscience, New York.

Grocott, J., 1977a. The northern margin of the Ikertok shear belt, West Greenland. Unpubl. Ph.D Thesis, Univ. Liverpool.

- 1977b. The relationship between Precambrian shear belts and modern fault systems. J. Geol. Soc. 133, 257 - 262.

- 1981. Fracture geometry of pseudotachylyte generation

zones: a study of shear fractures formed during seismic events. J. struct. Geol. 3, 169-178.

Hafner, S.S., Virgo, D. and Warburton, D., 1971. Oxidation state of iron in plagioclase from basalts. Earth Plan. Sci. Lett. 12, 159-166.

Hall, A.L. and Molengraaf, G.A.F., 1925. The Vredefort Mountain Land in the southern Transvaal and the northern Orange Free State. Shaler Memorial Series, Verhan. K. Akad. Wet. Amsterdam (Tweede sectie) 3, 1-183.

Hall, M.G. and Lloyd, G.E., 1982. The SEM examination of geological samples with a semiconductor backscattered electron detector. Amer. Miner. 66, 362-368.

Hall, S.H., 1983. Post Alpine tectonic evolution of S.E. Spain and the structure of fault gouges. Unpubl. Ph.D thesis, Univ. Lond.

Hammer, W. von, 1915. Das gebeit der Bundnerscheifer im Tirolischen oberinntal. Geol. Reichsanstalt 64, 443-567.

Hancock, P., 1972. The analysis of en-echelon veins. Geol. Mag. 109, 269-276.

Handin, J., 1957. Experimental deformation of rocks and minerals. Colorado Sch. Mines Quart. 52, 75-98.

Hanks, T.C., 1974. The faulting mechanism of the San Fernando earthquake. J. Geophys. Res. 79, 1215-1229.

- and Raleigh, C.B., 1980. The conference on magnitude of deviatoric stresses in the Earth's crust and uppermost mantle. J. Geophys. Res. 85, 60683-60685.

Harris, C. and Bell, J.D., 1982. Natural partial melting of syenite blocks from Ascesion Island. Contrib. Mineral. Petrol. 79, 107-113.

Harris, C.C., 1966. Onthe role of energy in comminution: a review of physical and mathematical principles. Trans. Inst. Min. Metal. C75, 37-56.

Harrison, T.M. and Watson, E.B., 1983a. The behaviour of apatite during crustal anatexis: equilibrium and kinetic considerations. Geochim. Cosmochim. Acta 48, 1467-1477.

- 1984. Kinetics of zircon dissolution and diffusion of zirconium in granitic melts of variable water content. Contrib. Mineral. Petrol. 84, 66-105.

Hartzell, S.H., Brune, J.N. and Prince, J., 1978. The October 6, 1974 Acapulco earthquake: an example of the importance of short-period surface waves in strong ground motion. Bull. Seis.

Soc. Amer. 68, 1663-1677.

- and Helmburger, D. V., 1982. Strong motion modelling of the Imperial Valley earthquake of 1979. Bull. Seism. Soc. Amer. 72, 571-596.

Hawkes, L., 1929. Pseudotachylyte. Geol. Mag. 66, 143-144.

Heissel, W., 1938. Gesteinsaufschmelzungen bei Otz im Otztal (Tirol). Jb. Geol. Bundesanst. 88, 207-215.

Hellman, P.L., Smith, R.E. and Henderson, P., 1977. Rare earth element investigation of the Cliefdon Outcrop, NSW, Australia. Contrib. Mineral. Petrol. 37, 91-109.

Helz, R.T., 1982. Phase relations and compositions of amphiboles produced in studies of the melting behaviour of rocks. Mineralogical Soc. Amer. Reviews in Mineralogy 9B, 279-353.

Henderson, P., 1982. Inorganic Geochemistry. Pergamon, 353pp.

Hibbard, M.J., 1981. The magma mixing origin of mantled feldspars. Contrib. Mineral. Petrol. 76, 158-170.

Higgins, M.W., 1971. Cataclastic rocks. U.S.G.S. Prof. Pap. 687.

Hobbs, B.E., 1968. Recrystallization of single crystals of quartz. Tectonophys. 6, 353-401.

Holdaway, M.J., 1980. Chemical formulae and activity models for biotite, muscovite, and chlorite applicable to pelitic metamorphic rocks. Amer. Mineral. 65, 711-719.

Holland, T., The charnockite series - a group of Archaean hypersphene rocks in peninsula India. Mem. Geol. Surv. India 28, 119-249.

Hukki, R.T., 1975. The principles of comminution: an analytical summary. Eng. Min. J. (May), 106-110.

Hundley, E.M. and Moody, J.B., 1977. TEM confirmation of glass in experimentally produced fault gouge in orthoquartzite. Geol. Soc. Amer. Abstr. Progs. 9, 1030-1031.

Husseini, M.I., Jovanovich, D.B., Randall, M.J. and Freund, L.B., 1975. The fracture energy of earthquakes. Geophys. J. R. Astr. Soc. 43, 367-385.

- and Randall, M.J., 1976. Rupture velocity and radiation efficiency. Bull. Seism. Soc. Amer. 66, 1173-1187.

Irwine, W.P. and Barnes, I., 1975. Effect of geological structure and metamorphic fluids on seismic behaviour of the San Andreas fault system in central and northern California. Geology 3, 713-716.

Jackson, R.E. and Dunn, D.E., 1974. Experimental sliding friction and cataclasis of rocks. Int. J. Rock Mech. Min. Sci. 11, 235-249.

Jaeger, J.C., 1957. The temperature in the neighbourhood of a cooling

intrusive sheet. Amer. J. Sci. 255, 306-318.

Jeffereys, H., 1942. On the mechanics of faulting. Geol Mag. 79, 291-329.

Jehu, T. J., 1923. Observations on flinty crush rocks. Trans. Edin. Geol. Soc. 11, 405-406.

- and Craig, R.M., 1923. Geology of the Outer Hebrides. Part 1 - The Barra Isles. Trans. Roy. Soc. Edin. 53, 419-441.

- 1925. Geology of the Outer Hebrides. Part 2 - South Uist and Eriskay. ibid. 53, 615-641.

- 1926. Geology of the Outer Hebrides. Part 3 - North Uist and Benbecula. ibid. 54, 467-489.

- 1927. Geology of the Outer Hebrides. Part 4 - South Harris. ibid. 55, 457-488.

Kanamori, H., 1977. The energy release during great earthquakes. J. Geophys. Res. 82, 2981-2987.

- and Anderson, D.L., 1975. Theoretical basis of some empirical relations in seismology. Bull. Seism. Soc. Amer. 65, 1073-1095.

Kasahara. K., 1981. Earthquake Mechanics. Cambridge Univ. Press, 248pp.

Keil, K., Fodor, R.V. and Bunch, T.E., 1972. Contributions to the mineral chemistry of Hawaiian rocks. II. Feldspars and interstitial material in rocks from Haleakala and West Mau volcanoes, Maui, Hawaii. Contrib. Mineral. Petrol. 37, 253-276.

Keith, H.D. and Padden, F.J, 1963. A phenomenological study of spherulitic crystallization. J. Appl. Phys. 34, 2409-2421.

Kasza, S.E., 1981. Cataclastic metamorphism in the south-eastern Adirondack Mountains, New York State. Unpubl. Master's thesis, State Univ. N.Y., Binghampton.

Kerrich, R., Alliison, I., Barnett, R.L., Moss, S. and Starkey, J., 1980. Microstructural and chemical transformations accompanying deformation of granite in a shear zone at Mieville, Switzerland; with implications for stress corrosion cracking and superplastic flow. Contrib. Mineral. Petrol. 73, 221-242.

- , Fyfe, W.S., Gorman. B.E. and Allison, I., 1977. Local modification of rock chemistry by deformation. Contrib. Mineral. Petrol. 65, 183-190.

Kieffer, S.W., Phakey, P.P. and Christie, J.M., 1976. Shock pressures in porous quartzite: Transmission electron microscope observations and theory. Contrib. Mineral. Petrol. 59, 41-93.

King, W. and Foote, R.B., 1864. On the geological structure of portions of the districts of Trichonopoly, Salem and South Arcot, Madras, included in sheet No. 79 of the Indian Atlas. Mem. Geol. Surv. India 4, 223-386.

Kirkpatrick, R.J., 1981. Kinetics of crystallization of igneous rocks, in Lasaga, A.C. and Kirkpatrick, R.J. (ed.s), Mineral. Soc Amer. Reviews in Mineralogy 8, 321-398.

Knopf, E.B., 1931. Retrogressive metamorphism and phyllonitization. Amer. J. Sci. 21, 1-27.

Kohlstedt, D.L. and Weathers, M.S., 1980. Deformation-induced microstructures, paleopiezometers, and differential stresses in deeply eroded fault zones. J. Geophys. Res. 85, 6269-6285.

Kurat, G. and Richter, W., 1972. Impactite von Kofels, Tirol. Tschermaks Mineral. Petrogr. Mitt. 17, 23-45.

Lachenbruch, A.H., 1980. Frictional heating, fluid pressure and the resistance to fault motion. J. Geophys. Res. 85, 6097-6112.

- and Sass, J. H., 1973. Thermomechanical aspects of the San Andreas fault system, in Proceedings of the conference on tectonic problems of the San Andreas fault system, edited by R.L.Kovach and A. Nur, pp. 192-205, Stanford Univ. Press, Palo Alto, Calif.

- 1980. Heat flow and energetics of the San Andreas fault zone. J. Geophys. Res. 85, 6185-6222.

Lacroix, A., 1926. Les veinules fondues des meteorites, leur analogie avec les "pseudotachylytes" des regions ecrasees. Compt. Rend. Acad. Sci. Paris 182, 1581-1584.

Lambeck, K., 1980. Estimates of stress differences in the crust from isostatic considerations. J. Geophys Res. 85, 6397-6402.

- and Nakiboylu, 1980. Seamount loading and stress in the ocean lithosphere. J. Geophys. Res. 85, 6403-6418.

Lapworth, C., 1885. The Highland controversy in British geology: its causes, course and consequences. Nature 32, 558-559.

Larsen, E.S. and Switzer, G., 1939. An obsidian-like rock formed from the melting of a granodiorite. Amer. J. Sci. 237, 562-568.

LeMaitre, R.W., 1974. Partially fused granite blocks from Mt Elephant, Victoria, Australia. J. Petrol. 15, 403-412.

- 1979. A new generalised petrological mixing model. Contrib. Mineral. Petrol. 71, 133-137.

Lockner, D.A. and Okubo, P.G., 1983. Measurements of frictional heating in granite. J. Geophys. Res. 88, 4313-4320.

Lofgren, G., 1971a. Experimentally produced devitrification textures in natural rhyolitic glass. Bull. Geol. Soc. Amer. 82, 111-124.

- 1971b. Spherulitic textures in glassy and crystalline rocks. J. Geophys. Res. 76, 5635-5648.

- 1974. An experimental study of plagioclase morphology: isothermal crystallization. Amer. J. Sci. 274, 243-273.

- 1977. Dynamic crystallization experiments bearing on the origin of textures in impact generated liquids. Proc. Lunar Sci. Conf. 8th, 2079-2095.

- 1980. Experimental studies on the dynamic crystallization of silicate melts, in Hargraves, R.B. (ed.), Physics of magmatic processes. Princeton.

- , Donaldson, C.H., Williams, R.J., Mullins, O. and Usselman, T.M., 1974. Experimentally reproduced textures and mineral chemistry of Apollo 15 quartz normative basalts. Proc. Lunar Sci. Conf. 5th, 549-567.

- and Norris, P.N., 1981. Experimental duplication of plagioclase seive and overgrowth textures. Geol. Soc. Amer. Abst. with Programs, , 498.

- , Smith, D.P. and Roy, D., 1978. Dynamic crystallization and kinetic melting of the lunar soil. Proc. Lunar Sci. Conf. 9th, 959-975.

Logan, J.M., Higgs, N.G. and Friedman, M., 1981. Laboratory studies of natural gouge from the U.S. Geological Survey Dry Lake Valley No. 1 Well, San Andreas Fault zone. Amer. Geophys. Union Monograph 24, 121-134.

Longhi, J., Walker, D. and Hays, J.F., 1976. Fe and Mg in plagioclase. Proc. Lunar Sci. Conf. 7th, 1281-1300.

Macaudiere, J. and Brown, W.L., 1982. Transcrystalline shear fracturing and pseudotachylyte generation in a meta-anorthosite (Harris, Scotland). J. Struct. Geol. 4, 395-406.

Macaudiere, J., Brown, W.L. and Ohnenstetter, D., 1985. Microcrystalline textures resulting from rapid crystallization in a pseudotachylyte melt in a meta-anorthosite. Contrib. Mineral. Petrol. 89, 39-51.

Maculloch, J., 1819. A description of the western isles.

Maddock, R.H., 1983. Melt origin of fault-generated pseudotachylytes demonstrated by textures. Geology 11, 105-108.

- 1986a. Frictional melting in landslide-generated frictionites (hyalomylonites) and fault-generated

pseudotachylytes - Discussion. Tectonophys. (in press)

- 1986b. Partial melting of lithic porphyroclasts in fault-generated pseudotachylytes. Neues Jahr. Mineral. (in press).

- , Grocott, J. and van Nes, M., 1986. Vesicles, amygdales and similar structures in fault-generated pseudotachylytes. Lithos (in press).

Martini, J.E.J., 1978. Coesite and stishovite in the Vredefort Dome, South Africa. Nature 272, 715-717.

Masch, L., 1973. Investigation of the molten state and deformation of the pseudotachylites of the Silvretta (Austria, Switzerland). Neues. Jahrb. Miner. Mh. Jg. 11, 485-509.

- 1979. Deformation and fusion of two faultrocks in relation to their depth of formation: the hyalomylonite of the Langtang (Himalaya) and the pseudotachylytes of the Silvretta nappe (Eastern Alps). Conf. on analysis of actual fault zones in bedrock, U.S.G.S. Open File Rep. 79-1239, 528-533.

- and Preuss, E., 1977. Das vorkhommen des hyalomylonites von Langtang, Himalaya (Nepal). Neues Jahrb. Miner. 129, 292-311

- , Wenk, H.R. and Preuss, E., 1985. Electron microscopy study of hyalomylonites - evidence for frictional melting in landslides. Tectonophys. 115, 131-160.

Maury, R. and Bizouard, H., 1974. Melting of acid xenoliths into a basanite: an approach to the possible mechanisms of crustal contamination. Contrib. Mineral. Petrol. 48, 275-286.

Mawer, C.K., 1985. Comment and reply on "Fault-related rocks: suggestions for terminology". Geology 13, 378-379.

McGarr, A., 1980. Some constraints on levels of shear stress in the crust from observations and theory. J. Geophys. Res. 85, 6231-6238.

- A., Zoback, M.D. and Hanks, T.C., 1982. Implications of an elastic analysis of the in-situ stress measurements near the San Andreas Fault. J. Geophys. Res. 87, 7797-7806.

McNutt, M., 1980. Implications of regional gravity for state of stress in the Earth's crust and upper mantle. J. Geophys. Res. 85, 6377-6396.

McKenzie, D. and Brune, J.N., 1972. Melting of fault planes during large eathquakes. Geophys. J. Roy. Astr. Soc. 29, 65-78.

Melosh, H.J., 1979. Acoustic fluidization: a new geologic process. J. Geophys. Res. 84, 7513-7520.

Mehnert, K.R., Busch, W. and Schneider, G., 1973. Initial melting at grain boundaries of quartz and feldspar in gneisses and granulites. N. Jb. Miner. Mh. 4, 165-183.

Mercier, J.G.C., 1980. Magnitude of the continental lithospheric stresses inferred from rheomorphic petrology. J. Geophys. Res. 85, 6293-6303.

Mevel, C., 1978. Mineralogy and chemistry of secondary phases in low temperature altered basalts from deep sea drill project legs 51, 52 and 53. Initial Rept. D.S.D.P. 53, 1299-1317.

Milton, D.H., 1964. Fused rocks from Kofels, Tirol. Tschermaks Mineral. Petrogr. Mitt. 9, 86-94.

van der Molen, I. and Paterson, M.S., 1979. Experimental deformation of partially-melted granite. Contrib. Mineral. Petrol. 70, 299-318.

Moore, H.E., 1980. Rock textures and microstructures related to cataclastic processes. Unpubl. Ph.D thesis, Univ. Lond. 215pp.

- and Sibson, R.H., 1979. Experimental thermal fragmentation in relation to seismic faulting. Tectonophys. 49, T9-T17.

Morrison, M.A., 1979. Igneous and metamorphic geochemistry of Mull lavas. Unpubl. Ph.D thesis, Univ. Lond.

Nabelek, P.I., Taylor, L.A. and Lofgren, G.E., 1978. Nucleation and growth of plagioclase and the development of textures in a high-alumina basaltic melt. Proc. Lunar Sci. Conf. 9th, 725-741.

Naney, M.T., 1983. Phase equilibria of rock-forming ferromagnesian silicates in granitic systems. Amer. J. Sci. 283, 993-1033.

Nedelec, A. and Paquet, J., 1981. La fusion naturelle et experimental de la biotite de gneiss du Haut-Allier (Massif Central). C. R. Acad. Sci. Paris 292, 1283-1286.

Nicholls, J. and Stout, M.Z., 1982. Heat effects of assimilation, crystallization and vesiculation in magmas. Contrib. Mineral. Petrol. 8, 328-339.

Nicolaysen, L., 1972. North American cryptoexplosion structures. Mem. Geol. Soc. Amer. 132, 605-620.

Nockolds, S.R., 1940. Petrology of rocks from Queen Mary Land. Australasian Antarctic Exped., 1911-1914. Sci. Repts. Ser. A, 4, 15-86.

Nur, A., 1972. Dilatancy, pore fluids and premonitory variations of t_s/t_p travel times. Bull. Seis. Soc Amer. 62, 1217-1222.

Nystrom, J.O., 1984. Rare earth element mobility in vesicular lava during low grade metamorphism. Contrib. Mineral. Petrol. 88,

328-331.

Obee, H.K., 1985. Fault rock and deformation studies of a major continental fault system. Unpubl. Ph.D thesis, Univ Lond. 238pp.

Okubo, P.G. and Dieterich, J.H., 1980. Fracture energy of stick-slip experiments in a large-scale biaxial experiment. Geophys. Res. Lett. 8, 887-890.

O'Neill, J.R. and Hanks, T.C., 1980. Geochemical evidence for water-rock interaction along the San Andreas and Garlock faults in California. J. Geophys. Res. 85, 6286-6291.

Papike, J.J., Cameron, K.L. and Baldwin, K., 1974. Amphiboles and pyroxenes: characterization of other than quadrilateral components and estimates of ferric iron from microprobe data. Geol. Soc. Amer. Abstr. with Progs. 6, 1053-1054.

Paquet, J., Francois, P. and Nedelec, A., 1981. Effect of partial melting on rock deformation: experimental and natural evidences on rocks of granitic compositions. Tectonophys. 78, 545-565.

Park, R. G., 1961. The pseudotachylyte of the Gairloch district, Ross-shire, Scotland. Amer. J. Sci. 259, 542 - 550.

Parker, R. J., 1980. Preparation of rock samples for XRF analysis. Technical report No XRF-3. Imperial College, 12pp.

- , R.J., 1983. Single pass X-ray fluorescence analysis of silicate rock samples using a Phillips 1212 spectrometer. X-ray Spectrom. 11, 100-108.

Passchier, C.W., 1982a. Mylonitic deformation in the Saint-Barthelmy massif, french Pyrenees, with emphasis on the genetic relationship between ultramylonite and pseudotachylyte. GUA Papers of Geology Series 1, No.16-1982.

- , C.W., 1982b.Pseudotachylyte and the development of ultramylonite bands in the Saint-Barthelmy massif, French Pyrenees. J. Struct. Geol. 4, 69-79.

Paterson, M.S., 1978. Experimental rock deformation - the brittle field. Springer-Verlag, 254pp.

Peach, B.N, Horne, J., Gunn, W., Clough, C.T., Hinxman, L.W. and Teall, J.J.H, 1907. The geological structure of the north-west highlands of Scotland. Mem. Geol. Surv. U.K.

Pecher, A., 1981. Experimental decrepitation and re-equilibration of fluid inclusions in synthetic quartz. Tectonophys. 78, 567-583.

Peredery, W.V., 1972. in Guy-Bray, J.V. (ed), New developments in Sudbury geology. Geol. Assoc. Can. Spec. Pap. 10, -.

Pettinga, J.R., 1982. Upper Cenozoic structural history, coastal

southern Hawke's Bay, New Zealand. N.Z. J. Geol. Geophys. 25, 149-191.

Philpotts, A.R., 1964. Origin of pseudotachylyte. Amer. J. Sci. 262, 1008-1035.

- and Miller, J.A., 1963. A pre-Cambrian glass from St. Alexis-des-Monts, Quebec. Geol. Mag. 100, 337-344.

Pichamuthu, C.S., 1959. Trap-shotten rock from the Biligirirangan Hills, Mysore State, India. Nature 183, 483-484.

Pichler, A., 1863. Zur geognosie Tirols. II. Die vulcanischen reste von Kofels. Jb. K.K Geol. Reichsanst. (Wien) 13, 591-594.

Poirier, J.P., 1985. Creep of crystals. Cambridge Univ. Press.

Prescott, W.H. and Nur, A., 1981. Accomodation of relative motion at depth on the San Andreas fault system in California. J. Geophys. Res. 86, 999-1004.

Preuss, E., 1971. Uber den bimmstein von Kofels/Tirol. Fortschr. Min. 49, S70.

- 1974. Der bimmstein von Kofels im Otztal/Tirol.

Price, G.D, Putnis, A. and Agrell, S.O., 1979. Electron petrography of shock-produced veins in the Tenham meteorite. Contrib. Mineral. Petrol. 7, 211-218.

Price, N.J., 1966. Fault and joint development in brittle and semi-brittle rocks. Pergamon, 176pp.

- 1970. Laws of rock behaviour in the earth's crust. In, W.H. Somerton (ed.), Rock Mechanics. Proc. 11th Symp. Rock Mechanics, Berkeley A.I.M., 1-23.

Raleigh, C. B., 1977. Frictional heating, dehydration and earthquake stress drops. In, Experimental studies of rock friction with applications to earthquake prediction, 291-304. National earthquake hazards reduction program, U.S. Geol. Surv.

Ramsay, J. G., 1980. The crack-seal mechanism of rock deformation. Nature 284, 135-139.

Reed, S.B.J., 1975. Electron microprobe analysis. Cambridge Univ. Press, pp.

Reid, H.F., 1910. The Calif. earthquake of April 18, 1906. Rept. State Earthquake Invest. Comm. v.II, Carnegie Inst. of Washington, Washington D.C., 192pp.

Reynolds, D.L., 1954. Fluidization as a geological process, and its bearing on the problem of intrusive granites. Amer. J. Sci. 252, 577-614.

Rice, J.R. and Simmons, D.A., 1978. The stabilization of spreading

shear faults by coupled deformation-diffusion effects in fluid-infiltrated porous materials. J. Geophys. Res. 81, 5322-5334.

Richards, P.G., 1976. Dynamic motions near an earthquake fault: a three dimensional solution. Bull. Seism. Soc. Amer. 66, 1-32.

Richter, 1958. Elementary seismology. W.H. Freeman, San Francisco.

Rickard, M.J. and Rixon, L.K., 1983. Stress configurations in conjugate quartz-vein-arrays. J. Struct. Geol. 6, 573-578.

Roberts, J.L., 1966. The emplacement of the Main Glen Coe Fault intrusion at Stob Mhic Mhartuin. Geol. Mag. 103, 299-315.

Robinson, P., Spear, F.C., Schumacher, J.C., Laird, J., Klein, C., Evans, B.W. and Doolan, B.L., 1982. Phase relations of metamorphic amphiboles: natural occurence and theory. Mineralogical Soc. Amer. Reviews in Mineralogy 9B, 1-227.

Roedder, E., 1979. Silicate liquid immiscibility in magmas. In, H.S. Yoder (ed.), The evolution of the igneous rocks. Princeton, 588pp.

Rudnicki, J.W. and Kanamori, H., 1981. Effects of fault interaction on moment, stress drop and strain energy release. J. Geophys. Res. 86, 1785-1793.

Rutter, E.H. and Mainprice, D., 1978. The effect of water on faulted and unfaulted sandstone. Pageophys. 116, 634-654.

- and White, S.H., 1979. The microstructure and rheology of fault gouges produced experimentally under wet and dry conditions at temperatures up to 400 C. Bull. Mineral. 102, 101-109.

- , Maddock, R.H., Hall, S.H. and White, S.H., 1986. Comparative microstructures of natural and experimentally produced fault gouges. Pageophys. (in press).

Salop, L.I., 1949. Pseudotachylyte from the Cis-Baikal and the western trans-Baikal regions and the problems of their genesis. Bull. Akad. Sci. U.S.S.R., ser. geol. 5, 40-56.

Savage, J.C. and Walsh, J.B., 1978. Gravitational energy and faulting. Bull. Seism. Soc. Amer. 68, 1613-1622.

Segall, P. and Pollard, D.D., 1980. Mechanics of discontinuous faults. J. Geophys. Res. 85, 4337-4350.

Schidlowski, M.O.G., 1963. Recrystallization of zircon as an indicator of contact metamorphism. Nature 197, 68-69.

Schiffman, P. and Lofgren, G.E., 1982. Dynamic crystallization studies on the Grande Ronde pillow basalts, central Washington. J. Geol.

90, 49-78.

Schleicher, H. and Lippolt, H.J., 1981. Magmatic muscovite in felsitic parts of rhyolites from southwest Germany. Contrib. Mineral. Petrol. 78, 220-224.

Scholz, C.H., 1980. Shear heating and the state of stress on faults. J. Geophys. Res. 85,

- , 1982. Scaling laws for large earthquakes: consequwences for physical models. Bull. Seism. Soc. Amer. 72, 1-14.

- , Molnar, P. and Johnston, T., 1972. Detailed studies of frictional sliding of granite and implications for the earthquake mechanism. J. Geophys. Res. 77, 6392-6406.

- , Sykes, L.R. and Agarwal, Y.P., 1973. Earthquake prediction: a physical basis. Science 181, 803-810.

- , Beavan, J. and Hanks, T.C., 1979. Frictional heating, argon depletion and tectonic stress on the Alpine Fault, New Zealand. J. Geophys. Res. 84, 6770- .

Schreyer, W. and Abraham K., 1978. Symplectic cordierite-orthopyroxene-garnet assemblages as products of contact metamorphism of pre-existing basement granulites in the Vredefort structure, South Africa, and their relations to pseudotachylite. Contrib. Mineral. Petrol. 68, 53-62.

Schwarzman, E.C., Meyer, C.E. and Wilshire, H.G., 1983. Pseudotachylyte from the Vredefort Ring, South Africa, and the origins of some lunar breccias. Bull. Geol. Soc. Amer. 94, 926-935.

Scott, J.S. and Drever, H. I., 1953. Frictional fusion along a Himalyan thrust. Proc. Roy. Soc. Edinburgh 65, 121-142.

Shaw, H.R., 1980. The fracture mechanisms of magma transport from the mantle to the surface, in, R.B. Hargraves (ed.), Physics of magmatic processes, Princeton Univ. Press, Princeton N.J., 201-264.

Shand, S.J., 1914. On tachylyte veins and assimilation phenomena in the granite of Parijs (Orange Free State). Abs. Proc. Geol. Soc. No. 964, 10-11.

- 1916. The pseudotachylyte of Parijs (OFS), and its relation to trap-shotten gneiss and flinty crush rock. J. Geol. Soc. 72, 198-221.

Sibson, R. H., 1973. Interactions between temperature and pore fluid pressure during earthquake faulting and a mechanism for partial or total stress relief. Nature Phys. Sci. 243, 66-68.

- 1974. Frictional constraints on thrust, wrench and normal faults. Nature 249, 542-544.
- 1975. Generation of pseudotachylyte by ancient seismic faulting. Geophys. J. Roy. Astr. Soc. 43, 775-794.
- 1977a. The Outer Hebrides Thrust: its structure, mechanism and deformation environment. Unpubl. Ph.D thesis, Univ. Lond.
- 1977b. Fault rocks and fault mechanisms. J. Geol. Soc. 133, 191-213.
- 1977c. Kinetic shear resistance, fluid pressures and radiation efficiency during seismic faulting. Pageophys. 115, 387-400.
- 1978. Radiant flux as a guide to relative seismic efficiency. Tectonophys. 51, T39-T46.
- 1980a. Power dissipation and stress levels in the upper crust. J. Geophys. Res. 85, 6239-6247.
- 1980b. Transient seismic discontinuities during ductile shear. J. Struct. Geol. 2, 165-171.
- 1981. Controls on low stress hydrofracture dilatancy in thrust, wrench and normal fault terrains. Nature 289, 665-667.
- 1982. Fault zone models, heat flow and the depth distribution of earthquakes in the continental crust of the United States. Bull. Seism. Soc. Amer. 72, 151-163.
- 1983. Continental fault structure and the shallow earthquake source. J. Geol. Soc. 140, 741-767.
- 1985. Stopping of earthquake ruptures at dilational fault jogs. Nature, 316, 248-251.
- Moore, J. McM. and Rankin, A. H., 1975. Seismic pumping - a hydrothermal fluid transport mechanism. J. Geol. Soc. 131, 653-659.
- White, S.H. and Atkinson, B.K., 1981. Structure and distribution of faultrocks in the Alpine Fault zone. In: K.R. McClay and N.J. Price (eds.), Thrust and Nappe Tectonics. Geol. Soc. Lond., 197-210.Sigurdsson, H., 1968. Petrology of acid xenoliths from Surtsey. Geol. Mag. 105, 440-453.

Sigurdsson, H., 1968. Petrology of acid xenoliths from Surtsey. Geol. Mag. 105, 440-453.

Sinha-Roy, S., 1981. Pseudotachylyte from a thrust zone in mylonite gneisses of major Bergen arc, southwest Norway. Neues. Jahr. Minerlogie Abh. 141, 150-160.

Smith, J.V., 1974. Feldspar minerals, vol. 2. Springer-Verlag, Berlin,

690pp.

Smythe, D.K., Dobinson, A., McQuillin, R., Brewer, J.A., Matthews, D.H., Blundell, D.J. and Kelk, B., 1982. Deep structure of the Scottish Caledonides as revealed by the MOIST reflection profile. Nature 299, 338-340.

Spry, A., 1969. Metamorphic textures. Pergamon, 350pp.

Statham, P., 1976. X-Ray Spectrom. 5, 154-168.

Staub, R., 1915. Petrographische untersuchungen im westlichen Berninagebirge. Vjschr. Naturf. Ges. Zurich 60, 71-91.

Stearns, D.W., 1968. Fracture as a mechanism of flow in naturally deformed, layered rocks. Proc. Conf. Research on Tectonics. Geol. Surv. Can. pp 68-80.

Stel, H., 1981. Crystal growth in cataclasites: diagnostic microstructures and implications. Tectonophys. 78, 585-600.

Stesky, R.M., 1978. Mechanisms of high temperature frictional sliding in Westerly granite. Can. J. Earth Sci. 15, 361-375.

Storzer, D., Horn, P. and Kleinmann, B., 1971. The age and origin of the Kofels structure, Austria. Earth Plan. Sci. Lett. 12, 238-244.

Studemeister, P.A., 1983. The greenschist facies of an Archaean near Wawa, Ontario. Can. J. Earth. Sci. 20, 1409-1420.

Stutzer, O., 1937. Die talweitung von Kofels im Otztal (Tirol) als meteorkrater. Zeitschr. Deutsch. Geol. Ges. 88, 523-525.

Suess, F. E., 1937. Der meteor-kraten von Kofels bei Umhausen im Otztale, Tirol. Neues. Jhrb. Min. Geol. Palaont. 72, 98-155.

Sutton, J. and Watson, J., 1951. The pre-Torridonian metamorphic history of the Loch Torridon and Scourie areas in the North-west Highlands and its bearing on the chronological classification of the Lewisian. J. Geol. Soc. 106, 241-307.

Sykes, L.R., 1971. Aftershocks of great earthquakes, seismicity gaps and earthquake prediction for Alaska and the Aleutians. J. Geophys. Res. 76, 8021-8041.

Termier, P. and Boussac, J., 1911. Sur les mylonites de la region de Savonne. Compt. Rend. Acad. Sci. 152, 1550-1556.

Tiller, W.A., 1964. Dendrites. Science 146, 871-879.

Teufel, L., and Logan, J., 1978. Effect of displacement rate on the real contact area and temperature generated during frictional sliding of Tennessee Sandstone. Pure Appl. Geophys. 116, 840-865.

Torske, T., 1975. Snowflake texture in Ordovician rhyolite from

Stord.Hordaland. Norges Geol. Unders. 319, 17-27.

Towers H. and Chipman, J., 1957. Diffusion of calcium and silicon in a lime-alumina-silica slag. Trans. Amer. Inst. Metal. 209, 769-773.

Tsuchiyama, A. and Takahashi, E., 1983. Melting kinetics of plagioclase feldspar. Contrib. Mineral. Petrol. 84, 345-354.

Tullis, J., Snoke, A.W. and Todd, V.R., 1982. Significance and petrogenesis of mylonitic rocks. Geology, 10, 227-230.

Tullis, J. and Yund, R.A. 1977. Experimental deformation of dry Westerly granite. J. Geophys Res. 82, 5705-5718.

Turcotte, D.L. and Oxburgh, E.R., 1968. A fluid theory for the deep stucture of dip-slip fault zones. Phys. Earth Plan. Int. 1, 381-386.

Turcotte, D.L., Tag, P.H. and Cooper, R.E.A., 1980. A steady state model for the distribution of stress and creep on the San Andreas fault. J. Geophys. Res. 85, 6224-6230.

Ujike, O., 1982. Microprobe mineralogy of plagioclase, clinopyroxene and amphibole as records of cooling rate in the Shirotori Hiketa dike swarm, northeastern Shikoku, Japan. Lithos 15, 281-293.

Varshneya, A.K. and Cooper, A.R., 1972. Diffusion in the system K_2O-SrO-SiO_2: cation self-diffusion coefficients. J. Amer. Ceram. Soc. 55, 226-223.

Voight, B. E. and Faust, C., 1982. Frictional heat and strength loss in some rapid landslides. Geotechnique 32, 43-54.

Voll, G., 1976. Recrystallization of quartz, biotite and feldspars from Erstfeld to the Levantina Nappe, Swiss Alps, and its geological significance. Schweiz. Mineral. Petrogr. Mitt. 56, 641-647.

Walker, D., Kirkpatrick, R.J., Longhi, J. and Hays, J.F., 1976. Crystallization history of lunar picrite basalt sample 12002: phase equilibria and cooling rate studies. Bull. Geol. Soc. Amer. 87, 646-656.

Waters, A.C. and Cambell, C.D., 1935. Mylonites from the San Andreas fault zone. Amer. J. Sci. 29, 473-503.

Waters, A.C. and Krauskopf, K.B., 1941. Protoclastic border of the Colville batholith. Bull. Geol. Soc. Amer. 52, 1355-1418.

Wallace, R.C., 1976. Partial fusion along the Alpine fault zone, New Zealand. Bull. Geol. Soc. Amer. 87, 1225-1228.

Watkins, P.J., 1980. Analysis of silicates using a single solution procedure. Technical Report No. 8, Imperial College.

Watts, M. J. and Williams, G. D., 1980. Fault rocks as indicators of progressive shear deformation in the Guincamp region, Brittany. J. Struct. Geol. 1, 323-332.

Weichert, R. and Schonert, K., 1974. On the temperature rise at the tip of a fast running crack. J. Mech. Phys. Solids 22, 127-133.

Weiss, L.E. and Wenk, H.R., 1983. Experimentally-produced pseudotachylyte-like veins in gabbro. Tectonophys. 96, 299-310.

Wenk, H.R., 1978. Are pseudotachylytes products of fracture or fusion? Geology 6, 507-511.

Wenk, H.R. and Weiss, L.E., 1982. Al-rich calcic pyroxene in pseudotachylyte: an indicator of high pressure and high temperature. Tectonophys. 84, 329-341.

Willemse, J., 1937. On the Old Granite of the Vredefort region and some of its associated rocks. Trans. Geol. Soc. S. Afr. 40, 43-119.

Wilshire, H.G., 1971. Pseudotachylite from the Vredefort Ring, South Africa. J. Geol. 79, 195-206.

Winkler, H.G.F., 1967. Petrogenesis of metamorphic rocks. Springer, New York, 237pp.

Whipple, E.R., 1974. A study of Wilson's determination of ferrous iron in silicates. Chem. Geol. 14, 223-238.

White, J.C. and White, S.H., 1983. Semi-brittle deformation within the Alpine Fault zone. J. Struct. Geol. 5, 579-589.

White, S.H., 1971. Natural creep deformation of quartzites. Nature Phys. Sci. 234, 276-278.

White, S. H., 1979. Palaeo-stress estimates in the Moine Thrust zone, Eriboll, Scotland. Nature 280, 222-223

- 1973. Syntectonic recrystallization and texture development in quartz. Nature 244, 276-278.

- 1976. The effects of strain on the microstructures, fabrics and deformation mechanisms in quartz. Phil. Trans. Roy. Soc. Lond. A283, 69-86.

- 1982. Fault rocks of the Moine Thrust: a guide to their nomenclature. Textures and Microstructures 4, 211-221.

- , Burrows, S.E., Carreras, J., Shaw, N. and Humphreys, F.J., 1979. On mylonites in ductile shear zones. J. Struct. Geol. 2, 175-187.

- and Johnson, D.J., 1981. A microstructural and microchemical study of cleavage lamellae in a slate. J. Struct. Geol. 3, 279-290.

Wise, D.U., Dunn, J.E., Engelder, J.T., Geiser, P.A., Hatcher, R.D., Kish, S.A., Odom, A.L. and Schamel, S., 1984. Fault-related rocks: suggestions for terminology. Geology 12, 391-394.

Wong, Teng-fong, 1982. Shear fracture energy of Westerly granite from post-failure behaviour. J. Geophys. Res. 87, 990-1000.

Wood, B.J., 1974. The solubility of alumina in orthopyroxene coexisting with garnet. Contrib. Mineral. Petrol. 46, 1-15.

Wood, M.M. and Weidlich, J.E., 1982. Empirical evaluation of fracture toughness: the toughness of quartz. Amer. Min. 1065-1068.

Wyllie, P.J., 1961. Fusion of Torridonian Sandstone by a picrite sill in Soay (Hebrides). J. Petrol. 2, 1-37.

Wu, F.T., Blatter, L. and Robertson, H., 1975. Clay gouges in the San Andreas fault system and their possible implications, Pageophys. 113, 87-95.

Yamashita, T., 1976. On the dynamical processes of fault motion in the presence of friction and inhomogeneous initial stress; Part I, Rupture propagation. J. Phys. Earth 24, 417-444.

Yuen, D.A., Fleitout, L., Schubert, G. and Froidevaux, C., 1978. Shear deformation zones along major transform faults and subducting slabs. Geophs. J. Roy. Astr. Soc. 54, 93-119.

Zoback, M.L. and Zoback, M.D., 1980. State of stress in the conterminous United States. J. Geophys. Res. 85, 6113-6156.

APPENDIX A1: Radiometric Age Dating of Pseudotachylytes

An attempt to date Outer Hebrides pseudotachylytes using the whole-rock Rb-Sr method was undertaken for the following reasons:-

(i) to establish the age of the thrust;
(ii) to compare the ages of pseudotachylytes from the main thrust with those from western forethrusts;
(iii) to place constraints on the duration of thrusting;
(iv) to test the general applicability of Rb-Sr dating of pseudotachylytes.

Analyses were kindly performed by Dr S. Moorbath at the Department of Geology and Mineralogy, Oxford University. Six samples of pseudotachylyte and one of host rock (sample series G801 - G806) from a concordant FV traceable nearly 40m in uniform paragneisses of SE Grimsay were chosen for dating. Preliminary XRF analyses (Appendix A4) indicated that sufficient variation in Rb/Sr ratios between samples existed to define a possible isochron.

The results are shown in Fig. A1.1. Regardless of the error in initial $^{87}Sr/^{86}Sr$ ratio, a least squares best fit isochron of 2640±210 (2σ) Ma may be defermined. This result is consistent with the probable Scourian age of the metasediments (Coward et al., 1969) but unfortunately meaningless with respect to the age of the pseudotachylyte. The anomalous age of the pseudotachylyte may in part be due to the presence of incompletely melted porphyroclasts in the sample, but is more likely a consequence of the power of closed-system melting to retain primary ages (S. Moorbath, pers. comm., 1982).

Using the K-Ar whole rock method on 19 samples of pseudotachylytes, cataclasites and phyllonites from the OHT, Sibson (1977a) obtained a spread of ages from 2056±86 to 394±16 Ma. Interestingly, 4 phyllonites which have undergone the most complete (metamorphic) recrystallization and metasomatism (the latter suggested by XRF analyses from this study) are grouped tightly about a late Caledonian age of 400 Ma. Isotopic homogenization (of Rb and Sr) has been observed elsewhere in high-strain/highly recrystallized mylonites allowing meaningful age determinations (e.g. Abbot, 1972). These data suggest that radiometric age dating of mylonites and phyllonites deformed and recrystallized in a high fluid activity environment, may be more forthcoming than pseudotachylytes.

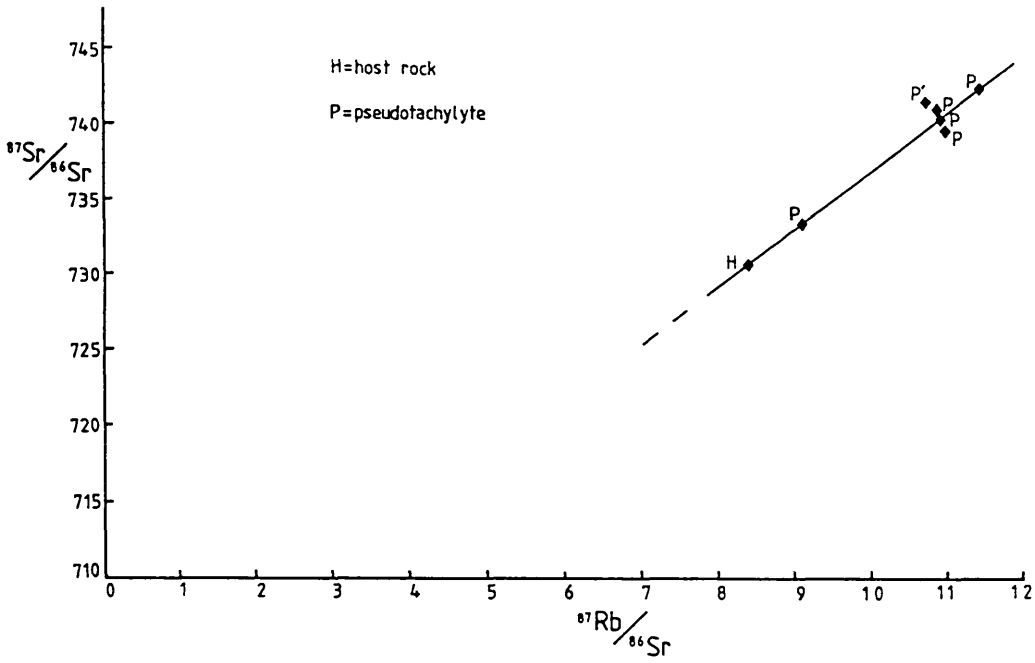


FIGURE A1.1 Rb - Sr isotope plot for sample series G80 (see text for discussion.

Philpotts and Miller (1963) claim meaningful ages for 3 Canadian pseudotachylytes dated by the K-Ar whole rock method. It can be inferred from their results that Ar-retentivity varied according to the texture of the pseudotachylyte. Glassy, plagioclase-microlitic and partially devitrified samples yielded progressively younger ages within a spread of ∿150 Ma. If the devitrification was achieved by heat and fluid flow, which would tend to cause Ar-loss, then an anomalously young age is expected (cf. Evernden and James, 1964).

In conclusion it seems that radiometric age dating of pseudotachylytes, at least by Rb-Sr and K-Ar whole rock methods, is rather unsatisfactory. This is unfortunate since a pseudotachylyte fault must surely provide the ultimate time plane in geology. Two future lines of attack present themselves. First, truly glassy pseudotachylytes (and especially landslide frictionites) might be dated by fission-track methods if suitable porphyroclasts, for example zircon, are present. Secondly, the isotopic composition of individual, newly-crystallized phases (e.g. mica or feldspar) might be measured by ion microprobe. The 'state of the art' of ion probe analysis would however seem to preclude this at the present time (P. Dennis, pers. comm., 1982).

APPENDIX A2: Analytical Techniques

1) Optical Microscopy Transmitted and reflected light microscopy of standard and polished thin sections was used for initial examination of the pseudotachylytes. For transmitted light study it was found to be beneficial to use ultra-thin sections (10-20 um thick); in this way useful and novel observations of the fine grained phases could be made (e.g. Maddock, 1983). Orthogonal thin sections of selected samples were prepared in some cases when the presence of a fabric was suspected, and to assist in determining the effect of sectioning on apparent crystal morphologies. Large format (10x7 cm) thin sections were prepared of some quasi-conglomerates.

2) Electron Microprobe Analysis Probe analyses were chiefly made using a Cambridge Instruments Microscan V instrument fitted with a Link Systems energy-dispersive (EDS) X-ray analyzer and on-line computer for ZAF corrections and data reduction (see Statham, 1976 for details). Jadeite, peridot and/or adularia standards were analyzed during each session to check accuracy and precision of analyses; summarized standards data is given in Table A2.1. All analyses were performed using an accelerating voltage of 15 kV, a beam current of ~80 uA and a 100s live counting time on C-coated polished thin sections.

Point, defocussed spot and raster analyses were made as applicable, the latter for fine grained phases less than 5 um diameter. In each case, standards were analysed in the same mode as the sample; differences in the results of standard analyses in the different modes were found to be insignificant. To locate the beam in fine grained phases up to 20 um across, a combination of optics, SEI, cathodoluminescence and specimen current had to be used.

Silicate mineral analyses have been recalculated using the FORTRAN computer program SUPFRECAL written by J.C. Rucklidge (University of California at Berkeley). Total iron is calculated as FeO with the exception of sphene, epidote and celadonite where Fe_2O_3 was used and amphiboles where the FeO/Fe_2O_3 ratio, assuming minimum Fe_2O_3, was calculated according to the method of Papike et al (1974).

3) Scanning Electron Microscopy (SEM) SEM studies were made using a JEOL 733 chiefly operating in the back-scattered electron imaging (BEI) mode. Machine parameters and specimen preparation were

TABLE A2.1 SUMMARIZED MICROPROBE STANDARDS DATA

	1		2		3	
SiO_2	59.59	(0.25)	40.98	(0.34)	64.45	(0.31)
TiO_2	0.00	-	0.00	-	0.00	-
Al_2O_3	25.13	(0.37)	0.00	-	18.37	(0.27)
FeO	0.05	(0.09)	8.83	(0.18)	0.00	-
MnO	0.00	-	0.00	-	0.00	-
MgO	0.05	(0.16)	49.25	(0.21)	0.00	-
CaO	0.28	(0.27)	0.00	-	0.00	-
Na_2O	14.87	(0.17)	0.00	-	1.68	(0.08)
K_2O	0.00	-	0.00	-	14.62	(0.16)
Total	99.97		99.06		99.12	
Formulae						
Si	2.004	(0.013)	1.007	(0.002)	2.992	(0.007)
Al	-	-	-	-	1.005	(0.007)
Al	0.996	(0.04)	-	-	-	-
Ti	-	-	-	-	-	-
Fe	0.001	(0.03)	0.181	(0.003)	-	-
Mn	-	-	-	-	-	-
Mg	0.002	(0.08)	1.804	(0.005)	-	-
Ca	0.010	(0.009)	-	-	-	-
Na	0.970	(0.001)	-	-	0.151	(0.006)
K	-	-	-	-	0.866	(0.016)
O	6.000		4.000		8.000	

1. Mean and Standard deviation (bracketed) of 13 analyses of jadeite Standards.
2. Mean and Standard deviation (bracketed) of 5 analyses of peridot Standards.
3. Mean and Standard deviation (bracketed) of 3 analyses of adularia Standards

essentially as for the microprobe and a similar EDS X-ray analyzer is fitted. Combined BEI, qualitative X-ray mapping and quantitative analysis in the SEM proved to be a particularly powerful tool for characterizing the phases and textures in pseudotachylytes on a scale of ~1 um to 1 cm. The theory and application of BEI/SEM to geological materials is fully discussed by Hall and LLoyd (1982). As a prefix to the presentation of the BSE micrographs a brief explanation of image contrast will be given here. Contrast in a BSE image is provided by atomic number (z) contrast in the sample. For compounds, the mean BSE coefficient, $\bar{\eta}$, may be defined (Reed, 1975):-

$$\bar{\eta} = \sum_{i=1}^{n} C(i)\eta(i) \qquad \text{A2.1}$$

where i is the concentration by weight of each element in the compound and $\eta(i)$ the BSE coefficient of each element. Plots of η against z and $\bar{\eta}$ against $\bar{z}$ are shown in Fig. A2.1. Note that the brightness of the image increases with increasing η and hence z. With the detector electronics in the JEOL 733 it is possible to resolve differences of z of ~0.1 throughout the range in carefully polished samples.

4) Transmission Electron Microscopy (TEM) TEM studies were performed using AEI, Phillips and JEOL 100 kV instruments in the Department of metallurgy at Imperial College. The JEOL 100CX is a scanning-transmission electron microscope (STEM) with a Link Systems EDS analyzer similar to that fitted to the microprobe (see White et al, 1979 for details of data reduction).

Samples for TEM were selected from uncovered (alcohol-soluble) "Lakeside" mounted thin sections and mounted on 3 mm CU-foils using (water-soluble) "Seccotine" cement. The foils are thinned to perforation by sputtering with Ar ion beams, accelerated to 6 kV. Some problems were experienced due to differential thinning rates of porphyroclasts and matrix, but reasonable results were generally obtained using a sputtering angle of 11-15°. The foils are C-coated to reduce charging and drift in the electron beam.

Attempts to produce accurate and reproducible analyses in the STEM were hampered for the following reasons:-

(i) the extremely fine grain size of some samples meant that some of the analyses included more than one phase; with inequant grains (e.g. phyllosilicates) this could sometimes be overcome by making the

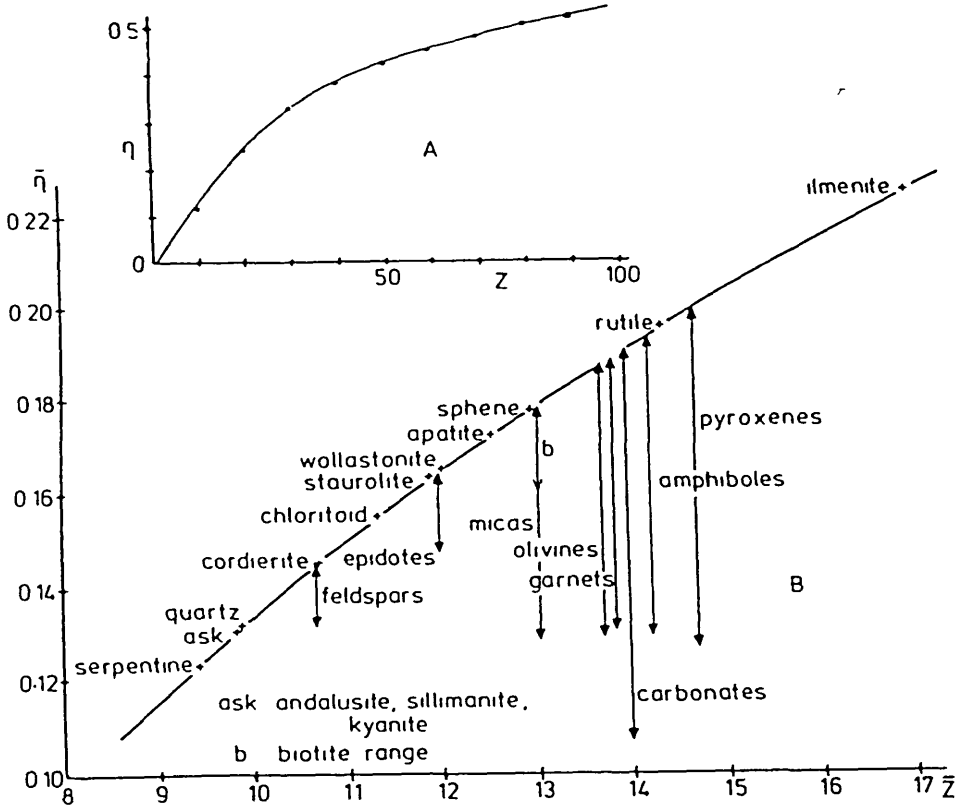


FIGURE A2.1 (A) relationship between back-scattered electron coefficient (η) and atomic number (z) for pure elements; (B) relationship between mean back-scattered electron coefficient ($\bar{\eta}$) and weighted mean atomic number (z) for common rock-forming minerals plotted on a curve of against z (from Hall and Lloyd, 1982).

TABLE A2.2 STEM TEST ANALYSIS OF QUARTZ (Sample X, Foil 6)

Oxide	Wt. %	Rejection or Acceptance
SiO_2	95.707	
TiO_2	0.223	$<2\sigma$
Al_2O_3	1.100	$<2\sigma$
FeO	0.600	$<2\sigma$
MnO	0.178	$<2\sigma$
MgO	0.600	$<2\sigma$
CaO	0.167	$<2\sigma$
Na_2O	1.426	$<2\sigma$
K_2O	0.000	$<2\sigma$
Total	100.000	

beam astigmatic and parallel to the larger dimension;
(ii) the analytical hardware is very temperature-sensitive and problems with the air-conditioning were persistent during the entire time the machine was used;
(iii) a given calibration is probably unsuitable for analysing the wide range of minerals determined; this is illustrated by a test analysis performed on quartz shown in Table A2.2;
(iv) up to 2.0 wt.% FeO was detected in most analyses of non Fe-bearing phases; this may be a consequence of the calibration, extraneous fluorescence of Fe K. radiation from the column or due to contamination of the foils during ion thinning.

For these reasons the analyses are considered semi-quantitative. 43 analyses from a total of about 80 determined are presented in Appendix A3 (many other qualitative 'fingerprints' were made). Analyses are norma lized to 100% during data reduction and subsequently oxide values with less than 2σ counting statistic certainty have been deducted (note, this has the effect of reducing the total of the normalized quartz analysis in Table A2.2 to 95.71%). An estimated foil thickness (required for data reduction) of 250 nm was used for all analyses as this parameter appears to have little effect on the analyses (D. Johnston, pers. comm., 1982) and is certainly insignificant compared to the above problems.

Despite these problems useful observations and analyses have been made and further application of STEM microanalysis to pseudotachylytes would be profitable.

STEM analyses were recalculated using program SUPERECAL largely for the purpose of tabulation.

5) X-ray Fluorescence Spectrometry (XRF) XRF whole rock analysis was performed using a Phillips 1212 automated XRF wavelength dispersive spectrometer. For major and minor elements fused glass beads were prepared (in duplicate or triplicate for 35% of the samples) by the Norrish method. H_2O^- was determined from sample weight loss after drying for 8 hours at 110°C; loss or gain on ignition was calculated from weight changes after ignition at 950° C for 1/2 hour. International rock standards were used to prepare calibration lines by a background iteration technique. Full details of sample preparation, instrument settings and data reduction are given by Parker (1983).

Trace element concentrations were determined from pressed powder briquettes, details of preparation are given by Parker (1980). A flexible trace element calibration method was used allowing emphasis to be placed on the best characterized international standards. Trace element standard concentrations used in the calibration were taken from Abbey (1980). Further details of instrument settings, data reduction, etc., are given by Parker (1979).

Precision data for major, minor and trace elements are given in Table A2.3, and detection limits and average relative errors for trace element standards given in Table A2.4

6) Inductively Coupled Plasma Spectroscopy (ICP) and Atomic Absorbtion Spectroscopy (AA) Trace Element Analysis For 11 whole rock samples of pseudotachylyte, insufficient material was available for manufacture of an XRF trace element briquette (i.e. <5g). For these samples, Rb was determined using a Perkin Elmer model 2722 atomic absorbtion spectrometer and Ba, Sr, V and Zr using an ARL ICP. A common attack was used for both analytical techniques involving fusion of rock powder with $LiBo_2$ flux and digestion in nitric acid (see Watkins, 1980 for details).

Precision data for the elements analysed by these methods are given in Table A2.5 and a comparison between XRF, AA and ICP analysis for Rb, Ba, Sr, V and Zr is given in Table A2.6. The least satisfactory results are the ICP values for V and Zr, although these are considered acceptable for the purposes of this study.

7) Ferrous Iron Determination FeO was determined from acid-digested rock powders titrated against potassium dichromate solution following the method of Whipple (1974).

TABLE A2.3 XRF WHOLE ROCK PRECISION DATA

	1		2	
SiO_2	62.10	(0.27)	62.19	(0.14)
TiO_2	0.45	(0.004)	0.44	(0.005)
Al_2O_3	15.59	(0.13)	15.71	(0.08)
Fe_2O_3	6.24	(0.09)	6.07	(0.04)
MnO	0.13	(0.002)	0.14	(0.05)
MgO	2.20	(0.17)	2.12	(0.12)
CaO	5.75	(0.04)	5.69	(0.04)
Na_2O	4.47	(0.30)	4.60	(0.35)
K_2O	2.22	(0.05)	2.29	(0.01)
P_2O_5	0.28	(0.03)	0.27	(0.03)
H_2O^-	0.02	(0.007)	0.02	-
LOI	0.43	(0.04)	0.43	-
Total	99.88		99.97	
Ba	795	(36)	843	(11)
Y	34	(1)	33	(1)
Rb	38	(2)	39	(1)
Sr	410	(5)	415	(2)
Th	12	(2)	11	(1)
V	89	(4)	86	(3)
Cr	56	(3)	54	(2)
Ni	26	(1)	26	(1)
Cu	53	(6)	47	(3)
Nb	8	(4)	7	(2)
Zr	147	(16)	147	(6)
Zn	80	(4)	78	(3)

1 Mean and Standard deviations (bracketed) for 9 preparations of sample GQ55.

2 Mean and Standard deviations (bracketed) for 10 aliquots prepared from 1 sample split of sample GQ55 (major elements); same disc analysed 10 times for trace elements.

TABLE A2.4 XRF TRACE ELEMENT DETECTION LIMITS AND AVERAGE RELATIVE ERROR OF ANALYSED STANDARDS

Element	Detection limit (ppm)	Average relative error %
Ba	21	1.32
Y	2	10.76
Rb	2	2.40
Sr	2	1.48
Th	4	5.74
V	2	8.45
Cr	2	14.80
Ni	2	12.12
Cu	3	10.13
Nb	6	6.30
Zr	7	3.60
Zn	3	5.28

Note: 1) detection limit (dl) calculated from formula:

$$dl = \frac{3}{m} \left(\frac{R_b}{T_b}\right)^{\frac{1}{2}}$$

where $m = \frac{R_p - R_b}{\text{std.conc.}}$

and R_p = peak counting rate

R_b = background counting rate

T_b = background counting time

determined for 3 or 4 Standards for each element with the average quoted.

2) average relative error determined from up to 14 Standards.

TABLE A2.5. AVERAGE RELATIVE ERROR FOR TRACE ELEMENT ANALYSIS BY ICP AND AA

Element	Method	Average relative error %
Rb	AA	3.90
Ba	ICP	1.87
Sr	ICP	2.25
V	ICP	22.80
Zr	ICP	16.44

Note: error determined on 6 and 5 international standards for AA and ICP respectively.

TABLE A2.6 COMPARISON OF XRF, AA AND ICP TRACE ELEMENT ANALYSIS

Element	Sample	Measured value		
		XRF	AA	ICP
Rb	MM2	11, 12	17	-
	R2	113, 113	112, 116	-
	G1A/H	22, 24	25	-
	GQ33	18	19	-
Ba	MM2	122, 145	-	143
	R2	847, 862	-	901, 923
	G1A/H	878, 901	-	910
	GQ33	139	-	173
Sr	MM2	1087, 1093	-	1114
	R2	449, 452	-	456, 458
	G1A/H	432, 434	-	445
	GQ33	145	-	156
V	MM2	217, 220	-	189
	R2	93, 104	-	98, 99
	G1A/H	281, 285	-	243
	GQ33	321	-	272
Zr	MM2	273, 281	-	176
	R2	205, 221	-	205, 237
	G1A/H	144, 155	-	164
	GQ33	78	-	110

Note: 2 values indicates duplicate preparations

TABLE A2.7 AVERAGE RELATIVE ERRORS FOR FeO DETERMINATIONS OF STANDARDS

Standard	FeO determined (wt%)	FeO accepted value (wt%)	Average relative error
91	1.41	1.41	
NIM-G	1.41	1.30*	0.08
SY-2	3.68	3.62*	0.02

* From Abbey (1980)

TABLE A2.8 PRECISION DATA FOR FeO DETERMINATION OF SAMPLES

	1	2	
	5.77 (0.32)	5.51 (0.35)	wt.%

1 Mean and standard deviation (bracketed) for 9 preparations of sample GQ55

2 Mean and standard deviation for 9 repeat determinations of sample GQ55/7

APPENDIX A3: Mineral Analyses

The mineral analyses with recalculated formulae are identified by title, column number and a key to the column numbers which includes the sample number and brief description. The analyses are arranged in the following order:-

Electron Microprobe

feldspars	
muscovite	
biotite	matrix and porphyroclast
amphibole	phases
clinopyroxene	
sphene	
feldspar	
mica	
chlorite	amygdale and microfracture
amphibole	phases
sphene	
epidote	
carbonates	

STEM

feldspars	
amphibole	matrix and porphyroclast
biotite	phases
chlorite	

SUPER RECAL — PROBE ANALYSIS OF FELDSPARS

	1	2	3	4	5	6	7	8
SIO2	59.93	41.49	60.35	59.74	62.66	60.88	64.00	63.70
TIO2	0	0	0	0	0	0	0	0
A203	24.08	22.90	24.32	24.43	22.29	23.50	22.25	22.85
FEO	.80	.65	.51	.60	.48	.39	0	0
MNO	0	0	0	0	0	0	0	0
MGO	0	0	0	0	0	0	0	0
CAO	6.25	4.58	6.04	6.48	3.82	5.21	3.75	3.96
NA2O	7.92	8.36	8.13	7.90	8.98	8.54	9.52	9.11
K2O	.32	.57	.32	.11	.38	.42	.25	.32
SUM	99.31	99.15	99.87	99.26	98.61	98.94	99.77	99.94
SI	2.693 *	2.754 *	2.696 *	2.687 *	2.813 *	2.740 *	2.833 *	2.814 *
AL	1.277 *	1.313 *	1.342 *	1.295 *	1.179 *	1.246 *	1.160 *	1.190 *
FE	.030 4.006	.020 4.002	.030 4.011	.023 4.005	.018 4.011	.015 4.001	0 3.993	0 4.004
TI	0 *	0 *	0 *	0 *	0 *	0 *	0 *	0 *
MN	0 *	0 *	0 *	0 *	0 *	0 *	0 *	0 *
MG	0 *	0 *	0 *	0 *	0 *	0 *	0 *	0 *
CA	.302 *	.331 *	.286 *	.312 *	.184 *	.251 *	.178 *	.187 *
NA	.691 *	.753 *	.705 *	.688 *	.782 *	.745 *	.817 *	.780 *
K	.018 1.012	.033 1.034	.013 1.007	.006 1.008	.022 .987	.024 1.020	.014 1.009	.010 .986
O	8.000 *	8.000 *	8.000 *	8.000 *	8.000 *	8.000 *	8.000 *	8.000 *
AN	29.85	31.33	28.74	30.99	18.61	24.62	17.63	19.01
AB	68.16	65.51	70.01	68.38	79.18	73.02	80.97	79.16
OR	1.82	3.15	1.25	.63	2.20	2.36	1.40	1.83
F/M	0	0	0	0	0	0	0	0
F/FM	0	0	0	0	0	0	0	0

1 SA3 MICROLITE 1
2 SA3 MICROLITE 2
3 SA3 MICROLITE 3
4 SA3 MICROLITE 4
5 SA3 MICROLITE 5
6 SA3 MICROLITE 6
7 SA3 PORPHYROCLAST 1
8 SA3 PORPHYROCLAST 2

SUPER RECAL — PROBE ANALYSIS OF FELDSPARS

	9	10	11	12	13	14	15	16
SIO2	62.74	63.57	64.36	56.08	59.26	59.11	55.45	54.41
TIO2	0	0	0	0	0	0	0	0
A203	22.71	22.76	18.56	21.28	25.50	25.74	28.40	29.21
FEO	0	0	0	0	0	0	0	.39
MNO	0	0	0	0	0	0	0	0
MGO	0	0	0	0	0	0	0	0
CAO	4.03	3.69	0	2.14	7.23	7.13	10.13	10.81
NA2O	9.41	9.20	.57	10.12	6.69	6.52	5.27	4.79
K2O	.17	.28	16.02	.19	.23	.20	0	0
SUM	99.05	99.50	99.51	99.81	98.91	98.70	99.25	99.61
SI	2.830 *	2.810 *	2.908 *	2.904 *	2.664 *	2.659 *	2.505 *	2.459 *
AL	1.195 *	1.189 *	1.015 *	1.102 *	1.351 *	1.365 *	1.512 *	1.556 *
FE	0 3.996	0 4.009	0 4.003	0 4.007	0 4.014	0 4.024	0 4.017	.015 4.029
TI	0 *	0 *	0 *	0 *	0 *	0 *	0 *	0 *
MN	0 *	0 *	0 *	0 *	0 *	0 *	0 *	0 *
MG	0 *	0 *	0 *	0 *	0 *	0 *	0 *	0 *
CA	.195 *	.175 *	0 *	.161 *	.348 *	.344 *	.490 *	.523 *
NA	.815 *	.791 *	.051 *	.862 *	.583 *	.569 *	.462 *	.420 *
K	.010 1.017	.016 .982	.049 1.100	.011 .974	.013 .944	.011 .924	0 .952	0 .943
O	8.000 *	8.000 *	8.000 *	8.000 *	8.000 *	8.000 *	8.000 *	8.000 *
AN	19.92	17.85	0	10.35	36.87	37.20	51.51	55.50
AB	81.13	80.54	5.13	78.56	61.73	61.56	48.49	44.50
OR	.95	1.61	94.87	1.09	1.40	1.24	0	0
F/M	0	0	0	0	0	0	0	0
F/FM	0	0	0	0	0	0	0	0

9 SA3 PORPHYROCLAST 3
10 SA3 PORPHYROCLAST 4
11 SA3 PORPHYROCLAST 5 F
12 SA3 PORPHYROCLAST 5 AB
13 GB0/4 PORPHYROCLAST 1
14 GB0/4 PORPHYROCLAST 2
15 GB0/4 MICROLITE 1
16 GB0/4 MICROLITE 2

SUPER RECAL — PROBE ANALYSES OF FELDSPARS

	17	18	19	20	21	22	23	24
SIO2	61.01	61.14	57.06	56.99	55.94	61.43	61.20	63.65
TIO2	0	0	0	0	0	0	0	.53
A2O3	23.92	23.74	25.60	25.51	26.64	23.44	23.58	18.06
FEO	0	0	1.24	1.08	.86	0	0	0
MNO	0	0	0	0	0	0	0	0
MGO	0	0	0	.23	0	0	0	0
CAO	5.69	5.70	8.48	8.51	9.49	5.70	5.70	.15
NA2O	8.80	8.83	6.92	6.62	6.50	8.60	8.21	.29
K2O	.11	0	.34	.36	.15	0	.52	16.53
SUM	99.53	99.41	99.64	99.30	99.58	99.17	99.21	99.21
SI	2.727 *	2.734 *	2.567 *	2.569 *	2.539 *	2.749 *	2.743 *	2.977 *
AL	1.260 *	1.251 *	1.358 *	1.356 *	1.425 *	1.236 *	1.245 *	.995 *
FE	0 3.986	0 3.984	.047 4.002	.041 3.996	.033 3.996	0 3.986	0 3.988	0 3.973
TI	0 *	0 *	0 *	0 *	0 *	0 *	0 *	.019 *
MN	0 *	0 *	0 *	0 *	0 *	0 *	0 *	0 *
MG	0 *	0 *	0 *	.016 *	0 *	0 *	0 *	0 *
CA	.272 *	.273 *	.412 *	.414 *	.461 *	.273 *	.274 *	.008 *
NA	.762 *	.765 *	.608 *	.593 *	.572 *	.746 *	.713 *	.026 *
K	.005 1.041	0 1.039	.020 1.046	.021 1.034	.009 1.042	0 1.020	.030 1.017	.986 1.039
O	8.000 *	8.000 *	8.000 *	8.000 *	8.000 *	8.000 *	8.000 *	8.000 *
AN	26.17	26.29	39.61	40.68	44.28	26.81	26.92	.74
AB	73.37	73.51	58.50	57.27	54.68	73.19	70.16	2.58
OR	.60	0	1.89	2.05	.83	0	2.92	96.68
F/M	0	0	0	2.635	0	0	0	0
F/FM	0	0	0	.725	0	0	0	0

17 R4 PORPHYROCLAST 1
18 R4 PORPHYROCLAST 2
19 R4 MICROLITE 1
20 R4 MICROLITE 2
21 R4 MICROLITE 3
22 SU80/2 PORPHYROCLAST 1
23 SU80/2 PORPHYROCLAST 2
24 SU80/2 PORPHYROCLAST 3

SUPER RECAL — PROBE ANALYSES OF FELDSPARS

	25	26	27	28	29	30	31	32
SIO2	61.54	62.05	60.69	61.29	60.69	61.97	61.70	61.02
TIO2	0	0	0	0	0	0	0	0
A2O3	23.99	22.24	22.81	23.45	24.02	24.08	24.00	24.34
FEO	0	.87	1.03	.68	0	0	0	0
MNO	0	0	0	0	0	0	0	0
MGO	0	0	0	0	0	0	0	0
CAO	5.90	4.31	5.24	5.56	5.63	5.34	5.16	5.59
NA2O	8.07	8.36	8.26	7.90	7.85	7.96	7.86	8.12
K2O	.48	.40	.29	.67	.98	1.05	.88	.37
SUM	99.97	98.28	98.32	99.55	99.17	100.40	99.60	99.44
SI	2.730 *	2.801 *	2.753 *	2.745 *	2.726 *	2.745 *	2.749 *	2.725 *
AL	1.256 *	1.184 *	1.219 *	1.237 *	1.271 *	1.257 *	1.260 *	1.281 *
FE	0 3.993	.033 4.019	.039 4.011	.025 4.007	0 3.997	0 4.001	0 4.009	0 4.005
TI	0 *	0 *	0 *	0 *	0 *	0 *	0 *	0 *
MN	0 *	0 *	0 *	0 *	0 *	0 *	0 *	0 *
MG	0 *	0 *	0 *	0 *	0 *	0 *	0 *	0 *
CA	.281 *	.200 *	.255 *	.267 *	.271 *	.253 *	.246 *	.267 *
NA	.695 *	.734 *	.726 *	.686 *	.684 *	.684 *	.679 *	.703 *
K	.027 1.004	.023 .964	.017 .998	.038 .991	.056 1.011	.059 .996	.050 .975	.021 .991
O	8.000 *	8.000 *	8.000 *	8.000 *	8.000 *	8.000 *	8.000 *	8.000 *
AN	29.00	21.58	25.52	26.92	26.81	25.44	25.26	26.97
AB	69.29	76.03	72.80	69.22	67.64	68.61	69.62	70.90
OR	2.71	2.38	1.68	3.86	5.55	5.95	5.13	2.13
F/M	0	0	0	2.635	0	0	0	0
F/FM	0	0	0	.725	0	0	0	0

25 SU80/2 PORPHYROCLAST 4
26 SU80/2 MICROLITE 1
27 SU80/2 MICROLITE 2
28 SU80/2 MICROLITE 3
29 R2 HOST 1
30 R2 HOST 2
31 R2 HOST 3
32 R2 HOST 4

SUPER I CAL — PROBE ANALYSES OF FELDSPARS

	33	34	35	36	37	38	39	40
SIO2	62.15	61.50	61.84	61.23	61.47	61.41	61.64	61.22
TIO2	0	0	0	0	0	0	0	0
A203	24.03	23.75	24.09	23.76	23.35	24.14	24.38	24.13
FEO	0	0	0	0	0	0	0	0
MNO	0	0	0	0	0	0	0	0
MGO	0	0	0	0	0	0	0	0
CAO	5.03	5.52	5.67	5.76	6.06	5.44	5.90	5.68
NA20	8.01	8.23	8.34	8.18	8.17	8.33	8.14	7.99
K20	.93	.17	.15	.15	.38	.29	.14	.37
SUM	100.17	99.37	100.10	99.08	99.43	99.61	100.20	99.39
SI	2.719 *	2.750 *	2.748 *	2.742 *	2.749 *	2.736 *	2.729 *	2.733 *
AL	1.384 *	1.249 *	1.258 *	1.254 *	1.231 *	1.267 *	1.272 *	1.270 *
FE	0 4.021	0 4.000	0 3.998	0 3.995	0 3.980	0 4.003	0 4.001	0 4.003
TI	0 *	0 *	0 *	0 *	0 *	0 *	0 *	0 *
MN	0 *	0 *	0 *	0 *	0 *	0 *	0 *	0 *
MG	0 *	0 *	0 *	0 *	0 *	0 *	0 *	0 *
CA	.241 *	.264 *	.269 *	.276 *	.290 *	.260 *	.260 *	.272 *
NA	.680 *	.712 *	.717 *	.710 *	.708 *	.719 *	.699 *	.692 *
K	.052 .301	.010 .986	.009 .995	.009 .995	.022 1.020	.016 .996	.008 .987	.021 .984
O	8.000 *	8.000 *	8.000 *	8.000 *	8.000 *	8.000 *	8.000 *	8.000 *
AN	24.56	26.78	27.06	27.77	28.46	26.08	28.37	27.60
AB	71.13	72.24	72.03	71.37	69.42	72.27	70.83	70.26
OR	5.31	.98	.91	.86	2.12	1.66	.80	2.14
F/*	0	0	0	2.635	0	0	0	0
F/FM	0	0	0	.725	0	0	0	0

33 R2 HOST 5
34 R2 PORPHYROCLAST 3
35 R2 PORPHYROCLAST 2
36 R2 PORPHYROCLAST 3

37 R2 PORPHYROCLAST 4
38 R2 PORPHYROCLAST 4(2)
39 R2 PORPHYROCLAST
40 R2 PORPHYROCLAST

SUPER PECAL — PROBE ANALYSES OF FELDSPARS

	41	42	43	44	45	46	47	48
SIO2	61.15	61.23	61.22	61.10	61.74	69.94	68.26	64.83
TIO2	0	0	0	0	0	0	0	0
A203	24.60	23.76	24.13	23.94	22.93	15.81	19.64	20.58
FEO	0	0	0	0	.99	.78	.26	.44
MNO	0	0	0	0	0	0	0	0
MGO	0	0	0	0	0	0	0	0
CAO	5.81	5.76	5.68	6.06	4.63	2.15	3.28	2.34
NA20	8.13	8.18	7.90	7.98	7.70	2.69	7.22	5.68
K20	.20	.15	.37	.22	2.21	9.08	1.72	6.48
SUM	99.90	99.03	99.39	99.30	100.20	100.45	100.38	100.35
SI	2.717 *	2.742 *	2.735 *	2.732 *	2.764 *	3.122 *	2.983 *	2.904 *
AL	1.288 *	1.254 *	1.270 *	1.262 *	1.210 *	.832 *	1.011 *	1.086 *
FE	0 4.004	0 3.995	0 4.003	0 3.994	.037 4.011	.029 3.983	.010 4.004	.016 4.007
TI	0 *	0 *	0 *	0 *	0 *	0 *	0 *	0 *
MN	0 *	0 *	0 *	0 *	0 *	0 *	0 *	0 *
MG	0 *	0 *	0 *	0 *	0 *	0 *	0 *	0 *
CA	.276 *	.276 *	.272 *	.290 *	.222 *	.103 *	.154 *	.112 *
NA	.700 *	.710 *	.692 *	.692 *	.668 *	.233 *	.612 *	.493 *
K	.010 .993	.009 .995	.021 .984	.013 .995	.126 1.017	.517 .853	.096 .861	.370 .976
O	8.000 *	8.000 *	8.000 *	8.000 *	8.000 *	8.000 *	8.000 *	8.000 *
AN	27.84	27.77	27.60	29.19	21.85	12.06	17.83	11.51
AB	70.50	71.37	70.26	69.55	65.74	27.31	71.03	50.55
OR	1.65	.86	2.14	1.26	12.41	60.63	11.13	37.94
F/*	0	0	0	2.635	0	0	0	0
F/FM	0	0	0	.725	0	0	0	0

41 R2 PORPHYROCLAST 9
42 R2 PORPHYROCLAST 10
43 R2 PORPHYROCLAST 11
44 R2 PORPHYROCLAST 12

45 R2 PCL4/P1/1
46 R2 PCL4/P2/3
47 R2 PCL4A/P1/1
48 R2 PCL4A/P1/2

SUPER RECAL — PROBE ANALYSES OF FELDSPARS

	49	50	51	52	53	54	55	56
SIO2	61.04	62.47	59.38	57.50	58.52	58.18	61.78	61.57
TIO2	0	0	0	.21	0	0	0	0
A203	22.41	21.85	24.97	25.69	25.98	26.06	24.65	24.10
FEO	.44	.39	1.22	1.06	1.07	1.18	0	1.34
MNO	0	0	0	0	0	0	0	0
MGO	.75	0	0	0	0	.39	0	0
CAO	5.96	3.84	6.76	8.25	7.99	8.23	5.71	5.29
NA20	7.45	6.86	7.27	6.42	6.84	6.71	8.40	8.42
K20	.39	3.75	.45	.28	.22	.31	.25	.32
SUM	98.45	99.15	100.05	99.61	100.62	101.06	100.79	101.04
SI	2.752 *	2.823 *	2.661 *	2.596 *	2.612 *	2.593 *	2.722 *	2.723 *
AL	1.190 *	1.163 *	1.319 *	1.377 *	1.367 *	1.368 *	1.280 *	1.256 *
FE	.016 * 3.996	.015 4.001	.046 4.026	.040 4.013	.040 4.019	.044 4.005	0 4.002	.050 4.028
TI	0 *	0 *	0 *	.007 *	0 *	0 *	0 *	0 *
MN	0 *	0 *	0 *	0 *	0 *	0 *	0 *	0 *
MG	.051 *	0 *	0 *	0 *	0 *	.026 *	0 *	0 *
CA	.241 *	.186 *	.325 *	.399 *	.382 *	.393 *	.270 *	.251 *
NA	.652 *	.600 *	.632 *	.562 *	.592 *	.580 *	.718 *	.722 *
K	.021 1.013	.228 1.602	.026 .982	.016 .984	.013 .987	.018 1.016	.014 1.001	.018 .991
O	8.000 *	8.000 *	8.000 *	8.000 *	8.000 *	8.000 *	8.000 *	8.000 *
AN	24.68	18.55	33.05	40.84	38.73	39.68	26.92	25.30
AB	67.16	59.83	64.33	57.51	60.00	58.54	71.67	72.88
OR	8.23	21.57	2.62	1.65	1.27	1.78	1.40	1.82
F/M	1.063	0	0	2.635	0	1.698	0	0
F/FM	.552	0	0	.725	0	.629	0	0

49 R2 POLAR/P1/1
50 R2 POLAR/P2/1
51 R2 MICROLITE 1
52 R2 MICROLITE 2
53 R2 MICROLITE 3
54 R2 MICROLITE 4
55 R2 PORPHYROCLAST 5
56 R2 MICROLITE 5

SUPER RECAL — PROBE ANALYSES OF FELDSPARS

	57	58	59	60	61	62	63	64
SIO2	61.35	59.74	58.03	58.61	57.53	58.23	60.40	61.60
TIO2	.23	0	0	0	0	0	0	0
A203	21.59	25.17	25.11	24.60	25.74	25.70	23.79	22.98
FEO	1.43	.89	1.07	1.11	.79	.77	.91	1.08
MNO	0	0	0	0	0	0	0	0
MGO	0	0	0	0	0	0	0	0
CAO	5.51	7.44	7.20	6.64	8.53	7.78	5.89	4.87
NA20	7.93	7.17	7.35	7.47	6.59	6.80	7.91	8.28
K20	.40	.23	.21	.38	.21	0	.25	.45
SUM	100.63	99.65	99.97	99.81	99.39	99.28	99.15	99.26
SI	2.727 *	2.744 *	2.648 *	2.675 *	2.602 *	2.625 *	2.718 *	2.764 *
AL	1.236 *	1.135 *	1.327 *	1.301 *	1.372 *	1.365 *	1.262 *	1.215 *
FE	.053 * 4.016	.033 4.009	.040 4.016	.042 4.016	.030 4.003	.029 4.019	.034 4.014	.041 4.020
TI	.008 *	0 *	0 *	0 *	0 *	0 *	0 *	0 *
MN	0 *	0 *	0 *	0 *	0 *	0 *	0 *	0 *
MG	0 *	0 *	0 *	0 *	0 *	0 *	0 *	0 *
CA	.262 *	.354 *	.346 *	.319 *	.413 *	.376 *	.284 *	.234 *
NA	.684 *	.636 *	.638 *	.650 *	.578 *	.594 *	.690 *	.720 *
K	.024 .969	.013 .969	.012 .997	.022 .991	.012 1.003	0 .970	.014 .989	.026 .980
O	8.000 *	8.000 *	8.000 *	8.000 *	8.000 *	8.000 *	8.000 *	8.000 *
AN	25.76	35.96	34.70	32.22	41.20	38.74	28.73	23.89
AB	67.77	62.72	64.10	65.59	57.60	61.26	69.82	73.49
OR	6.47	1.32	1.20	2.19	1.21	0	1.45	2.63
F/M	1.093	0	0	2.635	0	1.698	0	0
F/FM	.515	0	0	.725	0	.629	0	0

57 R2 MICROLITE 6
58 R2 MICROLITE 7
59 R2 MICROLITE 8A
60 R2 MICROLITE 8B
61 R2 MICROLITE 9
62 R2 MICROLITE 10
63 R2 MICROLITE 11 BB1
64 R2 MICROLITE 12 BB2

SUPER RECAL

PROBE ANALYSIS OF FELDSPARS

	65		66		67		68		69		70		71		72	
SIO2	57.89		57.36		58.40		60.71		60.55		61.33		67.52		65.56	
TIO2	0		0		0		0		0		0		0		0	
A2O3	26.22		26.19		25.81		24.09		24.64		24.17		20.50		21.71	
FEO	0		.49		.66		0		0		0		0		0	
MNO	0		0		0		0		0		0		0		0	
MGO	0		0		.53		0		0		0		0		0	
CAO	7.71		8.58		7.38		5.73		6.69		5.65		.77		2.75	
NA2O	7.03		6.33		7.41		8.13		7.83		8.39		10.58		10.18	
K2O	.66		.20		.19		.13		0		0		.25		.14	
SUM	99.51		99.14		100.81		98.79		99.91		99.54		100.02		100.34	
SI	2.607	*	2.594	*	2.603	*	2.727	*	2.694	*	2.732	*	2.953	*	2.875	*
AL	1.391	*	1.195	*	1.356	*	1.275	*	1.303	*	1.269	*	1.057	*	1.122	*
FE	0	3.999	.019	4.008	.025	3.983	0	4.002	0	3.997	0	4.001	0	4.010	0	3.997
TI	0	*	0	*	0	*	0	*	0	*	0	*	0	*	0	*
MN	0	*	0	*	0	*	0	*	0	*	0	*	0	*	0	*
MG	0	*	0	*	.035	*	0	*	0	*	0	*	0	*	0	*
CA	.372	*	.416	*	.376	*	.276	*	.319	*	.270	*	.036	*	.129	*
NA	.614	*	.555	*	.640	*	.708	*	.676	*	.725	*	.931	*	.866	*
K	.038	1.024	.012	.982	.007	1.059	.007	.991	0	.994	0	.994	.014	.981	.008	1.003
O	8.000	*	8.000	*	8.000	*	8.000	*	8.000	*	8.000	*	8.000	*	8.000	*
AN		36.34		42.32		36.77		27.82		32.07		27.12		3.68		12.89
AB		59.96		56.50		62.67		71.43		67.93		72.88		94.90		86.33
OR		3.70		1.17		.67		.75		0		0		1.42		.78
F/M		1.063		0		.699		2.635		0		1.698		0		0
F/FM		.515		0		.411		.725		0		.629		0		0

65 CT1 HOST 1
66 CT1 MICROLITE 1
67 CT1 MICROLITE 2
68 CT3 HOST 1
69 CT3 HOST 2
70 CT3 HOST 3
71 CT3 PORPHY 1 (DEFORMED)
72 CT3 PORPHY 2

SUPER RECAL

PROBE ANALYSES OF FELDSPARS

	73		74		75		76		77		78		79		80	
SIO2	61.61		60.93		61.42		60.99		61.02		60.96		59.75		62.61	
TIO2	0		0		0		0		0		0		0		0	
A2O3	24.29		24.19		24.14		24.25		23.97		23.98		25.34		23.31	
FEO	0		0		0		0		0		0		.40		0	
MNO	0		0		0		0		0		0		0		0	
MGO	0		0		0		0		0		0		0		0	
CAO	5.91		5.77		5.37		5.80		5.86		5.87		7.39		4.78	
NA2O	8.01		7.85		8.48		8.27		8.02		8.13		7.36		8.62	
K2O	0		.26		.32		.20		0		0		.15		.32	
SUM	99.81		99.99		99.73		99.51		98.87		98.94		100.39		99.64	
SI	2.734	*	2.723	*	2.734	*	2.723	*	2.735	*	2.732	*	2.659	*	2.781	*
AL	1.270	*	1.277	*	1.266	*	1.276	*	1.266	*	1.266	*	1.329	*	1.220	*
FE	0	4.004	0	4.006	0	4.001	0	3.998	0	4.001	0	3.999	.015	4.002	0	4.001
TI	0	*	0	*	0	*	0	*	0	*	0	*	0	*	0	*
MN	0	*	0	*	0	*	0	*	0	*	0	*	0	*	0	*
MG	0	*	0	*	0	*	0	*	0	*	0	*	0	*	0	*
CA	.282	*	.277	*	.256	*	.277	*	.281	*	.282	*	.352	*	.227	*
NA	.689	*	.682	*	.732	*	.716	*	.697	*	.706	*	.635	*	.742	*
K	0	.970	.015	.974	.018	1.006	.011	1.005	0	.978	0	.988	.009	.996	.018	.988
O	8.000	*	8.000	*	8.000	*	8.000	*	8.000	*	8.000	*	8.000	*	8.000	*
AN		28.96		29.45		25.45		27.61		28.76		28.52		35.38		23.03
AB		71.04		70.03		72.54		71.25		71.24		71.48		63.76		75.14
OR		0		1.53		1.81		1.13		0		0		.85		1.84
F/M		1.063		0		.699		2.635		0		1.698		0		0
F/FM		.515		0		.411		.725		0		.629		0		0

73 GQ12 HOST 1
74 GQ12 HOST 2
75 GQ12 HOST 3
76 GQ12 HOST 4
77 GQ12 HOST 5
78 GQ12 PORUPHYROCLAST 1 CORE
79 GQ12 PORPHYROCLAST 1 RIM
80 GQ12 PORPHYROCLAST 2 DEF

SUPER PROM PROBE ANALYSES OF FELDSPARS

	81	82
SIO2	69.73	57.45
TIO2	0	0
A2O3	21.50	24.60
FEO	.48	.80
MNO	0	0
MGO	0	0
CAO	2.21	8.65
NA2O	9.56	7.55
K2O	.50	.13
SUM	99.73	99.39

SI	2.924	*	2.676	*
AL	1.075	*	1.305	*
FE	.018	4.016	.030	4.012
TI	0	*	0	*
MN	0	*	0	*
MG	0	*	0	*
CA	.096	*	.321	*
NA	.824	*	.569	*
K	.027	.949	.007	.897
O	8.000	*	8.000	*
AN	10.10		32.18	
AB	86.61		67.07	
OR	2.99		.75	
F/M	1.000		0	
F/FM	.981		0	

81 G012 PORPHYROCLAST 2 DEF

82 G013 MICROLITE 1

SUPER RECAL — PROBE ANALYSES OF MUSCOVITES

	1	2	3	4	5	6	7	8
SIO2	44.68	45.35	45.14	45.05	45.43	46.21	47.30	45.14
TIO2	1.27	1.68	1.22	1.65	1.36	.55	.56	.98
A2O3	33.05	33.28	33.08	33.09	32.49	33.44	34.57	29.52
FEO	2.79	2.57	2.67	3.13	3.06	2.56	3.02	5.41
MNO	0	0	0	0	0	0	0	0
MGO	.62	.71	.69	.75	.80	.89	.68	1.40
CAO	0	0	.16	0	.17	.17	.17	0
NA2O	.23	.31	.29	.30	.21	0	.67	0
K2O	10.51	11.05	11.08	11.46	10.64	11.31	11.72	10.23
SUM	93.15	94.95	94.32	95.43	94.16	95.13	98.69	92.68

SI	6.147	*		6.135	*		6.154	*		6.102	*		6.197	*		6.228	*		6.179	*		6.322	*	
AL	1.853	8.000		1.865	8.000		1.846	8.000		1.898	8.000		1.803	8.000		1.772	8.000		1.821	8.000		1.678	8.000	
AL	3.506	*		3.440	*		3.468	*		3.383	*		3.419	*		3.538	*		3.500	*		3.193	*	
TI	.131	*		.171	*		.125	*		.168	*		.140	*		.056	*		.055	*		.103	*	
FE	.321	*		.291	*		.304	*		.355	*		.349	*		.289	*		.330	*		.634	*	
MN	0	*		0	*		0	*		0	*		0	*		0	*		0	*		0	*	
MG	.127	4.086		.143	4.044		.138	4.036		.151	4.057		.163	4.071		.179	4.061		.132	4.017		.292	4.222	
CA	0	*		0	*		.023	*		0	*		.025	*		.025	*		.024	*		0	*	
NA	.061	*		.081	*		.077	*		.079	*		.056	*		0	*		.170	*		0	*	
K	1.844	1.906		1.907	1.988		1.927	2.027		1.980	2.059		1.851	1.932		1.944	1.969		1.953	2.146		1.827	1.827	
O	22.000	*		22.000	*		22.000	*		22.000	*		22.000	*		22.000	*		22.000	*		22.000	*	
MUSC		96.78			95.91			96.17			96.17			97.09			100.00			92.00			100.00		
PARG		3.22			4.09			3.83			3.83			2.91			0			8.00			0		
F/M		2.525			2.031			2.203			2.342			2.146			1.614			2.492			2.168		
F/FM		.716			.670			.688			.701			.682			.617			.714			.684		

1 B1 HOST MUSC1
2 B1 HOST MSC2
3 B1 HOST MSC3
4 B1 HOST MSC4
5 B1 HOST MSC5
6 B1 P1 PORPHYROCLAST MSC 1
7 B1 P1 PORPHYROCLAST MSC2
8 X HOST MSC1

SUPER RECAL — PROBE ANALYSES OF MUSCOVITES

	9	10
SIO2	44.27	45.26
TIO2	.82	1.54
A2O3	28.87	28.40
FEO	4.77	3.84
MNO	0	0
MGO	1.39	1.29
CAO	0	.15
NA2O	.28	.38
K2O	9.94	10.14
SUM	90.34	91.00

SI	6.345	*		6.416	*	
AL	1.655	8.000		1.584	8.000	
AL	3.221	*		3.161	*	
TI	.088	*		.164	*	
FE	.572	*		.455	*	
MN	0	*		0	*	
MG	.297	4.178		.273	4.053	
CA	0	*		.023	*	
NA	.078	*		.104	*	
K	1.817	1.895		1.833	1.961	
O	22.000	*		22.000	*	
MUSC		95.89			94.61	
PARG		4.11			5.39	
F/M		1.925			1.670	
F/FM		.658			.625	

9 X HOST MSC3
10 X HOST MSC4

SUPER RECAL — PROBE ANALYSES OF BIOTITES

	1	2	3	4	5	6	7	8
SIO2	34.84	35.16	36.87	36.59	34.33	34.89	34.50	34.55
TIO2	2.78	2.72	2.58	2.67	2.63	2.70	2.79	2.71
A2O3	18.76	19.41	18.99	18.89	18.67	18.81	18.89	18.39
FEO	21.06	20.77	18.09	19.25	21.49	19.77	21.58	21.41
MNO	0	0	0	0	0	0	0	0
MGO	7.86	7.68	8.96	7.94	7.91	8.15	8.12	7.77
CAO	.15	0	0	.20	0	0	0	0
NA2O	.29	0	0	.31	.40	0	.29	.25
K2O	9.98	9.59	9.53	9.61	9.54	9.62	9.89	9.33
SUM	95.72	95.33	95.02	95.46	94.97	93.94	96.06	94.41
SI	5.354 *	5.384 *	5.565 *	5.545 *	5.324 *	5.409 *	5.295 *	5.376 *
AL	2.646 8.000	2.616 8.000	2.435 8.000	2.455 8.000	2.676 8.000	2.591 8.000	2.705 8.000	2.624 8.000
AL	.751 *	.886 *	.942 *	.918 *	.736 *	.844 *	.712 *	.749 *
TI	.321 *	.313 *	.293 *	.304 *	.307 *	.315 *	.322 *	.317 *
FE	2.706 *	2.660 *	2.283 *	2.440 *	2.787 *	2.563 *	2.770 *	2.786 *
MN	0 *	0 *	0 *	0 *	0 *	0 *	0 *	0 *
MG	1.800 5.578	1.753 5.612	2.016 5.534	1.793 5.455	1.828 5.658	1.883 5.605	1.858 5.661	1.802 5.654
CA	.025 *	0 *	0 *	.032 *	0 *	0 *	0 *	0 *
NA	.086 *	0 *	0 *	.091 *	.120 *	0 *	.086 *	.075 *
K	1.956 2.067	1.873 1.873	1.835 1.835	1.857 1.981	1.887 2.007	1.902 1.902	1.936 2.022	1.852 1.927
O	22.000 *	22.000 *	22.000 *	22.000 *	22.000 *	22.000 *	22.000 *	22.000 *
ANNT	60.05	60.28	53.11	57.63	60.39	57.65	59.86	60.72
PHLG	39.95	39.72	46.89	42.37	39.61	42.35	40.14	39.28
F/M	1.503	1.517	1.133	1.360	1.524	1.361	1.491	1.546
F/FM	.601	.603	.531	.576	.604	.576	.599	.607

1 B1 P1 BTE2
2 B1 P1 BTE3
3 B1 P1 BTE5
4 B1 P1 BTE6(A)
5 B1 P1 BTE6(B)
6 B1 P1 BTE6(A)2
7 B1 BTE7 TRAVERSE 1
8 B1 BTE7 TRAVERSE 2

SUPER RECAL — PROBE ANALYSES OF BIOTITES

	9	10	11	12	13	14	15	16
SIO2	41.59	36.69	36.90	36.41	36.20	37.51	37.29	38.38
TIO2	1.87	3.10	3.10	2.90	3.08	3.10	3.17	3.13
A2O3	26.80	15.49	15.51	15.42	15.70	15.98	15.78	16.26
FEO	17.74	17.19	16.28	16.60	16.38	16.67	16.53	17.01
MNO	0	0	.30	.24	.25	.25	.26	0
MGO	3.46	12.67	12.43	11.99	12.38	11.70	11.52	11.39
CAO	.86	0	0	.15	0	0	0	.32
NA2O	1.01	.30	0	0	.30	.37	.65	.74
K2O	5.06	9.75	9.78	9.45	9.60	10.08	9.42	9.23
SUM	98.39	95.19	94.30	93.16	93.89	95.66	94.62	96.46
SI	5.773 *	5.559 *	5.617 *	5.617 *	5.547 *	5.640 *	5.654 *	5.691 *
AL	2.227 8.000	2.441 8.000	2.383 8.000	2.383 8.000	2.453 8.000	2.360 8.000	2.346 8.000	2.309 8.000
AL	2.156 *	.324 *	.399 *	.421 *	.382 *	.471 *	.473 *	.532 *
TI	.195 *	.353 *	.355 *	.336 *	.355 *	.351 *	.361 *	.349 *
FE	2.059 *	2.178 *	2.072 *	2.142 *	2.099 *	2.096 *	2.096 *	2.109 *
MN	0 *	0 *	.039 *	.031 *	.032 *	.032 *	.033 *	0 *
MG	.716 5.126	2.861 5.717	2.820 5.685	2.757 5.688	2.828 5.696	2.622 5.571	2.603 5.567	2.517 5.507
CA	.128 *	0 *	0 *	.025 *	0 *	0 *	0 *	.051 *
NA	.272 *	.088 *	0 *	0 *	.089 *	.108 *	.191 *	.213 *
K	.896 1.295	1.884 1.972	1.899 1.899	1.860 1.884	1.876 1.965	1.933 2.041	1.822 2.013	1.746 2.009
O	22.000 *	22.000 *	22.000 *	22.000 *	22.000 *	22.000 *	22.000 *	22.000 *
ANNT	74.21	43.22	42.81	44.08	42.98	44.80	44.99	45.59
PHLG	25.79	56.78	57.19	55.92	57.02	55.20	55.01	54.41
F/M	2.877	.761	.749	.788	.754	.812	.818	.838
F/FM	.742	.432	.428	.441	.430	.448	.450	.456

9 B1 BTE7 TRAVERSE 3
10 GH4 HOST BTE1
11 GH4 HOST BTE2
12 GH4 HOST BTE3
13 GH4 HOST BTE4
14 GH4 PORPHYROCLAST BTE1
15 GH4 PORPHYROCLAST BTE2
16 GH4 PORPHYROCLAST VTE2(2)

SUPER RECAL PROBE ANALYSES OF BIOTITES

	17		18		19		20		21		22		23		24	
SIO2	38.63		39.35		36.96		36.67		37.57		36.39		35.76		36.29	
TIO2	2.67		3.10		3.30		3.15		3.14		2.37		2.04		3.15	
A203	16.72		16.08		16.06		15.47		15.59		17.46		17.43		16.72	
FEO	16.84		16.34		15.96		15.60		14.70		18.09		17.58		17.54	
MNO	.24		0		0		.33		.36		.20		.36		.24	
MGO	10.88		10.92		12.25		12.80		12.74		10.78		11.51		10.33	
CAO	.75		.76		0		0		0		0		.19		.15	
NA20	1.01		1.06		0		.31		0		0		0		0	
K20	9.03		8.78		9.87		9.83		9.75		9.04		8.17		9.03	
SUM	96.77		96.39		94.40		94.16		93.85		94.33		93.04		93.45	
SI	5.708	*	5.803	*	5.601	*	5.586	*	5.691	*	5.546	*	5.502	*	5.580	*
AL	2.292	8.000	2.197	8.000	2.399	8.000	2.414	8.000	2.309	8.000	2.454	8.000	2.498	8.000	2.420	8.000
AL	.619	*	.597	*	.468	*	.364	*	.474	*	.682	*	.662	*	.610	*
TI	.297	*	.344	*	.376	*	.361	*	.358	*	.272	*	.236	*	.364	*
FE	2.081	*	2.015	*	2.023	*	1.988	*	1.862	*	2.306	*	2.262	*	2.256	*
MN	.030	*	0	*	0	*	.043	*	.046	*	.026	*	.047	*	.031	*
MG	2.396	5.423	2.400	5.357	2.767	5.634	2.907	5.661	2.876	5.616	2.449	5.734	2.640	5.847	2.368	5.628
CA	.119	*	.120	*	0	*	0	*	0	*	0	*	.031	*	.025	*
NA	.289	*	.303	*	0	*	.092	*	0	*	0	*	0	*	0	*
K	1.702	2.110	1.651	2.075	1.908	1.908	1.910	2.002	1.884	1.884	1.757	1.757	1.603	1.635	1.771	1.796
O	22.000	*	22.000	*	22.000	*	22.000	*	22.000	*	22.000	*	22.000	*	22.000	*
ANNT		46.84		45.64		42.23		41.12		39.88		48.77		46.66		49.13
PHLG		53.16		54.36		57.77		58.88		60.12		51.23		53.34		50.87
F/M		.881		.840		.731		.698		.663		.952		.875		.966
F/FM		.468		.456		.422		.411		.399		.488		.467		.491

17 GH4 PORPHYROCLAST BTE3
18 GH4 PORPHYROCLAST BTE4
19 GH5 HOST BTE1
20 GH5 HOST BTE3
21 GH5 HOST BTE4
22 X HOST BTE1
23 X HOST BTE2
24 X HOST BTE3

SUPER RECAL PROBE ANALYSES OF BIOTITES

	25		26		27		28		29		30		31		32	
SIO2	35.85		35.08		35.24		35.85		36.89		41.34		43.19		41.07	
TIO2	3.47		2.77		3.07		3.25		2.74		2.47		2.44		2.11	
A203	16.13		15.85		15.94		16.15		16.85		12.58		11.61		12.43	
FEO	18.00		18.72		17.82		17.66		18.59		15.67		15.07		16.15	
MNO	.28		.38		.27		.34		0		.20		.22		.25	
MGO	10.49		11.06		10.63		10.44		10.68		14.43		14.05		14.06	
CAO	.17		0		.16		0		0		.31		.27		.22	
NA20	0		0		.21		0		.31		.35		.49		0	
K20	8.77		7.82		8.70		9.03		9.17		7.96		7.84		8.09	
SUM	93.16		91.68		92.04		92.72		95.23		95.31		95.18		94.38	
SI	5.549	*	5.520	*	5.530	*	5.573	*	5.585	*	6.097	*	6.331	*	6.131	*
AL	2.451	8.000	2.480	8.000	2.470	8.000	2.427	8.000	2.415	8.000	1.903	8.000	1.669	8.000	1.869	8.000
AL	.490	*	.459	*	.478	*	.531	*	.591	*	.283	*	.337	*	.318	*
TI	.404	*	.328	*	.362	*	.380	*	.312	*	.274	*	.269	*	.237	*
FE	2.330	*	2.464	*	2.339	*	2.296	*	2.354	*	1.933	*	1.847	*	2.016	*
MN	.037	*	.051	*	.036	*	.045	*	0	*	.025	*	.027	*	.032	*
MG	2.420	5.681	2.594	5.895	2.487	5.702	2.419	5.671	2.410	5.667	3.172	5.687	3.070	5.550	3.129	5.731
CA	.028	*	0	*	.027	*	0	*	0	*	.049	*	.042	*	.035	*
NA	0	*	0	*	.064	*	0	*	.091	*	.100	*	.139	*	0	*
K	1.731	1.759	1.570	1.570	1.741	1.832	1.790	1.790	1.771	1.862	1.497	1.646	1.466	1.648	1.540	1.576
O	22.000	*	22.000	*	22.000	*	22.000	*	22.000	*	22.000	*	22.000	*	22.000	*
ANNT		49.44		49.22		48.85		49.18		49.41		38.16		37.92		39.56
PHLG		50.56		50.78		51.15		50.82		50.59		61.84		62.08		60.44
F/M		.978		.969		.955		.968		.977		.617		.611		.655
F/FM		.494		.492		.488		.492		.494		.382		.379		.396

25 X HOST BTE4
26 X HOST BTE5
27 X HOST BTE7
28 X HOST BTE8
29 X HOST BTE9
30 X Z7 BTE1
31 X Z7 BTE2
32 X Z7 BTE3

SUPER RECAL PROBE ANALYSES OF BIOTITES

	33	34	35	36	37	38	39	40
SIO2	35.14	35.13	39.00	36.50	36.94	37.14	36.95	36.77
TIO2	3.21	3.25	2.31	2.82	1.02	3.37	2.21	1.76
A203	17.19	17.64	17.58	17.04	15.96	16.23	16.39	16.55
FEO	18.26	17.92	18.26	18.75	16.09	14.50	16.22	16.24
MNO	0	.25	0	0	0	0	.25	.32
MGO	8.78	8.63	7.26	7.95	12.37	13.01	12.34	12.16
CAO	0	0	0	0	0	0	0	0
NA20	0	0	0	0	0	0	0	0
K20	10.09	9.73	9.77	9.86	10.02	10.36	10.01	10.15
SUM	92.67	92.55	94.18	92.92	92.40	94.61	94.37	93.95
SI	5.510 *	5.497 *	5.922 *	5.687 *	5.726 *	5.590 *	5.615 *	5.621 *
AL	2.490 8.000	2.503 8.000	2.078 8.000	2.313 8.000	2.274 8.000	2.410 8.000	2.385 8.000	2.379 8.000
AL	.687 *	.749 *	1.067 *	.816 *	.642 *	.468 *	.551 *	.603 *
TI	.379 *	.382 *	.264 *	.330 *	.119 *	.381 *	.253 *	.202 *
FE	2.395 *	2.345 *	2.319 *	2.443 *	2.086 *	1.825 *	2.061 *	2.076 *
MN	0 *	.033 *	0 *	0 *	0 *	0 *	.032 *	.041 *
MG	2.052 5.512	2.013 5.522	1.643 5.293	1.846 5.436	2.858 5.704	2.919 5.593	2.795 5.692	2.771 5.694
CA	0 *	0 *	0 *	0 *	0 *	0 *	0 *	0 *
NA	0 *	0 *	0 *	0 *	0 *	0 *	0 *	0 *
K	2.018 2.018	1.942 1.942	1.892 1.892	1.960 1.960	1.981 1.981	1.989 1.989	1.940 1.940	1.979 1.979
O	22.000 *	22.000 *	22.000 *	22.000 *	22.000 *	22.000 *	22.000 *	22.000 *
ANNT	53.85	54.16	58.53	56.96	42.19	38.47	42.82	43.32
PHLG	46.15	45.84	41.47	43.04	57.81	61.53	57.18	56.68
F/M	1.167	1.182	1.411	1.323	.730	.625	.749	.764
F/FM	.539	.542	.585	.570	.422	.385	.428	.433

33 A HOST RTE1
34 A HOST RTE2
35 A PORPHYROCLAST RTE1
36 A PORPHYROCLAST RTE2
37 G1B HOST RTE1
38 G1B HOST RTE2
39 G1B HOST RTE3
40 G1B HOST RTE4

SUPER RECAL PROBE ANALYSES OF BIOTITES

	41	42	43	44	45	46	47	48
SIO2	36.82	35.42	41.41	36.57	37.27	39.05	37.42	39.14
TIO2	2.35	1.97	0	2.30	2.90	1.31	2.10	1.05
A203	15.91	15.29	15.50	16.85	17.27	16.91	17.58	17.20
FEO	17.01	19.38	16.67	16.10	15.81	13.86	14.61	12.87
MNO	.24	.25	.25	0	0	0	0	0
MGO	12.44	11.91	13.26	13.30	12.91	13.59	13.34	13.13
CAO	0	0	0	0	0	1.24	.19	1.60
NA20	0	0	1.30	0	.40	0	0	.27
K20	10.01	8.88	7.60	9.39	10.08	8.73	9.41	8.40
SUM	94.78	92.10	95.99	94.51	96.64	94.69	94.65	93.66
SI	5.599 *	5.572 *	6.063 *	5.523 *	5.513 *	5.777 *	5.585 *	5.820 *
AL	2.401 8.000	2.428 8.000	1.937 8.000	2.477 8.000	2.487 8.000	2.223 8.000	2.415 8.000	2.180 8.000
AL	.451 *	.407 *	.738 *	.522 *	.524 *	.724 *	.677 *	.834 *
TI	.269 *	.233 *	0 *	.261 *	.323 *	.146 *	.236 *	.117 *
FE	2.163 *	2.418 *	2.041 *	2.033 *	1.956 *	1.715 *	1.824 *	1.601 *
MN	.031 *	.033 *	.031 *	0 *	0 *	0 *	0 *	0 *
MG	2.820 5.733	2.793 5.884	2.894 5.704	2.994 5.810	2.846 5.648	2.997 5.581	2.968 5.705	2.910 5.463
CA	0 *	0 *	0 *	0 *	0 *	.197 *	.030 *	.255 *
NA	0 *	0 *	.369 *	0 *	.115 *	0 *	0 *	.078 *
K	1.942 1.942	1.782 1.782	1.419 1.788	1.809 1.809	1.902 2.017	1.647 1.844	1.791 1.822	1.593 1.926
O	22.000 *	22.000 *	22.000 *	22.000 *	22.000 *	22.000 *	22.000 *	22.000 *
ANNT	43.76	46.75	41.73	40.45	40.73	36.40	38.06	35.48
PHLG	56.24	53.25	58.27	59.55	59.27	63.60	61.94	64.52
F/M	.778	.878	.716	.679	.687	.572	.614	.550
F/FM	.438	.467	.417	.404	.407	.364	.381	.355

41 G1B HOST RTE5
42 G1B PORPHYROCLAST RTE1
43 G1B PORPHYROCLAST RTE2
44 G2D HOST RTE1
45 G2D HOST RTE2
46 G2D PORPHYROCLAST1
47 G2D PORPHYROCLAST2
48 G2D PORPHYROCLAST4

SUPER RECAL PROBE ANALYSES OF BIOTITES

	49	50	51	52	53	54	55	56
SIO2	40.09	37.35	37.13	36.95	37.28	37.03	35.93	36.20
TIO2	3.25	3.46	2.92	2.73	3.77	3.34	3.76	2.81
A2O3	14.38	13.45	15.18	15.13	14.53	14.44	14.08	14.28
FEO	18.31	20.62	9.42	9.51	10.56	12.13	14.38	13.86
MNO	.25	0	0	0	.21	0	0	0
MGO	9.54	10.64	16.83	16.26	14.70	14.72	12.96	13.06
CAO	.41	.15	0	.25	.21	.21	.23	.23
NA2O	1.65	.54	0	0	0	0	0	0
K2O	8.46	9.06	10.31	10.31	10.38	10.39	9.93	9.89
SUM	96.34	95.27	91.79	91.14	91.64	92.26	91.27	90.33
SI	5.972 *	5.736 *	5.632 *	5.653 *	5.708 *	5.675 *	5.633 *	5.709 *
AL	2.028 8.000	2.264 8.000	2.368 8.000	2.347 8.000	2.292 8.000	2.325 8.000	2.367 8.000	2.291 8.000
AL	.497 *	.170 *	.345 *	.381 *	.329 *	.283 *	.234 *	.363 *
TI	.364 *	.400 *	.333 *	.314 *	.434 *	.385 *	.443 *	.333 *
FE	2.281 *	2.648 *	1.195 *	1.217 *	1.352 *	1.555 *	1.885 *	1.828 *
MN	.032 *	0 *	0 *	0 *	.027 *	0 *	0 *	0 *
MG	2.118 5.292	2.436 5.653	3.805 5.679	3.708 5.620	3.355 5.497	3.362 5.584	3.028 5.590	3.070 5.595
CA	.065 *	.025 *	0 *	.041 *	.034 *	.034 *	.039 *	.039 *
NA	.477 *	.161 *	0 *	0 *	0 *	0 *	0 *	0 *
K	1.608 2.150	1.775 1.960	1.995 1.995	2.012 2.053	2.027 2.061	2.031 2.065	1.986 2.024	1.990 2.028
O	22.000 *	22.000 *	22.000 *	22.000 *	22.000 *	22.000 *	22.000 *	22.000 *
ANNT	52.19	52.09	23.90	24.71	29.14	31.62	38.37	37.32
PHLG	47.81	47.91	76.10	75.29	70.86	68.38	61.63	62.68
F/M	1.092	1.087	.314	.328	.411	.462	.623	.595
F/FM	.522	.521	.239	.247	.291	.316	.384	.373

49 SA3 BTE ADJ PCL2
50 SA3 BTE2
51 CT1 HOST BTE1
52 CT1 HOST BTE2
53 CT1 HOST BTE3
54 CT1 PORPHYROCLAST1
55 CT1 PORPHYROCLAST2
56 CT1 PORPHYROCLAST3

SUPER RECAL PROBE ANALYSES OF BIOTITES

	57	58	59	60	61	62	63	64
SIO2	37.02	37.33	38.22	38.79	35.43	36.56	38.86	36.93
TIO2	3.12	5.90	5.32	5.73	5.87	5.69	4.91	6.70
A2O3	14.20	14.98	14.84	15.57	15.62	16.16	16.55	16.18
FEO	11.19	11.33	10.63	15.06	16.34	14.88	13.67	14.53
MNO	0	0	0	0	0	0	.30	.38
MGO	15.49	15.63	16.91	11.23	12.16	13.65	12.28	12.49
CAO	.32	0	0	.29	.27	.23	.49	.62
NA2O	0	.46	.43	1.38	.43	.45	1.58	.72
K2O	10.10	9.89	9.95	9.39	9.77	10.17	9.06	9.56
SUM	91.44	95.52	96.30	97.44	95.89	97.79	97.70	98.11
SI	5.692 *	5.492 *	5.549 *	5.663 *	5.337 *	5.354 *	5.617 *	5.377 *
AL	2.308 8.000	2.508 8.000	2.451 8.000	2.337 8.000	2.663 8.000	2.646 8.000	2.383 8.000	2.623 8.000
AL	.265 *	.088 *	.087 *	.341 *	.110 *	.143 *	.436 *	.153 *
TI	.361 *	.653 *	.581 *	.629 *	.665 *	.627 *	.534 *	.734 *
FE	1.439 *	1.394 *	1.291 *	1.839 *	2.059 *	1.823 *	1.653 *	1.769 *
MN	0 *	0 *	0 *	0 *	0 *	0 *	.037 *	.047 *
MG	3.550 5.615	3.427 5.562	3.659 5.618	2.444 5.252	2.730 5.564	2.980 5.572	2.646 5.305	2.711 5.413
CA	.053 *	0 *	0 *	.045 *	.044 *	.036 *	.076 *	.097 *
NA	0 *	.131 *	.121 *	.391 *	.126 *	.128 *	.443 *	.203 *
K	1.981 2.034	1.856 1.987	1.842 1.963	1.748 2.184	1.877 2.046	1.900 2.064	1.670 2.189	1.775 2.075
O	22.000 *	22.000 *	22.000 *	22.000 *	22.000 *	22.000 *	22.000 *	22.000 *
ANNT	28.84	28.91	26.07	42.94	42.99	37.95	38.97	40.12
PHLG	71.16	71.09	73.93	57.06	57.01	62.05	61.03	59.88
F/M	.405	.407	.353	.752	.754	.612	.638	.670
F/FM	.288	.289	.261	.429	.430	.380	.390	.401

57 CT1 PORPHYROCLAST4
58 CT2 HOST BTE1
59 CT2 PORPHYROCLAST BTE1
60 R4/1 BTE5(1)
61 R4/1 BTE5(2)
62 R4/1 BTE6(1)
63 R4/1 BTE6(2)
64 R4/1 BTE6(3)

SUPER RECAL PROBE ANALYSES OF BIOTITES

	65	66	67	68	69	70	71	72
SIO2	39.91	36.41	36.29	45.62	42.56	36.35	39.55	36.15
TIO2	6.05	6.03	6.49	5.53	5.07	6.63	5.36	4.11
A2O3	14.19	15.61	15.07	13.67	15.65	15.16	17.45	15.73
FEO	14.36	14.66	15.13	12.93	13.09	15.01	13.44	18.66
MNO	0	.21	0	0	0	0	0	0
MGO	12.68	13.25	13.31	10.41	10.86	13.63	10.56	10.95
CAO	0	0	.15	.23	.40	.21	.75	0
NA2O	.58	.44	.37	.78	.66	.42	1.82	0
K2O	9.76	10.49	10.25	8.65	8.74	10.08	8.75	10.10
SUM	97.53	97.09	97.06	97.82	97.03	97.49	97.68	95.70
SI	5.788 *	5.383 *	5.375 *	6.410 *	6.072 *	5.352 *	5.681 *	5.497 *
AL	2.212 8.000	2.617 8.000	2.625 8.000	1.590 8.000	1.928 8.000	2.630 7.983	2.319 8.000	2.503 8.000
AL	.212 *	.103 *	.005 *	.673 *	.703 *	0 *	.635 *	.316 *
TI	.660 *	.670 *	.723 *	.584 *	.544 *	.734 *	.579 *	.470 *
FE	1.741 *	1.813 *	1.874 *	1.519 *	1.562 *	1.848 *	1.615 *	2.373 *
MN	0 *	.026 *	0 *	0 *	0 *	0 *	0 *	0 *
MG	2.741 5.354	2.920 5.533	2.938 5.540	2.180 4.957	2.309 5.119	2.991 5.574	2.261 5.090	2.482 5.641
CA	0 *	0 *	.024 *	.035 *	.061 *	.033 *	.115 *	0 *
NA	.163 *	.126 *	.106 *	.212 *	.183 *	.120 *	.507 *	0 *
K	1.805 1.968	1.976 2.103	1.936 2.066	1.550 1.797	1.590 1.834	1.893 2.046	1.603 2.226	1.959 1.959
O	22.000 *	22.000 *	22.000 *	22.000 *	22.000 *	22.000 *	22.000 *	22.000 *
ANNT	38.85	38.64	38.94	41.07	40.34	38.19	41.66	48.88
PHLG	61.15	61.36	61.06	58.93	59.66	61.81	58.34	51.12
F/M	.635	.630	.638	.697	.676	.618	.714	.956
F/FM	.389	.386	.389	.411	.403	.382	.417	.489

65 R4/1 BTE8(1)
66 R4/1 BTE8(2)
67 R4/1 BTE8(3)
68 R4/1 BTE8(4)
69 R4/1 BTE8(5)
70 R4/1 BTE8(7)
71 R4/1 BTE9(1)
72 GQ19 HOST BTE1

SUPER RECAL PROBE ANALYSES OF BIOTITES

	73	74	75	76	77	78	79	80
SIO2	36.36	36.56	33.96	35.09	33.21	32.49	36.10	35.12
TIO2	3.72	4.17	4.02	3.50	1.86	1.72	3.13	1.57
A2O3	15.78	16.70	14.96	15.01	15.38	15.11	15.12	16.25
FEO	18.78	17.98	22.84	21.97	21.15	21.40	20.05	20.34
MNO	0	0	0	0	0	0	0	.23
MGO	11.58	10.48	8.90	9.66	12.81	12.40	10.47	10.31
CAO	0	0	.10	.13	.15	0	.29	.74
NA2O	0	0	.39	.21	0	0	.79	.45
K2O	9.85	10.17	9.03	9.17	6.95	6.51	8.50	8.36
SUM	96.07	96.06	94.20	94.74	91.51	89.63	94.45	93.37
SI	5.499 *	5.506 *	5.374 *	5.477 *	5.302 *	5.302 *	5.573 *	5.500 *
AL	2.501 8.000	2.494 8.000	2.626 8.000	2.523 8.000	2.698 8.000	2.698 8.000	2.427 8.000	2.500 8.000
AL	.311 *	.470 *	.163 *	.238 *	.196 *	.207 *	.323 *	.499 *
TI	.423 *	.472 *	.478 *	.411 *	.223 *	.211 *	.363 *	.185 *
FE	2.375 *	2.265 *	3.022 *	2.868 *	2.824 *	2.920 *	2.588 *	2.664 *
MN	0 *	0 *	0 *	0 *	0 *	0 *	0 *	.031 *
MG	2.610 5.720	2.353 5.560	2.099 5.763	2.247 5.764	3.049 6.292	3.016 6.355	2.409 5.684	2.407 5.786
CA	0 *	0 *	.017 *	.022 *	.026 *	0 *	.048 *	.124 *
NA	0 *	0 *	.120 *	.064 *	0 *	0 *	.236 *	.137 *
K	1.900 1.900	1.954 1.954	1.822 1.959	1.826 1.911	1.415 1.441	1.355 1.355	1.674 1.958	1.670 1.931
O	22.000 *	22.000 *	22.000 *	22.000 *	22.000 *	22.000 *	22.000 *	22.000 *
ANNT	47.64	49.05	59.01	56.06	48.09	49.19	51.79	52.82
PHLG	52.36	50.95	40.99	43.94	51.91	50.81	48.21	47.18
F/M	.910	.963	1.440	1.276	.926	.968	1.074	1.120
F/FM	.476	.490	.590	.561	.481	.492	.518	.528

73 GQ19 HOST BTE2
74 GQ19 PORPHYROCLAST BTE1
75 GQ34 HOST BTE1
76 GQ34 HOST BTE2
77 GQ34 HOST BTE3 (ALT. TO CHLOR)
78 GQ34 HOST BTE4 (ALT. TO CHLOR)
79 GQ34 PORPHYROCLAST BTE1
80 GQ34 PORPHYROCLAST BTE2

SUPER RECAL — PROBE ANALYSES OF BIOTITES

	81	82	83	84	85	86	87	88
SIO2	34.61	34.40	31.56	29.71	35.71	34.58	35.85	34.77
TIO2	2.14	2.93	.53	.55	1.73	2.29	2.66	2.77
A203	16.45	14.04	17.14	17.32	16.23	15.46	15.47	15.06
FEO	19.01	20.55	22.07	23.19	20.50	21.25	16.70	16.21
MNO	0	0	.25	0	0	0	0	0
MGO	11.44	10.96	12.48	14.46	11.32	11.98	12.18	12.36
CAO	.31	0	.20	.39	.29	.11	0	.17
NA20	.69	.37	.52	.17	.50	.47	0	.33
K20	8.01	8.33	4.92	2.26	7.63	7.79	9.72	9.30
SUM	92.66	91.58	89.67	88.05	93.91	93.93	92.58	90.97

SI	5.416	*		5.515	*		5.130	*		4.883	*		5.517	*		5.391	*		5.579	*		5.513	*	
AL	2.584	8.000		2.485	8.000		2.870	8.000		3.117	8.000		2.483	8.000		2.609	8.000		2.421	8.000		2.487	8.000	
AL	.449	*		.167	*		.413	*		.238	*		.472	*		.231	*		.415	*		.327	*	
TI	.252	*		.353	*		.065	*		.068	*		.201	*		.268	*		.311	*		.330	*	
FE	2.488	*		2.755	*		3.000	*		3.188	*		2.649	*		2.771	*		2.173	*		2.149	*	
MN	0	*		0	*		.034	*		0	*		0	*		0	*		0	*		0	*	
MG	2.668	5.857		2.619	5.895		3.023	6.535		3.543	7.037		2.607	5.928		2.784	6.054		2.825	5.725		2.921	5.728	
CA	.052	*		0	*		.035	*		.069	*		.048	*		.018	*		0	*		.029	*	
NA	.209	*		.115	*		.164	*		.054	*		.150	*		.142	*		0	*		.101	*	
K	1.599	1.860		1.703	1.818		1.020	1.219		.474	.597		1.504	1.701		1.549	1.709		1.929	1.929		1.881	2.011	
O	22.000	*		22.000	*		22.000	*		22.000	*		22.000	*		22.000	*		22.000	*		22.000	*	
ANNT		48.25			51.27			50.09			47.36			50.40			49.88			43.48			42.39		
PHLG		51.75			48.73			49.91			52.64			49.60			50.12			56.52			57.61		
F/M		.932			1.052			1.004			.900			1.016			.995			.769			.736		
F/FM		.482			.513			.501			.474			.504			.499			.435			.424		

81 GQ34 PORPHYROCLAST BTE3
82 GQ34 PORPHYROCLAST BTE4
83 GQ34 PORPHYROCLAST BTE5 (ALT. TO CHLOR)
84 GQ34 PORPHYROCLAST BTE6 (ALT. TO CHLOR)
85 GQ34 PORPHYROCLAST BTE7
86 GQ34 PORPHYROCLAST BTE8
87 GQ38 HOST BTE1
88 GQ38 HOST BTE2

SUPER RECAL — PROBE ANALYSES OF BIOTITES

	89	90	91	92	93	94	95	96
SIO2	36.25	36.70	35.47	36.02	36.70	36.29	35.56	35.27
TIO2	2.91	2.80	2.51	2.18	.82	.99	1.72	.84
A203	15.64	15.57	15.61	16.20	18.00	16.89	16.53	16.90
FEO	17.66	16.91	19.84	19.33	18.16	18.56	19.77	18.90
MNO	.22	0	0	0	0	0	0	0
MGO	12.47	12.78	11.35	9.72	10.64	10.39	10.27	10.89
CAO	0	0	0	.36	.62	.42	0	0
NA20	0	.27	.34	.74	.40	.12	0	.34
K20	10.22	10.05	9.75	9.63	9.84	9.42	9.98	9.34
SUM	95.37	95.08	94.87	94.18	95.18	93.08	93.83	92.48

SI	5.515	*		5.568	*		5.481	*		5.586	*		5.574	*		5.641	*		5.543	*		5.542	*	
AL	2.485	8.000		2.432	8.000		2.519	8.000		2.414	8.000		2.426	8.000		2.359	8.000		2.457	8.000		2.458	8.000	
AL	.319	*		.352	*		.323	*		.546	*		.796	*		.735	*		.579	*		.671	*	
TI	.333	*		.319	*		.292	*		.254	*		.094	*		.116	*		.202	*		.099	*	
FE	2.247	*		2.146	*		2.564	*		2.507	*		2.307	*		2.413	*		2.577	*		2.484	*	
MN	.028	*		0	*		0	*		0	*		0	*		0	*		0	*		0	*	
MG	2.828	5.756		2.890	5.707		2.614	5.793		2.247	5.554		2.409	5.606		2.407	5.672		2.386	5.743		2.550	5.804	
CA	0	*		0	*		0	*		.060	*		.101	*		.070	*		0	*		0	*	
NA	0	*		.079	*		.102	*		.222	*		.118	*		.036	*		0	*		.104	*	
K	1.983	1.983		1.945	2.024		1.922	2.023		1.905	2.187		1.906	2.125		1.868	1.974		1.984	1.984		1.872	1.975	
O	22.000	*		22.000	*		22.000	*		22.000	*		22.000	*		22.000	*		22.000	*		22.000	*	
ANNT		44.59			42.61			49.51			52.74			48.92			50.06			51.92			49.34		
PHLG		55.41			57.39			50.49			47.26			51.08			49.94			48.08			50.66		
F/M		.805			.742			.981			1.116			.958			1.002			1.080			.974		
F/FM		.446			.426			.495			.527			.489			.501			.519			.493		

89 GQ38 HOST BTE3
90 GQ38 HOST BTE4
91 GQ38 HOST BTE5
92 GQ38 PORPHYROCLAST BTE1
93 GQ38 PORPHYROCLAST BTE2
94 GQ38 PORPHYROCLAST BTE3
95 GQ38 PORPHYROCLAST BTE4
96 GQ38 PORPHYROCLAST BTE5

SUPER RECAL PROBE ANALYSES OF BIOTITES

	97	98	99	100	101	102	103	104
SIO2	38.52	33.98	36.52	37.05	36.68	37.60	36.79	35.85
TIO2	1.20	8.43	4.13	3.86	3.94	3.04	2.68	3.11
A2O3	16.43	13.73	16.16	15.99	15.68	15.77	16.69	15.59
FEO	17.61	15.95	16.97	18.32	18.21	20.32	18.71	21.54
MNO	0	.21	0	0	0	.30	0	.36
MGO	11.85	8.96	11.74	11.55	11.52	10.12	9.84	10.89
CAO	1.81	6.34	0	0	0	.30	.73	.28
NA2O	.47	.32	0	0	.34	0	.74	.36
K2O	8.62	7.33	10.07	10.13	10.18	9.26	9.01	9.20
SUM	96.51	95.25	95.59	96.90	96.55	96.71	95.19	97.18

SI	5.719	*	5.207	*	5.505	*	5.538	*	5.518	*	5.657	*	5.594	*	5.439	*
AL	2.281	8.000	2.479	7.686	2.495	8.000	2.462	8.000	2.482	8.000	2.343	8.000	2.406	8.000	2.561	8.000
AL	.593	*	0	*	.376	*	.355	*	.298	*	.453	*	.585	*	.226	*
TI	.134	*	.971	*	.468	*	.434	*	.446	*	.344	*	.306	*	.355	*
FE	2.186	*	2.044	*	2.139	*	2.290	*	2.291	*	2.557	*	2.379	*	2.733	*
MN	0	*	.027	*	0	*	0	*	0	*	.038	*	0	*	.046	*
MG	2.622	5.536	2.046	5.089	2.638	5.621	2.573	5.652	2.583	5.618	2.270	5.662	2.230	5.500	2.462	5.822
CA	.288	*	1.041	*	0	*	0	*	0	*	.048	*	.119	*	.046	*
NA	.135	*	.095	*	0	*	0	*	.099	*	0	*	.218	*	.106	*
K	1.632	2.056	1.433	2.569	1.936	1.936	1.931	1.931	1.953	2.053	1.777	1.825	1.747	2.085	1.780	1.932
O	22.000	*	22.000	*	22.000	*	22.000	*	22.000	*	22.000	*	22.000	*	22.000	*
	ANNT	45.47		50.30		44.78		47.09		47.00		53.35		51.62		53.02
	PHLG	54.53		49.70		55.22		52.91		53.00		46.65		48.38		46.98
	F/M	.834		1.012		.811		.890		.887		1.143		1.067		1.129
	F/FM	.455		.503		.448		.471		.470		.533		.516		.530

97 GQ38 PORPHYROCLAST BTE6
98 GQ38 PORPHYROCLAST BTE7 (ALT. TO SPH)
99 GQ39 HOST BTE1
100 GQ39 HOST BTE2
101 GQ39 HOST BTE3
102 GQ39 PORPHYROCLAST BTE1
103 GQ39 PORPHYROCLAST BTE2
104 GQ39 PORPHYROCLAST BTE3

SUPER RECAL PROBE ANALYSES OF BIOTITES

	105	106	107	108	109	110	111	112
SIO2	35.43	34.94	37.50	37.07	36.15	35.03	35.64	35.56
TIO2	3.44	2.24	3.51	.68	3.90	1.14	9.63	3.43
A2O3	14.97	16.45	15.51	17.94	16.24	17.33	13.67	15.53
FEO	20.92	21.04	19.34	18.17	16.20	19.19	13.76	21.06
MNO	.29	.27	.30	.21	.17	.42	.25	.21
MGO	10.60	12.13	10.25	11.61	10.38	11.93	8.44	10.56
CAO	0	.26	1.53	.14	3.06	.48	7.91	.31
NA2O	.29	.33	.86	0	.27	.27	.37	.40
K2O	9.17	7.78	8.44	9.91	8.96	8.38	7.42	9.43
SUM	95.11	95.44	97.24	95.73	95.33	94.17	97.09	96.49

SI	5.482	*	5.345	*	5.602	*	5.584	*	5.473	*	5.400	*	5.305	*	5.433	*
AL	2.518	8.000	2.655	8.000	2.398	8.000	2.416	8.000	2.527	8.000	2.600	8.000	2.398	7.703	2.567	8.000
AL	.212	*	.311	*	.332	*	.769	*	.371	*	.547	*	0	*	.228	*
TI	.400	*	.258	*	.394	*	.077	*	.444	*	.132	*	1.078	*	.394	*
FE	2.707	*	2.692	*	2.416	*	2.289	*	2.051	*	2.474	*	1.713	*	2.691	*
MN	.038	*	.035	*	.038	*	.027	*	.022	*	.055	*	.032	*	.027	*
MG	2.445	5.802	2.766	6.061	2.282	5.463	2.607	5.769	2.343	5.230	2.741	5.949	1.872	4.695	2.405	5.745
CA	0	*	.043	*	.245	*	.023	*	.496	*	.079	*	1.261	*	.051	*
NA	.087	*	.098	*	.249	*	0	*	.079	*	.081	*	.107	*	.118	*
K	1.810	1.897	1.518	1.659	1.608	2.102	1.904	1.927	1.730	2.306	1.648	1.807	1.409	2.777	1.837	2.007
O	22.000	*	22.000	*	22.000	*	22.000	*	22.000	*	22.000	*	22.000	*	22.000	*
	ANNT	52.89		49.64		51.81		47.04		46.95		47.99		48.23		53.06
	PHLG	47.11		50.36		48.19		52.96		53.05		52.01		51.77		46.94
	F/M	1.123		.986		1.075		.888		.885		.923		.932		1.130
	F/FM	.529		.496		.518		.470		.469		.480		.482		.531

105 GQ39 PORPHYROCLAST BTE4 CORE
106 GQ39 PORPHYROCLAST BTE4 RIM
107 GQ39 PORPHYROCLAST BTE5
108 GQ39 PORPHYROCLAST BTE6
109 GQ39 PORPHYROCLAST BTE6 (ALT. TO SPH)
110 GQ39 PORPHYROCLAST BTE7
111 GQ39 PORPHYROCLAST BTE7 (ALT. TO SPH)
112 GQ39 PORPHYROCLAST BTE8(1)

SUPER RECAL PROBE ANALYSES OF BIOTITES

	113		114		115		116		117		118		119		120	
SIO2	36.85		36.98		37.43		36.15		35.93		36.84		36.65		36.38	
TIO2	.45		1.23		2.97		3.65		3.35		3.37		3.17		3.05	
A2O3	17.73		17.55		16.87		15.58		15.40		16.07		15.93		15.57	
FEO	17.77		18.20		19.29		18.60		18.10		18.08		20.05		20.56	
MNO	.35		.24		.23		0		.23		.27		.25		0	
MGO	11.56		11.22		9.76		11.06		10.89		11.37		10.72		9.54	
CAO	0		.58		2.18		0		0		0		0		.18	
NA2O	0		0		.39		.42		.41		.35		.21		.32	
K2O	9.67		9.76		9.30		9.79		9.77		10.07		10.14		9.79	
SUM	94.38		95.76		98.42		95.25		94.08		96.42		97.12		95.39	
SI	5.619	*	5.578	*	5.539	*	5.522	*	5.554	*	5.543	*	5.528	*	5.595	*
AL	2.381	8.000	2.422	8.000	2.461	8.000	2.478	8.000	2.446	8.000	2.457	8.000	2.472	8.000	2.405	8.000
AL	.804	*	.698	*	.480	*	.326	*	.359	*	.392	*	.359	*	.417	*
TI	.052	*	.140	*	.330	*	.419	*	.389	*	.381	*	.360	*	.353	*
FE	2.266	*	2.296	*	2.387	*	2.376	*	2.340	*	2.275	*	2.529	*	2.644	*
MN	.045	*	.031	*	.029	*	0	*	.030	*	.034	*	.032	*	0	*
MG	2.627	5.794	2.523	5.687	2.153	5.379	2.518	5.639	2.509	5.627	2.550	5.632	2.410	5.689	2.187	5.601
CA	0	*	.094	*	.346	*	0	*	0	*	0	*	0	*	.030	*
NA	0	*	0	*	.112	*	.124	*	.123	*	.102	*	.061	*	.095	*
K	1.881	1.881	1.878	1.972	1.755	2.213	1.907	2.032	1.926	2.049	1.932	2.035	1.951	2.012	1.921	2.046
O	22.000	*	22.000	*	22.000	*	22.000	*	22.000	*	22.000	*	22.000	*	22.000	*
ANNT		46.80		47.98		52.88		48.55		48.57		47.53		51.52		54.73
PHLG		53.20		52.02		47.12		51.45		51.43		52.47		48.48		45.27
F/M		.880		.922		1.122		.944		.945		.906		1.063		1.209
F/FM		.468		.480		.529		.485		.486		.475		.515		.547

113 GQ39 PORPHYROCLAST BTE9
114 GQ39 PORPHYROCLAST BTE9
115 GQ39 PORPHYROCLAST BTE10
116 GQ49 HOST BTE1
117 GQ49 HOST BTE2
118 GQ49 HOST BTE3
119 GQ49 PORPHYROCLAST BTE1
120 GQ49 PORPHYROCLAST BTE2

SUPER RECAL PROBE ANALYSES OF BIOTITES

	121		122		123		124	
SIO2	36.45		35.87		35.92		37.84	
TIO2	2.21		1.09		.92		.95	
A2O3	16.76		17.02		16.74		16.37	
FEO	21.37		20.00		20.01		19.28	
MNO	0		0		0		0	
MGO	10.12		9.91		9.80		9.93	
CAO	0		0		.16		1.34	
NA2O	.48		.45		0		0	
K2O	9.82		10.14		9.85		8.93	
SUM	97.21		94.48		93.40		94.64	
SI	5.510	*	5.562	*	5.620	*	5.777	*
AL	2.490	8.000	2.439	8.000	2.380	8.000	2.223	8.000
AL	.495	*	.672	*	.706	*	.721	*
TI	.251	*	.127	*	.108	*	.109	*
FE	2.701	*	2.594	*	2.618	*	2.461	*
MN	0	*	0	*	0	*	0	*
MG	2.280	5.727	2.290	5.683	2.285	5.717	2.259	5.551
CA	0	*	0	*	.027	*	.219	*
NA	.141	*	.135	*	0	*	0	*
K	1.893	2.034	2.005	2.141	1.966	1.992	1.739	1.958
O	22.000	*	22.000	*	22.000	*	22.000	*
ANNT		54.23		53.10		53.39		52.14
PHLG		45.77		46.90		46.61		47.86
F/M		1.185		1.132		1.146		1.089
F/FM		.542		.531		.534		.521

121 GQ49 PORPHYROCLAST BTE3
122 GQ49 PORPHYROCLAST BTE3(2)
123 GQ49 PORPHYROCLAST BTE4
124 GQ49 PORPHYROCLAST BTE5

SUPER RECAL PROBE ANALYSES OF AMPHIBOLES

	1	2	3	4	5	6	7	8
SIO2	43.62	48.75	49.58	49.32	52.81	49.93	46.49	48.41
TIO2	.78	.20	.51	.54	.47	.47	.81	.66
A203	15.52	11.08	4.67	5.01	3.79	3.72	6.02	5.50
F203	0	0	0	0	0	0	1.03	0
FEO	15.47	16.28	17.20	18.05	15.41	17.09	17.58	18.44
MNO	0	0	.27	.31	.37	.35	.33	.27
MGO	12.96	10.19	11.95	11.58	11.75	12.05	10.76	11.24
CAO	8.54	11.80	11.61	11.48	11.70	11.75	11.42	12.12
NA20	2.33	1.27	.96	1.01	1.08	1.22	1.04	1.43
K20	.50	0	.39	.99	.30	.63	.54	.61
SUM	99.72	99.57	97.14	98.29	97.68	97.21	96.02	98.68
SI	6.277 *	7.005 *	7.394 *	7.326 *	7.711 *	7.463 *	7.099 *	7.197 *
AL	1.723 8.000	.995 8.000	.606 8.000	.674 8.000	.289 8.000	.537 8.000	.901 8.000	.803 8.000
AL	.908 *	.881 *	.215 *	.203 *	.363 *	.119 *	.183 *	.161 *
TI	.084 *	.022 *	.057 *	.060 *	.052 *	.053 *	.093 *	.074 *
FE3+	0 *	0 *	0 *	0 *	0 *	0 *	.118 *	0 *
FE	1.862 *	1.956 *	2.145 *	2.242 *	1.882 *	2.136 *	2.245 *	2.293 *
MN	0 *	0 *	.034 *	.039 *	.046 *	.044 *	.043 *	.034 *
MG	2.780 5.634	2.182 5.041	2.656 5.107	2.564 5.108	2.557 4.900	2.685 5.037	2.449 5.131	2.491 5.052
CA	1.317 *	1.817 *	1.855 *	1.827 *	1.830 *	1.882 *	1.868 *	1.931 *
NA	.650 *	.354 *	.278 *	.291 *	.306 *	.354 *	.308 *	.412 *
K	.092 2.058	0 2.170	.074 2.207	.188 2.305	.056 2.192	.120 2.356	.105 2.282	.116 2.458
O	23.000 *	23.000 *	23.000 *	23.000 *	23.000 *	23.000 *	23.000 *	23.000 *
F/M	.670	.896	.820	.890	.754	.812	.934	.934
F/FM	.401	.473	.451	.471	.430	.448	.483	.483

1 SV15 MICROLITE 1
2 SV15 MICROLITE 2
3 SA3 MICROLITE 1
4 SA3 MICROLITE 2
5 SA3 MICROLITE 3
6 SA3 MICROLITE 4
7 SA3 MICROLITE 5
8 SA3 MICROLITE 6

SUPER RECAL PROBE ANALYSES OF AMPHIBOLES

	9	10	11	12	13	14	15	16
SIO2	42.62	42.53	42.48	43.13	42.51	43.08	42.98	42.88
TIO2	1.09	1.11	1.23	1.22	1.02	1.00	1.17	1.06
A203	12.04	12.15	12.16	11.58	12.38	11.61	11.85	12.06
F203	0	0	0	0	0	0	0	0
FEO	19.24	18.87	20.07	20.26	19.11	20.09	19.66	18.79
MNO	.34	.23	0	.34	.32	.42	.25	.24
MGO	8.29	8.49	8.34	8.90	8.42	9.02	8.93	8.48
CAO	11.07	11.04	11.07	10.36	11.39	10.03	10.48	10.71
NA20	1.65	1.74	1.57	1.64	1.90	1.73	1.65	1.60
K20	1.09	1.10	1.06	1.64	1.04	.99	1.01	1.10
SUM	97.43	97.26	97.98	99.07	98.09	97.97	97.98	96.92
SI	6.489 *	6.476 *	6.445 *	6.492 *	6.434 *	6.525 *	6.499 *	6.533 *
AL	1.511 8.000	1.524 8.000	1.555 8.000	1.508 8.000	1.566 8.000	1.475 8.000	1.501 8.000	1.467 8.000
AL	.649 *	.655 *	.620 *	.546 *	.642 *	.597 *	.610 *	.698 *
TI	.125 *	.127 *	.140 *	.138 *	.116 *	.114 *	.133 *	.121 *
FE3+	0 *	0 *	0 *	0 *	0 *	0 *	0 *	0 *
FE	2.450 *	2.403 *	2.547 *	2.550 *	2.419 *	2.545 *	2.486 *	2.394 *
MN	.044 *	.030 *	0 *	.043 *	.041 *	.054 *	.032 *	.031 *
MG	1.881 5.149	1.927 5.142	1.886 5.193	1.997 5.274	1.900 5.118	2.036 5.346	2.013 5.274	1.926 5.170
CA	1.806 *	1.801 *	1.800 *	1.671 *	1.847 *	1.628 *	1.698 *	1.748 *
NA	.487 *	.514 *	.462 *	.479 *	.558 *	.508 *	.484 *	.473 *
K	.212 2.505	.214 2.528	.205 2.467	.315 2.464	.201 2.605	.191 2.327	.195 2.376	.214 2.435
O	23.000 *	23.000 *	23.000 *	23.000 *	23.000 *	23.000 *	23.000 *	23.000 *
F/M	1.325	1.262	1.350	1.299	1.295	1.276	1.251	1.259
F/FM	.570	.558	.575	.565	.564	.561	.556	.557

9 GQ36 HOST 1
10 GQ36 HOST 1(2)
11 GQ36 HOST 2(1)
12 GQ36 HOST 2(2)
13 GQ36 HOST 3(1)
14 GQ36 HOST 3(2)
15 GQ36 HOST 4(1)
16 GQ36 HOST 4(2)

SUPER RECAL PROBE ANALYSES OF AMPHIBOLES

	17	18	19	20	21	22	23	24
SIO2	43.04	42.97	42.94	42.10	42.41	42.72	43.56	43.23
TIO2	.99	1.08	1.30	1.19	1.02	1.18	.82	1.03
A203	12.64	12.79	12.88	12.28	11.95	12.46	12.09	12.14
F203	0	0	0	0	0	0	0	0
FEO	18.99	18.74	18.63	18.56	19.65	19.13	18.94	18.82
MNO	.20	.28	.24	.29	.29	0	.24	.29
MGO	8.54	8.73	8.47	8.60	8.94	8.77	9.20	8.71
CAO	11.04	11.19	11.19	11.07	10.40	11.12	10.55	10.92
NA20	1.82	1.82	1.74	1.82	1.75	2.09	1.60	1.74
K20	.99	1.06	.99	1.05	.97	.99	1.07	.92
SUM	98.25	98.66	98.38	96.96	97.38	98.46	98.07	97.80
SI	6.473 *	6.437 *	6.441 *	6.430 *	6.462 *	6.427 *	6.547 *	6.524 *
AL	1.527 8.000	1.563 8.000	1.559 8.000	1.570 8.000	1.538 8.000	1.573 8.000	1.453 8.000	1.476 8.000
AL	.714 *	.695 *	.718 *	.641 *	.608 *	.635 *	.689 *	.682 *
TI	.112 *	.122 *	.147 *	.137 *	.117 *	.133 *	.093 *	.117 *
FE3+	0 *	0 *	0 *	0 *	0 *	0 *	0 *	0 *
FE	2.389 *	2.348 *	2.337 *	2.371 *	2.504 *	2.407 *	2.381 *	2.375 *
MN	.025 *	.036 *	.030 *	.038 *	.037 *	0 *	.031 *	.037 *
MG	1.914 5.154	1.949 5.149	1.894 5.126	1.958 5.143	2.030 5.296	1.966 5.142	2.061 5.254	1.959 5.170
CA	1.779 *	1.796 *	1.798 *	1.812 *	1.698 *	1.792 *	1.699 *	1.766 *
NA	.531 *	.529 *	.506 *	.539 *	.517 *	.610 *	.466 *	.509 *
K	.190 2.500	.203 2.527	.189 2.494	.205 2.555	.189 2.403	.190 2.592	.205 2.370	.177 2.452
O	23.000 *	23.000 *	23.000 *	23.000 *	23.000 *	23.000 *	23.000 *	23.000 *
F/M	1.261	1.223	1.250	1.230	1.252	1.224	1.170	1.231
F/FM	.558	.550	.556	.552	.556	.550	.539	.552

17 GQ36 HOST 5(1)
18 GQ36 HOST 5(2)
19 GQ36 HOST 6(1)
20 GQ36 HOST 6(2)
21 GQ36 HOST 7(1)
22 GQ36 HOST 7(2)
23 GQ36 HOST 8(1)
24 GQ36 HOST 8(2)

SUPER RECAL PROBE ANALYSES OF AMPHIBOLES

	25	26	27	28	29	30	31	32
SIO2	43.35	42.86	42.82	42.69	51.57	48.86	49.77	48.84
TIO2	1.04	1.22	1.24	.95	.63	.60	.37	.43
A203	11.85	11.98	11.96	11.68	7.52	6.56	6.13	7.06
F203	0	0	0	0	0	0	1.77	0
FEO	18.60	18.55	19.36	18.66	11.41	11.92	9.85	11.46
MNO	.36	0	.32	.23	.21	.37	.21	0
MGO	8.79	8.72	8.67	8.64	13.41	13.95	14.77	14.28
CAO	11.03	10.85	10.50	10.84	11.87	11.99	13.77	12.86
NA20	1.99	1.64	1.74	1.55	1.48	.84	.54	.65
K20	1.04	1.07	1.04	1.11	.83	1.26	.79	1.04
SUM	98.05	96.89	97.65	96.35	98.93	96.35	97.97	96.62
SI	6.534 *	6.522 *	6.495 *	6.547 *	7.332 *	7.215 *	7.193 *	7.166 *
AL	1.466 8.000	1.478 8.000	1.505 8.000	1.453 8.000	.668 8.000	.785 8.000	.807 8.000	.834 8.000
AL	.639 *	.670 *	.632 *	.658 *	.592 *	.356 *	.237 *	.387 *
TI	.118 *	.140 *	.141 *	.110 *	.067 *	.067 *	.040 *	.047 *
FE3+	0 *	0 *	0 *	0 *	0 *	0 *	.192 *	0 *
FE	2.345 *	2.361 *	2.456 *	2.393 *	1.357 *	1.472 *	1.190 *	1.406 *
MN	.046 *	0 *	.041 *	.030 *	.025 *	.046 *	.026 *	0 *
MG	1.975 5.122	1.978 5.148	1.960 5.231	1.975 5.166	2.842 4.883	3.070 5.011	3.182 4.867	3.123 4.964
CA	1.781 *	1.769 *	1.706 *	1.781 *	1.808 *	1.897 *	2.132 *	2.022 *
NA	.582 *	.484 *	.512 *	.461 *	.408 *	.240 *	.151 *	.185 *
K	.200 2.563	.208 2.461	.201 2.419	.217 2.459	.151 2.367	.237 2.375	.146 2.429	.195 2.401
O	23.000 *	23.000 *	23.000 *	23.000 *	23.000 *	23.000 *	23.000 *	23.000 *
F/M	1.211	1.194	1.274	1.227	.486	.494	.382	.450
F/FM	.548	.544	.560	.551	.327	.331	.277	.310

25 GQ36 HOST 9(1)
26 GQ36 HOST 9(2)
27 GQ36 HOST 10(1)
28 GQ36 HOST 10(2)
29 GQ36 PORPHYROCLAST 1
30 GQ36 PORPHYROCLAST 2
31 GQ36 PORPHYROCLAST 3
32 GQ36 PORPHYROCLAST 4

SUPER RECAL PROBE ANALYSES OF AMPHIBOLES

	33	34	35	36	37	38	39	40
SIO2	50.96	48.55	48.47	49.08	49.44	43.54	48.19	47.12
TIO2	.39	.38	.60	.58	.59	.44	.48	.52
A2O3	6.92	8.17	8.90	7.52	7.04	10.91	7.82	7.47
F2O3	0	0	0	0	0	0	0	0
FEO	10.86	11.60	11.48	11.39	11.52	15.48	13.01	12.46
MNO	.29	.24	.30	.21	0	.44	.56	.37
MGO	14.18	12.62	12.63	14.60	14.40	11.70	11.55	13.49
CAO	13.62	13.29	12.33	12.31	12.75	7.64	10.38	11.33
NA2O	.47	.65	.93	1.15	.90	.94	1.11	.55
K2O	1.59	1.32	1.76	.77	1.01	3.42	2.64	1.99
SUM	99.28	96.82	97.40	97.61	97.65	94.51	95.74	95.30
SI	7.268 *	7.133 *	7.078 *	7.118 *	7.175 *	6.718 *	7.226 *	7.083 *
AL	.732 8.000	.867 8.000	.922 8.000	.882 8.000	.825 8.000	1.282 8.000	.774 8.000	.917 8.000
AL	.431 *	.548 *	.610 *	.403 *	.379 *	.701 *	.608 *	.406 *
TI	.042 *	.042 *	.066 *	.063 *	.064 *	.051 *	.054 *	.059 *
FE3+	0 *	0 *	0 *	0 *	0 *	0 *	0 *	0 *
FE	1.295 *	1.425 *	1.402 *	1.381 *	1.398 *	1.997 *	1.632 *	1.566 *
MN	.035 *	.030 *	.037 *	.026 *	0 *	.058 *	.071 *	.047 *
MG	3.014 4.817	2.764 4.808	2.749 4.864	3.156 5.030	3.115 4.956	2.691 5.498	2.582 4.946	3.022 5.100
CA	2.081 *	2.092 *	1.929 *	1.913 *	1.982 *	1.263 *	1.668 *	1.825 *
NA	.130 *	.185 *	.263 *	.323 *	.253 *	.281 *	.323 *	.160 *
K	.289 2.500	.247 2.525	.328 2.520	.142 2.379	.187 2.423	.673 2.217	.505 2.495	.382 2.366
O	23.000 *	23.000 *	23.000 *	23.000 *	23.000 *	23.000 *	23.000 *	23.000 *
F/M	.441	.527	.523	.446	.449	.764	.660	.534
F/FM	.306	.345	.344	.308	.310	.433	.397	.348

33 GQ36 PORPHYROCLAST 5
34 GQ36 PORPHYROCLAST 6
35 GQ36 PORPHYROCLAST 7
36 GQ36 PORPHYROCLAST 8

37 GQ36 PORPHYROCLAST 9
38 GQ36 PORPHYROCLAST 10
39 GQ36 PORPHYROCLAST 11
40 GQ36 PORPHYROCLAST 12

SUPER RECAL PROBE ANALYSES OF AMPHIBOLES

	41	42	43	44	45	46	47	48
SIO2	40.95	41.31	41.31	42.08	43.63	43.89	45.02	44.22
TIO2	.86	.95	.94	.96	.75	.74	.75	.77
A2O3	13.61	14.01	13.87	11.70	10.93	10.74	10.75	10.92
F2O3	.73	0	0	1.65	0	1.18	.64	.69
FEO	13.51	13.30	13.74	11.44	15.91	15.40	15.56	15.65
MNO	.41	.47	.30	.28	.29	.51	.50	.48
MGO	10.80	11.15	10.80	12.37	10.64	10.82	10.86	10.92
CAO	11.72	11.51	11.97	11.82	11.80	11.49	11.71	11.61
NA2O	1.50	1.48	1.48	1.27	1.71	1.46	1.12	1.48
K2O	1.85	1.99	1.96	1.74	.94	.88	.89	.97
SUM	95.94	96.17	96.37	95.31	96.60	97.11	97.80	97.71
SI	6.237 *	6.251 *	6.255 *	6.393 *	6.601 *	6.600 *	6.692 *	6.606 *
AL	1.763 8.000	1.749 8.000	1.745 8.000	1.607 8.000	1.399 8.000	1.400 8.000	1.308 8.000	1.394 8.000
AL	.679 *	.749 *	.729 *	.487 *	.549 *	.504 *	.575 *	.529 *
TI	.098 *	.108 *	.107 *	.110 *	.085 *	.084 *	.084 *	.087 *
FE3+	.084 *	0 *	0 *	.189 *	0 *	.134 *	.072 *	.078 *
FE	1.721 *	1.683 *	1.740 *	1.453 *	2.013 *	1.937 *	1.934 *	1.955 *
MN	.053 *	.060 *	.038 *	.036 *	.037 *	.065 *	.063 *	.061 *
MG	2.452 5.087	2.515 5.115	2.437 5.052	2.801 5.076	2.399 5.084	2.425 5.148	2.406 5.135	2.432 5.141
CA	1.912 *	1.866 *	1.942 *	1.924 *	1.913 *	1.851 *	1.865 *	1.858 *
NA	.443 *	.434 *	.434 *	.374 *	.502 *	.426 *	.323 *	.429 *
K	.359 2.715	.384 2.684	.379 2.755	.337 2.635	.181 2.596	.169 2.446	.169 2.357	.185 2.472
O	23.000 *	23.000 *	23.000 *	23.000 *	23.000 *	23.000 *	23.000 *	23.000 *
F/M	.723	.693	.730	.532	.854	.825	.830	.829
F/FM	.420	.409	.422	.347	.461	.452	.454	.453

41 CT1 HOST 1
42 CT1 HOST 1
43 CT1 HOST 2
44 CT1 PORPHYROCLAST 1

45 GQ38 HOST 1
46 GQ38 HOST 2
47 GQ38 HOST 3
48 GQ38 HOST 4

SUPER RECAL PROBE ANALYSES OF AMPHIBOLES

	49		50		51		52		53		54		55		56	
SIO2	43.95		44.24		44.58		43.59		44.98		43.77		41.94		42.27	
TIO2	.64		1.05		.80		1.18		2.98		.82		1.69		1.62	
A203	10.76		10.54		11.12		11.47		7.77		10.70		10.75		11.12	
F203	1.34		0		0		.25		0		.46		0		.99	
FEO	15.40		16.75		15.16		17.28		13.75		15.54		18.69		17.85	
MNO	.42		.55		.52		.59		.41		.48		.33		0	
MGO	10.45		10.98		10.49		9.77		11.62		10.51		8.52		8.85	
CAO	11.76		8.07		12.04		11.60		10.64		11.83		11.12		11.84	
NA20	1.27		.84		1.17		1.38		.67		1.42		1.53		1.37	
K20	.90		3.85		.91		1.15		2.28		.95		.90		.94	
SUM	96.89		96.87		96.79		98.26		95.10		96.48		95.47		96.85	
SI	6.623	*	6.718	*	6.684	*	6.530	*	6.858	*	6.626	*	6.517	*	6.460	*
AL	1.377	8.000	1.282	8.000	1.316	8.000	1.470	8.000	1.142	8.000	1.374	8.000	1.483	8.000	1.540	8.000
AL	.534	*	.605	*	.649	*	.555	*	.254	*	.534	*	.486	*	.463	*
TI	.073	*	.120	*	.090	*	.133	*	.342	*	.093	*	.197	*	.186	*
FE3+	.152	*	0	*	0	*	.028	*	0	*	.052	*	0	*	.114	*
FE	1.941	*	2.127	*	1.901	*	2.165	*	1.753	*	1.967	*	2.429	*	2.281	*
MN	.054	*	.071	*	.066	*	.075	*	.053	*	.062	*	.043	*	0	*
MG	2.347	5.101	2.485	5.408	2.344	5.051	2.182	5.137	2.641	5.043	2.371	5.080	1.973	5.129	2.016	5.061
CA	1.899	*	1.313	*	1.934	*	1.862	*	1.738	*	1.919	*	1.851	*	1.939	*
NA	.371	*	.247	*	.340	*	.401	*	.198	*	.417	*	.461	*	.406	*
K	.173	2.443	.746	2.306	.174	2.448	.220	2.482	.443	2.380	.183	2.519	.178	2.491	.183	2.528
O	23.000	*	23.000	*	23.000	*	23.000	*	23.000	*	23.000	*	23.000	*	23.000	*
F/M		.850		.884		.839		1.027		.684		.856		1.253		1.132
F/FM		.459		.469		.456		.507		.406		.461		.556		.531

49 GQ38 HOST 5
50 GQ38 PORPHYROCLAST 1
51 GQ38 PORPHYROCLAST 2
52 GQ38 PORPHYROCLAST 3
53 GQ38 PORPHYROCLAST 4
54 GQ38 PORPHYROCLAST 5
55 GQ5 HOST 1
56 GQ5 HOST 2

SUPER RECAL PROBE ANALYSES OF AMPHIBOLES

	57		58		59		60		61		62		63		64	
SIO2	42.40		43.20		41.88		41.90		42.85		42.89		41.67		43.09	
TIO2	1.79		1.61		1.73		1.44		1.64		1.41		1.49		1.62	
A203	11.75		11.48		11.12		12.92		12.17		13.14		12.47		11.88	
F203	0		0		2.05		0		0		0		0		0	
FEO	18.33		18.01		17.73		18.16		17.55		17.58		18.85		18.95	
MNO	.51		0		.32		.28		0		.25		0		.29	
MGO	8.55		8.49		8.50		6.65		8.23		7.70		7.89		8.16	
CAO	11.26		11.61		11.52		9.75		11.39		11.27		10.65		10.88	
NA20	1.52		1.09		1.23		.92		1.14		1.18		1.24		1.20	
K20	.79		1.07		.84		.98		1.03		1.09		1.18		.99	
SUM	96.90		96.56		96.92		93.00		96.00		96.51		95.44		97.06	
SI	6.466	*	6.579	*	6.414	*	6.596	*	6.544	*	6.514	*	6.453	*	6.549	*
AL	1.534	8.000	1.421	8.000	1.586	8.000	1.404	8.000	1.456	8.000	1.486	8.000	1.547	8.000	1.451	8.000
AL	.578	*	.640	*	.421	*	.992	*	.735	*	.866	*	.729	*	.677	*
TI	.205	*	.184	*	.199	*	.170	*	.188	*	.161	*	.174	*	.185	*
FE3+	0	*	0	*	.236	*	0	*	0	*	0	*	0	*	0	*
FE	2.338	*	2.294	*	2.271	*	2.391	*	2.242	*	2.233	*	2.441	*	2.409	*
MN	.066	*	0	*	.042	*	.037	*	0	*	.032	*	0	*	.037	*
MG	1.943	5.130	1.927	5.045	1.940	5.109	1.560	5.151	1.873	5.038	1.743	5.035	1.821	5.165	1.849	5.156
CA	1.840	*	1.895	*	1.890	*	1.644	*	1.864	*	1.834	*	1.767	*	1.772	*
NA	.449	*	.322	*	.365	*	.281	*	.338	*	.347	*	.372	*	.354	*
K	.154	2.443	.208	2.424	.164	2.420	.197	2.122	.201	2.402	.211	2.392	.233	2.372	.192	2.317
O	23.000	*	23.000	*	23.000	*	23.000	*	23.000	*	23.000	*	23.000	*	23.000	*
F/M		1.237		1.190		1.192		1.556		1.196		1.299		1.340		1.323
F/FM		.553		.543		.544		.609		.545		.565		.573		.570

57 GQ5 HOST 3
58 GQ5 HOST 3(FRACT)
59 GQ5 HOST 4
60 GQ5 HOST 4(FRACT)
61 GQ5 PORPHYROCLAST 1
62 GQ5 PORPHYROCLAST 2
63 GQ5 PORPHYROCLAST 2(FRACT)
64 GQ5 PORPHYROCLAST 2(Y2)

SUPER RECAL PROBE ANALYSES OF AMPHIBOLES

	65	66	67	68	69	70	71	72
SIO2	43.19	49.32	42.02	42.82	42.64	43.14	43.89	45.75
TIO2	1.49	.93	1.81	1.41	1.62	1.44	2.96	1.27
A203	12.72	15.49	11.49	11.49	11.13	9.86	12.60	13.47
F203	0	0	.26	.12	0	.84	0	0
FEO	18.06	15.49	18.46	18.50	17.68	19.21	17.21	14.79
MNO	.30	0	.32	0	.49	.32	.35	.24
MGO	7.75	6.26	8.50	8.95	9.65	8.84	6.45	7.03
CAO	10.99	8.35	11.73	11.72	10.83	11.08	9.44	10.40
NA20	1.50	3.17	1.57	1.56	1.89	1.48	2.01	1.98
K20	.93	1.35	.83	.83	.64	.64	.45	.52
SUM	96.93	100.36	96.99	97.40	96.57	96.85	95.36	95.45
SI	6.542 *	6.977 *	6.427 *	6.495 *	6.502 *	6.612 *	6.678 *	6.847 *
AL	1.458 8.000	1.023 8.000	1.573 8.000	1.505 8.000	1.498 8.000	1.388 8.000	1.322 8.000	1.153 8.000
AL	.812 *	1.559 *	.498 *	.549 *	.502 *	.393 *	.937 *	1.223 *
TI	.170 *	.099 *	.208 *	.161 *	.186 *	.166 *	.339 *	.143 *
FE3+	0 *	0 *	.030 *	.014 *	0 *	.097 *	0 *	0 *
FE	2.288 *	1.832 *	2.361 *	2.347 *	2.255 *	2.462 *	2.190 *	1.851 *
MN	.038 *	0 *	.041 *	0 *	.063 *	.042 *	.045 *	.030 *
MG	1.750 5.058	1.320 4.810	1.938 5.077	2.024 5.094	2.193 5.200	2.020 5.180	1.463 4.974	1.568 4.816
CA	1.784 *	1.266 *	1.922 *	1.905 *	1.769 *	1.820 *	1.539 *	1.668 *
NA	.441 *	.869 *	.466 *	.459 *	.559 *	.440 *	.593 *	.575 *
K	.180 2.404	.244 2.379	.162 2.550	.161 2.524	.124 2.453	.125 2.385	.087 2.219	.099 2.342
O	23.000 *	23.000 *	23.000 *	23.000 *	23.000 *	23.000 *	23.000 *	23.000 *
F/M	1.329	1.388	1.240	1.160	1.057	1.240	1.528	1.200
F/FM	.571	.581	.554	.537	.514	.554	.604	.545

65 GQ5 PORPHYROCLAST 2(Y3)
66 GQ5 PORPHYROCLAST 3
67 GQ14 HOST 1
68 GQ14 HOST 2
69 GQ14 HOST 3
70 GQ14 HOST 4
71 GQ14 PORPHYROCLAST 1
72 GQ14 PORPHYROCLAST 2

SUPER RECAL PROBE ANALYSES OF AMPHIBOLES

	73	74	75	76	77	78	79	80
SIO2	47.25	43.47	44.03	42.88	43.72	43.45	43.01	42.34
TIO2	.46	1.35	1.32	1.44	1.31	1.41	1.47	1.66
A203	12.21	11.77	11.43	10.60	11.83	11.12	11.29	11.37
F203	0	.46	0	.46	0	0	0	0
FEO	13.72	17.16	18.70	18.30	17.83	16.68	18.36	18.41
MNO	0	.30	.25	.26	.23	0	.27	.27
MGO	8.53	9.63	10.45	9.91	9.31	10.27	9.14	8.97
CAO	7.77	11.29	9.93	9.69	10.37	11.80	11.75	11.67
NA20	2.25	1.29	1.63	1.31	1.27	1.77	1.78	1.79
K20	.53	.56	.52	.53	.70	.79	.89	.87
SUM	92.72	97.28	98.26	95.38	96.57	97.29	97.96	97.35
SI	7.158 *	6.536 *	6.566 *	6.598 *	6.611 *	6.540 *	6.496 *	6.446 *
AL	.842 8.000	1.464 8.000	1.434 8.000	1.402 8.000	1.389 8.000	1.460 8.000	1.504 8.000	1.554 8.000
AL	1.338 *	.622 *	.575 *	.520 *	.719 *	.513 *	.505 *	.486 *
TI	.052 *	.153 *	.148 *	.167 *	.149 *	.160 *	.167 *	.190 *
FE3+	0 *	.052 *	0 *	.053 *	0 *	0 *	0 *	0 *
FE	1.738 *	2.158 *	2.332 *	2.355 *	2.255 *	2.100 *	2.319 *	2.344 *
MN	0 *	.038 *	.032 *	.034 *	.029 *	0 *	.035 *	.035 *
MG	1.926 5.055	2.158 5.181	2.323 5.409	2.273 5.402	2.098 5.251	2.304 5.076	2.058 5.083	2.036 5.090
CA	1.261 *	1.819 *	1.587 *	1.598 *	1.680 *	1.903 *	1.901 *	1.904 *
NA	.661 *	.376 *	.471 *	.391 *	.372 *	.517 *	.521 *	.528 *
K	.102 2.025	.107 2.302	.099 2.157	.104 2.092	.135 2.187	.152 2.571	.171 2.594	.169 2.601
O	23.000 *	23.000 *	23.000 *	23.000 *	23.000 *	23.000 *	23.000 *	23.000 *
F/M	.902	1.018	1.018	1.051	1.089	.911	1.144	1.169
F/FM	.474	.504	.504	.512	.521	.477	.534	.539

73 GQ14 PORPHYROCLAST 3
74 GQ19 HOST 1
75 GQ19 HOST 2
76 GQ19 HOST 2(FRACT)
77 GQ19 PORPHYROCLAST 1
78 GQ6 HOST 1
79 GQ6 HOST 2
80 GQ6 HOST 3

SUPER RECAL PROBE ANALYSES OF AMPHIBOLES

	81		82		83		84		85		86		87		88	
SIO2	43.94		43.78		44.95		47.18		44.39		44.67		42.55		43.93	
TIO2	1.11		1.50		1.04		.91		1.39		1.87		1.36		1.19	
A2O3	10.19		10.93		10.81		11.14		10.87		12.47		11.54		12.00	
F2O3	0		0		0		0		0		0		0		0	
FEO	16.77		16.79		16.35		15.02		16.09		16.08		17.02		15.77	
MNO	0		.21		.24		0		.32		.29		0		0	
MGO	9.84		10.26		9.84		9.23		10.34		9.08		9.33		9.40	
CAO	11.62		11.82		11.68		11.74		12.15		11.61		11.43		11.55	
NA2O	1.50		1.65		1.58		1.64		1.34		1.78		1.26		1.73	
K2O	.78		.85		.73		.45		.73		.98		.96		.78	
SUM	95.75		97.79		97.22		97.31		97.62		98.83		95.45		96.35	
SI	6.708	*	6.562	*	6.729	*	6.947	*	6.629	*	6.577	*	6.534	*	6.620	*
AL	1.292	8.000	1.438	8.000	1.271	8.000	1.053	8.000	1.371	8.000	1.423	8.000	1.466	8.000	1.380	8.000
AL	.541	*	.492	*	.636	*	.880	*	.542	*	.740	*	.623	*	.751	*
TI	.127	*	.169	*	.117	*	.101	*	.156	*	.207	*	.157	*	.135	*
FE3+	0	*	0	*	0	*	0	*	0	*	0	*	0	*	0	*
FE	2.141	*	2.104	*	2.047	*	1.850	*	2.009	*	1.980	*	2.186	*	1.988	*
MN	0	*	.027	*	.030	*	0	*	.040	*	.036	*	0	*	0	*
MG	2.239	5.049	2.292	5.084	2.196	5.027	2.026	4.856	2.302	5.050	1.993	4.956	2.136	5.101	2.111	4.985
CA	1.901	*	1.898	*	1.873	*	1.852	*	1.944	*	1.831	*	1.881	*	1.865	*
NA	.444	*	.479	*	.459	*	.468	*	.388	*	.508	*	.375	*	.505	*
K	.152	2.496	.162	2.540	.139	2.471	.085	2.405	.139	2.471	.184	2.524	.188	2.444	.150	2.520
O	23.000	*	23.000	*	23.000	*	23.000	*	23.000	*	23.000	*	23.000	*	23.000	*
F/M		.956		.930		.946		.913		.891		1.012		1.024		.941
F/FM		.489		.482		.486		.477		.471		.503		.506		.485

81 GQ6 HOST 4
82 GQ6 HOST 4(CENT)
83 GQ6 PORPHYROCLAST 1
84 GQ6 PORPHYROCLAST 2
85 GQ6 PORPHYROCLAST 3
86 GQ6 PORPHYROCLAST 4
87 GQ6 PORPHYROCLAST 5
88 GQ6 PORPHYROCLAST 5(2)

SUPER RECAL PROBE ANALYSES OF AMPHIBOLES

	89		90		91		92		93		94		95		96	
SIO2	44.74		45.03		46.49		44.11		44.02		44.36		44.58		46.67	
TIO2	1.43		.94		.99		1.18		1.23		1.06		1.22		1.08	
A2O3	11.77		12.11		12.60		11.47		11.53		12.21		11.35		13.58	
F2O3	0		0		0		0		0		0		0		0	
FEO	15.23		15.50		15.16		16.48		17.03		15.89		15.92		14.44	
MNO	0		.30		.25		.23		.19		0		.27		0	
MGO	9.09		8.62		8.89		9.29		9.15		8.69		10.10		7.80	
CAO	10.30		10.97		10.88		11.08		11.10		11.10		10.45		10.22	
NA2O	1.28		2.00		2.21		1.41		1.28		1.84		1.47		2.31	
K2O	1.94		.83		.64		.73		.75		.67		2.00		1.13	
SUM	95.78		96.30		98.11		95.98		96.28		95.82		97.36		97.23	
SI	6.759	*	6.762	*	6.806	*	6.683	*	6.664	*	6.701	*	6.677	*	6.855	*
AL	1.241	8.000	1.238	8.000	1.194	8.000	1.317	8.000	1.336	8.000	1.299	8.000	1.323	8.000	1.145	8.000
AL	.854	*	.904	*	.980	*	.731	*	.721	*	.875	*	.680	*	1.205	*
TI	.162	*	.106	*	.109	*	.134	*	.140	*	.120	*	.137	*	.119	*
FE3+	0	*	0	*	0	*	0	*	0	*	0	*	0	*	0	*
FE	1.924	*	1.946	*	1.856	*	2.088	*	2.156	*	2.007	*	1.994	*	1.774	*
MN	0	*	.038	*	.031	*	.030	*	.024	*	0	*	.034	*	0	*
MG	2.047	4.988	1.929	4.924	1.940	4.916	2.098	5.081	2.065	5.106	1.957	4.960	2.255	5.101	1.708	4.806
CA	1.667	*	1.765	*	1.707	*	1.799	*	1.800	*	1.797	*	1.677	*	1.608	*
NA	.375	*	.582	*	.627	*	.414	*	.376	*	.539	*	.427	*	.658	*
K	.374	2.416	.159	2.506	.120	2.454	.141	2.354	.145	2.321	.129	2.465	.382	2.486	.212	2.478
O	23.000	*	23.000	*	23.000	*	23.000	*	23.000	*	23.000	*	23.000	*	23.000	*
F/M		.940		1.029		.973		1.009		1.056		1.026		.900		1.039
F/FM		.485		.507		.493		.502		.514		.506		.474		.509

89 GQ6 PORPHYROCLAST 6
90 GQ6 PORPHYROCLAST 7
91 GQ6 MGB 1
92 GQ6 MGB 2
93 GQ6 MGB 3
94 GQ6 MGB 4
95 GQ6 IG 1
96 GQ6 IG 2

SUPER RECAL PROBE ANALYSES OF AMPHIBOLES

	97	98	99	100	101	102	103	104
SIO2	44.69	46.25	41.40	42.61	41.84	41.90	41.39	42.40
TIO2	1.22	1.20	1.80	2.10	1.83	1.45	1.93	1.83
A203	11.51	9.91	11.12	12.15	11.74	11.66	11.69	11.86
F203	0	0	0	0	0	0	.61	1.17
FEO	16.77	15.18	19.13	19.27	19.61	19.57	20.01	19.36
MNO	.24	0	.50	.59	.38	.50	.42	.42
MGO	9.57	9.55	7.69	7.74	7.93	7.54	7.76	8.35
CAO	10.81	10.94	11.70	11.78	11.60	11.80	11.59	11.97
NA20	1.01	.83	1.67	1.62	1.67	1.40	1.39	1.42
K20	1.64	1.68	1.48	1.87	1.62	1.56	1.64	1.56
SUM	97.46	95.54	96.49	99.73	98.22	97.38	98.43	100.34
SI	6.689 *	6.982 *	6.427 *	6.389 *	6.381 *	6.441 *	6.325 *	6.331 *
AL	1.311 8.000	1.018 8.000	1.573 8.000	1.611 8.000	1.619 8.000	1.559 8.000	1.675 8.000	1.669 8.000
AL	.719 *	.745 *	.461 *	.535 *	.491 *	.553 *	.430 *	.418 *
TI	.137 *	.136 *	.210 *	.237 *	.210 *	.168 *	.222 *	.205 *
FE3+	0 *	0 *	0 *	0 *	0 *	0 *	.070 *	.131 *
FE	2.099 *	1.916 *	2.484 *	2.416 *	2.501 *	2.516 *	2.557 *	2.418 *
MN	.030 *	0 *	.066 *	.075 *	.049 *	.065 *	.054 *	.053 *
MG	2.135 5.121	2.149 4.947	1.779 5.000	1.730 4.993	1.803 5.053	1.728 5.029	1.768 5.101	1.858 5.084
CA	1.734 *	1.769 *	1.946 *	1.892 *	1.895 *	1.943 *	1.898 *	1.915 *
NA	.293 *	.243 *	.503 *	.471 *	.494 *	.417 *	.412 *	.411 *
K	.313 2.340	.323 2.336	.293 2.742	.358 2.721	.315 2.704	.306 2.667	.320 2.629	.297 2.623
O	23.000 *	23.000 *	23.000 *	23.000 *	23.000 *	23.000 *	23.000 *	23.000 *
F/M	.997	.892	1.433	1.440	1.415	1.494	1.478	1.329
F/FM	.499	.471	.589	.590	.586	.599	.596	.571

97 GQ6 IG 3
98 GQ6 IG 4
99 QD1 HOST 1
100 QD1 HOST 2
101 QD1 HOST 3
102 QD1 HOST 4
103 QD1 HOST 5
104 QD1 HOST 6

SUPER RECAL PROBE ANALYSES OF AMPHIBOLES

	105	106	107	108	109
SIO2	42.48	42.81	44.20	42.51	44.84
TIO2	1.80	1.71	1.29	1.59	1.52
A203	11.65	11.08	9.32	11.05	10.22
F203	.24	.50	0	.10	0
FEO	19.35	19.40	18.69	19.60	17.79
MNO	.32	.48	.37	.37	.39
MGO	8.11	8.40	9.08	8.12	8.01
CAO	11.74	11.60	11.91	11.88	12.61
NA20	1.04	1.25	1.15	1.37	1.28
K20	1.46	1.31	1.13	1.36	.96
SUM	98.19	98.54	97.14	97.95	97.62
SI	6.445 *	6.479 *	6.737 *	6.484 *	6.761 *
AL	1.555 8.000	1.521 8.000	1.263 8.000	1.516 8.000	1.239 8.000
AL	.528 *	.455 *	.411 *	.470 *	.576 *
TI	.205 *	.195 *	.148 *	.182 *	.172 *
FE3+	.027 *	.057 *	0 *	.011 *	0 *
FE	2.455 *	2.455 *	2.382 *	2.500 *	2.243 *
MN	.041 *	.062 *	.048 *	.048 *	.050 *
MG	1.834 5.091	1.895 5.118	2.063 5.052	1.846 5.058	1.800 4.842
CA	1.908 *	1.881 *	1.945 *	1.941 *	2.037 *
NA	.306 *	.367 *	.340 *	.405 *	.374 *
K	.283 2.497	.253 2.501	.220 2.505	.265 2.611	.185 2.596
O	23.000 *	23.000 *	23.000 *	23.000 *	23.000 *
F/M	1.361	1.328	1.178	1.380	1.274
F/FM	.576	.570	.541	.580	.560

105 QD1 TRAVERSE 1
106 QD1 TRAVERSE 2
107 QD1 TRAVERSE 2
108 QD1 TRAVERSE 4
109 QD1 TRAVERSE 5

SUPER RECAL — PROBE ANALYSES OF CLINOPYROXENES

	1		2		3		4		5		6		7		8	
SIO2	51.30		50.94		51.93		52.17		52.27		51.89		52.35		51.27	
TIO2	0		.15		.10		.11		0		0		.11		.17	
A203	1.91		1.99		2.35		2.45		2.31		2.07		2.25		2.38	
FEO	9.21		9.07		9.17		9.20		9.12		9.56		8.85		9.79	
MNO	.58		.28		.29		.41		.45		.21		.40		.41	
MGO	12.35		12.18		12.89		12.71		12.66		12.63		12.71		13.15	
CAO	21.45		21.85		22.06		22.24		21.89		22.09		22.74		21.50	
NA20	.69		.73		.96		1.03		.90		.78		.93		.74	
K20	0		0		0		0		0		0		0		0	
SUM	97.49		97.19		99.75		100.32		99.60		99.23		100.34		99.41	
SI	1.970	*	1.963	*	1.949	*	1.948	*	1.962	*	1.960	*	1.953	*	1.936	*
AL	.030	2.000	.037	2.000	.051	2.000	.052	2.000	.038	2.000	.040	2.000	.047	2.000	.064	2.000
AL	.057	*	.053	*	.053	*	.056	*	.064	*	.052	*	.052	*	.042	*
TI	0	*	.004	*	.003	*	.003	*	0	*	0	*	.003	*	.005	*
FE	.296	*	.292	*	.288	*	.287	*	.286	*	.302	*	.276	*	.309	*
MN	.019	*	.009	*	.009	*	.013	*	.014	*	.007	*	.013	*	.013	*
MG	.707	*	.700	*	.721	*	.708	*	.708	*	.711	*	.707	*	.740	*
CA	.883	*	.902	*	.887	*	.890	*	.880	*	.894	*	.909	*	.870	*
NA	.051	*	.055	*	.070	*	.075	*	.066	*	.057	*	.067	*	.054	*
K	0	2.012	0	2.015	0	2.031	0	2.032	0	2.019	0	2.023	0	2.028	0	2.033
O	6.000	*	6.000	*	6.000	*	6.000	*	6.000	*	6.000	*	6.000	*	6.000	*
EN	37.13		36.76		37.85		37.28		37.49		37.16		37.11		38.30	
FS	16.52		15.84		15.59		15.82		15.91		16.13		15.16		16.68	
WO	46.35		47.40		46.56		46.89		46.60		46.71		47.73		45.02	
F/M	.445		.431		.412		.424		.424		.434		.409		.435	
F/FM	.308		.301		.292		.298		.298		.303		.290		.303	

1 CT3 HOST CPX 1
2 CT3 HOST CPX 2
3 CT3 HOST CPX 3
4 CT3 HOST CPX 4
5 CT3 HOST CPX 5
6 CT3 PORPHYROCLAST CPX 1
7 CT3 PORPHYROCLAST CPX 2
8 CT3 PORPHYROCLAST CPX 3

SUPER RECAL — PROBE ANALYSES OF CLINOPYROXENES

	9		10		11		12		13		14		15		16	
SIO2	51.85		51.74		50.23		51.92		51.34		51.94		50.78		52.44	
TIO2	.11		.14		.32		.19		.27		0		.25		0	
A203	2.17		4.26		2.73		1.85		1.82		1.85		2.10		1.37	
FEO	8.97		8.86		11.88		11.19		11.73		10.78		10.86		10.16	
MNO	.43		.34		.37		.20		.49		.22		.29		.30	
MGO	12.34		13.88		11.64		11.28		11.01		11.63		11.37		11.93	
CAO	22.75		20.70		20.82		23.17		23.01		23.05		22.15		23.44	
NA20	.65		1.24		.60		.55		.48		.49		.43		.26	
K20	0		0		0		0		0		0		0		0	
SUM	99.27		101.16		98.59		100.35		100.15		99.96		98.23		99.90	
SI	1.957	*	1.905	*	1.929	*	1.958	*	1.949	*	1.962	*	1.952	*	1.976	*
AL	.043	2.000	.095	2.000	.071	2.000	.042	2.000	.051	2.000	.038	2.000	.048	2.000	.024	2.000
AL	.054	*	.089	*	.052	*	.040	*	.030	*	.044	*	.047	*	.037	*
TI	.003	*	.004	*	.009	*	.005	*	.008	*	0	*	.007	*	0	*
FE	.283	*	.273	*	.381	*	.353	*	.372	*	.340	*	.349	*	.320	*
MN	.014	*	.011	*	.012	*	.006	*	.016	*	.007	*	.009	*	.010	*
MG	.694	*	.762	*	.666	*	.634	*	.623	*	.655	*	.652	*	.670	*
CA	.920	*	.816	*	.857	*	.936	*	.936	*	.933	*	.912	*	.947	*
NA	.048	*	.089	*	.045	*	.040	*	.035	*	.036	*	.032	*	.019	*
K	0	2.015	0	2.043	0	2.022	0	2.015	0	2.020	0	2.015	0	2.009	0	2.003
O	6.000	*	6.000	*	6.000	*	6.000	*	6.000	*	6.000	*	6.000	*	6.000	*
EN	36.33		40.91		34.77		32.86		32.00		33.84		33.89		34.43	
FS	15.53		15.22		20.54		18.62		19.94		17.96		18.65		16.94	
WO	48.14		43.86		44.70		48.52		48.07		48.20		47.46		48.63	
F/M	.428		.372		.591		.567		.623		.531		.550		.492	
F/FM	.300		.271		.371		.362		.384		.347		.355		.330	

9 CT3 PORPHYROCLAST CPX 4
10 CT3 PORPHYROCLAST CPX 5
11 GQ6 HOST CPX 1
12 GQ6 HOST CPX 2
13 GQ6 HOST CPX 3
14 GQ6 PORPHYROCLAST CPX 2
15 GQ6 PORPHYROCLAST CPX 3
16 GQ6 PORPHYROCLAST CPX 4

SUPER RECAL PROBE ANALYSES OF SPHENES

	1	2	3	4	5	6	7	8
SIO2	30.64	30.76	31.67	31.58	29.80	30.11	30.32	30.32
TIO2	35.96	35.17	35.92	36.40	39.87	39.61	38.31	38.31
A203	1.71	1.84	2.20	2.14	.80	1.26	1.42	1.42
FEO	1.29	1.45	1.21	1.09	.42	.69	.61	.61
MNO	0.00	0.00	0.00	0.00	0.00	0.00	0.00	0.00
MGO	0.00	.24	0.00	0.00	0.00	0.00	0.00	0.00
CAO	28.27	27.77	28.65	28.72	28.67	28.72	28.77	28.77
NA20	0.00	.25	0.00	.36	.24	0.00	0.00	0.00
K20	0.00	.19	0.00	.14	0.00	0.00	0.00	0.00
SUM	97.87	97.67	99.65	100.43	99.80	100.39	99.43	99.43

SI	4.092	*	4.119	*	4.141	*	4.106	*	3.914	*	3.926	*	3.987	*	3.987	*
AL	-I	4.092	-I	4.119	-I	4.141	-I	4.106	.086	4.000	.074	4.000	.013	4.000	.013	4.000
AL	.269	*	.290	*	.339	*	.328	*	.038	*	.120	*	.207	*	.207	*
TI	3.612	*	3.542	*	3.532	*	3.559	*	3.938	*	3.884	*	3.788	*	3.788	*
FE	.144	4.025	.162	3.994	.132	4.003	.119	4.006	.046	4.022	.075	4.080	.067	4.062	.067	4.062
MN	0.000	*	0.000	*	0.000	*	0.000	*	0.000	*	0.000	*	0.000	*	0.000	*
MG	0.000	*	.048	*	0.000	*	0.000	*	0.000	*	0.000	*	0.000	*	0.000	*
CA	4.045	*	3.984	*	4.014	*	4.001	*	4.034	*	4.013	*	4.053	*	4.053	*
NA	0.000	*	.065	*	0.000	*	.091	*	.061	*	0.000	*	0.000	*	0.000	*
K	0.000	4.045	.032	4.129	0.000	4.014	.023	4.115	0.000	4.095	0.000	4.013	0.000	4.053	0.000	4.053
O	20.000	*	20.000	*	20.000	*	20.000	*	20.000	*	20.000	*	20.000	*	20.000	*
F/M		C.000		3.390		C.000		C.000		C.000		C.000		C.000		C.000
F/FM		C.000		.772		C.000		C.000		0.000		C.000		0.000		C.000

1 R2 HOST 1
2 R2 HOST 2
3 R2 PORPHYROCLAST 1
4 R2 PORPHYROCLAST 2
5 G06 HOST 1
6 G06 PORPHYROCLAST 1
7 G1A HOST 1
8 C1A HOST 2

SUPER RECAL PROBE ANALYSES OF SPHENES

	9
SIO2	28.98
TIO2	37.51
A203	1.20
FEO	1.00
MNO	0.00
MGO	.21
CAO	27.64
NA20	.12
K20	0.00
SUM	96.86

SI	3.928	*	
AL	.072	4.000	
AL	.119	*	
TI	3.823	*	
FE	.113	4.056	
MN	0.000	*	
MG	.042	*	
CA	4.014	*	
NA	.084	*	
K	0.000	4.140	
O	20.000	*	
F/M		2.672	
F/FM		.728	

9 G1A PORPHYROCLAST 1

SUPER RECAL — FELDSPAR IN MICROFRACTURES AND AMYGDALES

	1	2	3	4	5	6	7	8
SIO2	64.91	65.02	64.32	63.70	62.95	67.34	63.70	64.39
TIO2	0	0	0	0	0	0	0	0
A203	18.05	18.20	18.67	17.99	18.14	20.00	17.99	18.41
FEO	0	0	0	.24	.30	0	.24	.38
MNO	0	0	0	0	0	0	0	0
MGO	0	0	0	0	0	0	0	0
CAO	.13	.23	.17	.60	0	.15	.60	0
NA20	0	0	0	0	.78	11.30	0	.32
K20	15.57	15.47	16.91	15.83	15.93	.11	15.83	16.25
SUM	98.66	98.92	100.07	98.36	98.10	98.90	98.36	99.75
SI	3.022 *	3.018 *	2.981 *	2.995 *	2.977 *	2.973 *	2.995 *	2.989 *
AL	.990 4.013	.996 4.014	1.020 4.000	.997 3.992	1.011 3.988	1.040 4.013	.997 3.992	1.007 3.996
TI	0	0	0	0	0	0 .980	0 .989	0 1.006
FE	0 *	0 *	0 *	.009 *	.012 *	0 *	.009 *	.015 *
MN	0 *	0 *	0 *	0 *	0 *	0 *	0 *	0 *
MG	0 *	0 *	0 *	0 *	0 *	0 *	0 *	0 *
CA	.006 *	.011 *	.008 *	.030 *	0 *	.007 *	.030 *	0 *
NA	0 *	0 *	0 *	0 *	.072 *	.967 *	0 *	.029 *
K	.925 .931	.916 .927	1.000 1.008	.949 .989	.961 1.044	.006 .980	.949 .989	.962 1.006
O	8.000 *	8.000 *	8.000 *	8.000 *	8.000 *	8.000 *	8.000 *	8.000 *
AN	.70	1.23	.84	3.09	0	.72	3.09	0
AB	0	0	0	0	6.93	98.64	0	2.91
OR	99.30	98.77	99.16	96.91	93.07	.63	96.91	97.09
F/M	0	0	0	0	0	0	0	0
F/FM	0	0	0	0	0	0	0	0

1 X MFRACT 1(1)
2 X MFRACT 1(2)
3 G1A MFRACT 1
4 R15 AMYGDALE 1
5 R15 MFRACT 1
6 R15 MFRACT 1
7 R15 AMYGDALE 1
8 R15 AMYGDALE 2

SUPER RECAL — FELDSPAR IN MICROFRACTURES AND AMYGDALES

	9	10	11	12	13	14	15
SIO2	63.43	64.11	63.73	63.71	59.79	60.55	63.83
TIO2	0	0	0	0	0	0	0
A203	17.80	18.39	18.06	17.98	25.13	24.83	18.23
FEO	.25	0	0	0	0	0	0
MNO	0	0	0	0	0	0	0
MGO	0	0	0	0	0	0	0
CAO	0	0	0	0	6.91	6.51	0
NA20	.61	.51	.48	.49	7.53	8.09	.71
K20	15.92	16.49	16.25	16.14	0	0	16.10
SUM	98.02	99.50	98.52	98.32	99.36	99.98	98.87
SI	2.997 *	2.986 *	2.995 *	2.998 *	2.676 *	2.694 *	2.989 *
AL	.991 3.988	1.009 3.995	1.000 3.995	.997 3.995	1.326 4.002	1.302 3.995	1.006 3.995
TI	0 1.026	0 1.026	0 1.018	0 1.014	0 .985	0 1.008	0 1.026
FE	.010 *	0 *	0 *	0 *	0 *	0 *	0 *
MN	0 *	0 *	0 *	0 *	0 *	0 *	0 *
MG	0 *	0 *	0 *	0 *	0 *	0 *	0 *
CA	0 *	0 *	0 *	0 *	.331 *	.310 *	0 *
NA	.056 *	.046 *	.044 *	.045 *	.654 *	.698 *	.064 *
K	.959 1.026	.980 1.026	.974 1.018	.959 1.014	0 .965	0 1.008	.962 1.026
O	8.000 *	8.000 *	8.000 *	8.000 *	8.000 *	8.000 *	8.000 *
AN	0	0	0	0	33.65	30.78	0
AB	5.50	4.49	4.30	4.41	66.35	69.22	6.28
OR	94.50	95.51	95.70	95.59	0	0	93.72
F/M	0	0	0	0	0	0	0
F/FM	0	0	0	0	0	0	0

9 R15 AMYGDALE 3
10 R15 AMYGDALE 4
11 R15 AMYGDALE 5
12 R15 AMYGDALE 6
13 R15 AMYGDALE 979-1
14 R15 AMYGDALE 979-5
15 R15 AMYGDALE 978-1

SUPER RECAL MICA IN AMYGDALES

	1	2	3	4	5	6	7	8
SIO2	54.42	54.34	54.20	52.90	52.70	55.46	37.10	37.35
TIO2	0	0	0	0	0	0	2.51	2.47
A203	0	.34	0	0	0	.50	15.61	14.16
F203	20.53	21.14	21.26	23.78	21.03	22.03	0	0
FEO	0	0	0	0	0	0	16.36	17.03
MNO	0	0	0	0	0	0	.45	.16
MGO	7.94	6.74	7.22	6.56	7.10	7.78	13.24	14.29
CAO	.24	.68	0	.27	.57	.36	0	.33
NA20	0	0	0	0	0	0	C	0
K20	10.57	9.12	10.60	10.28	10.15	10.59	9.01	7.02
SUM	93.70	92.36	93.29	93.79	91.55	96.72	96.28	92.83

SI	7.937	*	7.984	*	7.953	*	7.797	*	7.897	*	7.851	*	5.560	*	5.707	*
AL	0	7.937	.016	8.000	0	7.953	0	7.797	0	7.897	.083	7.934	2.440	8.000	2.293	8.000
AL	0	*	.043	*	0	*	0	*	0	*	0	*	.317	*	.257	*
FE3+	2.253	*	2.337	*	2.348	*	2.637	*	2.371	*	2.347	*	0	*	0	*
FE	0	*	0	*	0	*	0	*	0	*	0	*	2.301	*	2.176	*
TI	0	*	0	*	0	*	C	*	0	*	0	*	.283	*	.284	*
MN	0	*	0	*	0	*	0	*	0	*	0	*	.057	*	.023	*
MG	1.726	3.979	1.476	3.856	1.579	3.927	1.441	4.078	1.586	3.957	1.642	3.988	2.958	5.915	3.255	5.994
CA	.038	*	.107	*	0	*	.043	*	.092	*	.055	*	0	*	.054	*
NA	0	*	0	*	C	*	0	*	0	*	0	*	0	*	0	*
K	1.966	2.004	1.709	1.815	1.984	1.984	1.932	1.975	1.940	2.032	1.912	1.967	1.722	1.722	1.368	1.422
O	22.000	*	22.000	*	22.000	*	22.000	*	22.000	*	22.000	*	22.000	*	22.000	*
	FE3+	56.62		61.29		59.78		64.67		59.93		58.84		C		C
	MG	43.38		38.71		40.22		35.33		40.07		41.16		100.00		100.00
	F/M	0		0		0		0		0		0		.797		.676
	F/FM	0		0		0		0		0		0		.444		.403

1 2070 CELADONITE IN AMYGDALE 1
2 2070 CELADONITE IN AMYGDALE 2
3 2070 CELADONITE IN AMYGDALE 3
4 2070 CELADONITE IN AMYGDALE 4
5 2070 CELADONITE IN AMYGDALE 5
6 2070 CELADONITE IN AMYGDALE 6
7 R15 AMYGDALE 2
8 R15 AMYGDALE 3

SUPER RECAL — CHLORITE IN MICROFRACTURES AND AMYGDALES

	1	2	3	4	5	6	7	8
SIO2	26.13	26.20	29.09	27.86	27.99	27.70	26.19	34.58
TIO2	.20	0	0	0	0	0	0	1.44
A2O3	17.90	18.32	15.45	17.91	16.71	17.37	18.94	15.88
FEO	34.35	34.24	23.55	24.09	26.17	25.42	20.99	19.16
MNO	0	0	0	.21	0	.27	0	0
MGO	8.31	8.21	17.33	17.05	15.61	16.37	17.42	15.99
CAO	.26	.15	.26	0	.09	0	0	.28
NA2O	0	0	0	.50	.34	.37	.40	0
K2O	0	0	0	0	0	0	0	2.78
SUM	87.21	87.12	85.68	87.62	86.91	87.50	83.94	90.11
SI	5.831 *	5.830 *	6.203 *	5.838 *	5.978 *	5.860 *	5.651 *	6.851 *
AL	2.169 8.000	2.170 8.000	1.797 8.000	2.162 8.000	2.022 8.000	2.140 8.000	2.349 8.000	1.149 8.000
AL	2.529 *	2.634 *	2.086 *	2.261 *	2.183 *	2.190 *	2.466 *	2.558 *
TI	.033 *	0 *	0 *	0 *	0 *	0 *	0 *	.215 *
FE	6.400 *	6.372 *	4.200 *	4.222 *	4.674 *	4.497 *	3.787 *	3.174 *
MN	0 *	0 *	0 *	.037 *	0 *	.048 *	0 *	0 *
MG	2.759 *	2.723 *	5.508 *	5.326 *	4.969 *	5.162 *	5.602 *	4.722 *
CA	.062 *	.036 *	.059 *	0 *	.021 *	0 *	0 *	.059 *
NA	0 *	0 *	0 *	.203 *	.141 *	.152 *	.167 *	0 *
K	0 11.784	0 11.765	0 11.853	0 12.049	0 11.988	0 12.049	0 12.023	.702 11.430
O	28.000 *	28.000 *	28.000 *	28.000 *	28.000 *	28.000 *	28.000 *	28.000 *
F/M	2.320	2.340	.762	.800	.941	.881	.676	.672
F/FM	.699	.701	.433	.444	.485	.468	.403	.402

1 GQ14 MFRACT 1
2 GQ14 MFRACT 2
3 GQ34 MFRACT 1
4 GQ34 MFRACT 2
5 GQ34 CAVITY FILLING (WITH CALCITE)
6 GQ34 CAVITY FILLING (WITH CALCITE)
7 G80/2 MFRACT 1
8 R15 AMYGDALE (AFTER BIOTITE) 1

SUPER RECAL — CHLORITE IN MICROFRACTURES AND AMYGDALES

	9
SIO2	34.00
TIO2	1.28
A2O3	15.07
FEO	19.08
MNO	.31
MGO	16.06
CAO	.31
NA2O	0
K2O	2.55
SUM	88.66
SI	6.864 *
AL	1.136 8.000
AL	2.450 *
TI	.194 *
FE	3.221 *
MN	.053 *
MG	4.833 *
CA	.067 *
NA	0 *
K	.657 11.475
O	28.000 *
F/M	.678
F/FM	.404

9 R15 AMYGDALE (AFTER BIOTITE) 2

SUPER RECAL — AMPHIBOLE IN AMYGDALES

	1	2	3	4	5	6	7
SIO2	54.01	53.41	55.03	53.65	53.17	52.24	54.66
TIO2	.37	.32	0	0	1.09	.80	0
A203	1.92	1.42	1.28	1.29	1.76	2.20	1.98
F203	0	.16	0	.84	1.30	1.21	0
FEO	11.65	14.20	16.27	13.89	10.91	11.57	13.03
MNO	.57	.52	.77	.70	.46	.41	.58
MGO	16.02	14.80	13.27	15.10	15.99	15.89	15.45
CAO	12.76	12.49	11.98	12.35	13.04	12.64	12.34
NA20	.36	.51	.39	.46	.13	.50	.48
K20	.19	0	0	0	0	0	0
SUM	97.84	97.67	98.99	97.44	96.55	96.25	98.52

SI	7.754	*	7.772	*	7.932	*	7.811	*	7.714	*	7.638	*	7.812	*
AL	.246	8.000	.228	8.000	.068	8.000	.189	8.000	.286	8.000	.362	8.000	.188	8.000
AL	.079	*	.015	*	.149	*	.032	*	.015	*	.017	*	.146	*
TI	.040	*	.035	*	0	*	0	*	.119	*	.088	*	0	*
FE3+	0	*	.018	*	0	*	.092	*	.142	*	.133	*	0	*
FE	1.399	*	1.728	*	1.961	*	1.691	*	1.324	*	1.415	*	1.557	*
MN	.069	*	.064	*	.094	*	.086	*	.057	*	.051	*	.070	*
MG	3.428	5.014	3.210	5.070	2.851	5.055	3.277	5.179	3.458	5.113	3.463	5.166	3.291	5.065
CA	1.963	*	1.947	*	1.850	*	1.926	*	2.027	*	1.980	*	1.890	*
NA	.100	*	.144	*	.109	*	.130	*	.037	*	.142	*	.133	*
K	.033	2.096	0	2.091	0	1.959	0	2.056	0	2.063	0	2.122	0	2.023
O	23.000	*	23.000	*	23.000	*	23.000	*	23.000	*	23.000	*	23.000	*
F/M		.428		.558		.721		.542		.399		.423		.495
F/FM		.300		.358		.419		.352		.285		.297		.331

1 R15 AMYGDALE 2
2 R15 AMYGDALE 4
3 R15 AMYGDALE 5
4 R15 AMYGDALE 6
5 R15 AMYGDALE 970-6
6 R15 AMYGDALE 979-4
7 R15 AMYGDALE 978-3

SUPER RECAL — SPHENE IN AMYGDALES

	1	2	3	4	5	6	7	8
SIO2	30.07	29.55	29.74	29.76	30.07	29.50	29.03	30.58
TIO2	35.76	35.60	36.24	36.67	36.08	35.44	37.20	36.14
A203	1.95	2.10	1.86	1.37	1.83	1.90	1.25	2.12
F203	1.99	1.18	1.51	1.26	1.11	1.26	1.74	2.04
FEO	0	0	0	0	0	0	0	0
MNO	0	0	0	0	0	0	0	0
MGO	0	0	0	0	0	0	0	0
CAO	28.36	28.19	28.14	28.33	28.71	27.69	28.07	28.07
NA20	0	0	0	0	0	0	0	0
K20	0	0	0	0	0	0	0	0
SUM	98.13	96.62	97.49	97.39	97.80	95.79	97.29	98.95

SI	4.010	*	3.996	*	3.989	*	3.998	*	4.019	*	4.020	*	3.916	*	4.033	*
TI	0	4.010	.004	4.000	.011	4.000	.002	4.000	0	4.019	0	4.020	.084	4.000	0	4.033
TI	3.586	*	3.617	*	3.643	*	3.703	*	3.626	*	3.632	*	3.690	*	3.584	*
AL	.306	*	.335	*	.294	*	.217	*	.288	*	.305	*	.199	*	.329	*
FE3+	.199	*	.120	*	.152	*	.127	*	.112	*	.129	*	.177	*	.202	*
FE	0	4.091	0	4.071	0	4.090	0	4.047	0	4.026	0	4.066	0	4.065	0	4.116
MN	0	*	0	*	0	*	0	*	0	*	0	*	0	*	0	*
MG	0	*	0	*	0	*	0	*	0	*	0	*	0	*	0	*
CA	4.052	*	4.085	*	4.043	*	4.078	*	4.111	*	4.043	*	4.057	*	3.967	*
NA	0	*	0	*	0	*	0	*	0	*	0	*	0	*	0	*
K	0	4.052	0	4.085	0	4.043	0	4.078	0	4.111	0	4.043	0	4.057	0	3.967
O	20.000	*	20.000	*	20.000	*	20.000	*	20.000	*	20.000	*	20.000	*	20.000	*
F/M		0		0		0		0		0		0		0		0
F/FM		0		0		0		0		0		0		0		0

1 R15 AMYGDALE 1
2 R15 AMYGDALE 2
3 R15 AMYGDALE 3
4 R15 AMYGDALE 4
5 R15 AMYGDALE 5
6 R15 AMYGDALE 6
7 R15 AMYGDALE 7
8 R15 AMYGDALE 8

SUPER RECAL — EPIDOTE IN MICROFRACTURES AND AMYGDALES

	1	2	3	4	5	6	7	8
SIO2	38.94	39.54	38.08	41.79	42.02	37.22	43.10	39.58
TIO2	.84	.83	1.36	.17	0	.80	.28	.28
A203	21.69	21.72	22.14	22.46	21.40	22.40	20.18	21.82
F203	12.92	12.93	13.40	12.36	13.27	14.46	12.57	13.77
FEO	0	0	0	0	0	0	0	0
MNO	0	0	0	0	0	.23	0	0
MGO	0	.59	0	.22	0	.63	.45	.33
CAO	23.06	22.12	23.66	21.80	22.16	22.50	21.97	22.80
NA20	0	.39	0	.41	0	0	0	.22
K20	0	0	0	0	0	0	0	0
SUM	97.47	99.17	98.64	99.21	98.85	97.44	99.07	98.80

SI	6.211 *	6.243 *	6.032 *	6.466 *	6.541 *	5.980 *	6.673 *	6.230 *
AL	0 5.211	0 5.243	0 6.032	0 6.466	0 6.541	.020 6.000	0 6.673	0 6.230
AL	4.074 *	4.041 *	4.133 *	4.095 *	3.925 *	4.220 *	3.681 *	4.047 *
FE3+	1.550 5.624	1.542 5.583	1.597 5.730	1.439 5.534	1.554 5.480	1.748 5.968	1.464 5.146	1.631 5.678
TI	.101 *	.099 *	.162 *	.020 *	0 *	0 *	.093 *	.033 *
FE	0 *	0 *	0 *	0 *	0 *	0 *	0 *	0 *
MN	0 *	0 *	0 *	0 *	0 *	.031 *	0 *	0 *
MG	0 *	.139 *	0 *	.051 *	0 *	.151 *	.104 *	.077 *
CA	3.939 *	3.742 *	4.015 *	3.614 *	3.696 *	3.873 *	3.644 *	3.845 *
NA	0 *	.119 *	0 *	.123 *	0 *	0 *	0 *	.067 *
K	0 4.039	0 4.099	0 4.177	0 3.807	0 3.696	0 4.055	0 3.841	0 4.023
O	25.000 *	25.000 *	25.000 *	25.000 *	25.000 *	25.000 *	25.000 *	25.000 *
AL	72.44	72.38	72.12	74.00	71.63	70.61	71.54	71.28
FE3+	27.56	27.62	27.88	26.00	28.37	29.19	28.46	28.72
F/M	0	0	0	0	0	.207	0	0
F/FM	0	0	0	0	0	.172	0	0

1 QD1 MFRACT 1(1)
2 QD1 MFRACT 1(2)
3 QD1 MFRACT 1(3)
4 QD1 MFRACT 1(4)
5 QD1 MFRACT 1(5)
6 QD1 MFRACT 1(6)
7 QD1 MFRACT 1(8)
8 QD1 MFRACT 1(9)

SUPER RECAL — EPIDOTE IN MICROFRACTURES AND AMYGDALES

	9	10	11	12	13	14
SIO2	38.86	38.74	37.19	37.24	34.83	34.95
TIO2	.55	0	0	0	0	0
A203	22.35	21.92	21.63	21.26	20.12	20.70
F203	13.17	13.67	14.51	13.54	14.25	13.76
FEO	0	0	0	0	0	0
MNO	0	0	.22	0	0	0
MGO	.23	0	0	0	0	0
CAO	22.99	23.49	22.53	21.43	19.87	19.40
NA20	0	0	0	0	0	0
K20	0	0	0	0	0	0
SUM	98.14	97.81	96.08	93.47	89.07	88.81

SI	6.153 *	6.176 *	6.064 *	6.194 *	6.106 *	6.118 *
AL	0 6.153	0 6.176	0 6.064	0 6.194	0 6.106	0 6.118
AL	4.170 *	4.118 *	4.156 *	4.167 *	4.156 *	4.270 *
FE3+	1.569 5.739	1.640 5.757	1.780 5.936	1.695 5.861	1.880 6.036	1.813 6.082
TI	.065 *	0 *	0 *	0 *	0 *	0 *
FE	0 *	0 *	0 *	0 *	0 *	0 *
MN	0 *	0 *	.030 *	0 *	0 *	0 *
MG	.054 *	0 *	0 *	0 *	0 *	0 *
CA	3.898 *	4.010 *	3.936 *	3.819 *	3.732 *	3.638 *
NA	0 *	0 *	0 *	0 *	0 *	0 *
K	0 4.018	0 4.010	0 3.966	0 3.819	0 3.732	0 3.638
O	25.000 *	25.000 *	25.000 *	25.000 *	25.000 *	25.000 *
AL	72.66	71.52	70.01	71.09	68.86	70.20
FE3+	27.34	28.48	29.99	28.91	31.14	29.80
F/M	0	0	0	0	0	.207
F/FM	0	0	0	0	0	.172

9 QD1 MFRACT 1(10)
10 QD1 MFRACT 1(11)
12 R15 AMYGDALE
13 R15 AMYGDALE

	1	2	3	4	5	6	7	8	9	10	11	12	13
FeO	0.28	0.23	3.40	3.88	2.73	4.35	3.71	0.96	14.67	8.75	11.27	10.63	4.57
MgO	0.19	0.19	18.54	18.27	19.77	16.96	19.49	0.77	12.25	16.38	14.62	16.06	17.58
MnO	0.00	0.32	0.90	0.68	0.73	1.03	0.63	0.37	0.41	0.30	0.57	0.00	0.60
CaO	55.73	55.74	29.26	29.43	29.56	31.06	30.74	55.17	27.62	29.43	28.36	29.28	28.10
CO_2*	44.14	44.32	45.86	45.86	46.92	46.21	48.08	44.98	44.31	46.54	45.49	47.04	44.43
SUM	100.34	100.80	97.96	98.12	99.71	99.61	102.65	102.25	99.26	101.40	100.31	103.01	95.28
Sid	0.39	0.32	4.54	5.18	3.57	5.77	4.73	1.31	20.29	11.52	15.18	13.85	6.30
Magn	0.47	0.47	44.15	43.51	46.01	40.08	44.26	1.87	30.19	38.43	35.09	37.28	43.21
Rhod	0.00	0.45	1.22	0.92	0.97	1.38	0.81	0.51	0.57	0.40	0.78	0.00	0.84
Calc	99.14	98.77	50.09	50.39	49.46	52.77	50.19	96.31	48.94	49.65	48.95	48.87	49.65

1 GQ34 Replacement pseudomorph
2 GQ34 Replacement pseudomorph
3 2070 Amygdale, Axial zone
4 2070 Amygdale, Axial zone
5 2070 Amygdale, Axial zone
6 2070 Amygdale, Axial zone
7 2070 Amygdale, Axial zone
8 2070 Amygdale, inclusion in barite
9 2070 Amygdale, Marginal zone
10 2070 Amygdale, Marginal zone
11 2070 Amygdale, Marginal zone
12 2070 Amygdale, Marginal zone
13 2070 Amygdale, Marginal zone

*CO_2 estimated from stoichiometry

SUPER RECAL — STEM ANALYSES OF FELDSPARS

	1	2	3	4	5	6	7	8
SIO2	59.11	54.42	59.55	56.52	62.53	64.13	53.99	54.52
TIO2	0	0	0	0	0	0	0	0
A203	25.00	25.32	26.58	22.67	21.45	22.44	26.35	21.43
FEO	1.30	1.61	0	2.28	2.40	1.95	3.53	4.91
MNO	0	0	0	0	0	0	0	0
MGO	0	0	0	0	0	0	0	0
CAO	4.90	5.74	5.39	5.31	1.27	1.70	6.18	6.75
NA20	8.88	11.18	6.70	10.58	10.12	9.42	9.14	11.50
K20	0	0	0	.82	0	0	0	0
SUM	99.19	98.26	98.22	98.18	97.77	99.64	99.19	99.11
SI	2.666 *	2.532 *	2.671 *	2.637 *	2.840 *	2.842 *	2.497 *	2.574 *
AL	1.329 3.995	1.388 3.920	1.405 4.076	1.246 3.883	1.148 3.987	1.172 4.014	1.436 3.932	1.192 3.767
TI	0 *	0 *	0 *	0 *	0 *	0 *	0 *	0 *
FE	.049 *	.063 *	0 *	.089 *	.091 *	.072 *	.137 *	.194 *
MN	0 *	0 *	0 *	0 *	0 *	0 *	0 *	0 *
MG	0 *	0 *	0 *	0 *	0 *	0 *	0 *	0 *
CA	0 1.062	0 1.357	0 .842	0 1.360	0 1.044	0 .962	0 1.262	0 1.588
NA	.777 *	1.009 *	.583 *	.957 *	.891 *	.809 *	.819 *	1.053 *
K	0 1.062	0 1.357	0 .842	.049 1.360	0 1.044	0 .962	0 1.262	0 1.588
O	8.000 *	8.000 *	8.000 *	8.000 *	8.000 *	8.000 *	8.000 *	8.000 *
AN	23.37	22.16	30.78	20.88	6.49	9.07	27.20	24.49
AB	76.63	77.90	69.22	75.28	93.51	90.93	72.80	75.51
OR	0	0	0	3.84	0	0	0	0
F/M	0	0	0	0	0	0	0	0
F/FM	0	0	0	0	0	0	0	0

1 SU80/3/6 FELDSPAR CLAST 1
2 SU80/3/6 MATRIX FELDSPAR LATH 1
3 X/6 MATRIX FELDSPAR 1
4 X/6 FELDSPAR CLAST 1 PLATE
5 GQ1A INTERSPHERULITE FELDSPAR 1
6 GQ1A INTERSPHERULITE FELDSPAR 2 PLATE
7 SU80/3/5 FELDSPAR CLAST 1 PLATE
8 SU80/3/5 MATRIX FELDSPAR LATH 1

SUPER RECAL — STEM ANALYSES OF FELDSPARS

	9	10	11	12	13	14	15	16
SIO2	54.86	56.82	55.66	61.33	57.40	59.59	59.11	54.42
TIO2	0	0	0	0	0	0	0	0
A203	25.59	25.49	25.99	19.33	25.66	25.18	25.00	25.31
FEO	2.31	1.03	3.03	1.67	1.31	3.26	1.30	1.61
MNO	0	0	0	0	0	0	0	0
MGO	0	0	.66	0	0	0	0	0
CAO	5.86	4.84	6.64	.78	5.56	4.15	4.90	5.74
NA20	9.65	9.46	7.32	1.14	9.37	5.32	8.88	11.18
K20	0	.46	0	14.41	0	0	0	0
SUM	98.27	98.09	99.30	98.66	99.30	97.50	99.19	98.26
SI	2.544 *	2.598 *	2.544 *	2.897 *	2.605 *	2.708 *	2.666 *	2.532 *
AL	1.398 3.942	1.378 3.971	1.400 3.944	1.076 3.973	1.372 3.977	1.348 4.057	1.329 3.995	1.388 3.920
TI	0 *	0 *	0 *	0 *	0 *	0 *	0 *	0 *
FE	.090 *	.074 *	.116 *	.066 *	.050 *	.124 *	.049 *	.063 *
MN	0 *	0 *	0 *	0 *	0 *	0 *	0 *	0 *
MG	0 *	0 *	.045 *	0 *	0 *	0 *	0 *	0 *
CA	0 1.248	0 1.176	0 1.135	0 1.078	0 1.144	0 .795	0 1.062	0 1.357
NA	.868 *	.839 *	.649 *	.104 *	.824 *	.469 *	.777 *	1.009 *
K	0 1.248	.027 1.176	0 1.135	.868 1.078	0 1.144	0 .795	0 1.062	0 1.357
O	8.000 *	8.000 *	8.000 *	8.000 *	8.000 *	8.000 *	8.000 *	8.000 *
AN	25.13	21.51	33.39	3.90	24.69	30.12	23.37	22.10
AB	74.87	76.06	66.61	10.32	75.31	69.88	76.63	77.90
OR	0	2.43	0	85.78	0	0	0	0
F/M	0	0	2.576	0	0	0	0	0
F/FM	0	0	.720	0	0	0	0	0

9 R2/6 MATRIX FELDSPAR 1
10 R2/6 MATRIX FELDSPAR 2
11 R2/6 MATRIX FELDSPAR 3
12 R2/6 MATRIX FELDSPAR 4
13 R2/3 MATRIX FELDSPAR 1
14 SU80/2/3 FELDSPAR PLATE
15 SU80/3/6 FELDSPAR CLAST 1
16 SU80/3/6 MATRIX FELDSPAR LATH 1

SUPER RECAL 17 — STEM ANALYSES OF FELDSPARS

	17		
SIO2	54.23		
TIO2	0		
A2O3	25.56		
FEO	3.13		
MNO	0		
MGO	1.72		
CAO	6.69		
NA2O	6.48		
K2O	1.22		
SUM	99.03		
SI	2.507	*	
AL	1.392	3.899	
TI	0	*	
FE	.121	*	
MN	0	*	
MG	.119	*	
CA	0	1.224	
NA	.581	*	
K	.072	1.224	
O	8.000	*	
AN		33.67	
AB		59.02	
OR		7.31	
F/M		1.021	
F/FM		.505	

17 X/6 FELDSPAR

SUPER RECAL — STEM ANALYSES OF AMPHIBOLES

	1		2		3	
SIO2	47.75		44.00		49.11	
TIO2	0		0		0	
A2O3	12.26		9.33		6.52	
FEO	15.85		14.37		9.27	
MNO	0		0		0	
MGO	9.79		11.66		18.68	
CAO	11.42		11.00		14.40	
NA2O	2.41		3.83		0	
K2O	0		1.05		0	
SUM	99.78		95.24		97.98	
SI	6.859	*	6.536	*	7.026	*
AL	1.141	8.000	1.458	7.994	.974	8.000
AL	.984	*	0	*	.125	*
TI	0	*	0	*	0	*
FE	1.904	*	1.785	*	1.109	*
MN	0	*	0	*	0	*
MG	2.096	4.984	3.467	5.253	3.983	5.217
CA	1.757	*	1.751	*	2.207	*
NA	.671	*	1.103	*	0	*
K	0	2.429	.199	3.223	0	2.207
O	23.000	*	23.000	*	23.000	*
MG		52.40		66.01		78.22
FEMN		47.60		33.99		21.78
F/M		.908		.515		.278
F/FM		.476		.340		.218

1 SU80/2/5 MATRIX HORNBLENDE 1 PLATE
2 SU80/3/5 MATRIX HORNBLENDE 1
3 SU80/3/6 MATRIX HORNBLENDE 1 PLATE

SUPER RECAL — STEM ANALYSES OF BIOTITES

	1	2	3	4	5	6	7	8
SIO2	39.45	37.24	39.66	35.21	40.90	38.96	37.19	38.75
TIO2	2.61	.97	2.99	1.88	1.74	2.56	2.35	2.76
A203	16.57	15.41	15.96	17.53	18.98	14.05	17.87	16.83
FEO	19.08	19.67	17.76	20.08	16.08	13.66	14.60	16.12
MNO	0	0	0	0	0	0	0	0
MGO	11.92	13.43	13.25	14.13	10.99	19.33	18.58	15.69
CAO	0	.63	1.71	.63	.92	0	0	0
NA20	0	0	0	1.76	2.73	0	0	0
K20	9.55	8.75	7.87	8.53	7.49	7.31	8.40	9.11
SUM	99.18	97.00	99.20	99.75	99.83	95.87	99.99	99.26
SI	5.712 *	5.429 *	5.684 *	5.167 *	5.760 *	5.657 *	5.286 *	5.532 *
AL	2.288 8.000	2.571 8.000	2.316 8.000	2.033 8.000	2.240 8.000	2.343 8.000	2.714 8.000	2.468 8.000
AL	.539 *	.256 *	.380 *	.198 *	.910 *	.061 *	.279 *	.364 *
TI	.284 *	.227 *	.322 *	.207 *	.184 *	.290 *	.251 *	.296 *
MN	0 *	0 *	0 *	0 *	0 *	0 *	0 *	0 *
MG	2.573 *	2.926 *	2.831 *	3.091 *	2.307 *	4.183 *	3.936 *	3.339 *
FE	2.310 5.706	2.405 5.914	2.129 5.662	2.464 5.960	1.894 5.295	1.659 6.183	1.736 6.202	1.925 5.924
CA	0 *	.099 *	.263 *	.099 *	.139 *	0 *	0 *	0 *
NA	0 *	0 *	0 *	.501 *	.745 *	0 *	0 *	0 *
K	1.704 1.704	1.632 1.730	1.439 1.701	1.597 2.196	1.345 2.230	1.354 1.354	1.523 1.523	1.659 1.659
O	22.000 *	22.000 *	22.000 *	22.000 *	22.000 *	22.000 *	22.000 *	22.000 *
ANN	47.32	45.11	42.92	44.36	45.08	28.39	30.60	36.57
PHLG	52.68	54.89	57.08	55.64	54.92	71.61	69.40	63.43
F/M	.990	.822	.752	.797	.821	.396	.441	.576
F/FM	.473	.451	.429	.444	.451	.284	.306	.366

1 R2/6 MATRIX BIOTITE 1
2 R2/6 MATRIX BIOTITE 2
3 R2/6 MATRIX BIOTITE 3
4 R2/3 MATRIX BIOTITE 1
5 R2/5 MATRIX BIOTITE 1
6 SU80/3/5 MATRIX BIOTITE LATH 1 PLATE
7 SU80/3/6 MATRIX BIOTITE LATH 1 PLATE.
8 SU80/3/6 MATRIX BIOTITE LATH 2 PLATE.

SUPER RECAL — STEM ANALYSES OF BIOTITES

	9	10	11	12	13	14
SIO2	37.35	41.05	39.77	40.43	40.13	38.14
TIO2	2.21	)	0	1.33	2.04	2.46
A203	17.81	15.33	15.17	13.03	16.69	18.43
FEO	14.82	14.27	16.21	10.75	15.74	17.10
MNO	0	0	0	0	0	0
MGO	16.76	9.42	8.14	14.12	13.90	13.71
CAO	.66	0	5.03	0	.90	1.15
NA20	0	0	0	2.06	0	1.24
K20	9.22	8.09	6.34	7.60	7.95	7.59
SUM	98.83	97.16	98.66	99.32	97.35	99.82
SI	5.354 *	5.769 *	5.622 *	5.543 *	5.779 *	5.428 *
AL	2.646 8.000	2.231 8.000	2.378 8.000	2.457 8.000	2.221 8.000	2.572 8.000
AL	.362 *	1.968 *	1.481 *	1.264 *	.612 *	.519 *
TI	.238 *	0 *	0 *	.137 *	.221 *	.263 *
MN	0 *	0 *	0 *	0 *	0 *	0 *
MG	3.581 *	1.762 *	1.715 *	2.805 *	2.984 *	2.908 *
FE	1.777 5.958	1.677 5.405	1.916 5.113	1.233 5.519	1.896 5.712	2.035 5.726
CA	.101 *	0 *	.762 *	0 *	.139 *	.175 *
NA	0 *	0 *	0 *	.548 *	0 *	.342 *
K	1.686 1.787	1.450 1.450	1.143 1.905	1.329 1.877	1.460 1.599	1.378 1.895
O	22.000 *	22.000 *	22.000 *	22.000 *	22.000 *	22.000 *
ANN	33.16	48.74	52.77	29.93	38.85	41.17
PHLG	66.94	51.26	47.23	70.07	61.15	58.83
F/M	.496	.951	1.117	.427	.635	.700
F/FM	.332	.487	.528	.299	.389	.412

9 SU80/3/6 MATRIX BIOTITE LATH 3
10 SU80/2/3 SPHERULITIC BIOTITE 1 PLATE
11 SU80/2 PLATE/3 MATRIX BIOTITE 2
12 X/11 SPHERULITIC BIOTITE 1 PLATE
13 X/6 SPHERULITIC BIOTITE 1
14 X/6 MATRIX BIOTITE LATH 1 PLATE

SUPER RECAL STEM ANALYSES OF CHLORITES

	1	2	3	4	5	6	7	8
SIO2	24.73	25.20	26.57	27.75	26.28	29.85	29.14	32.06
TIO2	0	0	0	0	0	0	0	0
A2O3	23.78	23.48	23.00	23.11	22.82	23.44	21.91	19.54
FEO	29.61	29.43	26.63	27.87	31.18	27.58	29.22	29.83
MNO	0	0	0	0	0	0	0	0
MGO	20.98	19.46	19.16	20.55	18.52	17.73	18.79	16.25
CAO	0	0	.78	0	0	0	0	.83
NA2O	0	0	2.78	0	0	0	0	0
K2O	0	0	0	0	0	0	0	.98
SUM	99.10	98.47	98.92	99.28	98.80	98.60	99.06	99.49

SI	4.693	*		4.864	*		5.021	*		5.170	*		5.020	*		5.548	*		5.459	*		6.010	*	
AL	3.307	8.000		3.136	8.000		2.978	8.000		2.830	8.000		2.980	8.000		2.452	8.000		2.541	8.000		1.990	8.000	
AL	2.011	*		2.225	*		2.143	*		2.243	*		2.156	*		2.683	*		2.296	*		2.327	*	
TI	0	*		0	*		0	*		0	*		0	*		0	*		0	*		0	*	
FE	4.699	*		4.607	*		4.209	*		4.342	*		4.981	*		4.287	*		4.578	*		4.677	*	
MN	0	*		0	*		0	*		0	*		0	*		0	*		0	*		0	*	
MG	5.935	*		5.620	*		5.397	*		5.706	*		5.273	*		4.912	*		5.247	*		4.541	*	
CA	0	*		0	*		.158	*		0	*		0	*		0	*		0	*		.167	*	
NA	0	*		0	*		1.019	*		0	*		0	*		0	*		0	*		0	*	
K	0	12.645		0	12.483		0	12.925		0	12.291		0	12.409		0	11.882		0	12.120		.234	11.946	
O	28.000	*		28.000	*		28.000	*		28.000	*		28.000	*		28.000	*		28.000	*		28.000	*	
	F/M	.792			.820			.780			.761			.945			.873			.873				1.030	
	F/FM	.442			.450			.438			.432			.486			.466			.466				.507	

1 GQ1A INTER-SPHERULITE CHLORITE 1
2 GQ1A INTER-SPHERULITE CHLORITE 2
3 GQ1A INTER-SPHERULITE CHLORITE 3
4 GQ1A INTER-SPHERULITE CHLORITE 4 PLATE
5 GQ1A INTER-SPHERULITE CHLORITE 5 PLATE
6 GQ1A INTER-SPHERULITE CHLORITE 6
7 GQ1A INTER-SPHERULITE CHLORITE 7 PLATE
8 SU80/2/3 SPHERULITIC CHLORITE PLATE

SUPER RECAL STEM ANALYSES OF CHLORITES

	9
SIO2	28.90
TIO2	0
A2O3	19.09
FEO	32.55
MNO	0
MGO	15.44
CAO	0
NA2O	3.32
K2O	0
SUM	99.30

SI	5.580	*	
AL	2.420	8.000	
AL	1.924	*	
TI	0	*	
FE	5.256	*	
MN	0	*	
MG	4.444	*	
CA	0	*	
NA	1.243	*	
K	0	12.867	
O	28.000	*	
	F/M	1.183	
	F/FM	.542	

9 SU80/2/3 SPHERULITIC CHLORITE 2 PLATE

APPENDIX A4: Whole Rock Analyses

Sample identification for the XRF whole rock analyses presented on the following pages follow a consistent scheme. The title data are explained as follows:-

R2	/	AV2	1	PLAG-MICROLITIC IV...etc		1070
sample number		number of duplicates	locality number	sample description and locality		(machine number)

"H" and "P" at the end of the sample number indicate host and pseudotachylyte vein respectively. Where the host-rock and vein samples are from the same handspecimen, the same sample number is used, viz. GQ1AH and GQ1AP. Host and vein samples not from the same handspecimen have different sample numbers and their field relationship is explained in the sample description.

The following abbreviations are used:-

AF - alkali feldspar
BT - biotite
CHL - chlorite
CPX - clinopyroxene
EP - epidote
GT - garnet
HB - hornblende
MT - magnetite
PL - plagioclase
QZ - quartz
SP - sphene
WM - white mica
IV - injection vein
FV - fault vein
ND - not determined

	R2	R4	SU802A	SU802B	SL80/3	SL80/4	SA3	E1	E5	MM2	GL2	GL12	GL8	LB20
SIO2	61.81	59.26	64.26	64.23	64.60	58.78	67.58	61.61	63.87	50.24	62.73	49.97	57.29	56.78
TIO2	.69	.94	.76	.65	.46	.88	.67	.66	.63	1.16	.80	.95	.66	.77
AL203	16.47	16.37	15.26	15.05	16.31	15.66	14.30	14.91	15.41	14.45	15.45	14.21	15.90	15.92
FE203	6.89	8.01	6.05	5.82	4.47	9.26	4.55	7.68	6.48	9.99	6.88	13.47	7.98	7.49
MNO	.09	.12	.10	.10	.07	.18	.07	.13	.11	.17	.10	.22	.14	.14
MGO	1.64	2.10	1.14	1.02	2.20	2.40	1.24	2.55	2.58	6.28	2.14	6.35	4.44	4.04
CAO	4.30	5.15	4.58	4.26	4.91	5.97	3.20	5.52	3.60	10.84	5.39	10.93	7.45	6.19
NA20	4.49	4.31	4.02	3.39	4.82	4.30	4.54	3.89	3.82	3.76	4.55	2.63	3.50	4.34
K20	2.89	2.44	1.89	2.56	1.44	1.80	2.85	1.93	2.42	.61	1.44	.61	1.72	2.43
P205	.26	.43	.33	.27	.16	.46	.20	.14	.15	.49	.20	.13	.23	.36
H20-	.04	.05	.12	.19	0	.04	.05	.05	.05	.05	.03	.01	.02	.07
LOI	.41	.34	.94	1.25	.31	.15	.67	.36	.77	1.27	.03	.19	.29	.55
TOTAL	99.98	99.52	99.45	98.79	99.75	99.88	99.92	99.43	99.89	99.31	99.74	99.67	99.62	99.08
K20/NA20	.64	.57	.47	.76	.30	.42	.63	.50	.63	.16	.32	.23	.49	.56
MGO/K20	.57	.86	.60	.40	1.53	1.33	.44	1.32	1.07	10.30	1.49	10.41	2.58	1.66
K20/CAO	.67	.47	.41	.60	.29	.30	.89	.35	.67	.06	.27	.06	.23	.39
CAO/MGO	2.62	2.45	4.02	4.18	2.23	2.49	2.58	2.16	1.40	1.73	2.52	1.72	1.68	1.53
V	99	106	72	ND	70	118	89	145	120	219	112	268	135	124
CR	14	12	27	ND	87	17	37	51	123	126	42	94	140	104
NI	11	7	8	ND	37	17	18	28	54	116	30	75	42	55
CU	20	20	24	ND	17	42	43	58	42	19	51	92	35	47
ZN	117	110	92	ND	69	135	62	85	113	100	101	98	79	37
TH	17	C	7	ND	C	9	8	8	6	C	C	C	1	C
RB	113	66	35	ND	52	73	108	71	94	12	34	16	48	43
SR	450	507	451	ND	550	378	333	378	386	1090	439	442	508	858
Y	9	25	20	ND	4	28	15	17	10	21	15	19	15	14
ZR	197	255	313	ND	75	169	190	131	145	236	158	57	124	189
NB	6	9	10	ND	4	11	14	7	8	3	4	3	3	6
BA	855	845	947	ND	508	243	522	306	529	134	530	360	576	1186
K/RB	212.	307.	448.	C	230.	205.	219.	226.	214.	422.	352.	317.	297.	469.
RB/SR	.251	.130	.076	C	.095	.193	.324	.188	.244	.011	.077	.036	.094	.050
TH/K	.0007	C	.0004	C	C	.0006	.0003	.0005	.0003	C	C	C	.0001	C

R2	/AV 2 1	PLAG-MICROLITIC IV, RUBHA ARDVULE, SOUTH UIST	1070
R4	/AV 2 2	PLAG-MICROLITIC IV, RUBHA ARDVULE, SOUTH UIST	1440
SU802A	/AV 1 3	PLAG-MICROLITIC IV, RUBHA ARDVULE, SOUTH UIST	1300
SU802B	/AV 1 3	BT-SPHERULITIC IV, RUBHA ARDVULE, SOUTH UIST	1590
SU80/3	/AV 1 4	PLAG-MICROLITIC IV, RUBHA ARDVULE, SOUTH UIST	1240
SU80/4	/AV 1 5	PLAG-MICROLITIC IV, RUBHA ARDVULE, SOUTH UIST	1410
SA3	/AV 1 5	AMPHIBOLE-MICROLITIC IV, VREDEFORT DOME, SOUTH AFRICA	1020
E1	/AV 1 7	MYLONITE, MAIN THRUST, ERISKAY	1050
E5	/AV 2 7	PSEUDOTACHYLYTE PAVEMENT, MAIN THRUST, ERISKAY	1100
MM2	/AV 1 7	PHYLLONITE, MAIN THRUST, RUBHA BOLUM, SOUTH UIST	1000
GL2	/AV 2 8	PSEUDOTACHYLYTE PAVEMENT, MAIN THRUST, SOUTH UIST	1220
GL12	/AV 1 8	PSEUDOTACHYLYTE PAVEMENT, MAIN THRUST, SOUTH UIST	1110
GL8	/AV 1 8	PSEUDOTACHYLYTE PAVEMENT, MAIN THRUST, SOUTH UIST	1180
LB20	/AV 1 8	PSEUDOTACHYLYTE PAVEMENT, MAIN THRUST, SOUTH UIST	1060

	G8C1/H	G8C1/P	G8C2/H	G8C2/P	G8C3/P	G8C4/P	G8C5/P	G8C6/P	G8C7/H	GC1A/H	GC1A/P	GC10/H	GC9/H	GC12/P
SIO2	60.64	59.94	60.06	60.67	61.12	60.14	60.92	59.62	62.22	49.13	48.54	67.01	47.38	55.60
TIO2	.57	.63	.63	.60	.61	.64	.64	.65	.55	1.18	1.27	.26	1.28	.74
AL203	16.63	17.42	16.53	16.92	17.02	17.55	17.16	17.22	16.50	13.41	14.56	15.76	13.61	18.14
FE203	7.31	7.27	7.19	6.94	7.09	7.54	7.39	7.48	6.56	14.63	14.88	3.41	14.81	8.31
MNO	.13	.12	.12	.10	.11	.12	.11	.13	.14	.25	.23	.06	.19	.11
MGO	3.89	4.13	4.36	4.21	3.97	4.25	4.23	4.28	3.53	6.00	6.24	2.01	6.70	3.22
CAO	3.37	3.44	3.44	3.94	3.48	3.62	3.51	3.58	3.33	10.62	8.66	4.99	11.25	7.16
NA20	3.23	3.67	3.82	3.32	3.35	3.57	3.06	3.46	3.51	3.01	2.63	5.17	2.76	5.39
K20	2.33	2.68	2.43	2.20	2.52	2.57	2.51	2.62	2.11	.83	.37	.47	.65	.67
P205	.16	.12	.27	.15	.11	.12	.09	.14	.16	.16	.11	.17	.15	.27
H2O-	.07	.07	.05	.15	.07	.01	0	.06	.11	.04	.08	.04	.06	.04
LOI	.60	.81	.66	.94	.70	.37	.45	.55	.66	.72	1.74	.20	.30	.18
TOTAL	98.93	100.30	99.56	100.14	100.15	100.50	100.07	99.79	99.38	99.98	99.31	99.55	99.14	99.83
K20/NA20	.72	.73	.64	.66	.75	.72	.82	.76	.60	.28	.14	.09	.24	.12
MGO/K20	1.67	1.54	1.79	1.91	1.58	1.65	1.69	1.63	1.67	7.23	16.86	4.28	10.31	4.81
K20/CAO	.69	.78	.71	.56	.72	.71	.72	.73	.63	.08	.04	.09	.06	.09
CAO/MGO	.87	.83	.79	.94	.88	.85	.83	.84	.94	1.77	1.39	2.48	1.68	2.22
V	162	144	153	131	140	144	138	149	145	344	362	60	365	145
CR	291	251	280	251	253	264	270	271	246	101	91	24	99	55
NI	72	109	134	106	124	115	113	117	57	71	73	17	75	47
CU	37	46	38	46	43	49	39	61	50	117	213	46	127	151
ZN	68	99	112	93	111	102	101	103	66	93	103	32	110	106
TH	6	7	6	8	9	8	9	8	7	0	0	5	0	1
RB	102	125	101	102	117	111	107	113	89	9	2	13	5	3
SR	301	311	332	319	300	294	280	296	332	161	122	575	167	590
Y	23	21	14	20	19	22	25	21	17	35	31	11	36	12
ZR	124	141	120	143	139	138	144	136	127	66	74	161	81	72
NB	5	11	10	8	7	8	5	6	5	8	6	0	3	4
BA	511	523	583	393	481	450	458	474	468	43	0	89	27	174
K/RB	190.	178.	200.	179.	179.	192.	195.	192.	197.	766.	1536.	300.	1079.	1854.
RB/SR	.339	.402	.304	.320	.390	.378	.382	.382	.268	.056	.016	.023	.030	.005
TH/K	.0003	.0003	.0003	.0004	.0004	.0004	.0004	.0004	.0004	0	0	.0008	0	.0002

G8C1/H	/AV 1 10	BT-CT-PL-AF-QZ PARAGNEISS, 0 M ALONG SECTION, GRIMSAY	10
G8C1/P	/AV 2 10	BT-SPHERULITIC FV CUTTING G8C1/H, 0 M ALONG SECTION, GRIMSAY	600
G8C2/H	/AV 1 11	BT-CT-PL-QZ-AF PARAGNEISS, 7.6 M ALONG SECTION, GRIMSAY	30
G8C2/P	/AV 2 11	BT-SPHERULITIC FV CUTTING G8C2/H, 7.6 M ALONG SECTION,	610
G8C3/P	/AV 2 12	BT-SPHERULITIC FV, 14.6 M ALONG SECTION, GRIMSAY	620
G8C4/P	/AV 2 13	BT-SPHERULITIC FV, 39.1 M ALONG SECTION, GRIMSAY	630
G8C5/P	/AV 2 14	BT-SPHERULITIC FV, 40.6 M ALONG SECTION, GRIMSAY	640
G8C6/P	/AV 2 15	BT-SPHERULITIC FV, 1.6 M ALONG SECTION, GRIMSAY	650
G8C7/H	/AV 1 15A	BT-CT-PL-QZ-AF PARAGNEISS, 2.2 M ALONG SECTION, GRIMSAY	40
GC1A/H	/AV 1 16	PL-HB AMPHIBOLITE, GRIMSAY	140
GC1A/P	/AV 2 16	CHL-SPHERULITIC FV CUTTING GC1A/H, GRIMSAY	1630
GC10/H	/AV 1 17	PL-QZ-HB GNEISS, GRIMSAY	160
GC9/H	/AV 1 17	PL-HB AMPHIBOLITE, GRIMSAY	150
GC12/P	/AV 2 17A	IV GENERATED AT CONTACT BETWEEN GC9/H AND GC10/H	1190

	GQ13/P	GQ4/P	GQ21/H	GQ22/H	GQ15/P	GQ16FP	GQ16IP	GQ17/P	GQ23/H	GQ23/P	GQ24/H	GQ24/P	GQ27/H	GQ25/P
SIO2	55.97	51.39	66.16	50.34	55.11	55.05	53.46	57.09	60.21	51.42	50.73	49.33	68.98	67.06
TIO2	.74	1.41	.34	1.11	.74	.71	.82	.75	.76	1.34	1.14	1.19	.31	.52
AL203	17.98	14.56	16.99	13.57	18.27	18.18	17.57	17.08	17.54	15.32	13.81	14.52	15.56	15.40
FE203	7.76	14.64	2.76	13.33	8.46	8.72	9.73	8.64	6.07	13.94	14.69	14.62	2.94	4.72
MNO	.12	.25	.11	.25	.11	.12	.11	.12	.12	.23	.26	.25	.16	.06
MGO	3.13	4.28	1.77	5.88	3.17	3.16	3.60	3.27	2.18	4.16	5.66	5.57	1.03	1.29
CAO	7.05	8.28	3.62	10.40	7.25	7.38	7.44	7.00	6.79	8.27	9.70	9.40	3.82	4.41
NA2O	5.28	2.86	5.94	3.23	4.95	5.06	4.99	4.71	5.10	3.40	2.79	3.06	5.14	4.58
K2O	.60	.78	1.16	.64	.66	.63	.65	.52	.44	.84	.66	.57	.79	.91
P2O5	.22	.19	.22	.20	.27	.41	.37	.20	.18	.19	.10	.11	.15	.11
H2O-	.06	.06	.07	.06	.02	0	.19	.05	.02	.05	.07	.36	.07	.12
LOI	.25	.27	.25	.31	.32	.12	.36	.17	.27	.14	.43	.89	.42	.66
TOTAL	99.16	98.97	99.59	99.32	99.33	99.50	99.29	99.60	99.68	99.30	100.03	99.87	99.37	99.87
K2O/NA2O	.11	.27	.20	.20	.13	.12	.13	.11	.09	.25	.24	.19	.15	.20
MGO/K2O	5.22	5.49	1.53	9.19	4.80	4.92	5.54	6.29	4.95	4.95	8.58	9.77	1.30	1.42
K2O/CAO	.09	.09	.30	.06	.09	.09	.09	.07	.06	.10	.07	.06	.21	.21
CAO/MGO	2.25	1.93	2.16	1.77	2.29	2.38	2.07	2.14	3.11	1.99	1.71	1.69	3.71	3.42
V	138	326	59	320	129	129	162	130	111	302	317	342	31	70
CR	53	29	45	99	ND	ND	43	75	26	31	84	103	20	ND
NI	50	44	31	65	ND	ND	63	46	35	46	61	82	17	ND
CU	116	125	9	99	ND	ND	147	46	72	148	70	236	10	ND
ZN	98	131	0	53	ND	ND	121	126	51	125	89	93	51	ND
TH	0	3	2	2	ND	ND	0	0	0	4	0	0	1	ND
RB	1	19	57	7	0	37	5	2	3	22	5	7	18	32
SR	583	231	645	183	602	597	528	501	550	280	150	150	294	274
Y	12	27	2	30	ND	ND	17	16	11	25	28	28	4	ND
ZR	78	88	0	301	67	7	109	175	27	82	59	73	122	141
NB	4	6	0	8	ND	ND	6	6	6	7	4	7	3	ND
BA	130	184	497	61	189	18	143	132	116	212	73	49	338	320
K/RB	4981.	341.	169.	759.	0	141.	1079.	2159.	1218.	317.	1096.	670.	364.	236.
RB/SR	.002	.082	.088	.038	0	.062	.009	.004	.005	.079	.033	.047	.061	.117
TH/K	0	.0005	.0002	.0004	0	0	0	0	0	.0006	0	0	.0002	0

GQ13/P	/AV 2 17A	IV GENERATED AT CONTACT BETWEEN GQ9/H AND GQ10/H	1610
GQ4/P	/AV 1 17A	IV GENERATED AT CONTACT BETWEEN GQ9/H AND GQ10/H	1620
GQ21/H	/AV 1 18	PL-QZ-HB GNEISS, GRIMSAY	180
GQ22/H	/AV 1 18	PL-HB AMPHIBOLITE, GRIMSAY	190
GQ15/P	/AV 1 18	FV GENERATED AT CONTACT BETWEEN GQ21/H AND GQ22/H	1660
GQ16FP	/AV 1 18A	FV GENERATED AT CONTACT BETWEEN GQ21/H AND GQ22/H	1680
GQ16IP	/AV 1 18A	IV GENERATED AT CONTACT BETWEEN GQ21/H AND GQ22/H	1350
GQ17/P	/AV 2 18B	FV GENERATED AT CONTACT BETWEEN GQ21/H AND GQ22/H	1360
GQ23/H	/AV 1 19	PL-QZ-HB GNEISS, GRIMSAY	1420
GQ23/P	/AV 1 19A	IV CUTTING GQ23/H	1080
GQ24/H	/AV 1 20	PL-HB AMPHIBOLITE, GRIMSAY	1120
GQ24/P	/AV 1 20	IV CUTTING GQ24/H	1320
GQ27/H	/AV 1 21	PL-QZ-HB GNEISS, GRIMSAY	200
GQ25/P	/AV 1 21	FV CUTTING GQ27/H	1480

	GQ33/H	GQ34/P	GQ36/P	GQ37/H	GQ38/P	GQ39/P	GQ42/H	GQ40/P	GQ41/P	GQ43/H	GQ47/H	GQ45/P	GQ51/H	GQ49/P
SIO2	50.73	53.53	51.83	52.04	49.63	49.24	63.03	58.08	56.62	68.74	57.95	57.32	62.11	58.00
TIO2	1.25	.78	.64	.87	1.08	1.02	.68	.69	.84	.52	.85	.85	.68	.81
AL2O3	12.98	14.53	15.50	17.45	16.46	16.30	16.22	18.16	18.53	14.76	16.11	16.97	15.77	16.69
FE2O3	14.92	10.24	9.55	9.79	11.27	10.66	5.42	5.81	6.12	3.46	7.78	7.61	6.20	7.61
MNO	.27	.17	.14	.19	.20	.18	.10	.07	.09	.09	.15	.08	.08	.14
MGO	5.66	6.46	6.57	4.45	5.83	5.29	2.66	2.05	2.06	1.51	3.55	2.84	2.91	2.99
CAO	9.15	7.81	8.60	7.27	6.64	8.00	5.19	7.51	7.80	4.25	6.54	3.59	5.28	6.66
NA2O	3.35	3.76	3.83	4.26	3.62	3.73	4.88	4.88	4.94	4.59	3.91	4.52	4.30	3.72
K2O	1.07	.97	.79	2.01	2.88	2.30	1.62	1.08	1.11	1.32	1.73	2.27	1.58	1.68
P2O5	.26	.11	.09	.43	.30	.33	.17	.32	.33	.29	.25	.18	.20	.18
H2O-	.02	.01	.04	.05	.03	.26	.02	.12	.12	.02	C	.94	.03	C
LOI	.53	1.20	1.83	.76	1.34	1.90	.32	.51	.67	.28	.39	2.19	.39	.77
TOTAL	100.19	99.57	99.41	99.57	99.28	99.21	100.33	99.28	99.23	99.83	99.21	99.36	99.53	99.25
K2O/NA2O	.32	.26	.21	.47	.80	.62	.33	.22	.22	.29	.44	.50	.37	.45
MGO/K2O	5.29	6.66	8.32	2.21	2.02	2.30	1.65	1.90	1.86	1.14	2.05	1.25	1.84	1.78
K2O/CAO	.12	.12	.09	.28	.43	.29	.31	.14	.14	.31	.26	.63	.30	.25
CAO/MGO	1.62	1.21	1.31	1.63	1.14	1.51	1.94	3.66	3.79	2.81	1.84	1.26	1.81	2.23
V	321	194	139	213	199	208	92	128	ND	76	139	125	99	122
CR	82	213	ND	22	ND	ND	72	ND	ND	43	86	ND	97	ND
NI	55	140	ND	11	ND	ND	39	ND	ND	25	40	ND	38	ND
CU	109	88	ND	16	ND	ND	32	ND	ND	30	30	ND	46	ND
ZN	133	114	ND	126	ND	ND	83	ND	ND	57	114	ND	96	ND
TH	2	1	ND	2	ND	ND	1	ND	ND	1	2	ND	2	ND
RB	18	44	43	60	139	115	55	12	ND	49	53	99	49	50
SR	145	218	309	469	549	708	411	427	ND	424	393	307	420	438
Y	33	16	ND	22	ND	ND	16	ND	ND	9	38	ND	33	ND
ZR	78	65	63	145	11	79	197	103	ND	246	154	215	147	219
NB	4	3	ND	14	ND	ND	5	ND	ND	3	14	ND	13	ND
BA	139	156	137	747	63	498	430	159	ND	370	384	488	461	352
K/RB	C	183.	153.	278.	172.	166.	245.	747.	C	224.	271.	190.	268.	279.
RB/SR	C	.202	.139	.128	.253	.162	.134	.028	C	.116	.135	.322	.117	.114
TH/K	C	.0001	C	.0001	C	C	.0001	C	C	.0001	.0001	C	.0002	C

GQ33/H /AV 1 23	GT-PL-HB GNEISS, GRIMSAY	220
GQ34/P /AV 2 23	IV/QUASI-CONGLOMERATE CUTTING GQ33/H	1290
GQ36/P /AV 2 23	IV DERIVED FROM GQ34/P, CUTTING GQ33/H	1530
GQ37/H /AV 1 24	PL-HB AMPHIBOLITE, GRIMSAY	230
GQ38/P /AV 1 24	FV CUTTING GQ37/H	1670
GQ39/P /AV 1 24	IV DERIVED FROM GQ38/P, CUTTING GQ37/H	1560
GQ42/H /AV 1 25	PL-QZ-HB GNEISS, GRIMSAY	240
GQ40/P /AV 1 25	FV CUTTING GQ42/H	1540
GQ41/P /AV 2 25	FV, 37 CM FROM GQ40/P, CUTTING GQ42/H	1470
GQ43/H /AV 1 26	PL-QZ-HB GNEISS, GRIMSAY	250
GQ47/H /AV 1 26	PL-HB-QZ GNEISS, GRIMSAY	270
GQ45/P /AV 1 26	FV CUTTING GQ43/H	1690
GQ51/H /AV 1 27	PL-HB AMPHIBOLITE, GRIMSAY	310
GQ49/P /AV 1 27	FV CUTTING GQ51/H	1650

	GQ55/H	GQ53/P	GQ52/P	GQ59/H	GQ58/P	GQ57/P	QD10/H	QD11/H	QD7/P	QD2/P	QD1/P	QD16/H	QD15/P	QD17MH
SIO2	61.96	57.55	62.27	60.41	61.28	59.72	48.39	68.95	55.11	53.03	55.97	48.83	49.27	49.17
TIO2	.45	.76	.61	.62	.75	.78	.96	.31	1.25	1.08	1.01	.89	.86	1.93
AL203	15.50	15.63	16.43	14.74	15.65	15.33	13.31	15.08	13.46	13.46	14.11	14.16	13.83	12.68
FE203	6.28	9.51	4.59	7.83	6.57	7.81	13.81	2.91	12.96	13.31	10.84	13.15	12.85	16.75
MNO	.15	.15	.09	.20	.11	.15	.23	.09	.20	.19	.15	.26	.25	.24
MGO	2.28	2.74	1.55	3.48	2.37	2.80	6.04	.81	3.12	2.47	2.80	7.30	6.35	4.94
CAO	5.76	6.87	4.99	7.30	5.19	5.93	10.86	3.87	7.35	11.93	9.09	11.50	10.91	9.28
NA20	4.37	3.80	5.12	4.42	4.04	3.54	3.42	6.62	3.06	.95	2.49	2.98	3.13	3.07
K20	2.25	1.32	2.54	.89	2.04	1.87	1.02	.85	.73	.17	.36	1.07	1.04	1.14
P205	.27	.22	.23	.14	.16	.17	.11	.14	.15	.12	.13	.09	.07	.23
H20-	.02	.08	.11	.01	.26	.15	.08	.06	.14	.16	.23	.06	.10	.05
LOI	.45	.47	.87	.28	.91	1.02	.72	.82	1.72	1.91	2.03	.46	.81	.27
TOTAL	99.74	99.40	99.39	100.32	99.33	99.27	98.95	100.51	99.25	98.78	99.21	100.75	99.47	99.75
K20/NA20	.51	.49	.50	.20	.50	.53	.30	.13	.24	.18	.14	.36	.33	.37
MGO/K20	1.01	1.51	.61	3.91	1.16	1.50	5.92	.95	4.27	14.53	7.79	6.82	6.11	4.33
K20/CAO	.39	.26	.51	.12	.39	.32	.09	.22	.10	.01	.04	.09	.10	.12
CAO/MGO	2.53	2.51	3.21	2.10	2.19	2.12	1.80	4.78	2.36	4.83	3.25	1.58	1.72	1.88
V	90	161	112	161	112	121	302	35	235	242	186	285	283	353
CR	50	47	45	162	ND	ND	157	21	ND	71	ND	136	114	83
NI	27	31	23	66	ND	ND	83	13	ND	46	ND	86	77	54
CU	60	59	318	65	ND	ND	132	74	ND	68	ND	37	45	50
ZN	81	113	63	86	ND	ND	101	29	ND	123	ND	92	105	143
TH	12	10	11	3	ND	ND	4	4	ND	6	ND	4	0	6
RB	37	38	61	5	90	69	16	36	16	2	18	8	6	13
SR	411	365	388	275	334	298	145	376	363	982	754	238	255	159
Y	33	33	23	26	ND	ND	29	3	ND	27	ND	21	19	48
ZR	154	178	219	93	151	206	57	132	124	102	145	71	40	127
NB	7	8	9	9	ND	ND	5	0	ND	6	ND	6	10	21
BA	809	459	885	73	432	324	114	251	299	57	130	105	109	130
K/RB	505.	398.	346.	1478.	198.	225.	529.	196.	337.	706.	166.	1110.	1439.	728.
RB/SR	.090	.099	.157	.018	.269	.232	.110	.095	.050	.002	.024	.034	.024	.082
TH/K	.0006	.0007	.0005	.0004	C	C	.0005	.0006	C	C	C	.0005	C	C

GQ55/H	/AV 2 28	PL-QZ-FE GNEISS, GRIMSAY	320
GQ53/P	/AV 1 28	FV CUTTING GQ55/H	1370
GQ52/P	/AV 1 28	FV CUTTING GQ55/H	1510
GQ59/H	/AV 1 29	PL-QZ-FB GNEISS, GRIMSAY	290
GQ58/P	/AV 1 29	FV CUTTING GQ59/H	1550
GQ57/P	/AV 2 29	FV, 40 CM FROM GQ58/P, CUTTING GQ59/H	1520
QD10/H	/AV 1 30	PL-QZ-FB GNEISS, HOWMORE QUARRY, SOUTH UIST	80
QD11/H	/AV 1 30	PL-FB-QZ GNEISS, HOWMORE QUARRY, SOUTH UIST	90
QD7/P	/AV 1 30	IV GENERATED AT CONTACT BETWEEN QD10/H AND QD11/H	1500
QD2/P	/AV 1 30	IV GENERATED AT CONTACT BETWEEN QD10/H AND QD11/H	1360
QD1/P	/AV 2 30	IV GENERATED AT CONTACT BETWEEN QD10/H AND QD11/H	1570
QD16/H	/AV 2 31	PL-FB AMPHIBOLITE, HOWMORE QUARRY, SOUTH UIST	670
QD15/P	/AV 2 31	FV CUTTING QD16/H	1560
QD17MH	/AV 1 32	PL-FB AMPHIBOLITE, HOWMORE QUARRY, SOUTH UIST	130

	QD17FH	QD17/F	QD18/H	QD18/F	QD24/H	QD24/F	QL1/H	QL1/F	X/H	X/F	SH1/H	SH1/F	SH2/H	SH2/F
SIO2	70.57	54.97	52.77	50.89	53.19	50.15	62.79	63.49	68.62	67.00	69.18	63.63	49.48	51.29
TIO2	.26	1.41	2.09	2.10	1.98	1.87	.47	.52	.46	.47	.34	.52	1.16	1.16
AL203	15.53	13.85	12.33	12.42	12.30	12.63	14.82	14.99	15.21	15.91	13.98	15.63	18.29	16.46
FE203	2.09	12.69	16.98	17.35	16.58	16.36	5.47	5.43	3.85	4.26	6.48	7.27	17.54	14.45
MNO	.05	.20	.26	.27	.25	.28	.12	.07	.08	.07	.11	.13	.23	.19
MGO	.84	3.22	2.91	3.39	2.94	4.01	3.61	3.04	1.12	1.22	.98	2.25	7.58	6.38
CAO	3.36	7.44	8.15	8.71	7.56	9.32	5.74	4.71	3.78	3.69	4.91	5.98	4.00	6.51
NA2O	5.24	4.06	2.63	3.33	2.80	3.10	4.30	4.37	4.47	5.16	2.81	3.36	1.66	2.40
K2O	1.14	1.17	.21	.87	1.10	1.16	1.26	2.42	1.60	1.59	.31	.55	.26	.15
P2O5	.12	.18	.25	.26	.24	.21	.18	.15	.12	.17	.11	.14	.03	.07
H2O-	.04	C	.02	C	.04	.04	.06	.08	.16	.05	.10	.07	.06	.06
LOI	.32	.45	C	C	.22	C	.27	.51	.42	.62	.35	.18	.04	.66
TOTAL	99.56	99.66	99.40	99.59	99.20	99.13	99.09	99.78	99.79	100.21	99.66	99.71	100.33	99.82
K2O/NA2O	.22	.29	.29	.26	.39	.37	.29	.55	.36	.31	.11	.16	.16	.07
MGO/K2O	.74	2.75	3.59	3.90	2.67	3.46	2.87	1.26	.70	.77	3.16	4.09	29.15	35.44
K2O/CAO	.34	.16	.10	.10	.15	.12	.22	.51	.42	.43	.06	.09	.07	.03
CAO/MGO	4.00	2.31	2.80	2.57	2.57	2.32	1.59	1.55	3.38	3.02	5.01	2.66	.53	1.02
V	26	265	336	386	355	356	97	86	56	60	70	131	256	307
CR	25	55	21	28	18	56	225	116	25	22	17	40	386	213
NI	12	35	26	32	26	45	57	44	15	16	13	20	121	95
CU	31	45	117	154	88	206	21	16	16	14	10	15	6	27
ZN	37	124	142	153	132	123	67	74	68	70	71	68	93	135
TH	3	C	C	C	2	1	3	C	1	5	C	C	0	C
RB	44	36	9	C	16	19	32	81	43	59	1	2	2	3
SR	573	270	236	198	230	176	472	345	412	412	409	479	350	224
Y	2	29	42	43	49	39	11	15	5	4	5	12	66	34
ZR	177	141	175	168	172	133	118	123	81	73	85	88	521	210
NB	1	12	14	20	20	15	C	8	3	3	2	3	4	7
BA	339	194	296	242	296	223	304	489	625	669	278	364	216	149
K/RB	215.	270.	747.	803.	571.	507.	327.	248.	309.	224.	2574.	2283.	1079.	496.
RB/SR	.077	.133	.038	.048	.070	.108	.068	.235	.104	.143	.002	.004	.006	.013
TH/K	.0003	0	C	C	.0002	.0001	.0003	C	.0001	.0004	C	C	C	C

QD17FH	/AV 1 32	PL-QZ-HE GNEISS, HOWMORE QUARRY, SOUTH UIST	120
QD17/F	/AV 1 32	FV GENERATED AT CONTACT BETWEEN QD17F/H AND QD17M/H	1700
QD18/H	/AV 1 33	PL-QZ-HE GNEISS, HOWMORE QUARRY, SOUTH UIST	1400
QD18/F	/AV 1 33	FV CUTTING QD18/H	1640
QD24/H	/AV 1 33A	PL-HB AMPHIBOLITE, HOWMORE QUARRY, SOUTH UIST	1710
QD24/F	/AV 1 33B	IV CUTTING QD24/H	1330
QL1/H	/AV 1 34	PL-HB AMPHIBOLITE, CALIBURGH QUARRY, SOUTH UIST	60
QL1/F	/AV 1 34	FV CUTTING QL1/H	70
X/H	/AV 1 35	QZ-AF-PL-BT-WM-EP-SF GNEISS, RUBHA ARDVLLE, SOUTH UIST	1040
X/F	/AV 1 35	IV/FV CUTTING X/H	1010
SH1/H	/AV 2 36	PL-QZ-BT-HE GNEISS, SOUTH HARRIS	1450
SH1/F	/AV 2 36A	PLAC-MICROLITIC FV CUTTING SH1/H	1390
SH2/H	/AV 2 37	GT-FL-BT-QZ GNEISS, SOUTH HARRIS	1720
SH2/F	/AV 1 37	PLAC-MICROLITIC FV CUTTING SH2/H	1460

	G1A/H	G1A/P	CT3/H	CT3/P	SA1B/H	SA1B/P	SA2/H	SA2/P	I2/H	I2/V	I7/H	I7/V
SIO2	54.35	54.05	49.05	48.68	72.05	69.89	52.12	55.08	46.71	45.09	45.10	44.22
TIO2	1.34	1.50	1.29	1.10	.38	.48	.46	.41	3.11	2.56	.14	.54
AL2O3	13.29	13.25	13.57	13.69	14.88	14.66	15.12	14.78	14.09	13.29	4.27	13.44
FE2O3	14.16	14.39	14.35	11.93	2.35	2.95	9.70	8.54	15.34	13.79	9.42	5.62
MNO	.20	.12	.21	.19	.06	.05	.20	.13	.24	.15	.15	.11
MGO	3.15	2.83	6.40	7.79	.40	.79	7.68	6.50	4.88	7.23	36.80	17.88
CAO	7.02	3.48	8.91	8.52	2.22	2.40	12.18	10.01	11.57	11.97	4.12	16.71
NA2O	2.56	3.28	3.94	4.29	4.81	4.52	1.76	2.36	3.29	2.55	.07	.44
K2O	1.81	4.58	.57	.28	2.60	2.79	.20	.69	.59	.37	0	.01
P2O5	.19	.21	.09	.08	.12	.16	.05	.06	.37	.34	0	.01
H2O-	.06	.27	.08	.19	.04	.11	.04	.08	.01	.03	.02	.01
LOI	1.04	1.36	.45	2.39	.38	.48	.61	.62	.31	2.16	.56	.34
TOTAL	99.17	99.32	98.91	99.13	100.29	99.28	100.12	99.26	100.51	99.53	100.65	99.33
K2O/NA2O	.71	1.40	.14	.07	.54	.62	.11	.29	.18	.15	0	.02
MGO/K2O	1.74	.62	11.23	27.82	.15	.28	38.40	9.42	8.27	19.54	0	*****
K2O/CAO	.26	1.32	.06	.03	1.17	1.16	.02	.07	.05	.03	0	.00
CAO/MGO	2.23	1.23	1.39	1.09	5.55	3.04	1.59	1.54	2.37	1.66	.11	.93
V	283	291	314	269	29	41	206	168	383	341	93	331
CR	10	7	167	159	12	21	250	310	39	219	1693	1145
NI	32	32	72	76	8	13	113	129	37	136	1575	1285
CU	34	47	102	117	10	16	104	99	191	102	27	91
ZN	142	98	68	123	47	61	64	66	114	85	46	109
TH	2	3	0	0	13	11	0	6	0	0	0	0
RB	23	90	19	6	104	119	2	61	8	19	1	0
SR	433	211	214	184	410	369	107	121	514	346	4	21
Y	29	30	31	25	10	11	16	13	39	30	5	19
ZR	138	158	65	62	194	247	36	56	205	164	3	14
NB	11	13	8	5	11	15	3	2	30	24	1	0
BA	890	2446	49	26	606	667	58	175	114	67	0	0
K/RB	653.	422.	249.	387.	208.	195.	830.	94.	612.	162.	0	0
RB/SR	.053	.427	.089	.033	.254	.322	.019	.504	.016	.055	.250	0
TH/K	.0001	.0001	0	0	.0006	.0005	0	.0010	0	0	0	0

G1A/H	/AV 1 37	PL-HB-EP-SP-AP-CHL GNEISS, GAIRLOCH, N W SCOTLAND	1150
G1A/P	/AV 1 37	FV CUTTING G1A/H	1490
CT3/H	/AV 1 39	PL-HB-CPX-MT GNEISS, TIREE, SCOTLAND	1130
CT3/P	/AV 2 39	AMPHIBOLE-MICROLITIC FV CUTTING CT3/H	1340
SA1B/H	/AV 2 40	GRANITE, VREDEFORT DOME, SOUTH AFRICA	1270
SA1B/P	/AV 1 40	IV CUTTING SA1B/H	1310
SA2/H	/AV 1 40	PL-HB AMPHIBOLITE, VREDEFORT DOME, SOUTH AFRICA	1170
SA2/P	/AV 1 40	IV CUTTING SA2/H	1030
I2/H	/AV 1 43	PYROXENE GRANULITE, IVREA ZONE, LOCARNO,ITALY	1210
I2/V	/AV 1 43	CATACLASITE CUTTING I2/H	1260
I7/H	/AV 1 44	PERIDOTITE, IVREA ZONE, BALMUCCIA, ITALY	1250
I7/V	/AV 2 44A	CATACLASITE CUTTING I7/H	1600

APPENDIX A5: FeO Determinations

Sample No.	1	2	3
GQ1AH	11.51	12.79	14.63
GQ9H	11.65	12.95	14.81
GQ10H	3.32	3.69	3.41
GQ21H	2.38	2.65	2.76
GQ22H	10.46	11.62	13.33
GQ28H	8.55	9.50	12.73
GQ33P	11.72	13.02	14.92
GQ37H	7.39	8.21	9.79
GQ42H	5.27	5.86	5.42
GQ43H	2.89	3.21	3.46
GQ47FH	5.23	5.81	5.16
GQ47MH	6.87	7.63	7.78
GQ48H	6.89	7.66	6.92
GQ51H	5.77	6.41	6.20
GQ54H	3.28	3.65	4.26
GQ55H	5.77	6.41	6.29
GQ59H	6.38	7.09	7.83
G801H	6.43	7.15	7.31
G801P	6.36	7.07	7.27
G802H	7.19	7.99	7.19
G802P	5.96	6.62	6.94
G803P	5.89	6.55	7.09
G804P	6.40	7.11	7.54
G805P	6.07	6.75	7.39
G806P	6.36	7.07	7.48
G807H	4.73	5.26	6.56
HR7	0.58	0.64	2.09
HR8	0.65	0.72	2.03
QD10H	9.49	10.55	13.81
QD11H	2.10	2.33	2.91
QD14H	12.26	13.62	16.61
QD16H	9.16	10.18	13.00
QD17FH	2.24	2.49	2.09
QD17MH	16.34	18.23	16.75
QL1H	4.04	4.49	5.47
QL1P	4.48	4.98	5.43

1 FeO determined by wet chemistry.
2 Column 1 as Fe_2O_3*.
3 Fe_2O_3* by XRF.
(all values as wt.%)

Literature Data
Mean Fe_2O_3/FeO of 12 host rocks = 0.29
Mean Fe_2O_3/FeO of 12 pseudotachylytes = 0.38
data from Bhattacharjee (1963), Ermanovics(1971), Masch (1974), Philpotts (1964), Salop (1945) and Sinha-Roy (1981).

APPENDIX A6: Sample Localities

Sample	Locality	Grid Ref.
A	Kanuku Mountains, Guyana (from H.I. Drever collection, University of St Andrews)	
B1	Market Stance Quarry, Benbecula	NF806537
CT1-CT2	W coast, Tiree	NL938442
CT3	E Vaul Bay, Tiree	NM057488
E1	E coast, Eriskay	NF809124
E5	E coast, Eriskay	NF808118
G1A-G1B	Roadside cutting, Gairloch (collected by R.H. Sibson)	NG831781
G2D	Track, Gairloch (collected by R.H. Sibson)	NG860776
G801-G807	SE Grimsay coast	NF877547
GH4-GH5	Greian Head, Barra	NF653046
GL2	Rubha Meall na Hoe, S Uist	NF828169
GL8	Rubha Dubh, S Uist	NF816132
GL12	Ru Melvick, S Uist	NF832131
GQ1A-GQ27	Roadside cutting, N Grimsay	NF867571
GQ33-GQ36	Roadside cutting, N Grimsay	NF869569
GQ37-GQ39	Roadside cutting, N Grimsay	NF868570
GQ40-GQ59	Roadside cutting, S Grimsay	NF855562
LB20	Clett, S Uist	NF808223
MM2	Rubha Bolum, S Uist	NF829284
QD1-QD24	Druidibeg Quarry, S Uist	NF766355
QL1	Askernish Quarry, S Uist	NF753218
R2	Rubha Ardvule, S Uist	NF712269
R4	Rubha Ardvule, S Uist	NF711297
R7	Rubha Ardvule, S Uist (beach pebble)	NF711301
R15	Rubha Ardvule, S Uist	NF715299
SA1A	Vredefort Dome, S Africa (collected by S. White)	
SA1B	Vredefort Dome, S Africa (collected by S. White)	
SA2	Vredefort Dome, S Africa (collected by S. White)	
SA3	Vredefort Dome, S Africa (collected by P. Suddaby)	
SH1-SH3	Rodelpark, S Harris	NG056838
SV15	Piz Urschai, Silvretta Alps (Landeskarte der Schweiz 1:25000 Blatt 1198)	GR81051935
SU802	Rubha Ardvule, S Uist	NF711299
SU803	Rubha Ardvule, S Uist	NF711299

SU804	Rubha Ardvule, S Uist	NF714302
X	Rubha Ardvule, S Uist (beach pebble)	NF711301
2070	Ikertoq Shear Belt, W Greenland (collected by J. Grocott)	
11256	Langtang Valley, Nepal (from H.I. Drever collection, University of St Andrews)	

Melt origin of fault-generated pseudotachylytes demonstrated by textures

R. H. Maddock
Department of Geology
Imperial College
London SW7 2BP, England

ABSTRACT

A petrographic and electron-microprobe study of fault-generated pseudotachylytes from the Outer Hebrides Thrust Zone, Scotland, demonstrates that the textures have resulted from the *primary* crystallization of a clast-laden melt rather than the devitrification of a glass, or by crushing and cataclasis. The observations are consistent with these pseudotachylytes having formed by frictional fusion followed by rapid quenching—implying faulting at shallow crustal depths.

INTRODUCTION

Pseudotchylytes are found as planar or ramifying vein networks in many major fault zones. Texturally they are rather variable: they may be holocrystalline, devitrified, or, rarely, glassy, but many appear cryptic and subopaque in thin section. Controversy exists over the origin of pseudotachylytes and particularly over the interpretation of their microstructure and texture. Sibson (1975) has suggested that fault-generated pseudotachylytes are formed by frictional fusion during seismic slip, and although reviews of the "pseudotachylyte problem" tend to favor melting in preference to ultratrituration (Philpotts, 1964; Francis, 1972), a recent paper favors a cataclastic origin (Wenk, 1978). Here I present mineral-textural and mineral-chemical data demonstrating the primary crystallization characteristic of some holocrystalline pseudotachylytes.

The pseudotachylytes were collected from several locations west of the base of the main Outer Hebrides Thrust Zone (Sibson, 1975), which cuts Precambrian (Lewisian) amphibolite-facies quartzofeldspathic gneisses. The photomicrographs presented here are from two samples and are representative of veins varying in thickness from 1 to 10 cm.

PETROGRAPHY

The pseudotachylytes are strongly porphyroclastic, with poorly sorted and rounded clasts of quartz and plagioclase typically constituting about 25 modal % of the rock. The apparent clast size of both quartz and feldspar varies from 0.5 cm to a few tens of microns, though the smallest clasts are invariably quartz (cf. Ermanovics et al., 1971). Larger clasts include polymineralic lithic aggregates. Clasts of magnetite, sphene, zircon, and relict ferromagnesian minerals (hornblende and biotite) make up less than 1 modal % of the pseudotachylyte. The paucity of ferromagnesian clasts is typical of pseudotachylytes.

The textural and mineralogical features of the porphyroclasts demonstrate incomplete equilibration during melting. Plagioclase porphyroclasts have melt-corroded rims and exhibit incipient to advanced melting along fractures (Fig. 1A) together with grain and subgrain boundaries—fingerprint textures peculiar to feldspars in buchites (Al-Rawi and Carmichael, 1967). Quartz clasts display similarly corroded margins (Fig. 1B). Ferromagnesian phases have broken down to produce showers of magnetite grains (Fig. 1C), again typical of buchites. In the absence of P_{H_2O} data, it is difficult to estimate the temperature of the melt, but the almost complete assimilation of the ferromagnesian clasts and partial assimilation of quartz and feldspar clasts implies a temperature of about 1,000 °C or greater.

The pseudotachylyte matrix comprises microlitic feldspar set in an ultra-fine-grained groundmass of chiefly plagioclase, quartz, biotite, and magnetite. The salient characteristics of the matrix feldspars are summarized in Table 1 and Figures 1 and 2. Every gradation exists from filled tabular forms to feldspars of highly skeletal and inequant shape, reflecting actual variation and apparent variation due to the sectioning process. The dominant form of the larger plagioclases is a skeletal-prism morphology; elongation parallel to (010) being more pronounced in the finer grained forms. Heterogeneous nucleation of the microlites on plagioclase, but not quartz, porphyroclasts is ubiquitous. Feldspars with these morphologies are typically found in submarine-quenched ocean-floor basalts (Bryan, 1972a) and as run products of dynamic crystallization experiments (Lofgren, 1974).

Fan and plumose spherulites (Lofgren, 1971a) composed of plagioclase intergrown with biotite extend from the blunt terminations of many of the microlites (Fig. 1F). Much of the finest groundmass, interstitial to the porphyroclasts and neocrystallized plagioclase, is composed of ultra-fine-grained (< 1 μm) plagioclase, quartz, and biotite, resolvable only by transmission electron microscopy (Fig. 1H).

Dendritic and granular magnetite (Figs. 1G and 1F, respectively) has also crystallized from the melt during rapid crystallization. Nucleation of the opaque phases on the feldspar microlite margins indicates late-stage precipitation of the former, late-stage dendritic opaques being common in rapidly chilled igneous rocks (Tiller, 1964).

Some or all of the above textural features have been described in fault-generated pseudotachylytes from Norway (Dietrichson, 1953), Canada (Philpotts, 1964), Greenland (Grocott, 1977), and Australia (Allen, 1979).

TABLE 1. CHARACTERISTICS OF PSEUDOTACHYLYTE MATRIX FELDSPARS

Crystal morphology:	Square tabular	Lath tabular	Acicular	Spherulitic
Maximum dimensions (m)	40 x 40	36 x 50	200 x 20	200 x 2
Maximum growth parallel to	(010), (001)	(010)	(010)	(010)
Composition	An_{25-45}	An_{25-45}	An_{25-45}	An_{22-25}
Form	Chiefly filled	Skeletal, filled	Skeletal, filled	-
Twinning	Albite, Pericline	Albite, Pericline	Albite, Pericline	-
Zoning	Sector, normal	Sector, normal	-	-
Example	Fig.2b	Fig.1d	Fig.1b,1e	Fig.1f

Note: terminology after Lofgren (1974)

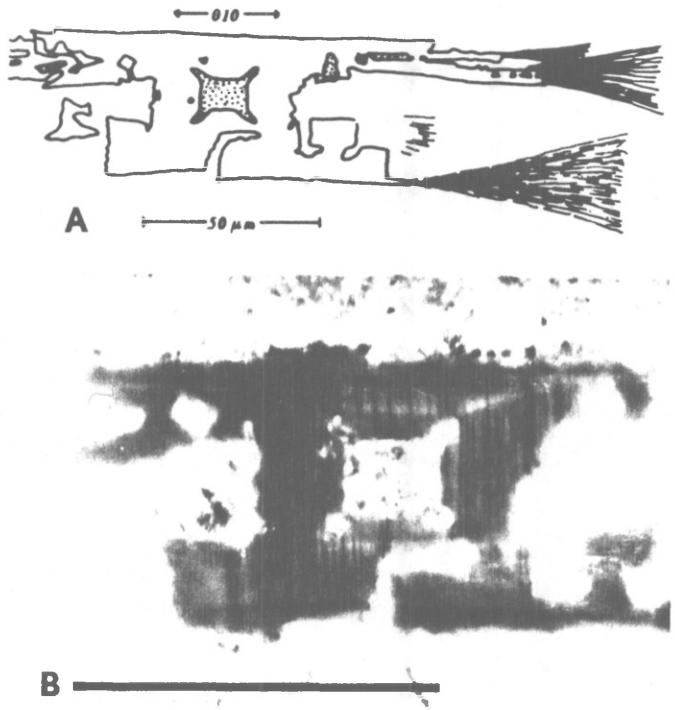


Figure 2. (A) Compound skeletal plagioclase showing three phases of growth: central tabular part of primary growth; secondary growth stage of skeletal acicular plagioclase elongated parallel to (010); and tertiary growth stage of fan-spherulite (mainly plagioclase) drawn from photograph. (B) Detail of central part of same crystal showing albite and pericline twinning, sector and normal zoning, and crystallographically controlled form of melt inclusion; scale bar = 50 μm.

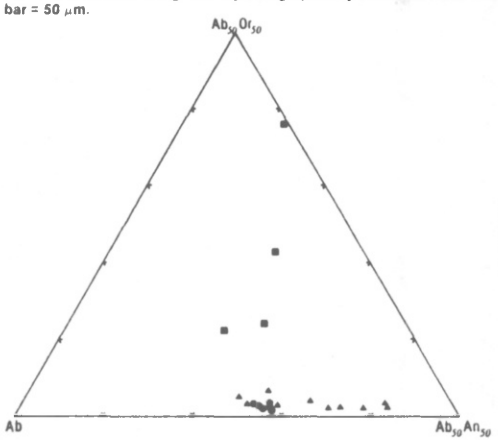


Figure 3. An-Ab-Or diagram. Dots = porphyroclasts; triangles = groundmass laths; squares = microlites from enclave within lithic porphyroclast.

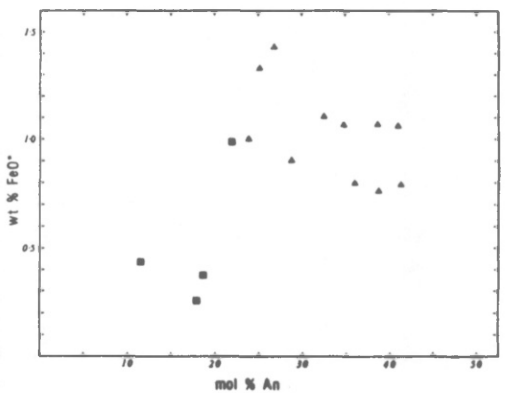


Figure 4. Plot of mol % An versus wt % FeO* (symbols as for Fig. 3).

FELDSPAR CHEMISTRY

The composition of representative feldspar porphyroclasts and microlites (analyzed by energy-dispersive electron microprobe) are plotted on an An-Ab-Or diagram in Figure 3. The plagioclase porphyroclasts all fall within a small field of oligoclase composition (An_{25}–An_{30}). The microlites span a much larger compositional range, from calcic oligoclase to calcic andesine (An_{25}–An_{45}). A few of the microlites analyzed plot in the alkali feldspar field; such microlites are always within enclaves in lithic porphyroclasts with relict biotite. The small size of the microlites did not allow determination of the compositional zoning, but the optical misorientation is slight and suggests variation of only a few mol % An.

All the feldspars have unusually high Fe content (up to 1.5 wt % FeO*) (Fig. 4). In many cases high concentrations of Fe in feldspars can be attributed to the presence of exsolved phases or mechanical impurities (Smith, 1974). However, examination of the microlites by high-magnification (up to ×2,300) back-scattered electron imagery in a scanning electron microscope and by concomitant X-ray analysis indicates that the microlites are homogeneous. The Fe must therefore be lattice bound. Such high Fe contents in naturally occurring plagioclases are restricted to lunar (Crawford, 1973) and ocean-floor (Bryan, 1972b) examples. Examination of the stoichiometry of the pseudotachylyte plagioclases does not allow obvious assignment of the Fe to either the tetrahedral or the octahedral sites.

The high Fe content of the microlites

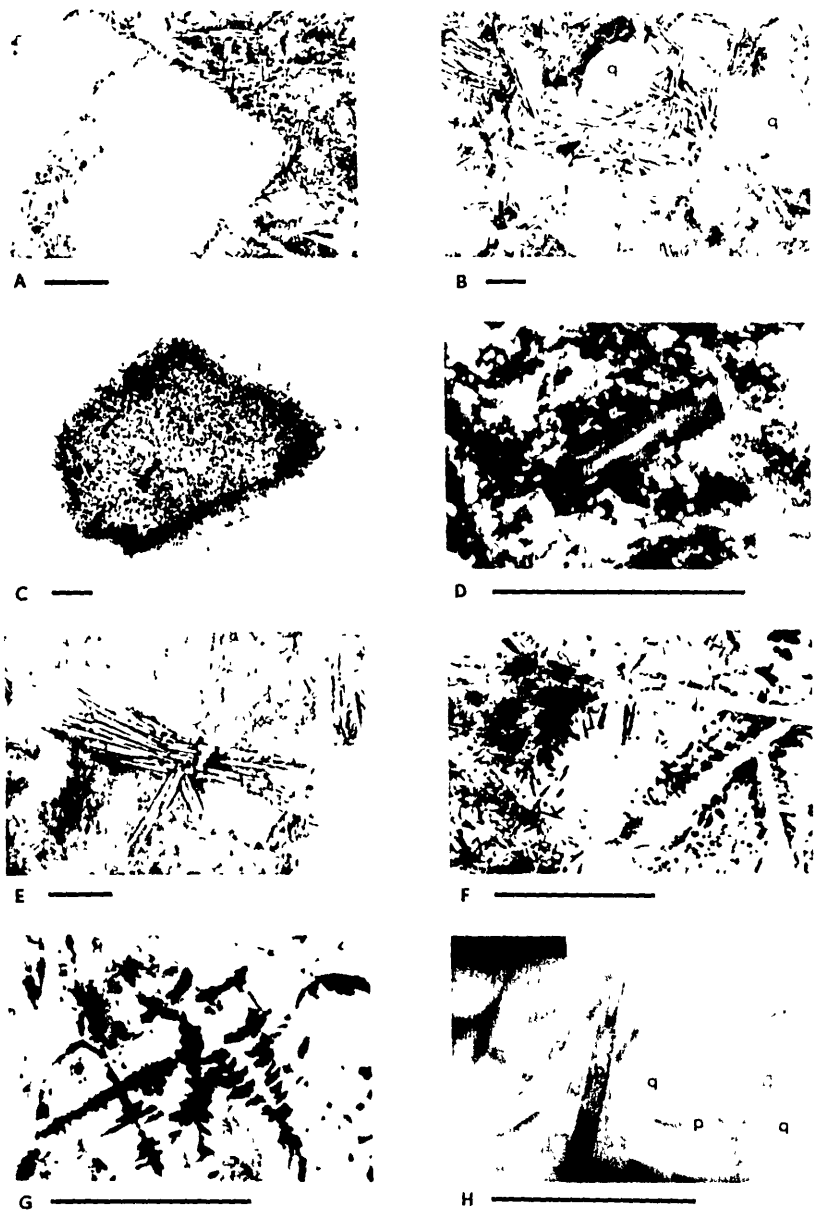


Figure 1 (A) Incipiently melted plagioclase porphyroclast showing fingerprint texture and mantle of new plagioclase. (B) Incipiently melted quartz clasts and new skeletal acicular plagioclases. (C) Disequilibrium melted biotite being replaced by magnetite. (D) Tabular zoned plagioclase lath. (E) Skeletal acicular plagioclases (F) Plumose fan-spherulite projecting from blunt termination of acicular plagioclase microlite fringed by magnetite (G) Dendritic opaques showing cruciform and "Christmas-tree" morphology (H) Transmission electron micrograph of finest groundmass between microlites, q = quartz, p = plagioclase, b = biotite. For A through G, scale bar = 100 μm For H, scale bar = 1 μm.

complements the morphological evidence for fast crystallization at rapid cooling rates, a poor correlation between Fe content and Ab component and morphology suggests that chemical and probably heat fluxes were strongly heterogeneous during the freezing of the melt-clast system

DISCUSSION

The composition, distribution, and melting of the porphyroclasts has governed the nucleation and growth of new phases from the melt and therefore had an overriding control on the texture of these pseudotachylytes Chemically specific heterogeneous nucleation dominated Heterogeneous nucleation tends to reduce the critical undercooling (ΔT) required for nucleation to occur because the surface energy of solid-solid interfaces is usually less than that of solid-liquid interfaces (Dowty, 1980), particularly if nucleation is epitaxial Heterogeneous nucleation also reduces the incubation time required for nucleation to occur once the requisite undercooling is attained The consequence of this is that in a rapidly chilled melt-clast system, such as the pseudotachylyte, nucleation can be expected to begin at relatively smaller values of ΔT, and growth can be expected to continue over a greater temperature range than would be the case for a homogeneous clast-free melt cooling at the same rate Thus, a greater variety of crystal morphologies is possible

The plagioclase morphologies listed in Table 1 from left to right reflect crystallization at increasingly greater values of ΔT The compound form of the plagioclase crystal in Figure 2A is directly analogous to the run products of isothermal drop experiments (cf. Lofgren, 1974) where the charge is repeatedly rapidly chilled and held at successively greater values of ΔT Crystallization of the pseudotachylytes may therefore also have occurred in stages at successively lower temperatures

It is extremely difficult to discriminate between primary spherulitic crystallization and spherulitic devitrification of glass (Lofgren, 1971b) Devitrification is much enhanced by the presence of fluids at high temperature (Marshall, 1961) The pseudotachylytes do not show extensive evidence for abundant fluid activity at high temperature causing devitrification The feldspars (clasts and microlites) are fresh, and perlitic cracks are absent Closely spaced parallel microjoints cutting the pseudotachylyte, although sometimes healed by chlorite and epidote, are generally barren and cut both microlites and spherulites This suggests that the spherulitic crystallization was primary and that glass may never have been present in these particular pseudotachylytes A corollary of this is that the presence or absence of glass should not be a prerequisite in identifying or classifying pseudotachylytes

The pseudotachylyte textures and the interpretation of them presented here differ considerably from those described by Wenk (1978), which include a sample from the same Hebridean locality The fault rocks described by Wenk, although having a field habit similar to that of pseudotachylyte, would seem to be better described as cataclasites (in the sense of Sibson, 1977) formed by fracture and crushing Textural similarities appear to be restricted to the finest quartz-feldspar microstructure (compare Fig 1H of this paper with Fig 3d of Wenk, 1978) Whereas Wenk attributed the equant fine-grained structure to the recrystallization of highly deformed regions, I suggest that the texture shown in Figure 1H is due to the final crystallization of the melt (interstitial to the feldspar microlites), or possibly devitrification of a glass

CONCLUSIONS

It appears that the inhomogenous texture of these pseudotachylytes has resulted from the rapid crystallization, largely of feldspar, from a clast-laden melt Nucleation was generally heterogeneous, and crystal growth varied The most important factor affecting the texture was the initial composition, density, and distribution of porphyroclasts prior to cooling Crystallization took place in a system that was "poorly stirred" with respect to chemical and, probably, heat fluxes The cooling rate was sufficiently slow (and nucleation sufficiently rapid) that glass probably did not form, but sufficiently rapid that strongly disequilibrious feldspar morphologies and chemistries resulted

The textures and microstructures described here support the idea that fault-generated pseudotachylytes are formed by frictional fusion at shallow depth, rather than by crushing and cataclasis Cataclasites formed by the latter processes may, however, occur in association with pseudotachylytes (Sibson, 1977)

REFERENCES CITED

Allen, A R , 1979, Mechanism of frictional fusion in fault zones Journal of Structural Geology, v 1, p 231–243

Al-Rawi, Y , and Carmichael, I S E 1967, A note on the natural fusion of feldspars American Mineralogist, v 52, p 1806–1814

Bryan, W B , 1972a, Morphology of quench crystals in submarine basalts Journal of Geophysical Research, v 77, p 5812–5819

— 1972b, Mineralogical studies of submarine basalts Carnegie Institution of Washington Yearbook 71, p 396–403

Crawford, M L , 1973, Crystallization of plagioclase in mare basalts Lunar Science Conference, 4th, Proceedings, p 705–717

Dietrichson, B , 1953, Pseudotachylit fra de kaledonske Skyvesoner i Jotenheimens forgarder, Gudbrandsdalen og deres dannelsbetingelser Norges Geologiske Undersokelse [Skrifter], v 184, p 23–70

Dowty, E , 1980, Crystal growth and nucleation theory and the numerical simulation of igneous crystallization, *in* Hargraves, R B , ed , Physics of magmatic processes Princeton, New Jersey, Princeton University Press, p 419–485

Ermanovics, I F , Helmstaedt, H , and Plant, A G , 1971, An occurrence of Archaean pseudotachylyte from southeastern Manitoba Canadian Journal of Earth Sciences, v 9, p 257–265

Francis, P W , 1972, The pseudotachylyte problem Comments on Earth Sciences – Geophysics, v 3, p 35–53

Grocott, J , 1977, The northern boundary of the Ikertoq shear belt, west Greenland [Ph D thesis] Liverpool, University of Liverpool

Lofgren, G E , 1971a, Experimentally produced devitrification textures in natural rhyolitic glass Geological Society of America Bulletin, v 82, p 111–124

— 1971b, Spherulitic textures in glassy and crystalline rocks Journal of Geophysical Research, v 76, p 5635–5648

— 1974, An experimental study of plagioclase crystal morphology Isothermal crystallization American Journal of Science, v 274, p 243–273

Marshall, R R , 1961, Devitrification of natural glasses Geological Society of America Bulletin, v 72, p 1493–1520

Philpotts, A R , 1964, Origin of Pseudotachylytes American Journal of Science, v 252, p 577–614

Sibson, R H , 1975, Generation of pseudotachylyte by ancient seismic faulting Royal Astronomical Society Geophysical Journal, v 43, p 775–794

1977, Fault rocks and fault mechanisms Geological Society of London Journal, v 133, p 191–213

Smith, J V , 1974, Feldspar minerals, Volume 2 New York, Springer-Verlag, 690 p

Tiller, W A , 1964, Dendrites Science, v 146, p 871–879

Wenk, H R , 1978, Are pseudotachylytes products of fracture or fusion? Geology, v 6, p 507–511

ACKNOWLEDGMENTS

Reviewed by J Grocott, J Nolan, and R H Sibson Supported by a Natural Environment Research Council research studentship G Lloyd performed the back-scattered electron imagery at the Centre for Materials Science, University of Birmingham The thin sections were skillfully prepared by A Jones Electron microscope facilities at Imperial College are assisted by Natural Environment Research Council Grant GR33848 I thank C Holloway for assistance

Manuscript received July 8, 1982
Revised manuscript received October 22, 1982
Manuscript accepted October 27, 1982

Elsevier Scientific Publishing Company P.O. Box 330, Amsterdam
Printed
Page 3 1st proof 173
IN ALL CORRESPONDENCE CONCERNING THIS PAPER REFER TO
TEC01443
AUTHOR

Tectonophysics, 128 (1986) TEC01443
Elsevier Science Publishers B.V., Amsterdam – Printed in The Netherlands

Discussion

FRICTIONAL MELTING IN LANDSLIDE-GENERATED FRICTIONITES (HYALOMYLONITES) AND FAULT-GENERATED PSEUDOTACHYLYTES–DISCUSSION

R.H. MADDOCK

Department of Geology, Royal School of Mines, Imperial College, London SW7 2BP (England)

(Received July 10, 1985; accepted March 25, 1986)

Masch and co-authors (1985) have presented evidence documenting frictional melting in the landslide-generated frictionites (hyalomylonites) of Köfels, Austrian Alps and Langtang, Nepal Himalaya. Their integrated approach utilizing electron petrography combined with microprobe analysis, analytical transmission electron microscopy (TEM) and conventional bulk chemical analysis is to be welcomed in the study of ultra-fine-grained fault-rocks. However, their conclusions are largely directed towards rejecting a frictional melting origin for fault-generated pseudotachylytes. This author contends that this is unwarranted and unsupported by published data.

Firstly the absence of glass in pseudotachylytes is used in their paper, and in others by one of the co-authors (Wenk, 1976, Weiss and Wenk, 1983), as evidence against frictional melting during pseudotachylyte generation. At least two reasons make the preservation of glass in pseudotachylytes unlikely (1) Many pseudotachylytes have a plagioclase-microlitic texture which has been inferred to indicate primary crystallization from a melt (e.g. Philpotts, 1964, Maddock, 1983) (2) The majority of pseudotachylytes described in the literature are tens or hundreds of millions of years old, and were generated at depths corresponding to higher P–T conditions than those for landslide frictionites. Thus time, heat energy and water—*the essential requirements for devitrification of glass* (Marshall, 1961) — are available to pseudotachylytes, whereas only water may be available to landslip frictionites which have been generated at depths of a few hundred metres within the last twenty thousand years or so. Significantly, glass is illustrated in a TEM micrograph of Alpine Fault Zone (New Zealand) pseudotachylyte (Sibson et al., 1981 fig. 3c p. 201), which may be as young as 0.5 Ma (R.H. Sibson, pers. commun., 1983).

Secondly, Masch et al suggest that feldspar microlites found in pseudotachylytes could result from metamorphic neo-/re-crystallization rather than crystallization from a melt, citing as an example albite crystallites in Silvretta (Alps) pseudotachylytes. In microlitic pseudotachylytes from Canada (Philpotts, 1964) and the Outer

0040-1951/86/$03.50 © 1986 Elsevier Science Publishers B.V.

Hebrides Thrust (Sibson, 1975, Maddock, 1983) the chemistry (An_{20}–An_{40}) skeletal habit and/or the structural state of the plagioclase (intermediate) are compelling evidence for primary crystallization from a melt phase. Clearly, post-generation metamorphism, alteration or deformation of pseudotachylyte is possible and may mask primary crystallization or devitrification textures (cf. Sibson, 1980, Troushek and Huber, 1982, Passchier, 1982).

Thirdly Masch et al note that frictional melting on the soles of landslides involves displacements which are three orders of magnitude greater than, and displacement rates which are two orders of magnitude greater than those associated with seismic/pseudotachylyte faulting. This is however misleading with respect to the rate of frictional heat generation which is a function of both displacement rate and shear stress. The rate of frictional heat generation per unit area, Q, is given by (e.g., Sibson, 1975)

$$\dot{Q} = \tau_f v \qquad (1)$$

where τ_f is the average frictional shear resistance during slip and v the average slip rate. For the simple case of slip on a dry horizontal fault plane the frictional shear resistance may be expressed as (Sibson, 1975)

$$\tau_f = \mu_k \sigma_n = \mu_k \rho g z \qquad (2)$$

where μ_k is the kinetic coefficient of friction, σ_n the normal stress across the fault plane, ρ the density, g the acceleration due to gravity and z the depth to the fault plane. Using this model with $\mu_k = 0.15$ Scholz (1980) estimated a value of 1.9 MPa for τ_f during slip on the Langtang landslide. Since pseudotachylyte is probably generated at depths at least an order of magnitude greater than landsliding, eqn. 2 predicts that τ_f should be an order of magnitude greater during pseudotachylyte faulting than landsliding. The theoretical studies of McKenzie and Brune (1972) and Cardwell et al. (1978) suggested that frictional heating sufficient to cause melting during (dry) earthquake faulting is possible for reasonable values of frictional shear resistance and displacement or displacement rate.

Additional evidence supporting a frictional melting origin for fault-generated pseudotachylytes includes the occurrence of partially melted porphyroclasts (Maddock, in prep.) and amygdales which occur in both plagioclase-microlitic and phyllosilicate-spherulitic textured pseudotachylytes (e.g., Philpotts, 1964, Beckholmen, 1982).

In conclusion, this author considers that the majority of published data on pseudotachylytes overwhelmingly supports an origin by frictional melting. The call by Masch and co-workers, for further experimental and analytical work on pseudotachylytes is, however, welcomed. Additionally there is a need for a consensus approach to the definition and terminology of pseudotachylyte, particularly in view of the varied hypotheses which have been proposed for the type locality pseudotachylytes of the Vredefort Dome (Shand, 1916).

ACKNOWLEDGEMENTS

The author's studies on pseudotachylytes were undertaken whilst in receipt of a NERC research studentship. The author is presently supported by NERC grant GR3/5109.

REFERENCES

Beckholmen, M., 1982. Mylonites and pseudotachylytes associated with thrusting of the Koli Nappes, *Taasfors/sket*, central Swedish Caledonides. Geol. Fören. Förh., 104: 23–32.
Cardwell, R.K., Chinn, D.S., Moore, G.F. and Turcotte, D.L., 1978. Frictional heating on a fault zone with finite thickness. Geophys. J.R. Astron. Soc., 52: 525–530.
Troushek, A. and Huber, M., 1982. Pseudotachylyte zones in the Leventina gneiss (Lepontine Alps, Ticino, Switzerland). Schweiz. Mineral. Petrogr. Mitt., 62: 313–325.
Maddock, R.H., 1983. Melt origin of pseudotachylytes demonstrated by textures. Geology, 11: 105–108.
Marshall, R.R., 1961. Devitrification of natural glasses. Geol. Soc. Am. Bull., 72: 1493–1520.
Masch, L., Wenk, H.R. and Preuss, E., 1985. Electron microscopy study of hyalomylonites—evidence for frictional melting in landslides. Tectonophysics, 115: 131–160.
McKenzie, D. and Brune, J.N., 1972. Melting on fault planes during large earthquakes. Geophys. J.R. Astron. Soc., 29: 65–78.
Passchier, C.W., 1982. Pseudotachylyte and the development of ultramylonite bands in the Saint-Barthelemy massif, French Pyrenees. J. Struct. Geol., 4: 69–79.
Philpotts, A.R., 1964. Origin of pseudotachylyte. Am. J. Sci., 262: 1008–1035.
Scholz, C.H., 1980. Shear heating and state of stress on faults. J. Geophys. Res., 85: 6174–6184.
Shand, S.J., 1916. The pseudotachylyte of Parijs (OFS), and its relation to trap-shotten gneiss and fluaty crush rock. Q.J. Geol. Soc., 72: 198–221.
Sibson, R.H., 1975. Generation of pseudotachylyte by ancient seismic faulting. Geophys. J.R. Astron. Soc., 43: 775–794.
Sibson, R.H., 1980. Transient discontinuities in ductile shear zones. J. Struct. Geol., 2: 165–171.
Sibson, R.H., White, S.H. and Atkinson, B.K., 1981. Structure and distribution of fault rocks in the Alpine Fault zone, New Zealand. In: K.R. McClay and N.J. Price (Editors), Thrust and Nappe Tectonics. Geological Society London, pp. 197–210.
Weiss, L.E. and Wenk, H.R., 1983. Experimentally produced pseudotachylyte-like veins in gabbro. Tectonophysics, 96: 299–310.
Wenk, H.R., 1976. Are pseudotachylytes products of fracture or fusion? Geology, 6: 507–511.

Min. Abh. 27

Neues Jahrbuch Miner. Abh.	■		000 - 000	Stuttgart, ■ 1986

Partial melting of lithic poryphyroclasts in fault-generated pseudotachylytes

By

R. H. Maddock, London

With 11 figures and 5 tables in the text

Maddock, R. H.: Partial melting of lithic porphyroclasts in faultgenerated pseudotachylytes – Neues Jahrbuch Miner. Abh. ■: 000 - 000, Stuttgart 1986

Abstract: Partially melted (s.l.) lithic porphyroclasts contained in fault generated pseudotachylytes have been examined by scanning electron microscopy (SEM) and microprobe analysis. Selective fusion/breakdown of hydrous ferromagnesian phases in the porphyroclasts suggests that melting occurred at temperatures in excess of 750 °C, and under vapour poor conditions. These observations provide further evidence for a melt origin for pseudotachylytes and may be pertinent to initial melting studies of anatexis.

Key words: Pseudotachylyte, initial melting, frictional fusion, Lewisian Gneiss, scanning electron microscopy

Introduction

Fault-generated pseudotachylytes are widely believed to form by frictional fusion during seismic (i.e. earthquake) faulting at depths of 2–15 km (Sibson, 1975, Watts & Williams, 1980, Passchier, 1982). In many examples unequivocal evidence of the presence of melt is demonstrated by igneous textures, for example plagioclase microlites or amygdales, in the pseudotachylyte groundmass (e.g. Philpotts, 1964, Maddock, 1983). Alternatively, it has been suggested that pseudotachylytes form principally by cataclastic deformation not involving melting (e.g. Wenk, 1978). This proposal has been argued for briefly on the basis of the examination and interpretation of ultrafine grained pseudotachylytes whose groundmasses are apparently devoid of obvious igneous textures (e.g. Wenk, 1978; Weiss & Wenk, 1983, Masch et al., 1985).

The purpose of this contribution is to describe the mineralogy and texture of partially melted porphyroclasts in 2 examples of ultrafine grained pseudotachylytes from classic localities in NW Scotland. The particular samples were chosen because the polymineralic composition of the porphyroclasts yields considerable information on the processes and conditions of melting.

0077-7757/86/0000-0000 $ 0.00
© 1986 E. Schweizerbart'sche Verlagsbuchhandlung, D-7000 Stuttgart 1

Sample Localities. The pseudotachylytes were sampled from the Outer Hebrides Thrust (OHT) and the crush belts of the Gairloch area, both of which affect the Archaean Lewisian Gneiss of NW Scotland. The OHT is believed to have been active in a thrust sense, with generation of pseudotachylyte, during Caledonian times (Sibson, 1977), and later reactivated as an extensional fault (Smythe et al., 1982). Pseudotachylytes from the OHT have been described in greatest detail by Jehu and Craig (1926, and companion papers referenced therein) and Sibson (1975). The Hebridean sample was collected from a steeply-dipping E–W trending vein cutting paragneiss, just W of the base of the main thrust, on the island of Grimsay near North Uist (G.R. NF877547). The NW-trending crush belts of the Gairloch area are late Laxfordian in age (Park, 1964). The pseudotachylytes were noted by Clough (1907), who termed them "flinty crush rocks", and their optical petrography has been described in some detail by Park (1961). The Gairloch sample was collected, by R. H. Sibson from a vein cutting gneiss in a roadside quarry (G.R. NG831781).

Method of Study. Under the microscope, the partially melted porphyroclasts appear virtually opaque and structureless in conventional 30 μm thin sections. Therefore, polished thin sections were examined using an JEOL 73 SEM fitted with a Link Systems energy dispersive X-ray analyser. The SEM was operated in the backscattered electron (BSE) imaging mode, providing mean atomic number contrast images (Hall and Lloyd, 1981). XRF whole-rock analyses were obtained using fused glass discs and a Phillips PW1212 wavelength dispersive machine following the method of Parker (1982). A thousand points were counted for each modal analysis.

Table 1. Chemical compositions of host-rocks and pseudotachylyte veins as determined by X-ray fluorescence spectrometry

	Outer Hebrides		Gairloch	
	host	vein	host	vein
SiO_2	60.06	60.67	54.35	54.05
TiO_2	0.63	0.60	1.34	1.50
Al_2O_3	16.53	16.92	13.29	13.25
Fe_2O_3*	7.19	6.94	14.16	14.39
MnO	0.12	0.10	0.20	0.12
MgO	4.36	4.21	3.15	2.83
CaO	3.44	3.94	7.02	3.48
Na_2O	3.82	3.32	2.56	3.28
K_2O	2.43	2.20	1.81	4.58
P_2O_5	0.27	0.15	0.19	0.21
H_2O^-	0.05	0.15	0.06	0.27
LOI	0.66	0.94	1.04	1.36
Total	99.56	100.14	99.17	99.32

Description

Outer Hebrides Sample. The host-rocks to the pseudotachylyte are medium grained homogeneous paragneisses, of tonalitic composition (Table 1), whose modal mineralogy is given in Table 2. The paragneiss has a weak foliation largely defined by the dimensional-preferred orientation of biotite (Fig. 1). The foliation-parallel pseudotachylyte vein, up to 3 cm thick, has a brown, fine grained matrix with a texture varying from globulitic to spherulitic. Optical microscopy, microprobe analysis, and analytical transmission electron microscopy indicate that the groundmass is largely composed of plagioclase, quartz, biotite and chlorite (Maddock, in prep.). It is believed that this groundmass is largely devitrified glass. The composition of the pseudotachylyte vein, including clasts, is almost identical to the host-rock (Table 1), demonstrating that it is derived from the surrounding host-rock.



Fig. 1. Backscattered electron (BSE) micrograph of host-rock paragneiss containing quartz (q), plagioclase (p) and biotite (b). Pseudotachylyte vein is labelled v. Outer Hebrides sample

The vein contains abundant quartz and feldspar porphyroclasts, a few lithic clasts, but no biotite porphyroclasts. The lithic clasts range in size up to 4 mm. A typical example is shown in Fig. 2, where the porphyroclast can be seen to be made up of 3 phases or assemblages: (i) plagioclase, (ii) quartz, (iii) zones composed of an assemblage of plagioclase microlites with minor sulphides and accessory phases, poikilitically enclosed by biotite and minor chlorite. A rather similar "external" zone mantles the entire porphyroclast (Figs. 2 and 3).

The internal microlitic zones constitute approximately 40 modal % of the porphyroclasts – i.e. slightly more than the modal proportion of biotite in the host-rock/protolith (Table 2; compare Figs. 1 and 2). The texture of the internal zones is shown in detail in Figs. 3 and 4. The plagioclase microlites ($8 \times 100\,\mu m$ max) are heterogeneously nucleated on the original plagioclase

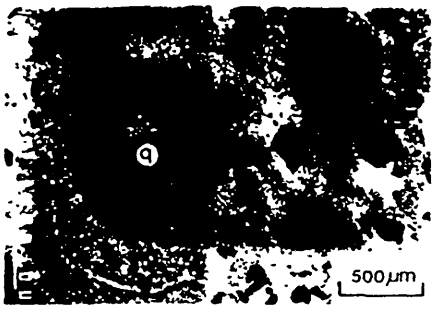


Fig 2 BSE micrograph of partially melted porphyroclast. Note distribution of microlitic melt zones (m) and absence of large biotite grains. Outer Hebrides sample



Fig 3 Detail of Fig. 2 showing relict quartz grains with sulphide blebs (bright) along microfractures, and contact between porphyroclast melt zones (m) and pseudotachylyte vein (v) marked by dashed line

grains of the lithic clast The margins of the plagioclase grains show slight enrichment in CaO (Fig 4) extending over distances of $<5\,\mu m$ This is believed to be due to either fractional melting or, "plating on" of new, more An-rich plagioclase Semi-quantitative analyses of the plagioclase microlites (their fine grain size precluded fully quantitative analysis) indicates that they are also more An-rich than the relict plagioclase grains (Table 3) Interstitial to the microlites is a non-pleochroic, freckly brown substrate with a texture varying from ill-defined spherulitic to platy, with optically recognizable plates of birefringent biotite ($<10\,\mu m$ dia) In the SEM this poikilitic matrix is found to be dominantly biotite with minor chlorite, sulphides and accessory phases The

sent in the host-rock Additionally, the quartz microfractures are decorated by minute blebs ($<5\,\mu m$ dia.) of sulphide.

2 Gairloch Sample The host-rock to this sample is a fine grained (?para-) gneiss whose composition is shown in Table 1 and modal mineralogy in Table 4 The pseudotachylyte vein (1 cm thick) has a well-developed spherulitic texture (Fig 6), also believed to have resulted from devitrification of a glass As in the previous sample, quartz and feldspar clasts are abundant but ferromagnesian mineral clasts are very scarce.

The scarce lithic clasts are typically ovoid, up to 3 mm in length, with their long axes aligned parallel to the vein margins and the host-rock foliation A typical example is shown in Fig. 7. *With the exception of hornblende and chlorite,*

Table 3 Electron microprobe analyses of mineral phases, Outer Hebrides sample

	1	2	3	4	5
SiO_2	59 61	56 57	37 06	38 44	26 77
TiO_2	0 00	0 00	2.88	1 89	0 00
Al_2O_3	25 62	25 79	16 59	16 95	19 37
FeO	0 00	0 38	15 15	14 44	20 38
MnO	0 00	0 00	0 00	0 00	0 00
MgO	0 00	0 00	14 10	13 95	19 09
CaO	7 44	8 71	0 00	0 07	0 00
Na_2O	6 71	5 63	0 00	0 28	0 40
K_2O	0 20	0.39	9 87	9 73	0 00
Total	99 58	97 47	95 65	95.75	86 01

1 Mean of 4 analyses of relict plagioclase grains.
2 Plagioclase microlite.
3 Mean of 6 analyses of host-rock biotites.
4 Mean of 6 analyses of new poikiloblastic biotite.
5 Chlorite in porphyroblast.



Fig. 5. Detail of Fig. 2 showing reacted zircon within melt zone which has recrystallized to a spherulitic habit.

biotite contains less TiO_2 but greater SiO_2 and Al^{iv} than the host biotite (Table 3) Amongst the accessory phases, zircon is of particular interest. Whereas in the pseudotachylyte groundmass proper, grains of zircon are simply darker coloured relative to those in the host-rock, the zircons in the porphyroclast have sufferred reaction and complete recrystallization to a spherulitic habit (Fig 5)

Table 2 Modal composition (volume %) of Outer Hebrides host-rock and experimentally melted gneiss of Winkler (1967)

	1	2	3
Quartz	23 5	26	21
Plagioclase	38 8	43	45
Biotite	28 0	31	30
Garnet	8 9	–	–
Opaque	0 8	–	–
Plagioclase composition	An_{38}	An_{38}	An_{21}

1 Host rock, Outer Hebrides
2 Same normalized to quartz + plagioclase + biotite = 100 %
3 Experimentally melted gneiss of Winkler (1967, p 215)

The microlitic habit and general texture of these zones indicate that they were once molten The external melt zones contain essentially the same phases as the internal zones, but the crystallites tend to exhibit a more platy habit (Fig 3)

Both the (relict) quartz and plagioclase grains show extensive brittle microfracturing and moderate to strongly undulose extinction, which are not pre-

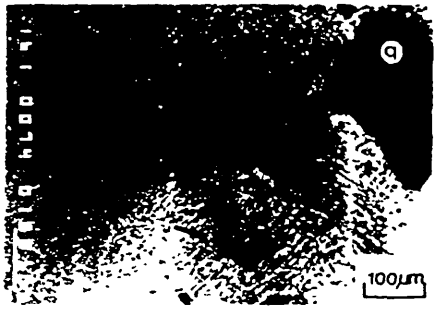


Fig 4 Detail of Fig 2 showing plagioclase microlites heterogeneously nucleated on relict grains of plagioclase which have An-enriched margins (arrowed)

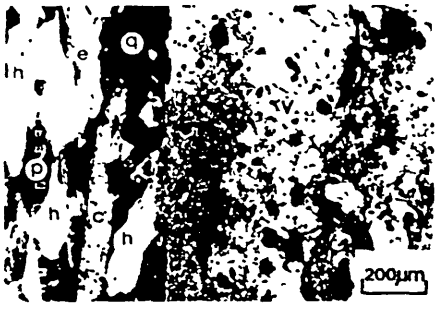


Fig 6 BSE micrograph showing contact between spherulitic pseudotachylyte vein (v) and host rock containing quartz (q), microperthite (k), hornblende (h), epidote (e) and chloritized hornblende (c) Gairloch sample.

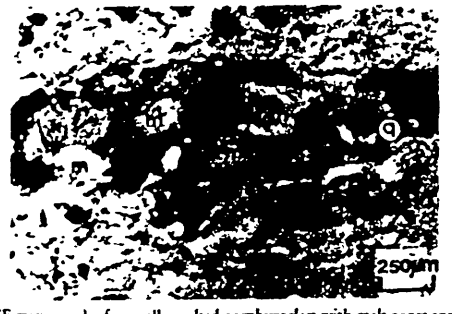


Fig. 7 BSE micrograph of partially melted porphyroclast with melt zones annotated m. Gairloch sample.

all of the phases present in the host rock (Table 4) occur with *broadly* similar habits, grain sizes and modal abundances in the lithic porphyroclast (Fig. 7). The inferred former sites of hornblende and chlorite are now occupied by fine grained, texturally and mineralogically complex zones – an analagous relationship to that of biotite in the previous sample. The fine grained zones are composed of epidote + chlorite + muscovite + sphene + magnetite + K-spar + plagioclase, varying in grain size from 1–30 μm (Figs. 8, 9 and 10). Their habit varies from platy/decussate, especially phyllosilicates and epidote, to dendritic/microlitic form favoured by sphene, magnetite and feldspar (Fig. 9). Analyses of some of the phases are given in Table 5. As in the previous sample un-

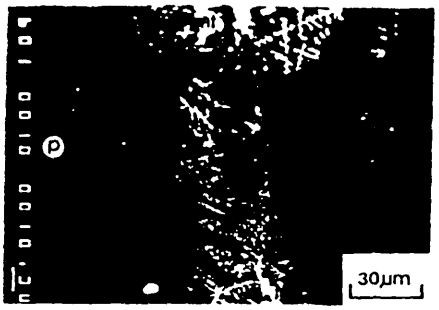


Fig 8 Detail of Fig. 7 showing fine grained melt zone within enclave in feldspar, composed of dendritic sphene (s) and magnetite (mt), epidote (e) and muscovite (mu)



Fig. 9 Detail of Fig 7 showing microlitic plagioclase heterogeneously nucleated on relict feldspar grain at margin of porphyroclast.

expected textures are shown by the accessory phases. In Fig 10 a relict grain of sphene is fringed (epitaxially?) by heterogeneously nucleated microlites of newly grown sphene; both have the same composition (Table 5)

These zones are also considered to be former melt zones, now largely devitrified glass, though the feldspar, sphene and magnetite microlites and dendrites may have grown directly from the melt

The relict quartz and plagioclase grains show brittle deformation features comparable to he last sample, although the microfractures are undecorated The plagioclase in both host-rock and clasts is heavily sericitized, in the latter however, it has a marked brown discolouration – perhaps due to exsolution of hematite, though this could not be resolved in the SEM

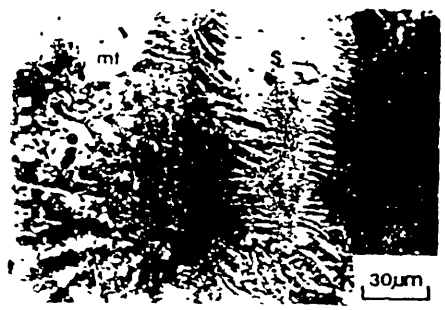


Fig 10 Detail of Fig 7 showing relict sphene (s) rimmed by sphene microlites and surrounded by a fine grained matrix of epidote, muscovite, magnetite and chlorite.

Discussion

The textures of the lithic porphyroclasts in these two pseudotachylytes indicates that melting occurred as a consequence of heat derived from the surrounding pseudotachylyte melt and transported over distances < 1000 μm.

In both examples melting was initiated at and advanced to the greatest degree, in and around sites formerly occupied by hydrous ferromagnesian minerals (principally biotite and hornblende). Also in both cases, feldspar has been 'wetted' by the melt to a greater degree than quartz (e g. Fig. 4). Selective fusion of hydrous ferromagnesian phases and preferential "melt-wetting" of feldspar relative to quartz has been observed in granitic and arkosic xenoliths in basalt (Ackermann & Walker, 1960; Al-Rawi & Carmichael, 1967, Sigurdsson, 1968) In these examples the temperature of the melt was about 1000 °C The pseudotachylyte porphyroclasts differ from the xenoliths, in that of the usual solid residua resulting from incongruent melting of biotite and hornblende, i e olivine pyroxene and magnetite, only magnetite is seen in the porphyroclasts

A number of partial melting experiments on granitoid/gneissic rocks, with mineralogies appropriate to the pseudotachylyte host-rocks/lithic clasts, are

Table 4 Modal composition (volume %) of Gairloch host-rock

Quartz	15 1
Plagioclase	19 6
Microperthite	12 4
Hornblende	36 2 (part chloritized)
Epidote	11 3
Sphene	3 0
Magnetite	2 4

Table 5 Electron microprobe analyses of mineral phases, Gairloch sample

	1	2	3	4	5
SiO_2	29 58	28 88	46 78	28 69	61 68
TiO_2	38 36	38 86	0 17	0 00	0 00
Al_2O_3	1 15	1 25	32 63	19 16	18 30
FeO	0 68	1.38	4 55	22 19	1 97
MnO	0 00	0 00	0 00	0 65	0 00
MgO	0 00	0 00	0 90	14 57	0 26
CaO	28 82	27 18	0 00	0 24	0 40
Na_2O	0 34	0 00	0 40	0 00	0 98
K_2O	0 00	0 00	10 24	0 00	14 11
Total	98 93	97 55	95 67	85 50	97 70

1 Relict sphene (Fig 10)
2 Sphene microlite (Fig. 10)
3 Muscovite (Fig 10)
4 Chlorite (Fig. 10)
5 K-spar microlite (Fig 9) – also contains BaO

pertinent to he porphyroclast observations In experiments where $P_{H_2O} = P_{total} \geq 200$ MPa, "equilibrium" partial melting begins at quartz + K-spar + plagioclase or quartz + plagioclase (K-spar absent) grain boundaries, breakdown or melting of hydrated ferromagnesian phases does not occur until higher temperatures are reached (e.g Mehnert et al , 1973, Büsch et al , 1974, Arzi, 1978, van der Molen & Paterson, 1979) In the ternary system, quartz + K-spar + plagioclase, at $P_{H_2O} = P_{total} = 200$ MPa, minimum melts may form at temperatures ≥ 670 °C, depending on the Ab/An ratio of the plagioclase (Winkler, 1967). In contrast to the above experiments, when $P_{H_2O} < P_{total}$ partial melting is delayed until higher temperatures are reached and is initiated in and around hydrated ferromagnesian phases (e g Auer et al., 1981, Paquet et al , 1981) These observations also concur with phase equilibria studies. Nanev (1983) for example, has shown that the thermal stability of biotite and hornblende increase as water is added to a granitoid system at $P_{H_2O} < P_{total} = 200$ MPa.

In general, such studies indicate that for confining pressures in the range 200–400 MPa (appropriate to equivalent depths of pseudotachylyte generation), dry melting of granitoid rocks requires temperatures 100–300 °C greater than melting under water-saturated conditions (e g. Brown & Fyfe, 1970).

Comparison of the textures seen in the lithic porphyroclasts and those of the above experimental studies strongly suggests that melting in the clasts occurred with $P_{H_2O} < P_{total}$. It is specifically noted that many quartz + plagioclase + microperthite triple point grain boundaries in the Gairloch sample are unwetted by melt (Fig. 7). If these observations are correct, then it may be further inferred that the pseudotachylyte melt itself was also undersaturated with respect to H_2O. Otherwise, the easy ingress of vapour allowed by mechanically and thermally induced fractures should have allowed "wet" initial melting. A

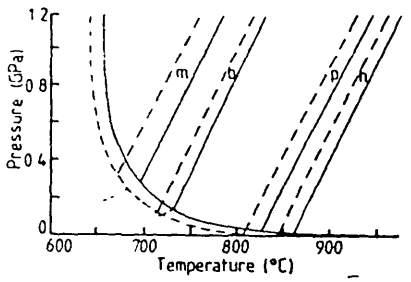


Fig 11 The beginning of melting of dry granitic (dashed lines) and dioritic (solid lines) mixtures resulting from the decomposition of muscovite (m), biotite (b), phlogopite (p) and hornblende (h) Water saturated solidus curves for granitic and dioritic mixtures also shown, after Brown & Fyfe (1970)

further consequence of dry melting is that heat transport from the surrounding pseudotachylyte melt must have been conductive rather than convective. Given the low thermal conductivity of silicates, a considerable overshoot must have existed between the temperature of the pseudotachylyte melt and the maximum temperature achieved by the porphyroclasts.

A generalized P–T diagram indicating the beginning of melting of granite and granodiorite mixed with various hydrated phases is shown in Fig. 11. Assuming $P_{total} \leq 200$ MPa, temperatures in excess of 740 and 860 °C should have been attained in the centres of the Hebridean and Gairloch samples, respectively The influence of much lower confining pressures (considered unlikely) and hydrated phase solid-solution are difficult to assess.

A further constraint on the *minimum* temperature of melting of the Hebridean sample may be made by comparison with experimental data reported by Winkler (1967) In this experiment, a biotite gneiss of similar mineralogy and chemistry to the host-rock of the Hebridean sample (Table 2) was melted at $P_{H_2O} = P_{total} = 200$ Mpa. Melting began at 690 °C and 50 % melt was formed at 720 °C Noting the higher An-content of the pseudotachylyte host-rock plagioclases (Table 2), more refractory behaviour would be expected in the latter compared to the experimental sample. During *dry* melting of a biotite gneiss at a confining pressure of 210 MPa, Nedelec & Paquet (1981) found that melting began at 770 °C.

In both the porphyroclast examples, formation of a melt phase has been assisted by water released during dehydration/breakdown of hydrous ferromagnesian minerals. Additionally, it may be anticipated that a $KAlSi_3O_8$ component released by biotite in the first sample and microperthite in the second, should tend to lower the liquidus temperature of any melt forming (Winkler, 1967, p. 214)

The textures of the accessory phases, zircon and sphene, suggest partial dissolution in the surrounding melt followed by heterogeneous nucleation and growth of new spherulitic/microlitic forms. Corrosion of these rather refractory phases, not seen in the main pseudotachylyte vein, may have been assisted by unusual local melt compositions in the porphyroclasts. Since a high proportion of the rare earth elements (RLE) and U reside in accessory phases such as zircon and sphene, the melting behaviour of these phases is of crucial importance in trace element, RLE and isotopic petrogenetic studies (cf. Harrison & Watson, 1983).

Conclusions

1. Lithic porphyroclasts in two fault-generated pseudotachylytes show evidence of selective breakdown and fusion of hydrous ferromagnesian phases, principally biotite and hornblende. By analogy with experimental studies of partial melting, this suggests that melting occurred under vapour-poor conditions (this could be tested by suitable experiments).

2. Partial melting of the porphyroclasts probably occurred at temperatures in excess of 750 °C. The bulk of the pseudotachylyte melt (i.e. the vein) must have been substantially hotter, perhaps 850–1000 °C.

3. Reaction of normally refractory phases (zircon and sphene) may have resulted from unusual local melt compositions. If this occurs widely during anatectic melting it will be significant in trace element, REE and isotopic petrogenetic studies.

Acknowledgements

R. G. Park provided details of field localities in Gairloch. The supervision and field assistance of J. Nolan and R. H. Sibson is gratefully acknowledged. M. Fowler kindly commented on an initial draft of this paper. This work was carried out whilst the author was in receipt of a NERC research studentship. The author is presently supported by NERC grant GR3/5109.

References

Ackermann, P. B. & Walker, F. (1960). Vitrification of arkose by Karoo dolerite near Heilbron, Orange Free State. – J. Geol. Soc., 116: 239–254.

Al-Rawi, Y. & Carmichael, I. S. E. (1967). A note on the natural fusion of granite. – Amer. Miner., 52: 1806–1814.

Arzi, A. A. (1978). Fusion kinetics, water pressure, water diffusion and electrical conductivity in melting rock, interrelated. – J. Petrol., 19: 153–169.

Auer, F., Beaucheimer, H. & Oehlschlegel, G. (1981). Steady state creep of fine grain granite at partial melting. – J. Geophys., 49: 89–92.

Brown, G. C. & Fyfe, W. S. (1970). The production of granitic melts during ultrametamorphism. – Contr. Mineral. Petrol., 28: 310–318.

Busch, W., Schneider, G. & Mehnert, K. R. (1974). Initial melting at grain boundaries. Part II. Melting in rocks of granodioritic, quartzdioritic and tonalitic composition. – N. Jb. Miner. Mh., 1974, 8: 345–370.

Lithic porphyroclasts in fault generated pseudotachylytes 13

Clough, C. T. (1907). In the geological structure of the north west Highlands of Scotland. – Mem. Geol. Surv. Great Britain.

Hall, M. G. & Floyd, G. F. (1981). The SEM examination of geological samples with a semiconductor backscattered electron detector. – Amer. Miner., 66: 362–368.

Harrison, T. M. & Watson, E. B. (1983). Kinetics of zircon dissolution in granitic melts of variable water content. – Contr. Mineral. Petrol., 84: 66–72.

Jehu, T. J. & Craig, R. M. (1926). Geology of the Outer Hebrides, Part 3. – North Uist and Benbecula. – Trans. Roy. Soc. Edin., 17: 419–441.

Maddock, R. H. (1983). Melt origin of pseudotachylytes demonstrated by textures. – Geology, 11: 105–108.

Masch, L., Wenk, H. R. & Preuss, E. (1985). Electron microscopy study of hyalomylonites – evidence for frictional melting in landslides. – Tectonophys., 115: 131–160.

Mehnert, K. R., Busch, W. & Schneider, G. (1973). Initial melting at grain boundaries of quartz and feldspar in gneisses and granulites. – N. Jb. Miner. Mh., 1973, 4: 165–183.

van der Molen, I. & Paterson, M. S. (1979). Experimental deformation of partially-melted granite. – Contr. Mineral. Petrol., 70: 299–318.

Naney, M. T. (1983). Phase equilibria of rock forming silicates in granitic systems. – Amer. J. Sci., 283: 993–1033.

Nedelec, A. & Paquet, J. (1981). La fusion naturelle et experimental de la biotite de gneiss du Haut Allier (Massif Central). – C. R. Acad. Sci. Paris, 292: 1283–1286.

Paquet, J., Francois, P. & Nedelec, A. (1981). Effect of partial melting on rock deformation: experimental and natural evidences on rocks of granitic compositions. – Tectonophys., 78: 545–565.

Para, R. G. (1961). The pseudotachylyte of the Gairloch district, Ross-shire, Scotland. – Amer. J. Sci., 259: 542–550.

– (1964). The structural history of the Lewisian rocks of Gairloch, Wester Ross, Scotland. – J. Geol. Soc., 120: 397–433.

Parker, R. J. (1982). Single pass X-ray fluorescence analysis of silicate rock samples using a Phillips 1212 spectrometer. – X ray Spectrom., 11: 100–108.

Passchier, C. W. (1982). Pseudotachylyte and the development of ultramylonite bands in the Saint Barthelmy massif, French Pyrenees. – J. Struct. Geol., 4: 69–79.

Philpotts, A. R. (1964). Origin of pseudotachylytes. – Amer. J. Sci., 262: 1008–1035.

Sibson, R. H. (1975). Generation of pseudotachylyte by ancient seismic faulting. – Geophys. J. R. Astron. Soc., 43: 775–794.

– (1977). Fault rocks and fault mechanisms. – J. Geol. Soc., 133: 191–213.

Sigurdsson, H. (1968). Petrology of acid xenoliths from Surtsey. – Geol. Mag., 105: 440–451.

Smythe, D. K., Dobinson, A., McQuillin, R., Brewer, J. A., Matthews, D. H., Blundell, D. J. & Kelk, B. (1982). Deep structure of the Scottish Caledonides revealed by the MOIST reflection profile. – Nature, 299: 338–340.

Watts, M. J. & Williams, G. D. (1980). Fault rocks as indicators of progressive shear deformation in the Guincamp region, Brittany. – J. Struct. Geol., 1: 323–332.

Weiss, L. E. & Wenk, H. R. (1983). Experimentally produced pseudotachylyte-like veins in gabbro. – Tectonophys., 96: 299–310.

Wenk, H. R. (1978). Are pseudotachylytes products of fracture or fusion? – Geology, 6: 507–511.

Winkler, H. G. F. (1967). Petrogenesis of metamorphic rocks. Springer, New York, 237 p.

Manuscript received by the editor September 12, 1985, ready for print November 8, 1985.

VESICLES, AMYGDALES AND SIMILAR STRUCTURES IN FAULT-GENERATED PSEUDOTACHYLYTES

R. H. Maddock, Department of Geology, Royal School of Mines, Imperial College, London SW7 2BP.

J. Grocott, School of Geological Sciences, Kingston Polytechnic, Penrhyn Road, Kingston upon Thames KT1 2EE, England.

M. van Nees, Instituut voor aardwetenschappen, Budapestlaan 4, 3508 TA Utrecht, Netherlands.

Accepted for publication in Lithos

Abstract

Fault-generated pseudotachylytes from Scotland, Greenland and elsewhere contain amygdales whose presence and mineral assemblages may be used to infer limits to the depth of generation and subsequent geological history of these rocks. Using published data relating vesicle abundance and solubility functions for H_2O and CO_2 to pressure, a palaeoseismic depth estimate of about 1.6 km is inferred for the Greenland pseudotachylytes described in this paper. Other 'filled cavities', resembling amygdales in form and mineralogy, are *recognized as replacement pseudomorphs after porphyroclasts.*

Introduction

Fault-generated pseudotachylytes (hereafter simply termed pseudotachylytes) are believed to form by frictional melting during earthquake faulting, predominantly in cold dry crystalline rocks (Sibson, 1975), although an essentially cataclastic origin has also

been proposed (Wenk, 1978). They form at depths ranging from perhaps in excess of 15 km, where the dominant mode of deformation is ductile (*e g.* Sibson, 1980, Passchier, 1982), to as little as 0 5 km - for example along the Alpine Fault zone, New Zealand (R H. Sibson, pers. comm., 1982). Pseudotachylytes which can be shown unequivocally to have cooled from a melt (e.g. Philpotts, 1964, Maddock, 1983) occasionally contain amygdales, permitting refinement of estimates of depth of generation - i.e. palaeoseismic depths according to the model of Sibson (1975). More commonly however pseudotachylytes are non-amygdaloidal but are intensely jointed, the joints being visible in thin-section as healed microfractures A third type of structure resembling a filled cavity, results from in-situ alteration and replacement of porphyroclasts, forming pseudomorphs which may superficially resemble amygdales The purpose of this contribution is to describe the form and mineralogy of these structures in an attempt to deduce certain environmental conditions (temperature, fluid composition and especially confining pressure) during and after pseudotachylyte generation.

Method of Study

Polished thin sections of pseudotachylyte were examined optically and by scanning electron microscopy (SEM) operating in the backscattered electron (BSE) mode, which is particularly well-suited to study of these fine-grained and mineralogically heterogeneous rocks (cf. Hall and Lloyd, 1981). Quantitative and semi-quantitative mineral analyses were obtained in the SEM and a Cambridge Instruments Microscan V electron microprobe, both fitted with Link Sysytems energy-dispersive X-ray analysers Both instruments were operated at

15 kV excitation voltage and a beam current of - uA, well characterized mineral standards were analyzed at the same time as the samples.

Sample Localities

The pseudotachylytes of this study were collected from the Outer Hebrides Thrust (OHT), NW Scotland and the Ikertoq Shear Belt, W Greenland. Both of these major fault zones have a long history of deformation and contain abundant pseudotachylyte, cataclasite and mylonite series faultrocks

The OHT cuts Lewisian Gneisses and the pseudotachylyte faulting probably occurred during Caledonian times (Sibson, 1977a), the main thrust was subsequently reactivated as a major extensional fault (Smythe et al., 1982) A suite of amygdaloidal pseudotachylytes were collected from a sub-vertical quasiconglomerate vein complex (see Sibson, 1975 for terminology) cutting amphibolite facies quartzofeldspathic gneiss at Rubha Ardvule, South Uist (Grid reference NF7130), some 8 km W of the main thrust base The NW-trending, sub-vertical pseudotachylytes at this locality antedate gently E-dipping vein systems (Maddock, in prep) Amygdaloidal pseudotachylytes have not previously been reported from the OHT, their reported absence having been used to infer a minimum depth of generation of 2 km (cf Sibson, 1975)

The Ikertoq Shear belt is a major shear zone in which the main displacements occurred in the period 2700-1650 Ma, when the gneisses in the belt were reworked under amphibolite and granulite facies conditions (Bak et al., 1975; Grocott, 1979). Since then the shear belt has been reactivated several times (Watterson, 1975). In the N

part of the belt, where material for this study was collected, palaeomagnetic data from seven sites point to a late Proterozoic reactivation of the belt, either at ca. 1220 Ma or at ca 600 Ma (Piper, 1981a). Unfortunately the palaeomagnetic data cannot discriminate between these results, and although Piper (op. cit) believes the latter age to be that of pseudotachylyte formation, his arguments are equivocal

The gneisses of the shear belt are cut by a suite of kimberlite and lamproite dykes (Scott, 1981) Field relationships between faults on which pseudotachylyte was generated and certain lamproite dykes in the northern part of the shear belt clearly show that faulting and dyke intrusion were contemporaneous The field relationships between pseudotachylyte faults and kimberlite dykes are not yet known, although incorrect observations have unfortunately been published (Piper, 1981b, p 172). Lamproite dykes from elsewhere in the belt yield an age of 1227 + 12 Ma (Smith, 1979), but the range of published ages for rocks of the W Greenland carbonatite-lamproite-kimberlite suite is so large (Larsen et al., 1983), that one hesitates to discriminate between the possible palaeomagnetic ages on this evidence

The pseudotachylyte of this study lies along the contact between a biotite tonalitic gneiss and the pipe-like intrusion of the kimberlite-lamproite suite described by Scott (1981, pages 5 and 18). The pseudotachylyte cuts the pipe, but is believed to have been generated in the tonalitic gneiss. Detailed descriptions of the pseudotachylytes at the northern boundary of the shear belt are given by Grocott (1977, 1981).

Description and Mineralogy of Structures

Amygdales, Outer Hebrides Thrust

The pseudotachylyte veins, 3 cm in maximum thickness, have a plagioclase-microlitic texture indicating primary crystallization from a silicate melt (Maddock, 1983). The veins contain approximately 20 modal % porphyroclasts of brittly deformed quartz and plagioclase. The amygdales vary from almost perfectly circular (believed spherical in 3D) to elliptical with increasing size over the range 20 - 200 um maximum dimension. The larger elliptical examples are flattened parallel to the vein walls and have maximum aspect ratios of 2 (thin-section cut normal to vertical dip of vein) There is no evidence of microlite nucleation on the vesicle walls, but locally the microlite long axes are aligned parallel to the elongation of the vesicles. Segregation vesicles (Smith, 1967) were not observed. The modal proportion of amygdales is 3 - 5% and they are randomly distributed apart from being absent within 1 mm of the vein margin.

The mineralogy of the amygdales is shown in Table 1. Each amygdale contains 3 - 7 subhedral grains of one or more of the 'essential' phases which occupy most of the volume and exhibit quasi-drusy habit; the 'accessory' phases occupy the grain boundaries and inclusions within the essential phases (Plate 1). Extreme modal mineralogical variation from one amygdale to another is considered prima facie evidence that they are indeed amygdales and not immiscible silicate liquid droplets (cf. Roedder, 1979, p.44). In amygdales where quartz or alkali-feldspar dominate, sometimes to the total exclusion of all other phases (e.g. Plate 1H), substantial optical misorientation exists between the grains but there is no optical evidence of strain. Little chemical variation in essential or

accessory phases exists within or between amygdales.

The accessory phases occur in varying proportions and restricted combinations, neither of the pairs actinolite and biotite or magnetite and sulphide were observed coexisting in the same amygdale. Epidote 2 is found as laths (10 x 40 um max) within epidote 1 (Plate 1A and B), and contains up to 10 wt.% CeO and LaO substituting for CaO - estimated from semi-quantitative analyses (Fig. 1c). Actinolite perhaps the most abundant accessory phase, occurs as needles (15 x 100 um max.) which are included within and cross without deflection, grain boundaries between the major phases (Plate 1C and D). This textural relationship implies growth of actinolite and subsequent inclusion within the other phases. The actinolite approaches end-member composition (Fig. 1a) containing very low Al_2O_3 and total alkalis. Laths and plates of biotite have an average composition shown in Table 1, but some of the grains are partially chloritized.

Pyrite, the most abundant opaque phase, sometimes achieves dimensions comparable to the essential phases (Plate 1E and F) Magnetite occurs as small, rounded grains to 40 um diameter. Both pyrite and magnetite are altered marginally and along grain boundaries to a brown/red Fe-hydroxide of bladed habit

In one amygdale, a large angular grain of plagioclase of composition similar to the porphyroclasts (Fig 1b) was found (Plate 1G). The origin of this grain is uncertain, although it appears to contain inclusions of actinolite, it seems most likely that it is a clast that was trapped during vesiculation.

The amygdale walls vary from sharp boundaries to narrow zones (<10 um wide) of replacement/alteration of the pseudotachylyte matrix by the phases within the amygdale proper

The pseudotachylyte is cut by two generations of microfractures

The earliest microfractures (<10 um wide) appear to have been healed, mainly by K-spar, contemporaneously with the infilling of the amygdales. However, a minority of the amygdales are seen to be connected to microfractures. A later set of microfractures (up to 100 um wide), demonstrably postdates the infilling of the amygdales and are healed by a xenoblastic intergrowth of albite and K-spar (Fig. 1b)

Porphyroclast Replacement Pseudomorphs, Outer Hebrides Thrust

Porphyroclast replacement pseudomorphs are distinguished from amygdales by their more irregular form and generally larger dimensions. In the amygdaloidal pseudotachylytes described above, incipient marginal alteration of the plagioclase porphyroclasts to epidote + clinozoisite + sericite + calcite has occurred especially adjacent to the microfractures. Similar marginal alteration of porphyroclasts has been noted by Philpotts (1964) (see Table 3).

In a more general sense, the pseudomorphs are best developed in pseudotachylytes with a high content of chlorite in their groundmass (probably devitrified glass) and with a high density of microfractures The petrography and mineralogy of one example (in a non-amygdaloidal pseudotachylyte) is shown in Plate 2C and D. The plate shows a porphyroclast largely replaced by a rim of fibrous chlorite enclosing plates of weakly ferroan calcite, 200 um across and with finely saw-toothed grain boundaries. Detailed examination in the SEM/microprobe reveals that the chlorite is replacing actinolitic hornblende and that the calcite includes small grains of quartz (Plate 2D). The concentric pattern of replacement could result from nucleation effects or partial dissolution followed by void infilling,

or both. Chlorite healed microfractures occur in close proximity to the replacement pseudomorph (Plate 2C).

Amygdales, Ikertoq Shear Belt

The pseudotachylyte vein, up to 1.5 cm thick is conspicuously zoned The central zone is brown and spherulitic with amygdales, the marginal zones are for the most part black and opaque and lack amygdales The volume fraction of amygdales is 3 - 5%, and the lower figure is used in subsequent calculations The amygdales show aspect ratios up to 10 or more, perhaps resulting from simple shear or flattening of the still hot and viscous pseudotachylyte.

The larger amygdales (Plate 2A and B) contain a zoned arrangement of chiefly carbonate minerals whose composition is given in Table 2. The pattern of zonation from amygdale centre to margin follows an increasingly complex mineralogy and decreasing grain size The overall structure suggests vesicle infilling with nucleation dominating over growth initially (marginal zone) followed by growth dominating over nucleation (axial zone) Similar patterns, and indeed mineralogies, are frequently seen in vug and pore-space cementation and are explicable in terms of changing substrate structure and chemistry during crystallization Growth of non-carbonate phases (barite, celadonite and magnetite) in the amygdales may have been relegated to grain boundary environments for similar reasons The dolomite is presumably secondary - perhaps after calcite, although no porosity increase is apparent It is not clear whether the zoning in the dolomite is 'primary' (i e it formed during growth of the dolomite) or a later exsolution feature.

Celadonite, distinguished from glauconite by the former's

and van Nes, 1986 in prep.). One important source parameter is the drop in shearing stress in the plane of the fault during slip, and this parameter is limited during shallow earthquakes by the lithostatic pressure. If a method can be found whereby the formation depth of amygdaloidal pseudotachylyte can be estimated, the path would be open to more straightforward determination of palaeoseismic source parameters, and the search for scaling relationships between such source parameters could begin. In this section the possibilities for determining the depth of formation of pseudotachylyte using amygdales are reviewed, and a depth estimate is made for the Greenland pseudotachylyte described in detail in this paper.

In an unconfined igneous system it may be possible to estimate the depth of lava eruption on the sea floor if vesiculation has occurred (e.g. Moore, 1965, 1979). Bubbles form in the magma when the partial fictive vapour pressure of a dissolved gas phase exceeds the liquid pressure. They will only be preserved if this condition is maintained until the magma is largely solidified. In an unconfined body this can occur when the magma has access to the sea floor, and the liquid pressure is hydrostatic. The volume fraction of bubbles which form in a melt depends on the liquid pressure, temperature, the mass fraction of each gas phase and the solubility function of each gas phase (Macpherson, 1984).

Pseudotachylyte generation zones have no access to the surface and are thus confined systems. However, amygdaloidal pseudotachylyte is not uncommon (Table 3), and it is necessary to consider the circumstances in which the partial fictive vapour pressure of one or more of the gas phases could exceed the liquid pressure, at least transiently, in confined systems. Generation of pseudotachylyte on fault surfaces involves rapid, near-total, non-equilibrium melting

(unpublished data of one of us (RHM) suggests that a degree of selective melting can occur during pseudotachylyte genesis). For rocks of tonalitic composition, melting will involve a volume increase of about 12% (Clark, 1966). Consequently a high liquid pressure will tend to develop in the melt on the fault surface, but is limited by the strength of the surrounding rocks.

Veins of pseudotachylyte occur in three settings within pseudotachylyte generation zones; as lenses on non-planar generation surfaces, as veins which dilate pre-existing second order fractures and as injection veins (Grocott, 1981) Injection veins occupy simple extensional fractures and are commonly observed to have left planar pseudotachylyte generation surfaces at right angles. When melt is generated, liquid pressure (P_{liq}) may exceed lithostatic pressure (P_{lith}) due to volume change. (It is clear from field relationships that melt may continue to be generated on fault surfaces in spite of the expected reduction in friction.) If the differential stress is small, P_{liq} may approach a value of $-P_{lith} + t'$, where t is the tensile strength (Fig. 2a) When extension failure occurs, P_{liq} will fall and it is assumed that vesiculation occurs at this stage in the injection vein. Preservation of bubbles is favoured by rapid solidification of pseudotachylyte veins which are rarely wider than one or two cm.

In order to determine the depth of formation of amygdaloidal pseudotachylyte, data on the mass fraction of each gaseous component and their solubility functions are required. Solubility functions for H_2O in basalt and andesite at 1100 C have long been available (Hamilton et al., 1964), and more recently the solubility functions for CO_2 in basalt and andesite have been determined (Harris, 1981, Spera and Bergman, 1980). Macpherson (1984) makes use of these data to

predict the volumes of vesicles in submarine basalts, and his model may be used conditionally as a palaeodepth indicator if vesicle volume fractions are known. One problem with the method concerns the use of one solubility function for a wide range of basalt compositions, and there is certainly disagreement over the applicability of the results of Hamilton et al (1964) to all andesite compositions (Sakuyama and Kushiro, 1979). The results of Hamilton et al (1964) are difficult to apply to pseudotachylyte of andesitic composition formed at relatively shallow levels in the crust, because the solubility function for water in andesite is poorly defined at low pressures Furthermore pseudotachylyte liquids may easily become superheated On the other hand, Spera and Bergman (1980) show that the solubility of CO_2 is similar in both tholeiitic and andesitic melts at low pressures especially when the temperature exceeds 1450 C In addition solubility of CO_2 is almost independent of temperature in andesitic magma at pressures below 4 kb.

With these results and reservations in mind, the solubility functions for basalt may be applied to the pseudotachylytes of this study, noting that even at pressures below 1 kb the solubility of water in andesite is not more than double that in basalt. Provided differences in the solubility function for CO_2 in andesite and basalt are indeed low under conditions relevant to amygdaloidal pseudotachylyte, use of basalt solubility data on the pseudotachylytes studied here should provide a depth estimate to within a factor of two or three This estimate will be improved as more solubility data becomes available.

The mass fraction of gaseous components originally in solution can be obtained from analysis of the country rocks of the pseudotachylyte since near-total non-equilibrium melting was involved.

negligible Al^{VI} content (Buckley et al., 1978), occurs as verdant wispy laths to 75 x 15 um maximum dimensions (Plate 2B) Analyses of this phase contain less than 8 formula units Si per 22 O and little or no Al (Table 2) suggesting that some of the (inferred) Fe^{3+} might be tetrahedrally coordinated. Celadonite is also found as an alteration product after biotite in the pseudotachylyte matrix and in the host-rock.

Carbonate and barite bearing microfractures intersect some of the amygdales with textures clearly demonstrating coeval filling of both structures (Plate 2A and B). As with the Hebridean example however, by no means all the amygdales are visibly connected to microfractures.

Discussion

Physical Conditions of Amygdale Formation

In the himalayan Langtang and alpine Kofels landslides, frictionites with unequivocal vesicular texture are observed (Plate 3, Scott and Drever, 1953, Erismann et al., 1977) The vesicles are testament to the exsolution of a vapour phase from the melt under conditions of low lithostatic pressure, estimated at 200 bars by Masch et al (1985) for the Langtang slide Amygdaloidal pseudotachylytes have been described from at least four other localities in addition to the Ikertoq shear belt and the Outer Hebrides Thrust (Table 3).

Determination of the physical conditions of vesicle/amygdale formation is of importance in attempts to specify the palaeoseismic source parameters of the earthquakes during which pseudotachylyte generation zones were formed (cf. Sibson, 1975, Grocott, 1981, Grocott

In the Ikertoq shear belt the country rock temperature was below 250 C when most of the pseudotachylyte was generated (Grocott, 1977, Piper, 1981a), and there are no reasons to suppose that country rock compositions away from generation zones have changed since that time. Whole rock analyses of eight amphibolite facies tonalitic gneisses from the north part of the shear belt have an average H_2O content of 0.38 wt.% (standard deviation 0.07) (Grocott 1977, Table 2-2b, p.100). Unfortunately CO_2 has not been determined for the same rocks, but other tonalitic gneisses from the North Atlantic Shield yield consistent values in the range 0.1 - 0 2 wt.% CO_2 (Beach, 1976, p. ...).

The Greenland pseudotachylyte sample contains a volume fraction of amygdales of 3%, and we assume that H_2O and CO_2 are the only vesicle forming components of importance (cf. Macpherson, 1984, p.73). Carbon dioxide has a much lower solubility than H_2O in silicate melts, and a maximum liquid pressure, assuming that 0 2 wt.% CO_2 is the only vesicle forming gas component, is given by:

$$CO_2 \text{ (wt.\%)} = 0.0005 + 0\ 059\ P \text{ (kb)} \quad \text{(Harris, 1981)}$$

This equation gives a pressure of 3.38 kb which would have obtained at a depth of about 13 5 km, assuming $P_{liq} = P_{lith}$ when vesiculation occurred.

This estimate for the depth of formation of this sample is probably too deep since the rocks show no sign of subsequent greenschist facies metamorphism. It can be refined however by incorporating the H_2O content in the calculation, together with the observed volume fraction of amygdales. Using a graph of volume % vesicles against pressure for 0.2 wt.% CO_2 and 0.5 wt.% H_2O

(Macpherson, 1984, Fig. 2), a lithostatic pressure of 410 bars is obtained corresponding to a depth of 1.6 km.

These results of course are only as good as the solubility functions used to obtain them and depend on the validity of the assumptions made to justify their use. Given solubility data truly applicable to pseudotachylytes, together with appropriate analyses for volatiles, determination of formation depths of amygdaloidal pseudotachylyte should be possible.

Allen (1979) has suggested that vesicles and (feldspar) microlites are mutually exclusive in pseudotachylytes and that both are related to depth of generation This is demonstably not the case in the present Hebridean example and in Canadian pseudotachylytes described by Philpotts (1964) (see Table 3). The presence or absence of microlites should not therefore be used to infer the depth of pseudotachylyte generation, their occurrence is more likely a function of host-rock/pseudotachylyte melt composition, maximum melt temperature and crystal nucleation kinetics (Maddock, in prep.)

Significance of Amygdale Mineral Assemblages

Leaving aside the Hebridean amygdaloidal pseudotachylytes, a marked mineralogical uniformity exists between the vein material in microfractures, the replacement pseudomorphs, the Greenland pseudotachylyte amygdales and those described in the literature (Table 3) The widespread phase assemblage quartz + epidote + chlorite + carbonate indicates growth of these phases under conditions of low temperature and pressure - below those of greenschist facies metamorphism (Winkler, 1967). Notably, the common occurrence of carbonate suggests that cavity filling took place under conditions of

moderate partial pressure of CO_2 - favouring breakdown of Ca-silicates yielding calcite and an aluminous phase (especially chlorite). Microprobe analyses demonstrate chemical heterogeneity (i.e. disequilibrium) between, for example, chlorite in the replacement pseudomorph and the microfracture of Plate 2C and D). For this reason it is difficult to write precise reactions describing the alteration/replacement/cavity filling processes. However, for the replacement pseudomorph described above an appropriate end-member reaction involving the phases present is (Deer at al., 1966)

$$\text{Actinolite} + \text{Clinozoisite} + CO_2 + H_2O = \text{Chlorite} + \text{Calcite} + \text{Quartz}$$

with reaction tending to the r h.s. favoured by moderate to high P_{H2O} and P_{CO2}.

Summarizing, the mineralogy indicates that a low temperature (<200 C) assemblage was precipitated from a hydrous fluid, locally or temporally enriched in CO_2 and containing solutes Si, Al, Ca, K, Fe, Mg and S The timing of vesicle infilling and origin of the infilling fluids is difficult to ascertain. Philpotts (1964) suggested that pseudotachylyte amygdale minerals might be precipitated directly from vapour phases exsolved from the pseudotachylyte melt. This possibility seems unlikely in the present examples because of the mineralogy of the amygdales. Further, it is clear that in at least some cases vesicle infilling was related to healing of the microfractures (e.g. Plate 2A and B), and the sub-drusy habit is good evidence that the amygdales contain a primary assemblage precipitated in vesicle void space. In addition to the microfractures, the vesicles themselves may have locally provided a gross porosity allowing ingress of fluids.

In contrast to the mineralogy discussed above, the mineralogy of the Hebridean pseudotachylyte amygdales constitute a much higher temperature assemblage, similar to that found in greenschist facies metavolcanics (e.g. Morrison, 1979, Studemeister, 1983). The assemblage (albite+) actinolite + epidote + quartz + sphene is indicative of greenschist facies conditions with T > 350 C and P > 2 kb (Winkler, 1967). Further, the absence of carbonate suggests a low partial pressure of CO2. The chemistry and mineralogy of these amygdales suggests that the phases were precipitated from a hydrous fluid enriched in Si, K, Ca, Ti, Al and Fe, with lesser amounts of Mg, S, P, Na, Ce and La. The LREE content of the epidote confirms that short range LREE mobility at least is possible in a hydrous fluid at low metamorphic grade (cf Hellman et al , 1977, Nystrom, 1984), and that the LREE's are preferentially partitioned into epidote rather than sphene. The minimal compositional variation between analyses of the same phase suggests that a reasonable degree of equilibrium was obtained The extreme modal variation is perhaps due to different times of filling and kinetic nucleation effects

As with the amygdales and filled cavities described above, this mineral assemblage appears to be restricted to structures with suitable mechanical pathways allowing fluid ingress Thus the plagioclase microlites (An_{25}-An_{40}) and porphyroclasts (An_{25}) show no sign of albitization or adularization

A problem arises with the Hebridean pseudotachylytes as to how vesicles, shown above to be likely to have formed at depths <2 km, may contain a greenschist facies mineral assemblage implying T > 350 C. A palaeogeothermal gradient of 175 C km^{-1} is unlikely even in a potentially shear-heated thrust fault environment' An explanation for this may lie in the geological setting of these particular

pseudotachylytes.

It was noted earlier that the sub-vertical quasiconglomerate vein systems at Ruhba Ardvule, in which the amygdales occur, represent the earliest stages of pseudotachylyte generation, followed by E to W directed low angle thrusting. Sibson (1977b) has estimated a finite vertical component of thrust-sense movement across the main Outer Hebrides Thrust of 4.2 + 2.1 km. Ignoring the subaerial erosion that must accompany thrusting, it is possible that the early amygdaloidal pseudotachylytes were buried by a substantial thrust pile, with higher P-T conditions achieved through a combination of burial and shear-heating.

Conclusions

1) The occurence of amygdales in pseudotachylytes from various localities strengthens the case for an origin by melting for these faultrocks (*cf.* Wenk, 1978, Masch *et al.*, 1985).

2) Using reasonable values for the H_2O and CO_2 contents of pseudotachylyte melt assumed to approximate andesite in composition, a depth of 1.6 km is estimated for the Greenland pseudotachylyte described in this paper.

3) The carbonates and associated phases filling amygdales in Greenland pseudotachylytes and other examples described in the literature, are consistent with vesicle infilling at shallow depths.

4) Amygdales are reported from Outer Hebrides Thrust pseudotachylytes for the first time.

5) The greenschist facies mineral assemblage in Outer Hebrides Thrust pseudotachylyte amygdales strongly suggests that the pseudotachylytes were buried to greater depths subsequent to their formation. This is consistent with field evidence and Sibson's (1977b) model for the thrust-sense movement of the Outer Hebrides Thrust.

6) Structures superficially resembling amygdales in pseudotachylytes are recognized as porphyroclast replacement pseudomorphs

Acknowledgments

RHM acknowledges the support of a NERC research studentship. Work on fault-rocks in W. Greenland was supported by the Stichting Zuivereardwetenschappelyk Onderzoek (Z.W.O.) grant number 1811021 and the Stichting Dr. Schurmannfonds grant numbers 1983/01 and 1984/05. MVN also acknowledges receipt of a Z W O. research studentship. SEM and electron microprobe work was performed at Imperial College. Silicate mineral analyses were recalculated using program SUPREC written by J.C Rucklidge Adrian Jones guided us into the literature on solubility data.

References

Allen, A.R., 1979. Mechanism of frictional fusion in fault zones. J. Struct. Geol. 1: 231-243.

Bak, J., Sorensen, K., Grocott, J., Korstgard, J.A., Nash, D. and Watterson, J., 1975. Tectonic implications of Precambrian shear belts in western Greenland. Nature 254: 567-569.

Beach, A., 1976. The interrelations of fluid transport, deformation, geochemistry, and heat flow in early Proterozoic shear zones in the Lewisian complex. Phil Trans. R. Soc. A280: 569-604.

Beckholmen, M., 1982. Mylonites and pseudotachylytes associated with thrusting of the Koli Nappes, Tannforafaltet, central Swedish Caledonides Geol. Foren. Forh 104. 23-32.

Bischoff, A.A., 1962 The pseudotacgylyte of the Vredefort Dome Trans. Geol Soc. S Africa, 65. 207-225.

Buckley, H.A., Bevan, J.C , Brown, K M. and Johnson, L.R., 1978. Glauconite and celadonite two separate mineral species. Mineral. Mag 42: 373-382.

Clark, S.P , 1966. Handbook of physical constants. Geol Soc Amer Mem 97.

Deer, W.A., Howie, R A. and Zussman, J., 1966. An introduction to the rock-forming minerals Longman, London 528pp

Erismann, Th., Heuberger, H. and Preuss, E , 1977. Das bimsstein von Kofels (Tirol), ein bergsturtz-"friktionit". Tscher Min. Petr. Mitt. 24 67-119

Grocott, J , 1977 The northern boundary of the Ikertoq Shear Belt, West Greenland. Ph.D. thesis (unpubl.), Univ. Liverpool, 179pp.

Grocott, J., 1981. The fracture geometry of pseudotachylyte generation zones: a study of shear fractures formed during seismic events. J.

Harris, D.M., 1981 The concentration of CO_2 in submarine tholeiitic basalts. J. Geol. 89. 689-701

Hellman, P.L., Smith, R E. and Henderson, P., 1977. Rare earth element investigation of the Cliefdon Outcrop, N S W., Australia. Contrib. Mineral. Petrol. 37: 91-109

Larsen, L M., Rex, D.C. and Secher, K., 1983. The age of carbonatites, kimberlites and lamprophyres from southern West Greenland: recurrent alkaline magmatism during 2500 million years Lithos 16 215-221.

Macpherson, G.J., 1984 A model for predicting the volumes of vesicles in submarine basalts. J. Geol. 92 73-82

Maddock, R.H., 1983. Melt origin of pseudotachylytes demonstrated by textures. Geology 11: 105-108

Masch, L , Wenk, H.R and Preuss, E., 1985. Electron microscopy study of hyalomylonites - evidence for frictional melting in landslides. Tectonophys. 115 131-160.

Moore, J.G , 1965 Petrology of deep-sea basalt near Hawaii. Amer. J. Sci 263. 40-52

Moore, J G., 1979 Vesicularity and CO_2 in mid-ocean ridge basalt. Nature 282 250-253.

Morrison, M.A , 1979 Igneous and metamorphic geochemistry of Mull lavas. Ph D. thesis (unpubl.), Univ London , xxxpp.

Nockolds, S R., 1940 Petrology of rocks from Queen Mary Land Australasian Antarctic Exped., 1911 - 1914 Sci Rept a Ser. A, 4: 15-86

Nyatrom, J.O., 1984. Rare earth element mobility in vesicular lava during low grade metamorphism Contrib Mineral. Petrol. 88: 328-331

Papike, J.L., Cameron, K.L. and Baldwin, K., 1974. Amphiboles and pyroxenes characterization of other than quadrilateral components and estimates of ferric iron from microprobe data. Geol Soc. Amer. Abstr.

Struct. Geol. 3 169-178.

Hall, M.G. and Lloyd, G E., 1981. The SEM examination of geological samples with a semiconductor backscattered electron detector. Amer. Mineral. 66: 362-368.

Hamilton, D.L., Burnham, C.W. and Osborn, E.F., 1964. The solubility of water and effects of oxygen fugacity and water content on crystallization in mafic magmas. J. Petrol. 5. 21-39.

with Progs. 6: 1053-1054.

Passchier, C.W., 1982. Pseudotachylyte and the development of ultramylonite bands in the Saint-Barthelmy massif, French Pyrenees. J. Struct. Geol. 4· 69-79.

Philpotts, A.R., 1964. Origin of pseudotachylytes. Amer. J. Sci 262· 1008-1035.

Piper, J.A., 1981a. Palaeomagnetism of pseudotachylytes from the Ikertoq Shear Belt, and their relationship to the kimberlite-lamprophyre province, central-west Greenland. Bull. Geol. Soc. Den. 30. 51-61.

Piper, J.A., 1981b. Palaeomagnetic study of the (late Precambrian) West Greenland kimberlite-lamprophyre suite defnition of the Hadrynian Track. Phys. Earth Plan. Int. 27. 164-186.

Roedder, E., 1979. Silicate liquid immiscibility in magmas. In, Yoder, H. S. (ed.), The evolution of the igneous rocks. Princeton, 588pp.

Sakuyama, M. and Kushiro, I., 1979. Vesiculation of hydrous andesitic melt and transport of alkalies by separated vapour phase. Contrib. Mineral. Petrol. 71: 61-66.

Scott, B.H., 1981. Kimberlite and lamproite dykes from Holsteinborg, West Greenland. Medd. Gronland Geosci. 4 24pp

Scott, J.S. and Drever, H.I., 1953. Frictional fusion along a Himalayan thrust. Proc. Roy. Soc. Edin. B65 121-140.

Sibson, R.H., 1975. Generation of pseudotachylyte by ancient seismic faulting. Geophys. J. R. Astron. Soc. 43: 775-794.

Sibson, R.H., 1977a. Fault rocks and fault mechanisms. J Geol. Soc. 133: 191-213.

Sibson, R H., 1977b. The Outer Hebrides Thrust its structure, mechanism and deformation environment. Ph.D thesis, (unpubl.), Univ London, 254pp.

Sibson, R H., 1980. Transient discontinuities in ductile shear zones. J. Struct. Geol. 2· 165-171.

Smith, R.E , 1967. Segregation vesicles in basaltic lava. Amer J. Sci. 265 696-713.

Smith, C.B., 1979. Rb-Sr mica ages of various kimberlites. - Chairman's summaries and poster session abstracts, Kimberlite

Symposium II, Cambridge, 61-66.

Smythe, D.K., Dobinson, A., McQuillin, R., Brewer, J.A., Matthews, D.H., Blundell, D.J. and Kelk, B , 1982. Deep structure of the Scottish Caledonides revealed by the MOIST reflection profile. Nature 299 338-340.

Spera, F.J. and Bergman, S.C., 1980. Carbon dioxide in igneous petrogenesis I. Aspects of the dissolution of CO_2 in silicate liquids. Contrib. Mineral. Petrol. 74 55-66

Studemeister, P.A., 1983. The greenschist facies of an Archaen assemblage near Wawa, Ontario Can J Earth Sci. 20 1409-1420.

Watterson, J., 1975. Mechanism for persistence of tectonic lineaments Nature 253 520-522.

Winkler, H.G.F , 1967. Petrogenesis of metamorphic rocks Springer Verlag, New York, 237pp.

Wenk, H.R., 1978. Are pseudotachylytes products of fracture or fusion? Geology 6 507-511.

Figure Captions

Figure 1. Diagrams showing the compositions of selected phases in amygdales in Outer Hebrides Thrust pseudotachylytes (a) Plot of Si vs. $Mg/(Mg + Fe^{2+})$ formula units based on 23 (O) showing composition of acicular amphiboles (Fe^{2+} estimated by method of Papike et al (1974)). (b) An-Ab-Or diagram, . = K-spar in amygdales, . = (?)relict feldspar porphyroclast in amygdale, . = feldspars in microfractures (c) Peak intensity (I) vs. energy (KeV) plot showing qualitatively the presence of La and Ce in epidote 2 (lowest energy peaks only are annotated). Corresponds to Fig 5.19 of thesis

Figure 2 (a) Mohr diagram with a stress circle representing the state of stress in a pseudotachylyte generation zone at the stage of melt generation . The differential stress is low (a large fraction of the stress drop preceeds melt generation (Grocott, 1981)), and a state of plane stress is assumed with lithostatic pressure equal to the mean stress.

(b) Due to volume change on melting, pseudotachylyte is generated with a high fluid pressure. Pressure in the liquid will act against the lithostatic pressure On the Mohr diagram this can be represented as a shift of the stress circle towards the origin Extension failure occurs when the stress circle becomes tangent to the failure envelope In the limit represented by a vanishingly small stress circle, the difference between the lithostatic pressure, P_{lith}, and the effective lithostatic pressure, P_{le}, approaches a value of $-P_{lith} + t$, where t is the tensile strength This is the maximum possible value of the liquid pressure. When fracturing occurs, liquid pressure is assumed to revert to lithostatic pressure, and under this condition the melt

vesiculates.

Plate 1. Backscattered electron (BSE) micrographs and line drawings of amygdales in plagioclase microlitic pseudotachylyte from the OHT. a = actinolite, b = biotite, e = epidote, f = Fe-hydroxide, k = K-spar, p = pyrite (diagonal hachuring in F), pl = plagioclase, q = quartz, s = sphene. Scale in microns. Corresponds to Plate 5.24 of thesis

Plate 2. BSE micrographs of amygdale (Greenland) and porphyroclast replacement pseudomorph (OHT). Scale bar = 100 um. (A) A flattened vesicle with intersecting microfracture are infilled by large grains of carbonate with barite, celadonite and magnetite along grain boundaries. (B) Detail of A showing irregularly zoned plates of ferroan dolomite (d) and grain boundary location of barite (b), celadonite (c) and magnetite (m). Note increase in grain size away from margin and continuity of microfracture and amygdale infilling. (C) Porphyroclast replacement structure in chlorite-rich pseudotachylyte.; note proximity of chlorite healed microfracture (m). (D) Detail of C showing zoned arrangement with rim of chlorite (c) enclosing calcite (d) with small grains of quartz. Corresponds to Plate 5.25 of thesis

Plate 3. BSE micrograph of highly vesicular landslide frictionite from Langtang, Himalayas. Corresponds to Plate 5.26 of thesis

MAP 1 : GEOLOGICAL MAP OF THE OUTER HEBRIDES

58°30'N

N

0 km 25

58°00'N

57°30'N

57°00'N

7°30'W

7°00'W

6°30'W

Butt of Lewis

Tolsta Head

LEWIS

Gallan Head

Stornoway

Eye Peninsula

Seaforth Line

Seaforth Head

SCARP

NORTH HARRIS

TARANSAY

Tarbert

SCALPAY

SOUTH HARRIS

Toe Head

FAULT

MINCH

Renish Point

BERNERAY

NORTH UIST

Lochmaddy

MONACH ISLANDS

RONAY

GRIMSAY

BENBECULA

WIAY

Usinish

SOUTH UIST

Rubha Ardvule

Stuley Is.

Lochboisdale

ERISKAY

Greian Head

BARRA

Tangaval

Castlebay

VATERSAY

SANDRAY

PABBAY

MINGULAY

BERNERAY

Barra Head

KEY

PERMO-TRIASSIC

STORNOWAY BEDS;

OUTER HEBRIDES THRUST

THRUST

MAJOR CRUSH ZONE; pseudotachylyte-ultracataclasite

PHYLLONITE BELT

CRUSH MELANGE; cataclased, sheared and mylonitized gneisses with some pseudotachylyte; much low-grade alteration

p PSEUDOTACHYLYTE; W of main thrust base

LINEAMENT; post-dating main thrust movements

LEWISIAN GNEISS COMPLEX

GREY GNEISS; biotite and/or hornblende quarto-feldspathic gneiss; strongly reworked during Laxfordian; includes some metabasites

LAXFORDIAN GRANITE-MIGMATITES

gneiss veined by granite

dominantly granite

l area of weak Laxfordian reworking

LATER SCOURIAN ROCKS

acid

intermediate

pyroxene-granulite metabasite

anorthosite

intrusive originally

metasediment-metabasite assemblage

dip and trend of Laxfordian F_3 structures

I 0 – 30°

II 30 – 60°

III 60 – 90°

Map compiled from: Sibson (1977a)
Coward et al (1970)
IGS 1:100 000 Outer Hebrides Geological Map
personal observation

R H Maddock Ph.D 1986

MAP 2 : GEOLOGICAL MAP OF GREIAN HEAD, BARRA , (NF6504)

N

0 m 250

KEY

acid ('grey') gneiss showing trend of foliation and extent of exposure

dip of foliation
0 - 30°
30 - 60°
60 - 90°

basic gneiss (amphibolite) bodies

zones of abundant pseudotachylyte veining, quasi-conglomerate or net-veining

basalt dyke (presumed Tertiary)

A — A' line of section (see map 2a)

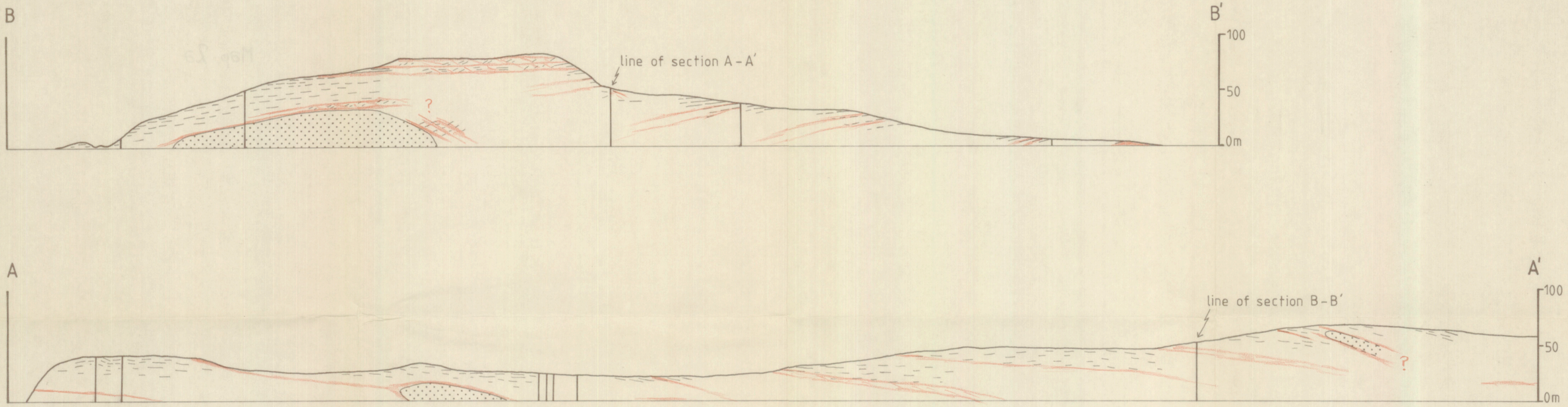
4.3 location and number of text-Plate and map 2b

For location see map 1



733 poles to foliation, contoured at 12, 9, 6, 3, 1 and 0·15 % per 1% area

R H Maddock PhD 1986



KEY

- trace of foliation in grey gneiss
- basic gneiss (amphibolite) bodies
- pseudotachylyte fault zone
- basalt dyke (presumed Tertiary)

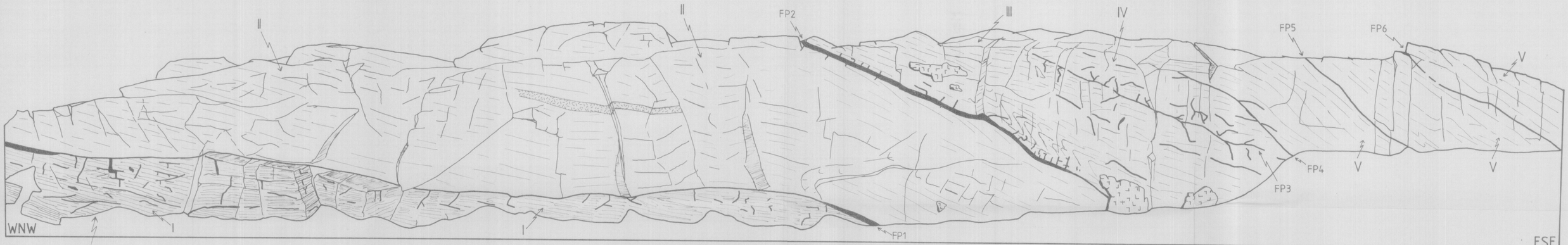
0 m 250

HS=VS

MAP 2a : SCHEMATIC GEOLOGICAL CROSS-SECTIONS OF GREIAN HEAD

R H Maddock Ph.D 1986

MAP 2b: SKETCH SECTION, GREIAN HEAD, BARRA (NF653046)



detail shown in Plate 4.3

KEY

- basic gneiss (platey foliation)
- acid gneiss (coarse foliation)
- pegmatite
- basalt
- pseudotachylyte

0 m 5

LITHOLOGIC UNITS

I Well-foliated platey gneiss; high colour index; dip 15–25°ENE; weak joint set trends 100°, 165°; intense pst. faulting

II Massive/blocky pink granitic-gneiss; strong joint set trends 100°, 165°; pst. absent

III Well-foliated/banded gneiss; moderate colour index; ENE dip, minor NW-plunging folds; intense pst. faulting especially close to TP3 and parallel to foliation

IV Well-foliated/banded granitic gneiss; much pst. veining; wedge-shape outcrop between TP3 and TP4

V Well-banded granitic gneiss/pegmatite/amphibolite; regular 30–40° dip to ENE; foliation parallel pst. faulting

FAULT-ZONES

FP1 Fault-zone includes most of lithology dip 15–25° ENE, locally discordant w.r.t. foliation; pst. to 5 cm thick, local quasi-conglomerate, pst. injection into lithology I only

FP2 Fault-zone 10–50 cm of quasi-conglomerate; ?ENE dip

FP3 Fault-zone to 5 cm thick, pst. injection above and below; pitches 30° to E

FP4 Fault-zone sub-barren to 5 cm thick; pitches 40° to E, locally discordant w.r.t. foliation

FP5,TP6 2 Foliation-parallel FVs to 3 cm thick; dip 30–40° to ENE

R H Maddock PhD 1986

MAP 3 : GEOLOGICAL MAP OF RUBHA ARDVULE, S UIST (NF7130)

KEY

acid ('grey') gneiss

basic gneiss (amphibolite) bodies

zones of extensive sub-horizontal or gently-dipping foliation-parallel pseudotachylyte veining and quasi-conglomerate

sub-vertical pseudotachylyte fault-vein, injection-vein and quasiconglomerate zones

b basalt dyke (presumed Tertiary)

4.7 location and number of text plate and map 4

For location see map 1

dip of foliation

- 0-30°
- 30-60°
- 60-90°
- horizontal

N

0 m 250

Geodha Mór

Geodha Garbh

Geodha an t-Sruthain

Loch Ardvule

Pond

map4 4.9 4.10

4.8

4.7

SAND

mean high water spring

mean low water spring

Cròic a Deas

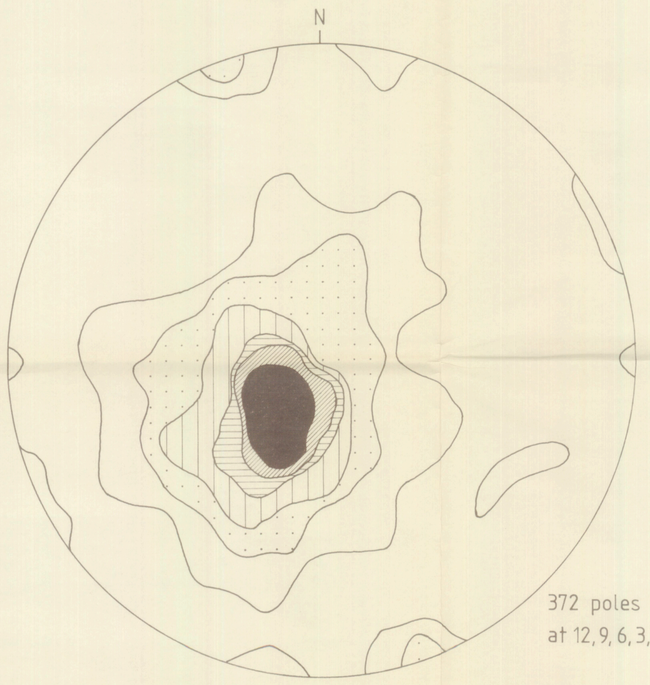
300

295

710

715

720



372 poles to foliation, contoured at 12, 9, 6, 3, 1 and 0·33 % per 1% area

R H Maddock Ph.D 1986

MAP 4 : QUASI-CONGLOMERATE ZONE , RUBHA ARDVULE , S UIST (NF70982983)

KEY

- well-foliated, acid ('grey') gneiss, locally with feldspar augen
- basic gneiss (amphibolite)
- quartzo-feldspathic pegmatite
- pseudotachylyte and quasi-conglomerate
- 123/15 orientation of foliation
- joint

max. relief of outcrop = 1m

Map compiled from scale drawings and photographs

see Plates 4.9 & 4.10 for detail



R H Maddock Ph.D 1986